# The geological and geodynamic evolution of the Northumberland Trough Region: insights from numerical modelling

Linda Austin

Submitted for the degree of Doctor of Philosophy

Keele University

2014

The world is the geologist's great puzzle-box; he stands before it like the child to whom the separate pieces of his puzzle remain a mystery till he detects their relation and sees where they fit, and then his fragments grow at once into a connected picture beneath his hand.

Louis Agassis
Geological Sketches (1866)

# Acknowledgements

There are many people without whom this research would not be possible. I would like to thank my principal supervisor Dr Stuart Egan for his time and support during this project, his advice on the geodynamic modelling aspect of the research was invaluable. I would also like to thank Dr Stuart Clarke, for passing on his extensive knowledge about the geology of northern England and his help with the GoCAD 3D modelling. In addition Dr Gary Kirby and Dr Dave Milward have contributed their assistance particularly with regards to their comments upon my thesis, which were gratefully received. I would also like to thank the British Geological Survey and Keele University for providing funding for this research.

Anyone who has done this type of research will understand how important the support of their colleagues is during this time and I have been lucky to be surrounded by a wonderful group of staff and research students whilst completing this work. Friday afternoon cake time in particular provided a great environment for exchanging ideas.

Lastly I need to thank my family for the enduring support and encouragement. I owe them everything. I would like to dedicate this thesis to the memory of my father Brian Albert Austin without whom it may never have been completed.

# Abstract

The geological and geodynamic processes that have controlled the evolution of the Northumberland Trough Region in Northern England have been investigated to expand understanding of the evolution of continental extensional basins. The region has experienced a number of extensional, compressional and wrench tectonic events throughout Late Palaeozoic, Mesozoic and Cenozoic times. These events have led to a complex subsidence and uplift history.

A kinematic model has been developed in two-dimensions to simulate the structural deformation caused by extension by faulting and pure shear, thermal processes and the flexural isostatic due to tectonic loading. The stratigraphy varies across the region between the block and basins, which has been addressed within the modelling by the development of algorithms to simulate palaeobathymetry, compaction and erosion.

Extension within the crust was taken up on multiple faults generating an average total heave of approximately 10-15km. Model results indicate there was non-uniform extension of the lithosphere with greater extension below the fault detachment depth where ductile deformation is the principal deformation mechanism. Results generated using a modelling approach that utilises multiple tectonic events generate stratigraphic patterns of syn-rift and post-rift deposition that support extension at multiple time stages within the Northumberland Trough Region during the early-Carboniferous period.

Models that reconcile the observed amount of fault-controlled deformation with the magnitude of overall thinning of the crust generate comparable amounts of subsidence to that observed in the basin structures. In contrast, these models over-estimated the amount of subsidence on the block structures. It has been hypothesised that this mismatch was due to the North Pennines Batholith, which acts as a negative load upon the lithosphere.

Development of an algorithm to model the isostatic response of the lithosphere to the North Pennines Batholith has provided insights into the influence of igneous intrusions on the post-emplacement structural development of the area. Model results incorporating the batholith indicate the generation of a significant amount of uplift coincident with the presence of the batholith, and show a realistic geometry and uplift-subsidence pattern across the Alston Block and adjacent basins.

# Contents

# Figure List

## Chapter 1: Introduction



## Chapter 2: Geology of the Northumberland Trough Region



## Chapter 3: Data analysis; Regional cross-sections, seismic analysis and borehole data

**Chapter 4: Two-dimensional modelling of the deformation resulting from extension**

**Chapter 5: Integrated lithosphere-scale modelling of basin development in two-dimensions**

## Chapter 6: Two-dimensional modelling of the Northumberland Trough Region

## Chapter 7: Three-dimensional modelling of the Northumberland Trough Region

# 1 Introduction

## 1.1 Background

The Northumberland Trough Region is a late Devonian – early Carboniferous extensional system with a basin and block architecture. It includes the Northumberland Trough, its westerly continuation, the Solway Basin, the Alston Block, a geomorphological high situated to the south of the Northumberland Trough, the Vale of Eden Basin to the west of the Alston Block and the Stainmore Trough to the south of the Alston block (Figure 1.1). The Alston Block is underlain by the North Pennines Batholith, a per-aluminous granite that was emplaced 398.3±1.6Ma (Selby *et al.*, 2008).

The region has experienced a number of extensional, compressional and wrench tectonic events throughout Late Palaeozoic, Mesozoic and Cenozoic times. These events have led to a complex subsidence-uplift history that cannot be adequately explained by basin formation due to uniform lithosphere extension.

Extensional basin formation occurs in a tectonic regime where the tensile normal stresses cause strain in the lithosphere as a result of pulling on the vertical plane. In response to these tensile stresses there are two opposing processes that are involved in lithospheric extension; crustal thinning and thinning of the mantle lithosphere. Crustal thinning is the structural response to lithosphere extension and may occur as a result of pure shear (stretching) or simple shear (faulting). This deformation is

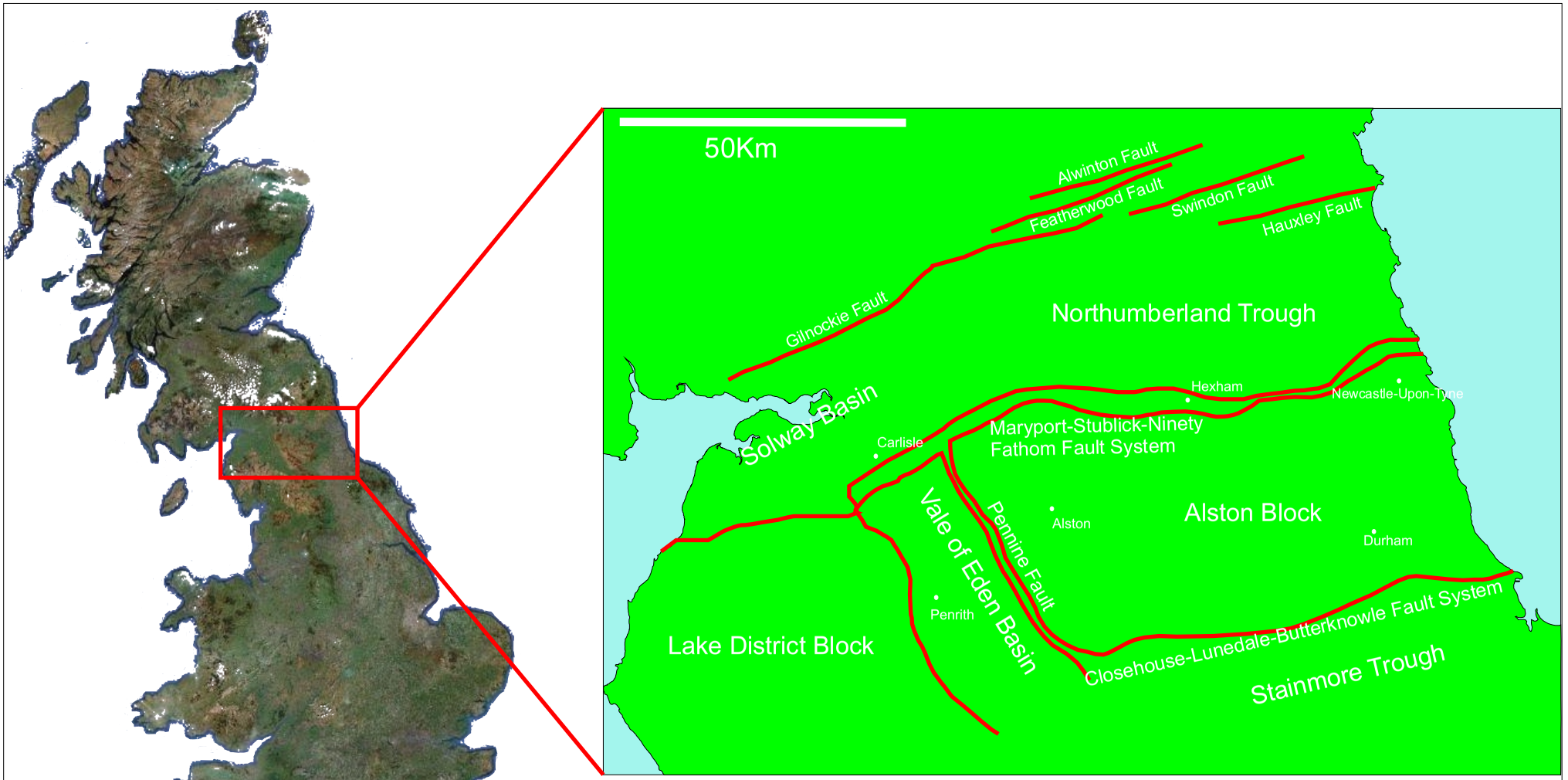


Figure 1.1. Location of study area. The Northumberland Trough Region comprises a major east-west orientated asymmetrical half-graben system that extends across Northern England into the Northern Irish Sea.
Map © 2009 Google - Imagery © 2009 TerraMetrics

permanent; the brittle crust cannot regain its original thickness, unless it is thickened by a later compressional event (Allen and Allen, 1990). Thinning of the lithosphere and uplift generated by thermal perturbations are transient. Thermally-induced uplift is generated as the crust and mantle lithosphere are thinned raising hotter material, i.e. the basal lithosphere boundary, closer to the surface, resulting in uplift. Subsequently the geotherm re-equilibrates, as heat is lost from the surface via convection, and subsidence occurs (Turcotte and Emerman, 1983).

## 1.2 Aims and objectives

The main emphasis of this project is to investigate the geological and geodynamic processes that have controlled the evolution of the Northumberland Trough Region in Northern England. This is achieved by:

- Analysis of surface and sub-surface data to provide input parameters for the modelling approach developed in addition to providing a basis for comparison.
- Further development and application of two-dimensional and three-dimensional lithosphere-scale tectonic modelling techniques to produce an integrated model.
- Utilise computer modelling to determine the interplay of geological and geodynamic processes that have controlled the region.
- Including examining the role of subsidence and uplift mechanisms responsible for basin formation as well as their influence on depocentre-migration and stratigraphy.

- Model results are used to provide insights into the importance of deep-processes such as depth dependent extension and how they interact with basin-controlling processes such as infill.
- Insights gained from the Northumberland Trough Region will have implications for understanding the evolution of similar Carboniferous intra-continental basin settings.
- When initial results could not explain the subsidence and uplift history of the Alston Block within the region the project aimed to develop a modelling technique to explain the geodynamic influence of the batholith on the region post-emplacement. This has implications for other settings where an igneous intrusion may have affected subsidence.

## 1.3 Methodology

Regional scale cross-sections, constructed from subsurface data, provide input parameters for numerical modelling. In addition, burial history modelling, constrained by well and subsurface data, determines trends in subsidence and uplift within the study area

The computer modelling of the interaction of geological and geodynamic processes is a valuable tool for explaining the causes and magnitude of regional subsidence and uplift in response to continental tectonics. Geodynamic modelling is an important technique as it can be used to investigate the effects of deep processes that are poorly constrained by geophysical subsurface data and surface field data.

The modelling approach that has been used is mature (Egan, 1992; Kusznir and Egan, 1989; Hodgetts *et al.*, 1998; Meredith and Egan, 2002) and enables forward modelling of extensional basin evolution in two and three dimensions. The modelling integrates a variety of geological and geodynamic processes, including structural deformation of the crust and mantle lithosphere, perturbation and subsequent re-equilibration of the lithosphere temperature field, flexural isostatic adjustments and surface processes. Using Java, an object oriented programming language, further development of existing and new modelling algorithms that integrate a variety of geological and geodynamic processes at both lithosphere and basin scale provide insights into lithosphere deformation and basin evolution.

### *1.3.1 Introduction to structural and geodynamic modelling of lithosphere extension*

A kinematic modelling approach that defines the dimensions of a system and the relationships that characterise interactions within that system has been adopted to enable forward modelling of extensional basin evolution. This modelling approach integrates information on the geometry, displacement and types of strain involved in crustal deformation as well as thermal, isostatic and surface processes. The geodynamic influence of these processes on basin development can be predicted (Kearey and Vine, 1990).

This modelling approach quantifies mechanical thinning of the lithosphere by pure and/or simple shear according to the amount of crustal thinning that can be observed. This exerts a strong control on the initial basin geometry and depth (Meredith and Egan, 2002). It is possible to simulate the effects of thermal perturbations of the lithosphere temperature field on basin formation as it influences the rate and magnitude of uplift and subsidence. In adition, the isostatic response of the lithosphere to loading exerts a strong control on basin geometry and can be calculated based on the elastic strength of the lithosphere. Surface processes such as sediment infill and erosion can further influence basin geometry by affecting the magnitude of subsidence and in the case of sediment infill, the physical dimensions of the basin (Meredith, 2003).

Early models of basin formation introduced fundamental concepts such as crustal extension modelled by pure shear (McKenzie, 1978; Royden and Keen, 1980) or by simple shear (Wernicke, 1985), and isostasy modelled using Airy Isostasy (Airy, 1855).

The lithosphere is the outermost layer of the earth and consists of the crust and part of the upper mantle, usually referred to as the mantle lithosphere. The lithosphere is 125 km thick on average however the thickness is variable and decreases strongly under young orogenic regions (Artyushkov, 1980). It overlies the asthenosphere, which is part of the upper mantle.

The crust is the outermost shell of the earth, and can be separated into oceanic and continental crust, which differ in thickness, density and

composition. The continental crust varies in thickness from less than 20km in shelf areas to greater than 70km within collisional regimes. The granitic crystalline basement of the continental crust is more inhomogeneous than the basaltic oceanic crust including a gradation in properties, such as increasing seismic velocity and density, from top to bottom and more regional variations in thickness and composition (Garland, 1971; Meissner, 1986). The base of the crust is defined by the Mohorovičić discontinuity or Moho. This marks an increase in seismic velocity resulting from the variation in composition and other physical parameters between the crust and mantle.

The mantle lithosphere is comprised of olivine rich peridotites and pyroxinites (Menzies, 1990) with an average density of ~ 3300 $kgm^{-3}$. It demonstrates lateral variations associated with the relationship between active tectonic regions and more stable regions (Anderson, 1990).

The base of the lithosphere is usually represented by the isotherm at which mantle rocks approach their solidus (1100$^{o}$C -1330$^{o}$C) (Pollack and Chapman, 1977). The boundary between the lithosphere and underlying asthenosphere is therefore a gradual transition zone where the approach of the solidus temperature results in a weakening and partial melting of the material. The asthenosphere corresponds with the lower part of the upper mantle which is the portion of the mantle where material is considerably more ductile (Meissner, 1986).

### *1.3.2 Structural, thermal and Isostatic processes due to lithosphere extension*

Basin formation consists of three related components arising as a consequence of lithosphere extension; structural deformation resulting in crustal thinning, perturbation of the geotherm giving rise to uplift followed by subsidence as it re-equilibrates and the isostatic response of the lithosphere responding to varying loads upon the lithosphere.

Structural deformation of the lithosphere in response to an extensional force can be modelled by simple shear (i.e. faulting) or pure shear (i.e. stretching). In reality these mechanisms represent end-members in lithosphere deformation and a combination of the two processes are responsible for extensional basin formation (Coward, 1986). Simple shear is a three-dimensional constant volume rotational strain in which the maximum and minimum strain axes are re-orientated in relation to their original positions (Twiss and Moores, 1992; Davis and Reynolds, 1996). In the case of lithosphere extension this occurs as faulting where the rock on one side of a fracture moves with respect to the rock on the other side. Sedimentary basins form within the hanging wall of major basement faults. These faults present a key control on the geometry of the resultant basin (Gibbs, 1984).

These major faults appear to be restricted to the cool, brittle, top 10-20km of the upper lithosphere (Kusznir and Egan, 1989) at which point they must detach horizontally within the continental crust (Kusznir *et al.*, 1987; Kusznir and Park, 1987; Kusznir and Matthews, 1988). Beneath the

region of faulting the lithosphere deforms by a plastic mechanism, which can be approximated to pure shear (Jackson and McKenzie, 1983; Kusznir and Park, 1987). Pure shear is a three-dimensional coaxial flattening strain in which principle strain axes remain parallel to their respective principle stress axes during deformation (Park, 1989). Large scale normal faulting and pure shear results in thinning of the lithosphere that can be simulated geometrically.

Thinning of the lithosphere raises the lithosphere/asthenosphere boundary, which increases the geothermal gradient (Kusznir and Egan, 1989). This disturbance of the temperature field produces thermal expansion determined by the volumetric coefficient of thermal expansion, and results in uplift. Following rifting the temperature field re-equilibrates and subsidence occurs as a result of thermal contraction. These perturbations of the geotherm can be calculated assuming that the lithosphere cools by gradual heat loss due to conduction (McKenzie, 1978).

Isostasy is the response of the lithosphere to the imposition or removal of large loads. Airy isostasy assumes that the Earth's crust is of a relatively constant density ($\rho_c$) and the mantle has a higher density ($\rho_m$). With this theory, isostatic equilibrium is achieved and maintained by varying the thickness of the two layers (Airy, 1855). Airy isostasy assumes the lithosphere to have no lateral strength. This is a major simplification; the lithosphere is relatively rigid and behaves like an elastic plate in response to loading, such that any load added to or removed from the lithosphere will generate regional uplift or subsidence, rather than local uplift or

subsidence as a result of the load only. These observations lead to the development of a new theory to explain isostasy; flexural Isostasy (Walcott, 1970; Watts *et al.*, 1982). The lithosphere is assumed to behave as an elastic sheet overlying a fluid substratum on which loads are compensated regionally. The flexural isostatic response of the lithosphere to negative loading caused by crustal thinning generates regional uplift as the underlying lithosphere compensates for the loss of crust at the surface. The resultant isostatically compensated lithosphere shows not only uplift within the basin but also uplift of the basin flanks, particularly uplift of the footwalls of the basin controlling faults.

### *1.3.3 Uniform lithosphere extension*

The processes described in section 1.3.2 were used as a foundation for the development of early models of extensional basin formation. The McKenzie model, or uniform lithosphere extension model (McKenzie, 1978) was one of the first quantitative kinematic models to study lithospheric extension and sedimentary basin formation. Figure 1.2 demonstrates the main features of the McKenzie model, where at time t = 0 a unit length of continental lithosphere is extended by a factor ß (equivalent to 1 + strain), causing the lithosphere including the crust to thin and the asthenosphere to rise as a result of isostatic compensation. The amount of isostatic compensation determines the final resting place of the surface, the Moho and the base of the lithosphere. As a result of thinning of the lithosphere, perturbation of the geotherm results in

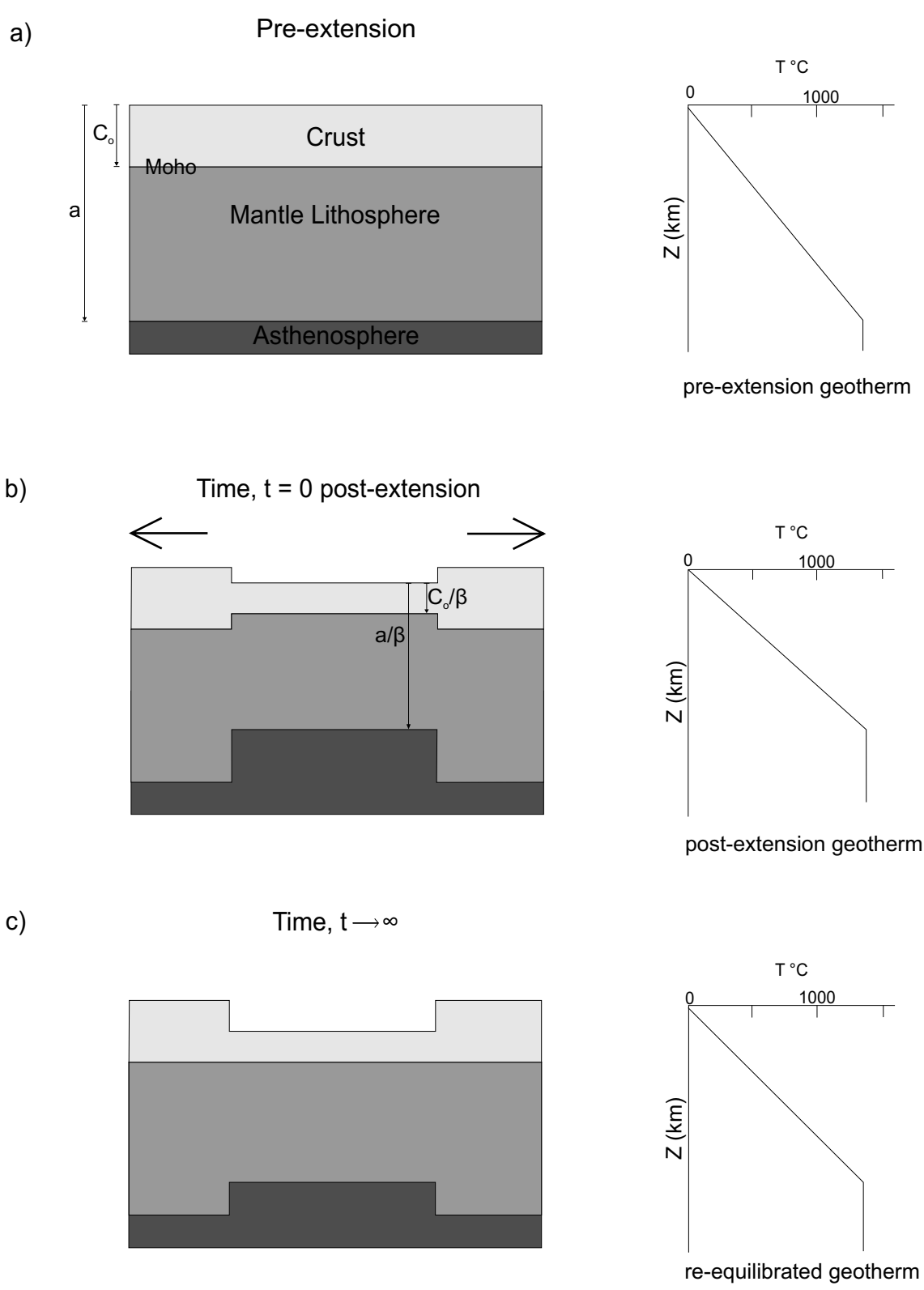


Figure 1.2. The McKenzie Model of uniform lithosphere extension. a) Extension has not yet occurred, the original crustal thickness, $C_o$, and original lithosphere thickness, a are observed. The geotherm is in equilibrium. b) At time, t = 0; the crust and mantle lithosphere has been thinned by the extension factor β. The asthenosphere has risen, resulting in heating of the temperature field as hotter material is moved closer to the surface. c) Over geological time the geotherm has returned to an eqilibrated state, resulting in subsidence (After McKenzie, 1978).

thermal expansion and uplift. Over time the thermal disturbance re-equilibrates causing subsidence as the temperature field cools.

The McKenzie model assumes that extension is instantaneous and uniform throughout the lithosphere, and that deformation is a result of pure shear (i.e. stretching). There are several weaknesses with the McKenzie model, most of which are related to the assumptions about the rifting process. The model assumes that extension occurs as a singular instantaneous event, whereas in reality extension occurs over a millions of years and possibly as several discreet episodes. The model also assumes the mechanism of extension is by pure shear which does not simulate the effects of faulting accurately; this is an important limitation because faulting has significant control on basin formation. In addition, the model calculations presuppose that any accommodation space created by subsidence is infilled to sea level with water. It would be more realistic to include sediment loading or partial infilling of the basin.

The other major restriction of the model as proposed by McKenzie is that it is one-dimensional. In its published form, the model represents the subsidence of a single vertical section of lithosphere. It is possible to generate a pseudo two-dimensional basin model by defining the ß factor at a series of positions laterally across the basin. Inputting the ß value for each position into the model produces a sequence of basement elevation values which when plotted against their lateral position produces a two-dimensional basin shape.

### *1.3.4 Simple shear models of lithosphere extension*

Wernicke (1985) created a qualitative model, based on the Basin and Range Province in the western USA, to highlight the role of faulting in extensional tectonics (Figure 1.3). The model features a fault dipping from the surface and detaching at the base of the lithosphere. At the surface this creates a half-graben. In the lower lithosphere, movement along the fault raises hotter asthenospheric material nearer to the surface resulting in thermal expansion and uplift. The Wernicke model is the opposite of the McKenzie model such that it assumes deformation is entirely by the process of simple shear.

### *1.3.5 Non-uniform lithosphere extension*

The McKenzie model assumes that extension is uniform through the depth of the lithosphere but as its rheological properties vary with composition, temperature and pressure, i.e. with depth, the lithosphere can not be expected to deform in a homogeneous manner (Kusznir and Park, 1987). Royden and Keen (1980) suggested an adaptation of the McKenzie model to account for this behaviour of the lithosphere (Figure 1.4). Their model, the non-uniform lithosphere extension model, assumes that the lithosphere can be decoupled at depth and deformed as two more-or-less separate sections. The division between the two sections is often located at the Moho, as it represents a compositional change, or at the depth of the fault detachment. Above the decoupling depth, the upper lithosphere extends by a factor $\beta_C$, below the decoupling depth the lower lithosphere

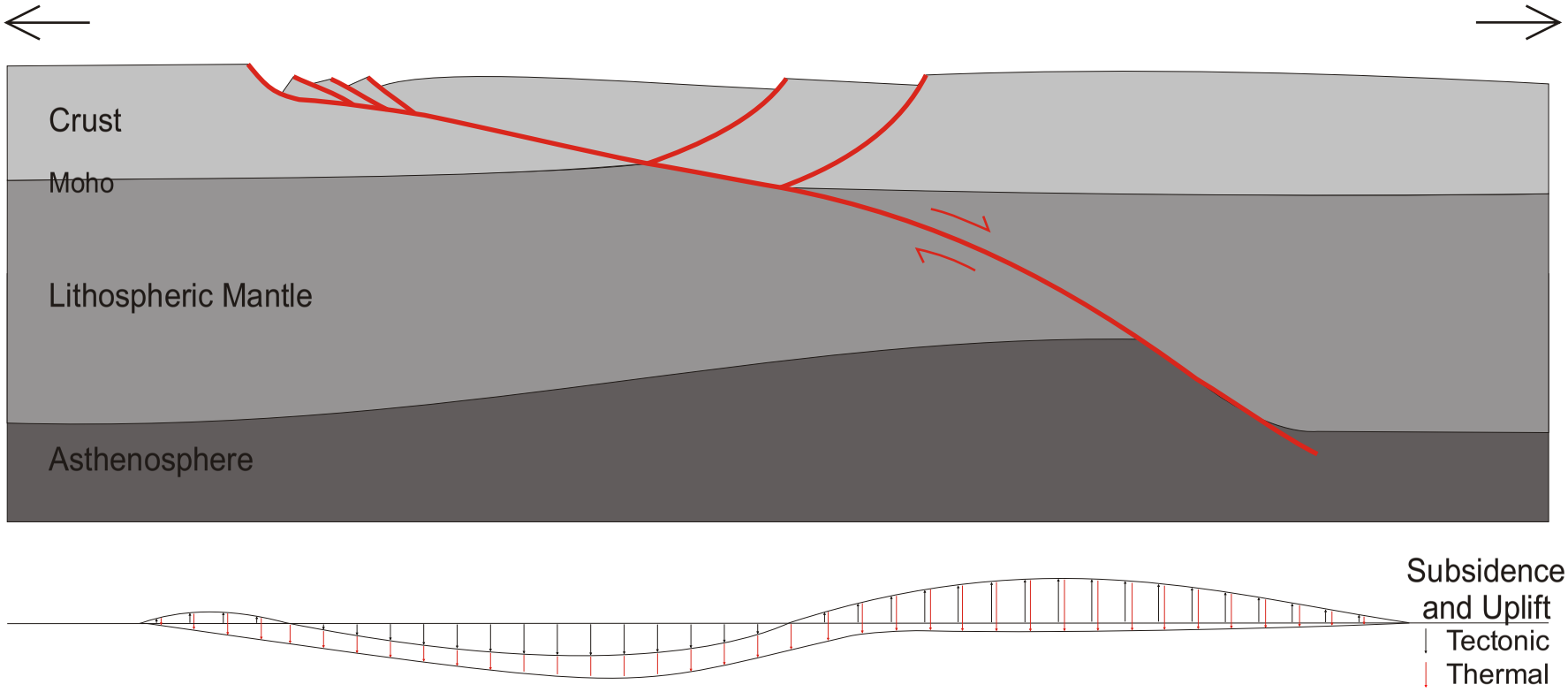


Figure 1.3. The Wernicke Model, a qualitative model based on observations from the Basin and Range province, USA. The model features a fault dipping from the surface and detaching at the base of the lithosphere. The model generates a series of grabens at the surface as a result of normal movement along the fault. Movement along the fault in the lower lithosphere raises hotter material nearer the surface causing uplift. (After Wernicke, 1985)

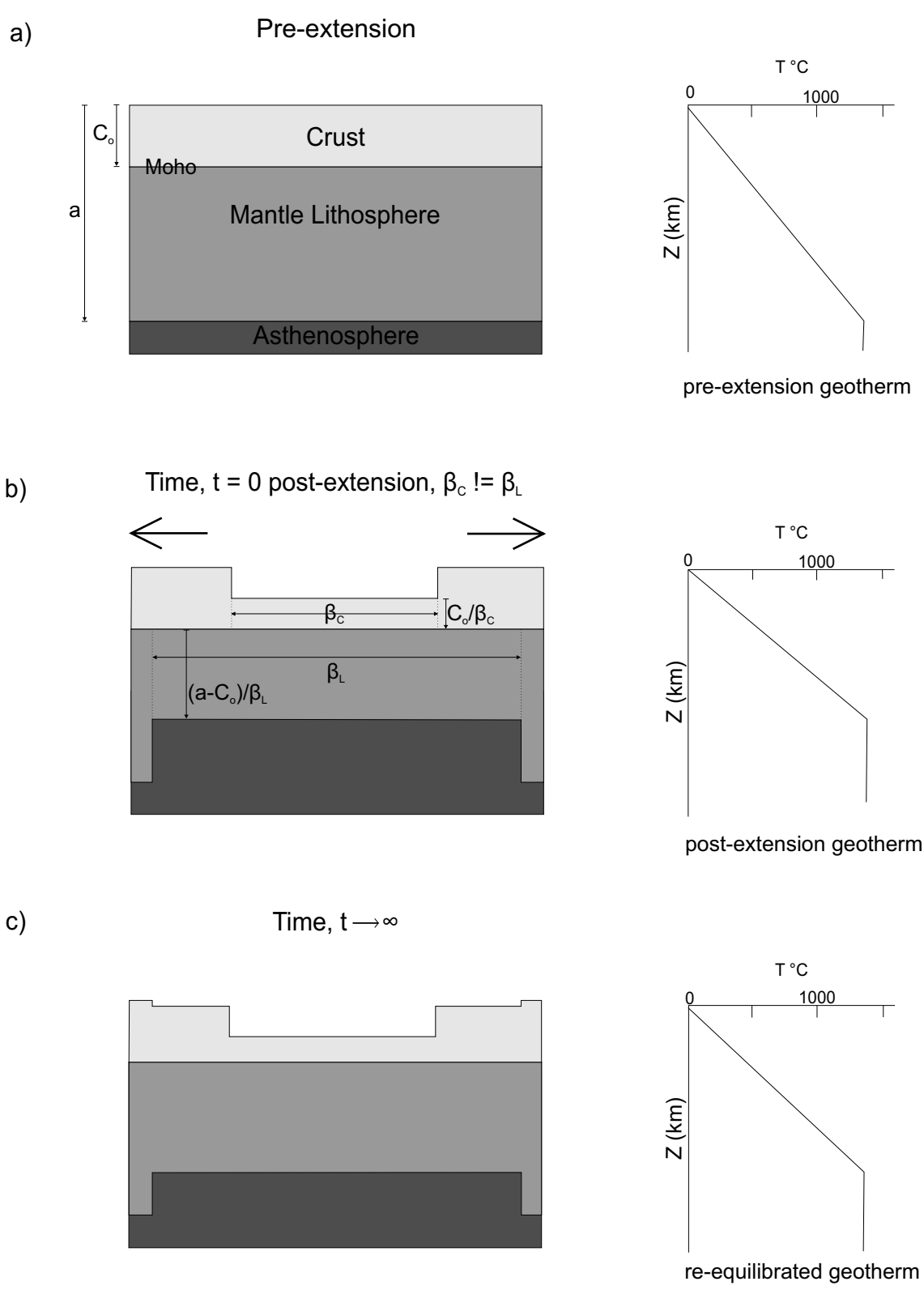


Figure 1.4. The Non Uniform Lithosphere Extension Model. a) Extension has not yet occurred and the geotherm is in equilibrium. b) At time, t = 0; the crust has been thinned by the extension factor $\beta_C$. The lithosphere mantle has been thinned by the extension factor $\beta_L$. The asthenosphere has risen, resulting in heating of the temperature field as hotter material is moved closer to the surface. c) After time has passed, the geotherm has returned to an equilibrated position, resulting in subsidence (After Royden and Keen, 1980).

extends independently by a factor $\beta_L$. Uniform extension (the McKenzie model) occurs when $\beta_C = \beta_L$.

Although this model explains the subsidence and uplift of some basins that the McKenzie model does not, it is still accompanied by a major limitation. The model still assumes that the mechanism of basin deformation is pure shear. Whilst this may be the case below the decoupling boundary in the more ductile mantle lithosphere, deformation in the upper lithosphere is accommodated by simple shear.

### *1.3.6 Integrated simple and pure shear models of lithosphere extension*

The McKenzie model and the Wernicke model are end-members of a range in crustal extension models (Coward, 1986). The majority of real world examples lie somewhere in between the two; the crust deforms by simple shear and the lower lithosphere below the fault detachment depth deforms by pure shear. Numerical models that simulate crustal thinning by simple shear, pure shear or a combination of the two methods have been developed and enable forward modelling of extensional basins due to rifting (Kusznir *et al.*, 1987; Kusznir and Egan, 1989; Egan, 1992; Hodgetts *et al.*, 1998; Meredith and Egan, 2002). Numerical modelling techniques have progressed to produce a model that integrates crustal deformation, thermal, isostatic and surface processes in both two- and three-dimensions (Figure 1.5). The model assumes that all of the faults have a common detachment depth, usually at mid to lower crustal levels which represents the brittle-ductile transition, below which deformation is

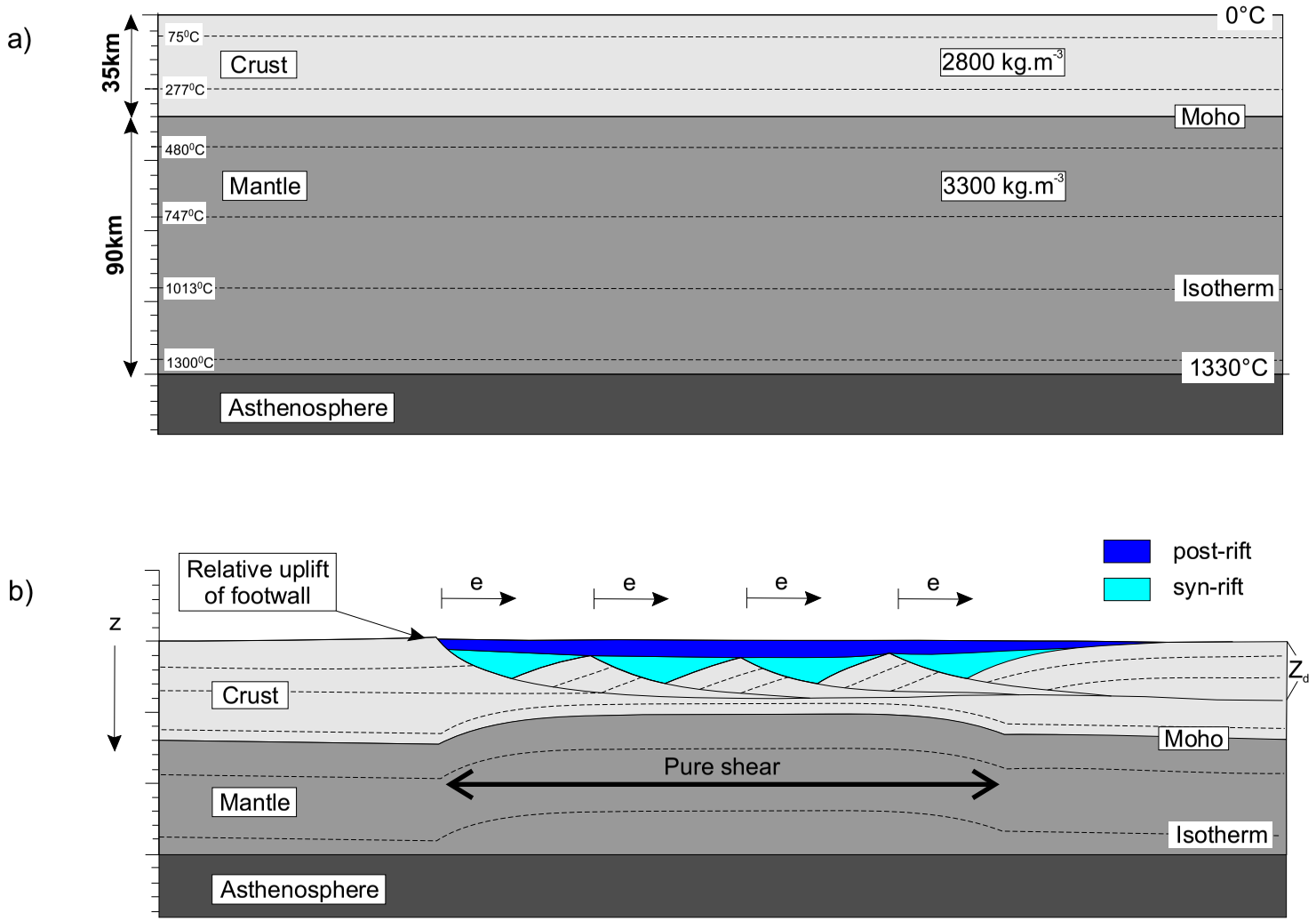


Undeformed model with geotherm in equilibrium.

Model of lithosphere deformation due to faulting and pure shear.

Figure 1.5. Integrated Simple and Pure Shear Model of Lithosphere Extension (After Meredith and Egan 2002).

assumed to be as a result of pure shear (Kusznir and Park, 1987). The pure shear thinning of the lower crust and mantle lithosphere is regional and defined in terms of a lateral position, width and magnitude, expressed as a sequence of beta values, all of which can be independent of the deformation by faulting in the upper crust (Kusznir *et al.*, 1987; Meredith and Egan, 2002).

## 1.4 The structural and geodynamic evolution of the Northumberland Trough Region: Previous studies

Previous research conducted on the evolution of the Northumberland Trough Region has presented several explanations of the mechanisms that have controlled subsidence. Bott (1976) and Leeder (1976) presented theories that attributed the subsidence to a combination of regional thinning of the crust by creep of the lower crustal material to the south where the mid-European marginal sea was closing by subduction of the northern continental margin, and wedge subsidence of the upper crust to form the block and trough structures. Leeder (1982) proposed an alternative theory based on the pure shear stretching mechanism of the McKenzie model. This theory proposes an initial extension event, which thinned the lithosphere by stretching during Dinantian times, resulting in the block and trough structures. This initial stretching event also caused the asthenosphere to rise, raising the geothermal gradient. Subsequently as the lithosphere cooled during the Westphalian stage, regional thermal subsidence affected both the block and trough regions.

Bott *et al.* (1984) suggested a subsidence mechanism, based on geodynamic observations, which is a modification of these two previous hypotheses with more emphasis on the lithosphere stretching with subordinate thermal effects. The Westphalian subsidence observed is considerably greater than the maximum amount of subsidence predicted by the McKenzie model, indicating that thermal subsidence was not the only factor affecting subsidence during the upper Carboniferous. The Westphalian succession is almost twice as thick as that of the Namurian, indicating an increased rate of subsidence rather than the expected exponential decay as a result of thermal subsidence. The stretching mechanism is likely to have remained active throughout the Carboniferous Period. This is also supported by the presence of the Whin Sill Suite intruded in upper Carboniferous times.

Differential stretching (Royden and Keen, 1980) has been proposed as part of this mechanism, with the ductile part of the lithosphere undergoing greater stretching and thinning than the upper brittle layer including the continental crust. Shearing between the two layers would be required to accommodate the differential strain. This scenario would occur if the upper layer subducts more slowly on average than the main ductile part of the lithosphere. The upper layer is affected by a concentration of the stress as the viso-elastic deformation of the ductile layer gives rise to larger tensions within the brittle layer (Kusznir and Bott, 1977), resulting in deformation by faulting (simple shear) rather than stretching (pure shear). The presence of low density granite within the crust influences the

formation of the block and trough structure, with blocks forming above the buoyant granites and troughs forming between them (Bott, 1967; 1976). The deformation of the brittle layer by simple shear being responsible for the block and trough structure is supported by the presence of a Moho with almost uniform depth. If this deformation was the result of pure shear the Moho would be significantly shallower beneath the blocks than the trough (Bott *et al.*, 1984).

## 1.5 Summary of thesis content

### *1.5.1 Chapter 2: Geology of the Northumberland Trough Region:*

This chapter contains a summary of the geology of the Northumberland Trough Region. Consideration of the Early Palaeozoic evolution of Northern England includes the significance of its location in the context of the Iapetus Suture Zone; the nature and timing of Caledonian igneous emplacement; and the nature of the Lower Palaeozoic stratigraphy. The late Devonian/early Carboniferous structure and stratigraphy of the Northumberland Trough Region are considered as either syn- or post-extensional. Subsequent structural, depositional and erosional events are also detailed.

### *1.5.2 Chapter 3: Data Analysis; Regional cross-sections, seismic analysis and borehole data:*

Data for the analysis of the development of the Northumberland Trough Region has been provided in the form of seismic, gravity and borehole data. The analyses of surface data and subsurface geophysical data have

been collated within a GIS environment and used to produce regional cross-sections showing the present day structure and stratigraphy of the study area. These have been used to provide input parameters for the modelling and will also form the basis for a comparison with the modelling results.

### *1.5.3 Chapter 4: Two-dimensional modelling of the deformation resulting from extension:*

This chapter considers possible methods of modelling fault deformation in two dimensions. The chosen method of modelling fault deformation, the inclined shear construction, is examined in greater detail, including its application to fault systems containing multiple faults and investigation of the parameters that affect the resultant basin geometry. This chapter will also examine the means by which the ductile lower crust is deformed by pure shear. The method of modelling pure shear within a coupled simple-shear/pure-shear model of lithosphere extension is explored.

The thermal processes resulting from lithosphere extension, thermal uplift and the subsequent thermal subsidence, are also examined in this chapter. Quantitative modelling of these thermal processes provides insights into their influence on basin development.

In response to any force that generates or removes a load, the Earth reacts to re-establish isostatic equilibrium. Several isostatic hypotheses have been put forward to explain the mechanism by which isostatic equilibrium is restored.

### *1.5.4 Chapter 5: Integrated lithosphere-scale modeling of extensional basin development*

This chapter considers the application of the methods discussed in chapter 4 into an integrated lithosphere-scale model. This is achieved by examining the performance of the inclined shear construction in a basinal setting containing multiple faults. In addition consideration is given to the flexural isostatic response to the mechanical, thermal and isostatic processes associated with extension of the lithosphere. A number of surface processes, including infilling the basin with water or sediment, compaction of sediments and erosion of material raised above sea level are also investigated.

### *1.5.5 Chapter 6: Modelling of the subsidence history of the Northumberland Trough Region in two-dimensions:*

Burial history modelling, constrained by borehole and subsurface data, has been utilised to provide constraints on the timing and magnitude of extension. The integrated tectonic, thermal, isostatic and stratigraphic modelling approach developed in chapters 4-5 has been applied to the Northumberland Trough Region in order to investigate its structural and stratigraphical evolution.

Modelling Results supports a non-uniform mode of lithosphere extension with multiple phases of extension responsible for the development of the configuration of stratigraphy within the basins. The presence of the North Pennines Batholith has influenced the structure of the region post-

emplacement by supporting the Alston Block and enhancing the basin and block architecture that resulted from extension.

### *1.5.6 Chapter 7: Modelling of the subsidence history of the Northumberland Trough Region in three-dimensions:*

Table 1.1 provides a summary of model parameter that are used throughout the thesis, along with their units and, where applicable, the values assumed.

| Symbol | Parameter | Value/Unit |
|---|---|---|
| $\alpha$ | flexural parameter | |
| $\alpha_s$ | angle of shear | |
| $\alpha_T$ | volumetric co-efficient of thermal expansion | $3.28 \times 10^{-5}$ $K^{-1}$ |
| $\beta$ | expansion factor | For extension $\beta$ has a value between 1 and $\infty$ |
| $\beta_C$ | expansion factor for the upper lithosphere | |
| $\beta_L$ | expansion factor for the lower lithosphere | |
| $\beta_{Max}$ | the maximum value of $\beta$ at the peak of the sinusoidal distribution | |
| $\beta_o$ | $\beta_{Max}$ -1 | |
| $\varepsilon$ | principal strains | |
| $\theta$ | angle of dip of the fault | |
| $\kappa$ | thermal diffusivity | |
| $\lambda$ | bulk modulus ratio of hydrostatic pressure to the dilation it produces | |
| $\lambda_f$ | wavelength of the flexural deflection of the lithosphere | |
| $\nu$ | Poisson's Ratio | 0.25 |
| $\rho$ | density per unit mass | $kgm^{-3}$ |
| $\rho'$ | depth dependent density of the lithosphere | $kgm^{-3}$ |
| $\rho_a$ | density of crust beneath sea level under an elevated region – Pratt isostasy | $kgm^{-3}$ |

| Symbol | Parameter | Value/Unit |
|---|---|---|
| $\rho_b$ | density of crust beneath sea level under a region of reduced topography –Pratt isostasy | $kgm^{-3}$ |
| $\rho_m$ | mantle density | 3300 $kgm^{-3}$ |
| $\rho_c$ | crustal density | 2800 $kgm^{-3}$ |
| $\rho_i$ | density of basin infill | 2500 $kgm^{-3}$ |
| $\rho_{air}$ | density of air | 1 $kgm^{-3}$ |
| $\rho_w$ | density of water | 1000 $kgm^{-3}$ |
| $\rho_s$ | bulk sediment density | 2500 $kgm^{-3}$ |
| $\rho_g$ | density of intrusion | 2630 $kgm^{-3}$ |
| $\sigma$ | principal stresses | |
| $\tau$ | thermal time constant of the lithosphere | 62.8 Ma |
| $\phi_s$ | surface porosity | 49% |
| $\phi_z$ | porosity at depth z | |
| $a$ | thickness of the lithosphere | 125 km |
| $A$ | constant dependent upon $\beta$ and $T_0$ | |
| $A_{(x,t)}$ | accommodation space | |
| $B_{(x)}$ $B_{(x,t)}$ | basin profile | |
| $c$ | compaction co-efficient | 0.27 |
| $C$ | amount of compaction of each unit | km |
| $C_f$ | degree of flexural compensation | |
| $C_s$ | cumulative amount of compaction | km |
| $C_o$ | original crustal thickness | 35 km |
| $C_L$ | lower crustal thickness | km |
| $C_{th}$ | crustal thickness | km |
| $C_p$ | specific heat at a constant pressure | |
| $CTPS_{(x)}$ | crustal thinning as a result of pure shear | |
| $d$ | denudation rate | |
| $d_f$ | fault displacement | |
| $d_w$ | depth of sea | |
| $D$ | flexural rigidity of the lithosphere | $7.8 \times 10^{11}$ N m |
| $e$ | horizontal extension | 10 km |
| $e_r$ | percentage erosion | |
| $e_t$ | elevation to which the lithosphere subsides at time, t | km |
| $E$ | Young's modulus | $7 \times 10^{10}$ Pa |
| $F_{(x)}$ | depth to individual faults | |
| $Flt_{(x)}$ $Flt_{(x,t)}$ | model fault profile | |
| $g$ | acceleration due to gravity | 9.81 $ms^{-2}$ |
| $G$ | modulus of rigidity | |
| $G_{(x)}$ | thickness of igneous intrusion | |
| $h$ | heave | |

| Symbol | Parameter | Value/Unit |
|---|---|---|
| $h_r$ | length scale for decrease in $H$ with depth | |
| $h_u$ | height of uplifted topography | |
| $H$ | radiogenic heat production rate per unit mass | |
| $H_s$ | surface radiogenic heat production rate per unit mass | |
| $H_T$ | total amount of horizontal extension by simple shear | |
| $HW_{(x)}$ | depth to the hanging wall | |
| $HT_{(x)}$ | deformation of the hanging wall in the x',y' co-ordinate system | |
| $ISO_{PS(x)}$ | Airy isostatic compensation due to extension by pure shear | |
| $j$ | ▪ fault number<br>▪ integer for an array | |
| $k$ | ▪ integer for an array<br>▪ lithology dependent compaction co-efficient | |
| $K$ | co-efficient of thermal conductivity | 3.3 $Wm^{-1} K^{-1}$ |
| K | Kelvin | |
| $L_{(x)}$ | pressure exerted by the applied load | |
| $m$ | integer which expresses the order of the iteration | |
| $M$ | bending moment | |
| $M_{(x)}$ $M_{(x,t)}$ | profile of the Moho | |
| $n$ | ▪ integer which expresses the order of the harmonic Fourier Transform<br>▪ number of repeats in iterative modelling | 20 |
| $N$ | maximum number of values within a Fast Fourier Transform | |
| $Nflt$ | total number of faults | |
| $p$ | pore fluid pressure | Pa |
| $P$ | pressure applied to a compensation level by a volume of rock | Pa |
| $P_E$ | pressure applied to a compensation level by an elevated region | Pa |
| $P_S$ | pressure applied to a compensation level by a column of rock below sea level | Pa |
| $P_U$ | pressure an undisturbed column of rock exerts upon the compensation level | Pa |

| Symbol | Parameter | Value/Unit |
|---|---|---|
| $P_{ab}$ | actual palaeobathymetry level | km |
| $P_b$ | maximum palaeobathymetry level | km |
| $P_{(x)}$ | crustal thinning produced by extension of the lower crust by pure shear | |
| $PS_S$ | position where pure shear deformation starts | |
| $PS_F$ | position where pure shear deformation finished | |
| $PS_W$ | width of pure shear distribution | |
| $q$ | heat flux | $mWm^{-2}$ |
| $q_s$ | surface heat flux | $mWm^{-2}$ |
| $r$ | radius of curvature | |
| $r_a$ | thickness of the anti-root of mantle material | km |
| $r_c$ | thickness of the crustal root | |
| $R$ | regional datum | |
| $Resp_1$ | response function to filter data in the Fast Fourier Transform | |
| $Resp_2$ | response function to filter data in the Fast Fourier Transform | |
| $s$ | vertical compressive stress | |
| $s_z$ | steady state component of the temperature of the lithosphere at depth z | |
| $S_i$ | initial subsidence McKenzie model | |
| $S_t$ | thermal subsidence | |
| $S_M$ | McKenzie model total subsidence | |
| $S_{(x)}$ | crustal thinning produced by extension of the upper crust by faulting | |
| $ST_{(x,ts)}$ | Thickness of stratigraphy created at time step, ts | |
| $t$ | time | Ma |
| $t_f$ | fault throw | |
| $ts$ | time step in model | |
| $T$ | temperature | |
| $\Delta T$ | temperature perturbation of the lithosphere | |
| $T_0$ | temperature at the base of the lithosphere | 1333°C |
| $T_s$ | surface temperature | |
| $Te$ | effective elastic thickness of the lithosphere | 5 km |
| $Ts$ | solid thickness of unit | |
| $Tp$ | pore thickness of unit | |

| Symbol | Parameter | Value/Unit |
|---|---|---|
| $u_{z,t}$ | unsteady state component of the temperature of the lithosphere at depth z and time, t | |
| $U_{(x)}$ | Uplifted basement above sea-level | |
| $UB_{(x)}$ | Uplifted basin above sea-level | |
| $V$ | volume per unit mass | $m^3$ |
| $w$ | vertical deflection of the plate | |
| $W$ | width of region undergoing pure shear | km |
| $W_{(x)}$ | flexural isostatic response of the lithosphere to a load | |
| $x$ | Cartesian co-ordinate on the horizontal axis | |
| $x'$ | x co-ordinate in an inclined plane | |
| $x_f$ | horizontal position of the surface outcrop of a fault | |
| $xH$ | x co-ordinate of the hanging wall profile following rotation | |
| $y$ | Cartesian co-ordinate on the vertical axis (depth) | |
| $y'$ | y co-ordinate in an inclined plane | |
| $y_p$ | thickness of pore space | |
| $y_s$ | thickness of sediment grains | |
| $y_t$ | thickness of sediment layer | |
| $z$ | distance measured upwards from the base of the lithosphere | |
| $Zd$ | detachment depth of fault | 20 km |

Table 1.1 List of parameters used in thesis

# 2 Geology of the Northumberland Trough Region

The Northumberland Trough Region consists of the Northumberland Trough and its westerly continuation, the Solway Basin. In addition to adjacent areas including the Alston Block, a structural high situated to the south of the Northumberland Trough, the northern part of the Stainmore Trough to the south of the Alston Block, the Lake District Block and the Vale of Eden Basin. This area of northern England has developed a basin and block architecture as a result of crustal extension from late Devonian through to Carboniferous times. The present day structural geometry of the region is illustrated in Figure 1.1.

## 2.1 Early Palaeozoic evolution of Northern England

The Northumberland Trough Region lies within the tectonic framework of the Iapetus Suture Zone. The Iapetus Ocean was a Neoproterozoic to Early Palaeozoic 'proto-Atlantic' ocean (Wilson, 1966). Closure of the Iapetus Ocean was responsible for the Caledonian Orogeny and has a complex convergence history between Laurentia, Avalonia and Baltica (Figure 2.1), with rotation of the continents and changes in subduction polarity (Soper *et al.* 1992a; Andreasson *et al.*, 2003; Torsvik and Rhenström, 2003). Evidence suggests that the final stages of closure of the Iapetus Ocean began when Avalonia and Baltica docked sinistrally against Laurentia in mid-Silurian times ~420Ma. At this time, faunal provinciality, as defined by 'Pacific' vs 'Atlantic' faunal provinces, ended (Cocks and Fortey, 1982; Cocks, 2000). Avalonia was subsequently shifted

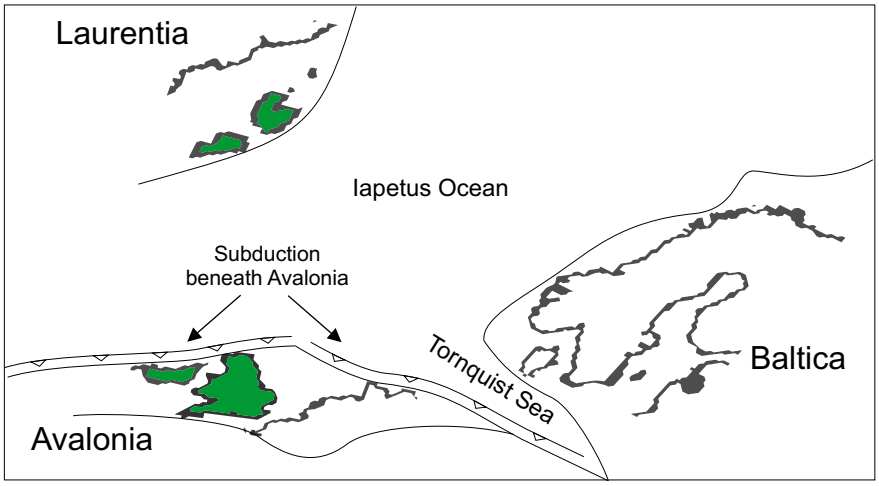


Ordovician - Katian c. 455Ma

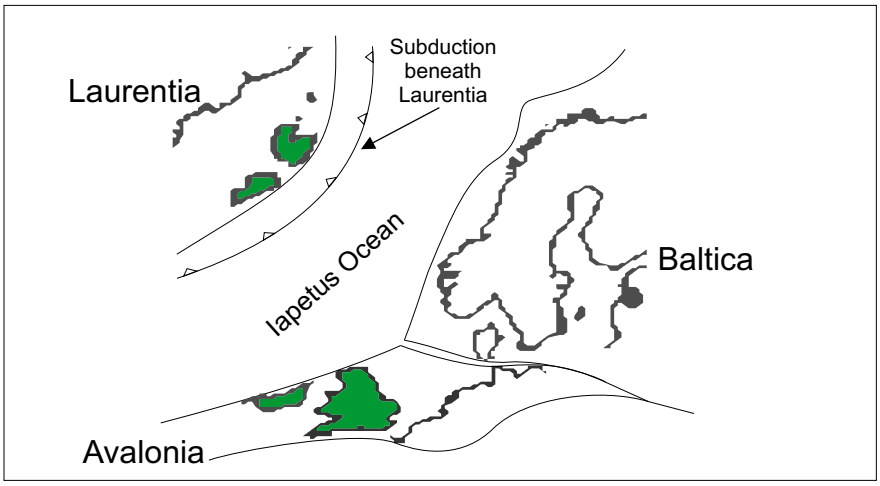


Silurian - Rhuddanian c. 440Ma

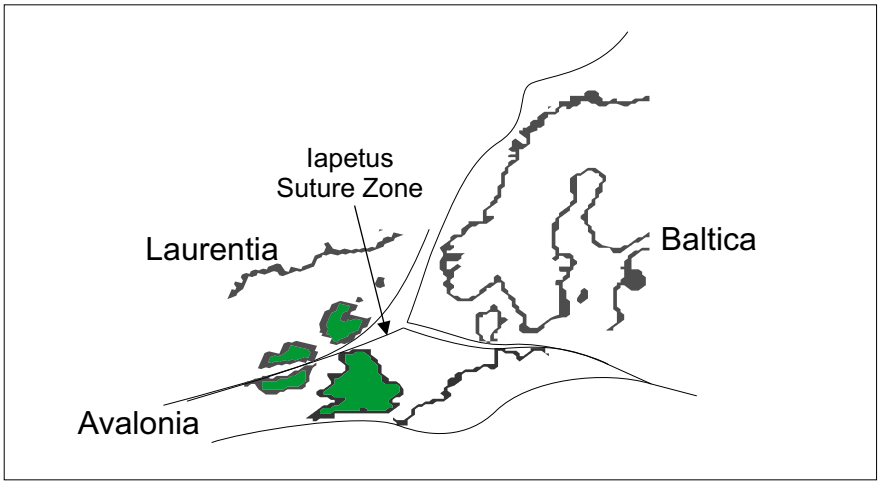


Silurian - Ludfordian c. 420Ma

Figure 2.1. Palaeoreconstruction of Laurentia, Baltica and Avalonia during the Ordovician and Silurian periods (After Torsvik and Rehnström, 2003).

dextrally during the Acadian Orogeny affecting final closure of the Iapetus Ocean (Soper *et al.*, 1992a; Dewey and Strachan, 2003). This shift occurred due to a collision between southern Avalonia and Armorica, a rifted fragment of Gondwana, as a result of the closure of the Rheic Ocean (Woodcock *et al.*, 2007). This deformation during the Acadian Orogeny resulted in pervasive cleavage development which has been dated by K-Ar techniques to 397±7Ma and by Ar-Ar techniques as 396.1±1.4Ma (Merriman *et al.*, 1995; Sherlock *et al.*, 2003). The Iapetus Suture marks the junction between the Laurentian basement of the Southern Uplands to the north and the Avalonian basement to the south (Leggett *et al.*, 1983; Beamish and Smythe, 1986; McKerrow and Soper, 1989; Soper *et al.*, 1992b). Its geographical position is identified by deep seismic reflection profiles.

The Western Isles North Channel (WINCH) deep seismic reflection profile and the North East Coast (NEC) line, British Institutions Reflection Profiling Syndicate (BIRPS) multichannel seismic reflection profiles (offshore), have been studied along with magnetotelluric data (onshore) to investigate the deep structure of the Iapetus Suture Zone (Figure 2.2) (Beamish and Smythe, 1986; Hall *et al.*, 1984; Freeman *et al.*, 1988). A north-dipping (c. 25°) seismic reflector offshore beneath the Southern Uplands has been interpreted from the WINCH line and has been suggested to represent the Iapetus Suture (Beamish and Smythe, 1986). However, the suture at depth is not likely to be represented by a single surface, but by a major shear or fault zone.

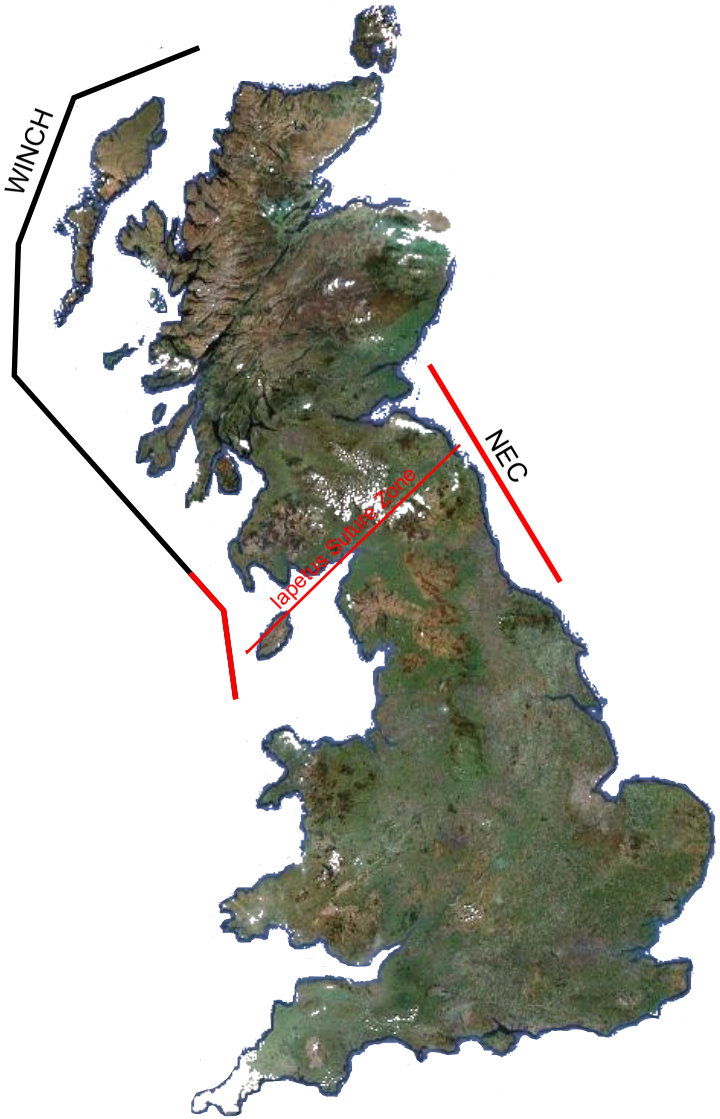


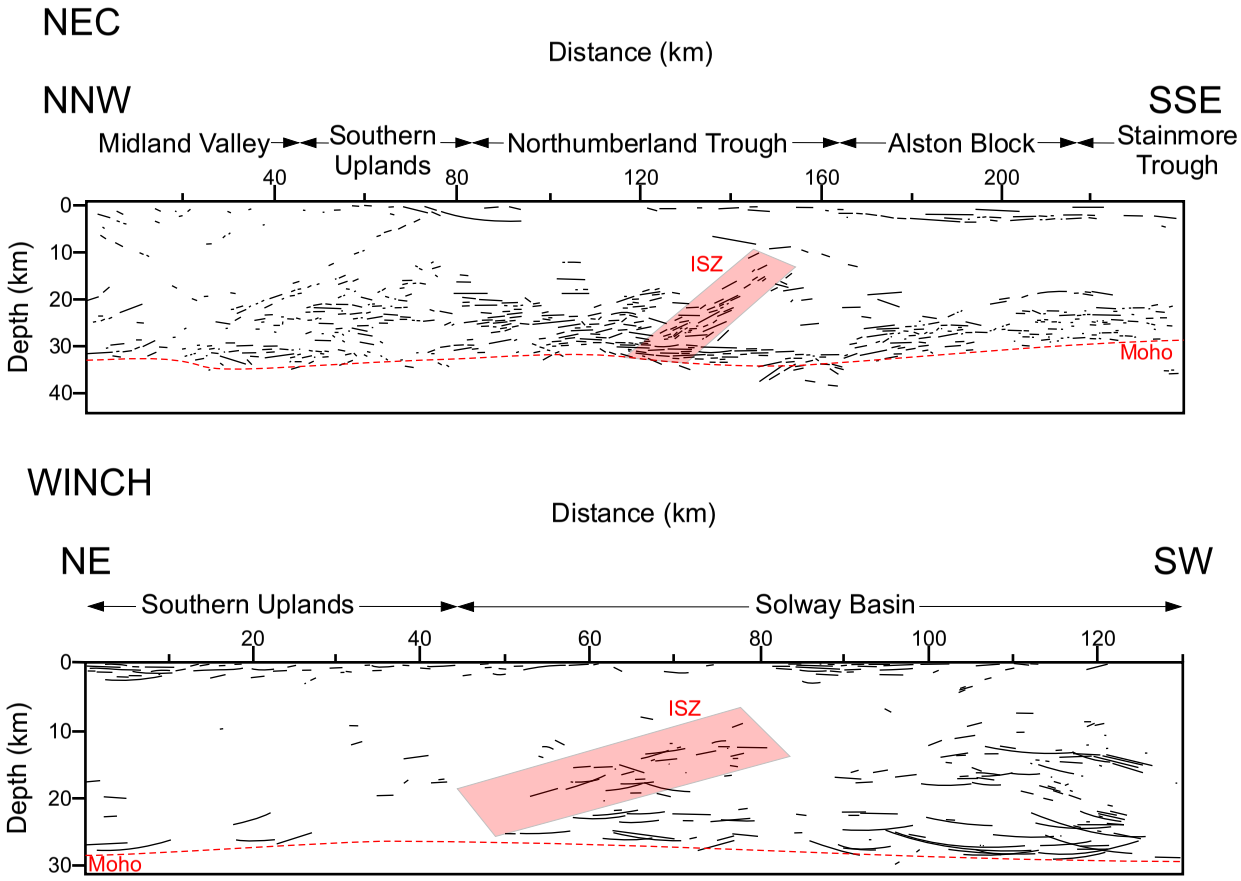


Figure 2.2. Interpretations of WINCH and NEC migrated and depth converted deep seismic lines. The Iapetus Suture Zone (ISZ) is interpreted on both sections, as is the depth of the Moho. (NEC after Freeman *et al.* 1988, WINCH after Brewer *et al.* 1983; Beamish and Smythe, 1986. Map © 2009 Google - Imagery © 2009 TerraMetrics)

A northwards dipping reflective zone, roughly planar in form, can be identified on the NEC line (Freeman *et al.*, 1988). These reflections may be generated within the Iapetus Suture Zone, where fractured and modified rocks will have different acoustic properties from those of the country rocks. Magnetotelluric data also reveal a single highly reflective area at mid to lower crustal depths, corresponding to the onshore continuation of the offshore seismic feature. The presence of a major shear zone would result in enhanced conductivity as it is common for free fluids or hydrous mineral assemblages to be present which allow ionic transfer and increase conductivity (Chadwick and Holliday, 1991). This highly conductive layer can also be explained as resulting from the Iapetus Suture Zone.

### *2.1.1 Structural Significance of the Iapetus Suture Zone*

At lower crustal levels, the Iapetus Suture Zone marks the boundary between the Laurentian crust and the underthrust Avalonian crust. The presence of a major crustal shear zone beneath northern England has important structural implications with regards to the subsequent Carboniferous extensional basin evolution, which is being investigated as part of this research.

The Northumberland Trough and the Solway Basin, which lie above the Iapetus Suture Zone, comprise a major east-west orientated asymmetrical half-graben system that extends across northern England into the northern Irish Sea (Figure 2.3).

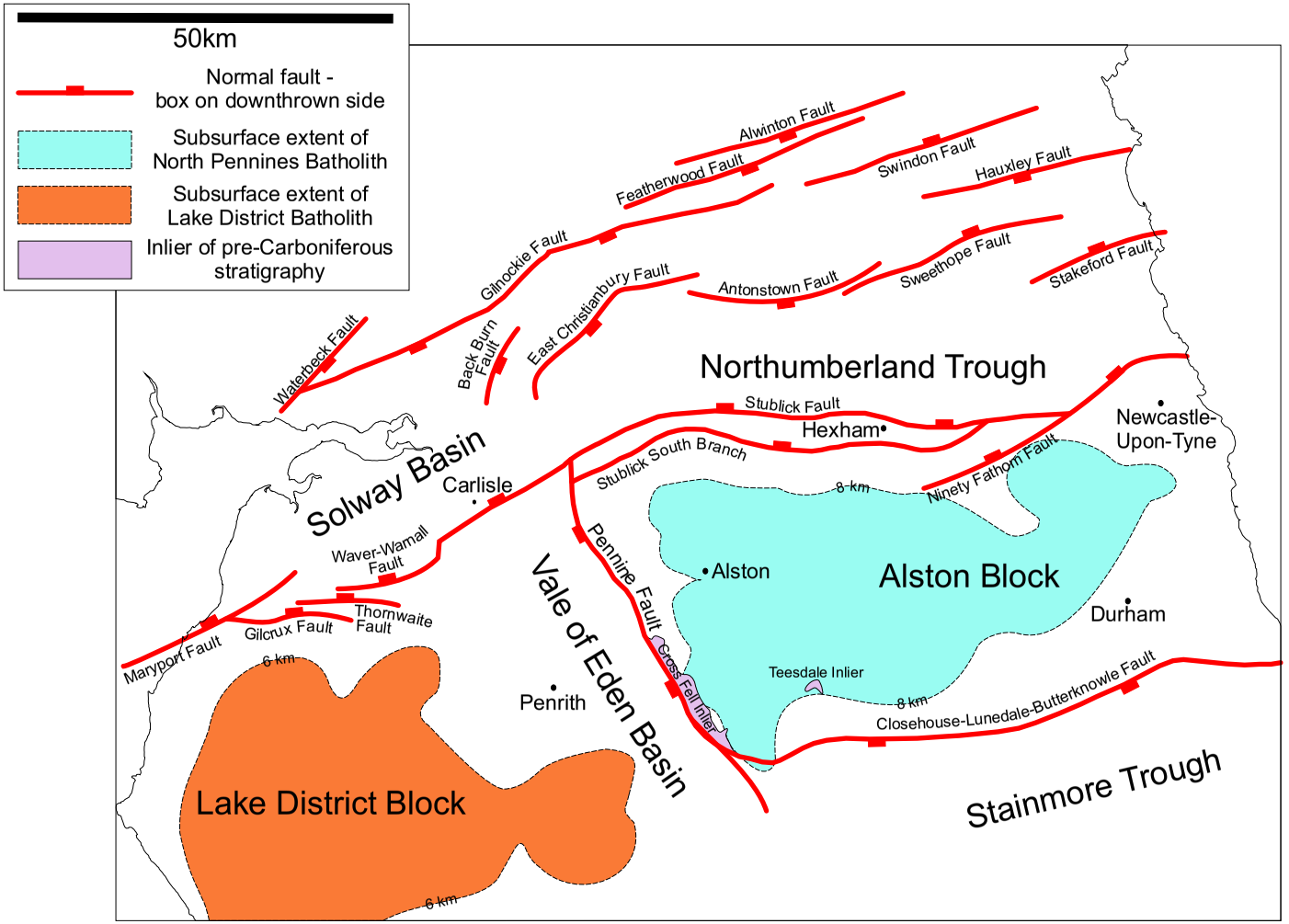


Figure 2.3. Carboniferous structure of the Northumberland Trough Region. (Chadwick *et al*. 1995; Stone *et al*., 2010; North Pennines Batholith data reproduced by permission of the British Geological Survey ©NERC. All rights reserved)

The east-north-east trend of the basins is reminiscent of the prominent structural trend of the lower Palaeozoic era. However, north-south orientated tension has imparted a significant component of dextral slip to the fault movement generating a wrench-dominated domain. In this wrench-dominated domain, the angle between the bulk displacement direction and the regionally recognised basin- and domain-bounding faults, and therefore the component of dextral tension, has been calculated with an approximate value of 30° (De Paola *et al.*, 2005). The basins lie within the hanging wall of the Iapetus Suture Zone which suggests that the major extensional faults responsible for basin formation are a result weakness within the older 'basement' features of the shear zone (Kimbell *et al.*, 1989).

### *2.1.2 Caledonian igneous emplacement*

Towards the end of the Caledonian Orogeny, a number of granitoid igneous intrusions were emplaced within the crust of Laurussia. In Northern England and southern Scotland, the Caledonian igneous intrusions can also be divided broadly into two groups. During middle to late Ordovician times, subduction-related intrusive rocks were emplaced at the margin of Avalonia, with the majority of the intrusions occurring at ~ 450Ma, significantly later than those in northern Scotland (Stephenson *et al.*, 1999). These late Ordovician intrusive rocks comprise the Ennerdale microgranite intrusion (452±4Ma), Eskdale granite pluton (450±3Ma), Broad Oak granodiorite pluton and the Threlkeld microgranite intrusion (451±1.1Ma) all of which form part of the Lake District Batholith

(Hughes *et al.*, 1996; Millward and Evans, 2003). The Ennerdale, Broad Oak and Threlkeld intrusions have a similar geochemical signature to the contemporaneous continental margin volcanic rocks of the Eycott Volcanic and Borrowdale Volcanic groups with which they are associated (Millward *et al.*, 2000; Millward, 2002; 2004). These were the result of subduction-related partial melting of the lithospheric mantle (MacDonald *et al.*, 1988).

The second group of igneous intrusions in Northern England and Southern Scotland, the Trans-Suture Suite were emplaced during Devonian times ~ 395-405Ma (Brown *et al.*, 2008). The Trans-Suture Suite comprises the Cairnsmore of Fleet intrusion (392±2Ma), the Crieffel pluton (397±2Ma) and the Cheviot intrusion (395±2.9Ma) of the Galloway Suite (Highton, 1999) in addition to the North Pennines Batholith (399±0.7Ma) and the Skiddaw (399±0.4Ma) and Shap (404±0.5Ma) granite plutons of the Lake District Batholith (Halliday *et al.*, 1979; Cox *et al.*, 1996; Brown *et al.*, 2008; Stone *et al.*, 2010). The intrusions of the Galloway Suite of southern Scotland have been included with the granitic intrusions of northern England despite being on opposite sides of the Iapetus suture on the basis of their age, tectonic setting and petrogenesis (Brown *et al.*, 2008). The intrusions of the Trans-Suture Suite were emplaced during the latter part of, and after, the Acadian Orogeny, a period of high heat flow and crustal thickening. These granites have S-types characteristics consistent with sedimentary input to the petrogenesis of the parent magma, with

derivation from Avalonian crust material (Stephens and Halliday, 1984; O'Brien *et al.*, 1985).

#### 2.1.2.1 The North Pennines Batholith

The North Pennines Batholith, a non-porphyritic, per-aluminous granite, known previously as the Weardale Granite, underlies the Alston Block (Bott; 1967; Holland and Lambert, 1970) (Figures 2.3 & 2.4).

The main constituent minerals of the granite include albite, potassium feldspars, muscovite, biotite and quartz. (Dunham *et al.*, 1965; Bott, 1967). The rock exhibits a foliation dipping between 0° and 20° as a result of the parallel alignment of the mica and quartz crystals. This foliation is less obvious below a depth of 670 m, which corresponds with a distinct change in the chemistry of the granite (Dunham *et al.*, 1965). Holland (1967) suggested that this geochemical differentiation is consistent with the intrusion of two granites from a common magma source, the lower granite being a latter magmatic fraction compared to the upper granite. The granite also contains thin veins of aplites and pegmatites, whose chemistry is similar to the granite, but lacking biotite and chlorite (Dunham *et al.*, 1965). These veins are interpreted as having formed at a late magmatic stage as end members of magmatic differentiation (Holland, 1967).

The date of emplacement of the North Pennines Batholith has been studied using isotope analysis. Initial dating using $^{87}Rb/^{86}Sr$ and $^{87}Sr/^{86}Sr$ techniques for whole rock samples and acquired a date of 410±10My for

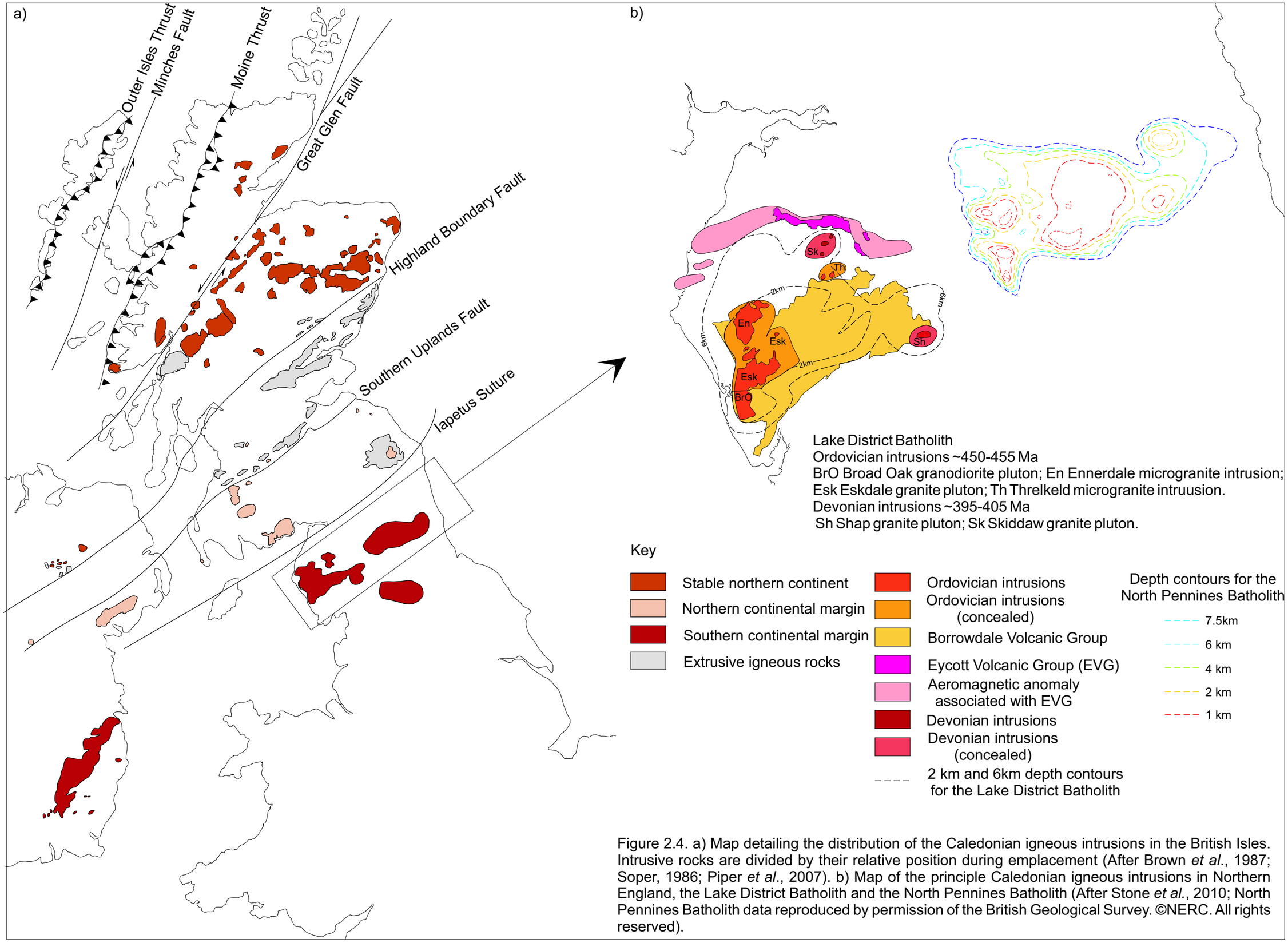


Figure 2.4. a) Map detailing the distribution of the Caledonian igneous intrusions in the British Isles. Intrusive rocks are divided by their relative position during emplacement (After Brown *et al*., 1987; Soper, 1986; Piper *et al*., 2007). b) Map of the principle Caledonian igneous intrusions in Northern England, the Lake District Batholith and the North Pennines Batholith (After Stone *et al.*, 2010; North Pennines Batholith data reproduced by permission of the British Geological Survey. ).

the North Pennines Batholith, with an age of 390±8My was obtained for the aplite samples (Holland and Lambert, 1970). Fitch and Miller (1965) interpret the results of their K/Ar dating as an initial magmatic event at approximately 410±10My followed by reactivation and gneissification of the early intrusion, followed by further intrusive activity before 392±6My. More recent studies using U-Pb and molybdenite Re-Os techniques give more precise dates for the emplacement of the North Pennines Batholith. A date of 398.3±1.6Ma has been presented for the emplacement and co-magmatic molybdenitic mineralisation of the North Pennines Batholith (Selby *et al.*, 2008). The U-Pb date of 399.3±0.7 Ma given by Kimbell *et al.* (2010) also falls within this range.

## 2.2 Syn-Extensional structural basin development

The present-day Northumberland Trough is an asymmetrical half-graben bounded at its southern margin by the Maryport-Stublick-Ninety Fathom Fault system (Kimbell *et al.*, 1989). The extensional displacement is accommodated by a series of en-échelon faults linked by a series of relay ramps. It was this fault system that controlled the structural evolution of the basin during Carboniferous and post-Carboniferous times. Early development of the basin may have been controlled by extensional faults in a more distal position than the Stublick fault (Chadwick and Holliday, 1991). It has been suggested that the series of normal faults that accounts for the displacement of the basin are caused by the manner of reactivation of the shear zone. Extension along the middle part of the shear zone caused subsidence in the hanging wall block, creating normal faulting and

some smaller antithetic faults. Extensional strain decreases upwards within the shear zone, with the shallowest areas exhibiting limited reactivation (Chadwick and Holliday, 1991). The faults of the Maryport-Stublick-Ninety Fathom Fault system dip moderately between 45°and 60° and have a maximum throw of ~5 km at the level of the top of the pre-Carboniferous Basement.

The northern margin of the Northumberland Trough is bounded by a series of en-échelon faults that are antithetic and subsidiary to the Maryport-Stublick-Ninety Fathom Fault system. These faults, the Waterbeck, Gilnockie, Featherwood, Alwinton and Hauxley faults (Figure 2.3), dip to the south by ~ 60° and have a maximum throw of ~1 km. Towards the east of the Hauxley Fault the throw is significantly less (Chadwick and Holliday, 1991). The northern margin of the Northumberland Trough is dominated by shelf processes with sediments in the east thinning into and over the Cheviot Block (Johnson, 1984; Barrett, 1988). The extensional phase of the Northumberland Trough's evolution is characterised by a close association between sedimentation and contemporaneous faulting (Chadwick *et al.*, 1995).

The development of the Solway Basin may have been controlled by movement upon the northern margin, along the east-north-east trending North Solway Fault, with a transfer zone along the Bewcastle Anticline separating the Northumberland Trough from the Solway Basin (Barrett, 1988). However, seismic evidence suggests that the development of the

| Chronostratigraphy | | | | | Lithostratigraphy | | |
|---|---|---|---|---|---|---|---|
| International | | European | | | Cheviot Block | Northumberland-Solway Trough | Alston Block |
| Subsystem | Stage | Subsystem | Stage | Substage | | | |
| Pennsylvanian | Gzhelian | Silesian* | Autunian | | | | |
| | Kasimovian | | Stephanian | | | | |
| | Moscovian | | Westphalian | Westphalian D | | | |
| | | | | Bolsovian | | | |
| | Bashkirian | | | Duckmantian | | | |
| | | | | Langsettian | | | |
| | | | Namurian | Yeadonian | | | |
| | | | | Marsdenian | | | |
| | | | | Kinderscoutian | | | |
| | | | | Alportian | | | |
| | | | | Chokierian | | | |
| Mississippian | Serpukhovian | | | Arnsbergian | | | |
| | | | | Pendleian | | | |
| | Visesn | Dinantian* | Visean | Brigantian | | | |
| | | | | Asbian | | | |
| | | | | Holkerian | | | |
| | | | | Arundian | | | |
| | | | | Chadian | | | |
| | Tournaisian | | Tournaisian | Courceyan | | | |

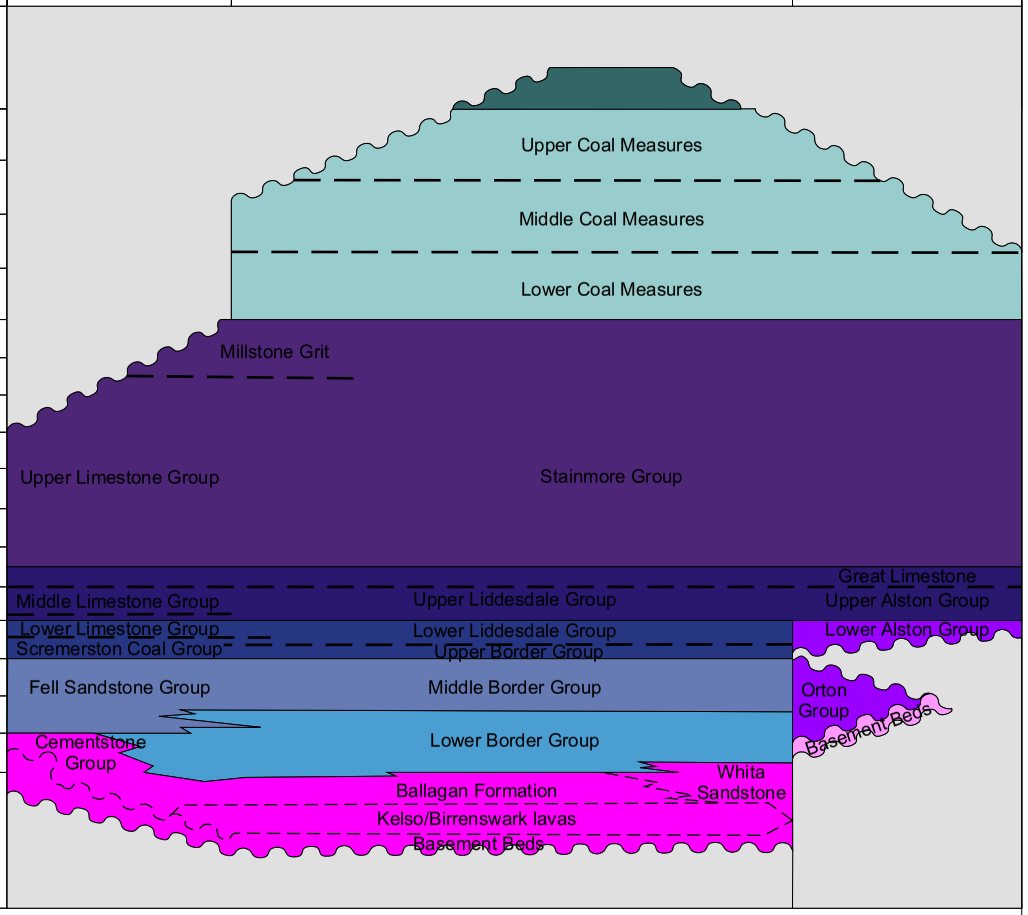


Figure 2.5. Correlation for traditional Carboniferous lithostratigraphy (*labelled on figure*) and newly adopted regional lithostratigraphy (*identified by colour and key*) (After Stone *et al.*, 2010).
*The terms Dinantian and Silesian are no longer used following a recommendation by the International Commission on Stratigraphy.

Current Regional Stratigraphy

Border Group: Fell Sandstone Formation; Lyne Formation; Inverclyde Group

Yoredale Group: Stainmore Formation; Alston Formation; Tyne Limestone Formation

Warwickshire Group; Pennine Coal Measures Group; Great Scar Limestone Group; Ravonstonedale Group

Solway Basin was controlled by movement along the Maryport Fault at its southern margin (Chadwick *et al.*, 1995).

## 2.3 Syn-Extensional stratigraphy

Evidence from palaeomagnetic studies indicate that Britain was situated near to the equator during the Tournasian and Viséan stages (Scotese and McKerrow, 1990). Terrestrial strata deposited during this time indicate a semi-arid climate with seasonal fluctuations in precipitation as evidenced by periodic desiccation (Waters and Davies, 2006). The Northumberland Trough was a centre of deposition during this time, surrounded by emergent land: the Southern Uplands and Cheviot Block to the north and the Alston Block and the Lake District Block to the south (Johnson, 1984; Cope *et al.*, 1992).

The sediments deposited syn-extensionally in the Northumberland Trough and Solway Basin during early Carboniferous times form the Inverclyde Group and the Border Group. An alternative lithostratigraphy is applied to describe the deposits of the Alston Block, the Stainmore Trough and the Vale of Eden Basin. The Ravenstonedale Group and the Great Scar Limestone Group form the sedimentary sequence to the south of the Maryport-Stublick-Ninety Fathom fault system. Figure 2.5 compares the current nomenclature to that used in previous publications.

### *2.3.1 The Inverclyde Group*

The oldest Carboniferous strata preserved within the Northumberland Trough are situated along its northern margin and are similar to those of

the Inverclyde Group of the Midland Valley of Scotland and as a consequence they are assigned to the same group (Cope *et al.*, 1992; Stone *et al.,* 2010). These strata consist of conglomerates and sandstones and grey mudstones with bands of sandstone representing a continental fluvial facies. The sandstone bands become more prominent towards the top of the sequence (Johnson, 1984) and are interpreted to be the result of deposition within a peritidal environment. In addition, there are thin bands of impure limestones that are indicative of occasional marine incursions from the east (Leeder, 1974a; Waters and Davies, 2006). Leeder (1974a) suggested deposition occurred within coastal plain and deltaic environments.

The Solway Basin was at this time a marine influenced gulf and the sediments of the Inverclyde Group within the basin comprise carbonates and silts (Cope *et al.*, 1992).

### *2.3.2 The Border Group*

The Border Group forms the main component of the syn-rift sedimentary fill within the Northumberland Trough and Solway Basin. It can be subdivided into the Lyne Formation and the Fell Sandstone Formation. These two formations are dominantly diachronous, most probably the result of fluctuations in sea level, although in the west, between Bewcastle and Bellingham, the Fell Sandstone Formation conformably overlies the Lyne Formation (Stone *et al.,* 2010).

#### 2.3.2.1 The Lyne Formation

The Lyne Formation consists of fine-grained, subarkosic sandstones, siltstones, mudstones and lacustrine limestones up to ~ 1 km in thickness interbedded with anhydrite (Leeder, 1974a; 1974b; Ward, 1997) (Figure 2.6). These sediments represent predominantly shallow water facies (Taylor *et al.*, 1971). Large-scale cycles of these strata were deposited in environments that fluctuated between peritidal, deltaic and fluvial conditions as a result of uniform subsidence rates and fluctuations in the relative sea level (Leeder, 1976). The Southern Uplands to the north and the Alston and Lake District blocks to the south provided locally sourced sediment and a major river system flowing from the north-east provided a large siliciclastic input into the basin (Leeder, 1974a). There are over 120 discrete anhydrite beds that range in thickness from 30 cm to 6 m (Ward, 1997). The anhydrite beds generally have sharp boundaries with adjacent lithologies and densities approximating 2950 $kgm^{-3}$ indicating that they were precipitated as gypsum in a subaqueous, salina rather than a subareial, sabkha environment (Warren and Kendall, 1985; Kendall, 1992). Occasional marine incursions resulted in thin marine mudstone deposits. The first marine limestones developed within the north-east of the basin towards the top of the succession due to an increase in marine influence.

#### 2.3.2.2 The Fell Sandstone Formation

The Fell Sandstone Formation reaches a maximum thickness of approximately 350m. Crustal extension continued during the deposition of

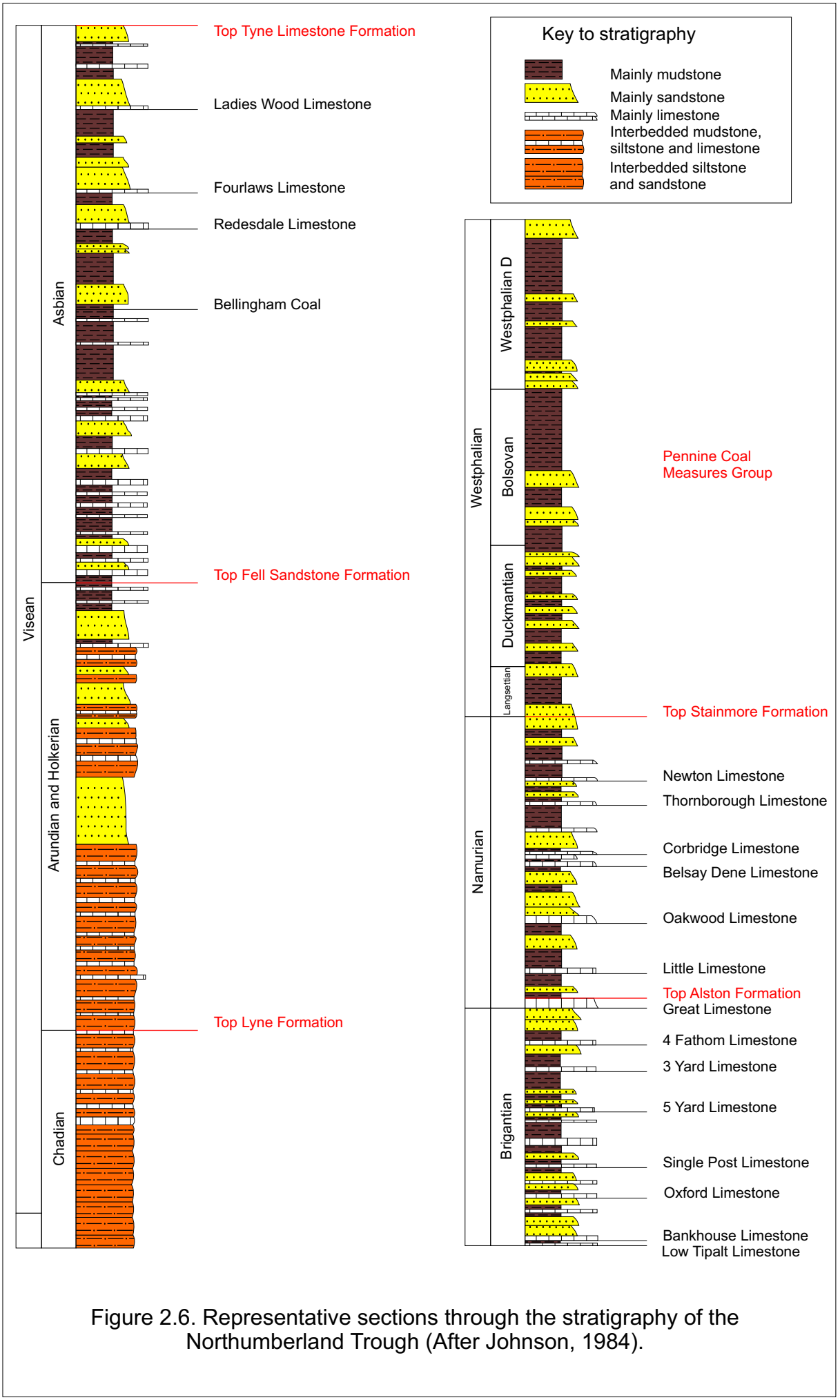


Figure 2.6. Representative sections through the stratigraphy of the Northumberland Trough (After Johnson, 1984).

the Fell Sandstone Formation but the rate of subsidence was considerably less than during deposition of the Lyne Formation, which accounts for the difference in thickness between the two formations (Fraser and Gawthorpe, 1990; Lawrence *et al.*, 2007). The environment of deposition varied laterally across the region within Fell Sandstone Formation times (Figure 2.7b). In the east of the Northumberland Trough, fluvial sediments - medium-grained sands sparsely interbedded with mudstones - were deposited by braided rivers. These pass westwards diachronously into a combination of fluvio-deltaic and shallow-marine environments with the deposition of finer grained sandstones with greater proportions of interbedded siltstone and mudstone layers (Figure 2.6) (Stone *et al.,* 2010). Transgression of the sea into northern England from Ireland increased the marine influence within the Solway Basin which is dominated by increased carbonate content and limited siliciclastic input (Cope *et al.*, 1992; Turner et al., 1997).

### *2.3.3 The Ravenstonedale Group*

The lower Ravonstonedale Group, which is restricted in extent to the western margin of the Stainmore Trough, consists of mudstone, fine-grained sandstone and dolomitised limestone deposited within a tidal flat environment during a marine transgression (Holliday *et al.*, 1979; Higgins and Varker, 1982; Collier, 1991).

Over much of the Stainmore Trough, the Ravonstonedale Group consists of a quartz-pebble conglomerate that contains fragments of lithified

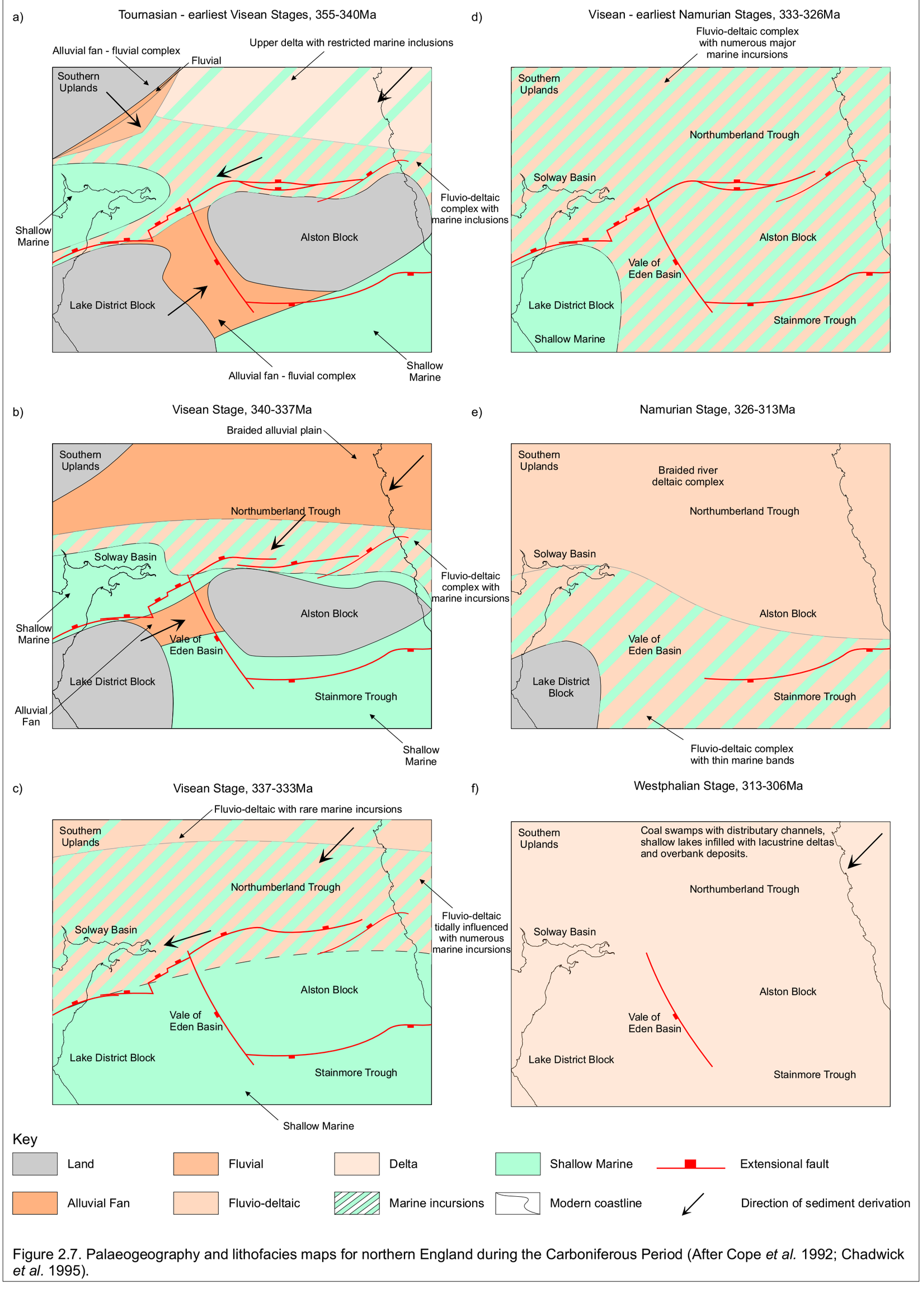


Figure 2.7. Palaeogeography and lithofacies maps for northern England during the Carboniferous Period (After Cope *et al.* 1992; Chadwick *et al.* 1995).

sandstones and mudstones derived from the Alston Block (Burgess and Harrison, 1967).

The uppermost unit of the Ravenstonedale Group comprises algal limestones with thin dolostones, sandstones and calcareous mudstones deposited in peritidal conditions following a marine transgression (Waters and Davies, 2006).

The Ravenstonedale Group on the Alston Block is restricted in extent to the edges of the block and comprises a succession that is almost entirely of marine origin representing where the margins of the Block were being encroached upon by the sea during the marine transgression (Cope *et al.*, 1992). On the Alston Block, the Ravenstonedale Group unconformably overlies the Skiddaw Group (Johnson, 1967; Waters *et al.*, 2007).

### *2.3.4 The Great Scar Limestone Group*

The lowest constituent of the Great Scar Limestone Group is the Ashfell Sandstone Formation within the Stainmore Trough. The Ashfell Sandstone Formation constitutes fluvio-deltaic deposits consisting of trough cross-stratified sandstone (Collier, 1991) that are approximately contemporaneous with the Fell Sandstone Formation in the Northumberland Trough and Solway Basin (Higgins and Varker, 1982). The Ashfell Limestone Formation intrudes onto the margins of the Alston Block as a result of a marine transgression (Ramsbottom, 1973).

Marine regression during early Asbian times resulted in the emergence of the Alston Block and deposits of this age are absent (George *et al.*, 1976).

The Melmerby Scar Limestone Formation unconformably rests on the Ashfell Limestone Formation (Burgess and Holliday, 1979), after a large-scale marine transgression re-established marine conditions across the region (Stone *et al.*, 2010). Deposits of the Melmerby Scar Limestone Formation represent a sediment-starved marine carbonate platform environment subject to oscillating relative sea level (Collier, 1991). The Melmerby Scar Limestone Formation is contemporaneous with the Tyne Limestone Formation of the Yoredale Group and is overlain by the Alston Formation of the Yoredale Group.

## 2.4 Post-Extensional structural basin development

The rate of displacement on the extensional faults at the basin margins was reduced following deposition of the Fell Sandstone Formation, approximately 337Ma. Minor extensional faulting continued into the 'post-extension' phase including localised movement on the basin-bounding Maryport-Stublick-Ninety Fathom and Closehouse-Lunedale-Butterknowle fault systems. As a result of this reduced structural influence, sedimentation became more regional including encroachment onto the previously emergent blocks. The rate of sediment supply matched the rate of the regional thermal subsidence and consequently fluvio-deltaic and shallow-marine conditions dominating deposition (Chadwick *et al.*, 1995).

## 2.5 Post-Extensional Stratigraphy

The Carboniferous sediments deposited post-extensionally form the Yoredale Group, the Pennine Coal Measures Group and the Warwickshire Group. On the Alston Block, the Alston Formation is underlain by the Melmerby Scar Limestone Formation of the Great Scar Limestone Group, which is contemporaneous with the Tyne Limestone Formation of the Yoredale Group. Figure 2.5 compares the current nomenclature to that used in previous publications.

### *2.5.1 The Yoredale Group*

Within the Yoredale Group there are conflicting influences on the depositional environment with continuing marine transgression from the west and south-west and fluvio-deltaic sediment supply from the east and north-east (Leeder *et al.*, 1989; Chadwick *et al.*, 1995). This resulted in the deposition of cyclic sedimentary sequences known as Yoredale Cyclothems. The Yoredale Group is divided into three formations based on the relative composition of the cyclothems: The Tyne Limestone Formation, the Alston Formation and the Stainmore Formation.

Cyclic sedimentary sequences, known as Yoredale Cyclothems, were deposited as part of the Yoredale Group. A complete cycle (Figure 2.8) includes limestone at its base, as a result of delta abandonment and marine transgression. This is followed by mudstone coarsening upwards into sandstone. The clastic component is derived from delta lobes prograding into the marine environment; the delta top is often colonised

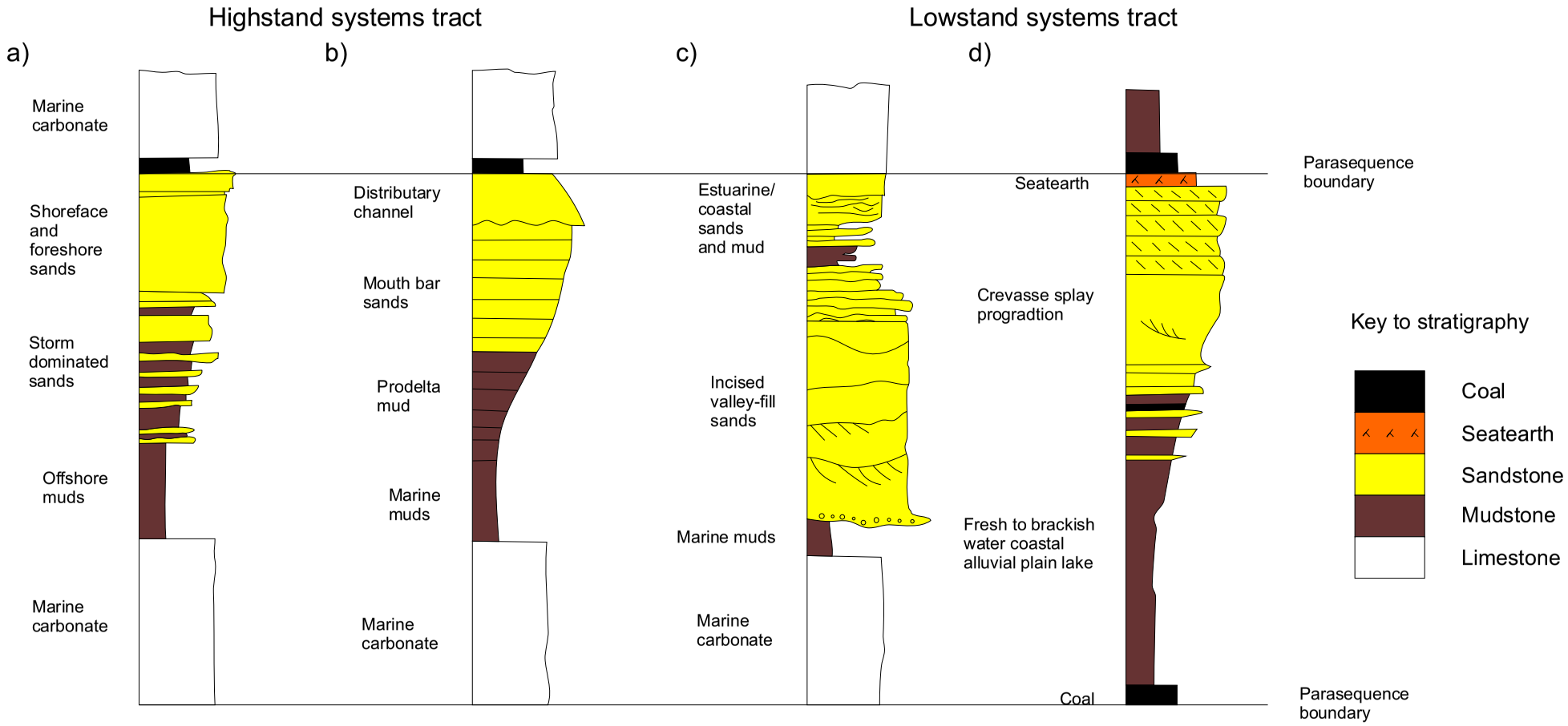


Figure 2.8. Illustrative logs for parasequences within the Yoredale and Pennine Coal Measures Group. a) Shoreline succession. b) typical delta-dominated Yoredale cyclothem. c) Incised valley-fill parasequence. d) Coal measures cyclothem. Within the Yoredale Group, the cyclothems of the Alston Formation are parasequences within the highstand systems tract and the parasequences within the Stainmore Formation form part of the lowstand systems tract (After Tucker *et al.*, 2003; Stone *et al.*, 2010).

by plants forming seatearth (palaeosol) and coals (Waters and Davies, 2006; Lawrence *et al.*, 2007). This coarsening upwards cycle is related to a fall in relative sea level, caused primarily by sediment infill. The cyclothems exhibit a varying degree of complexity across the area and many are incomplete, missing one or more of the characteristic units. Coal is commonly the absent unit. Some sequences are truncated by erosion which is subsequently infilled by fluvial sandstone bodies (Elliot, 1974; 1975). In addition, there is a regional difference in the constitution of the cycles between the Northumberland Trough and the Alston Block (Frost and Holliday, 1980). It has been observed during fieldwork that the cyclothems tend to be thicker in the basin where more accommodation space would have been available and there is a larger proportion of sandstone as a result of its proximity to the palaeocoastline.

#### 2.5.1.1 Cyclothems vs. Sequence Stratigraphy

Sequence stratigraphy techniques provide an alternative approach to established methods for the correlation and interpretation of the cyclic Carboniferous sediments of Northern England. Sequence stratigraphy involves dividing the rock record into a series of cycles relating vertical changes in lithology to corresponding changes in relative sea level during the infilling of a sedimentary basin. The concepts associated with sequence stratigraphy are particularly valuable when high magnitude and frequency fluctuations in sea level occur as a result of global eustasy (Hampson *et al.*, 1997), as is the case in the Northumberland Trough Region during late Carboniferous times (Stephenson *et al.*, 2008).

Sediments are commonly deposited in a predictable pattern from shoreline to open water within a basin. A cycle of sea level fall and rise causes the shoreline to migrate and as a result, a vertical cyclic succession of alternating shallow to deep water sediments will be deposited. A sequence is defined as a relatively conformable succession of genetically related strata bounded by an unconformity or correlative conformity (Sloss, 1963). These unconformities develop when there is a fall in relative sea level and deposition is interrupted. Sequences are subdivided into system tracts, which are defined by their position within the sequence and their relationship with relative sea level (Van Wagoner *et al.*, 1988). Each systems tract is composed of parasequences. Parasequences are defined as conformable successions of related beds bounded by marine-flooding surfaces or their correlative equivalent (Van Wagoner, 1985; Posamentier and Vail, 1988). Parasequences within a systems tract can be grouped into sets of related parasquences which have distinctive stacking characteristics such as progradational, aggredational or retrogradational patterns. These sets of parasequences are often bounded by more significant flooding surfaces (Galloway, 1989). Sedimentary cycles within the Yoredale Group represent parasequences within a parasequence set, with no significant unconformity between them. An example of a parasequence from the Yoredale Group is illustrated in Figure 2.8.

For geological mapping purposes, however, it is not possible to map sequence boundaries due to a lack of outcrop. Individual lithological units can be mapped despite the lack of outcrop due to the weathering

characteristics of the lithologies; for example, the bases of the limestones form features in the landscape which can be mapped. It is then possible to consider the lithologies in terms of cyclothems and sequences.

#### 2.5.1.2 The Tyne Limestone Formation

The Tyne Limestone Formation is restricted to the Northumberland Trough and the Solway Basin, where it is approximately 400 m thick. Limestones and sandstones are absent from parts of the succession, particularly towards the north where the limestones units thin and discontinue (Johnson, 1984). These limestone units also thicken towards the top of the formation as the marine influence is increased (Figure 2.6). Coal seams are well developed towards the east within the lower part of the Tyne Limestone Formation, where there is an eastwards transition to lacustrine and deltaic influenced environments (Figure 2.7c) (Stone *et al.*, 2010).

#### 2.5.1.3 The Alston Formation

The Alston Formation is deposited over much of the Alston Block, up to approximately 250m in thickness. Within the Northumberland Trough and Solway Basin, the formation is considerably thicker ranging from a maximum thickness of approximately 400m in the Northumberland Trough to over 1000m in the Solway Basin (Stone *et al.*, 2010). The quantity and thickness of limestone units are greater in the Alston Formation than within the underlying Tyne Limestone Formation (Figure 2.6) and have resulted from more frequent and enduring marine

incursions (Figure 2.7d) (Ramsbottom, 1977). The limestone units are laterally uniform in thickness, lithology and fossil content.

#### 2.5.1.4 The Stainmore Formation

The Stainmore Formation conformably overlies the Alston Formation and reaches a thickness of approximately 290m upon the Alston Block, increasing to about 500m thick within the Northumberland Trough. Within the Stainmore Formation, the marine influence is less evident such that the limestone units are relatively thin, impersistent and become difficult to distinguish from calcareous sandstones; they are the result of sporadic marine incursions. This distinguishes the Stainmore Formation from the underlying Alston Formation (Waters and Davies, 2006). Deposition of this formation occurred dominantly within a fluvio-deltaic environment (Dunham and Johnson, 1962) (Figure 2.7e) with a cyclical succession of upwards coarsening terrigenous mudstone, to siltstone, to fine sandstones, to very coarse grained erosive channel sandstones, to seatearths and thin coal seams. Mudstones dominate the lower part of the formation with sandstone beds thicker and in greater abundance in the upper part of the formation (Figure 2.6).

### *2.5.2 The Pennine Coal Measures Group*

Sedimentation became more regional during the Bashkirian to Moscovian stages. The sediments of the Pennine Coal Measures Group were deposited within a single province known as the Pennine Basin, bounded by the Southern Uplands to the north and by the Wales-Brabant Massif to

the south (Stone *et al.,* 2010). Deposition occurred within a prograding lacustrine deltaic environment, with wetland forest, delta distributary channels and flood plains (Figure 2.7f). Infrequent marine incursions occurred during periods of eustatic sea level rise, depositing thin layers of sediment (Waters and Davies, 2006). The position of the Northumberland Trough on the northern margin of the Pennine Basin results in the more proximal characteristics of the sediments deposited, Including reduced marine influence and later deposition within the upper delta plain (Fielding, 1984a). The Pennine Coal Measures Group is characterised by upward coarsening successions of grey-black mudstones, grey siltstones, fine to medium-grained sandstone, seatearths and relatively thick coal seams (Figure 2.6). These successions are thinner than those in the underlying Yoredale Group and also more numerous, with at least 40 cycles known in the Coal Measures of County Durham (Stone *et al.,* 2010). The Pennine Coal Measures Group is divided into three formations, the Pennine Lower Coal Measures Formation, the Pennine Middle Coal Measures Formation and the Pennine Upper Coal Measures Formation.

#### 2.5.2.1 The Pennine Lower Coal Measures Formation

The Pennine Lower Coal Measures Formation comprises up to 220 m of sediments, the lower portion of which exhibits similar in stratigraphy to those of the Stainmore Formation of the Yoredale Group. The formation as a whole, however, contains a higher proportion of mudstones and coals. Marine beds are distributed throughout the formation (Fielding, 1984b). Coal seams become thicker and more productive upwards in the

succession with several significant coal seams present (Stone *et al.,* 2010). This change is interpreted to be a consequence of progradation of the delta system, establishing fresh water conditions (Fielding, 1984b).

#### 2.5.2.2 The Pennine Middle Coal Measures Formation

This is the main coal-bearing succession; it is over 180 m thick, with relatively few marine bands. It formed within swamp conditions that were maintained during deposition within the upper delta plain (Fielding, 1984b; Stone *et al.,* 2010).

#### 2.5.2.3 The Pennine Upper Coal Measures Formation

This Formation marks a return to relatively thin coal seams and more numerous marine deposits. The 150 m of sediments that form the Pennine Upper Coal Measures Formation are dominated by grey-black mudstones and grey siltstones (Waters and Davies, 2006; Stone *et al.*, 2010).

### *2.5.3 Warwickshire Group*

In the Canonbie area of the Solway Basin, the Pennine Coal Measures Group is overlain by the Warwickshire Group (Stone *et al.*, 2010). A maximum thickness of ~ 700 m has been estimated from seismic data at the centre of the Solway Syncline (Picken, 1988). The deposits of the Warwickshire Group are represented by stratigraphy deposited in an alluvial plain setting with braided rivers flowing to the north (Besley, 1988; Waters *et al.*, 2007; Morton *et al.*, 2010). Primary depositional red strata are characteristic of the Warwickshire Group; however the

reddening is not uniform and alternates with unreddened strata (Jones and Holliday, 2006).

## 2.6 Variscan structures and tectonic inversion

The Variscan Orogeny, a result of continental collision between the Avalonian part of Laurussia to the north and Gondwana to the south took place during late Carboniferous times. In Northern England, the foreland to the Variscan Orogeny, syn-orogenic deformation (Figure 2.9) was less pervasive than in Southern England behind the Variscan Front. The main deformational stresses affecting the Northumberland Trough Region occurred after Pennsyilvanian deposition, and were mostly, although not exclusively, restricted to the reactivation of pre-existing basement structures (Leeder, 1982).

The major Variscan deformation of the region lies within the Solway Basin. The Carboniferous rocks are folded into a north-north-east trending syncline, the Solway Syncline, which is complimented by the Carlisle Anticline. The Carlisle Anticline is bound in the east by the Brackenhill Fault, a north-east to south-west trending, westerly dipping thrust fault, with evidence of a significant strike-slip component (Chadwick *et al.*, 1995). Several faults have undergone reactivation and a reversal of sense of movement. The Maryport Fault underwent partial reversal and was accompanied by inversion of the southern part of the Solway Basin, including formation of the Crosby Anticline as rollover into the Maryport Fault was tightened (Eastwood, 1930; Chadwick *et al.*, 1993).

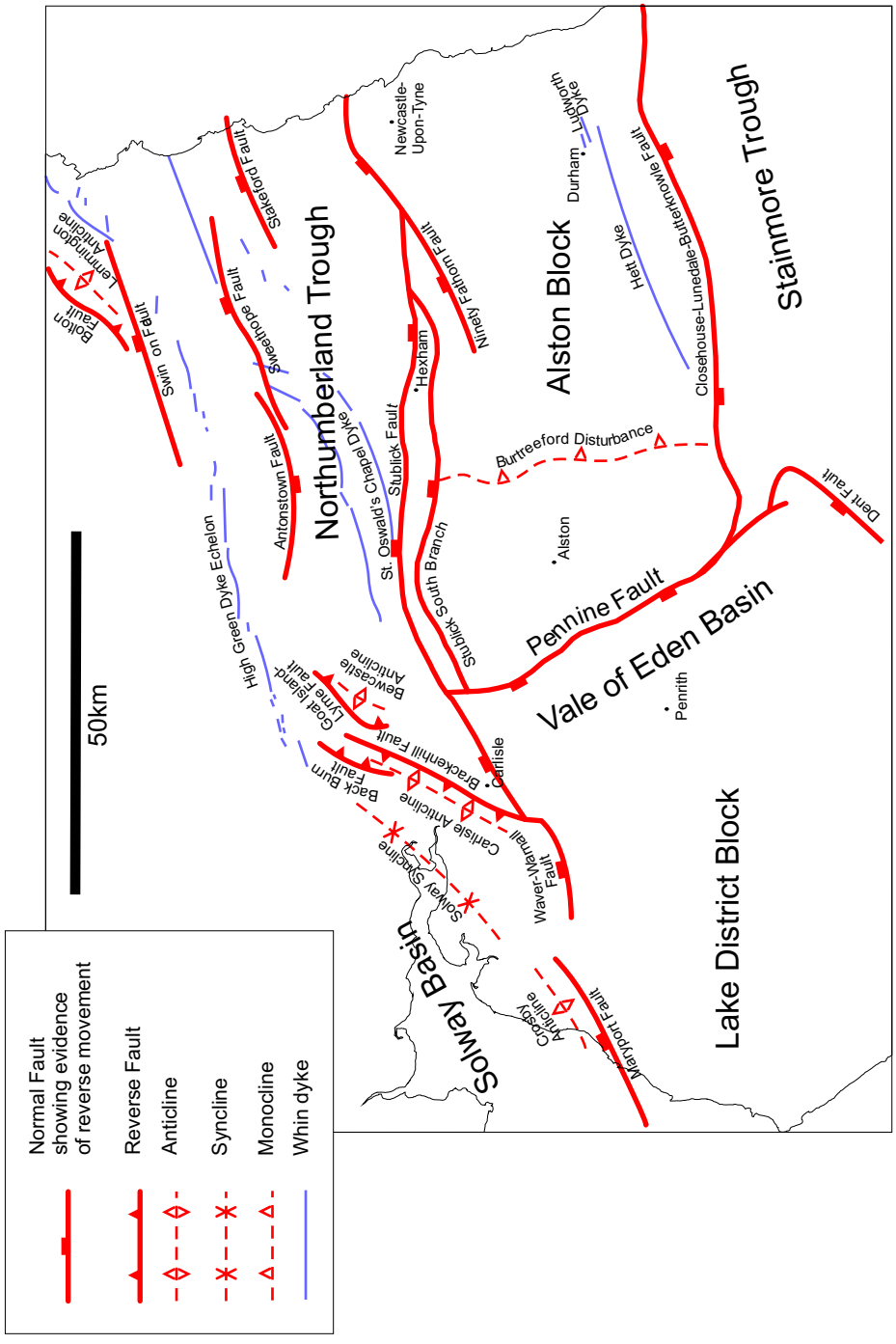


Figure 2.9. Variscan structure of the Northumberland Trough Region including the tholeiitic dyke swarm associated with the Whin Sill. (After Chadwick *et al.* 1995; Liss *et al.* 2004)

The orientation of faults and folds in the northern and western Northumberland Trough indicates the axis of maximum compressive stress having been in the range east-west to east-north-east to west-south-west (Leeder *et al.*, 1989). However, evidence of deformation from south of the Variscan Front presents a case for north-west to south-east Variscan shortening (Gayer *et al.*, 1998). It has been proposed that faults oblique to the north-west to south-east trend have been rotated clockwise in a dextrally transpressive stress field (Woodcock and Rickards, 2003).

There is an absence of thrust faulting in the south and east of the basin compared to the north and west. The Antonstown-Sweethope Fault system, a synthetic-antithetic pair, shows signs of minor inversion including folding of the strata between the faults into an anticline (Chadwick *et al.*, 1995). Collier (1989) suggests that this area of the basin was transported westwards as a single coherent unit. An alternative explanation, that of partitioned transtension, has been suggested such that the south and east of the Northumberland Trough forms part of an extension-dominated domain (De Paola *et al.*, 2005). This explanation also allows for the emplacement of the Whin Sill-swarm and associated Northern England Tholeiitic Dyke-swarm in an extensional regime.

### *2.6.1 The Whin Sill-swarm*

The Whin Sill-swarm, and its associated Northern England Tholeiitic Dyke-swarm, was intruded towards the end of the Variscan Orogeny, when magmatism associated with rifting in the northern foreland of the

Variscan orogenic belt was widespread across Europe (McCann *et al.*, 2006; Timmerman *et al.*, 2009). The Whin Sill-swarm is sub-divided into four geographically separate sills, from north to south these are the Farne Island Sill, the Alnwick Sill, the Great Whin Sill and the Little Whin Sill. The Little Whin Sill can also be distinguished on the basis of its geochemistry (Dunham and Kaye, 1965). The Great Whin Sill has a uniform mineralogy and petrology with little systematic variation. It is a quartz-dolerite with chemical characteristics between alkaline and tholeiitic types. The Little Whin Sill is a quartz-dolerite that contains phenocrysts of olivine and is lower in concentrations of silica, potassium and rubidium but higher in content of total iron than the Great Whin Sill (Dunham and Kaye, 1965). The Little Whin Sill is believed to be near to the composition of the parent magma for the Great Whin Sill (Wadge *et al.*, 1972). K-Ar analysis of the Little Whin Sill produces an age of approximately 300Ma (Miller and Mussett, 1963). This date supports the theory that the Great Whin Sill is a later differentiate of the Little Whin Sill as the age of the Great Whin Sill dolerite has been estimated using K-Ar analysis as 295±6Ma (Fitch and Miller, 1967) and using U-Pb analysis 297.4±0.4Ma (c.f. Armstrong *et al.*, 2001). Four major east-north-east trending doleritic dykes are associated with the Whin Sill-swarm, from north to south these are the Holy Island Dyke, the High Green Dyke, the St Oswald's Chapel Dyke and the Hett Dyke (Liss *et al.*, 2004). It has been suggested that these dykes could be feeders for the Whin sheets (Holmes and Harwood, 1928; Francis, 1982), evidence for this relationship

between the dykes and sills has been demonstrated by studies of the geochemistry (Thorpe and MacDonald, 1985). It has been proposed that the emplacement of the Whin Sill-swarm and its associated Northern England Tholeiitic Dyke-swarm, occurred within an extension-dominated domain of a partitioned transtensional regime (DePaola *et al.*, 2005).

## 2.7 Post-Variscan events

Following the inversion and uplift of the Variscan Orogeny, extension and deposition continued into the Permian and Triassic in Northern England. Later erosion of the Permo-Triassic and younger sediments has removed a large amount of the sedimentary cover.

### *2.7.1 Permian*

Uplift of the Northumberland Trough Region as a result of the Variscan Orogeny resulted in considerable erosion of the Carboniferous strata during the early Permian period resulting in the Permian Unconformity (Stone *et al.,* 2010). This was followed by a period of extension initiated by early Atlantic rifting during the break-up of Pangaea (Bott, 1982a; Anderson *et al.*, 1995). Throughout the whole of the Permian Period structural development and sedimentary deposition occurred independently in the east and west of the Northumberland Trough Region; these areas of lowland being separated by an upland area corresponding to the current position of the Pennines (Stone *et al.,* 2010).

In Western England, early Permian sediments were deposited in the Carlisle Basin, the offshore Solway Firth Basin and the Vale of Eden

Basin. The Vale of Eden Basin was largely developed during the Permian Period with a north-north-west, south-south-east trend (Holliday *et al.*, 2004). The sedimentary deposits of the early Permian Period are represented by the Penrith Sandstone Formation (Murchison and Harkness, 1864) of the Appleby Group. Fine to medium grained, moderately rounded and sorted, red to brown sandstones with large scale cross-stratification and breccia accumulations including coarse, well rounded and sorted grains of Carboniferous origin are observed. These are interpreted as representing an aeolian environment, with palaeowind directions between east and south-east, interbedded with fluvial and alluvial fan deposits (Waugh, 1965; 1970; Arthurton and Wadge, 1981; Holliday *et al.*, 2004).

During the early Permian Period, North-Eastern England formed part of the Southern North Sea Basin, which itself was part of the much larger Southern Permian Basin (Glennie, 1998). The sediments deposited in the Southern Permian Basin are described as the Rotliegend due to their dominant red colour. In North-Eastern England these sediments are yellow at outcrop and form the Yellow Sands Formation. The Yellow Sands Formation consists of basal breccias and aeolian sandstones. Clasts within the breccias are mostly locally sourced sub-Permian material including Carboniferous limestones and mudstones. These fragments are poorly sorted and angular to sub-angular within a sandy matrix (Robson, 1981). The aeolian sandstones are fine to medium grained and poorly cemented (Smith, 1970).

Widespread marine transgression occurred in the mid-late Permian following global sea level rise as a result of Permian deglaciation (Glennie, 1998). The Boreal Ocean to the north flooded into Northern England forming the Zechstein sea in the east (Smith, 1970; 1992; Ruffell *et al.*, 2006) and the Bakevillia sea in the west (Smith *et al.*, 1994). Marine conditions were established in the basins with extensive evaporitic sabkhas in the margin areas.

In the north-west, late Permian age rocks form the Eden Shales Formation. These strata are conformable with the underlying Penrith Sandstone Formation. Sedimentation was more widespread during the late Permian, deposits between the Carlisle Basin and Vale of Eden Basin are continuous, not restricted to the basinal depocentres as was the case in the early Permian (Holliday *et al.*, 2004). The Eden Shales formation consists of red-brown siltstones interbedded with very-fine to medium grained sandstones and occasional breccia and conglomerate horizons of aeolian origin with periodic sheet floods establishing evaporitic conditions (Arthurton and Wadge 1981; Holliday *et al.*, 2001; 2004). These deposits are divided by Holliday et *al.*, 2001 into three recognisable lithostratigraphical units ES1, ES2 and ES3.

In North-Eastern England, a shallow lagoonal environment with periodic flooding and evaporation as a result of transgression of the Zechstein sea lead to a cyclic sequence of carbonates and evaporates (Stone *et al.,* 2010). These cyclic sequences are called English Zechstein sequences (EZ) with four main cycles relating to four major transgressions and regressions

(Smith, 1970). Each EZ sequence consists of evaporitic anhydrite and halite deposited during the lowstand systems tract followed by clastic rocks then carbonates and sulphates as transgression occurs (Stone *et al.,* 2010).

### *2.7.2 Triassic*

Few sediments younger than those already described are preserved in the north-east of England (Chadwick *et al.*, 1995). During the early Triassic Period the basin development established in the Carlisle and Vale of Eden basins in mid-late Permian times continued with two to three en-echelon east-north-east, west-south-west to north-east, south-west trending synclines acting as depositional centres (Holloway, 1985).

Sediments of the Sherwood Sandstone Group have a conformable gradational boundary with the underlying Eden Shales Formation, and at the basin margins rest unconformably on the youngest Carboniferous deposits (Holliday *et al.*, 2004). Deposits are comprised of very-fine to fine grained red-brown fluvial sandstones, which have a locally patchy blue-green colour, interbedded with siltstones and mudstones (Holliday *et al.*, 2001) deposited by the Budleighensis River (Wills, 1956; Warrington and Ivimey-Cook, 1992; Hounslow and Ruffell, 2006). Towards the top of the Sherwood Sandstone Group aeolian influences become more dominant (Arthurton *et al.*, 1978; Hounslow and Ruffell, 2006).

A return to coastal and marine conditions resulting from marine transgression is observed in the deposits of the mid-late Triassic Period,

the Mercia Mudstone Group (Holloway, 1985). The Mercia Mudstone Group is comprised of red-brown mudstones with frequent siltstone layers occasionally interbedded with fine grained sandstones. These deposits are interpreted as having been deposited in shallow water bodies such as broad playa lakes and intertidal sabkhas (Holliday *et al.*, 2004).

### *2.7.3 Erosion*

Post-Triassic evolution of the Northumberland Trough Region is uncertain due to the absence of any rocks younger than Triassic in age, with the exception of an isolated deposit of earliest Jurassic age in the Carlisle Basin (Holliday, 1993a). Evidence that these rocks have been uplifted and removed by erosion in Cenozoic times is provided by fission track dating (Fleischer and Price, 1964) applied to apatite from samples in Northern England (Green, 1986; Lewis *et al.*, 1992). Apatite fission track analysis is used to determine the thermo-tectonic history by ascertaining maximum palaeotemperatures and the time at which cooling from these temperatures began (Green *et al.*, 1989; Lewis *et al.*, 1992). Results indicate palaeotemperatures in the region of 70-125°C (Green, 1986) and a time of cooling of 65±5Ma (Lewis *et al.*, 1992). Green, (1986) suggest two thermo-tectonic histories consistent with these results. Heating as a result of long-term burial with a normal geothermal gradient followed by 3-4km of uplift and erosion, this argument is supported by Lewis *et al.*, (1992) who claim that evidence suggests that the geothermal gradient was not elevated during the Late Cretaceous and therefore predict 3km of uplift and erosion. Alternatively, short lived burial with heating of the geotherm

as a result of igneous activity accompanied by uplift and erosion in the region of 1-2km. More recently evidence of elevated heat flow from borehole studies provides data that indicate palaeogeothermal gradients that are 50-100% higher than present-day values, which has led Green (2002) to propose exhumation and erosion of between 0.7 km from mountainous areas and 1.5 – 2 km from coastal areas. It has been suggested (Chadwick *et al.,* 1995) that the regional uplift is a result of the opening of the Atlantic Ocean in the west and subsidence of the North Sea Basin to the east began during the Miocene times.

## 2.8 Summary

The Northumberland Trough Region has a complex geological history. A summary of the tectonic and stratigraphic evolution of the region is provided in Figure 2.10.

The Iapetus Suture Zone is a major crustal shear zone, which formed as a result of the convergence and collision of Laurentia and Avalonia as the Iapetus Ocean was closed by the Caledonian Orogeny. As a result of the compressional tectonic events of the Caledonian Orogeny, the late Devonian and Carboniferous rocks of the Northumberland Trough Region overlie the earlier Palaeozoic basement rocks unconformably. The North Pennines Batholith, underlying the Alston Block, was one of a number of granitoid igneous intrusions that were emplaced towards the end of the Caledonian Orogeny. The North Pennines Batholith is a transitional granitoid dated to approximately 410±10Ma.

| Erathem Era | System Period | Series Epoch | Stage Age | Age Ma |
|---|---|---|---|---|
| Mesozoic | Cretaceous | Upper | Maastrichtian | 65.5 ±0.3 |
| | | | Campanian | 70.6 ±0.6 |
| | | | Santonian | 83.5 ±0.7 |
| | | | Coniacian | 85.8 ±0.7 |
| | | | Turonian | 89.3 ±1.0 |
| | | | Cenomanian | 93.5 ±0.8 |
| | | Lower | Albian | 99.6 ±0.9 |
| | | | Aptian | 112.0 ±1.0 |
| | | | Barremian | 125.0 ±1.0 |
| | | | Hauterivian | 130.0 ±1.5 |
| | | | Valanginian | 136.4 ±2.0 |
| | | | Berriasian | 140.2 ±3.0 |
| | Jurassic | Upper | Tithonian | 145.5 ±4.0 |
| | | | Kimmeridgian | 150.8 ±4.0 |
| | | | Oxfordian | 155.7 ±4.0 |
| | | Middle | Callovian | 161.2 ±4.0 |
| | | | Bathonian | 164.7 ±4.0 |
| | | | Bajocian | 167.7 ±3.5 |
| | | | Aalenian | 171.6 ±3.0 |
| | | Lower | Toarcian | 175.6 ±2.0 |
| | | | Pliensbachian | 183.0 ±1.5 |
| | | | Sinemurian | 189.6 ±1.5 |
| | | | Hettangian | 196.5 ±1.0 |
| | Triassic | Upper | Rhaetian | 199.6 ±0.6 |
| | | | Norian | 203.6 ±1.5 |
| | | | Carnian | 216.5 ±2.0 |
| | | Middle | Ladinian | 228.0 ±2.0 |
| | | | Anisian | 237.0 ±2.0 |
| | | Lower | Olenkian | 245.0 ±1.5 |
| | | | Induan | 249.7 ±0.7 |
| Palaeozoic | Permian | Lopingian | Changhsingian | 251.0 ±0.4 |
| | | | Wuchiapingian | 253.8 ±0.7 |
| | | Guadalupian | Capitanian | 260.4 ±0.7 |
| | | | Wordian | 265.8 ±0.7 |
| | | | Roadian | 268.0 ±0.7 |
| | | Cisuralian | Kungurian | 270.6 ±0.7 |
| | | | Artinskian | 275.6 ±0.7 |
| | | | Sakmarian | 284.4 ±0.7 |
| | | | Asselian | 294.6 ±0.8 |
| | Carboniferous | Pennsylvanian Upper | Gzhelian | 299.0 ±0.8 |
| | | | Kasimovian | 303.9 ±0.9 |
| | | Pennsylvanian Middle | Moscovian | 306.5 ±1.0 |
| | | Pennsylvanian Lower | Bashkirian | 311.7 ±1.1 |
| | | Mississippian Upper | Serpukhovian | 318.1 ±1.3 |
| | | Mississippian Middle | Visean | 326.4 ±1.6 |
| | | Mississippian Lower | Tournasian | 345.3 ±2.1 |
| | Devonian | Upper | Famennian | 359.2 ±2.5 |
| | | | Frasnian | 374.5 ±2.6 |
| | | Middle | Giventian | 385.3 ±2.6 |
| | | | Eifelian | 391.8 ±2.7 |
| | | Lower | Emsian | 397.5 ±2.7 |
| | | | Pragian | 407.0 ±2.8 |
| | | | Lockovian | 411.2 ±2.8 |
| | Silurian | Pridoli | | 416.0 ±2.8 |
| | | Ludlow | Ludfordian | 418.7 ±2.7 |
| | | | Gorstian | 421.3 ±2.6 |
| | | Wenlock | Homerian | 422.9 ±2.5 |
| | | | Sheinwoodian | 426.2 ±2.4 |
| | | Llandovery | Telychian | 428.2 ±2.3 |
| | | | Aeronian | 436.0 ±1.9 |
| | | | Rhuddanian | 439.0 ±1.8 |
| | Ordovician | Upper | Hirnantian | 443.7 ±1.5 |
| | | | Stage 6 | 445.6 ±1.5 |
| | | | Stage 5 | 455.8 ±1.6 |
| | | Middle | Darriwilian | 460.9 ±1.6 |
| | | | Stage 3 | 468.1 ±1.6 |
| | | Lower | Stage 2 | 471.8 ±1.6 |
| | | | Tremadocian | 478.6 ±1.7 |
| | | | | 488.3 ±1.7 |

Tectonics

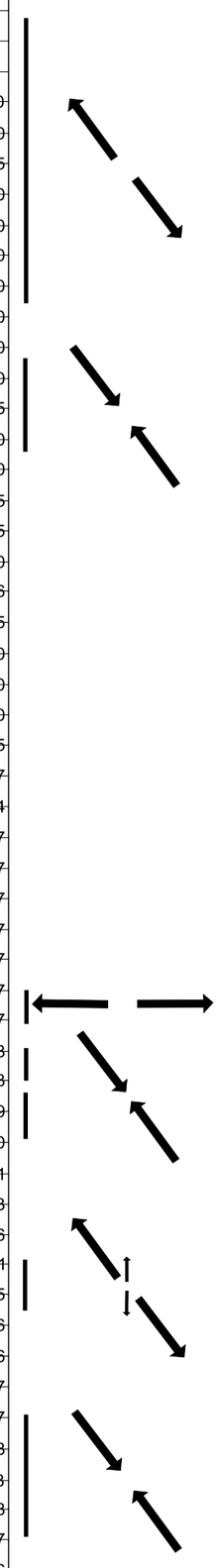

Sedimentation

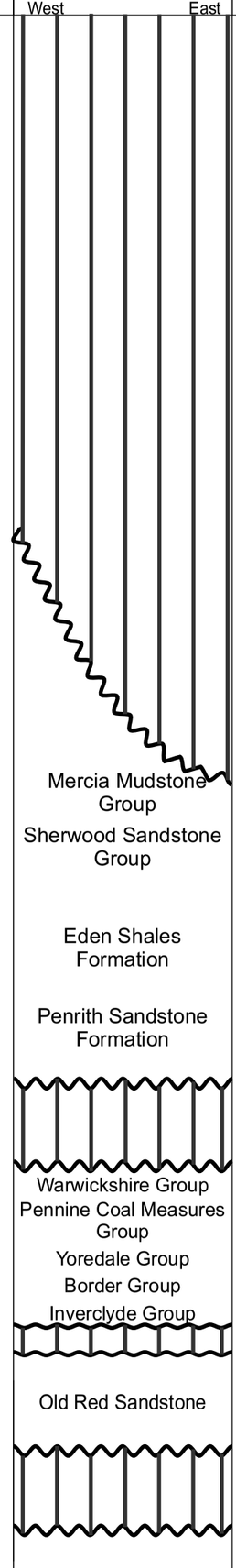


Magmatism




Remarks including Major Regional Events

Opening of the Atlantic Ocean in the west and subsidence of the North Sea Basin to the east (Ziegler, 1990).

Uplift of the North Sea Dome (Ziegler 1990).

Erosion of Permo-Triassic and younger sediments has removed a large amount of sedimentary cover. The thickness and extent of rocks that have been eroded is estimated to be up to 3km (Green 2002). There are considerably more Triassic and Jurassic sediments preserved in the north-west of England than in the north-east of England (Chadwick *et al*., 1995).

In late Permian to early Triassic times, there was a transition from a predominantly marine to a continental environment across northern England (Holliday *et al*., 2004).

Variscan Orogeny- Collision between the Avalonian part of Laurussia to the North and Gondwana to the South. Uplift of the Carboniferous basins resulted in considerable erosion of the Carboniferous strata during the Permian Period (Chadwick *et al*., 1995).

The extensional phase of the Northumberland Trough's evolution is characterised by a close association between sedimentation and contemporaneous faulting (Chadwick *et al*., 1995).

Acadian Orogeny - Final closure of the Iapetus Ocean as Avalonia is shifted dextrally against Laurentia, as a result of the collision between Avalonia and Amorica to the south (Soper *et al*., 1992).

Legend


Figure 2.10. Tectonostratigraphic chart, summarising the structural and stratigraphical development of the Northumberland Trough Region during the Ordovician to Cretaceous Periods.

Crustal extension was initiated in late Devonian to early Carboniferous times. The east-north-east to west-south-west trend of the basins in the Northumberland Trough region is influenced by the underlying Iapetus Suture Zone. It has been suggested that the major faults responsible for the formation of the Northumberland Trough and the Solway Basin are a reactivation of the basement shear zone. The structural highs of the Lake District Block and Alston Block also trend east-north-east to west-south-west, which is consistent with the trend of their underlying granitoid intrusions.

The syn-extensional strata of were mostly restricted to the basins. Post-extension deposition became more regional as a result of the reduced structural influence on the basins and the onset of regional subsidence. Sedimentation mostly kept pace with contemporaneous faulting and post-extensional subsidence. Post-extensional deposition includes cyclic sedimentary sequences known as Yoredale Cyclothems. A cycle of relative sea level fall and rise results in a predictable pattern of sedimentation as the shoreline migrates. A vertical cyclic succession of alternating deep to shallow water sediments are deposited.

Sedimentation ceased in the late Carboniferous times as the Northumberland Trough Region was uplifted and inverted by the Variscan Orogeny. Variscan deformation in Northern England was much less pervasive than in Southern England and was mostly restricted to reactivation of faults along pre-existing lines of weakness. Towards the end of the Variscan orogeny, the Whin Sill, a dyke and sill complex was

intruded. The discordant nature of the intrusion in places helps to constrain the timing of structural events.

Variscan uplift of the basins resulted in considerable erosion of the Carboniferous strata resulting in the Permian Unconformity. When sedimentation recommenced during the Permian Period marine conditions were established over much of Northern England. In late Permian to early Triassic times there was a transition from a predominantly marine to continental environment. There are considerably more sediments of Triassic age preserved in the north-west than in the north-east of England. Regional uplift as a result of opening of the Atlantic Ocean to the west and subsidence of the North Sea Basin to the east in Cenozoic times led to erosion that removed as much as 2km of the Permo-Triassic and younger sediments.

The present day structure of the region retains the basin and block architecture resultant from the Carboniferous extension.

# 3 Data analysis: Regional cross-sections, seismic analysis and borehole data.

Data for the analysis of the development of the Northumberland Trough Region has been provided by the British Geological Survey (BGS) in the form of seismic, gravity and borehole data. Interpretation of these data have been carried out whilst consideration has been given to previous interpretation and analyses. Interpretations of seismic data over the Northumberland Trough Region carried out by the BGS has been used to develop a number of structural and stratigraphic cross-sections across the region that will provide input parameters for the modelling and will also form the basis for a comparison with the model results. This is complimented by an analysis of some seismic data from the Northumberland Trough and the Alston Block carried out as part of this study. In addition, gravity data has been used, particularly in the analysis of the North Pennines Batholith beneath the Alston Block. Borehole data provides information about the stratigraphy within the basin, which will allow interpretations to be made about the depositional environment, including palaeobathymetry and sediment density, as well as providing estimates of porosity which have been used to carry out burial history modelling. This chapter will also provide a regional interpretation of the evolution of the Northumberland Trough Region.

### *3.1.1 Seismic Data*

Good quality seismic data have been acquired over much of the Northumberland Trough Region as a result of the economic importance of the Carboniferous age rocks in the region. These data have been interpreted by BGS geoscientists and made available for this study in the form of depth and structural contours, and isopach maps for each formation, for example, Figure 3.1 shows depth and structural contours to the top of the pre-Carboniferous basement. In addition a number of seismic lines have been re-interpreted as part of this study to compliment the data provided by the BGS. The location of the seismic lines is illustrated in Figure 3.2. Additionally the seismic data used as part of this study are summarised in Table 3.1.

| Line | Data Type | Vintage | Date Acquired |
|---|---|---|---|
| TOC-87-V111 | Post-stack Seg-Y and Navigation | Horizon 1987 | 27/02/2009 |
| TOC-87-V112 | Migrated Stack | Horizon 1987 | |
| TOC-87-V113 | Migrated Stack | Horizon 1987 | |
| TOC-86-V103 | Migrated Stack | SSL 1986 | |
| TOC-88-V118 | Migrated Stack | Geco 1988 | |
| TOC-88-V119 | Migrated Stack | Geco 1988 | |
| TOC-88-V123 | Migrated Stack | Geco 1988 | |
| BGS-86-02 | Coherency Filtered & | 1986 | 20/06/2008 |
| BGS-86-03 | No Post-stack Processing & Migration, No Post-Migration Processing | 1986 | |
| BGS-86-04 | CMP Stack, Filtered & | 1986 | |
| BGS-86-05 | Migrated Stack | 1986 | |
| BGS-86-06 | | 1986 | |

Table 3.1. Summary of Seismic Data

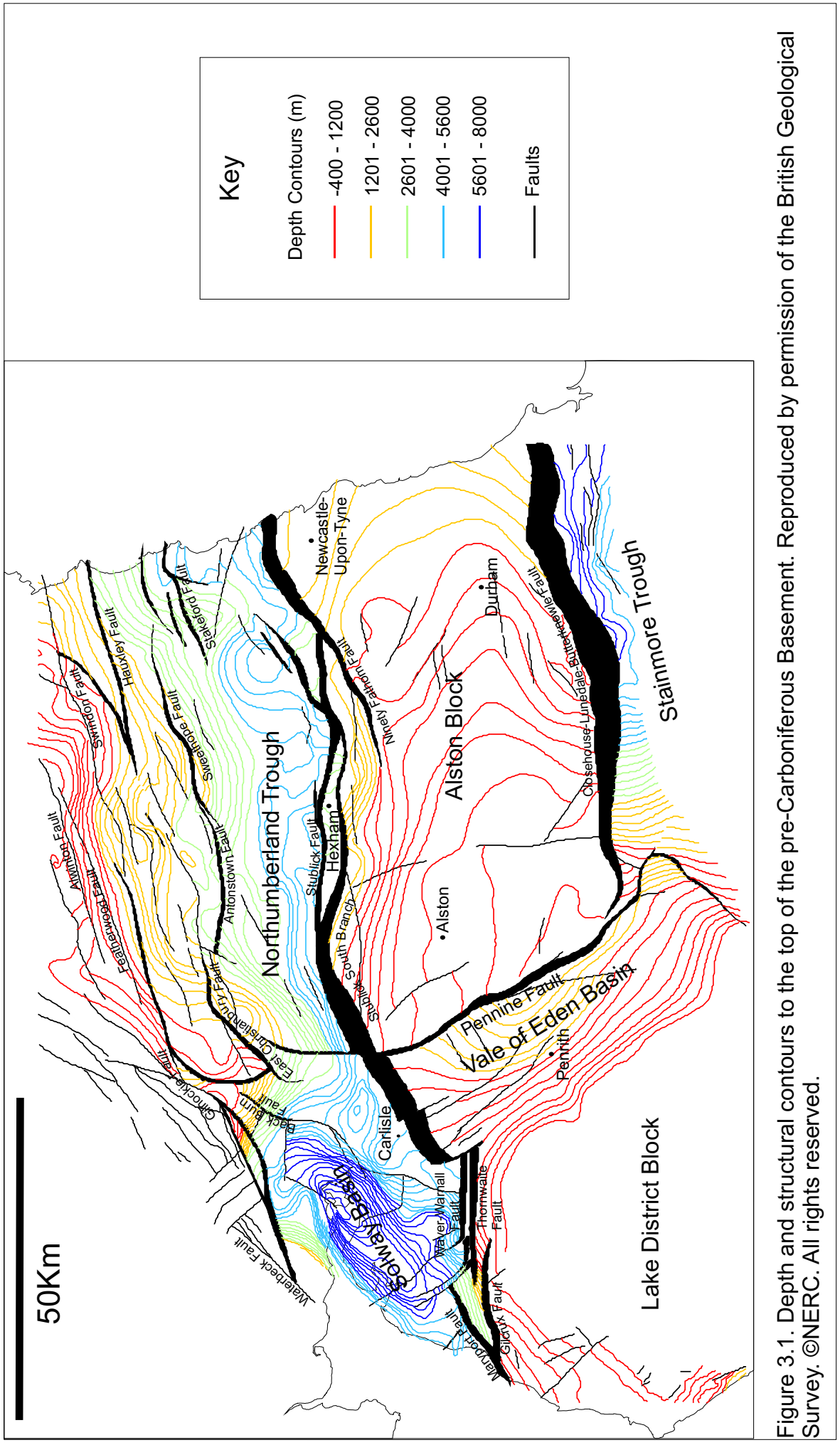


Figure 3.1. Depth and structural contours to the top of the pre-Carboniferous Basement. Reproduced by permission of the British Geological Survey. ©NERC. All rights reserved.

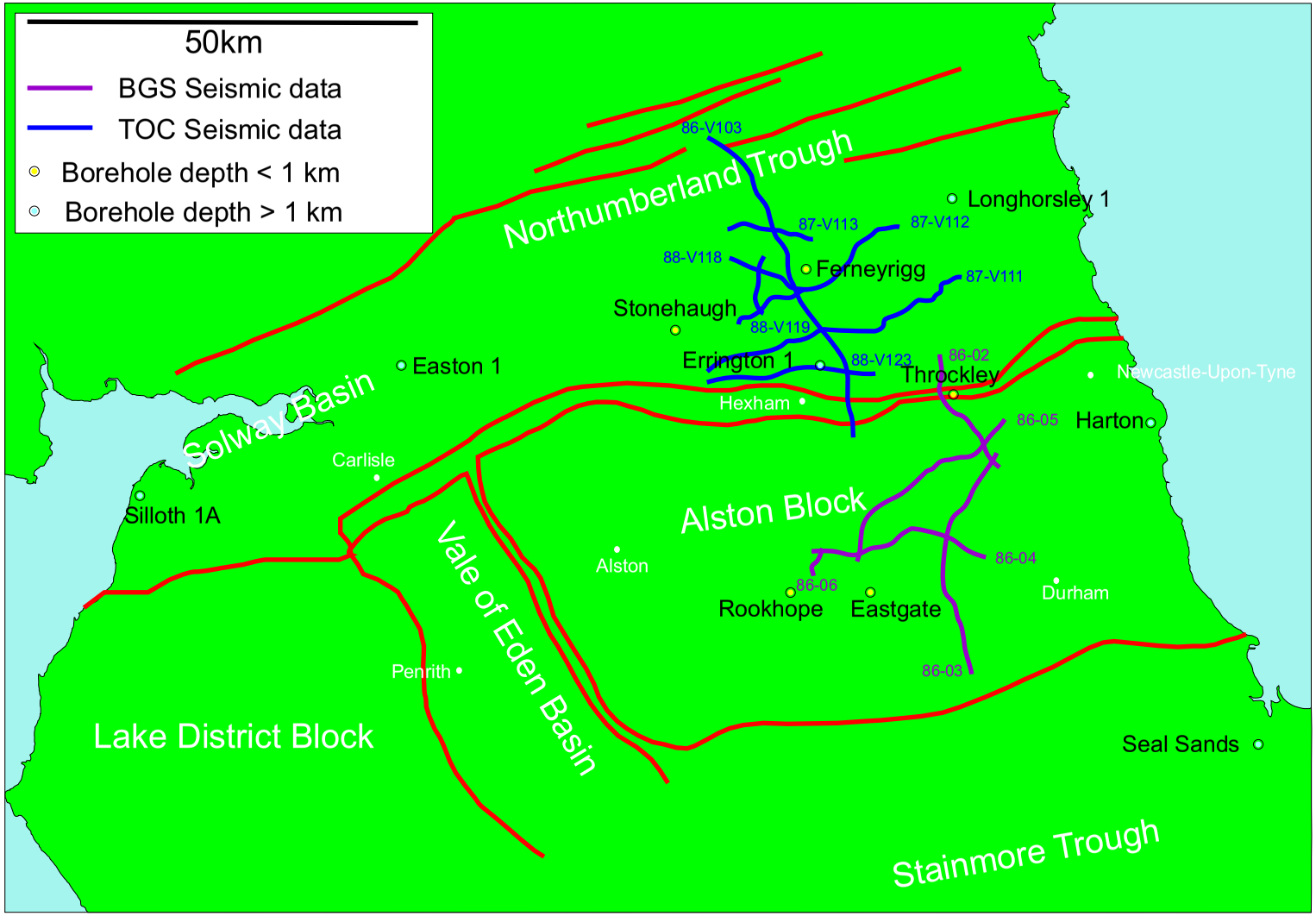


Figure 3.2. Location and position of the seismic lines and boreholes interpreted as part of this study. The TOC seismic lines were shot by Tricentrol/Arco over the Northumberland Trough for hydrocarbon exploration. The BGS (British Geological Survey) lines were shot over the Alston Block. TOC88-V103 and BGS86-02 both cross the basin-bounding Stublick-Ninety Fathom Fault System. The boreholes have been used to examine the stratigraphy of the Northumberland Trough Region and correlate it across the study area.

### *3.1.2 Borehole Data*

There are several boreholes that have been drilled in the Northumberland Trough Region for a number of purposes, including hydrocarbon exploration, coal exploration, mineral exploration, hydrogeology, geothermal energy potential and regional geology studies.

The locations of the borehole data used as part of this study are presented in Figure 3.2. The data from several of these boreholes have been used for burial history analysis.

The Seal Sands borehole is one of the deepest onshore boreholes in Britain, drilled to a depth of 4170 m. It is located in the east of the study area within the Stainmore Trough. On the Alston Block, three boreholes, the Harton, Rookhope and Eastgate boreholes, have been studied. The Harton borehole is a deep hydrocarbon exploration well on the eastern edge of the Alston Block, where it achieves a maximum depth of 1769 m. The Rookhope borehole was drilled to investigate the zonal mineralisation patterns upon the Alston Block (Dunham *et al.*, 1965). This was the first borehole to intercept the North Pennines Batholith, achieving a total depth of 808 m. The Eastgate borehole was drilled by Newcastle University to investigate the geothermal potential beneath the Alston Block. The borehole penetrates the North Pennines Batholith and achieves a total depth of 975 m.

Within the Northumberland Trough, two deep hydrocarbon exploration wells, Longhorsley 1 and Errington 1, have been studied. These boreholes

achieve total depths of 1829 m and 2200 m, respectively. In addition, several shallow boreholes with total depths less than 1000 m have been drilled by the BGS. These include, from east to west, the Throckley, Fernyrigg and Stonehaugh boreholes, which attain total depths of 605 m, 458 m, and 601 m, respectively.

In the Solway Basin, two hydrocarbon exploration wells have been studied. Easton 1 has a maximum depth of 2200 m and Silloth 1A, at the western edge of the onshore Solway Basin, has a maximum depth of 1342 m. The boreholes used as part of this study are summarised in Table 3.2.

| Borehole | Data Type | Depth | Date Acquired |
|---|---|---|---|
| Archerbeck | Stratigraphy | 0-1363m | 27/02/2009 |
| Easton1 | Gamma-ray and Stratigraphy | 1050-2200m | 27/02/2009 |
| | Data missing between 1830&1900m | | |
| Errington1 | Gamma-ray and Stratigraphy | 0-2300m | 03/03/2009 |
| Ferneyrigg | Gamma-ray and Stratigraphy | 0-450m | 27/02/2009 |
| Harton | Stratigraphy | 0-1796m | 27/02/2009 |
| Longhorsley | Gamma-ray and Stratigraphy | 1300-1750m | 03/03/2009 |
| Rookhope | Gamma-ray and Stratigraphy | 0-600m | 27/02/2009 |
| Seal Sands | Gamma-ray and Stratigraphy | 0-740m | 27/02/2009 |
| Silloth 1A | Gamma-ray and Stratigraphy | 0-1339m | 27/02/2009 |
| Stonehaugh | Gamma-ray and Stratigraphy | 0-600m | 27/02/2009 |
| Throckley | Gamma-ray and Stratigraphy | 0-600m | 27/02/2009 |

Table 3.2. Summary of Borehole Data

### *3.1.3 Gravity Data*

The BGS gravity dataset for Southern Scotland and Northern England comprises onshore measurements from land stations with a distribution density of ~1 station per 1 km$^2$ and offshore measurements from sea-

bottom and marine observations (Kimbell *et al.*, 2006). The combined land and marine gravity data have been gridded on a 0.5 km mesh using the surface algorithm from the Generic Mapping Tools package (Wessel and Smith, 1991). Figure 3.3 illustrates the gravity data for the study area and the location of the gravity profiles within the study area. Profiles 1-4 are gravity models produced by Kimbell *et al.* (2006) using the BGS GRAVMAG program (Busby, 1987; Pedley, 1991). These models were produced assuming a simple density structure where the upper crustal density is 2780 $kgm^{-3}$ between 0 and 20 km depth, lower crustal density is 3000 $kgm^{-3}$ between 20 km depth and the Moho and the density of the upper mantle is 3300 $kgm^{-3}$ (Kimbell *et al.*, 2006). Profiles 5-6 are produced from three-dimensional modelling of the Caledonian granites within the pre-Carboniferous basement carried out by Kimbell *et al.* (2006). The Gmod wavenumber domain program (Dabek and Williamson, 1999) was used to calculate the gravity effect of the sedimentary cover in order that its effect could be removed from the models. The geometry of the granite bodies were then determined using the spatial-domain GM3D program (Rollin, 1988).

## 3.2 Development of regional cross-sections

The analyses of surface data and subsurface geophysical data have been collated within a GIS environment and used to produce regional cross-sections showing the present day structure and stratigraphy of the study area.

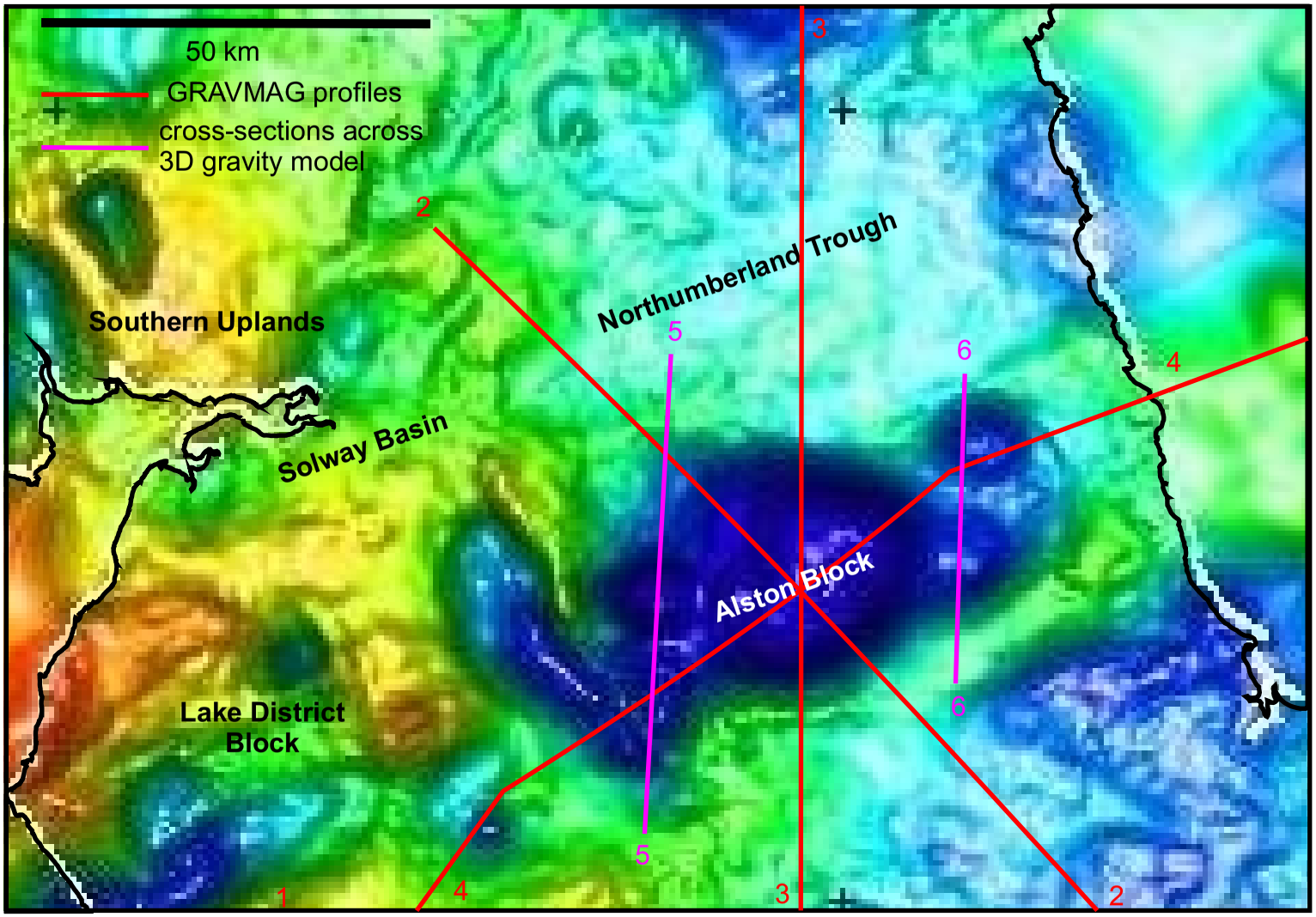


Figure 3.3. Gravity data for Northern England and Southern Scotland including location and position of the gravity profiles. The Alston Block is characterised by an area of low gravity. The Solway Basin is characterised by a positive gravity anomaly and the Northumberland Trough appears to exhibit little effect on the gravity field. Profiles 1-4 are two-dimensional models produced using BGS GRAVMAG program. Profiles 5 and 6 are cross-sections through a three-dimensional model of the North Pennines Batholith within the pre-Carboniferous basement.

### *3.2.1 Method of Construction*

The cross-sections were constructed by plotting manually the depth data for each formation and the major fault structures along the selected path of the section at a 1:100,000 scale. A vertical exaggeration of 300% was used to enhance the structural features within the cross-sections.

The locations of the interpreted sections are highlighted in Figure 3.4. Sections A-A' to I-I' strike approximately north to south and are perpendicular to the main structural trends within the region, including the basin controlling fault systems. Sections J-J' and K-K' strike from west to east and have been constructed to tie all of the sections together in order to enable three-dimensional interpretation of the region to be carried out.

The datasets used to produce the cross-sections are divided into formations using the stratigraphical nomenclature of Chadwick *et al.* (1995) who performed the initial interpretation. Some of this nomenclature has subsequently been revised (Stone *et al.*, 2010). The correlation between the old and new stratigraphical nomenclature summarised in Figure 2.5 has been included in the key provided with the cross-sections (e.g. Figure 3.5). The sections below provide a summary of each of the cross-sections constructed as well as nearby boreholes in order to provide an overview of the variation in structure and stratigraphy across the Northumberland Trough Region.

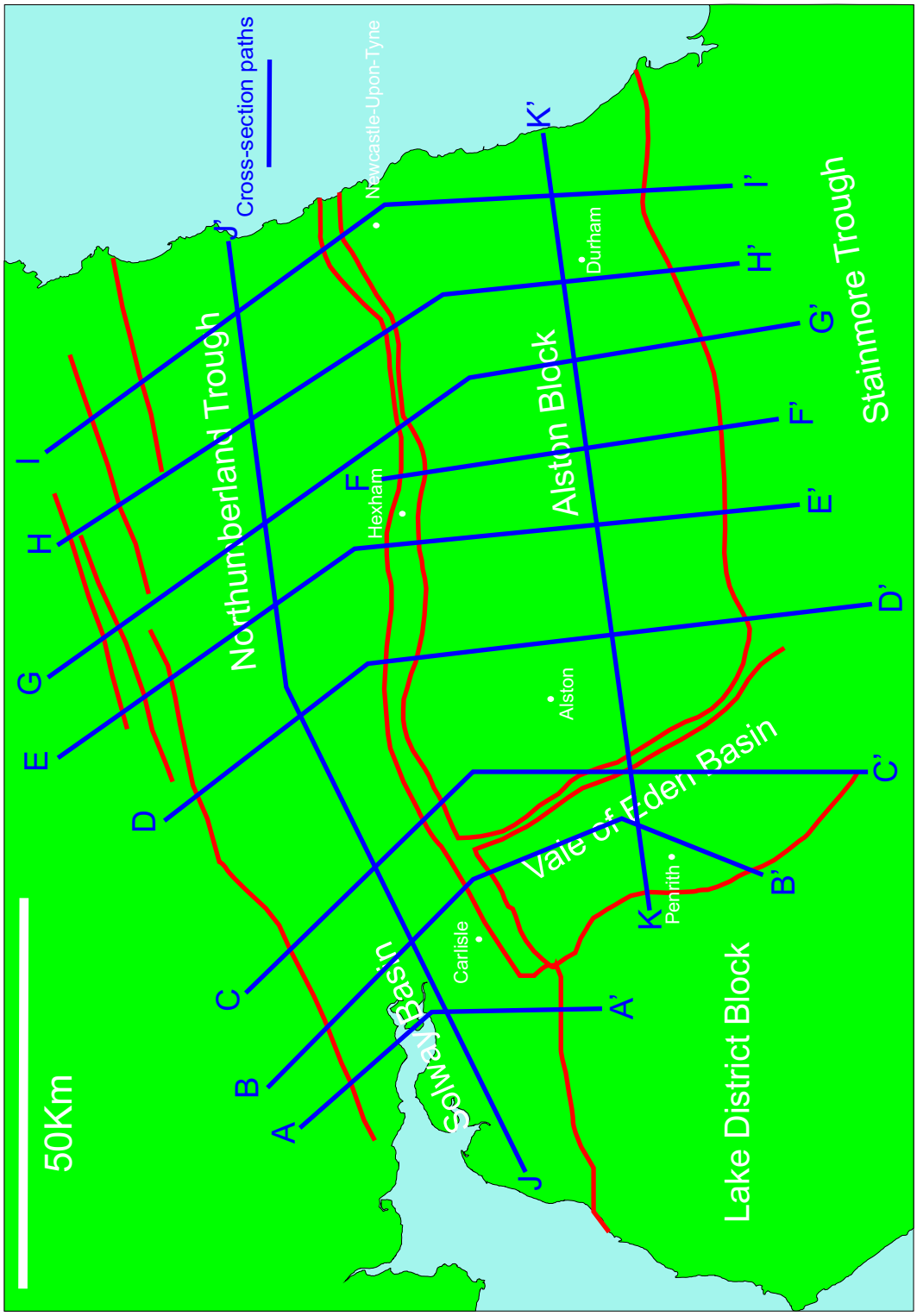


Figure 3.4. Location and position of the cross-sections. Cross-sections A-A' to I-I' are perpendicular to the strike of the main structural features within the Northumberland Trough Region. Cross-sections J-J' and K-K' have been constructed to tie the data together ready for three dimensional interpretation.

### *3.2.2 Section A - A'*

Cross-section A-A' (Figure 3.5) is located in the west of the region. It covers a distance of 44 km and illustrates the structure and stratigraphy of the central Solway Basin.

Development of the Solway Basin was controlled by movement of the Waver-Warnall Fault and the Thornthwaite Fault, which are en-echelon continuations of the Maryport Fault (Chadwick and Evans, 2005). The Thornthwaite Fault has a maximum throw of 3.5 km at this location. The maximum throw on the Waver-Warnall fault is 0.86 km at this locality, and shows evidence of re-activation with a reverse sense of movement. There is no evidence of faulting at the northern margin of the basin, generating an asymmetrical half-graben. The Solway basin attains a maximum depth of 8 km in the centre of the basin, which has been subjected to folding.

The syn-rift deposits of the Lyne Formation and the Fell Sandstone Formation thicken towards the basin controlling faults. The depocentre of the post-rift Carboniferous sequences has moved to the centre of the basin. All of the rocks of Carboniferous age are affected by the folding. Permian and Triassic sequences unconformably overlie the Carboniferous successions. These have not been subjected to folding.

Folding of the Carboniferous stratigraphy and the compressional reactivation of faulting suggest that the Solway Basin was subjected to

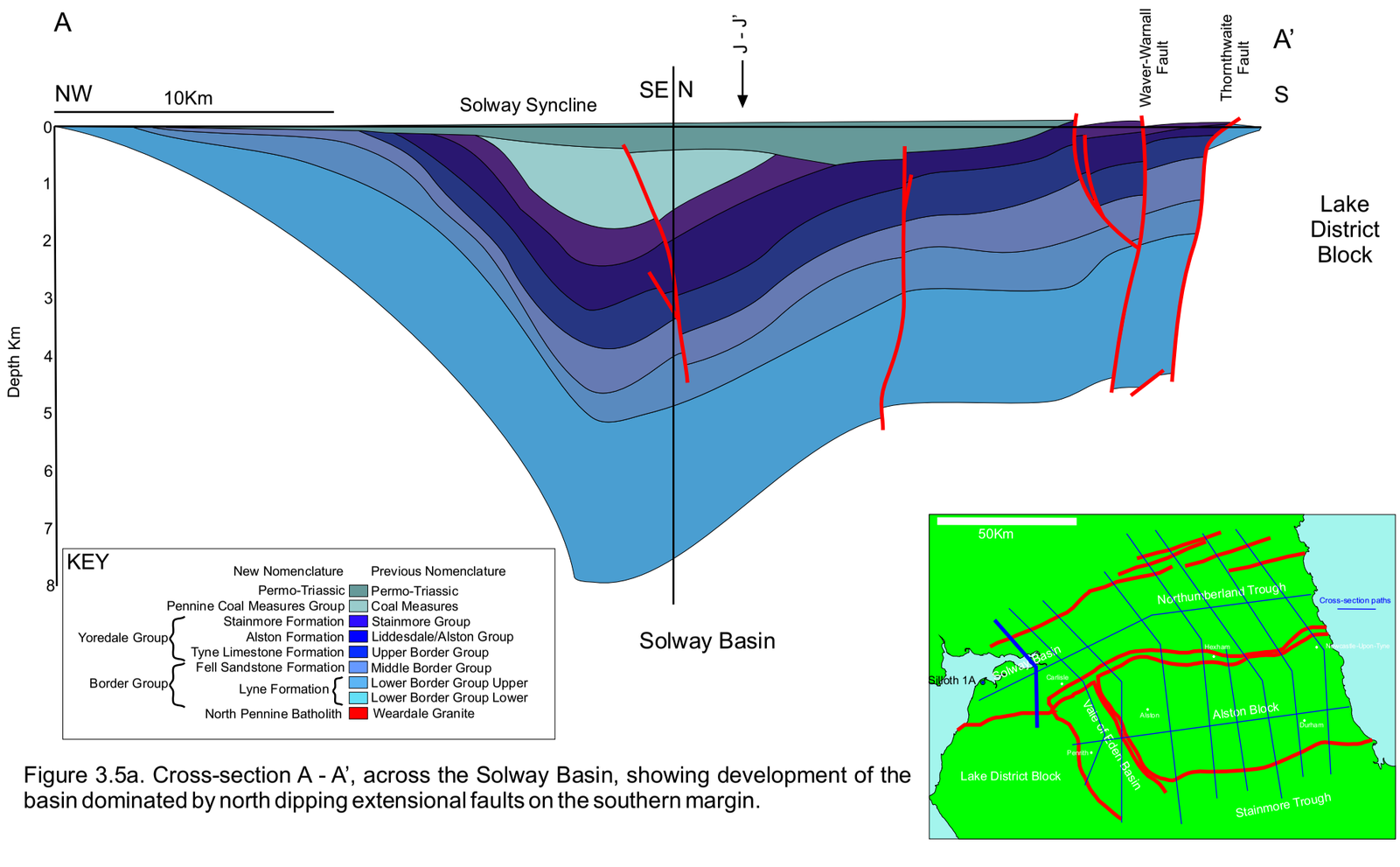


Figure 3.5a. Cross-section A - A', across the Solway Basin, showing development of the basin dominated by north dipping extensional faults on the southern margin.

Figure 3.5b. Silloth 1A borehole stratigraphy and gamma-ray logs. The Silloth 1A borehole provides a near complete section through the Permian and Triassic strata deposited within the Carlisle

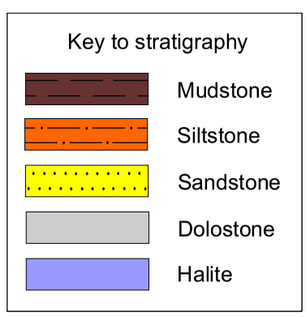


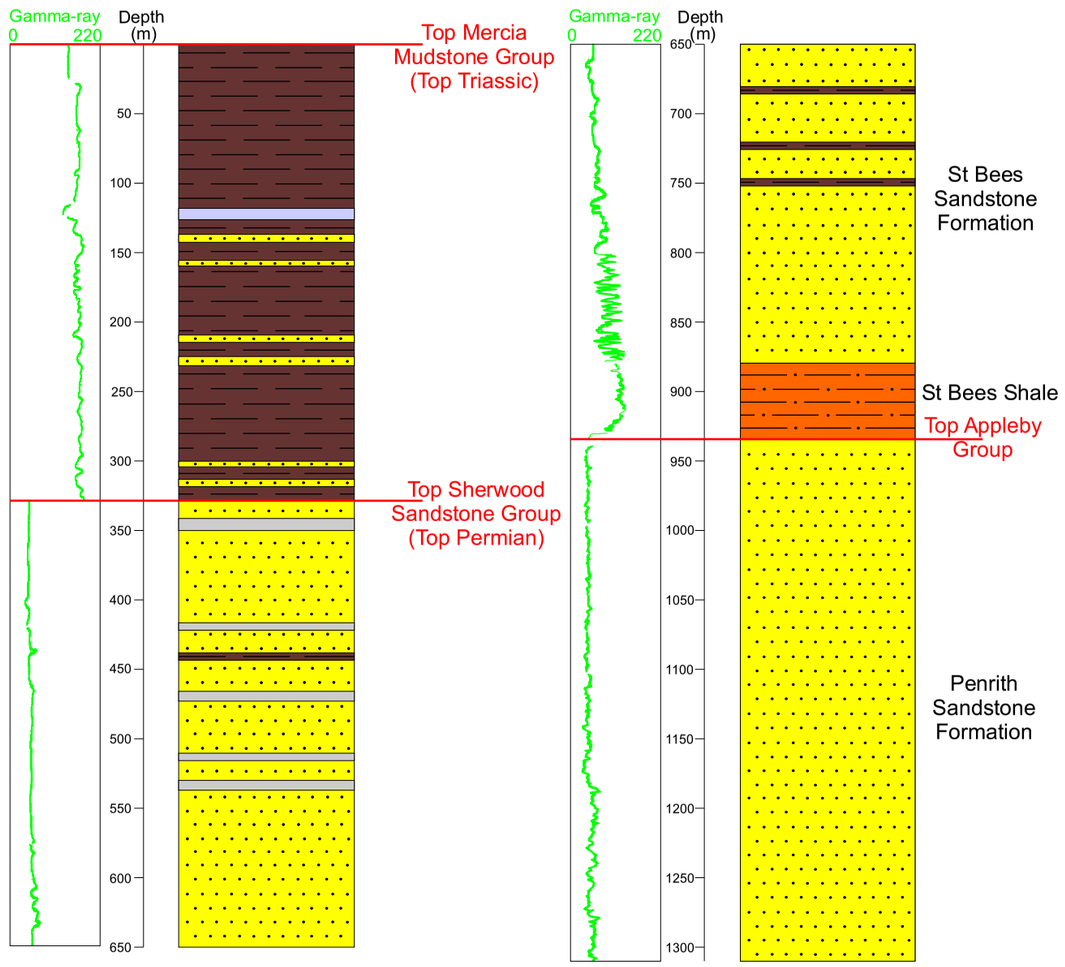


Data analysis: Regional cross-sections, seismic analysis and borehole data

compression related to the Variscan Orogeny creating the Solway Syncline (Chadwick *et al.*, 1993).

Located 20 km to the west of cross-section A-A', within the Solway Basin, the Silloth 1A borehole provides a near complete section through the Permian and Triassic strata deposited within the Carlisle Basin unconformably overlying the deposits within the Solway Basin (Smith *et al.*, 1986; Holliday, 1993b; Holliday *et al.*, 2001). Interpretations of the borehole have been carried out based on mud logs and geophysical logs (Holliday, 1993b; Smith *et al.*, 1994; Jackson *et al.*, 1995; Holliday *et al.*, 2001). Figure 3.5b presents an interpretation of the Silloth 1A borehole data for the Permian and Triassic Periods.

The Permian age Penrith Sandstone Formation comprises medium-coarse grained sandstones of aeolian origin (Waugh, 1970). From the base of the Penrith Sandstone Formation at 1310 m, the radioactivity denoted by the gamma-ray log decreases as depth in the borehole decreases. This may be indicative of a slight coarsening upwards trend. From 1100 m to the top of the Penrith Sandstone Formation at 940 m, the gamma-ray log presents a uniform level of radioactivity suggesting the formation consists of a uniform sandstone body at this level. The late Permian age Eden Shales Formation is divided into three lithostratigraphical units, which consist of mudstones and siltstones interbedded with fine to coarse grained sandstones.

The Triassic age St Bees Sandstone Formation of the Sherwood Sandstone Group is comprised of mudstones and very-fine to fine grained sandstones

deposited in a fluvial environment (Jackson *et al.*, 1995; Holliday *et al.*, 2001). The St Bees Sandstone Formation is 395 m thick in the Silloth 1A borehole. At the base of the formation, fluctuations in the gamma-ray log are interpreted as mudstones interbedded with sandstone (Jackson *et al.*, 1995). Higher in the formation, the gamma-ray log becomes more uniform, related to a decrease in the number and thickness of mudstone beds. The Triassic age Mercia Mudstone Group comprises mudstones with frequent siltstone layers and occasional fine grained sandstone layers deposited in shallow water (Holliday *et al.*, 2004). The base of the succession is represented by high radioactivity on the gamma-ray log interpreted as a higher proportion of calcareous material (Jackson *et al.*, 1995). One halite bed can be distinguished by its low gamma-ray signature relative to the surrounding material. This supports the theory of deposition within a playa lake or intertidal sabkha environment (Holliday *et al.*, 2004).

### *3.2.3 Section B - B'*

Cross-section B-B' (Figure 3.6) covers a distance of 74 km and shows the structure and stratigraphy of the eastern Solway Basin and the Vale of Eden Basin.

The development of the Solway Basin is controlled by the Maryport Fault, which has a maximum throw of 3.6 km. However, unlike in cross-section A-A', there are major antithetic extensional faults in the north of the basin, including the Gilnockie Fault which has a maximum throw of 2.5km. The Solway Basin reaches a maximum depth of 7km in this

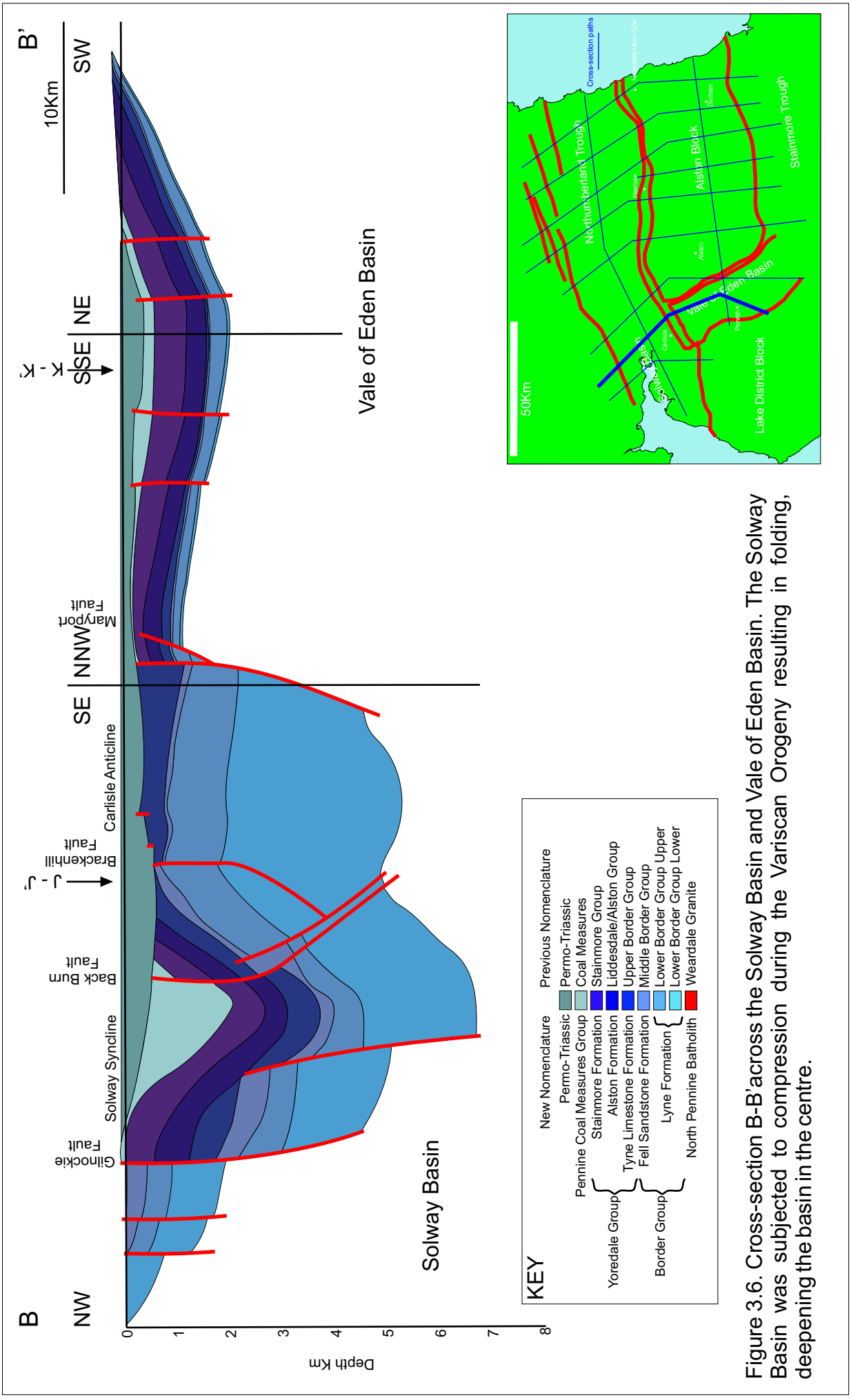


Figure 3.6. Cross-section B-B'across the Solway Basin and Vale of Eden Basin. The Solway Basin was subjected to compression during the Variscan Orogeny resulting in folding, deepening the basin in the centre.

section, which is partly a result of Variscan folding steepening the dip of the beds. The Solway Syncline and associated Carlisle Anticline, both of which are Variscan, can be observed in this section. The Back Burn Fault and the Brackenhill Fault, in the centre of the basin, demonstrate a reverse sense of movement as a result of this compression.

The syn-rift deposits of the Lyne Formation and the Fell Sandstone Formation have a maximum thickness of ~4.5 km within the Solway Basin. The predominantly post-rift Stainmore, Alston and Tyne Limestone formations of the Yoredale Group thicken towards the Gilknockie fault, suggesting that they are contemporaneous with faulting in the north of the basin. As in cross-section A-A', the Carboniferous age strata of the Solway Basin are blanketed by sediments of Permian and Triassic age.

The structure and stratigraphy illustrated within the cross-section suggests that initial development of the Solway Basin was controlled by faulting at the southern margin on the Maryport fault, generating an asymmetrical half-graben structure. This was followed by faulting at the northern margin, generating a more symmetrical graben structure. The Variscan orogeny resulted in uplift of the Carboniferous stratigraphy above the sea level datum, where it was subject to erosion.

The southern end of the cross-section traverses the Vale of Eden Basin. The main fault controlling basin formation, the Pennine Fault, runs parallel to this cross-section and is not crossed by this section. As the orientation of the cross-section changes towards the south-west, the basin

shallows towards the Lake District Block where the basin is not fault-controlled.

Like those of the Solway Basin, the Carboniferous age strata of the Vale of Eden Basin are blanketed by sediments of Permian and Triassic age. This is consistent with deposition in the regional Pennine Basin.

### *3.2.4 Section C - C'*

Cross-section C-C' (Figure 3.7) covers a distance of 90 km and traverses the easternmost part of the Solway Basin, its transition into the Northumberland Trough, the Alston Block and Vale of Eden Basin.

The section crosses the Bewcastle Anticline from the Solwat Basin into the south western tip of the Northumberland Trough. The Bewcastle Anticline is an asymmetrical fold that originated during the Variscan orogeny as a broad dome with a pre-dominantly east-west trend. There is evidence of erosion of the Carboniferous age strata deposited above the Tyne Limestone Formation. Permo-Triassic strata are not affected by the folding but are not present at the crest of the fold, which was uplifted above sea level at the time of deposition.

In the far west of the Northumberland Trough, the basin is controlled by the Stublick Fault. There is a maximum throw of 4.5 km upon the fault at this location. There is an increase in thickness of the syn-rift Lyne and Fell Sandstone formations as the section approaches the Stublick fault. These deposits have a maximum thickness of 3.5 km.

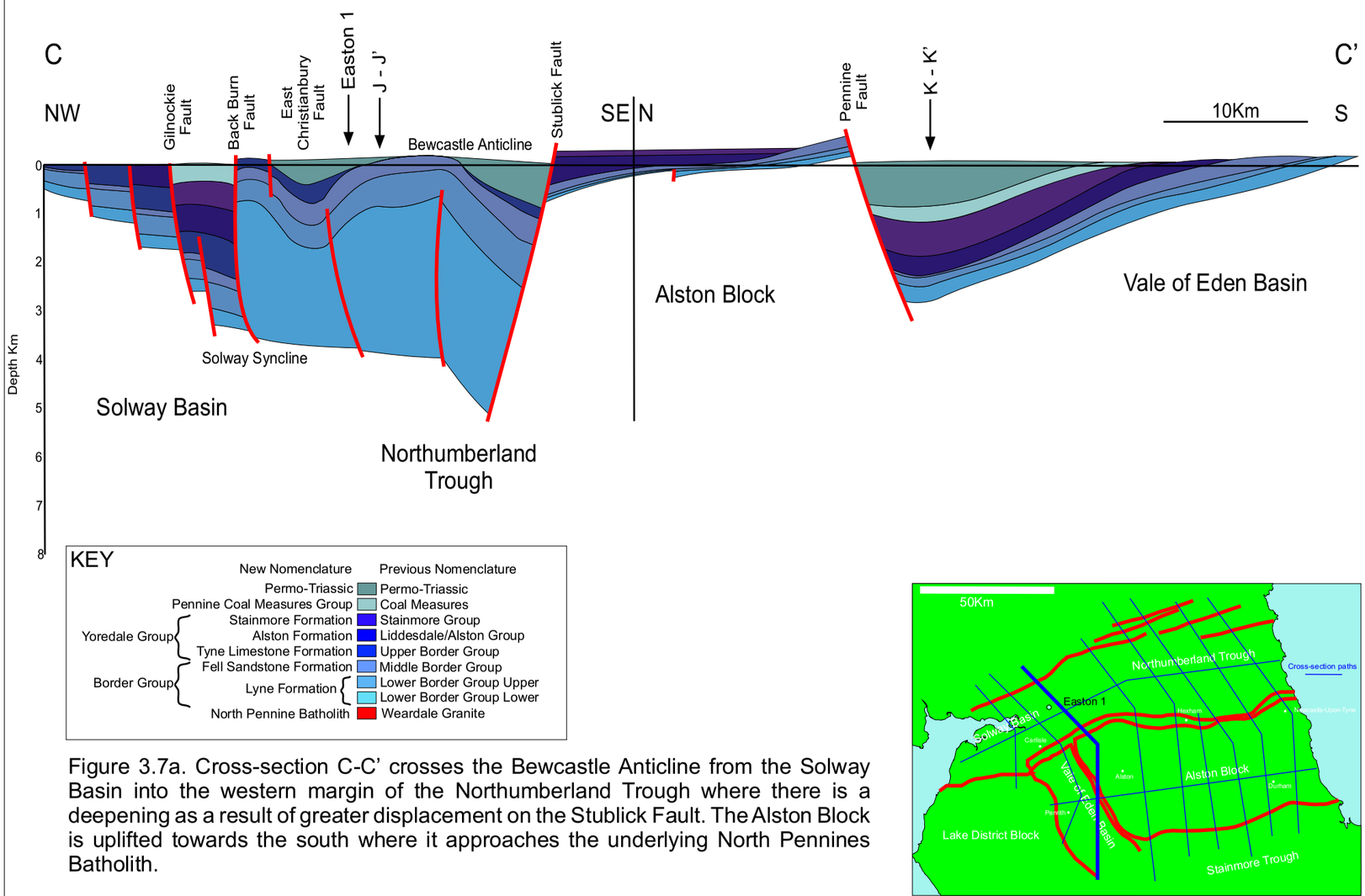


Figure 3.7a. Cross-section C-C' crosses the Bewcastle Anticline from the Solway Basin into the western margin of the Northumberland Trough where there is a deepening as a result of greater displacement on the Stublick Fault. The Alston Block is uplifted towards the south where it approaches the underlying North Pennines Batholith.




Figure 3.7b.
Easton 1 borehole stratigraphy and gamma-ray logs. The Easton 1 borehole provides a section through the Lyne Formation deposited within the Solway Basin. (After Ward, 1997)

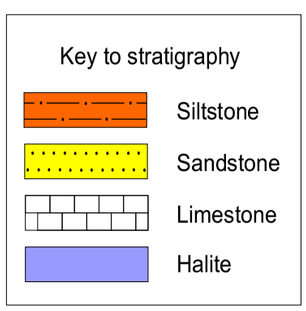


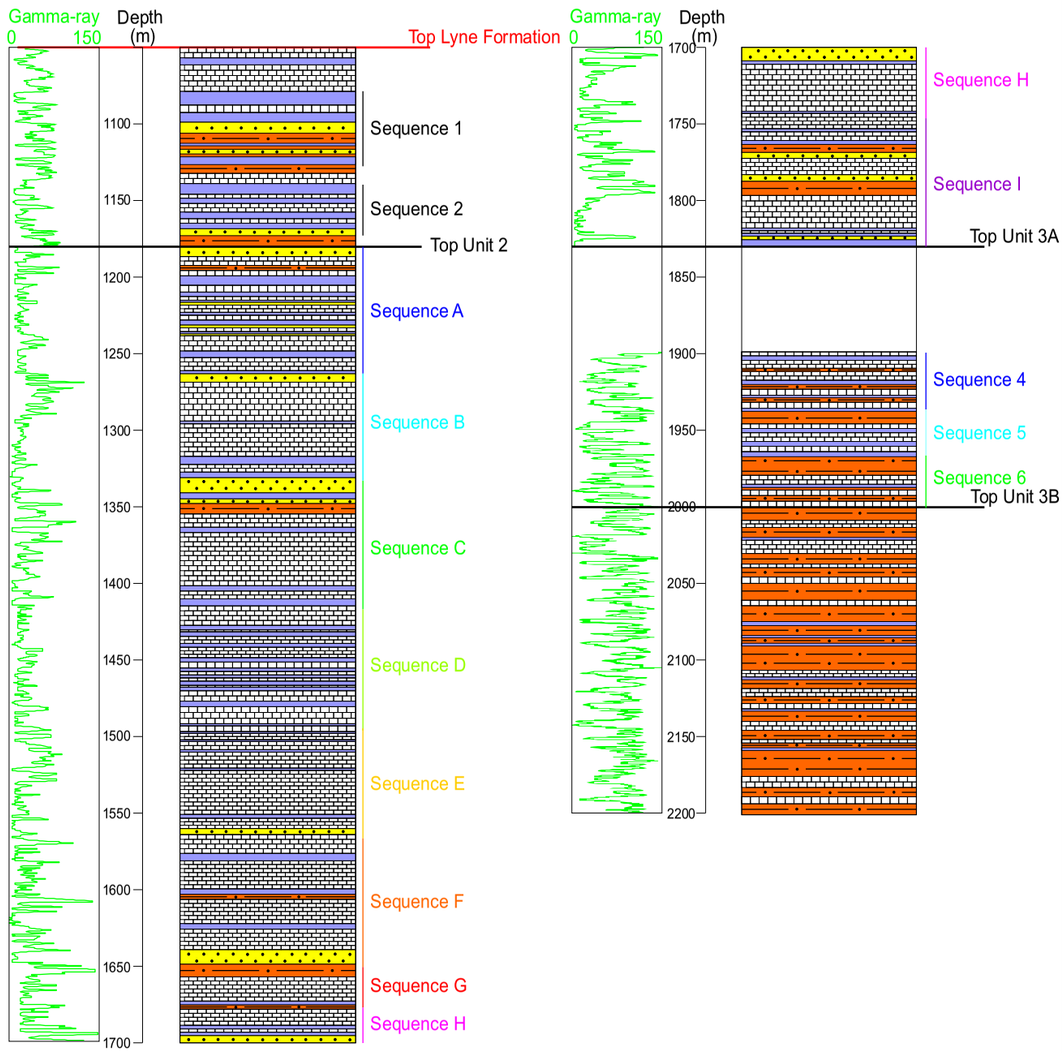


Data analysis: Regional cross-sections, seismic analysis and borehole data

The section displays the north western edge of the Alston Block, which is uplifted toward the Pennine Fault as a result of footwall uplift. As a result of this uplift the deposits of the Tyne Limestone Formation, Alston Formation and Stainmore Formation are not present on the western edge of the block.

The north-north-westerly trending Pennine Fault is oblique to the main east-north-east west-south-west fault trend. The Fault has a throw of 3km to the west creating the Vale of Eden Basin. Movement on the Pennine Fault commenced during the Permian period.

As in cross-section B-B', the Lyne and Fell Sandstone formations were deposited as a result of regional subsidence within this region of low topography and are therefore pre-rift in this area.

The Easton 1 borehole is situated 1 km to the south-west of cross-section C-C'. The borehole penetrates over 2 km of Carboniferous sediments deposited within the Solway Basin. Figure 3.7b illustrates the strata and gamma-ray logs for the Lyne Formation between 1054 m and 2195 m depth within the borehole. The interpretation of the borehole data was carried out by Ward (1997) based on the geophysical characteristics.

The Lyne Formation consists of clastic and carbonate rocks interbedded with anhydrite (Leeder, 1974a). The anhydrite deposits are interpreted as subaqueous salina evaporates (Warren and Kendall, 1985). The succession at Easton can be divided into three units based on their geophysical log signatures. Unit 1 (1054 m - 1181 m) contains two sequences of upwards

thickening anhydrite, interbedded with limestones, siltstones and sandstones (Ward, 1997). Unit 2 (1181 m – 1820 m) can be further subdivided into nine sequences, A-I from top to bottom. These sequences generally consist of a thick limestone near the base with anhydrite beds below the main limestone and above many of the other limestone beds within the sequence (Ward, 1997). There is a greater proportion of limestone material within unit 2 compared to the clastic content. This is reflected in the gamma-ray logs where there is a reduction in the high values reflecting the siltstone beds. Unit 3 (1820-2195) can also be further divided into two sub-units 3A and 3B. Within unit 3 there is a greater proportion of siltstone within the succession. This is reflected in the gamma-ray log, which exhibits a greater fluctuation between the low values that represent the anhydrite and limestone beds, and the high radioactivity values that are representative of the siltstone beds.

The deposits of the Lyne Formation are representative of deposition within a shallow water environment (Taylor *et al.*, 1971), with cycles related to rapid subsidence and sedimentation in combination with fluctuating sea level (Ward, 1997). The cyclic nature of these deposits within the syn-extensional Lyne Formation, support the proposal of Kimbell *et al.* (1989) that the extensional phase of the development of the Northumberland Trough Region occurred as a period of continuous subsidence resulting from faulting as opposed to multiple faulting events with irregular movements of varying magnitude (Ward, 1997).

### *3.2.5 Section D - D'*

This cross-section, (Figure 3.8) covers a distance of 97 km and represents the structure and stratigraphy of the western Northumberland Trough, Alston Block and Stainmore Trough.

The northern segment of the section is dominated by two major north-dipping extensional faults, which have generated a half-graben. These two faults are en-echelon branches of the Stublick Fault system, and have a total throw of 4 km. This is greater than the throw observed on the Maryport Fault and its associated faults in the Solway Basin of ~3.5 km (sections A-A' and B-B' Figures 3.5 and 3.6). To the north of the basin, there are several extensional faults that are antithetic to the main basin-bounding faults. There is evidence of reverse movement along some of these faults as a result of reactivation during the Variscan Orogeny. The compressional effects of the Variscan Orogeny are much less pervasive in the Northumberland Trough than the Solway Basin, with none of the large-scale folding observed in cross-sections A-A' and B-B' evident.

The total thickness of strata in the Northumberland Trough reaches 5.5 km in this section, adjacent to the basin bounding faults. The greater maximum thickness of strata in the Solway Basin of 7 km is due to the folding resulting from Variscan compression and located within the centre of the basin where the Solway Syncline has steepened the inclination of the beds. The syn-rift deposits of the Lyne and Fell Sandstone formations are up to 4.5km thick in the deepest part of the Northumberland Trough against the more proximal of the two basin-bounding faults of the Stublick

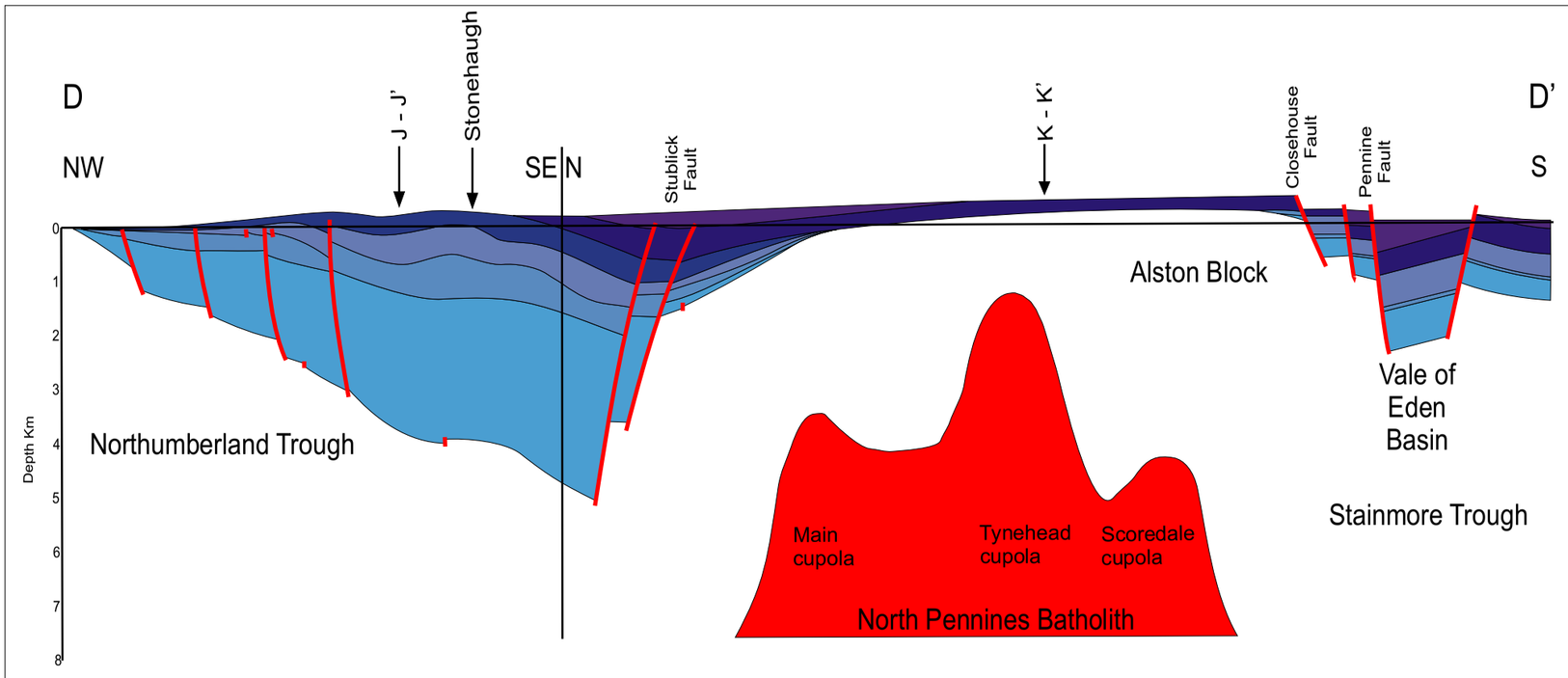


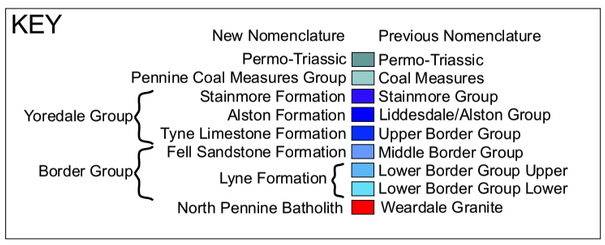


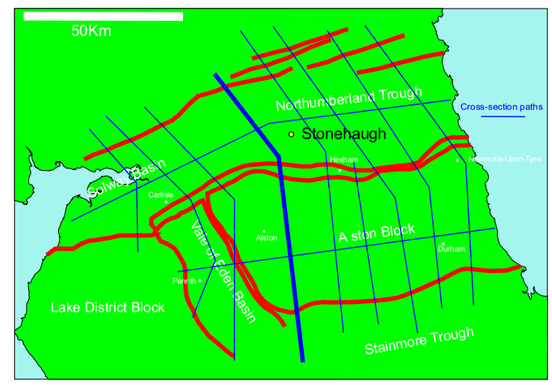


Figure 3.8a. Cross-Section D-D' across the Northumberland Trough, Alston Block and Stainmore Trough. The Northumberland Trough is deepest at the southern margin where most extension took place. The Alston Block is underlain by the North Pennines Batholith, which has a complex shape and maintained the Alston Block as a structural high during the early Carboniferous, with the youngest deposits across the centre of the block belonging to the Alston Formation.

Figure 3.8b. Stratigraphy and gamma-ray profile for the Stonehaugh borehole between 300 m and the base at 601m.Stonehaugh borehole penetrates the Visean sediments of the Fell Sandstone Formation and its upper boundary with the Tyne Limestone Formation. (After Frost and Holliday, 1980; Smith and Holliday, 1991; Corex, 2002)

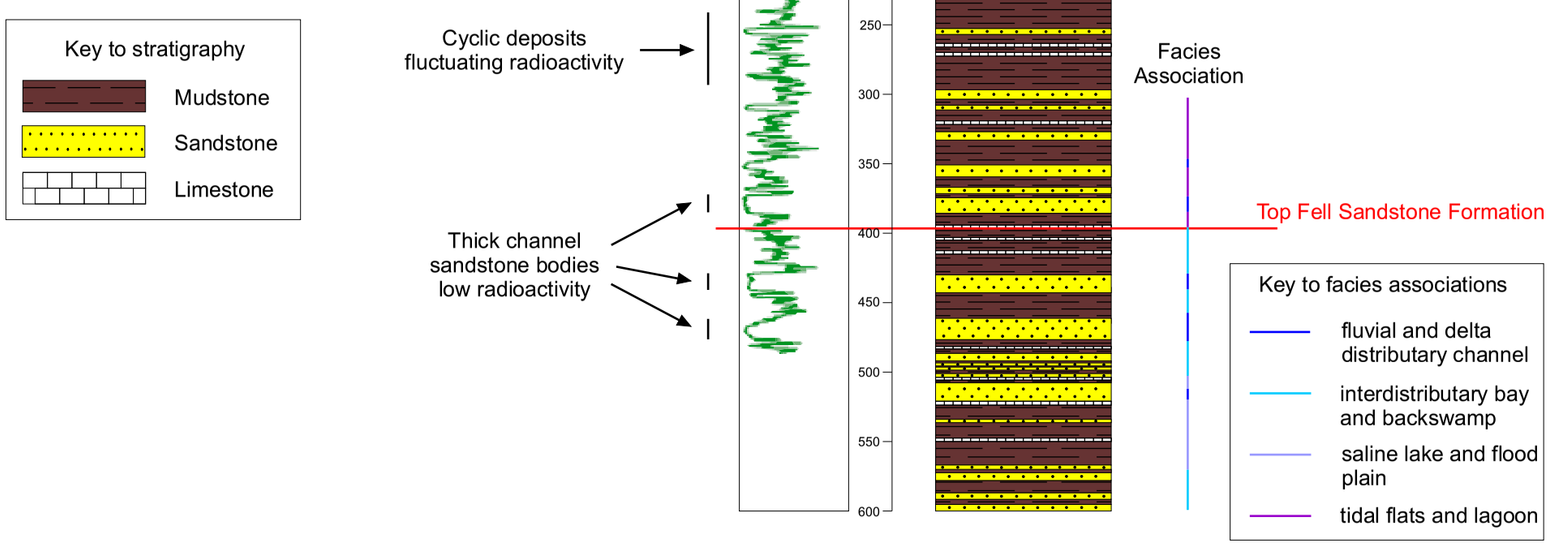


Data analysis: Regional cross-sections, seismic analysis and borehole data

Fault system. The thickness of these syn-rift deposits suggests that the first phase of extension was accommodated by the more proximal of these two faults, with extension being taken up on the more distal fault later.

On the flanks of the Alston Block there are some earlier deposits, belonging to the Tyne Limestone Formation, particularly on the northern margin with the Northumberland Trough, where the influence of the North Pennines Batholith is reduced and early Carboniferous sedimentation onlapped the margin of the Block. The North Pennines Batholith has a complex structure beneath this section, with three cupolas branching west from the central batholith. The top of the batholith reaches a minimum depth of 2km beneath the basement of the Alston Block and is separated from the deposits of the Alston Formation by pre-Carboniferous basement.

The cross-section also traverses the western margin of the Stainmore Trough. Displacement is taken up on the Closehouse Fault and a more proximal fault to the south, both south-dipping extensional faults, with a combined displacement of 1km. Much of the post-rift strata, the Yoredale Group and Pennine Coal Measures Group, have been removed by erosion following uplift above sea level.

The Stonehaugh borehole is located 9 km to the east of cross-section D-D', within the Northumberland Trough. The Stonehaugh borehole penetrates the Visean sediments of the Fell Sandstone Formation and its upper boundary with the Tyne Limestone Formation. The borehole does not penetrate the base of the Fell Sandstone Formation which is therefore at

least 200 m thick at this location (Frost and Holliday, 1980). The borehole was cored by the BGS and gamma-ray data is available to a depth of 480 m. Figure 3.8b illustrates the stratigraphy and gamma-ray profile for the Stonehaugh borehole between 300 m and its base at 601 m.

Three facies associations have been identified within the strata of the Fell Sandstone Formation in the Stonehaugh borehole (Smith and Holliday, 1991). These are:

- Fluvial and delta distributary channels, represented by thick sandstone bodies with interbedded mudstones.
- Interdistributary bays and backswamps, represented by coarsening upwards cyclothems of limestone, sandstone, seatearth and coal.
- Saline lakes and flood plains which are represented by siltstone, seatearth containing calcareous and ferruginous nodules and algal limestone (Frost and Holliday, 1980; Smith and Holliday, 1991).

The boundary between the Fell Sandstone Formation with the Tyne Limestone Formation is marked by a transition into marine influenced environments from fluvially dominated coastline to tidally dominated coastline. A new facies association is identified that represents deposition within tidal flats and lagoons, which are characterised by sandstones and mudstones that are heterolithic and bioturbated (Smith and Holliday, 1991).

The presence of the central cupola of the North Pennines Batholith has been proven by boreholes at Rookhope (Dunham *et al.*, 1965) and Eastgate (Manning *et al.*, 2007). Observation of mineralisation (Cann and Banks, 2001; Bouch *et al.*, 2006) and increased heat flow (Evans *et al.*, 1988) away from the central cupola provide evidence for the existence of the other cupolas. These observations are supported by the gravity data Figure 3.9, which provides strong evidence for the shape of the surrounding cupolas. The gravity profiles over the Alston Block contain a relatively low gravity anomaly, which is a result of the presence of a large granite intrusion within the basement of the Alston Block. A granite density of 2630 $kgm^{-3}$ is used for the North Pennines Batholith and assuming a country rock density of 2780 $kgm^{-3}$, model results suggest that the depth of the granite is approximately 10 km (Kimbell *et al.*, 2006).

Figure 3.9 presents a north-south section across the western end of the North Pennines Batholith. The profile contains three cupolas of the North Pennines Batholith; the western extent of the main cupola to the north, the Tynehead cupola and the Scordale cupola furthest to the south. The main cupola is situated beneath a greater amount of pre-Carboniferous basement than the Tynehead and Scordale cupolas and, as such, has a reduced effect upon the gravity profile. At the point at which this section crosses the Tynehead cupola, it is symmetrical, which is reflected in the symmetrical nature of the gravity profile between 25 and 35 km. The Scoredale cupola is hummocky in cross-section where it is crossed by this profile. Additional gravity and seismic data is available in Appendix A.

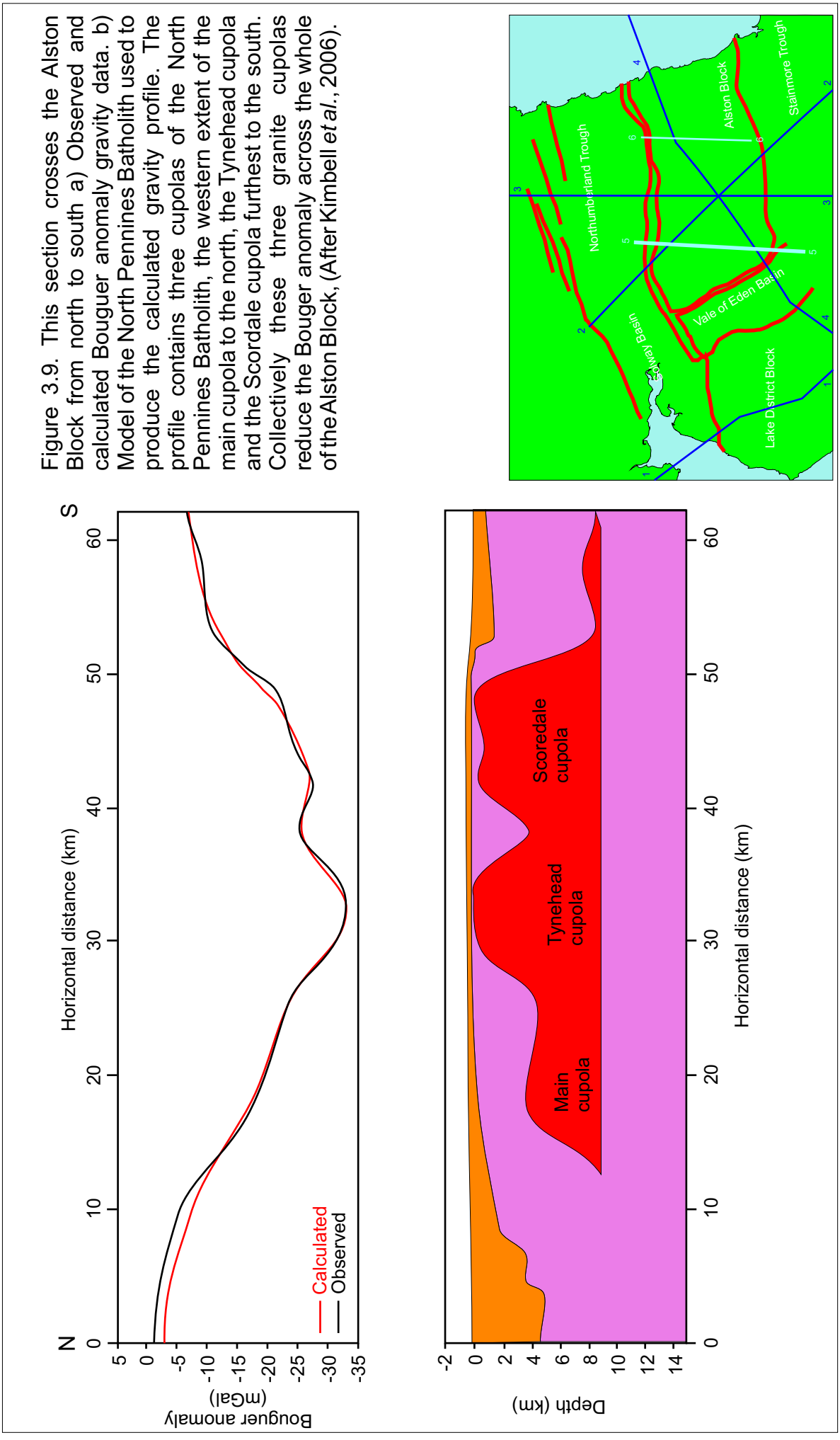


Figure 3.9. This section crosses the Alston Block from north to south a) Observed and calculated Bouguer anomaly gravity data. b) Model of the North Pennines Batholith used to produce the calculated gravity profile. The profile contains three cupolas of the North Pennines Batholith, the western extent of the main cupola to the north, the Tynehead cupola and the Scordale cupola furthest to the south. Collectively these three granite cupolas reduce the Bouger anomaly across the whole of the Alston Block, (After Kimbell *et al.*, 2006).

### *3.2.6 Section E - E'*

Cross-section E-E' (Figure 3.10) is located approximately 1 km to the east of cross-section D-D'. This cross-section traverses from north-west to south-east through the centre of the Northumberland Trough and from north to south across the centre of the Alston Block and into the Stainmore Trough.

Extension within the Northumberland Trough occurs along three major en-echelon faults on the southern margin of the trough. The two faults that are within the basin are en-echelon segments of the Stublick Fault (as in cross-section D-D'), whilst the more proximal fault that forms the southern margin of the basin, on which only a small amount of displacement has occurred, is the Ninety Fathom Fault.

The Lyne Formation accounts for the majority of the syn-rift deposits. The maximum thickness of the Lyne Formation, 3 km, occurs adjacent to the segment of the Stublick Fault in the most distal position within the basin. This is the fault that has accommodated most of the extension within the basin.

The North Pennines Batholith in this cross-section has a much simpler structure than in cross-section D-D'. It forms one central batholith of granite that has a minimum depth beneath the basement of the Alston Block that varies from approximately 1.5km to 0 km. In the centre of the Alston Block, where sediments have been deposited directly onto the North Pennines Batholith, only the Alston Formation has been deposited;

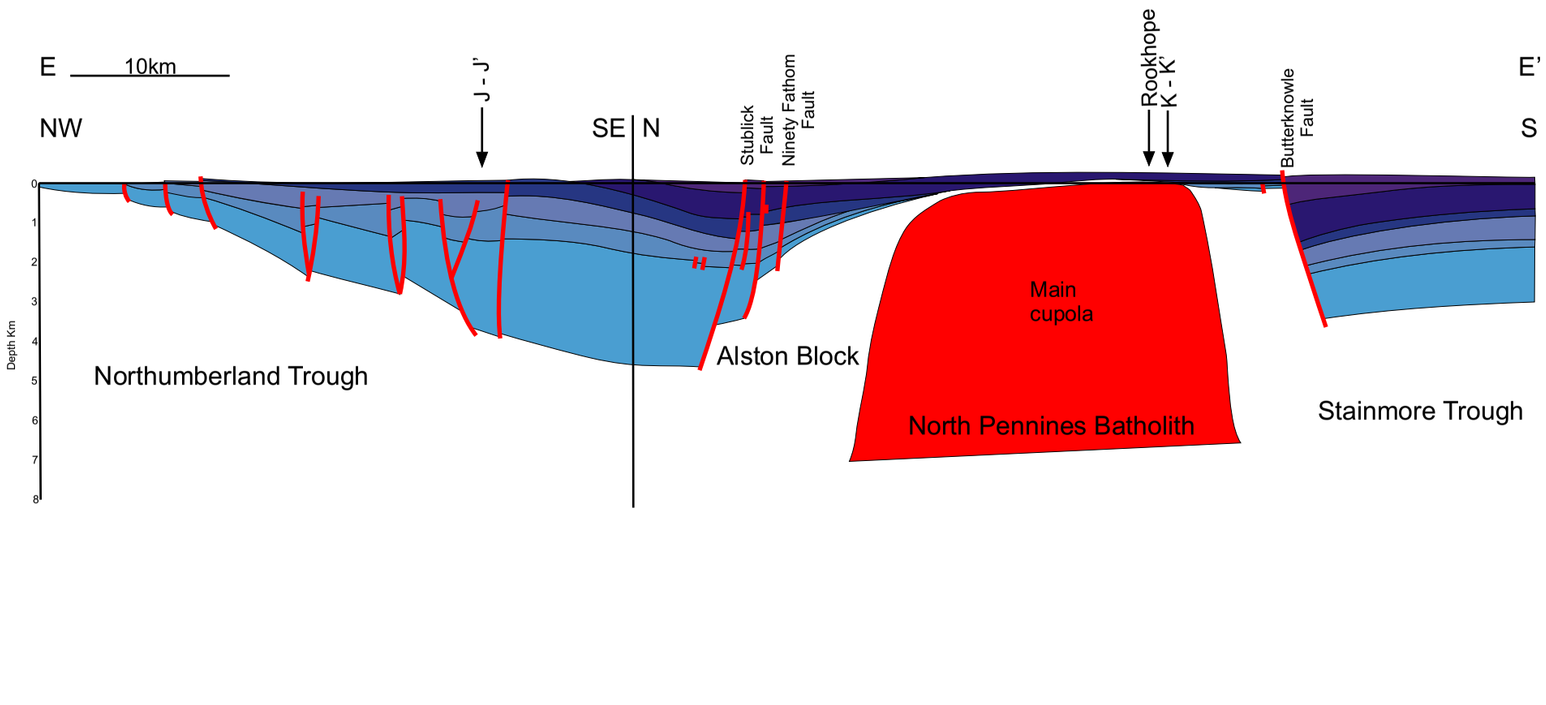


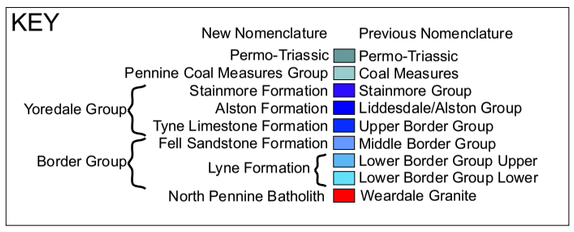


Figure 3.10a. Cross-Section E-E' across the Northumberland Trough, Alston Block and Stainmore Trough. As in cross-section D-D' the Northumberland Trough forms a half graben with extension occurring along three major faults on the southern margin of the trough. The two faults most proximal to the basin are branches of the Stublick Fault. The more distal fault, the Ninety Fathom Fault only takes up a small amount of the extension.

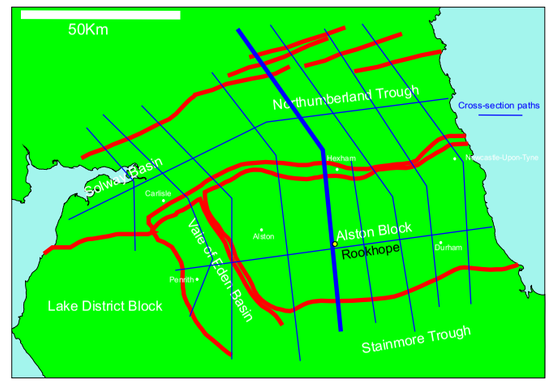


Figure 3.10b. Stratigraphy and gamma-ray profile for the Rookhope borehole to a depth of 650m.The Rookhope borehole penetrates the North Pennines Batholith, the Alston Formation and its upper boundary with the Stainmore Formation. (After Dunham *et al.*, 1965)

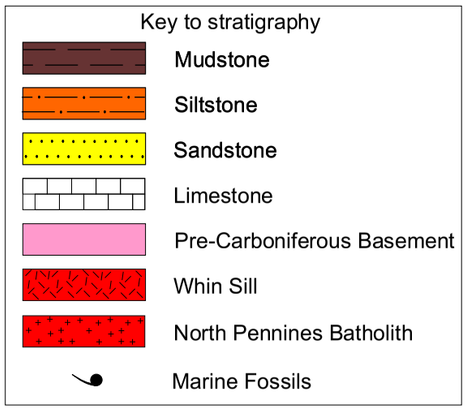


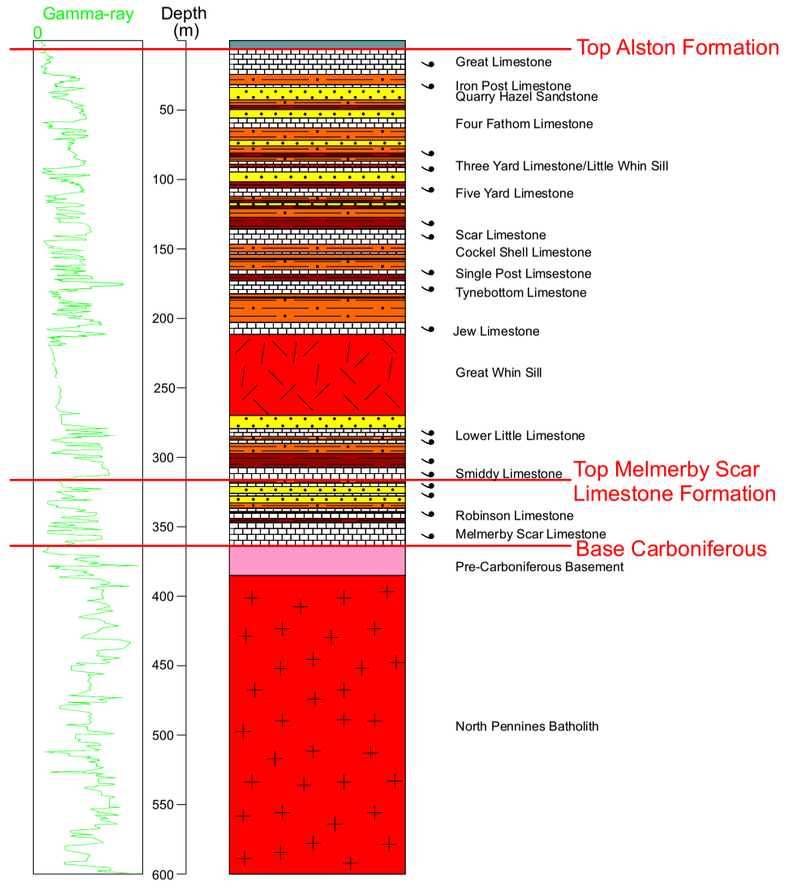

it is assumed that the Alston Block was exposed and eroded prior to this (Chadwick *et al.*, 1995).

The development of the Stainmore Trough is controlled in this cross-section by displacement on the Butterknowle Fault. Within the Stainmore Trough the depth to the pre-Carboniferous basement reaches a maximum depth of 3.5km with a maximum 3km of throw on the Butterknowle Fault, which is considerably deeper than observed in cross-section D-D' to the east. Thickening of the deposits of the Yoredale Group towards the Butterknowle Fault implies a second phase of extensional movement occurred on the fault contemporaneously to the deposition of these strata.

The Rookhope borehole is situated 2.5 km to the west of cross-section E-E', on the Alston Block. The borehole penetrates the boundary between the Stainmore Formation and the Alston Formation at the top and extends through the Alston Formation and Melmerby Scar Formation into the pre-Carboniferous basement and the North Pennines Batholith. Figure 3.10b illustrates the stratigraphy and gamma-ray log for the Rookhope borehole to a depth of 600m.

The Melmerby Scar Limestone Formation is 50 m thick in the Rookhope borehole and contains about 50% clastic material (Dunham *et al.*, 1965). The Alston Formation consists of a succession of thin limestones, mudstones, siltstones, sandstones and thin coals in cyclothems (Dunham *et al.*, 1965). Five facies associations have been identified within the Alston Formation within the Rookhope borehole. These are:

- Offshore carbonate platform; represented by grey bioclastic limestones with thin calcareous mudstone beds.
- Shallow-water marine environments below the wave base; these consist of mudstone, siltstone and fine sandstone beds.
- Relatively high-energy near-shore marine facies; represented by interbedded mudstone, siltstone and sandstone with thin bioclastic limestone bands.
- Shoreline, littoral and estuarine facies; composed of interbedded sandstone, micaceous siltstone and mudstones.
- Subaerial delta plain; represented by coals and seatearths of sandstone and siltstone (Johnson and Nudds, 1995).

The sequences of strata within each cyclothem can be assigned to one of these facies associations.

### *3.2.7 Section F - F'*

Cross-section F-F' (Figure 3.11) is relatively short at 50 km in length. It displays the structure and stratigraphy of the Alston Block and its margins with the Northumberland Trough to the north and the Stainmore Trough to the south.

The North Pennines Batholith has a similar structure to that in cross-section E-E'. Carboniferous age deposits do not directly overlie the batholith in this cross-section but are separated by approximately 100 m of pre-Carboniferous basement. The oldest deposits that are continuous

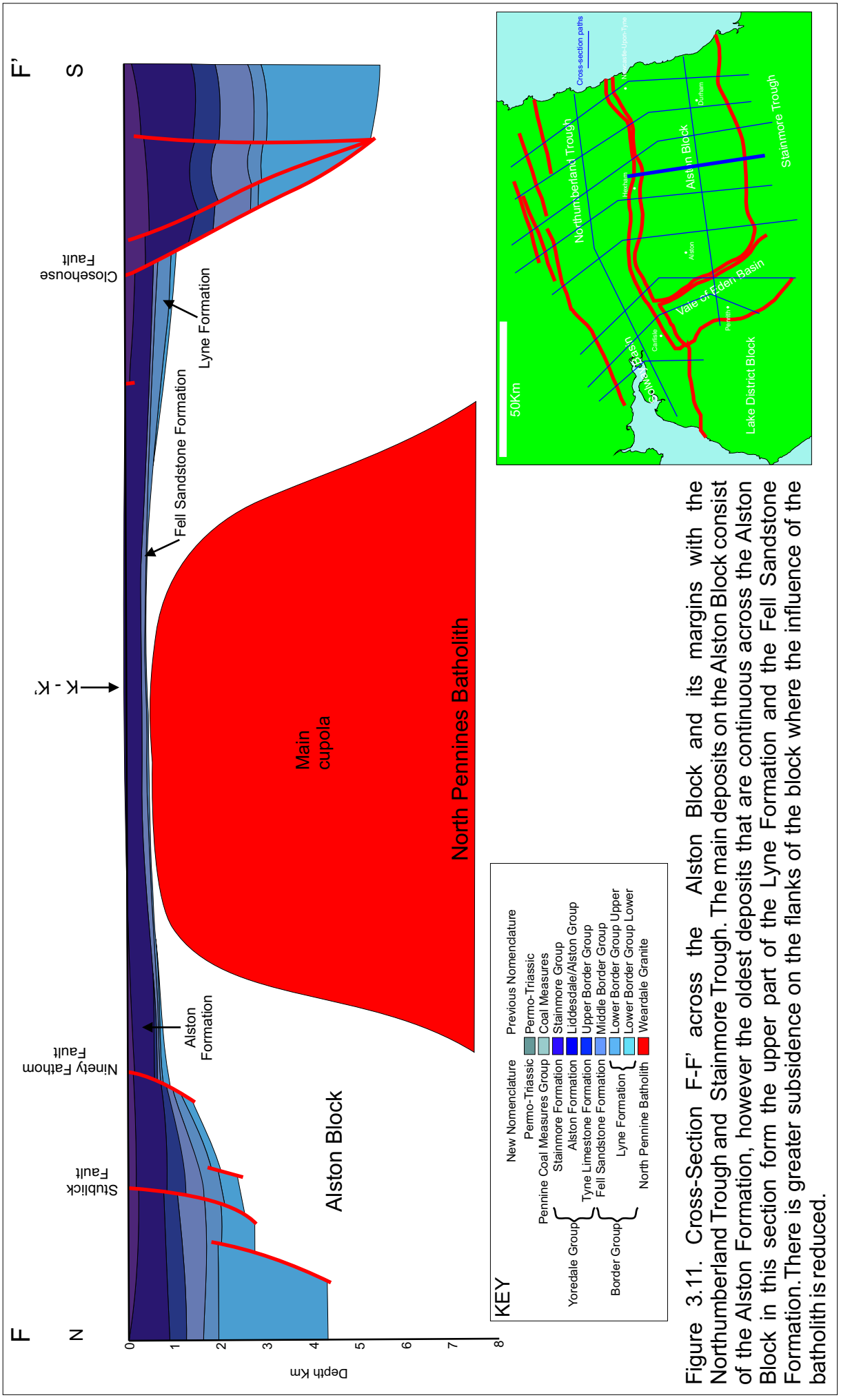


Figure 3.11. Cross-Section F-F' across the Alston Block and its margins with the Northumberland Trough and Stainmore Trough. The main deposits on the Alston Block consist of the Alston Formation, however the oldest deposits that are continuous across the Alston Block in this section form the upper part of the Lyne Formation and the Fell Sandstone Formation.There is greater subsidence on the flanks of the block where the influence of the batholith is reduced.

across the Alston Block in this section form the upper part of the Lyne Formation and the Fell Sandstone Formation. The Tyne Limestone Formation is absent indicating a relative fall in sea level over the block during this period (Johnson, 1984). The main deposits on the Alston Block consist of the Alston Formation. There is greater subsidence on the flanks of the block where the influence of the batholith is reduced. As a result deposits belonging to the Stainmore Formation encroach upon the margins of the Alston Block.

### *3.2.8 Section G - G'*

Cross-section G-G' (Figure 3.12) covers 103 km across the Northumberland Trough, Alston Block and Stainmore Trough. The section shows that the Northumberland Trough has a large number of subsidiary faults from the centre to the north of the half graben, both synthetic and antithetic to the main basin controlling faults, with the antithetic faults generally in a more northerly position.

There is evidence of reverse movement on some of the faults as a result of the Variscan Orogeny, including the basin-bounding faults. The Stublick Fault has an extensional displacement of 2.5km between the footwall and hanging wall deposits of the Lyne Formation. Further up the succession within the Fell Sandstone Formation and Alston Formation the hanging wall deposits have been thrust 200m above the footwall deposits.

The North Pennines Batholith beneath this cross-section represents two cupolas to the east of the main batholith. This section crosses the western

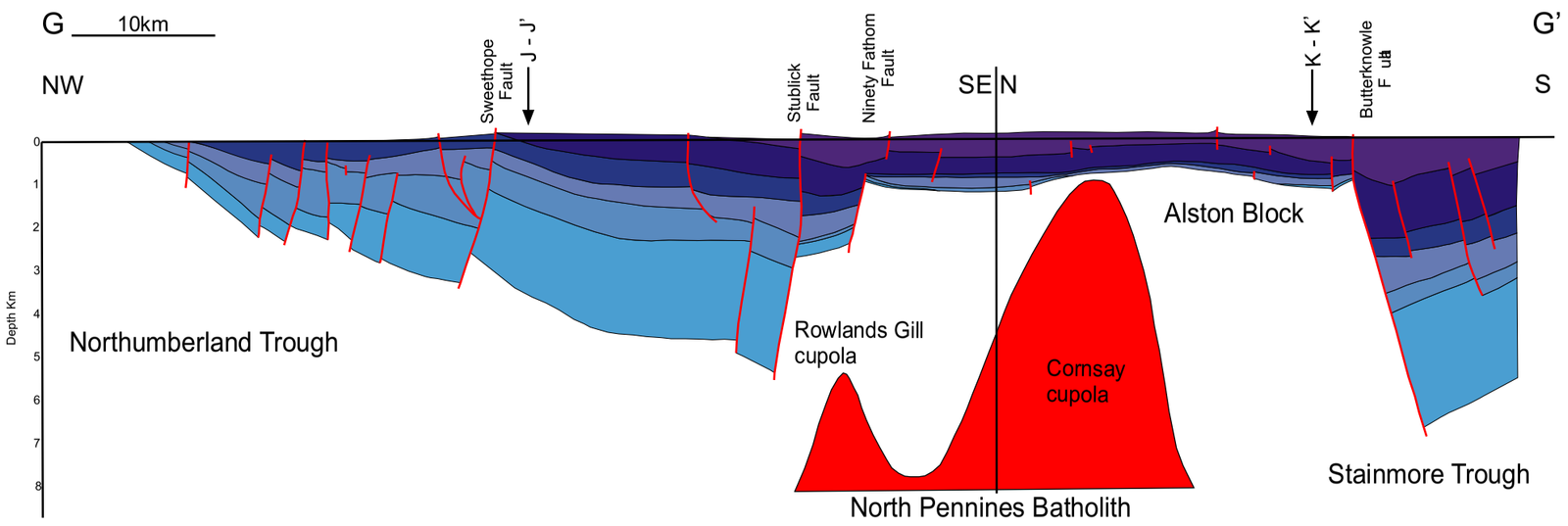


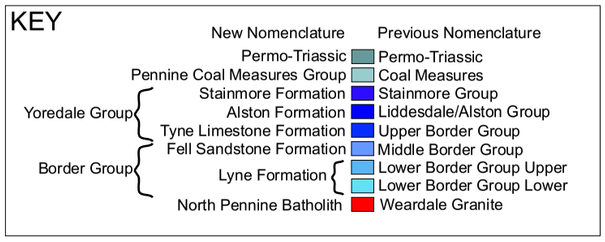


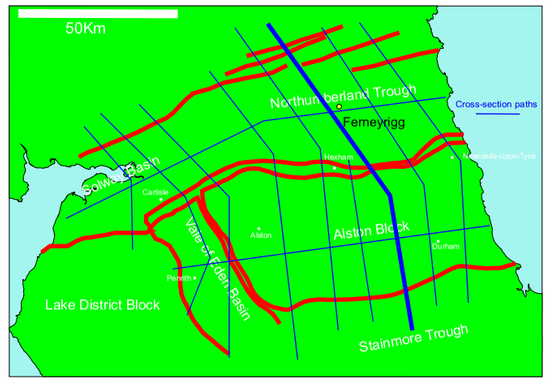


Figure 3.12. Cross-Section G-G' across the Northumberland Trough, Alston Block and Stainmore Trough. The majority of the extension in the basin is taken up on the Stublick Fault, with displacement later taken up by the Ninety Fathom Fault. The North Pennines Batholith beneath this cross-section represents two cupolas to the east of the main batholith.

Figure 3.12b. Stratigraphy and gamma-ray profile for the Ferneyrigg borehole. The Ferneyrigg borehole penetrates the Tyne Limestone Formation and the base of the Alston Formation. (After Frost and Holliday, 1980)

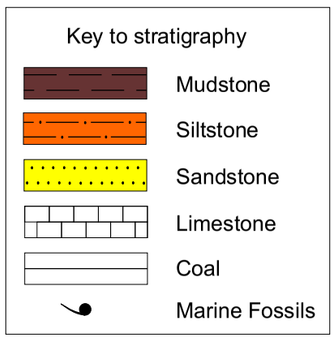


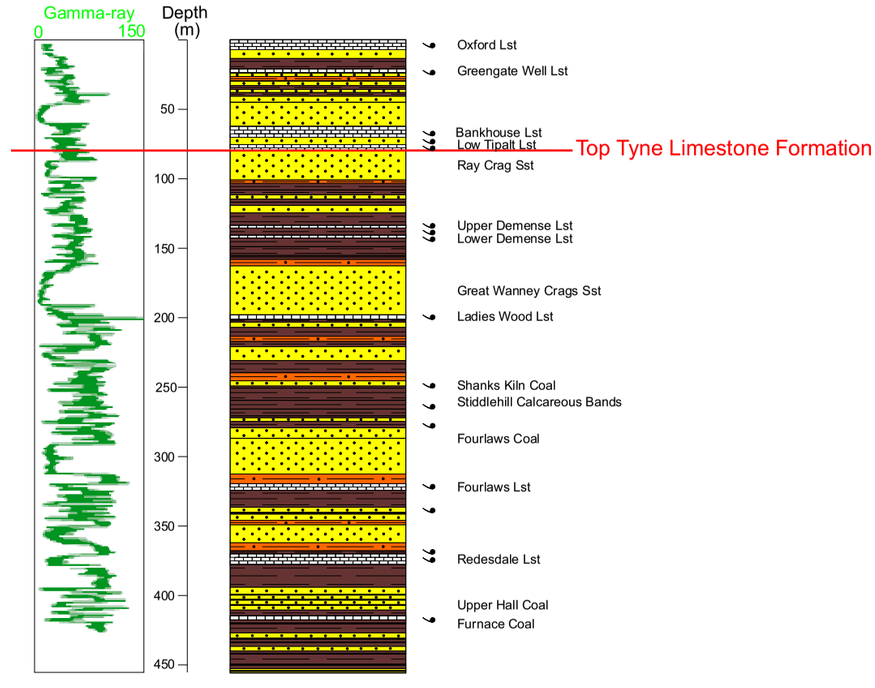


Data analysis: Regional cross-sections, seismic analysis and borehole data

edge of the north of the two cupolas and across the centre of the cupola to the south. These Carboniferous sedimentary deposits are 1 to 1.5km thick which is greater than in the cross-sections to the west (sections D-D' to F-F'). The Carboniferous sequence is thickest between the two cupolas indicating the buoyancy effect of the granite intrusion on the uplift and subsidence history of the Alston Block.

The Stainmore Trough has a maximum depth in this cross-section of 6.5km against the Butterknowle Fault, which has a maximum throw of 5km within the Lyne Formation reducing to 0.5km at the base of the Stainmore Formation. There are some extensional faults that cut through the Stainmore Formation and into the Fell Sandstone Formation or the top of the Lyne Formation. Movement on these faults occurred later than on the extensional faults responsible for the evolution of this system of half grabens as there is no evidence for syn-rift sedimentation in the hanging wall of the faults.

The Ferneyrigg borehole is located 3 km to the west of cross-section G-G', within the Northumberland Trough. It passes through the base of the Alston Formation and the Tyne Limestone Formation. Figure 3.12b illustrates the stratigraphy and gamma-ray log for the Ferneyrigg borehole to a depth of 455 m.

The Tyne Limestone Formation is comprised of fossiliferous mudstones, sandstones and coals with thin limestone beds. The following facies associations are recognised within the Tyne Limestone Formation:

- Shallow-water tidal flat facies; represented by thin limestone beds and fossiliferous mudstones.
- Delta-front facies; represented by a coarsening upwards sequence from fossiliferous mudstone to sandstone.
- Coastal plain facies; comprising a fining upwards sequence from sandstone, possibly containing an erosive base, to siltstone and mudstone with seatearths and coals (Frost and Holliday, 1980).

The Alston Formation demonstrates an increase in the quantity and thickness of the limestone beds as the marine influence increases.

### *3.2.9 Section H - H'*

Cross-section H-H', (Figure 3.13) lies 10-12 km to the east of cross-section G-G'. It covers a distance of 96 km and passes across the eastern Northumberland Trough, Alston Block and Stainmore Trough.

In this cross-section, the main basin-controlling fault within the Northumberland Trough is the Ninety Fathom Fault, which has a maximum throw of 2 km. This is significantly less than observed in the west of the basin in cross-sections C-C', D-D' and E-E'.

The North Pennines Batholith represents the eastern edge of the two cupolas to the east of the main intrusion seen in cross-section G-G'. In this cross-section the two cupolas have an equal minimum depth of 5 km and are the same size with only a small low between them.

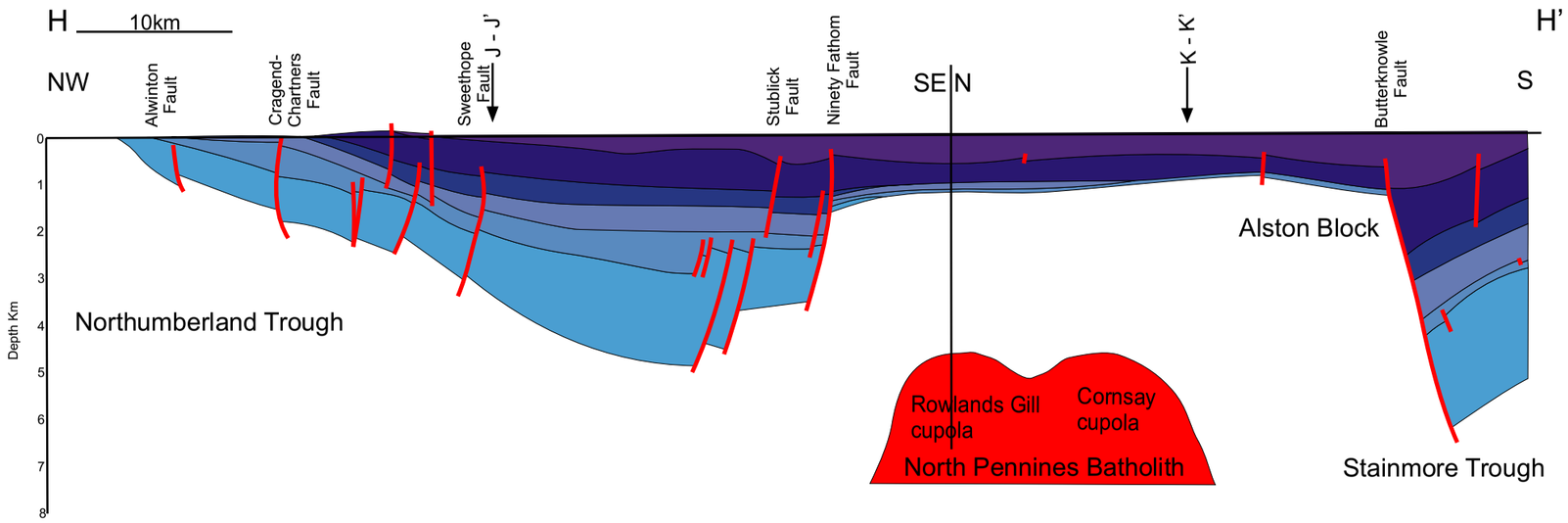


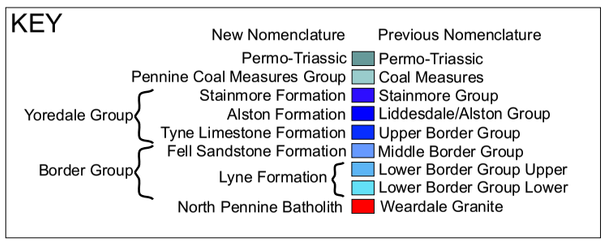


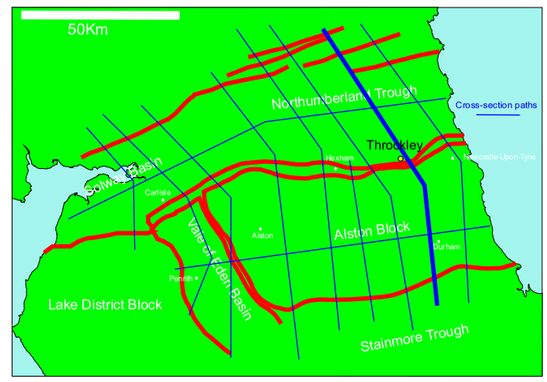


Figure 3.13a. Cross-Section H-H' across the Northumberland Trough, Alston Block and Stainmore Trough. In this cross-section the main basin controlling fault within the Northumberland Trough is the Ninety Fathom Fault, which has a maximum throw of 2km. Movement occurred on the Stublick Fault earlier than the Ninety Fathom Fault with the basin being deepest in the hanging wall of the Stublick Fault where the deposits of the Lyne Formation are thickest.

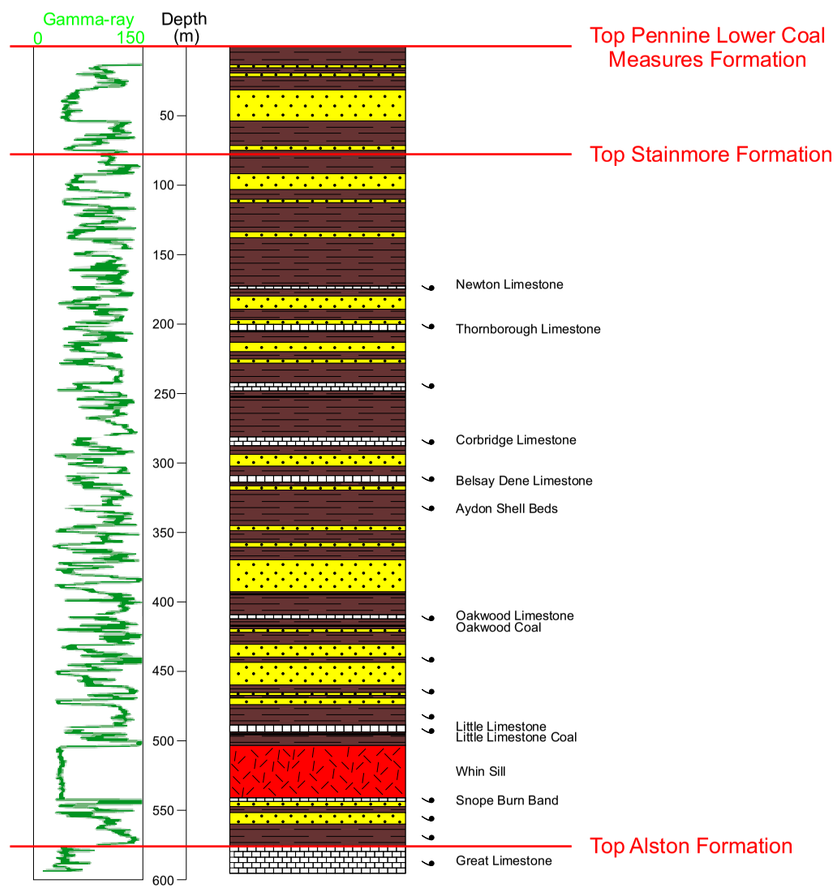


Figure 3.13b. Stratigraphy and gamma-ray profile for the Throckley borehole. The Throckley borehole penetrates the Top of the Alston Formation, the Stainmore Formation and the bottom of the Pennines Lower Coal Measures Formaion (After Frost and Holliday, 1980).

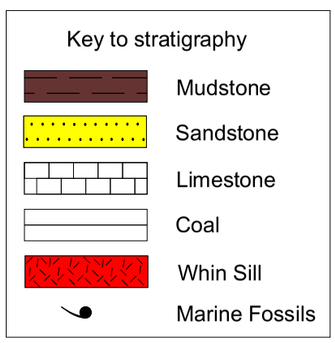

In the Stainmore Trough extension along the Butterknowle Fault appears to have continued longer than in the Northumberland Trough, with syn-rift deposition evidenced by thickening towards the fault demonstrated in the Lyne, Fell Sandstone, Tyne Limestone, Alston formations. The Stainmore Formation is continuous across the Stainmore Trough, the Alston Block and the Northumberland Trough indicating that the basins and the block were subsiding at an equal rate during its deposition.

The Throckley borehole is located 2 km to the west of cross-section H-H'. The borehole penetrates the base of the Pennine Lower Coal Measures Formation, the Stainmore Formation and the Great Limestone Member at the top of the Alston Formation. Figure 3.13b illustrates the stratigraphy and gamma-ray profile for the Throckley borehole.

The Great Limestone is the thickest limestone within the Yoredale Group. It is now officially included within the Alston Formation (Stone *et al.*, 2010). The strata of the Stainmore Formation can be divided into cyclothems, as with the Alston Formation, and include limestones, mudstones and sandstones with seatearths and coals. The strata between the Great Limestone and the Little Limestone can be divided into two sequences (Johnson, 1959). The lower sequence is a coarsening upwards sequence from mudstone to sandstone deposited within a lobate delta system (Elliot, 1974). The upper sequence consists of fosilliferous mudstones and limestones of marine origin deposited following delta lobe abandonment (Frost and Holliday, 1980). The strata between the Little Limestone and the Oakwood Limestone can be divided into three cycles,

with limestone or calcareous mudstone at the base followed by sandstone, seatearths and coals (Frost and Holliday, 1980). The Oakwood Limestone cyclothem consists of an argillaceous limestone overlain by mudstone and sandstone containing coal (Clarke, 2007). The Beslay Dene and Corbridge Limestone cyclothems contain bioclastic limestones at their base, overlain by mudstone and fine grained sandstones (Young, 2006). The top of the Stainmore Formation is characterised by the absence of limestone beds and the presence of erosive channel sandstones.

### *3.2.10 Section I - I'*

Cross-section I-I' (Figure 3.14) is the easternmost section, and covers 98 km through the Northumberland Trough, the Alston Block and the Stainmore Trough. This cross-section illustrates that the formation of the Northumberland Trough has been controlled by the Ninety Fathom Fault in this area. There is a greater amount of subsidiary faulting in the basin close to the main Ninety Fathom Fault. The Stakeford Fault shows evidence of extensional faulting with some reverse reactivation. To the north of the fault the Lyne Formation is 0.5 km thicker than adjacent to the fault to the south. However, the top of the Lyne Formation on the southern side of the fault has been displaced by at least 0.8 km in a reverse sense. All of the deposits of the Border and Yoredale groups have been affected by this fault re-activation, which implies that the movement occurred after they had been deposited and is likely to be a result of Variscan compression.

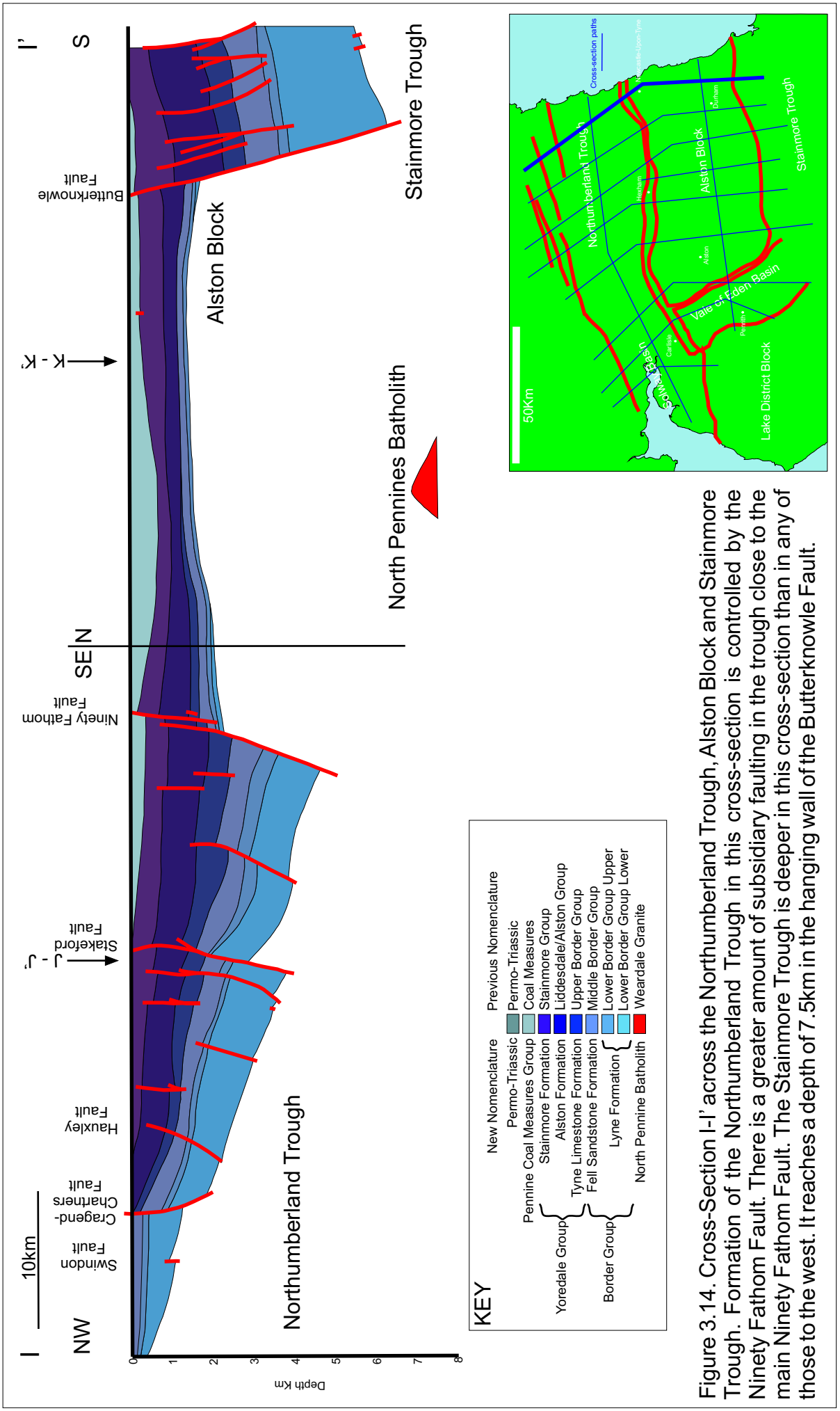


Figure 3.14. Cross-Section I-I' across the Northumberland Trough, Alston Block and Stainmore Trough. Formation of the Northumberland Trough in this cross-section is controlled by the Ninety Fathom Fault. There is a greater amount of subsidiary faulting in the trough close to the main Ninety Fathom Fault. The Stainmore Trough is deeper in this cross-section than in any of those to the west. It reaches a depth of 7.5km in the hanging wall of the Butterknowle Fault.

This cross-section includes the far eastern edge of the North Pennines Batholith where it is only 6km wide and at a minimum depth of 7km. The Carboniferous deposits on the Alston Block have a maximum thickness of 2.5km, thicker than observed in the cross-sections to the east, which is interpreted as a result of the diminishing influence of the buoyancy generated by the North Pennines Batholith. Deposits of the Lyne Formation cover the whole of the Alston Block over the extent of the section.

The Stainmore Trough is deeper in this cross-section than in any of those to the west. It reaches a depth of 7.5 km in the hanging wall of the Butterknowle Fault.

Rocks belonging to the Pennine Coal Measures Group are deposited regionally across the Northumberland Trough, Alston Block and Stainmore Trough and are thickest on the Alston Block implying development of a regional basin.

### *3.2.11 Section J - J'*

Cross-section J-J' (Figure 3.15) is 126 km long and crosses from west to east across the Solway Basin and Northumberland Trough. It runs parallel to the main structural features of the Northumberland Trough Region including the Maryport-Stublick-Ninety Fathom Fault system. It is also perpendicular to cross-sections A-A' to I-I' in the northern part of the area.

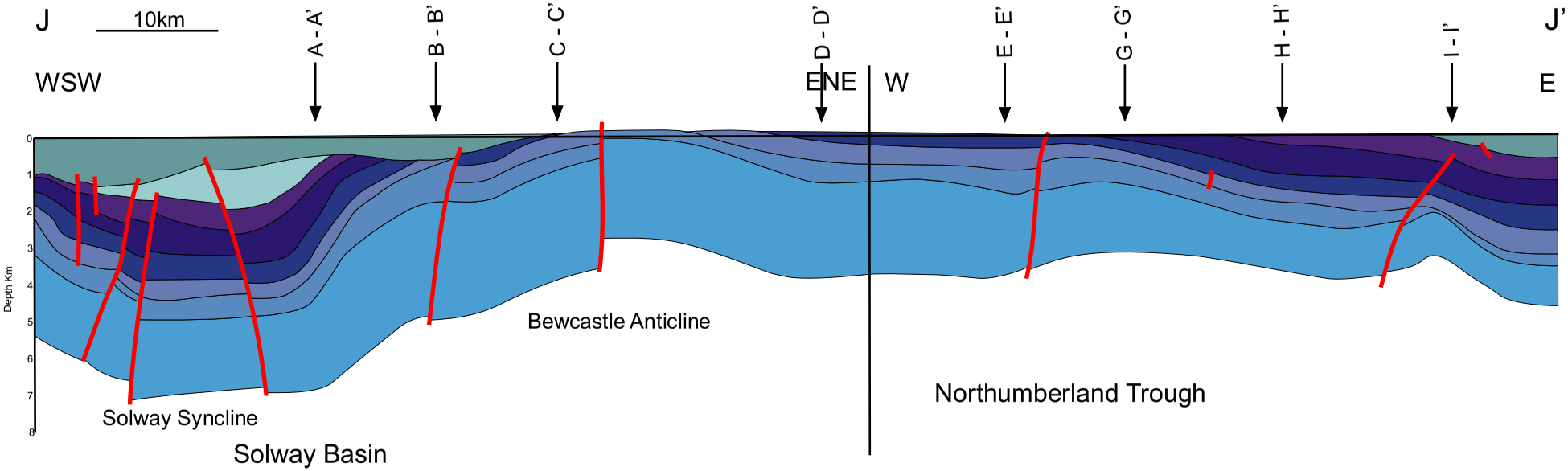


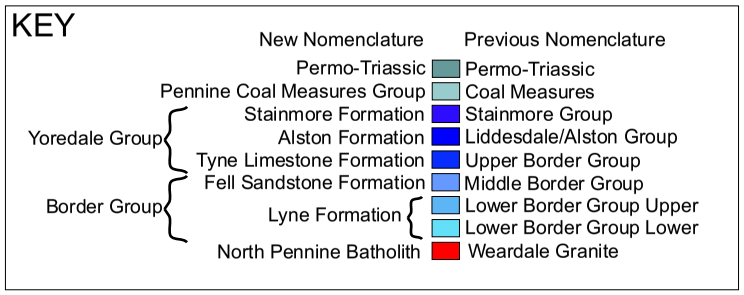


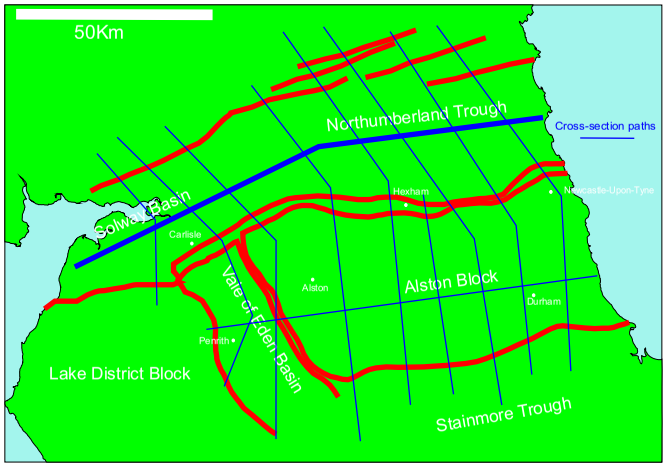


Figure 3.15. Cross-Section J-J' runs perpendicularly to the main structural features of the Northumberland Trough Region such as the Maryport-Stublick-Ninety Fathom Fault System. In the Solway Basin post-rift Carboniferous age deposits have been eroded and they are unconformably overlain by the Permian and Triassic age sequences. The Solway Basin passes into the Northumberland Trough via the Bewcastle Anticline, where all but the Lyne Formation has been uplifted and eroded.

The north-east to south-west trending Solway Syncline is crossed from west to east. The syn-rift deposits of the Lyne and Fell Sandstone formations thin slightly from east to west. The post-rift deposits of the Yoredale Group and the Pennine Coal Measures Group thicken towards the centre of the basin implying that their deposition was concurrent with folding. The Pennine Coal Measures Group reaches a thickness of 1 km in the centre if the basin. In the east of the basin, some of the post-rift Carboniferous age deposits have been eroded and they are unconformably overlain by the Permian and Triassic age sequences.

The Solway Basin passes into the Northumberland Trough via the Bewcastle Anticline which has a steeply inclined western limb and a shallow eastern limb. The syn-rift Lyne Formation and Fell Sandstone Formation deposits of the Northumberland Trough thin towards the east. This could be explained as a result of greater extension on the basin-controlling Stublick Fault in the west. The post-rift deposits have been eroded in the west where the basin has been folded to form the Bewcastle Anticline.

Figure 3.16 presents the gravity data and model that crosses the Northumberland Trough, Alston Block and Stainmore Trough. The position of the Iapetus Suture Zone has been inferred from seismic data acquired to the east and west of the region to lie beneath the Northumberland Trough (Figure 2.2). The structure of the Northumberland Trough in this model is based on the seismic interpretation of Chadwick *et al.* (1995), with the exception of a thicker

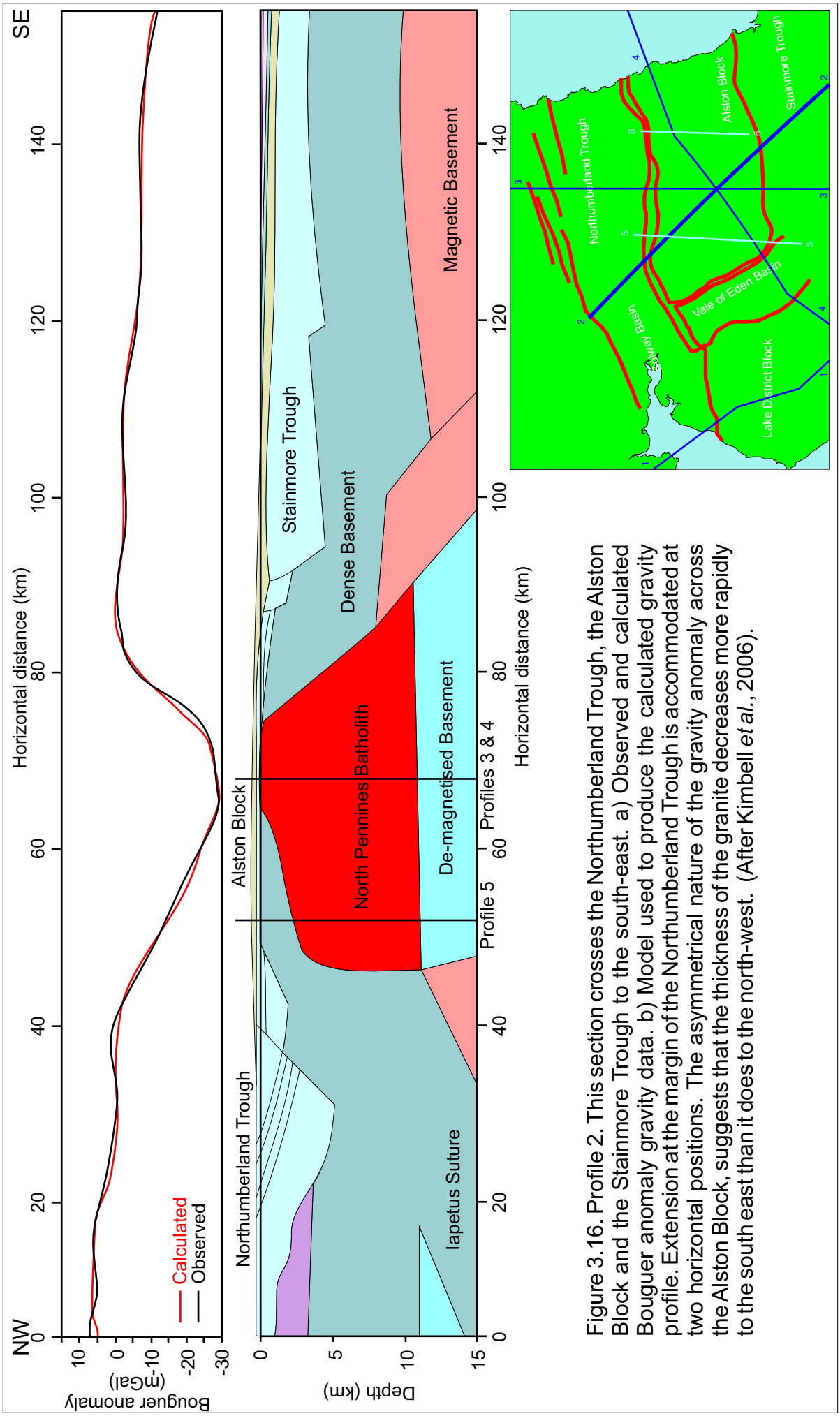


Figure 3.16. Profile 2. This section crosses the Northumberland Trough, the Alston Block and the Stainmore Trough to the south-east. a) Observed and calculated Bouguer anomaly gravity data. b) Model used to produce the calculated gravity profile. Extension at the margin of the Northumberland Trough is accommodated at two horizontal positions. The asymmetrical nature of the gravity anomaly across the Alston Block, suggests that the thickness of the granite decreases more rapidly to the south east than it does to the north-west. (After Kimbell *et al.*, 2006).

sequence of Carboniferous sediments towards the northern edge of the Alston Block, which is required to provide a better fit for the calculated gravity to the observed gravity (Kimbell *et al.*, 2006). This interpretation agrees with the data presented in cross-section D-D'. Additional gravity and seismic data is available in Appendix A.

### *3.2.12 Section K - K'*

This cross-section (Figure 3.17) traverses 99 km from west to east across the Vale of Eden Basin and the Alston Block. The Vale of Eden Basin is an asymmetrical half-graben that is oblique to the east-north-east to west-south-west structural trend of the troughs. The basin is fault-controlled at its eastern margin by the west-dipping Pennine Fault. The western margin is not fault-controlled and the basin fill onlaps the Lake District Block.

The complex structure of the North Pennines Batholith is illustrated clearly in this cross-section. There are two cupolas to the west of the main batholith and one to the east. The sediments are thickest where the North Pennines Batholith is not present beneath the Alston Block on the eastern edge of the block, where there has been greater subsidence.

Figure 3.18 illustrates the interpreted seismic line BGS-86-04, which cross part of the Alston Block. from east to west (Figure 3.2). The North Pennines Batholith can be identified within the crust by its poorly reflective nature. The increase in reflectivity at 4.9 s two-way travel time (twtt) (~13 km depth) is interpreted as marking the boundary between the

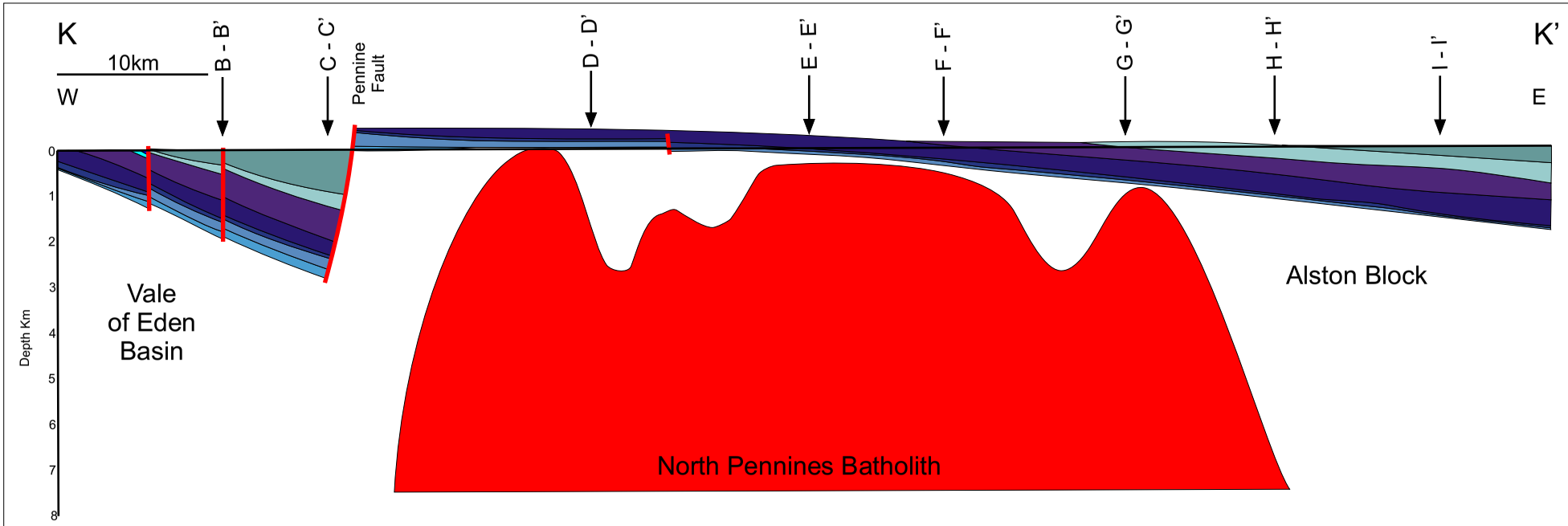


KEY

| | New Nomenclature | Previous Nomenclature |
|---|---|---|
| | Permo-Triassic | Permo-Triassic |
| | Pennine Coal Measures Group | Coal Measures |
| Yoredale Group | Stainmore Formation | Stainmore Group |
| | Alston Formation | Liddesdale/Alston Group |
| | Tyne Limestone Formation | Upper Border Group |
| Border Group | Fell Sandstone Formation | Middle Border Group |
| | Lyne Formation | Lower Border Group Upper |
| | | Lower Border Group Lower |
| | North Pennine Batholith | Weardale Granite |

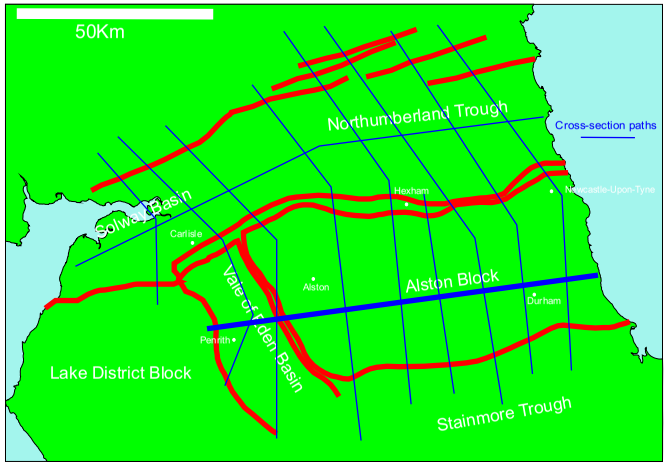


Figure 3.17. Cross-Section K-K'. The Vale of Eden Basin is an asymmetrical half-graben that is oblique to the main east north east to west south west trend and controlled at its eastern margin by the Pennine Fault. The complex structure of the North Pennines Batholith beneath the Alston Block is illustrated in this cross-section. The sediments are thickest where the North Pennines Batholith is not present beneath the Alston Block on the eastern edge of the block, where there has been greater subsidence.

Figure 3.18. Interpretation of seismic lines BGS-86-04 across the Alston Block. The North Pennines Batholith can be identified in the crust by its poor reflective nature.BGS-86-04 The main cupola lies almost directly beneath the carboniferous sediments in this line. Towards the east, the Cornsay cupola lie deeper within the crust and is separated from the Carboniferous sequence by pre-Carboniferous basement.
A strong reflector at 10 s two way travel time is interpreted to be the Moho.

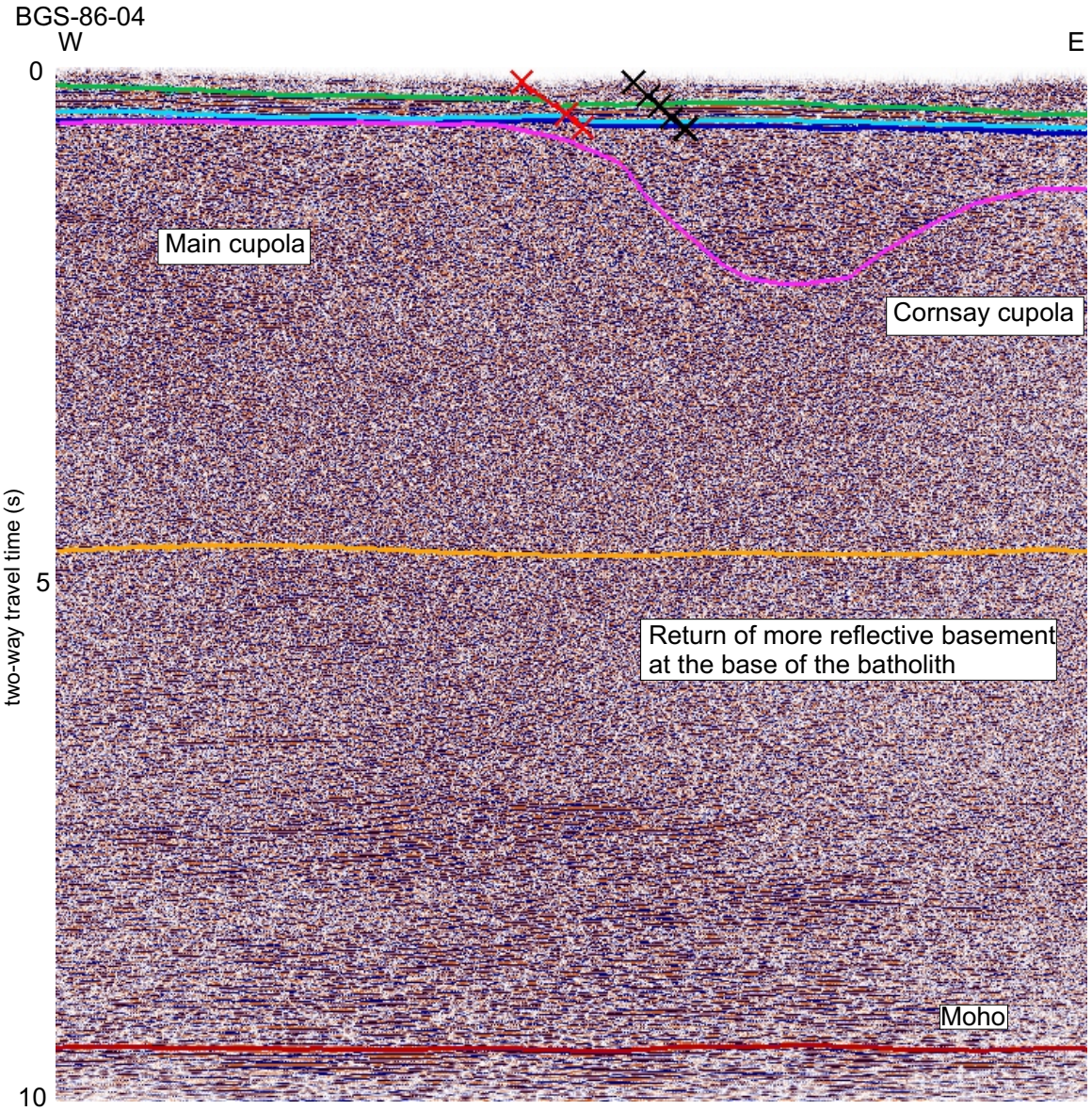


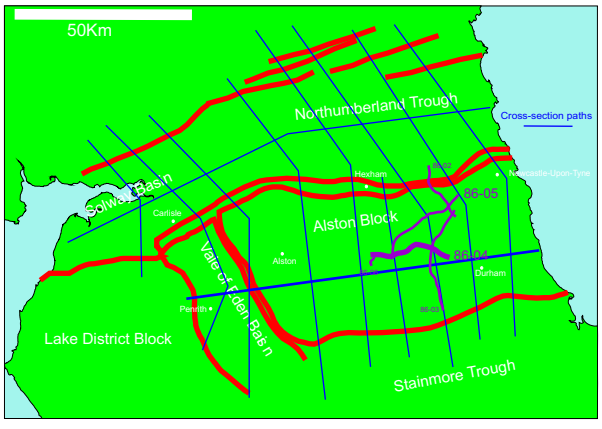


Key

- Top pre-Carboniferous basement
- Top batholith
- Base Batholith
- Top Alston Formation
- Top Stainmore Formation
- Faults
- Moho

relatively homogeneous granite intrusion and the more reflective country rock. At approximately 10 s twtt (~ 29 km depth) within section BGS-86-04, the strength of reflectors within the lower crust increase. This is interpreted as the position of the Moho (Chadwick and Evans, 2005).

Section BGS-86-04 crosses over the eastern edge of the main cupola, where it lies almost directly beneath the Carboniferous sediments. The section then runs eastwards over the Cornsay cupola, which is deeper within the crust and separated from the Carboniferous sequence by pre-Carboniferous basement rocks.

### 3.3 Summary

Analysis of the seismic, gravity and borehole data from the Northumberland Trough region has provided insights into the timing and magnitude of fault movement, depositional environments and the shape and depth of the North Pennines Batholith, all of which can be incorporated into the modelling aspect of this study. In addition, burial history modelling, described in chapter 6, constrained by borehole and subsurface data, provides a quantitative analysis of trends in subsidence and uplift across the Northumberland Trough Region.

# 4 Two-dimensional modelling of the deformation resulting from extension.

Several processes can be identified in response to a singular period of extension. Deformation results from the application of stress to the lithosphere. Extensional deformation is controlled by the strength of the lithosphere, which itself is a result of its rheology (Kusznir and Park, 1987). The lithosphere is not a homogeneous layer. It comprises a brittle layer in the upper crust that varies in thickness between approximately 10 and 30 km (Bott, 1971; 1976) in which deformation occurs dominantly by faulting and a deeper ductile layer where deformation is more likely to occur as a result of regionally distributed pure shear deformation.

Structural deformation of the lithosphere has consequences for heat transfer resulting in thermal disturbances. Thermal disturbances within the Earth are equally a motivating force for, and a product of, tectonic processes (Hu *et al.*, 2001). It is important, therefore, to consider geothermal processes and their influence upon basin evolution when modelling lithosphere extension. The structural deformation of the lithosphere also generates alterations in the distribution of mass within the lithosphere producing an isostatic response. The word isostasy is derived from the Greek 'iso' and 'stasis' which, when translated, mean equal standing. It describes the condition of equilibrium that the Earth tends towards in the absence of any disturbance of pressure, density and loading (Watts, 2001).

This chapter examines the established theory relating to modelling these processes. Faulting is an important factor in controlling basin development. As such, understanding fault geometry and hanging wall deformation is of critical importance to an analysis of extensional basin evolution. This chapter will also consider the strength of the lithosphere and the factors that affect the brittle-ductile transition within it and the means by which the ductile lower crust is deformed by pure shear. The thermal processes resulting from lithosphere extension, thermal uplift and subsequent thermal subsidence, are examined. The isostatic response to the loading resulting from extension of the lithosphere has an important influence upon basin evolution and therefore stratigraphical development. Several isostatic hypotheses have been put forward to explain the mechanism by which isostatic equilibrium is restored. The two most widely recognised hypotheses to emerge from early studies of isostatic theory are Airy isostasy (Airy, 1855) and Pratt isostasy (Pratt, 1859). However, neither hypothesis is able to adequately explain regional isostatic compensation. In order to accomplish this, the theory of flexural isostasy was developed (Walcott, 1970). This chapter will consider these isostatic hypotheses, including the methods of modelling isostatic compensation.

## 4.1 Two-dimensional modelling of the structural deformation resulting from fault movement.

Faulting (simple shear) is a mechanism that deforms the lithosphere in response to an applied force. At low temperatures and pressures, rocks

behave as brittle solids and large stresses cause fractures in the rock. A fault is a surface along which the rock has fractured and the rock on one side has moved relative to that on the other side, in a direction parallel to the surface (Twiss and Moores, 1992). The hanging wall and footwall blocks are fault-bounded volumes of rock that lay above and below a dipping fault surface, respectively. In the case of a normal or extensional fault, the hanging wall is down thrown relative to the footwall.

Fault surfaces can be defined by two main geometries; planar and listric. Planar faults exhibit constant dip with depth and may be characterised as rotational or non-rotational depending on whether the faults and beds within the hanging wall and footwall blocks maintain their orientation or are progressively rotated with respect to each other (Wernicke and Burchfiel, 1982; Twiss and Moores, 1992). The fault blocks may be substantially rotated, but they suffer only minor internal deformation and the upper surfaces of the fault blocks are essentially planar after extension (Kusznir and Egan, 1989). In contrast, listric faults have a curved fault profile that is generally convex towards the footwall strata (Wernicke and Burchfiel, 1982). They do not exhibit a constant dip, instead they show a progressive decrease in dip with depth until the fault profile is near horizontal, forming a detachment surface (Twiss and Moores, 1992). Extensional movement on a listric fault pulls the blocks apart such that a gap develops between the footwall and hanging wall blocks (Figure 4.1). This void is filled by collapse of the hanging wall onto the fault surface under the influence of gravity (Egan *et al.*, 1999). The

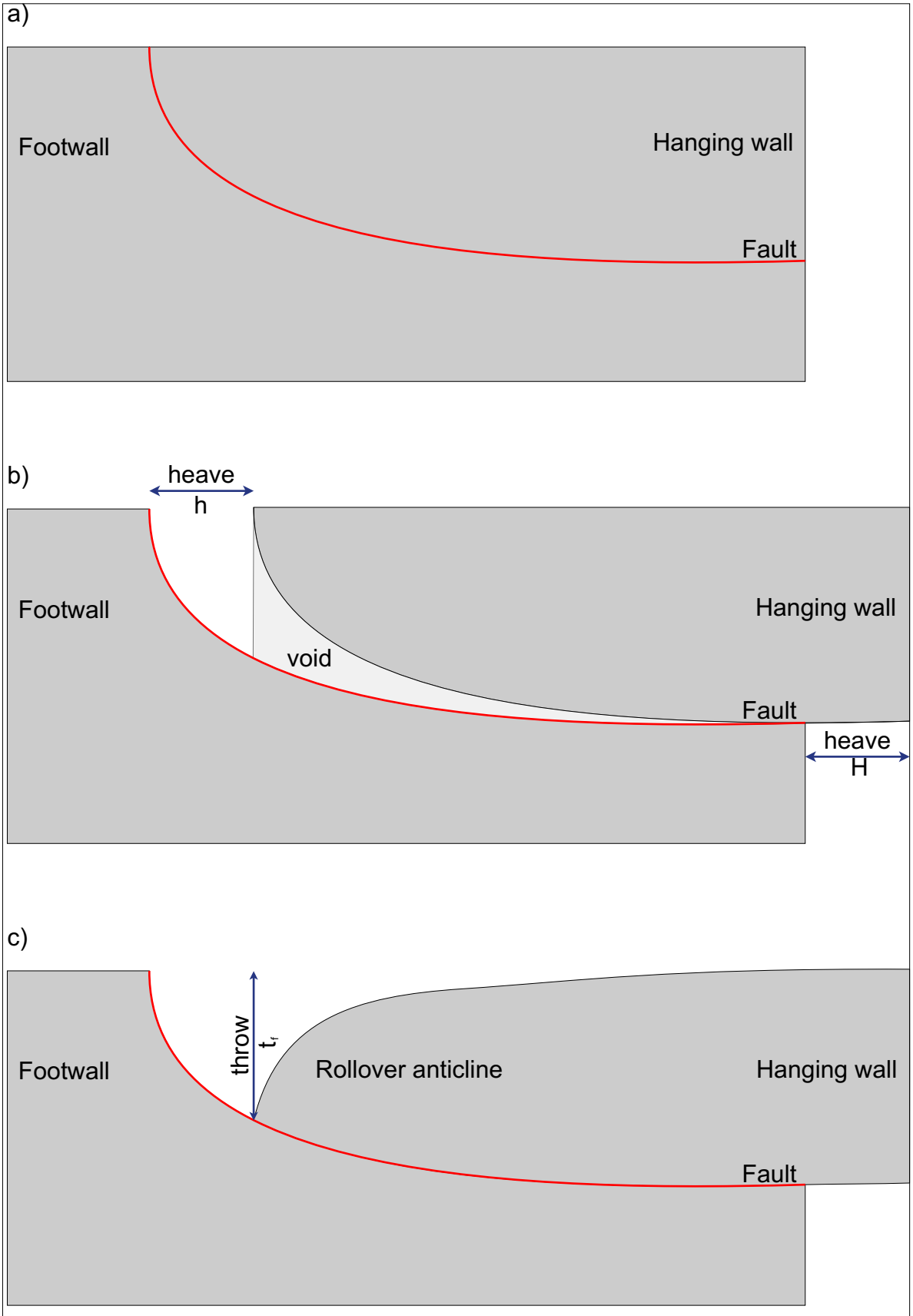


Figure 4.1. a) Profile of a listric fault. The hanging wall block lies above the fault. The footwall block lies beneath the fault. b) Extensional movement along the fault, by an amount of heave (h), pulls the blocks apart such that a void develops between the footwall and hanging wall blocks. c) The potential void is filled by collapse of the hanging wall onto the fault under the influence of gravity along an infinite number of vertical shear planes generating a rollover anticline. (After White *et al*., 1986).

deformation of the hanging wall generates a fold geometry known as a rollover anticline (Hamblin, 1965; Xiao and Suppe, 1992). Subsidiary faults can also develop in response to the curvature of the fault plane at depth (Gibbs, 1984; Peacock *et al.*, 2000).

Wernicke (1985) proposed that in areas of large-magnitude extension, low-angle, planar faults are the main structures responsible for overall extension. However, this assumption introduces both volume and geometrical problems with regard to the basal detachment and within the adjacent fault blocks (Gibbs, 1984). Seismic reflection data indicate that many faults in extensional regimes have a listric profile (Gibbs, 1983; Williams and Vann, 1987). The generation of folds and subsidiary faults within the hanging wall in response to displacement eliminate some of the space problems associated with the assumption of listric faults as the main structures responsible for extension (Gibbs, 1984).

### *4.1.1 Methods of modelling fault deformation*

Modelling of the structural deformation resulting from normal fault movement requires an understanding of the relationship between the geometry of the fault and the strata in the hanging wall (White *et al.*, 1986). The vertical shear (Chevron) construction (Gibbs, 1983; 1984; Verrall, 1981) and the inclined shear construction (White *et al.*, 1986) are methods of modelling the geometry of the hanging wall for a given amount of extension along a fault. These methods use geometrical constructions to model hanging wall deformation as it moves over the underlying and

footwall that is assumed to be rigid. The slip-line construction (Williams and Vann, 1987) is an alternative method of modelling hanging wall deformation from the profile of a fault, which conserves displacement along the fault. The inclined shear construction is particularly suitable for the modelling being carried out as part of this research as it allows the geometry of the hanging wall away from the fault surface to be established (Clarke, 2002) and in many cases it approximates hanging wall deformation more realistically than the vertical shear and modified chevron construction models (Dula, 1991). The assumption that hanging wall deformation occurs along a shear plane that is at an inclined angle is supported by evidence of subsidiary faulting within the hanging wall block of the Northumberland Trough that can be observed in the cross-sections shown in chapter 3 and in the interpreted seismic data. The method of modelling the inclined shear construction is considered below. A discussion of the alternative methods of modelling the structural deformation resulting from fault movement can be found in appendix B.

#### 4.1.1.1 The inclined shear construction

A major weakness with the vertical shear construction and its derivatives is that the collapse of the hanging wall following extension is restricted to simple shear on vertical planes (Egan *et al.*, 1999). Subsidiary faults observed within hanging wall blocks are generally not vertical (White *et al.*, 1986). This can be observed within the Northumberland Trough where subsidiary faults both synthetic and antithetic to the basin-bounding fault are observed. This implies that hanging wall shear occurs

at an inclination to the vertical. The inclined shear construction is a modification to the vertical shear construction that allows for non-vertical simple shear within the hanging wall (White *et al.*, 1986). The inclined shear construction is based on the same technique as the vertical shear construction except that the construction lines overlying the cross-section, and along which the hanging wall is displaced, are at an inclination to vertical (Figure 4.2).

The inclined shear construction can be defined numerically in several ways. The method presented here follows that of Egan *et al.* (1999). The geometry of the fault profile is modelled using equation [4.1].

$F_{(x)} = 0$ for $x < x_f$

$$F_{(x)} = Zd\left[1 - \exp\left(-\frac{x - x_f}{Zd}\right)\right] \text{ for } x \geq x_f \qquad [4.1]$$

where: $x_f$ is the horizontal position of the surface outcrop of the fault.

$Zd$ is the detachment depth of the fault.

A profile of the geometry of the hanging wall surface prior to deformation ($HW_{(x)}$) is also required. For simplicity it is assumed to be flat, such that:

$HW_{(x)} = 0$ for all values of x [4.2]

The plane in which simple shear of the hanging wall occurs ($y'$) is not vertical, but inclined by $\alpha_s$. To calculate the resultant hanging wall deformation by the inclined shear construction method, the model profiles are translated from the two-dimensional Cartesian co-ordinates ($x,y$) into

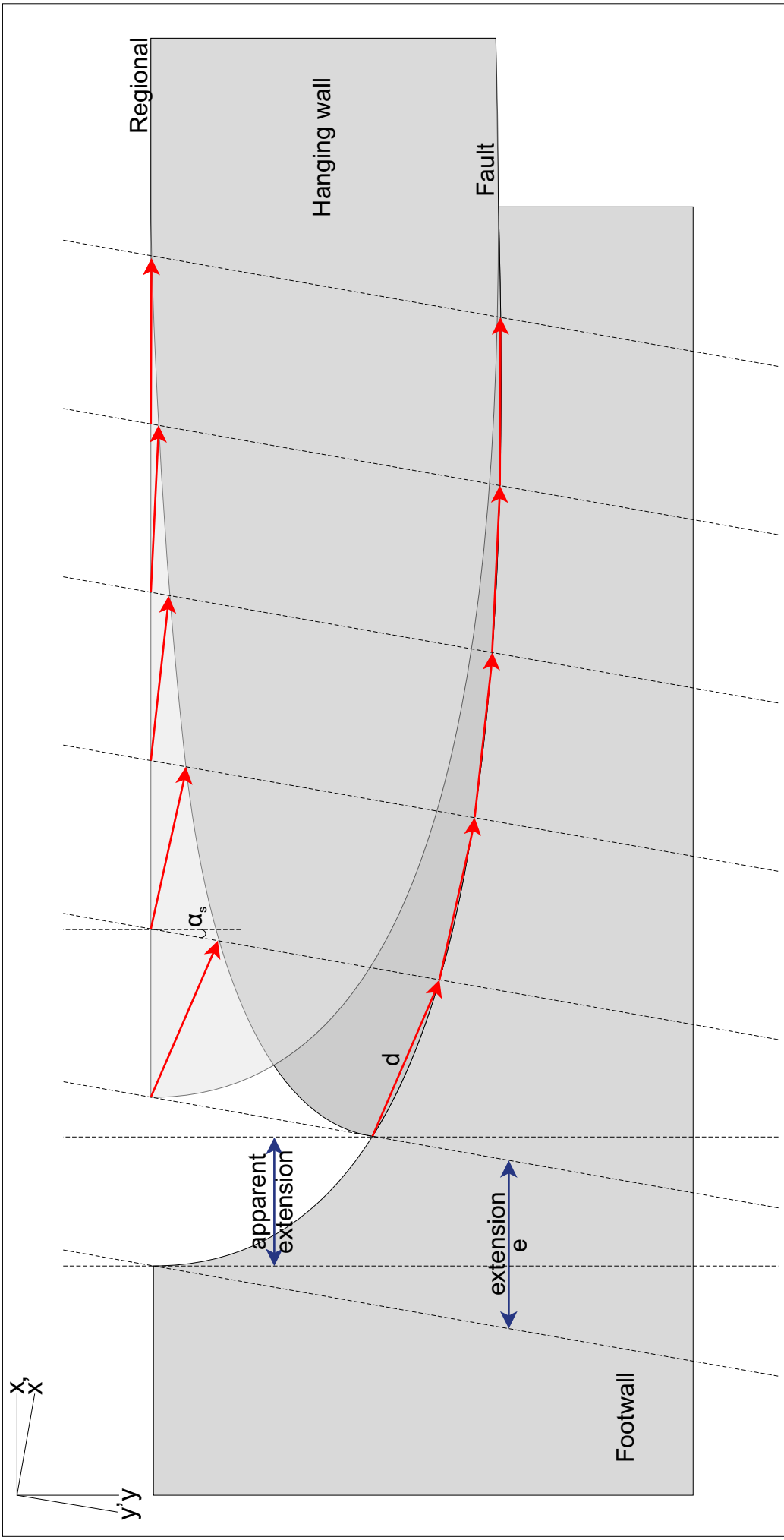


Figure 4.2. The Inclined Shear Construction. In order to numerically define the inclined shear construction, it is necessary to rotate the model profiles into a new co-ordinate system such that y' is vertical. The observed horizontal extension or apparent extension on a fault upon which deformation of the hanging wall has occurred by inclined simple shear will not be a reflection of the true value of extension (After White *et al.*, 1986).

a new co-ordinate system $(x', y')$ such that the shear plane is vertical (Figure 4.3). This is achieved using equations [4.3]-[4.7].

Both $F_{(x)}$ and $HW_{(x)}$ have the same $x$ co-ordinates, therefore their rotated profiles have the same $x'$ coordinates:

$$x' = \left(x \cos(\alpha_s)\right) + \left(F_{(x)} \sin(\alpha_s)\right) \quad [4.3]$$

The $y'$ coordinates of the fault and hanging wall profiles are given by:

$$F_{(x)}' = \left(-x \sin(\alpha_s)\right) + \left(F_{(x)} \cos(\alpha_s)\right) \quad [4.4]$$

$$HW_{(x)}' = -x' \tan(\alpha_s) \quad [4.5]$$

and the heave in the $x'y'$ coordinate system is given by:

$$e' = e \cos(\alpha_s) \quad [4.6]$$

These rotated profiles are used to model deformation of the hanging wall by modifying equation [B4.2] from the vertical shear construction. It is necessary to account for the profile of the hanging wall prior to deformation in the new coordinate system in order to calculate the depth of the hanging wall following deformation. The deformation of the hanging wall is determined by:

$$HT_{(x)}' = \left(F_{(x)}' - HW_{(x)}'\right) - \left(F_{(x-e')}' - HW_{(x-e')}'\right) \quad [4.7]$$

The method necessary to determine $x - e'$ is given in appendix B.

The profile of the deformed hanging wall is determined by adding the deformation of the hanging wall calculated in equation [4.8] to the profile of the undeformed hanging wall [4.5], such that:

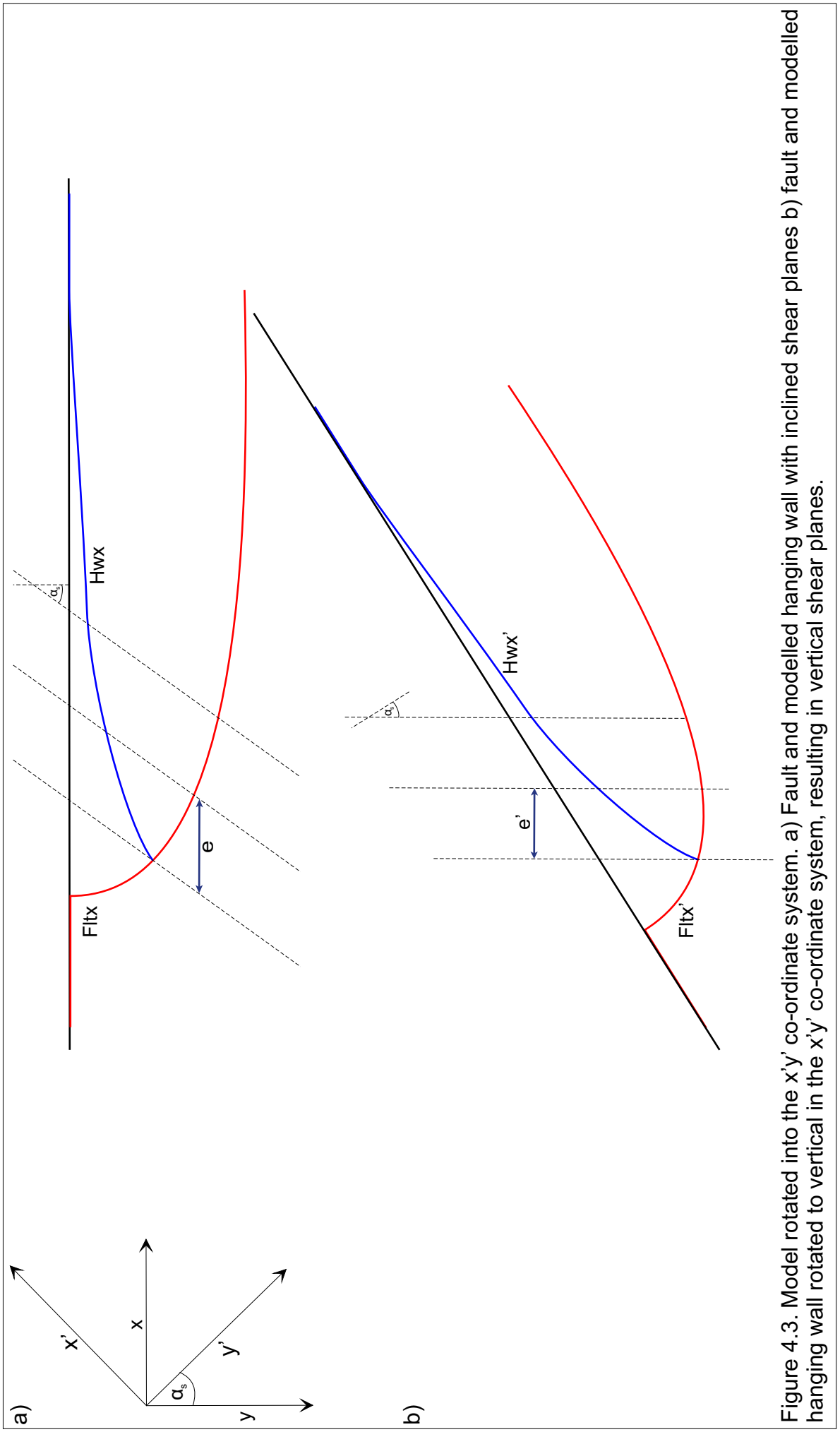


Figure 4.3. Model rotated into the x'y' co-ordinate system. a) Fault and modelled hanging wall with inclined shear planes b) fault and modelled hanging wall rotated to vertical in the x'y' co-ordinate system, resulting in vertical shear planes.

$$HW_{(x)}{}' = HW_{(x)}{}' + HT_{(x)}{}' \quad [4.8]$$

Once the deformed hanging wall profile has been calculated it is necessary to rotate the hanging wall profile back into the $x,y$ coordinate frame. Rotation of the $x$ coordinate of the hanging wall $x_H$ is achieved by:

$$x_H = \left(x' \cos(\alpha_s)\right) - \left(HW_{(x')} \sin(\alpha_s)\right) \quad [4.9]$$

The $x$ coordinates of the hanging wall profile may no longer be the same as the value of the $x$ coordinates of the fault profile. The $y$ coordinate of the hanging wall profile is rotated by applying the following equation:

$$HW_{(x_H)} = \left(x' \sin(\alpha_s)\right) + \left(HW_{(x')} \cos(\alpha_s)\right) \quad [4.10]$$

Similar to the vertical shear construction, the inclined shear construction assumes that the footwall remains rigid and does not deform under extension. However, this assumption may not be entirely the case with deeper basement faults that are responsible for crustal scale extension, which may be deformed during deformation as a result of other deep processes (White *et al.*, 1986).

Another weakness of the inclined shear model is the need to estimate the shear angle ($\alpha_s$). The value of $\alpha_s$ used in the model is an apparent shear value; the assumption of a single shear angle is a simplification. In reality, the shear angle varies spatially and temporally within the hanging wall, increasing with distance from the fault, and decreasing with increasing extension (Dula, 1991). Measuring the orientation of minor subsidiary faulting in the hanging wall block is a method of estimating $\alpha_s$

(White *et al.*, 1986). However, as has been shown in chapter 3, subsidiary faulting can occur with a variety of orientations, including both synthetic and antithetic subsidiary faulting. In these cases the orientations of the minor faults cannot be used to obtain an estimate of apparent shear angle (Dula, 1991). The apparent shear angle $\alpha_s$ can also be determined from observation of the geometry of two or more beds within the hanging wall, since fault geometry remains unchanged. If the pre-extensional geometry of the beds within the hanging wall and the magnitude of displacement on the fault are known, then assuming a constant angle of shear, the direction and angle of shear can be determined by inverting the section iteratively until the modelled results fit the observed beds. (Bruce, 1973; White *et al.*, 1986). An alternative method for determining the apparent shear angle involves iterative modelling whilst systematically varying the shear angle and comparing the resultant hanging wall model to the geometry of the observed hanging wall (Dula, 1991).

It is also important to consider that if inclined shear is the method by which the hanging wall of the fault has been deformed, the observed amount of horizontal extension will not reflect the true value of extension. The movement of the hanging wall away from the footwall has been changed by the internal deformation of the hanging wall necessary to fill the potential void beneath it (White *et al.*, 1986). This 'apparent extension' is the result of displacement of the hanging wall along an inclined plane. For an angle of shear synthetic to the fault, the observed horizontal

extension will be greater than the true value of extension. Conversely, for a shear angle antithetic to the fault, the observed horizontal extension will be smaller than the true value of extension.

The accommodation space created by the deformation of the hanging wall as a result of the application of the inclined shear construction for a given fault geometry and value of heave is constant, and cross sectional area is conserved. However, the hanging wall geometry produced as a result of this modelling varies depending on the angle and sense of shear (White *et al.*, 1986; Egan *et al.*, 1999). A shear angle of $\alpha_s = 0°$ is the equivalent of vertical shear (Figure 4.4). As the distance from the fault increases, the hanging wall profile returns to the regional datum (i.e. $R = 0$ where $R$ is the regional datum). Closer to the fault outcrop, the inclination of the shear plane is responsible for the depth of the resultant basin. The larger the value of the synthetic shear angle, the deeper the basin that results from deformation of the hanging wall. Similarly the larger the value of the antithetic shear angle, the shallower the resultant basin. For example, extension with $\alpha_s = -45°$ (antithetic) generates a narrower, shallower, asymmetrical half-graben compared to the half-graben structure with $\alpha_s = 0°$ . In contrast, $\alpha_s = 45°$ (synthetic) generates a wider, deeper asymmetrical half-graben (Figure 4.4).

The inclined shear construction is based on the same analytical technique as the vertical shear construction with the exception that the construction lines upon which the hanging wall is deformed are at an inclination to

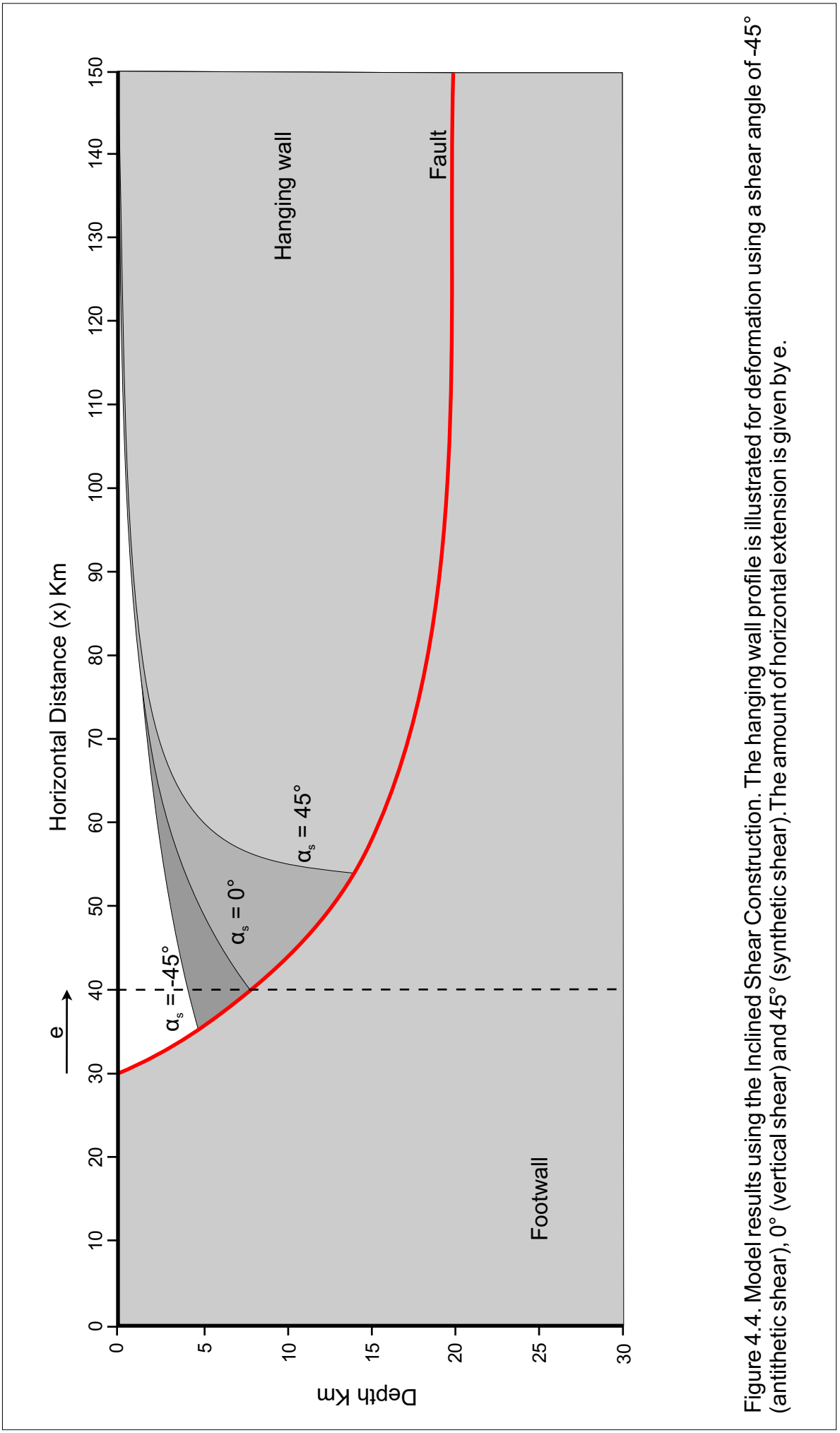


Figure 4.4. Model results using the Inclined Shear Construction. The hanging wall profile is illustrated for deformation using a shear angle of -45° (antithetic shear), 0° (vertical shear) and 45° (synthetic shear). The amount of horizontal extension is given by e.

vertical. The direction and angle of shear deforming hanging wall block has a strong influence on the resultant shape of the horizons within it.

Extensional basins are characterised by faulted margins upon which the majority of the displacement is generally accommodated by a small number of major faults. These major faults are accompanied by a number of subsidiary faults that accommodate smaller amounts of displacement and provide minor structural adjustments required for the major faults to accommodate the larger scale displacements. It is therefore necessary to model fault systems with multiple synthetic and antithetic subsidiary faults. This can be done by adapting the geometry of any subsequent faults and their hanging walls to consider the geometry of preceding faults. The application of fault deformation to extensional basins will be considered in chapter 5.

## 4.2 Pure shear deformation of the lithosphere

The brittle layer and the ductile layer are separated by the brittle-ductile transition; a competent elastic region (Sibson, 1977; Rutter, 1986; Kohlstedt *et al.*, 1995). The transition from brittle to ductile behaviour depends on factors including the strength of the lithosphere and the strain rate. The strength of the lithosphere is determined by the relationship between the composition of the crust, its thickness and the geothermal gradient (Kusznir and Park, 1986; 1987). Subsidence within basins can be related to these lithosphere scale processes that act upon them (Quinlan *et al.*, 1993).

The role of rheology in kinematic modelling is implicit in that the model is sensitive to the initial conditions imposed upon it (Negredo *et al.*, 1995; Fernandez and Ranalli, 1997). The existence of low strength regions within the lithosphere influences the position of the brittle-ductile transition and therefore the detachment horizons of faults (Kusznir *et al.*, 1987). As previously stated, the brittle layer deforms by faulting and although deformation due to fault movement is an important factor in lithosphere deformation, it is restricted to relatively shallow, brittle levels of the crust (Kusznir and Egan, 1989). The mid-lower crust and the lithospheric mantle are assumed to deform in a ductile manner (Artemjev and Artyushkar, 1971). Deformation within this ductile layer occurs by pure shear, which is a three-dimensional co-axial flattening strain in which the principal strain axes remain parallel to their respective principal stress axes during deformation (Figure 4.5) (Park, 1989).

It has been proposed that pure shear extension in the lower crust occurs along sets of low angle anastomosing shear zones (Reston, 1988). Evidence for this mechanism is provided by seismic data where strongly reflective zones and transparent zones in the lower crust are interpreted as mylonitic shear zones and low-strain zones, respectively, with the shear zones converging and diverging around less deformed lozenges (Klemperer, 1988; Reston, 1988; 1990a). In addition, some mantle reflections observed on deep seismic profiles have also been interpreted as shear zones (Reston 1990b). Similar localised shear zones are observed in high-grade metamorphic terrains which deformed under similar

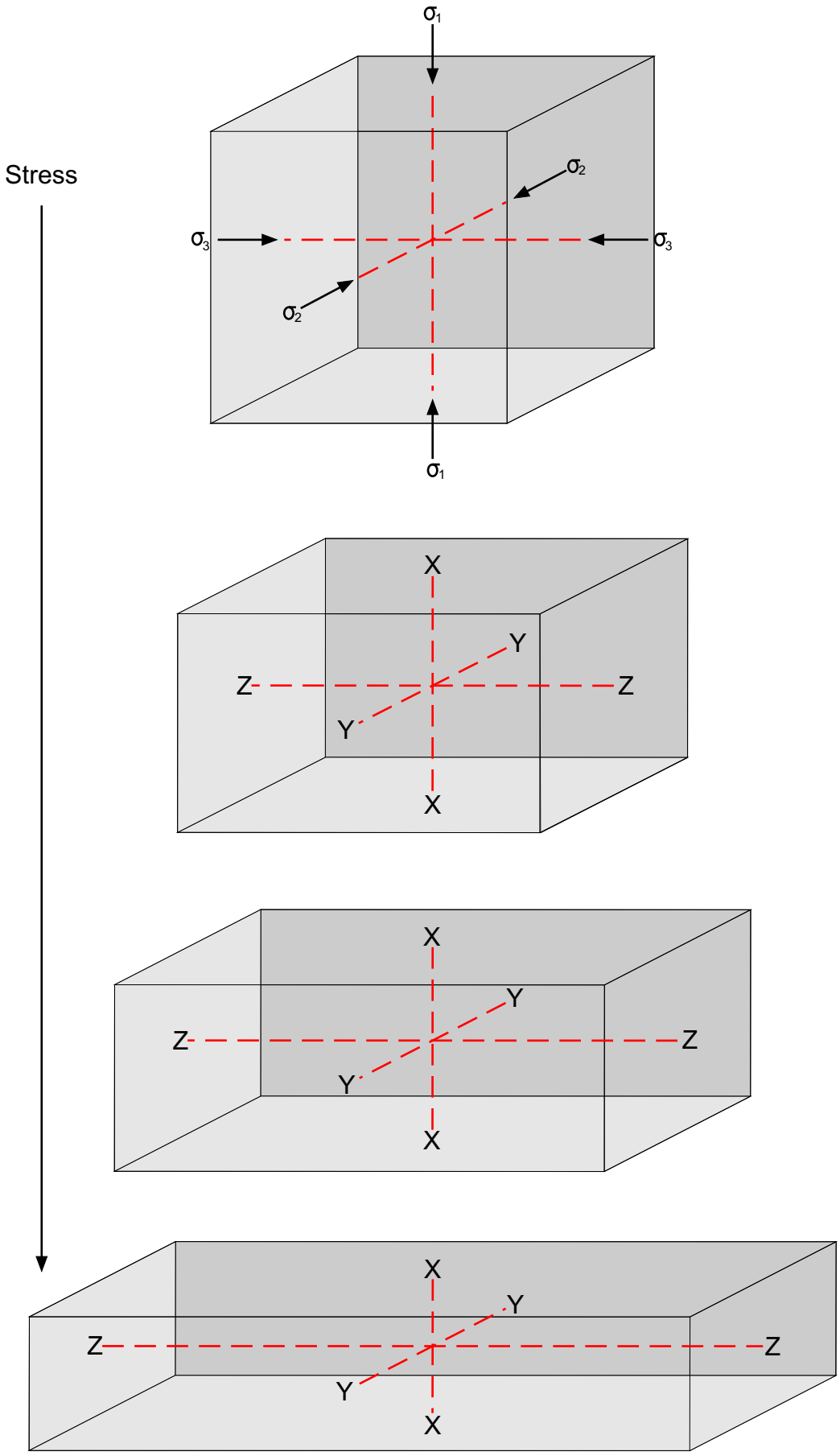


Figure 4.5. Pure shear, a co-axial flattening strain in which the principal strain axes (X, Y and Z) remain parallel to their respective principal stress axes ($\sigma_1$, $\sigma_2$ and $\sigma_3$) during deformation (After Park, 1989).

conditions to those found within the lower crust (Ramsey, 1980; Dawson *et al.*, 1986; Reston 1990a).

#### 4.2.1.1 Uniform extension

The McKenzie model (McKenzie, 1978) (Figure 1.2) provides a quantitative representation of the extensional deformation of the lithosphere by pure shear and can be used to provide a good approximation of deformation in the ductile layers of the lithosphere. The McKenzie model is divided into two phases of basin development, initial subsidence and thermal subsidence. The model assumes that at time $t = 0$, a unit of lithosphere is extended by a factor of $\beta$, resulting in thinning of the lithosphere. The amount of extension, $\beta$, is defined by the ratio of the extended length of the lithosphere to its initial length such that:

$$\beta = \frac{length_{final}}{length_{initial}} \qquad [4.11]$$

The initial subsidence, $S_i$, given by equation [4.12] (McKenzie, 1978; Allen and Allen, 1990), represents the mechanical thinning of the lithosphere by pure shear after extension at time $t = 0$. The equation also quantifies the amount of thermal uplift generated by raising of the lithosphere-asthenosphere boundary, as well as isostatic compensation.

$$S_i = \frac{a\left[\left(\rho_m - \rho_c\right)\frac{C_o}{a}\left(1 - \alpha_T T_o \frac{C_o}{2a}\right) - \frac{\alpha_T T_o \ \rho_m}{2}\right]\left(1 - \frac{1}{\beta}\right)}{\rho_m\left(1 - \alpha_T T_o\right) - \rho_i} \qquad [4.12]$$

where: $a$ is the thickness of the lithosphere

$C_o$ is the initial thickness of the crust

$\rho_m$ is the density of the mantle

$\rho_c$ is the density of the crust

$\rho_i$ is the density of the basin filling material i.e. sediment and/or sea water

$\alpha_T$ is the thermal expansion co-efficient of the lithosphere

$T_o$ is the temperature at the base of the lithosphere

$\beta$ is the expansion factor; for extension $\beta$ has a value between 1 and $\infty$

Some average values, applied to the above parameters, can be found in Table 1.1.

Figure 4.6 Illustrates the resulting initial subsidence, $S_i$, for a variety of initial crustal thicknesses, $C_o$, and extension factors, $\beta$, to show the importance of pure shear deformation upon surface elevation. These results indicate that the value of $S_i$ is not always positive (i.e. subsidence). For initial crustal thicknesses of 18.5 km or less, $S_i$ is negative, indicating that there is uplift at the surface. In this case, the amount of thermal uplift, resulting from raising of the lithosphere-asthenosphere boundary, is greater than the amount of subsidence generated by the crustal thinning. When crust with an initial thickness greater than 18.5 km is extended, the amount of subsidence generated by crustal thinning is greater than the thermal uplift. Increasing the extension factor, $\beta$, results in a greater amount of uplift or subsidence respectively.

#### 4.2.1.2 Depth-dependent extension

There are several weaknesses that limit the usefulness of the McKenzie model, most of which are related to assumptions about rifting processes.

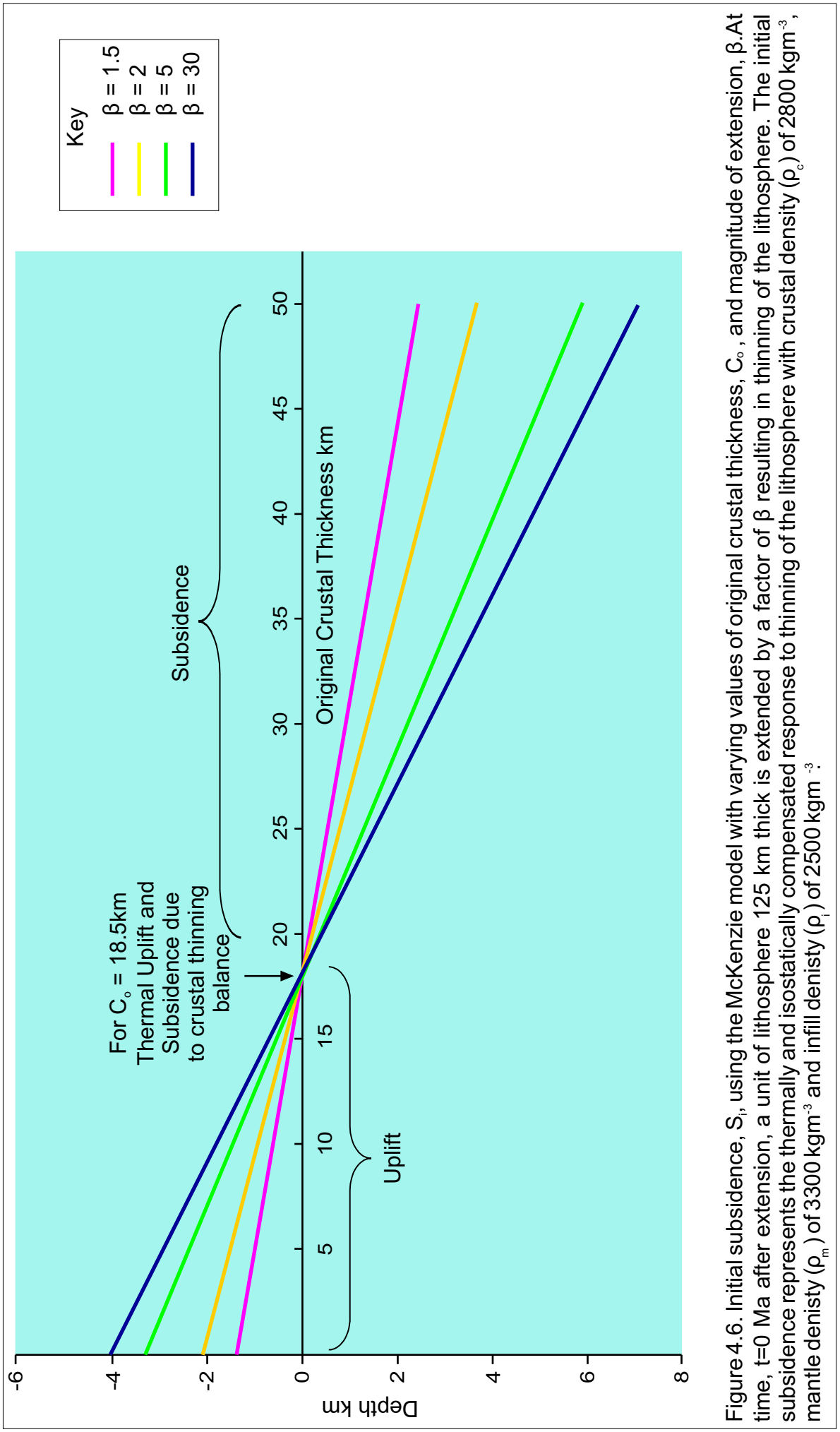


Figure 4.6. Initial subsidence, $S_i$, using the McKenzie model with varying values of original crustal thickness, $C_o$ , and magnitude of extension, β.At time, t=0 Ma after extension, a unit of lithosphere 125 km thick is extended by a factor of β resulting in thinning of the lithosphere. The initial subsidence represents the thermally and isostatically compensated response to thinning of the lithosphere with crustal density ($\rho_c$) of 2800 kgm$^{-3}$, mantle denisty ($\rho_m$) of 3300 kgm$^{-3}$ and infill denisty ($\rho_i$) of 2500 kgm $^{-3}$.

The model assumes that extension of the whole lithosphere occurs exclusively as a result of pure shear and it is not able to describe the deformation by faulting that takes place in the upper crust. It also assumes that extension is uniform throughout the lithosphere. However, the lithosphere is not a homogeneous body; it has rheological properties that vary with temperature, pressure and composition (section 1.2.1). Consequently, it cannot be expected to deform in a homogeneous manner, either laterally or with respect to depth, when stress is applied (Kusznir *et al.*, 1987). In response to these weaknesses Royden and Keen (1980) formulated the non-uniform lithosphere extension model (Figure 1.4) which is an adaptation of the McKenzie model and that accounts for the heterogeneous nature of the lithosphere. This model allows the lithosphere to be decoupled at a specific depth and deformed as separate sections, each extended by a different β factor.

Although the non-uniform lithosphere extension model still assumes that the sole mechanism of basin deformation is pure shear, the concept of non-uniform lithosphere extension or depth-dependent extension has some merit. Evidence acquired from many rifted margins suggests a discrepancy between the observed extension by simple shear in the upper crust and the estimate for overall lithosphere extension (Kington and Goodliffe, 2008). This mismatch can be explained as a result of varying amounts of extension in the upper and lower lithosphere above and below the decoupling depth, respectively. The decoupling depth can be interpreted as the point where there are depth-dependent changes in the

deformation mechanism such as the transition from brittle to ductile deformation, either as a distinct detachment or a distributed shear zone (Rowley and Sahagian, 1986). For example, Rosenbaum *et al.* (2008) suggest that the significant role of detachment faults in controlling structural evolution in extensional regimes implies that depth-dependent extension should be considered the prominent mechanism by which extension is accommodated in the lithosphere.

## 4.3 Coupled simple shear/pure shear model of continental lithosphere extension

Modelling the extension of the lithosphere by coupled simple shear and pure shear deformation allows for a quantitative model of lithospheric extension that can account for the major processes responsible for crustal thinning. Numerical models that simulate crustal thinning by coupling simple shear and pure shear mechanisms of deformation have been developed to enable forward modelling of extensional basins (Kusznir *et al.*, 1987; Kusznir and Egan, 1989). These models assume that all faults have a common detachment depth, which also represents the brittle-ductile transition, below which deformation results from pure shear.

It is possible to produce a coupled simple-shear/pure-shear model of lithosphere extension by modelling the geometry of the pure shear extension beneath an assumed fault detachment horizon. Algorithms have been developed to model the deformation by pure shear below the

detachment depth based on the methodology described in Kusznir *et al.* (1987) (Equations [4.13] - [4.16]). In addition, Figure 4.7 illustrates the parameters responsible for thinning of the lower crust by pure shear.

The extension factor of pure shear, $\beta$, is modelled with a sinusoidal distribution:

$$\beta_{(x)} = 1 + \beta_o \sin\left(\pi \frac{x}{W}\right) \qquad [4.13]$$

where: $(\beta_o + 1)$ is the maximum $\beta$ value at the peak of the sinusoidal distribution

$W$ is the width of the region undergoing pure shear deformation

$x$ is horizontal distance.

If the amount of extension by pure shear is balanced by the total amount of extension by simple shear in the upper crust, then the amount of extension ($e$) is given by:

$$e = \int_0^{W'} \left[\beta_{(x)} - 1\right] dx = 2\beta_o \frac{W'}{\pi} \qquad [4.14]$$

where: $W'$ is the width of the pure shear region pre-extension and:

$$W' = W - e \qquad [4.15]$$

Rearranging equation [4.16] gives $\beta_o$:

$$\beta_o = \frac{\pi}{2} \frac{e}{(W - e)} \qquad [4.16]$$

Within the numerical model it is necessary to define the positions at which the deformation resulting from pure shear starts and finishes; parameters

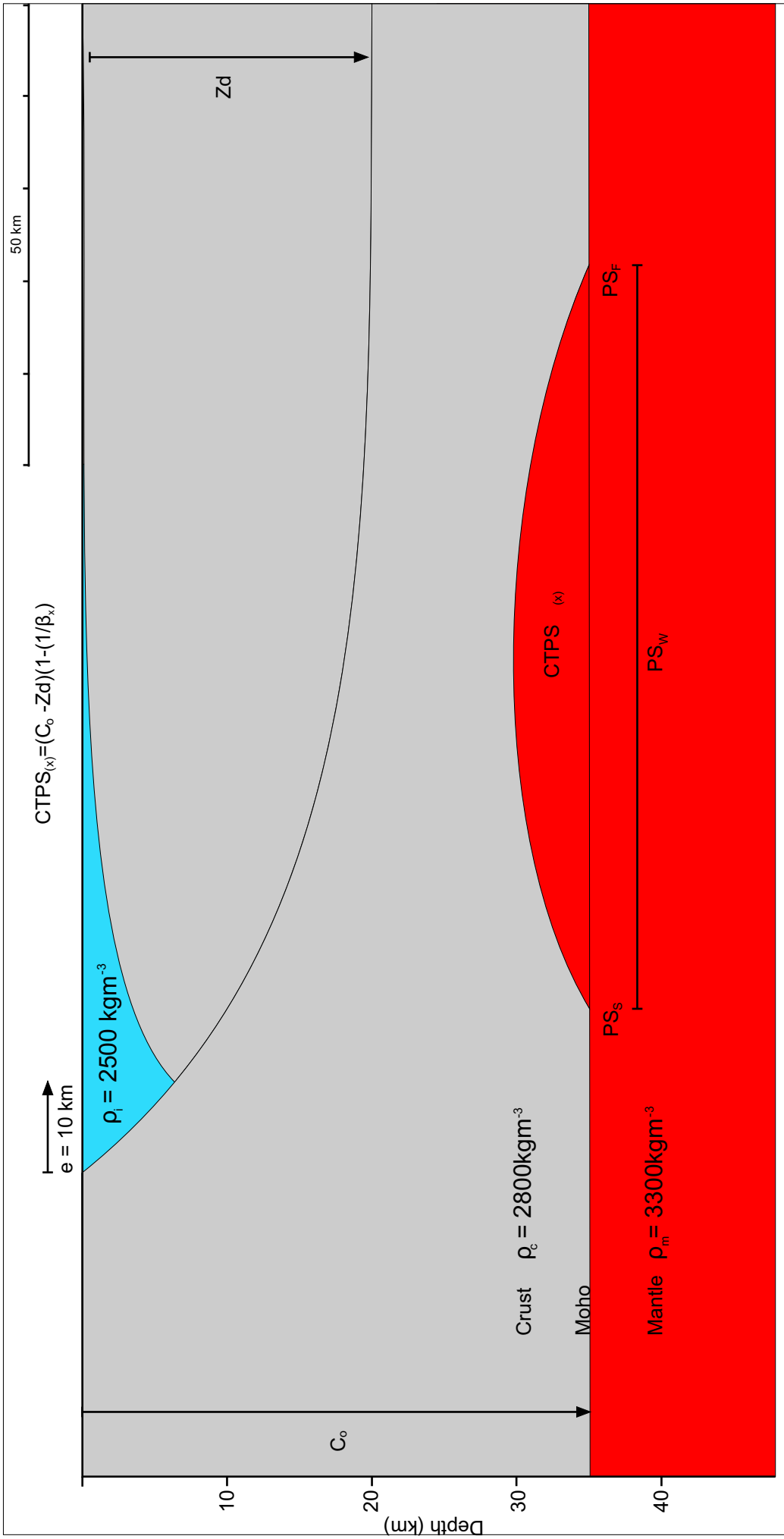


Figure 4.7. Thinning of the crust by faulting and pure shear. The upper crust is thinned by faulting with extension e = 10 km. The lower crust is thinned by pure shear between the horizontal positions $PS_S$ and $PS_F$. The amount of thinning of the lower crust $CTPS_{(x)}$ is related to the thickness of lower crust being deformed ($C_o$-Zd) and the β value.

$PS_S$ and $PS_F$, respectively. To determine the width of the region undergoing extension by pure shear, $PS_W$ is given by:

$$PS_W = PS_F - PS_S \quad [4.17]$$

If the amount of extension by pure shear is balanced by the amount of extension by simple shear, the value of $\beta_o$ can then be calculated using equation [4.18] such that:

$$\beta_o = \frac{\pi}{2}\frac{H_T}{\left(PS_W - H_T\right)} \quad [4.18]$$

where: $H_T$ is the amount of horizontal extension by simple shear.

It is possible to model pure shear that does not balance the amount of simple shear in the upper lithosphere in order to simulate depth-dependent extension. This can be done in two ways; either by replacing the value of $H_T$ with a specific value (Equation [4.19]), or by setting the value of $\beta_{Max}$ (Equations [4.19] – [4.20]).

$$\beta_o = \frac{\pi}{2}\frac{PS_T}{\left(PS_W - PS_T\right)} \quad [4.19]$$

$$\beta_{Max} = \left(\beta_o + 1\right) \quad [4.20]$$

$$\beta_o = \beta_{Max} - 1 \quad [4.21]$$

It is then possible to calculate the value of $\beta$ for each value of $x$ based on equation [4.13] such that:

$$\beta_{(x)} = \left(1 + \beta_o \sin\left(\pi \frac{\left(x - PS_S\right)}{PS_W}\right)\right) \text{ for } x \geq PS_S \text{ and } x \leq PS_F \quad [4.22]$$

and

$$\beta_{(x)} = 1 \text{ for } x < PS_S \text{ and } x > PS_F \quad [4.23]$$

The magnitude by which the crust has thinned by pure shear, $(CTPS)$, at each lateral position $(x)$ is given by:

$$CTPS_{(x)} = \left(C_o - Zd\right)\left(1 - \left(\frac{1}{\beta_{(x)}}\right)\right) \text{ for } x \geq PS_S \text{ and } x \leq PS_F \quad [4.24]$$

and

$$CTPS_{(x)} = 0 \text{ for } x < PS_S \text{ and } x > PS_F \quad [4.25]$$

where: $Zd$ is the fault detachment depth

In order to appreciate the effect that extension by pure shear has on basin geometry it is necessary to consider the isostatic effects that result from the crustal thinning generated by this deformational mechanism. The local (Airy) isostatic effect due to the thinning, $ISO_{PS(x)}$, can be determined by:

$$ISO_{PS(x)} = CTPS_{(x)}\left(\frac{\rho_m - \rho_c}{\rho_m}\right) \quad [4.26]$$

For extension, $ISO_{PS(x)}$ defines the isostatically compensated subsidence that is generated by thinning of the lower crust by pure shear. The profile

of the resultant basin, $B_{(x)}$, following a coupled simple shear and pure shear deformation is given by:

$$B_{(x)} = Flt_{(x)} + Iso_{PS(x)} \quad [4.27]$$

where: $Flt_{(x)}$ is the subsidence due to thinning of the upper crust by simple shear (i.e. faulting)

$ISO_{PS(x)}$ is the isostatic compensation

In addition, the isostatically compensated depth of the Moho, $M_{(x)}$, is given by:

$$M_{(x)} = C_o - CTPS_{(x)} + ISO_{PS(x)} \quad [4.28]$$

The position of the brittle-ductile transition depends upon the strength of the lithosphere. As such it is determined by the relationship between crustal composition and thickness as well as the geothermal gradient. Pure shear is a three-dimensional stretching mechanism in which the principal strain axes (X, Y and Z) remain parallel to their respective stress axes ($\sigma_1$, $\sigma_2$ and $\sigma_3$) during deformation.

The isostatic response of the lithosphere to the thinning of the lower crust by pure shear creates a sag basin in the surface profile above the area of extension (Figure 4.8). This subsidence occurs in response to thinning of the lower crust, which raises the Moho leading to low density crust being replaced with higher density material of the mantle lithosphere. This denser material acts as a load upon the lithosphere and results in subsidence (Figure 4.8b).

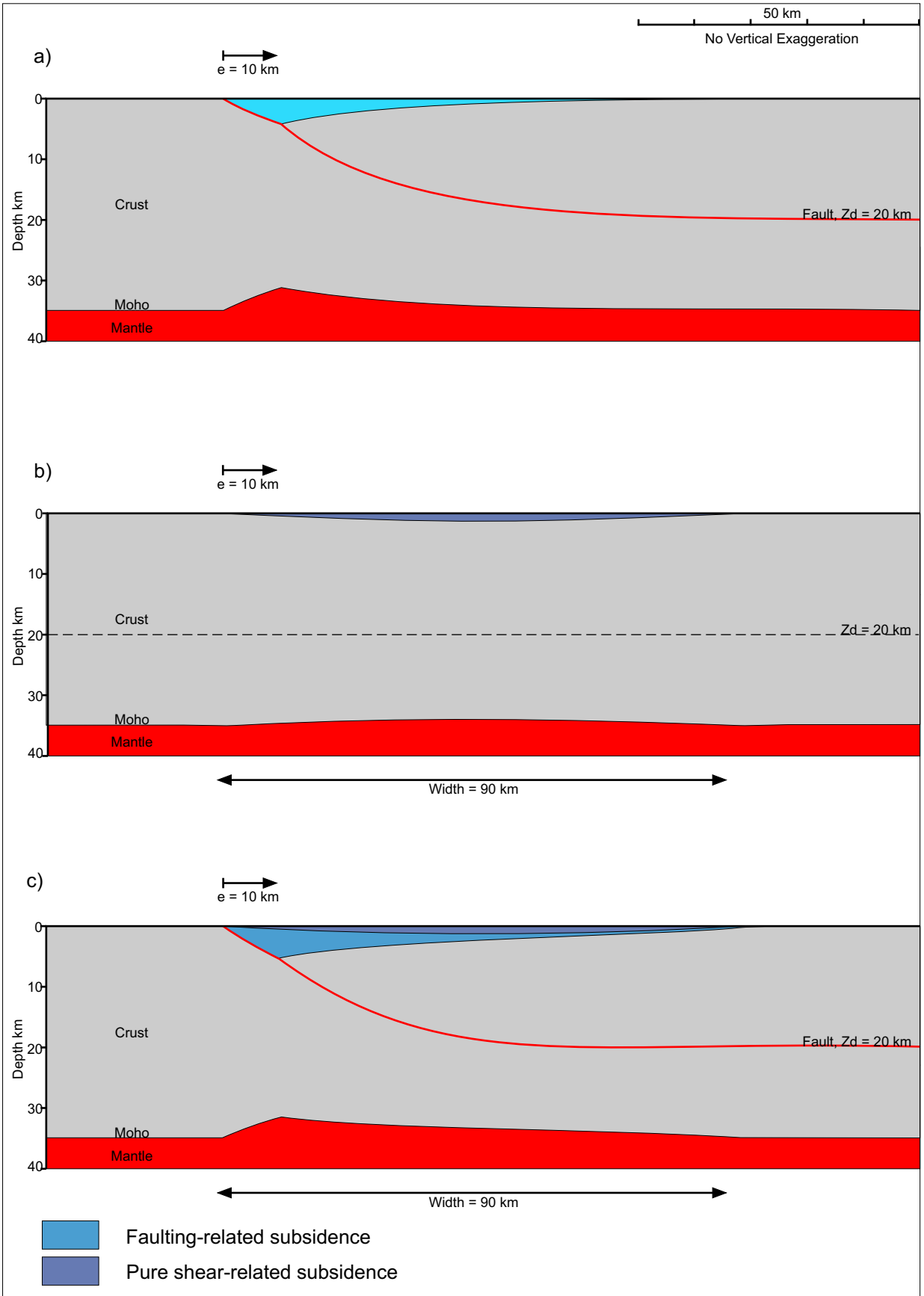


Figure 4.8. a) Model of fault profile following extension, e = 10 km with detachment depth, Zd = 20 km. b) Model of sag basin produced by thinning of the lower crust by pure shear (overall deformation is balanced to that by faulting in part a). Material removed by lower crustal thinning as a result of pure shear is replaced by denser mantle material adding a positive isostatic load to the lithosphere resulting in subsidence. c) Coupled simple-shear/pure-shear model of extensional basin formation.

As a result of increasing the magnitude of extension, the crust is thinned by a greater amount and the pure shear-related sag basin is deeper. The distribution of the pure shear extension also affects the resultant basin. Increasing the width of the pure shear distribution, results in the extension being distributed over a larger area of lower crust and the resultant sag basin is wider and shallower. Changing the lateral position of the pure shear relative to the fault-related extension controls the position of the basin depocentre.

## 4.4 Thermal processes and the thermal consequences of lithosphere extension

Structural deformation causes perturbation of the lithosphere geotherm. These thermal perturbations induce density changes in the lithosphere which, as a result of isostasy, alter basin geometry.

Conduction is the dominant mechanism of heat transfer in the lithosphere, the lowermost asthenospheric mantle and the core (Bott, 1982b). Heat transfer by conduction occurs when energy is exchanged, in the presence of a temperature gradient, from an area of high temperature to an area of low temperature (Ozisik, 1980).

Thinning of the lithosphere as a result of extension raises the lithosphere/asthenosphere boundary, which increases the geothermal gradient. This perturbation of the geotherm results in thermal expansion and uplift. Following extension, the temperature field re-equilibrates and

subsidence occurs as a result of thermal contraction (Sleep and Snell, 1976).

#### 4.4.1.1 Thermal Uplift

Extension as a result of passive rifting thins the lithosphere in response to regional stress. As the lithosphere material extends laterally, the asthenosphere ascends to replace the thinned lithosphere material and maintain volume (Morgan, 1984). On account of this uplift of hot asthenospheric material, the lithosphere will experience changes in its thermal properties, raising the geotherm (Beaumont *et al.*, 1982). As a consequence of heating, the lithospheric material expands (Bott, 1980). This thermal expansion is determined by the volumetric co-efficient of thermal expansion, $\alpha_T$, which represents the change in volume with temperature for a constant pressure (Zharkov, 1998).

$$\alpha_T = \frac{1}{V}\left(\frac{\delta V}{\delta T}\right)_p \qquad [4.29]$$

where: $V$ is the specific volume or volume per unit mass

$(\delta V/\delta T)_p$ is the partial differential of volume with respect to temperature at a constant pressure

The specific volume, $V$, of a material is inversely proportional to its density (Turcotte and Schubert, 2002):

$$V = \frac{1}{\rho} \qquad [4.30]$$

Therefore, thermal expansion is responsible for decreasing the density of the lithosphere, which as a consequence reacts by uplift to restore isostatic equilibrium (Bott, 1980).

#### 4.4.1.2 Thermal subsidence

Studies of the behaviour of oceanic crust as it moved laterally away from the mid-ocean ridges established the relationship between subsidence and cooling of the crust (Hess, 1962; Langseth *et al.*, 1966; McKenzie, 1967; Turcotte and Oxburgh, 1967; Vogt & Ostenso, 1967; Sleep, 1969; Parsons & Sclater, 1977). Thermal subsidence is not as simple to explain with regard to continental lithosphere, as a mechanism for the initial heating of the lithosphere must be incorporated (Mareschal, 1981). However, evidence of thermal subsidence related to continental extension is present in the sedimentary record, where deposition at rifted margins adheres to the exponential behaviour that characterises the thermal cooling observed at the mid-ocean ridges (Buck *et al.*, 1988). For example, the subsidence of the continental shelf of the Atlantic continental margin of the USA is reflected in the thickness of sediment deposited, which decrease exponentially as time since extension increases, with a time constant of 50 Ma (Sleep, 1971).

Thermal subsidence results from a gradual thermal contraction of the lithosphere as it cools by conduction in an attempt to restore thermal equilibrium (Sleep and Snell, 1976; McKenzie, 1978). This cooling increases the density due to the relationship between volume and density

that is expressed by equation [4.30]. Isostatic compensation for this increased density results in subsidence, usually referred to as post-rift subsidence or thermal sag. The amount of time it takes for the heat to be lost by conduction is related to its co-efficient of thermal diffusivity, $\kappa$, and the distance over which the heat must be conducted, $y$, according to equation [B4.20].

## 4.5 Modelling of thermal processes

It is possible to quantitatively define the outcome of these thermal processes on basin evolution assuming that the lithosphere was initially in a state of thermal equilibrium (Keen, 1985) and that the heat loss from the lithosphere is due to conduction (McKenzie, 1978).

The McKenzie model (McKenzie, 1978) quantitatively describes uniform lithosphere extension. It assumes instantaneous extension of the crust and mantle lithosphere by pure shear, taking into account the thermal and isostatic implications of extension, which results in thermal uplift as a consequence of elevation of the lithosphere/asthenosphere boundary increasing the temperature (Keen, 1987). The thermal perturbations that result from elevation of the lithosphere/asthenosphere boundary are transient, consequently so are the resultant elevation changes experienced at the surface. Following extension, re-equilibration of the temperature field results from cooling of the lithosphere, which leads to thermal subsidence (Le Pichon *et al.*, 1982; Alvarez *et al.*, 1984).

In order to calculate the amount of post-rift thermal subsidence, it is necessary to understand the behaviour of heat flow through time. The increase in heat flow in response to a rifting event predicted by the McKenzie model is assumed to be instantaneous. However, following extension the heat flow decreases at an exponential rate in order to re-establish the thermal equilibrium. Instantaneous extension increases the heat flow by the extension factor, $\beta$, at $t = 0$ such that after extension, the temperature variation is given by the following equations (McKenzie, 1978):

$$T = T_0 \text{ for } 0 < \frac{z}{a} < \left(1 - \frac{1}{\beta}\right) \qquad [4.31]$$

where: $z$ is distance measured upwards from the base of the lithosphere before extension

$T_0$ is the temperature at the base of the lithosphere

$a$ is the thickness of the lithosphere

$$T = T_0 \beta \left(1 - \frac{z}{a}\right) \text{ for } \left(1 - \frac{1}{\beta}\right) < \frac{z}{a} < 1 \qquad [4.32]$$

Assuming that lateral temperature gradients in the lithosphere are smaller than vertical gradients and, as a consequence, heat flow is unidirectional in a vertical sense, and that the internal heat production ($H$) is negligible, the one-dimensional unsteady (time-dependent) heat flow equation given by equation [4.39] can be solved by assuming the following boundary conditions:

$$T = 0 \text{ at } z = a \qquad [4.33]$$

$$T = T_0 \text{ at } z = 0 \quad [4.34]$$

The unsteady heat flow equation is solved by Fourier expansion (Lubimova and Nikitina, 1975; McKenzie, 1978). The temperature at any position in the lithosphere, $z$, and time, $t$, ($T_{(z,t)}$), assuming a linear geotherm, is made up of a steady state component, $s_{(z)}$, [4.35], and an unsteady-state component, $u_{(z,t)}$, [4.36].

$$s_{(z)} = T_0\left(1 - \frac{z}{a}\right) \quad [4.35]$$

$$u_{(z,t)} = \sum_{n=0}^{\infty} An \sin\left(\frac{n\pi z}{a}\right) \exp^{\frac{-n^2\pi^2\kappa t}{a^2}} \quad [4.36]$$

where: n is an integer which expresses the order of the harmonic Fourier Transform

A is a constant dependent on $T_0$ and $\beta$ such that:

$$An = \left[\frac{2}{\pi}(-1)^{n+1}\frac{\beta}{n\pi}\sin\left(\frac{n\pi}{\beta}\right)\right]T_0 \text{ at } t = 0 \quad [4.37]$$

It is possible to approximate the summation component of the equation by considering only the case of the lower bound of the summation, in this case $n = 1$ such that equation [4.37] becomes [4.38] (Allen and Allen, 1990):

$$An = \left[\frac{2\beta}{\pi^2}\sin\left(\frac{\pi}{\beta}\right)\right]T_0 \quad [4.38]$$

Therefore the solution for $T_{(z,t)}$ is the sum of equations [4.35] and [4.36]:

$$T_{(z,t)} = T_0\left(1 - \frac{z}{a}\right) + \sum_{n=1}^{\infty}\frac{2}{\pi}(-1)^{n+1}\left[\frac{\beta}{n\pi}\sin\left(\frac{n\pi}{\beta}\right)\right]T_0 \sin\left(\frac{n\pi z}{a}\right)\exp^{\frac{-n\pi^2\kappa t}{a^2}} \quad [4.39]$$

This can be simplified to:

$$\frac{T_{(z,t)}}{T_0} = \left(1 - \frac{z}{a}\right) + \frac{2}{\pi}\sum_{n=1}^{\infty} \frac{(-1)^{n+1}}{n}\left[\frac{\beta}{n\pi}\sin\left(\frac{n\pi}{\beta}\right)\right]\sin\left(\frac{n\pi z}{a}\right)\exp^{\frac{-n^2 t}{\tau}} \qquad [4.40]$$

where: $\tau$ represents the thermal time constant of the lithosphere given by:

$$\tau = \frac{a^2}{\pi^2 \kappa} \qquad [4.41]$$

For the case $n = 1$, equation [4.41] can be approximated by equation [4.32]:

$$\frac{T_{(z,t)}}{T_0} = \left(1 - \frac{z}{a}\right) + \frac{2}{\pi}\left[\frac{\beta}{\pi}\sin\left(\frac{\pi}{\beta}\right)\right]\sin\left(\frac{\pi^2}{a}\right)\exp^{\frac{-t}{\tau}} \qquad [4.42]$$

The surface heat flux, $q_s$, calculated by Fourier's law in equation [B4.14] is given by:

$$q_s = \frac{\alpha_T T_0}{a}\left\{1 + 2\sum_{n=1}^{\infty}\left[\frac{\beta}{n\pi}\sin\left(\frac{n\pi}{\beta}\right)\right]\exp^{\frac{-n^2 t}{\tau}}\right\} \qquad [4.43]$$

For the case $n = 1$, this can be approximated by:

$$q_s = \frac{\alpha_T T_0}{a}\left\{1 + 2\left[\frac{\beta}{\pi}\sin\left(\frac{\pi}{\beta}\right)\right]\exp^{-\frac{t}{\tau}}\right\} \qquad [4.44]$$

Assuming Airy isostasy, the elevation at a given time, $t$, to which the lithosphere subsides, $e_t$ is given by:

$$e_{(t)} = \frac{a\rho_m \alpha_T T_0}{\rho_m - \rho_i}\left\{\frac{4}{\pi^2}\sum_{m=0}^{\infty}\frac{1}{(2m+1)^2}\left[\frac{\beta}{(2m+1)\pi}\sin\frac{(2m+1)\pi}{\beta}\right]\exp^{-(2m+1)^2\frac{t}{\tau}}\right\} \qquad [4.45]$$

where: $\rho_m$ is the density of the mantle

$\rho_i$ is the density of the basin infill

$m$ is the integer which expresses the order of the harmonic Fourier Transform

Figure 4.9 illustrates the parameters involved in the calculation of $e_t$. The average values applied to the above parameters can be found in Table 1.1. For the lower bounding case, $m = 0$, an approximation can be generated:

$$e_{(t)} = \frac{4a\rho_m \alpha_T T_0}{\pi^2 (\rho_m - \rho_i)} \left[ \frac{\beta}{\pi} \sin\left(\frac{\pi}{\beta}\right) \right] \exp^{\frac{-t}{\tau}} \qquad [4.46]$$

The amount of thermal uplift generated following lithosphere extension, is represented by the surface elevation, $e_0$, at time, $t = 0$, calculated using equation [4.45]. There is no exponential component to the thermal uplift as the exponential function in the equation becomes $\exp^0$ which is equal to 1.

The amount of thermal subsidence, $S_t$, at any time since rifting is measured by the amount of surface elevation resulting from thermal uplift at $t = 0$ ($e_{(0)}$) minus the surface elevation at time, $t$($e_{(t)}$):

$$S_t = e_{(0)} - e_{(t)} \qquad [4.47]$$

The total amount of subsidence generated by the McKenzie model, $S_M$, is given by equation [4.48]:

$$S_M = S_i + S_t \qquad [4.48]$$

The amount of thermal subsidence, $S_t$, given by equation [4.47] represents the cumulative amount of thermal subsidence at any time after extension.

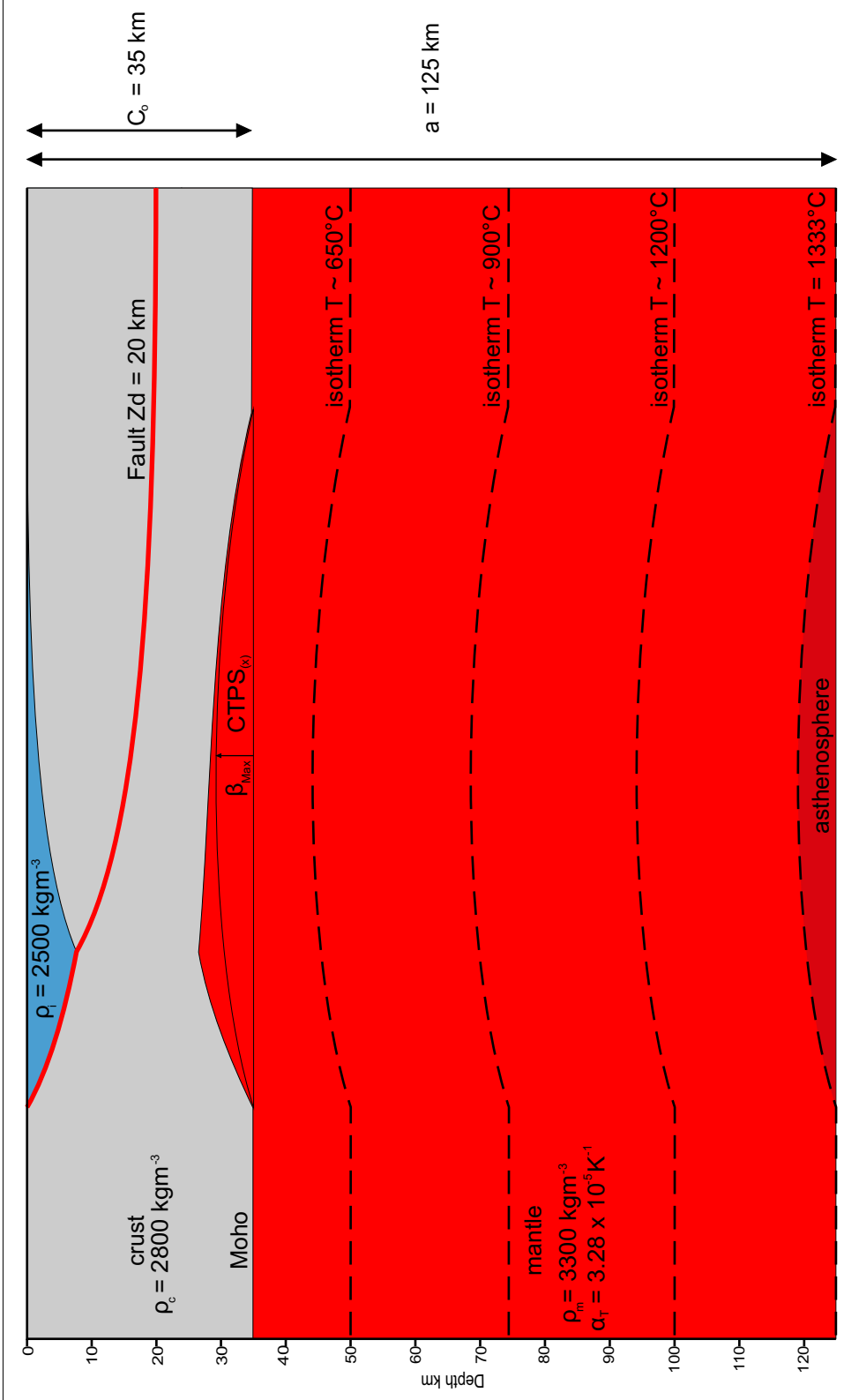


Figure 4.9. Parameters for the calculation of thermal processes. Thinning of the crust by faulting and pure shear perturbates the geotherm. The amount of thinning of the lower crust (CTPS$_{(x)}$) is related to the thickness of lower crust being deformed ($C_o$ -Zd) and the $\beta_x$ value. The effect of thermal processes on basin evolution is controlled by the magnitude of extension, $\beta$, the thickness of the lithosphere, a, the co-efficient of thermal expansion, $\alpha_T$, and the density of the mantle $\rho_m$.

In order to calculate the amount of subsidence generated between two time periods, $t=t_1$ and $t=t_2$, the difference in surface elevation between the two time periods is required. The difference is obtained using equation [4.47] such that:

$$S_t = e_{(t_1)} - e_{(t_2)} \qquad [4.49]$$

There are some limitations to this method of modelling the thermal processes that result from lithosphere extension. These include the initial assumptions of the McKenzie model such as instantaneous rifting, a linear geotherm, and the absence of radiogenic heating and lateral heat conduction (Alvarez *et al.*, 1984; Meredith, 2003). In addition the method presented above relies on Airy isostasy. An approach utilising flexural isostasy will be considered in section 5.2.

Figure 4.10a illustrates the response to thermal processes combined with the effects of coupled simple shear and pure shear extension, whilst Figure 4.10b isolates the effect of the thermal processes. The thermal response of the lithosphere at 0Ma after extension raises the geotherm, which results in uplift of the basin and Moho (Figure 4.10ai & 4.10bi). Following the initial thermally generated uplift, re-equilibration of the geotherm commences, resulting in subsidence. After 5Ma the amount of subsidence generated results in a small sag basin that overlies the rift phase of basin subsidence (Figure 4.10bii). As basin evolution continues the cumulative amount of thermally-generated subsidence increases although the rate at which the subsidence is generated decreases (Figure 4.10biii & biv).

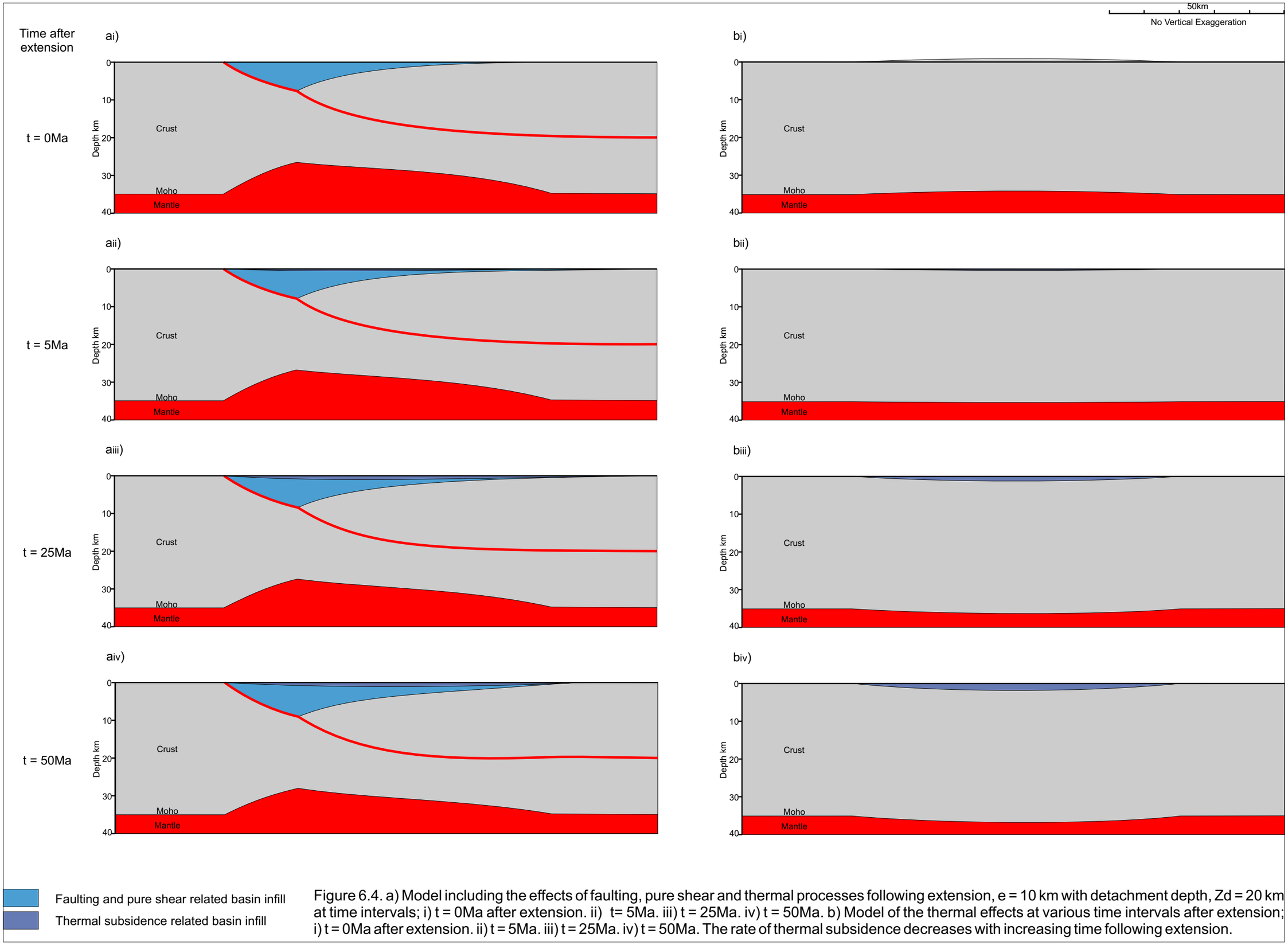


Figure 6.4. a) Model including the effects of faulting, pure shear and thermal processes following extension, e = 10 km with detachment depth, Zd = 20 km at time intervals; i) t = 0Ma after extension. ii) t= 5Ma. iii) t = 25Ma. iv) t = 50Ma. b) Model of the thermal effects at various time intervals after extension; i) t = 0Ma after extension. ii) t = 5Ma. iii) t = 25Ma. iv) t = 50Ma. The rate of thermal subsidence decreases with increasing time following extension.

## 4.6 The isostatic response to lithosphere extension

In addition to the thermal response of the lithosphere to tectonic activity, there is also an isostatic response. In response to any force that generates or removes a load, the Earth reacts to re-establish this equilibrium.

Both Airy and Pratt isostasy counteract variations in mass locally, equalising the pressure applied by columns of lithosphere to a level or depth of compensation within the Earth. The models compensate for the additional mass that results from an area of land elevated above sea level, by a reduction in the density of the region below the elevation. The reduction in mass that results from an area of land depressed below sea level is counterbalanced by a denser region beneath. The Airy and Pratt hypotheses differ in how they achieve this compensation, which is examined in Appendix B (Lyustikh, 1960; Lowrie, 1997). However, neither hypothesis adequately explains the regional nature of isostatic compensation observed in real world examples.

A regional approach to isostasy, flexural isostasy, in which the lithosphere responds to loading as a thin elastic plate overlying a fluid substratum, was developed to explain situations in which local isostasy models were unable to account for the observed topography and gravity measurements (Vening Meinesz, 1937; 1941; Gunn, 1949; Walcott, 1970; 1972). This flexural model of isostasy is similar to Airy isostasy in that loads are supported by variations in crustal thickness, the difference being that flexural isostasy considers the lithosphere to have a lateral strength and the pressure exerted upon the compensation depth due to loading is

spread regionally rather than locally (Karner and Watts, 1982) (Figure 4.11). Regional isostatic compensation is linked to the flexural strength of the lithosphere (Putnam, 1930), which is determined by the flexural rigidity of the lithosphere, $D$. The flexural rigidity of a material defines its resistance to bending and in the context of the lithosphere determines the maximum amplitude and wavelength of the deflection of the lithosphere in response to applied loads (Walcott, 1970). It is measured in Newton meters ($Nm$) and is calculated by (Love, 1944):

$$D = \frac{ETe^3}{12\left(1-\nu^2\right)} \qquad [4.50]$$

where: $E$ is Young's modulus, the ratio of compression to extension in a solid that is under axial compression and that is unrestricted laterally

$\nu$ is Poisson's ratio, the ratio of lateral extension to longitudinal extension in a solid that is under axial compression and that is unrestricted laterally

$Te$ is the effective elastic thickness of the lithosphere

The wavelength of the flexural deflection of the lithosphere in response to loading, $\lambda$, is defined by (Walcott, 1970):

$$\lambda = 2\pi\alpha \qquad [4.51]$$

where: $\alpha$ is the flexural parameter, such that:

$$\alpha = \left(\frac{4D}{\left(\rho_m - \rho_i\right)g}\right)^{\frac{1}{4}} \qquad [4.52]$$

where: $\rho_i$ is the density of the basin infill

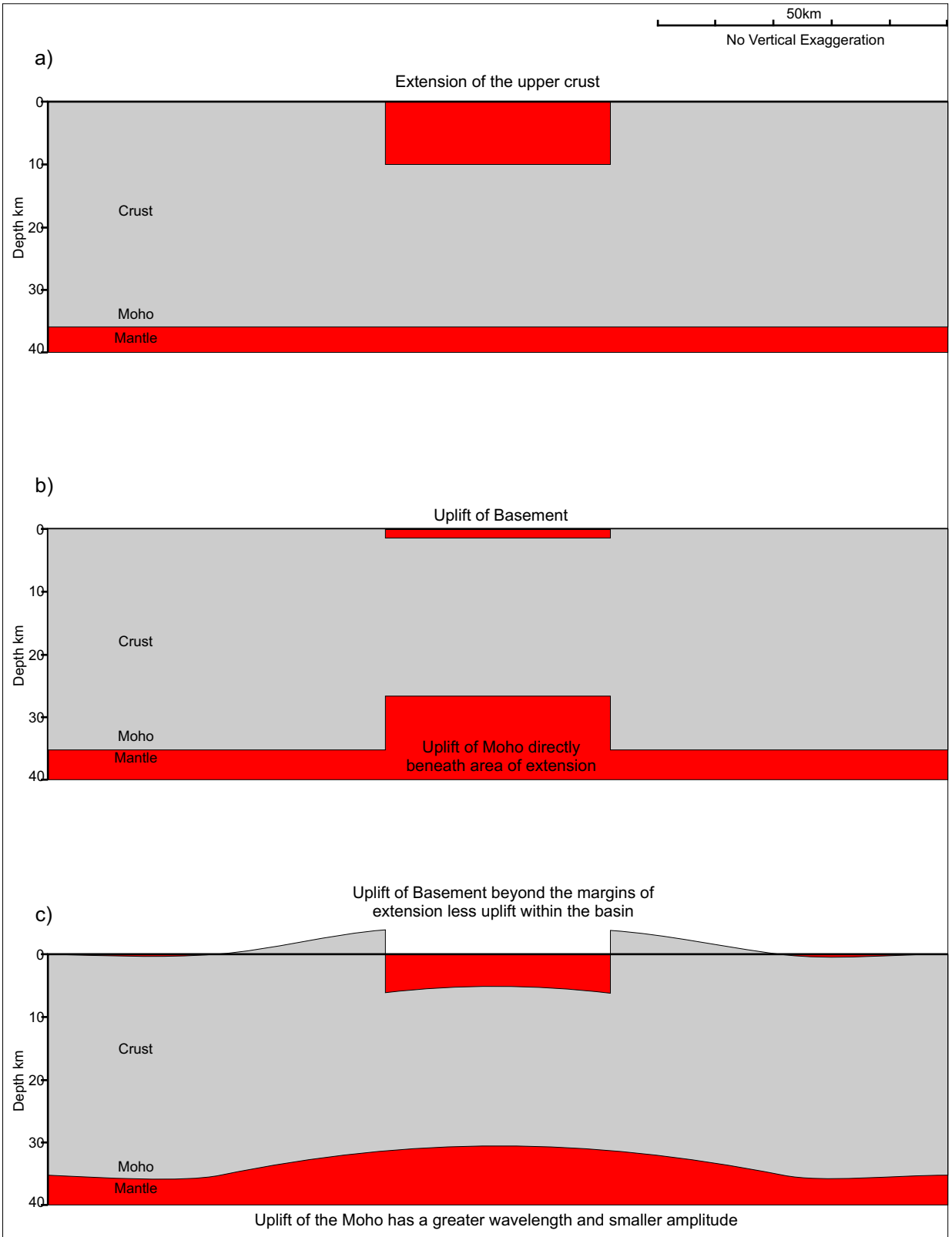


Figure 4.11. Basement and Moho profiles developed in response to extension of the lithosphere. a) Extended upper crust prior to isostatic compensation. b) Extended upper crust with Airy isostatic compensation. c) Extended upper crust with flexural isostatic compensation, in which the negative load associated with extension of the upper crust is compensated regionally.

The flexural wavelength is therefore dependent upon the flexural rigidity of the lithosphere and the density contrasts between the mantle and the material infilling the basin. The effect of infilling the basin will be discussed in chapter 5. In addition, the elastic thickness of the lithosphere has a significant influence upon the flexural rigidity of the lithosphere; flexural rigidity is proportional to the cube of the elastic thickness. Figure 4.12a illustrates the relationship between flexural rigidity and elastic thickness.

### *4.6.1 The effective elastic thickness of the lithosphere*

In engineering terms, the elastic thickness of an isotropic plate is simply related to the thickness of the plate and as such it is an easily measurable parameter (Hodgetts *et al.*, 1998). However, in the case of the lithosphere, determining the elastic thickness of the plate is not so simple. The continental lithosphere consists of multiple rheological layers which also vary laterally (Murrell, 1976; Kirby 1983). Instead of a true elastic thickness, an effective elastic thickness is assumed for the lithosphere and is generally referred to by the abbreviation *Te*. The *Te* of the lithosphere defines what the thickness of the plate would be if it were isotropic, and therefore it reflects the integrated strength of the brittle, elastic and ductile elements of the lithosphere (Watts and Burov, 2003). As such it is unrelated to any physical boundaries within the lithosphere and cannot therefore be measured directly (McNutt *et al.*, 1988; Burov and Diament, 1995; Hodgetts *et al.*, 1998).

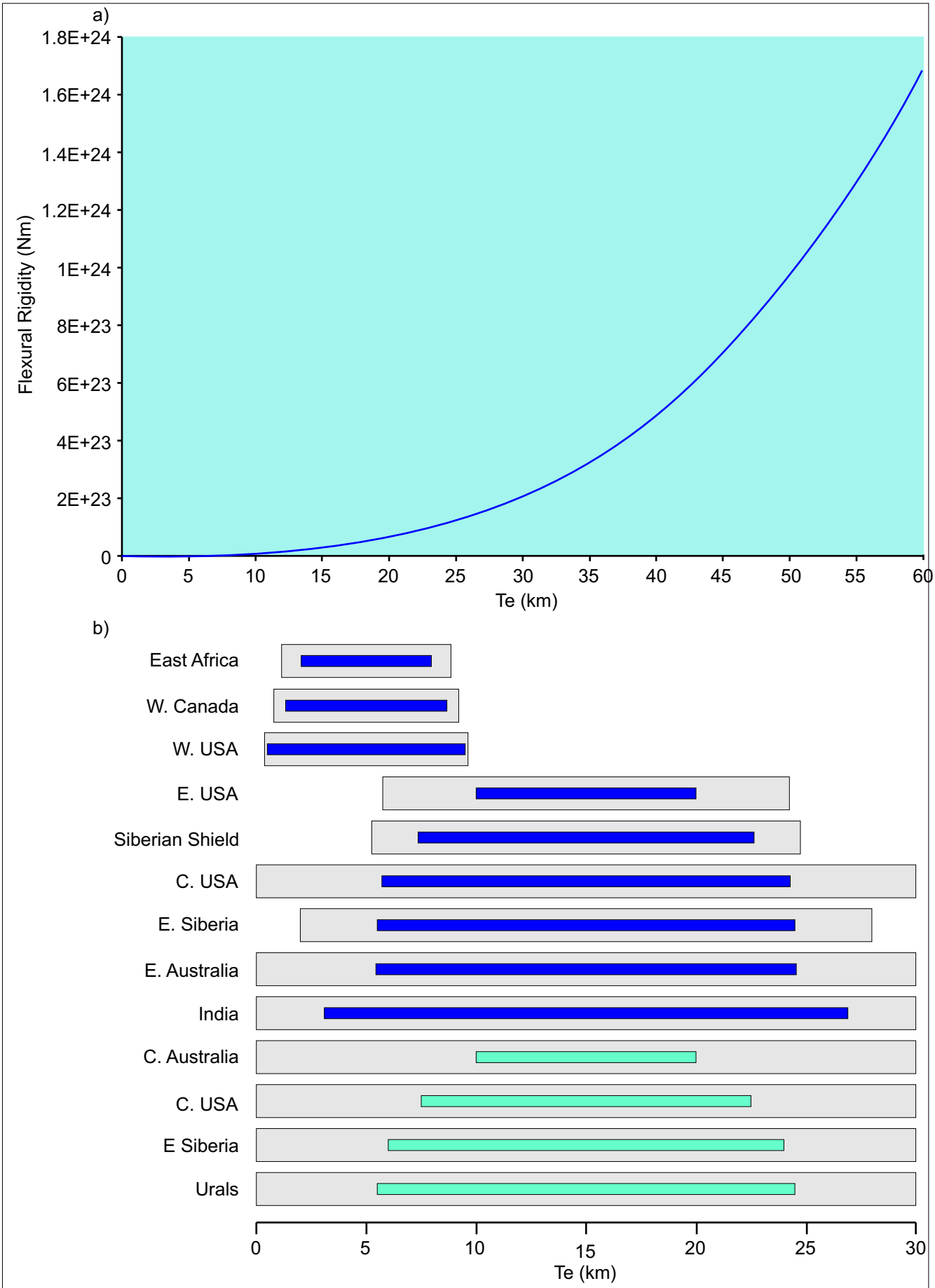


Figure 4.12. a) The relationship between flexural rigidity and the elastic thickness of the lithosphere. b) Estimates of Te from free air admittance and from free air gravity profiles including the range corresponding to the misfit between the observed and calculated free air gravity anomalies . Where the range exceeds 30 km, the results are truncated (After McKenzie and Fairhead, 1997).

In oceanic lithosphere it has been demonstrated that the *Te* is determined by the thermal structure of the lithosphere, which itself is determined by its thermal age (Caldwell and Turcotte, 1979; Watts *et al.*, 1980; Kusznir and Karner, 1985). Estimates for the *Te* of the oceanic lithosphere range between 2 and 50 km (Watts and Burov, 2003). There are several lithospheric parameters that act to determine the *Te* of the continental lithosphere (McNutt *et al.*, 1988; Watts, 1992); the thermal state of the lithosphere is not the only contributing factor. In addition, decoupling at the crust-mantle interface, the thickness of the crust and lithospheric mantle, and the local curvature of the plate as a result of the bending stress also contribute to the *Te* of the continental lithosphere (Burov and Diament, 1995). Estimates of the *Te* of the continental lithosphere have generated substantial debate (Banks *et al.*, 2001). It can be determined either by iterative modelling processes relating the observed deflection of the plate to the deflection calculated by the model, or by statistical methods (Burov and Diament, 1995; Hodgetts *et al.*, 1998). Estimates of the *Te* of the continental lithosphere exceeding 130 km have been presented, although it has been argued that some methods of modelling *Te* provide an upper bound rather than an estimate of *Te* (Forsyth, 1985; McKenzie and Fairhead, 1997; Banks *et al.*, 2001). Basins generated as a result of extensional regimes are associated with values of *Te* the effective elastic thickness of between 5 and 15 km, which have been linked to heating of the lithosphere during rifting (Watts and Burov, 2003).

Figure 4.12b provides estimates of *Te* from gravity data for continental lithosphere.

### *4.6.2 Modelling flexural isostasy*

In order to model flexural isostasy, the lithosphere is considered to be an isotropic, elastic solid in the form of a plate that deforms when a force is applied and returns to its original shape when the force is removed. The elastic properties of the plate are independent of orientation (Jaeger 1969; Turcotte and Schubert, 2002). Assuming the principal stresses are linearly proportional to the principal strains:

$$\sigma_1 = (\lambda + 2G)\varepsilon_1 + \lambda\varepsilon_2 + \lambda\varepsilon_3$$

$$\sigma_2 = \lambda\varepsilon_1 + (\lambda + 2G)\varepsilon_2 + \lambda\varepsilon_3$$

$$\sigma_3 = \lambda\varepsilon_1 + \lambda\varepsilon_2 + (\lambda + 2G)\varepsilon_3 \qquad [4.53]$$

where: $\lambda$ is the bulk modulus defined by the ratio of hydrostatic pressure to the dilation it produces

$G$ modulus of rigidity defined by the ratio of the shear stress to the shear strain in simple shear

These can be represented in their inverse form:

$$\varepsilon_1 = \frac{1}{E}\sigma_1 - \frac{\nu}{E}\sigma_2 - \frac{\nu}{E}\sigma_3$$

$$\varepsilon_2 = -\frac{\nu}{E}\sigma_1 + \frac{1}{E}\sigma_2 - \frac{\nu}{E}\sigma_3$$

$$\varepsilon_3 = -\frac{\nu}{E}\sigma_1 - \frac{\nu}{E}\sigma_2 + \frac{1}{E}\sigma_3 \qquad [4.54]$$

The relationship between $E$, $\lambda$ and $G$ is given by:

$$E = \frac{G(3\lambda + 2G)}{(\lambda + G)} \qquad [4.55]$$

The relationship between $\nu$ , $\lambda$ and $G$ is given by:

$$\nu = \frac{\lambda}{2(\lambda + G)} \qquad [4.56]$$

The elastic behaviour of a material can be shown by stipulating the values of either $\lambda$ and $G$ or $E$ and $\nu$.

Timoshenko (1958) has shown that any distortion of a plate than is considerably longer than it is wide is limited to the extreme edges of the plate. This being the case, it is possible to model the deformation of the lithosphere as a beam instead of a plate. It is however, necessary to take the stresses and strains that would act upon the beam were it part of a larger plate into consideration (Watts, 2001) (Figure 4.13). This is achieved by applying plane stress; that is the beam is stressed in the x and z directions but only free to move in the y direction such that:

$$\sigma_1 \neq 0 \ \sigma_2 \neq 0 \ \sigma_3 = 0 \text{ or } \sigma_x \neq 0 \ \sigma_z \neq 0 \ \sigma_y = 0 \qquad [4.57]$$

The stress applied in the z direction acts to prevent strain in the z direction as if the beam were part of a larger plate. The stress in the x direction results from the bending of the beam (Watts, 2001).

Given these stress conditions, the strains can be determined by substitution into equation [4.54] such that (Jaeger, 1969):

$$E\varepsilon_x = \sigma_x - \nu\sigma_z$$

$$E\varepsilon_y = \nu(\sigma_x + \sigma_z)$$

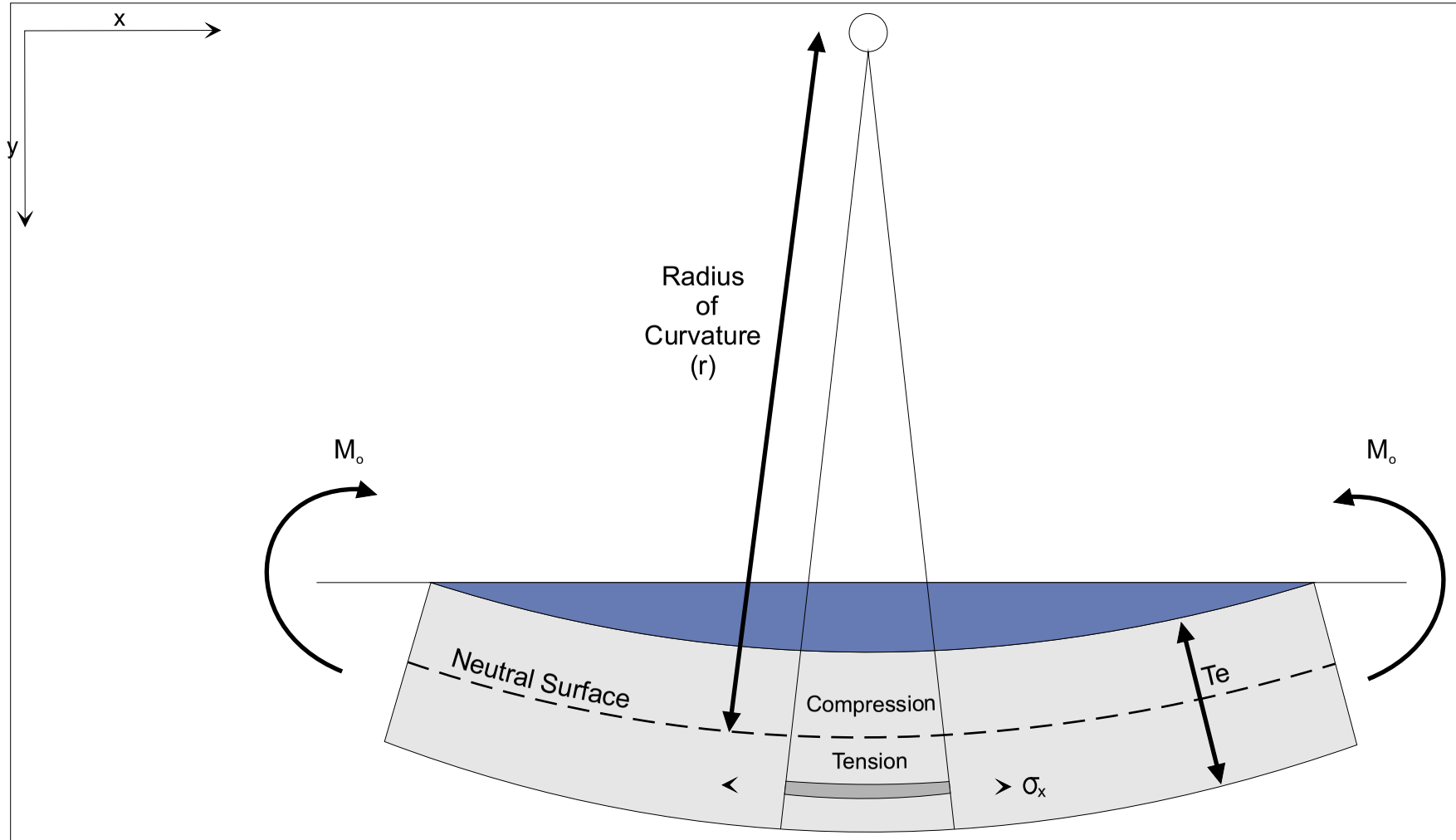


Figure 4.13. The bending of an elastic beam by an applied bending moment, $M_o$. The lower half of the beam is under tension, $\sigma_x$, whilst the upper half of the beam experiences compression. The neutral surface is the surface within the beam that experiences neither compression nor extension and therefore is not under strain (After Watts, 2001).

$$E\varepsilon_z = \sigma_z - \nu\sigma_x \qquad [4.58]$$

Given that there is no strain in the z direction, $\varepsilon_z = 0$ and the principal stresses can be presented in terms of the principal strain, $\varepsilon_x$, such that (Watts, 2001):

$$\sigma_x = \frac{E\,\varepsilon_x}{\left(1-\nu^2\right)}$$

$$\sigma_z = \frac{E\,\varepsilon_x\,\nu}{\left(1-\nu^2\right)} \qquad [4.59]$$

The bending moment, $M$, that acts in the plane of the cross-section of the beam, is defined by:

$$M = \frac{ETe^3}{12\left(1-\nu^2\right)r} \quad \text{or} \quad M = \frac{D}{r} \qquad [4.60]$$

where: $r$ is the radius of curvature which is given by the change in slope with horizontal distance such that:

$$\frac{1}{r} = -\frac{d^2w}{dx} \qquad [4.61]$$

where: $w$ is the vertical deflection of the plate

The two dimensional flexural isostatic response of the lithosphere, $W_{(x)}$, to a load is defined by the bending moment and the upward hydrostatic force such that (Turcotte and Schubert, 1982):

$$\frac{d^2}{dx^2}D\frac{d^2W_{(x)}}{dx^2} + \left[\left(\rho_m - \rho_i\right)gW_{(x)}\right] = L_{(x)} \qquad [4.62]$$

where: $L_{(x)}$ is the pressure exerted by the applied load which may vary with the horizontal x co-ordinate.

$\left(\rho_m - \rho_i\right) g W_{(x)}$ is the upward hydrostatic force per unit area.

The flexural isostatic hypothesis provides an explanation for regional isostatic compensation that cannot be provided by the local Airy and Pratt hypotheses of isostatic compensation. The flexural isostatic model assumes the lithosphere to have a lateral strength and supports loads by regional variations in crustal and mantle thickness. Changes in crustal thickness resulting from deformation of the hanging wall following fault movement and thinning of the crust by pure shear deformation impose loads upon the lithosphere. In addition, density changes from perturbations of the geotherm also impose loads upon the lithosphere. The lithosphere responds isostatically to these loads, the results of which can be quantified within the integrated tectonic, thermal and isostatic model that has been produced.

In addition to the mechanical, thermal and isostatic processes associated with extension of the lithosphere, a number of surface processes; including infilling of the basin with water and/or sediment, compaction of the sediments and erosion of material uplifted above the sea-level datum affect basin evolution. The isostatic effect of these surface processes are considered in chapter 5.

# 5 Integrated lithosphere-scale modelling of extensional basin development

One of the main aims of this project is to produce an integrated model of extensional deformation of the lithosphere. A computer model has been developed using Java Standard Edition (SE) version 6, an object oriented programming language and the NetBeans IDE 6.5, a modular development tool.

The methods discusses in chapter 4 provide the basis for the development of the modelling code. Faulting is an important factor in controlling basin development. The Northumberland Trough Region has experienced a number of tectonic events that make it necessary to consider the implication of fault deformation when analysing the development of the region. This chapter will consider the application of the inclined shear construction to fault systems containing multiple faults. This chapter will also examine the variations in mass resulting from extension of the continental lithosphere and the flexural isostatic response to these variations. The isostatic response to the loading resulting from extension of the lithosphere has an important influence upon basin evolution and therefore stratigraphical development. This chapter also gives consideration to infilling of the accommodation space created by extension and sedimentary processes. In order to determine the load applied to the lithosphere by infilling of the basin, the nature of the load needs to be established; this includes the effect of palaeobathymetry. In addition, the

effect of compaction of sediments must be taken into account. Finally, erosion of uplifted basement material, and/or sediments, and the isostatic implications of such erosion are considered to produce an integrated isostatically compensated, mechanical, thermal and stratigraphical model. The modelling code is presented in appendix C in addition to the results of sensitivity testing carried out on the model.

## 5.1 Application of fault deformation to extensional basins

Extensional basins are characterised by faulted margins upon which a variety of normal faults are active as a system of associated faults during deformation (Wernicke and Burchfiel, 1982; Twiss and Moores, 1992). Regional systems of extensional faults may define distinct structural provinces. Within such an extensional province, the majority of the displacement is generally accommodated by a small number of major faults. These major faults are accompanied by a number of subsidiary faults that accommodate smaller amounts of displacement and provide minor structural adjustments required for the major faults to accommodate the larger scale displacements (Twiss and Moores, 1992).

The modelling techniques described in chapter 4 are applicable to movement on a single fault. The inclined shear algorithm can be modified to simulate the formation of extensional basin systems with multiple faults.

### *5.1.1 Fault systems including synthetic subsidiary faults*

Figure 5.1 represents a fault system with a detachment fault and a subsidiary fault that is synthetic to the detachment fault. These faults are assigned fault numbers ($j$) based on the order in which they occurred. In this example the detachment fault is assigned the number $j = 0$ and the subsidiary fault is assigned the number $j = 1$.

The fault profile ($F_{(x_j)}$) for each fault can be calculated using equation [4.1]. However, equation [4.1] assumes that the crust is previously undeformed. The fault profile for the subsidiary fault (j=1) must be adjusted for the deformation of the crust caused by the detachment fault (Figure 5.2). Deformation of the crust as a result of faulting is represented in the hanging wall profile of the fault. The hanging wall profile for the main detachment fault is added to the fault profile to correct for the previous deformation such that:

$$F_{(x_1)} = F_{(x_1)} + HW_{(x_0)} \qquad [5.1]$$

The hanging wall geometry must also be modified to account for deformation caused by movement along the detachment fault (Figure 5.2), such that:

$$HW_{(x_1)} = HW_{(x_1)} + HW_{(x_0)} \qquad [5.2]$$

### *5.1.2 Fault systems including antithetic subsidiary faults*

Figure 5.3 represents a system in which there is a subsidiary fault antithetic to the main detachment fault. As in the previous example, the

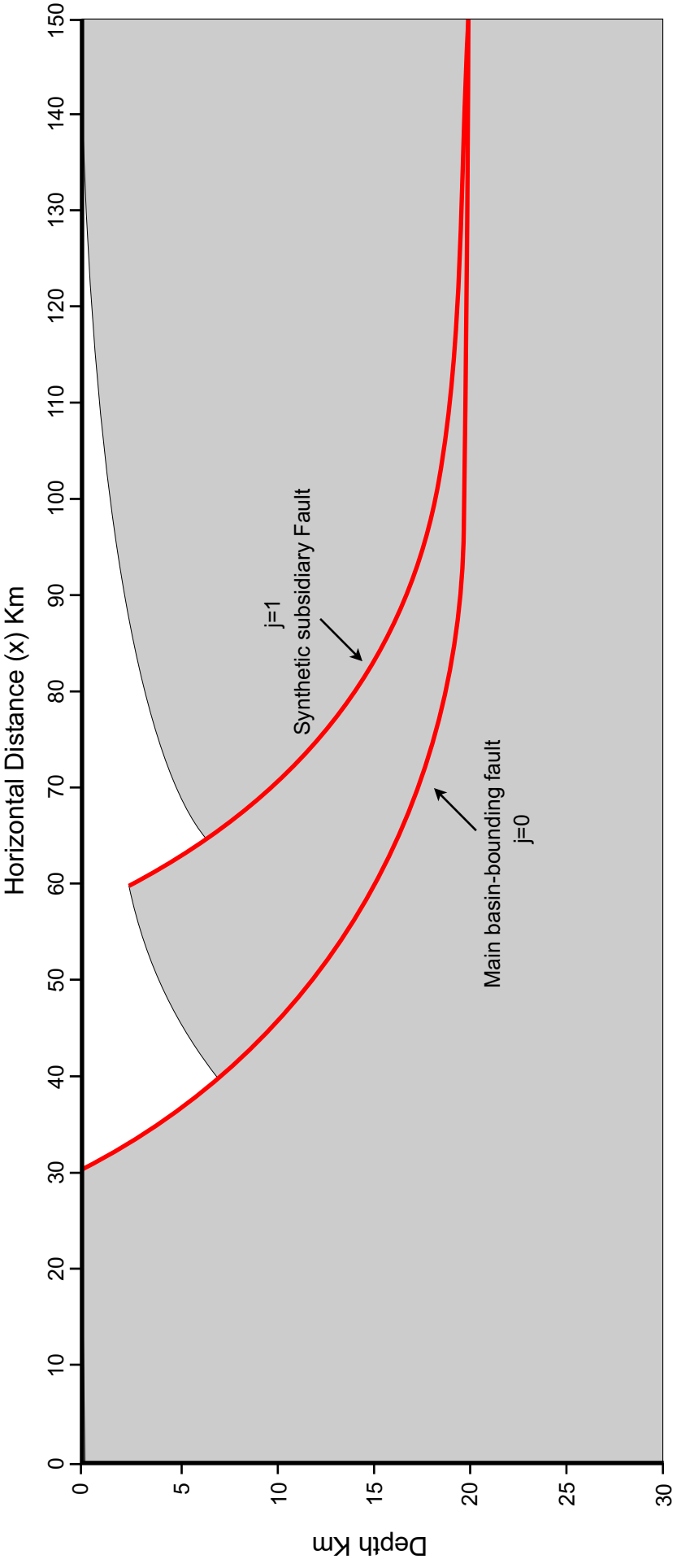


Figure 5.1. Cross-section containing basin-bounding detachment fault with synthetic subsidiary fault. The faults have been numbered starting with the main basin bounding fault as j = 0 and the subsidiary fault as j = 1.

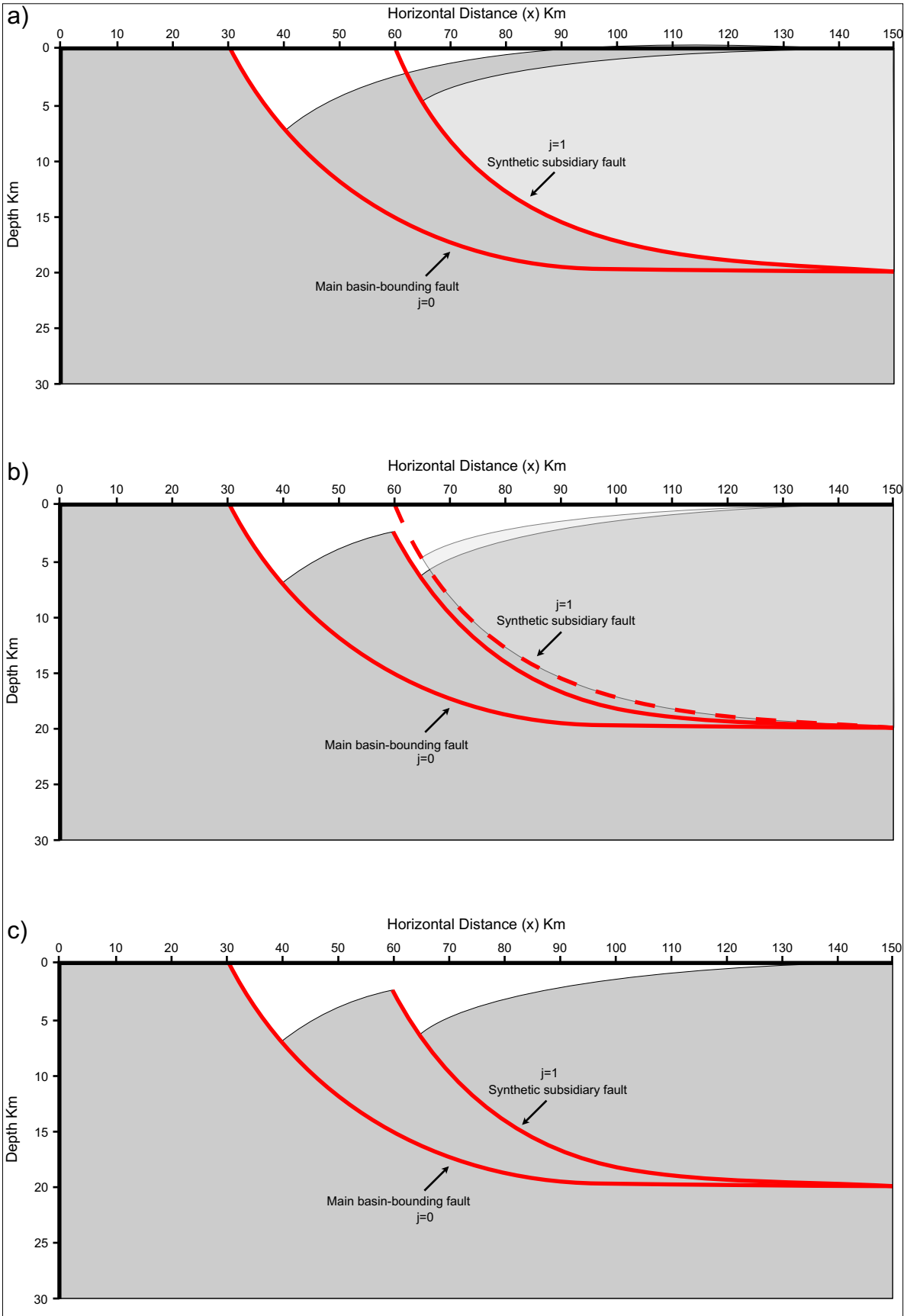


Figure 5.2. The fault and hanging wall profiles of the subsidiary fault must be adjusted to account for the deformation of the crust as a result of movement along the main basin-bounding fault. a) The unadjusted fault and hanging wall profiles. b) Adjustment of subsidiary fault and hanging wall profiles. c) The adjusted fault and hanging wall profiles.

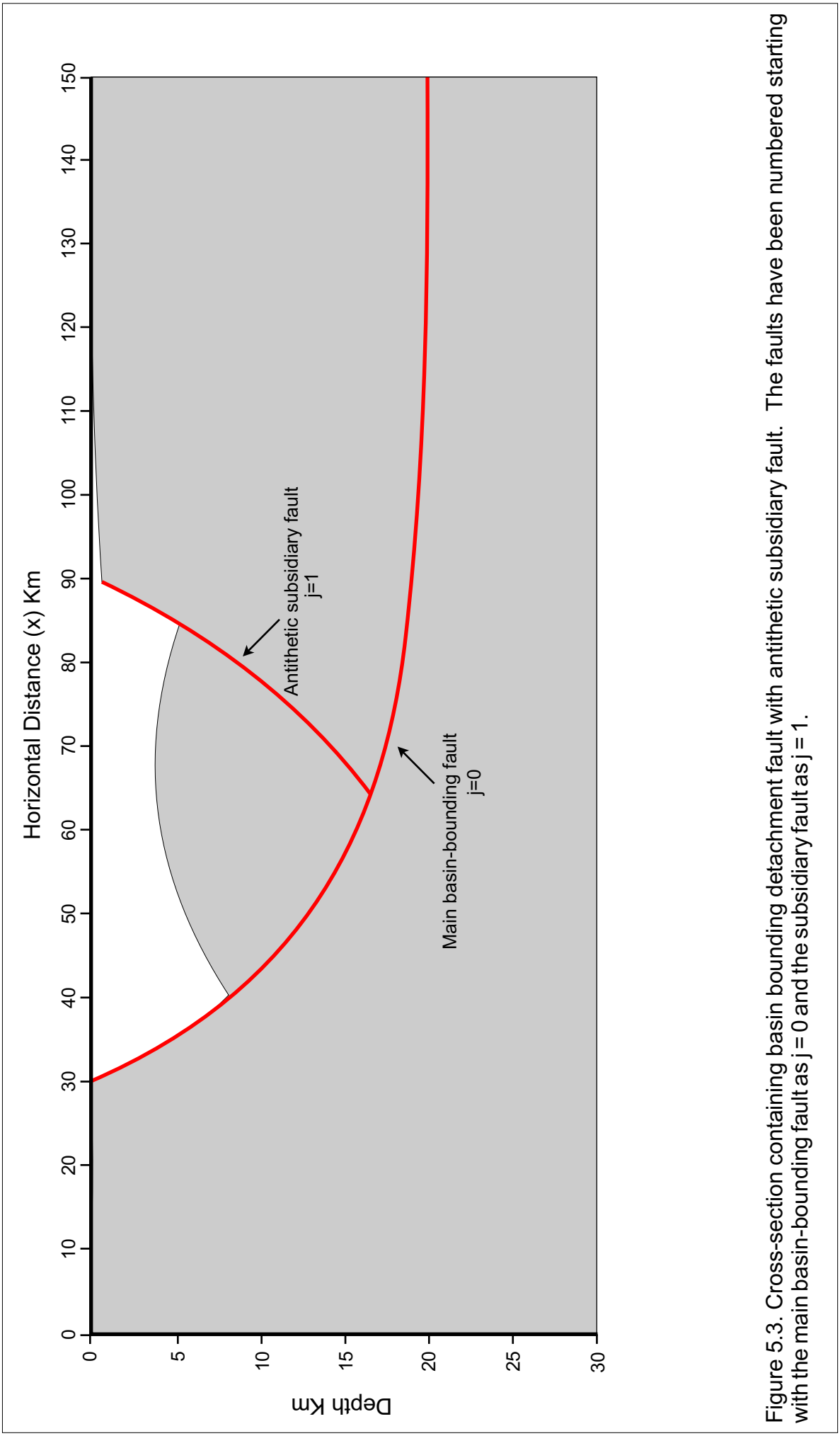


Figure 5.3. Cross-section containing basin bounding detachment fault with antithetic subsidiary fault. The faults have been numbered starting with the main basin-bounding fault as j = 0 and the subsidiary fault as j = 1.

faults are numbered, with the detachment fault being assigned $j = 0$ and subsidiary fault $j = 1$. The deformation of the footwall and hanging wall of the subsidiary fault in response to the main detachment fault is modelled in the same way as in the previous example using equations [5.1] and [5.2] (Figure 5.4). However, it is necessary to further modify the shape of the subsidiary fault whereby the footwall geometry of the subsidiary fault is adapted to follow the hanging wall geometry of the detachment fault using [5.3](Figure 5.4).

$$F_{(x_1)} = HW_{(x_0)} \qquad \text{if } x > x_{f_0} \qquad [5.3]$$

Where the fault profiles intersect, the subsidiary fault profile becomes deeper than the detachment fault as a consequence of the modelling method used. Therefore, the profile of the fault must also be modified to adjust for where the two faults intersect, which is achieved by adapting the geometry of the subsidiary fault to mirror the geometry of the detachment fault:

$$F_{(x_1)} = F_{(x_0)} \qquad \text{if } F_{(x_1)} < F_{(x_0)} \qquad [5.4]$$

### *5.1.3 Fault systems with synthetic and antithetic subsidiary faults*

It is possible to model fault systems with multiple synthetic and antithetic subsidiary faults. If there is more than one basin-controlling detachment fault within a cross-section, the faults can be divided into two independent fault systems that are defined by the direction of dip of the main basin-controlling fault within the system. For the purpose of this research, a

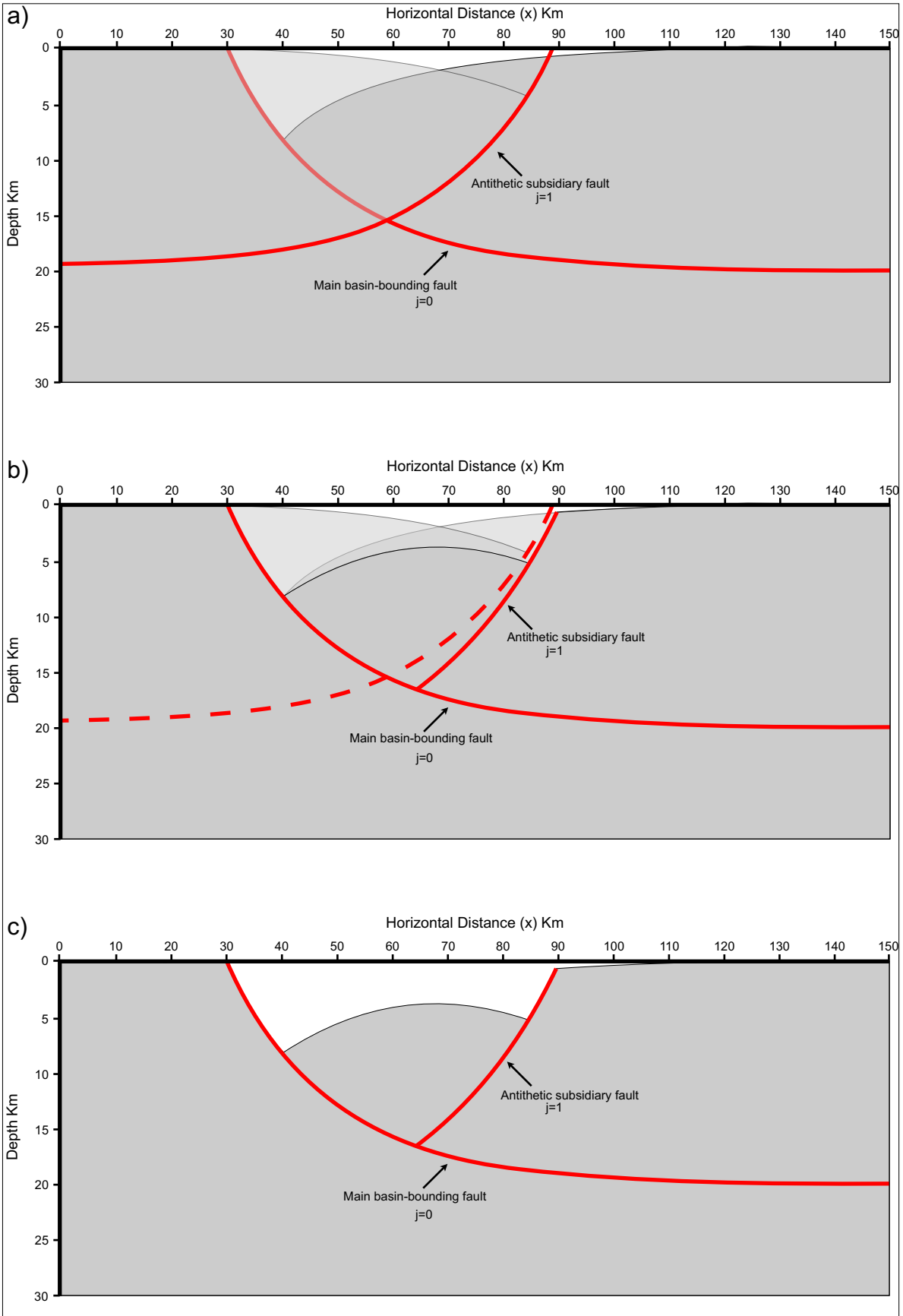


Figure 5.4. The fault and hanging wall profiles of the subsidiary fault must be adjusted to account for the deformation of the crust as a result of movement along the main detachment fault. a) The unadjusted fault and hanging wall profiles. b) Adjustment of subsidiary fault and hanging wall profiles. c) The adjusted fault and hanging wall profiles.

system of faults in which the detachment fault dips towards the end (right) of the cross-section ($x \mapsto x_{max}$) will be termed forwards dipping, and those that dip towards the start (left) of the cross-section ($x \mapsto 0$) will be described as backwards dipping. Within the model the order in which the fault systems are modelled does not influence the overall modelling results. Figure 5.5 illustrates a cross-section through a basin with multiple faults divided into systems.

All of the faults in the cross-section to be modelled are assigned a fault number ($j$) from 0 to the total number of faults ($NFlt$), which must be defined. This is an important step in the process, as the fault number dictates the order in which modelling occurs. Within each fault system, the faults should be numbered starting with the main detachment fault and working outwards with any subsidiary faults numbered with increasing distance from the basin-controlling fault (Figure 5.5).

The fault profile ($F_{(x_j)}$) for each fault, can be calculated using equation [4.1]. The fault profile for all of the faults, with the exception of the first fault ($j = 0$), must be adjusted for the deformation of the crust caused by any previous faults. Adjustment of the fault profiles is achieved using equation [5.5]:

$F_{(x_j)} = F_{(x_j)} + HW_{(x_k)}$ for values of $k$ between 0 and j-1 and with $k$ increasing incrementally by 1 [5.5]

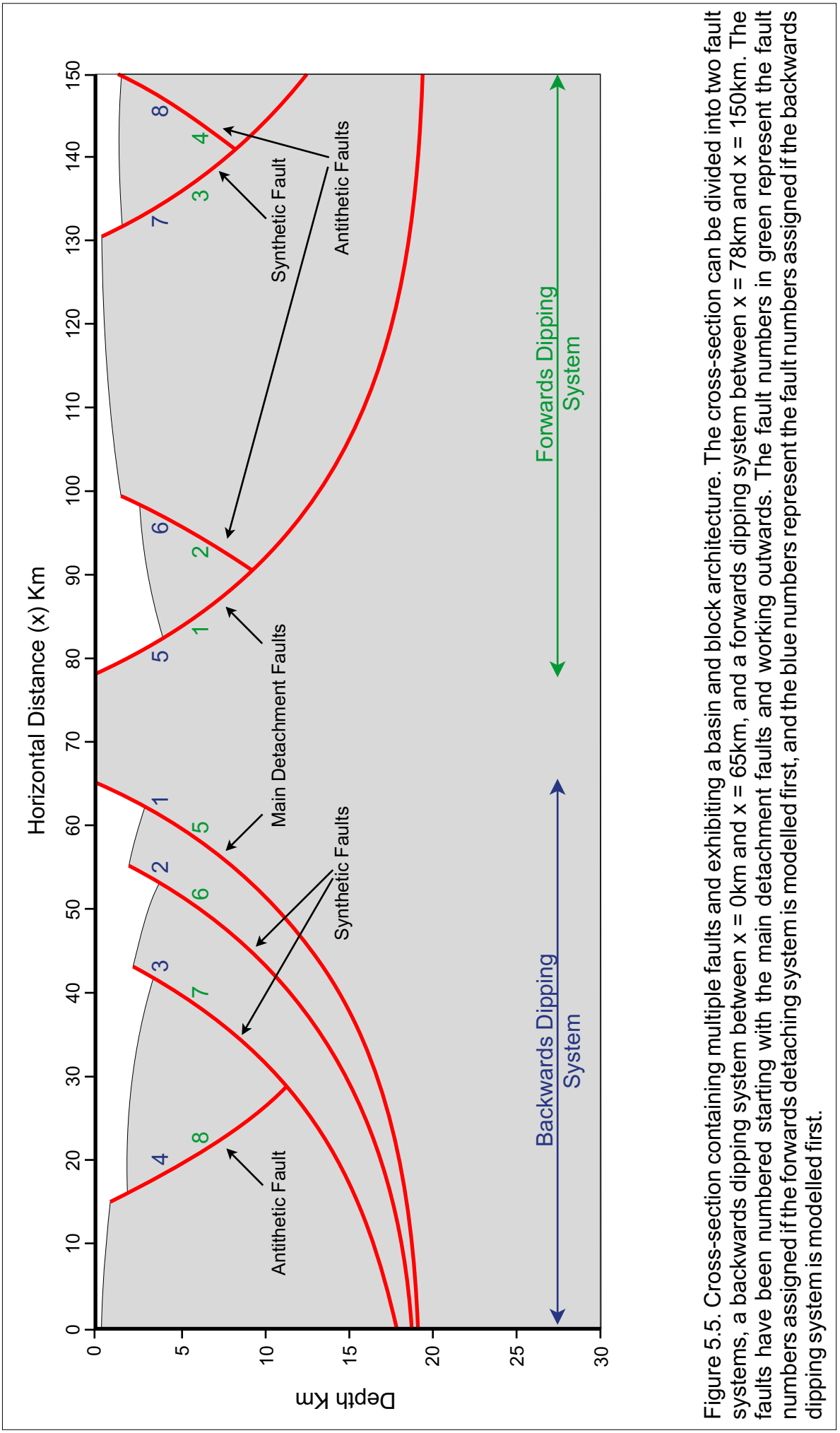


Figure 5.5. Cross-section containing multiple faults and exhibiting a basin and block architecture. The cross-section can be divided into two fault systems, a backwards dipping system between x = 0km and x = 65km, and a forwards dipping system between x = 78km and x = 150km. The faults have been numbered starting with the main detachment faults and working outwards. The fault numbers in green represent the fault numbers assigned if the forwards detaching system is modelled first, and the blue numbers represent the fault numbers assigned if the backwards dipping system is modelled first.

Each fault within a system causes progressive deformation of the crust. A summation of the hanging wall profile for each fault from 0 to $j$-1 is added to the fault profile to correct for previous deformation.

It is also necessary to take into account the shape of previous faults that may interact with the fault being modelled. The method of dealing with these modifications varies depending on whether the fault system is forwards or backwards dipping and whether the faults are synthetic or antithetic to the previous faults. A number of different fault interactions are illustrated in Figure 5.5.

Within a forward dipping system, faults that are synthetic to the main detachment fault can be modelled with the application of equation [5.5], however its relationship with previously modelled faults i.e. the main detachment fault, must be considered. For $j < k \geq 0$:

$$F_{(x_j)} = F_{(x_k)} \qquad \text{if } x < x_{f_j} \qquad [5.6]$$

This process adapts the geometry of the footwall of the fault to reflect the earlier faults.

If a subsidiary fault ($j$) is antithetic to the main detachment fault, two modifications must be made after equation [5.5] has been applied:

$$F_{(x_j)} = HW_{(x_k)} \qquad \text{if } x > x_{f_k} \qquad [5.7]$$

This process alters the footwall geometry of the fault to adapt to the hanging wall geometry of the fault to which it is antithetic. It is also necessary to consider the fault profile where the antithetic fault intersects

any synthetic fault. This is achieved by adapting the fault geometry to mirror the geometry of the conjugate fault where the value for the fault profile becomes deeper than that of the synthetic fault. For $j < k \geq 0$:

$$F_{(x_j)} = F_{(x_k)} \quad \text{if } F_{(x_j)} < F_{(x_k)} \text{ and } k \text{ represents a synthetic fault} \qquad [5.8]$$

Within a backwards dipping system, subsidiary faults that are synthetic to the main detachment fault are modified using equation [5.9] which alters the footwall geometry to demonstrate the effect of any previous faults.

$$F_{(x_j)} = F_{(x_k)} \quad \text{if } x \geq x_{f_j} \qquad [5.9]$$

Antithetic subsidiary faults within the backwards dipping system are modified in the same way as antithetic faults within a forward dipping system. The footwall geometry of the fault is revised to reflect the hanging wall geometry of the fault to which it is antithetic using equation [5.10].

$$F_{(x_j)} = HW_{(x_k)} \quad \text{if } x < x_{f_k} \qquad [5.10]$$

The fault profile of the antithetic fault where it intersects its conjugate synthetic fault is modelled using equation [5.8].

The hanging wall geometry for each subsequent fault must also be modified to correspond to deformation caused by movement along preceding faults. Each fault has a cumulative effect on the overall basin geometry that is calculated by equation [5.11].

$$HW_{(x)} = HW_{(x)} + \sum_{j=1}^{j=Nflt} HW_{(x_j)} \qquad [5.11]$$

These equations provide the basis for the development of algorithms to produce a computer modelling program capable of modelling multiple combinations of synthetic and antithetic faults.

## 5.2 Loading resulting from extension of the continental lithosphere

The modelling approach outlined in chapter 4 determines the deformation of the hanging wall following movement over a fault surface. Additionally, the lower crust and lithosphere mantle is assumed to deform by a pure shear mechanism. Changes in crustal thickness resulting from these processes impose loads upon the lithosphere, which responds by isostatic adjustment. In addition, density changes resulting from perturbations of the geotherm also impose loads upon the lithosphere, as detailed in section 4.5. Algorithms have been developed to quantify the flexural isostatic response to these loads (Egan, 1992). The profile of the flexural isostatic response to these processes is then integrated with the results from the structural modelling to generate profiles of isostatically compensated footwall, hanging wall and Moho surfaces.

The load arising from extension of the lithosphere by normal faulting, $L_{(s)x}$, is determined by:

$$L_{s(x)} = -\rho_c g S_{(x)} \qquad [5.12]$$

where: $S_{(x)}$ is the distribution of crustal thinning produced by extension along the fault.

Adapting equation [4.62], the flexural isostatic response to extension of the lithosphere by normal faulting, $W_{s(x)}$, can be defined as:

$$\frac{d^2}{dx^2} D \frac{d^2 W_{s(x)}}{dx^2} + \left[ \left( \rho_m - \rho_{air} \right) g W_{s(x)} \right] = -\rho_c g S_{(x)} \qquad [5.13]$$

where: $\rho_{air}$ is the density of the air, which assumes no water or sediment infill to the basin at this stage.

The load arising from ductile deformation of the lower crust by pure shear, $L_{P(x)}$, is given by:

$$L_{P(x)} = \left( \rho_m - \rho_c \right) g P_{(x)} \qquad [5.14]$$

where: $P_{(x)}$ is the distribution of crustal thinning produced by extension of the lower crust by pure shear.

Substituting this into equation [4.62] gives the flexural isostatic response to extension by pure shear, $W_{P(x)}$:

$$\frac{d^2}{dx^2} D \frac{d^2 W_{P(x)}}{dx^2} + \left[ \left( \rho_m - \rho_{air} \right) g W_{P(x)} \right] = \left( \rho_m - \rho_c \right) g P_{(x)} \qquad [5.15]$$

The flexural isostatic effects of temperature disturbances of the lithosphere, $W_{th(x,t)}$, can be calculated at any point in time (Egan, 1992):

$$\frac{d^2}{dx^2} D \frac{d^2 W_{th(x,t)}}{dx^2} + \left[ \left( \rho_m g W_{th(x,t)} \right) \right] = \int_a^0 \alpha_T \, \Delta T \, p' \, g \, dz \qquad [5.16]$$

where: $\alpha_T$ is the co-efficient of thermal expansion

$\Delta T$ is the temperature perturbation

$p'$ is the density of the lithosphere, which is dependent on depth

$a$ is the thickness of the lithosphere

The load generated by thermal perturbation of the temperature field, $L_{(th)x}$, at any time is calculated by:

$$L_{th(x)} = \rho_m S_{(t,x)} \quad [5.17]$$

where: $S_{(t,x)}$ represents the thermal perturbation of the lithosphere, such that (McKenzie, 1978; Allen and Allen, 1990):

At time, t = 0 Ma after extension:

$$S_{(0,x)} = -e_{(0,x)} \quad [5.18]$$

At any time after extension:

$$S_{(t,x)} = e_{(t,x)} - e_{(0,x)} \quad [5.19]$$

where:

$$e_{(t,x)} = a\alpha_T T_0 \left\{ \frac{4}{\pi^2} \sum_{m=0}^{\infty} \frac{1}{(2m+1)^2} \left[ \frac{\beta}{(2m+1)\pi} \sin \frac{(2m+1)\pi}{\beta} \right] e^{-(2m+1)^2 \frac{t}{\tau}} \right\} \quad [5.20]$$

The profile of the basin, relative to sea level, $B_{(x,t)}$, can be calculated by:

$$B_{(x,t)} = S_{(x)} + W_{s(x)} + W_{p(x)} + W_{th(x,t)} \quad [5.21]$$

The depth of the Moho profile, $M_{(x,t)}$, is given by:

$$M_{(x,t)} = C_o - P_{(x)} + W_{s(x)} + W_{P(x)} + W_{th(x,t)} \quad [5.22]$$

where: $C_o$ is the original crustal thickness

The geometry of the isostatically compensated fault profile is given by:

$$F_{(x,t)} = F'_{(x)} + W_{s(x)} + W_{P(x)} + W_{th(x,t)} \quad [5.23]$$

where: $F'_{(x)}$ is the original fault profile

Equations [5.13], [5.15] and [5.16] are rearranged and solved for $W_x$ by the Fast Fourier Transform technique.

### *5.2.1 Fast Fourier Transform*

The Fast Fourier Transform (FFT) is an efficient form of discrete Fourier transform (DFT). Fourier transforms are commonly used to transform a function in the time domain into a function in the frequency domain (Bracewell, 1986). A DFT requires that the input function is discrete, a finite set of values that are either real or complex numbers. A sequence of $N$ values $x_0 \ldots x_{N-1}$ is transformed into a sequence of $N$ values $X_0 \ldots X_{N-1}$, where $N$ is the maximum number of values (Elliot and Rao, 1982; Cormen *et al.*, 2001). The DFT is calculated using equation [5.24]:

$$X_{(j)} = \sum_{k=0}^{N-1} x_k e^{-\frac{2\pi i}{N} jk} \qquad \text{for } 0 < j > N \text{ and } j = j + 1 \qquad [5.24]$$

Where: $e^{-\frac{2\pi i}{N}}$ is the N$^{th}$ root of unity.

The inverse DFT, which transforms the function in the frequency domain back to the function in the time domain, is given by equation [5.25]:

$$x_{(k)} = \frac{1}{N} \sum_{j=0}^{N-1} X_j e^{\frac{2\pi i}{N} jk} \qquad \text{for } 0 < k > N \text{ and } k = k + 1 \qquad [5.25]$$

The FFT algorithm implemented in the model is based on the algorithm presented by Cooley and Tukey (1965). The algorithm for the FFT is derived by assuming $N$ is a composite of even and odd indexed values, such that the DFT is calculated separately for even indexed values

$x_0, x_2, \ldots x_{N-2}$ and for the odd indexed values $x_1, x_3, \ldots x_{N-1}$. These are then combined to produce the DFT for the whole sequence such that:

$$X_{(j)} = \sum_{k=0}^{\left(\frac{N}{2}\right)-1} x_{2k}\, e^{-\frac{2\pi i}{N}(2k)j} + \sum_{k=0}^{\left(\frac{N}{2}\right)-1} x_{2k+1} e^{-\frac{2\pi i}{N}(2k+1)j} \quad \text{for } 0 < j > N \text{ and } j = j+1 \quad [5.26]$$

These smaller DFTs have a length $N/2$ and for this length, the outputs for $N/2 \leq j < N$ are the same as the outputs for $0 \leq j < N/2$. For this reason the FFT is a more efficient version of the DFT because it requires fewer operations to complete. A DFT using equation [5.24] would require $N^2$ operations, whereas using the FFT requires $2N\log_2 N$ operations.

Once the data has been passed through the FFT routine it is filtered using the following response functions:

$$Resp_1 = \left(\frac{2\pi x}{N \times 1000}\right)^4 \quad [5.27]$$

$$Resp_2 = \frac{1}{\left(\rho_m g\right) + \left(D \times Resp_1\right)} \quad [5.28]$$

The isostatic response is then calculated:

$$W_{(x)} = L_{(x)} \times Resp_2 \quad [5.29]$$

Once the data have been filtered and the isostatic response calculated using equation [5.29] it is passed through the inverse FFT.

## 5.3 The effect of flexural isostasy on basin evolution

A model has been produced incorporating extension by faulting and pure shear and thermal uplift at time, t = 0 Ma after rifting, with isostatic

equilibrium maintained by applying the principles of flexural isostasy. Following the initial extension phase, a post-extensional thermal subsidence is applied to the model, also compensated using flexural isostasy. Models have been produced to examine the effect of applying flexural isostasy, by comparing the flexural isostatic response to the Airy isostatic response at each stage in the process. Several models have been produced at time intervals of 0, 5, 25, 50, 75 and 100 Ma after extension has occurred.

Figure 5.6 provides an overview of the model and the input parameters assumed, including an original crustal thickness of 35 km and a lithosphere thickness of 125 km. Extension by faulting in the upper crust with a magnitude of 10 km is balanced by extension by pure shear in the lower crust, with an intercrustal detachment between the two extension mechanisms at 20 km. The co-efficient of thermal expansion is assumed to be $3.28 \times 10^{-5}$ $K^{-1}$ and the temperature at the base of the lithosphere is 1333°C. Any accommodation space created in the basin is assumed to have been infilled by sediment with a density of 2500 $kgm^{-3}$. A Te of 5 km has been assumed. The effect of filling the basin is addressed in section 5.4. The model has been recalculated in order to observe the effect of individual variables on the isostatic response to lithosphere extension. In particular, the effects of varying the elastic thickness of the lithosphere, the density of the mantle, and the density crust have been investigated.

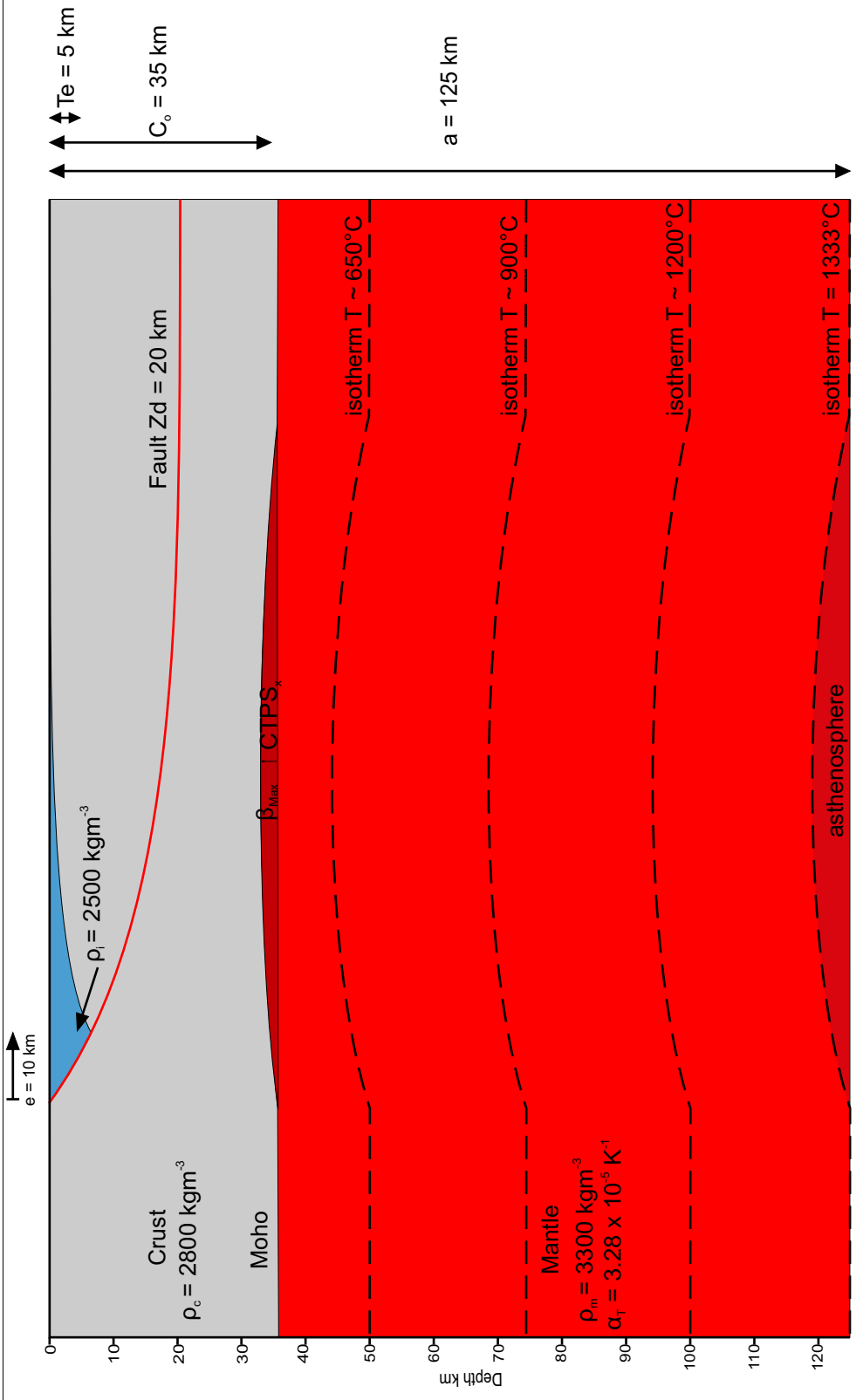


Figure 5.6. Parameters for the calculation of integrated model with flexural isostatic compensation. Extension of the upper crust by faulting is balanced by pure shear of the lower crust, which raises the lithosphere/asthenosphere boundary and perturbs the geotherm. Accommodation space created in the basin is assumed to have been filled with sediment. The effect of flexural isostasy on basin evolution is controlled by the flexural rigidity of the lithosphere, which is determined by its effective elastic thickness. The density of the mantle, $\rho_m$, and the density of the crust, $\rho_c$, also affect the flexural response.

### *5.3.1 The flexural isostatic response to extension due to faulting*

Figure 5.7 illustrates the isostatic response to extension of the lithosphere by faulting. Extension due to faulting imposes a negative load upon the lithosphere, where the crust is thinned, forming a basin. In order to restore isostatic equilibrium, uplift occurs. The Moho is raised introducing additional denser mantle material into the system. It should be considered, that the negative load imposed by the replacement of upper crustal material by the upper mantle may be subject to overestimation (Meredith, 2003). The value of density assigned to the crust for the purposes of modelling is an average for the whole crust. In reality, crustal density increases with depth such that at the surface, the density of the lower crust will be reduced, enlarging the contrast between the density of the crust and the density of the lithospheric mantle, reducing the size of the negative load upon the lithosphere and resulting in reduced uplift.

The Airy isostatic response to faulting (Figure 5.7b) is accommodated directly beneath the basin, producing a Moho whose profile is a mirror image of the basin. The fault profile is deformed by the uplift resulting from the isostatic rebound and the original basin is substantially shallower.

The flexural isostatic response to faulting (Figure 5.7c) is more regional and the geometry of the flexural rebound is broader and shallower as a result. The Moho and basin profile are uplifted by the amount of the flexural rebound. This uplift is greatest where the basin is deepest, corresponding to the greatest mass deficiency resulting from the faulting.

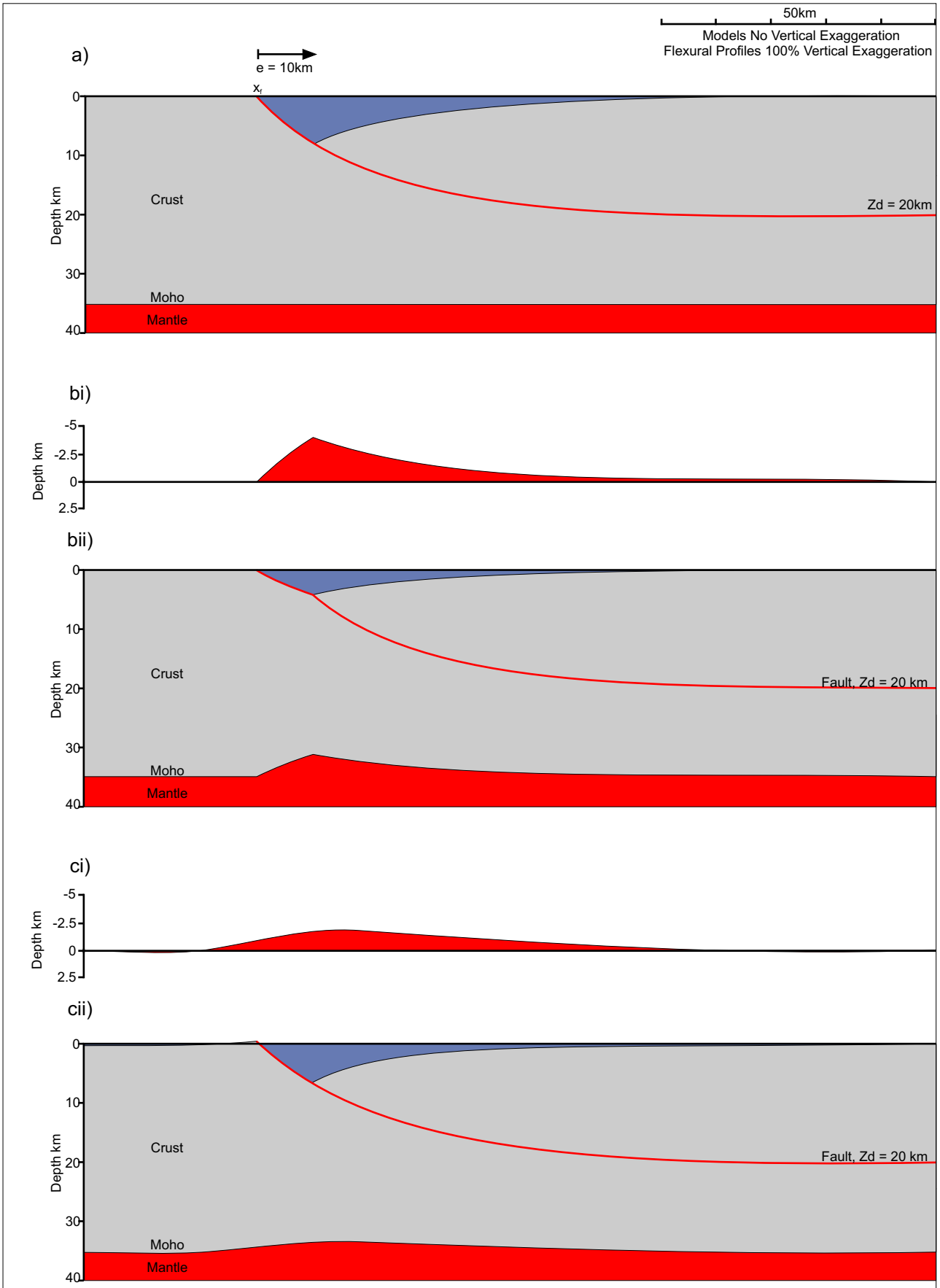


Figure 5.7. The isostatic response to extension of the lithosphere by faulting. a) Fault model, uncompensated. bi) Uplift profile assuming Airy isostatic compensation. bii) Fault model compensated using Airy isostasy. ci) Uplift profile assuming flexural isostatic compensation. cii) Fault model compensated using flexural isostasy.

However, the amount of uplift where the basin is deepest is less than the uplift associated with Airy isostasy at this location and, as a consequence, the resultant basin is deeper when flexural isostasy is applied. The regional response of flexural isostasy is also responsible for uplift in the footwall of the fault. This footwall uplift occurs as the flexural rebound extends laterally beyond the position of the fault intersection with the surface.

### *5.3.2 The flexural isostatic response to extension by pure shear*

Figure 5.8 illustrates the isostatic response to extension of the lithosphere by pure shear. Extension by pure shear is assumed to occur below a detachment depth of 20 km. This thins the lower crust, raising the Moho and imposing a positive load upon the lithosphere. The lithosphere responds by inducing subsidence.

The Airy isostatic response to extension by pure shear is shown in Figure 5.8bi. The isostatic induced subsidence occupies the same width and position as the pure shear that stimulates it. As a result a sag basin forms at the surface, and the topography of the Moho, which has been raised by the thinning of the lower crust is reduced, although it remains raised above its original position as the amount of thinning of the crust is greater than the isostatic subsidence. Figure 5.8bii displays the combined effect of faulting and pure shear with Airy isostatic compensation. The fault and basin profile is subjected to increased deformation as the subsidence resulting from pure shear enhances the amount of subsidence

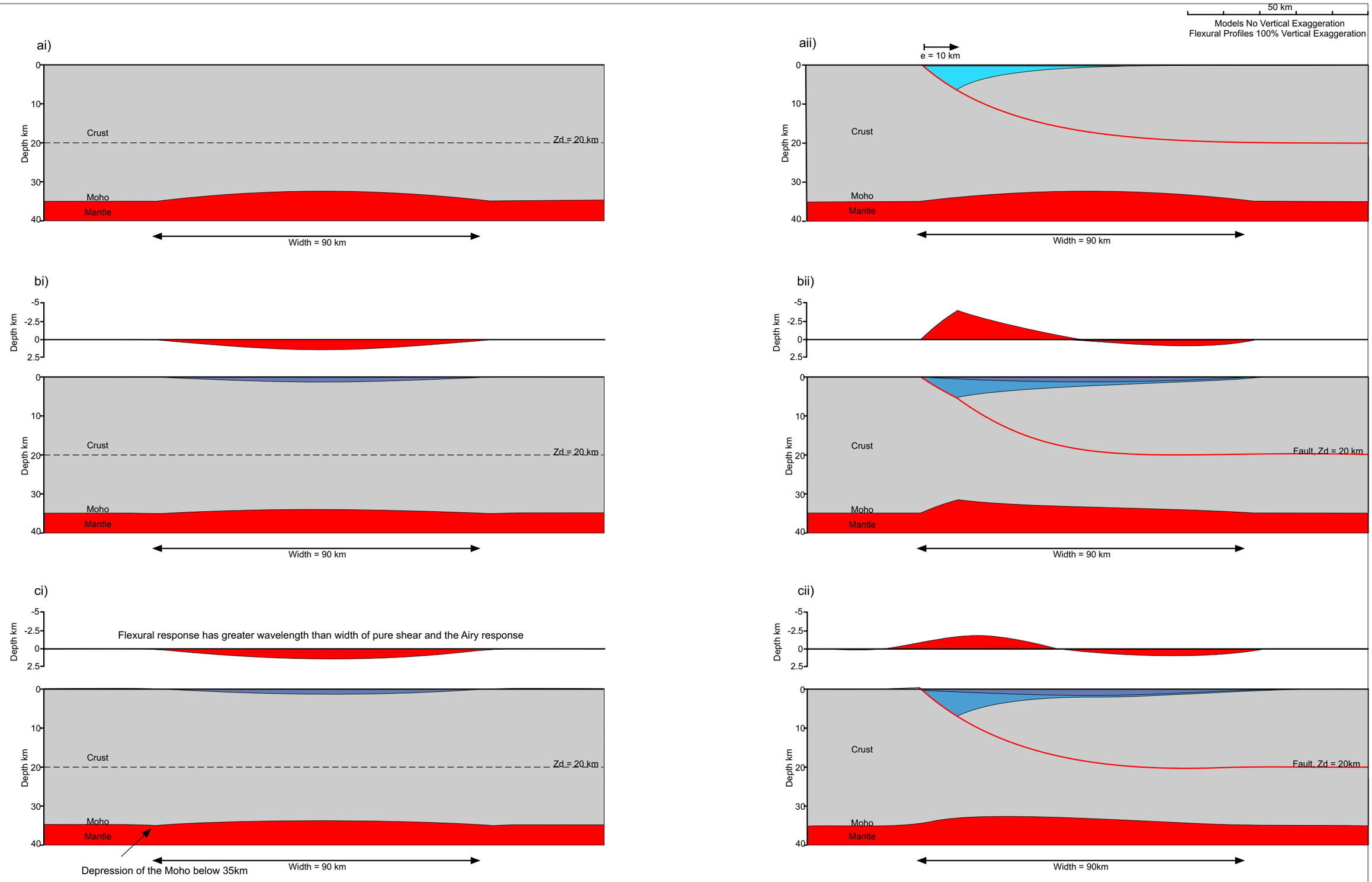


Figure 5.8. The isostatic response to extension of the lithosphere by pure shear. ai) Pure shear model, uncompensated. aii) Structural model, isostatically uncompensated. bi) Pure shear model assuming Airy isostasy, and showing isostatic subsidence. bii) Structural model compensated using Airy isostasy, including isostasy. ci) Pure shear model assuming flexural isostasy, including profile of flexural isostatic compensation. cii) Structural model compensated using flexural isostasy, including flexural isostasy profile.

at the surface. The combined isostatic effect results in uplift in the proximal region of the basin as the amount of isostatic uplift resulting from the crustal thinning due to faulting is greater than the amount of subsidence resulting from the pure shear. However, in a more distal position, the isostatic subsidence resulting from pure shear is greater than the fault related uplift and the overall outcome is subsidence.

The flexural isostatic effect of extension by pure shear is represented in Figure 5.8ci. The isostatic subsidence that is generated in response to the mass imposed upon the lithosphere is broader than the width of the pure shear. The maximum subsidence still occurs at the point of maximum crustal thinning, though the amount of subsidence is reduced. Likewise the resultant sag basin is broader and shallower than that produced by Airy isostasy. The profile of the Moho is reduced by subsidence however, it is not reduced as much as when Airy isostasy is applied at the location of the pure shear. Due to the fact that the flexural subsidence is broader than the width of the pure shear, the profile of the Moho at the edge of the region of pure shear has been subsided, such that it is depressed beneath its original depth of 35 km.

The combined flexural isostatic effect of extension by faulting and pure shear (Figure 5.8cii) reduces the amount of footwall uplift. The subsidence beyond the position of the pure shear counteracts the uplift that is a consequence of the isostatic response to crustal thinning due to faulting. Likewise, the depression of the Moho outside of the position of the pure

shear is counteracted by the fault related uplift. The profile of the Moho is shallowest beneath the deepest point in the basin.

### *5.3.3 The flexural isostatic response to thermal uplift*

Thermal uplift occurs in response to the thinning of the lithosphere caused by extensional tectonics. In particular, this thinning raises the basal lithosphere boundary, causing hotter asthenospheric material to be raised to a shallower depth to replace the amount of lithosphere that has been thinned. The hot asthenosphere represents a buoyancy load on the lithosphere which reacts by uplift to restore isostatic equilibrium. Figure 5.9 Illustrates the isostatically compensated thermal uplift in response to lithosphere extension immediately following rifting, that is at time, t = 0 Ma. The Airy isostatic response (Figure 5.9ai) is directly associated with the position of the pure shear extension of the lithosphere as this is where the geotherm has been disturbed and hotter material raised closer to the surface. The combined effect of extension and thermal uplift at t = 0 Ma after rifting is displayed in Figure 5.9aii. The thermal uplift counteracts some of the subsidence that occurs due to faulting and pure shear, decreasing the depth of the basin, particularly in the distal region of the basin.

The flexural isostatic response, illustrated in Figure 5.9bi, has a greater wavelength and reduced amplitude when compared to the Airy isostatic response. In this model, with an elastic thickness of 5 km, the maximum thermal uplift (amplitude) is ~60% of the maximum thermal uplift when

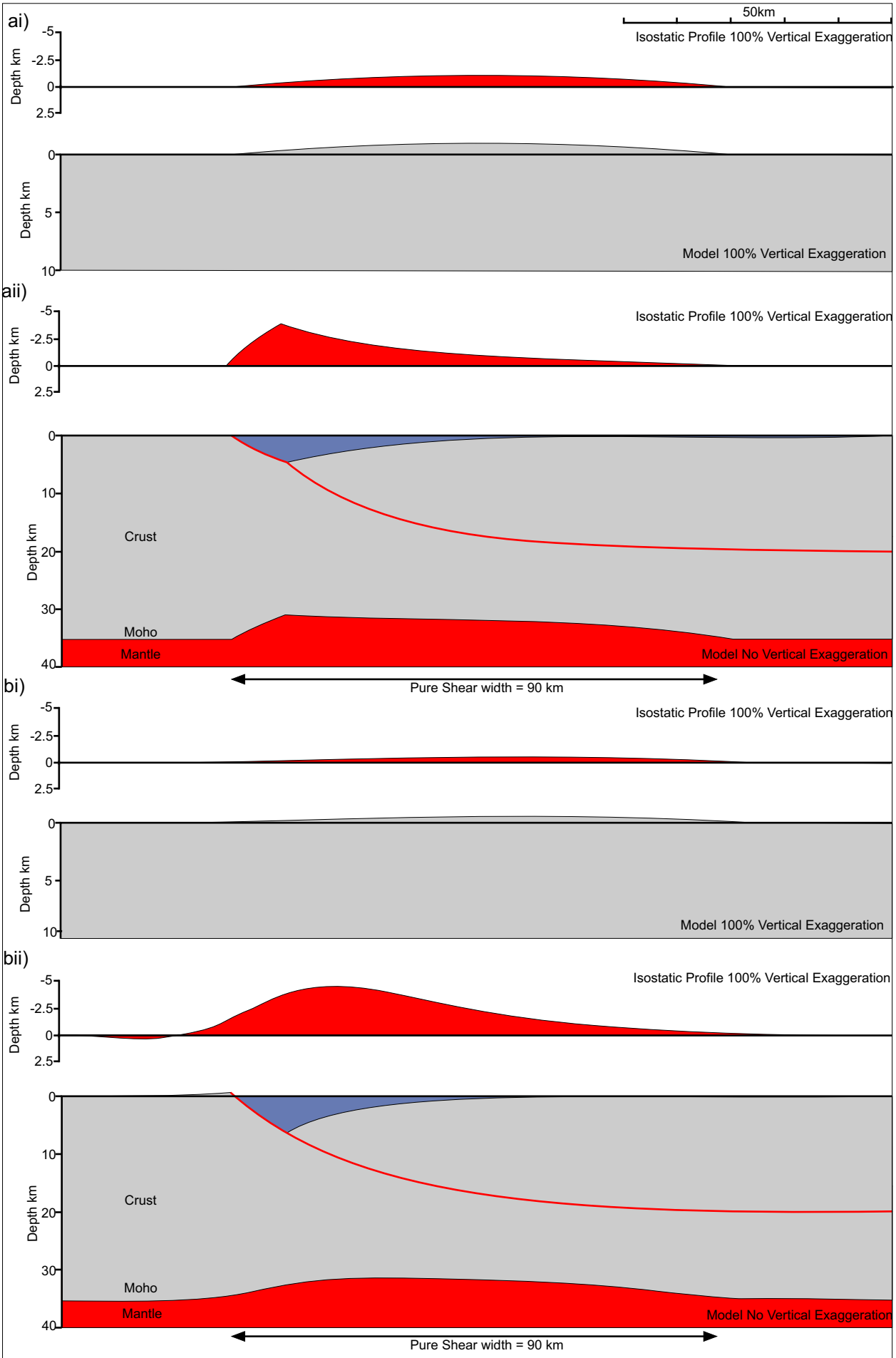


Figure 5.9. The isostatic effect of thermal uplift at time, t = 0 Ma after extension. ai) Model of Airy isostatically compensated thermal uplift with isostatic profile. aii) Integrated model with Airy isostatic compensation. bi) Model of flexurally compensated thermal uplift. bii) Integrated model with flexural isostatic compensation.

Airy isostasy is applied. The width of the flexurally compensated thermal uplift (wavelength) extends ~10 km beyond the limits of the Airy isostatic response. Figure 5.9bii demonstrates the flexural isostatic response to thermal and extensional processes at t = 0 Ma after rifting. The maximum depth of the basin generated is greater than that resulting from the application of Airy isostasy. The more distal regions have been subjected to greater uplift, and the resultant basin is shallower than its Airy isostasy counterpart. Uplift of the footwall of the fault above the datum is maintained.

### *5.3.4 The flexural isostatic response to thermal subsidence*

Figure 5.10 presents the effect of isostasy on thermal subsidence and the model at time, t = 100 Ma after extension. Following extension, thermal subsidence occurs as the geotherm returns to its original state. As the lithosphere material cools, its density increases and subsidence is induced in order to maintain isostatic equilibrium.

The Airy isostatic response to thermal subsidence is displayed in Figure 5.10ai. Similar to the Airy isostatic response to raising the geotherm, the subsidence resulting from thermal re-equilibration occurs in the area where the geotherm was raised, corresponding to the position of the pure shear extension of the lower crust and mantle lithosphere. The basin generated at t = 100 Ma after rifting (Figure 5.10aii) is widened by the maximum subsidence occurring in a position that is offset from the fault. In this position the total subsidence is greater than the total uplift.

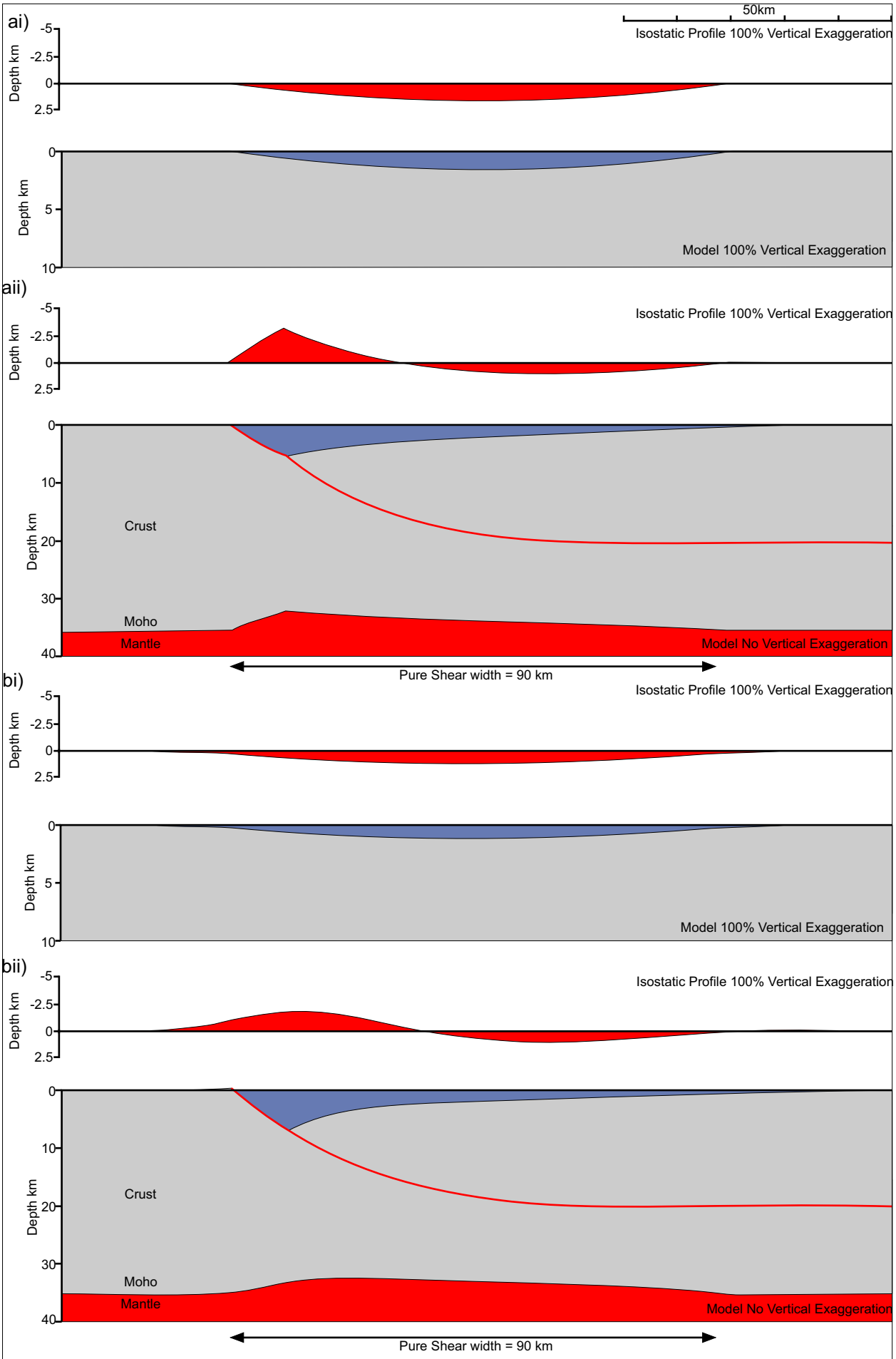


Figure 5.10. The isostatic response to thermal subsidence at time, t = 100 Ma after extension. ai) Model of Airy isostatically compensated thermal subsidence with isostatic profile above. aii) Integrated model with Airy isostatic compensation. bi) Model of flexurally compensated thermal subsidence. bii) Integrated model with flexural isostatic compensation.

The flexural isostatic response to thermal subsidence is shown in Figure 5.10bi. Similar to the thermal uplift response, the flexurally compensated thermal subsidence has a greater wavelength and smaller amplitude than when Airy isostasy is applied. Figure 5.10bii illustrates the combined model at $t = 100$ Ma after extension, showing that the combined isostatic response is uplift in the proximal region of the basin, whereas the overall isostatic response is subsidence in the distal region.

## 5.4 Surface Processes

In addition to the mechanical, thermal and isostatic processes associated with extension of the lithosphere, a number of surface processes need to be considered. These include infilling the basin with water and/or sediment, compaction of sediments and erosion of material raised above sea level. The structural extension of the lithosphere, as well as the thermal and flexural response to lithosphere extension are important factors in defining the stratigraphy that is deposited in the resultant basin. In addition, the rate of sediment supply and eustasy also play significant roles in determining the sedimentary sequences (Reynolds *et al.*, 1991) as these parameters interact to establish the palaeobathymetry. A model that integrates the tectonic, thermal and flexural responses to lithosphere extension with the surface processes of erosion and sedimentation, including isostatic adjustments, has been produced.

### *5.4.1 Basin Infill*

Flexurally compensated extension of the crust by faulting generates a basin at the surface. Basin subsidence is augmented by flexural subsidence resulting from pure shear of the lower crust and diminished by thermal uplift at the time of rifting. These mechanical and thermal processes control the initial creation of accommodation space which is often rapidly infilled by a combination of water and sediment. The infilling material acts as a further load upon the lithosphere which induces isostatic subsidence.

The load arising from the infilling of accommodation space, $L_{i(x,t)}$, is determined by:

$$L_{i(x,t)} = B_{(x,t)} \rho_i g \qquad [5.30]$$

where: $B_{(x,t)}$ defined the basin depth to be infilled

$\rho_i$ is the density of the infilling material

The flexural isostatic response to the basin infill, $W_{i(x,t)}$ is calculated using equation [7.26] such that (Watts *et al.*, 1982):

$$\frac{d^2}{dx^2} D \frac{d^2 W_{i(m,x,t)}}{dx^2} + \left[ \left( \rho_m - \rho_{air} \right) g W_{i(m,x,t)} \right] = B_{(x,t)} \rho_i g \qquad [5.31]$$

Equation [5.31] is solved for $W_{i(x,t)}$ using the fast Fourier transform method outlined in section 5.2.1. The data are passed through the forward FFT and filtered using the following response function:

$$Resp_2 = \frac{1}{\left(\rho_m - \rho_i\right) g + \left(D \, x \, Resp_1\right)} \qquad [5.32]$$

where: $Resp_1$ is given by equation [5.27]

The isostatic response is calculated using equation [5.29] before the data is passed through the inverse FFT.

It should be noted that this method of calculating the isostatic response to basin infill generates approximate values for the amount of flexural subsidence. The assumption of a constant density contrast ($\rho_m - \rho_i$) across the model profile results in an inaccurate amount of flexural subsidence particularly at the basin flanks (Egan, 1992). A more accurate method of calculating the flexural subsidence due to basin infill involves an iterative process of sequential basin infilling and isostatic compensation. The initial basin infill generates flexural subsidence. This extra accommodation space is then itself infilled. The load generated by this additional infill is then isostatically compensated. This process is then repeated iteratively until the additional subsidence generated becomes insignificant. The initial load is given by equation [5.30]. The flexural response to the initial load, $W_{i(m,x,t)}$ is given by:

$$\frac{d^2}{dx^2} D \frac{d^2 W_{i(m,x,t)}}{dx^2} + \left[\left(\rho_m - \rho_{air}\right) g W_{i(m,x,t)}\right] = B_{(x,t)} \rho_i \, g \qquad [5.33]$$

where: $m$ is the number of the iteration and = 0 for the initial load

This equation is solved for $W_{i(m,x,t)}$, using the FFT method and using the response function given by equation [5.28] to filter the data. The load, $L_{i(m,x,t)}$, generated by infilling of the newly created accommodation space at each iteration, *m*, is given by:

$$L_{i(m,x,t)} = W_{i(m-1,x,t)} \rho_i g \qquad [5.34]$$

The flexural response is therefore given by:

$$\frac{d^2}{dx^2} D \frac{d^2 W_{i(m,x,t)}}{dx^2} + \left[ \left( \rho_m - \rho_{air} \right) g W_{i(m,x,t)} \right] = W_{i(m-1,x,t)} \rho_i g \qquad [5.35]$$

and the total flexural response to the infilling of the basin, $W_{i(x,t)}$, is given by:

$$W_{i(x,t)} = \sum_{m=0}^{m=n} W_{i(m,x,t)} \qquad [5.36]$$

where: *n* is the number of iterations

The profile of the basin relative to sea level, $B_{(x,t)}$, can be calculated by:

$$B_{(x,t)} = S_{(x)} + W_{s(x)} + W_{p(x)} + W_{th(x,t)} + W_{i(x,t)} \qquad [5.37]$$

The thickness of each unit of stratigraphy at any point in the basin, $ST_{(x,ts)}$ created with each new time step can be calculated. At time, t = 0 Ma after rifting, the stratigraphy fills the basin such that:

$$ST_{(x,t,ts=0)} = B_{(x,t=0)} \quad \text{if} \quad B_{(x,t=0)} > 0$$

$$ST_{(x,t,ts=0)} = 0 \quad \text{if} \quad B_{(x,t=0)} < 0 \qquad [5.38]$$

where: *ts* is the number of the time step in which the stratigraphy was created

At any time step following the initial rifting event, the stratigraphy fills the additional subsidence generated such that:

$$ST_{(x,t,ts)} = \left(W_{th(x,ts)} + W_{i(x,ts)}\right) - \left(W_{th(x,ts-1)} + W_{i(x,ts-1)}\right)$$

$$\text{if } ST_{(x,t,ts)} < 0, \quad ST_{(x,t,ts)} = 0 \qquad [5.39]$$

The depth of the Moho profile, $M_{(x,t)}$, is given by:

$$M_{(x,t)} = C_o - P_{(x)} + W_{s(x)} + W_{P(x)} + W_{th(x,t)} + W_{i(x,t)} \qquad [5.40]$$

The geometry of the fault profile is given by:

$$F_{(x,t)} = F'_{(x)} + W_{s(x)} + W_{P(x)} + W_{th(x,t)} + W_{i(x,t)} \qquad [5.41]$$

### *5.4.2 Palaeobathymetry*

In order to simulate the effect of palaeobathymetry, at each time step, the accommodation space generated by structural deformation, thermal processes and isostatic compensation is infilled assuming an initial water infill. The basin is then infilled with sediment to a level that accounts for the bathymetry. The method presented here corresponds to a maximum palaeobathymetry level that is fixed over time.

The load, $L_{b(x,t=0)}$ and flexural response, $W_{b(x,t=0)}$ arising from the initial filling of the accommodation space by water at time, t = 0 Ma after extension is given by equations [5.30] & [5.31] such that:

$$L_{b(x,t=0)} = B_{(x,t=0)} \rho_w g \qquad [5.42]$$

$$\frac{d^2}{dx^2} D \frac{d^2 W_{b(x,t=0)}}{dx^2} + \left[ \left( \rho_m - \rho_{air} \right) g W_{b(x,t=0)} \right] = B_{(x,t=0)} \rho_w g \qquad [5.43]$$

This is solved for $W_{b(x,t)}$ using the FFT method described in section 5.2.1 and the response function given by equation [5.28].

$P_{b(x)}$ is the maximum level of the palaeobathymetry, if the basin is shallower than maximum palaeobathymetry (i.e. $B_{(x,t)} < P_{b(x)}$) the actual palaeobathymetry, $P_{ab(x)}$, is equal to the basin depth such that:

$$P_{ab(x,t)} = B_{(x,t)} \qquad \text{if } B_{(x,t)} < P_{b(x)}$$

$$P_{ab(x,t)} = P_{b(x)} \qquad \text{if } B_{(x,t)} \geq P_{b(x)} \qquad [5.44]$$

The additional load generated by infilling the basin to the level of the palaeobathymetry, $L_{sed(x)}$, is given by:

$$L_{sed(x)} = \left( B_{(x,t=0)} - P_{ab(x,t=0)} \right) \left( \rho_s - \rho_w \right) g \qquad [5.45]$$

The density of the initial sediment infill is simulated to be lighter than the specified bulk sediment density, $\rho_s$, by an amount equivalent to the value of the density of the water, $\rho_w$. This adjustment takes into account that the accommodation space was loaded with water in the first instance, which has already exerted a load upon the lithosphere that has been isostatically compensated for in equation [5.43].

The flexural response to this additional loading is calculated by:

$$\frac{d^2}{dx^2} D \frac{d^2 W_{sed(x)}}{dx^2} + \left[ \left( \rho_m - \rho_{air} \right) g W_{sed(x)} \right] = \left( B_{(x,t=0)} - P_{ab(x,t=0)} \right) \left( \rho_s - \rho_w \right) g \quad [5.46]$$

The amount of additional accommodation space created by the loading of the basin by infilling with water and sediment, $A_{(m=0,\,x,t=0)}$, is given by:

$$A_{(m=0,\,x,t=0)} = W_{b(x)} + W_{sed(x)} \quad [5.47]$$

This additional accommodation space is then infilled with either water, sediment or a combination of both depending upon the depth of the basin and the maximum palaeobathymetry. The process of filling the basin and isostatically compensating for the loading is repeated $n$ times until the subsidence becomes negligible.

The additional accommodation space generated at time, t = 0 Ma after extension by each additional iteration of the model, where $m > 0$, is given by:

$$A_{(m,\,x,t=0)} = W_{Pbi(m-1,x,t=0)} \quad [5.48]$$

where: $W_{Pbi(m-1,x,t=0)}$ is the additional subsidence generated by the previous iteration

If the basin is deeper than the maximum palaeobathymetry before the basin infill load generated subsidence is added, $B_{(x,t)} \geq P_{b(x)}$ the newly created accommodation space is infilled with sediment with bulk density, $\rho_s$, such that the new load generated by infilling the accommodation space, $L_{a(m,x,t)}$, is given by :

$$L_{a(m,x,t)} = A_{(m,x,t)} \rho_s g \qquad [5.49]$$

If the basin, including the newly created loading subsidence, $B_{(x,t)} + \sum_{m=0}^{m=n} A_{(m,x,t)}$, is shallower than or equal in depth to the maximum palaeobathymetry depth, $P_{b(x)}$, the additional accommodation space is filled by water such that:

$$L_{a(m,x,t=0)} = A_{(m,x,t=0)} \rho_w g \qquad [5.50]$$

If however, the basin at t = 0 Ma was shallower than the maximum palaeobathymetry, $B_{(x,t)} < P_{b(x)}$ prior to the addition of the newly accommodation space, and the subsided basin is deeper than the maximum palaeobathymetry, $B_{(x,t)} + \sum_{m=0}^{m=n} A_{(m,x,t)} > P_{b(x)}$, the load infilling the new accommodation space within the basin will be a combination of water and sediment. The difference between $B_{(x,t)}$ and $P_{b(x)}$ will be accommodated by infilling with water, any additional accommodation space will by infilled by sediment, such that:

$$L_{a(m,x,t)} = \left(P_{b(x)} - P_{ab(x,t)}\right)\rho_w g + \left(A_{(m,x,t)} - \left(P_{b(x)} - P_{ab(x,t)}\right)\right)\rho_s g \qquad [5.51]$$

The flexural response of the basin to the additional loading of the basin considering palaeobathymetry, $W_{Pbi(m,x,t)}$, is given by:

$$\frac{d^2}{dx^2} D \frac{d^2 W_{Pbi(m,x,t)}}{dx^2} + \left[\left(\rho_m - \rho_i\right) g W_{Pbi(m,x,t)}\right] = L_{a(m,x,t)} \qquad [5.52]$$

where: $\rho_i$ is the density of the infill and depends upon the density of the loading material

Equation [5.52] is re-arranged and solved for $W_{Pbi(m,x,t)}$ using the FFT and filtered using the response function given in section 5.2.1 by equation [5.28].

$$W_{Pbi(x,t)} = \sum_{m=0}^{m=n} W_{Pbi(m,x,t)} \quad [5.53]$$

When time is greater than 0 Ma, the amount of accommodation space, $A_{(x,t)}$ is equal to the amount of thermal subsidence such that:

$$A_{(x,t)} = W_{th(x,t)} - W_{th(x,t-1)} \quad [5.54]$$

The accommodation space created by thermal subsidence is then initially infilled with water in the same manner as the original basin infill. The load generated by the infilling with water and the flexural response to such infilling are given by:

$$L_{b(x,t)} = A_{(x,t)} \rho_w g \quad [5.55]$$

$$\frac{d^2}{dx^2} D \frac{d^2 W_{b(x,t)}}{dx^2} + \left[ \left( \rho_m - \rho_w \right) g W_{b(x,t)} \right] = A_{(x,t)} \rho_w g \quad [5.56]$$

Equation [5.56] is solved using the FFT method and the data is filtered using the response function given by:

$$Resp_2 = \frac{1}{\left( \rho_m - \rho_w \right) g + \left( D \, x \, Resp_1 \right)} \quad [5.57]$$

where: $Resp_1$ is given by equation [5.27].

This compensates for the additional subsidence assuming a water infill.

At time > 0 Ma, infilling the basin with sediment is modelled as a single step without iteration to reduce the model processing overheads. If the basin is deeper than the maximum palaeobathymetry before the thermally generated accommodation space was added and infilled by water, $B_{(x,t-1)} > P_{b(x)}$, the newly created accommodation space, including that generated by the water infill filled completely with sediment that has a density of $\rho_s - \rho_w$ to account for the fact that the load has already been isostatically compensated for water infill. The load generated by this sediment infill is given by:

$$L_{a(x,t)} = \left( A_{(x,t)} + W_{b(x,t)} \right) \left( \rho_s - \rho_w \right) g \qquad [5.58]$$

The flexural response is given by substituting $L_{a(x,t)}$ into equation [5.52] considering m = 0. $W_{Pbi(x,t)}$ is then solved using the FFT method and filtered using the response function given by:

$$Resp_2 = \frac{1}{\left( \rho_m - \left( \rho_s - \rho_w \right) \right) g + \left( DxResp_2 \right)} \qquad [5.59]$$

If the basin at time, t, after thermal subsidence and water loading is shallower than the maximum palaeobathymetry, $B_{(x,t-1)} + W_{th(x,t)} + W_{b(x,t)} < P_{b(x)}$, there is no infilling of the basin with the additional sediment and the flexural response is given by:

$$W_{Pbi(x,t)} = 0 \qquad [5.60]$$

If the basin was shallower than the maximum palaeobathymetry before the thermally generated subsidence was created and loaded, and deeper than the maximum palaeobathymetry following the thermal and loading subsidence, $B_{(x,t-1)} < P_{b(x)}$ and $B_{(x,t-1)} + W_{th(x,t)} + W_{b(x,t)} > P_{b(x)}$, then the space that is additional to the basin, once the maximum palaeobathymetry has been achieved, is infilled with sediment of density $\rho_s - \rho_w$. The load that results from this sediment infill is given by:

$$L_{a(x,t)} = \left( \left( A_{(x,t)} + W_{b(x,t)} \right) - \left( P_{b(x)} - P_{ab(x,t-1)} \right) \right) \left( \rho_s - \rho_w \right) g \qquad [5.61]$$

The flexural response, achieved by substituting equation [5.61] into [5.52], is solved for $W_{Pbi(x,t)}$ using the FFT. The data are filtered using the response function given by:

$$Resp_2 = \frac{1}{\left( \rho_m - \rho_s \right) g + \left( D \, x \, Resp_1 \right)} \qquad [5.62]$$

The additional space created by this loading will be infilled by sediment in order to maintain the palaeobathymetry level at the maximum palaeobathymetry, which has already been achieved. The true bulk density of the sediment, $\rho_s$, is used as the accommodation space has not previously been loaded with water.

The amount of subsidence generated by infilling of the basin, $W_{i(x,t)}$, is given by:

$$W_{i(x,t)} = W_{b(x,t)} + W_{sed(x)} + W_{Pbi(x,t)} \qquad [5.63]$$

The profile of the basin relative to sea level, $B_{(x,t)}$, is given by substituting equation [5.63] into equation [5.37]. The profile of the Moho, $M_{(x,t)}$, is calculated using equations [5.40] and [5.63], while the deformed fault profile, $F_{(x,t)}$, is given by substituting equation [5.63] into equation [5.41]. The actual palaeobathymetry, $P_{ab(x,t)}$, at any time is given by equation [5.44].

At t = 0 Ma after rifting, the thickness of the stratigraphy of the basin is dependent upon the isostatically compensated basin depth and the palaeobathymetry such that:

$$ST_{(x,t,ts=0)} = B_{(x,t=0)} - P_{ab(x,t=0)} \quad \text{if } B_{(x,t=0)} > 0$$

$$ST_{(x,t,ts=0)} = 0 \quad \text{if } B_{(x,t=0)} < 0 \qquad [5.64]$$

At t > 0 Ma after rifting, the thickness of the stratigraphy of the basin is dependent upon the amount of thermal subsidence, the palaeobathymetry, and the isostatic effect of loading the thermal subsidence such that:

$$ST_{(x,t,ts)} = \left(B_{(x,t)} - B_{(x,t-1)}\right) - \left(P_{ab(x)} - P_{ab(x,t-1)}\right) \qquad [5.65]$$

### *5.4.3 Compaction*

Compaction is a mechanical process that occurs as deposition of sediment increases the overburden stress. The overburden or effective stress is the weight of the granular matrix of the overlying sediment layer (Lerche, 1990). It has been shown from principles of soil mechanics that this weight is supported by the matrix of the sediment column and by fluid pressure in

the pore space of the sediment column such that (Terzaghi and Peck, 1948; Hubbert and Rubey, 1959):

$$\sigma = s - p \qquad [5.66]$$

where: $\sigma$ is the effective stress
$s$ is the vertical compressive stress
$p$ is the pore fluid pressure

Compaction produces changes in the porosity and permeability of the underlying sediment column. Initially, the increase in the sediment load is compensated for by an increase in fluid pressure. Over time, compaction proceeds as fluid escapes the rock, reducing the pore fluid pressure and increasing the effective stress. This increase in $\sigma$ results in a reduction in porosity and therefore compaction of the sediment column (Lerche, 1990; Allen and Allen, 1990).

Compaction of the underlying sediment column generates new accommodation space in the areas of active deposition (Thorne and Swift, 1991; Reynolds *et al.*, 1991), which can be a significant proportion of the total accommodation space as infilling with sediment induces additional subsidence (Reynolds *et al.*, 1991). Figure 5.11 illustrates the effect of compaction upon basin and stratigraphical development. Unit A is deposited at time, t = 0 Ma after extension (Figures 5.11ai & bi). Unit B is deposited at t1 after extension as a result of infilling accommodation space generated by thermal subsidence (Figures 5.11aii & bii). Unit B directly overlies the initial deposits, unit A. This applies pressure on unit A, which reacts by reducing pore space generating compaction and new

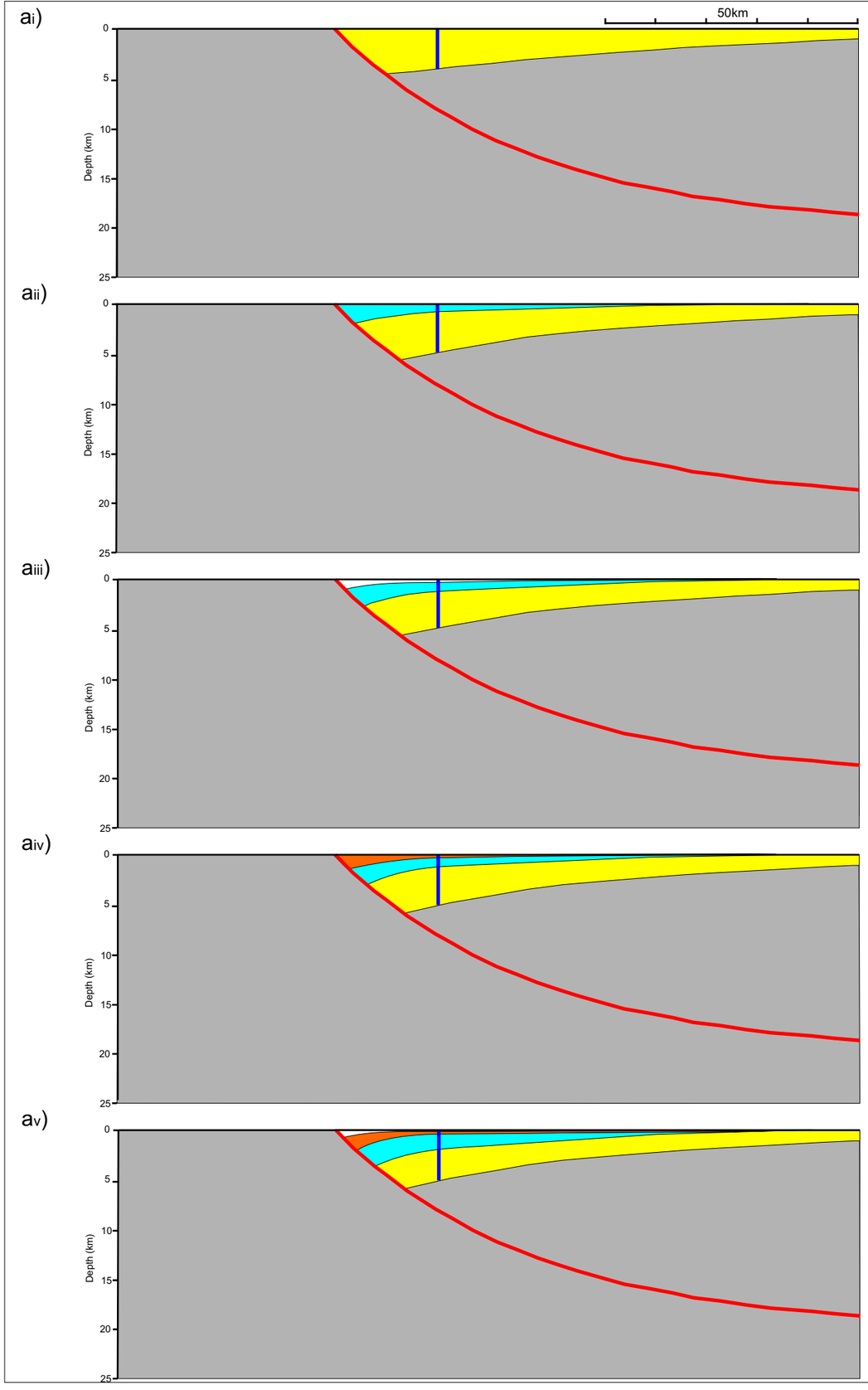


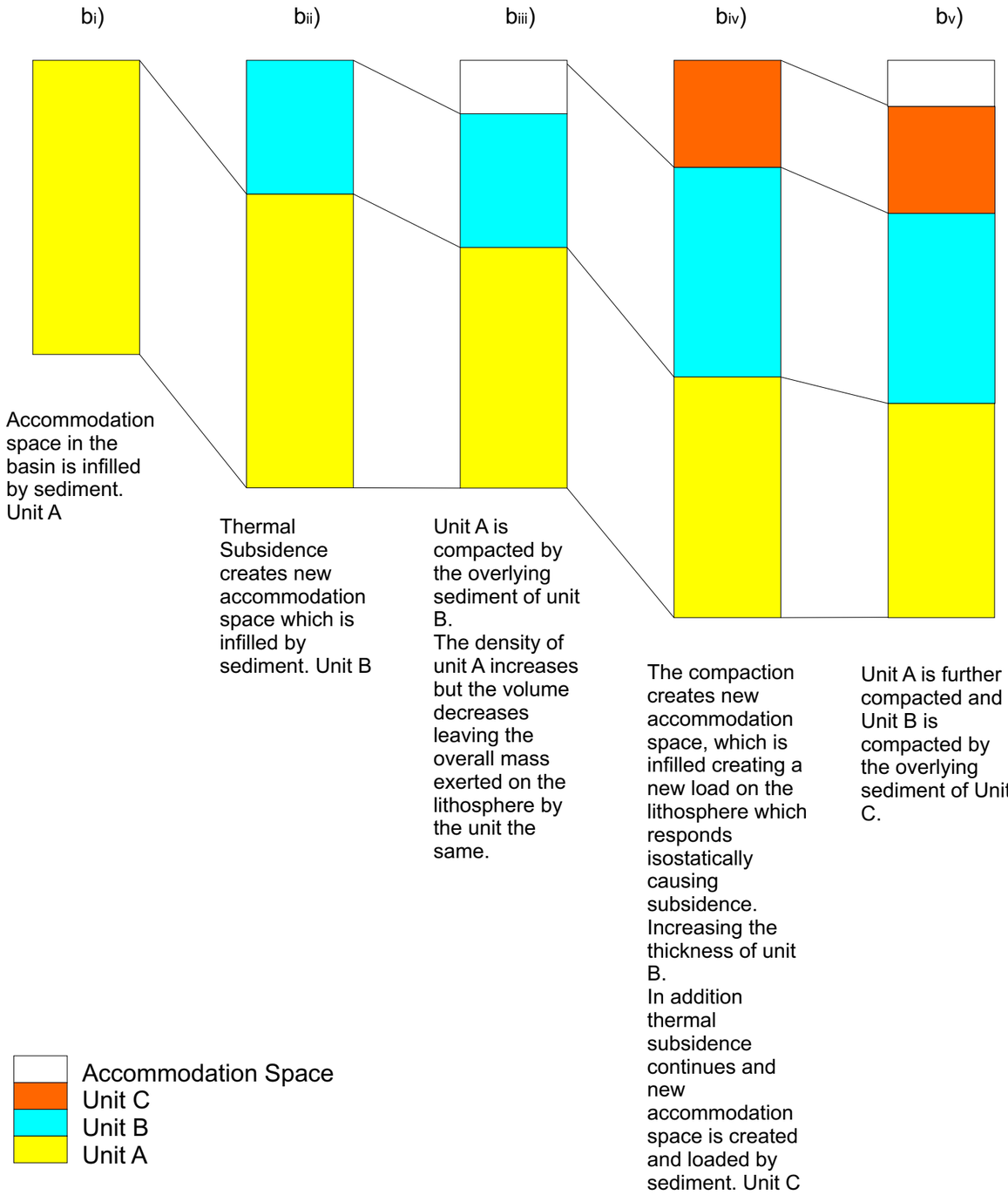


Figure 5.11. The stratigraphical and isostatic effect of compaction. a) Models showing stages of compaction. ai) Time step 0, t = 0 Ma after rifting the basin is infilled. aii) Time step 1, thermal subsidence generates additional accommodation space. aii) Additional accommodation space created by compaction of underlying sediments aiv) Time step 2, thermal subsidence generates more accommodation space. av) compaction of underlying sediments generates more accommodation space. b) Logs through the models showing the effect of compaction on the stratigraphy.

accommodation space at the surface (Figures 5.11aiii & biii). This accommodation space is loaded with sediment, generating additional isostatic subsidence, which is also infilled with sediment forming part of unit B. Thermal subsidence generates new accommodation space which is loaded with sediment, unit C (Figures 5.11aiv & biv). The pressure exerted by unit C further compacts unit A and compacts unit B generating new accommodation space which can be loaded by infilling with sediment (Figures 5.11av & bv).

The amount of compaction generated by deposition of sediment on a column of rock is complicated by the interaction of variables including lithology, overpressuring, diagenesis and chemical compaction (Allen and Allen, 1990). For example, mudstones, which comprise 60-70% of basin infill, have a surface porosity in the region of 60-75%, whereas sandstones typically have a surface porosity around 50% (Aplin *et al.*, 1995; Lerche, 1990). Mudstones also have a strong influence on the development of overpressure (Bredehoeft and Hanshaw, 1968; Smith, 1971). Additionally in carbonate rocks, chemical compaction, the dissolution of grains, diffusion and transport of dissolved material and precipitation of minerals, may be an important contributor to compaction even at shallow depths and low temperatures (Waples and Kamata, 1993).

In order to model the effects of compaction, a general relationship between the rate of sedimentation and porosity loss that is applicable over a large depth range and for a number of lithologies is required (Allen and Allen,

1990). Sediment compaction and the corresponding porosity variations can be modelled by understanding porosity-depth relations.

#### 5.4.3.1 The relationship between porosity and depth

Several porosity-depth relationships have been quantified. These include power-law and exponential relationships as well as complex numerical models that include the effect of variable sedimentation rates and diagenesis (Athy, 1930; Hubbert and Rubey, 1959; Rubey and Hubbert, 1959; Sclater and Christie, 1980; Falvey and Middleton, 1981; Das, 1983; Baldwin and Butler, 1985; Steckler *et al.*, 1988). Whilst some engineering applications require the use of complex numerical solutions, the general trend for the relationship between porosity and depth can be used to determine the probability that an unobserved sedimentary body has the assigned porosity (Bahr, 1997; Bahr *et al.*, 2001).

Recent observations of empirical data for a number of lithologies demonstrate that the relationship between porosity and depth is exponential (Bahr *et al.*, 2001). This supports previous analyses that have an exponential relationship between porosity and depth (Hubbert and Rubey, 1959; Rubey and Hubbert, 1959; Sclater and Christie, 1980; Falvey and Middleton, 1981; Das, 1983).

Rubey and Hubbert (1959) demonstrate that under normal pressure conditions, the porosity at depth $y$, $\phi_y$, is given by:

$$\phi_y = \phi_s e^{-cy} \qquad [5.67]$$

where: $\phi_s$ is the surface porosity

$c$ is the compaction co-efficient that determines the slope of the $\phi$-depth curve

$y$ is the depth

Sclater and Christie (1980) developed a model for the relationship between porosity and depth to fit data from the North Sea, which also show an exponential decrease in porosity with depth. Table 5.1 presents the parameters for the relationship between porosity and depth for North Sea lithologies.

| | $\Phi_s$ | c x10$^{-3}$cm$^{-1}$ |
|---|---|---|
| Shale | 0.63 | 0.51 |
| Sand | 0.49 | 0.27 |
| Chalk | 0.70 | 0.71 |
| Shaley Sand | 0.56 | 0.39 |

Table 5.1 Parameters for the exponential relationship between porosity and depth for the North Sea. From Sclater and Christie (1980).

Figure 5.12a illustrates the relationship between porosity and depth using the data in Table 5.1 and equation [5.67]. Sand has the lowest surface porosity and compaction co-efficient. The surface porosity and compaction co-efficient increases through silty sand, silt to chalk which has the highest surface porosity and compaction co-efficient. The porosity decreases more rapidly with depth the higher the initial porosity and compaction co-efficient. By 1 km depth, the porosity relationship has reversed such that chalk has the lowest porosity and sand the highest.

Falvey and Middleton (1981) argue that at shallow depths, the exponential porosity-depth relationship does not fit the data well. They

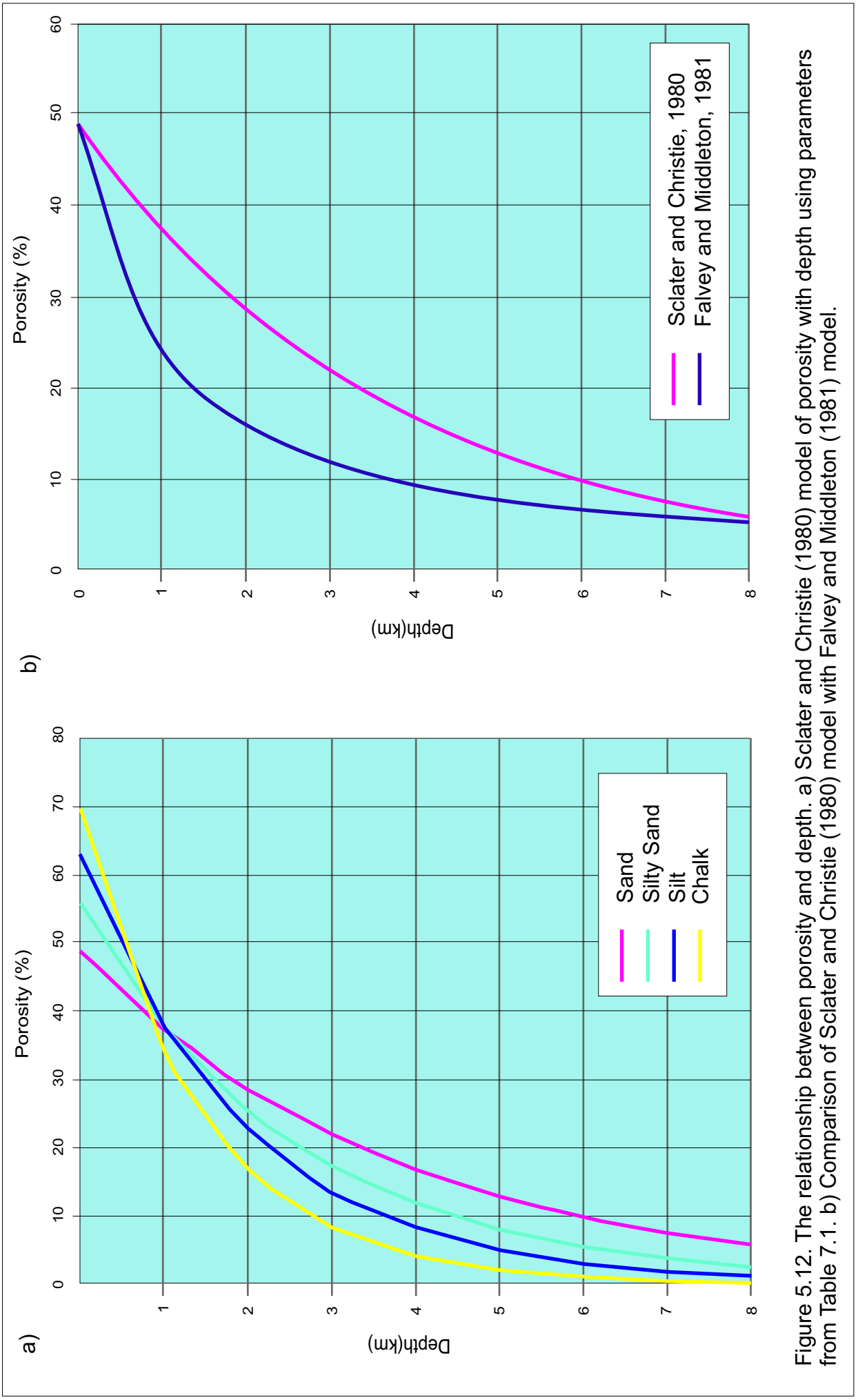


Figure 5.12. The relationship between porosity and depth. a) Sclater and Christie (1980) model of porosity with depth using parameters from Table 7.1. b) Comparison of Sclater and Christie (1980) model with Falvey and Middleton (1981) model.

have proposed an alternative porosity-depth relationship based on a differential change in the load such that:

$$\frac{1}{\phi_y} = \frac{1}{\phi_s} + ky \qquad [5.68]$$

where: $k$ is a lithology dependent co-efficient

Figure 5.12b compares the Sclater and Christie (1980) model with the Falvey and Middleton (1981) model for sandstone with $\phi_s$ = 0.49, $c$ = 0.27, $k$ = 2.18. Porosity decreases more rapidly with depth at small values of depth within the Falvey and Middleton model.

Compaction is assumed to take place at each time step following t = 0 Ma after extension. In order to model compaction, at each time step it is necessary to calculate the original unit thickness of the stratigraphy deposited by that time step. In addition at the first time step after t = 0 it is necessary to determine the original thickness of the unit of stratigraphy deposited at t = 0 when the basin was created. The un-compacted thickness of the first unit deposited is given by:

$$ST_{(x,t1,ts=0)} = B_{(x,t=0)} - P_{ab(x,\,t=0)} \qquad [5.69]$$

where: $B_{(x,t=0)}$ is given by equation [5.37]

The original thickness of any unit deposited after t = 0 is given by:

$$ST_{(x,\,t,ts=t)} = W_{th(x,t)} + W_{i(x,t)} - \left(P_{ab(x,t)} - P_{ab(x,t-1)}\right) \qquad [5.70]$$

where: $W_{i(x,t)}$ is given by equation [5.63]

For each unit it is necessary to work out the thickness if the unit that is made up of solid grains. This remains unchanged with compaction, whilst the thickness of the unit occupied by pore space decreases with increasing compaction. The solid thickness of the unit (*Ts*) is given by:

$$Ts_{(x,ts)} = ST_{(x,t=ts,ts)}\left(1-\phi_s\right) \qquad [5.71]$$

At each time step, each of the units deposited prior to that time step are compacted. This occurs by decreasing the amount of pore space within the unit. The change in pore thickness with compaction is calculated for each unit deposited before the current time step by:

$$Tp_{(x,t,ts)} = \frac{Ts_{(x,ts)}}{\left(1-\phi_y\right)}\phi_y \qquad [5.72]$$

where: $\phi_y$ is given by equation [5.67] or [5.68]

The thicknesses of these units after compaction are given by:

$$ST_{(x,t,ts)} = \left(Ts_{(x,ts)} + Tp_{(x,t,ts)}\right) \qquad [5.73]$$

The amount by which each unit has been compacted is given by:

$$C_{(x,t,ts)} = ST_{(x,t-1,ts)} - ST_{(x,t,ts)} \qquad [5.74]$$

The total amount of compaction at any time step is the sum of the compaction of each unit:

$$Cs_{(x,t)} = \sum_{n=0}^{n=t-1} C_{(x,t,ts=n)} \qquad [5.75]$$

The load generated by sediment infill of the space created by compaction is given by:

$$L_{c(x,t)} = Cs_{(x,t)} \rho_s g \qquad [5.76]$$

The flexural response to this load, $W_{c(x,t)}$, is give by:

$$\frac{d^2}{dx^2} D \frac{d^2 W_{c(x,t)}}{dx^2} + \left[ \left( \rho_m - \rho_i \right) g W_{c(x,t)} \right] = Cs_{(x,t)} \rho_s g \qquad [5.77]$$

This equation is solved for $W_{c(x,t)}$ using the FFT and the data is filtered using the response function given by:

$$Resp_2 = \frac{1}{\left( \rho_m - \rho_i \right) g + D \, x \, Resp_1} \qquad [5.78]$$

where: $Resp_1$ is given by equation [5.27]

The profile of the basin, $B_{(x,t)}$, following compaction is given by:

$$B_{(x,t)} = B_{(x,t)} + W_{c(x,t)} \qquad [5.79]$$

where: $B_{(x,t)}$ is given by equation [5.37]

The thicknesses of the units deposited prior to the current time step are given by equation [5.73]. The thickness of the stratigraphic unit deposited at the current time step has been increased from that calculated in equation [5.70] by the addition of new material as a result of infilling the space generated by compaction and the flexural response to this infill. As such the thickness of the stratigraphy deposited during the current time step, when *ts=t*, is given by:

$$ST_{(x,t,ts=t)} = W_{th(x,t)} + W_{i(x,t)} + Cs_{(x,t)} + W_{c(x,t)} - \left(P_{ab(x,t)} - P_{ab(x,t-1)}\right) \quad [5.80]$$

The solid thickness of the unit, $Ts_{(x,ts)}$, will also have changed as the new sediment material was added and should therefore be calculated again using equation [5.71].

The depth of the Moho profile, $M_{(x,t)}$, is given by:

$$M_{(x,t)} = M_{(x,t)} + W_{c(x,t)} \quad [5.82]$$

where: $M_{(x,t)}$ is given by equation [5.40]

The profile of the fault geometry, $F_{(x,t)}$, is given by:

$$F_{(x,t)} = F_{(x,t)} + W_{c(x,t)} \quad [5.83]$$

where: $F_{(x,t)}$ is given by equation [5.41]

### *5.4.4 Subaerial erosion*

Subaerial erosion has an important influence on extensional sedimentary basin evolution, particularly in the context of footwall uplift which may reach heights of over a kilometer. It is essential, therefore, that erosion should be considered when modelling extensional basin development. Subaerial erosion provides a sediment input and modifies the topography of the eroded area. In addition, erosional unloading generates additional uplift through isostatic adjustments (Enos, 1991; Gilchrist *et al.*, 1994; Champagnac *et al.*, 2009). Footwall uplift, resulting from the flexural response to thinning of the upper crust during lithosphere extension, is

rarely preserved in the geological record. Instead, it is often the case that there is a 'breakup' unconformity between the syn-rift and post-rift deposits. Subaerial erosion and the flexural response to such erosion have been proposed as one of the mechanisms responsible for the development of such an unconformity (Braun and Beaumont, 1989; Egan, 1992; Burov and Poliakov, 2003).

The rate of erosion is dependent upon factors such as the elevation of topography, lithology, climate and vegetation. For example, the erosion of a carbonate terrain is fundamentally different from that of a terrigenous terrain in terms of the erosive material generated and its subsequent deposition. Carbonate material is mostly subject to chemical erosion resulting in dissolution, evidenced by an increase in porosity without initial impact upon topography with no direct production of new material (Purdy, 1974; Bosence and Waltham, 1990). Conversely, terrigenous material is physically removed from the surface, reducing the relief of the topography and this material is potentially re-deposited elsewhere within the system. An empirical relationship between the rate of erosion and the elevation of the topography derived by Ahnert (1970) is given by:

$$d = 0.1515h \qquad [5.83]$$

where: $d$ is the denudation rate in mm/$10^3$yr
$h$ is the height of the uplifted topography

Schumm (1963) gives an average rate of 30-90 mm/$10^3$yr based on evidence collected from the United States. Given the uncertainties surrounding the implementation of differential erosion and the fact that

the factors responsible for erosion are not being investigated as part of this study, the amount of erosion will be defined as a percentage of the topography elevated above the sea-level datum. This results in erosion along the slopes of the uplifted footwall with preferential removal of material where the elevation is greatest, corresponding to observed erosion rates (van der Beek *et al.*, 1995; Burov and Cloetingh, 1997).

Erosion of the topography elevated above the sea-level datum imposes a negative load upon the lithosphere, which results in flexural isostatic uplift. If $Te > 0$ km, the uplift generated will have a wider distribution than that of the eroded topography (Figure 5.13) In the first instance, at time, t = 0 Ma after rifting, the load generated by erosion, $L_{er(x)}$, is calculated by:

$$L_{er(x)} = \left( U_{(x,t=0)} e_r \right) \rho_c g \qquad [5.84]$$

where: $U_{(x,t=0)}$ is the uplift of the basement at time, t = 0 Ma after rifting

$e_r$ is the percentage of erosion

The subsequent flexural response can be calculated by substituting $L_{er(x)}$ into equation [4.62] such that:

$$\frac{d^2}{dx^2} D \frac{d^2 W_{er(x)}}{dx^2} + \left( \rho_m - \rho_{air} \right) g W_{er(x)} = \left( U_{(x,t=0)} e_r \right) \rho_c g \qquad [5.85]$$

This uplifted topography is then further eroded in an iterative process until the amount of uplift generated is negligible. However due to the fact that the newly uplifted topography has a greater wavelength than the

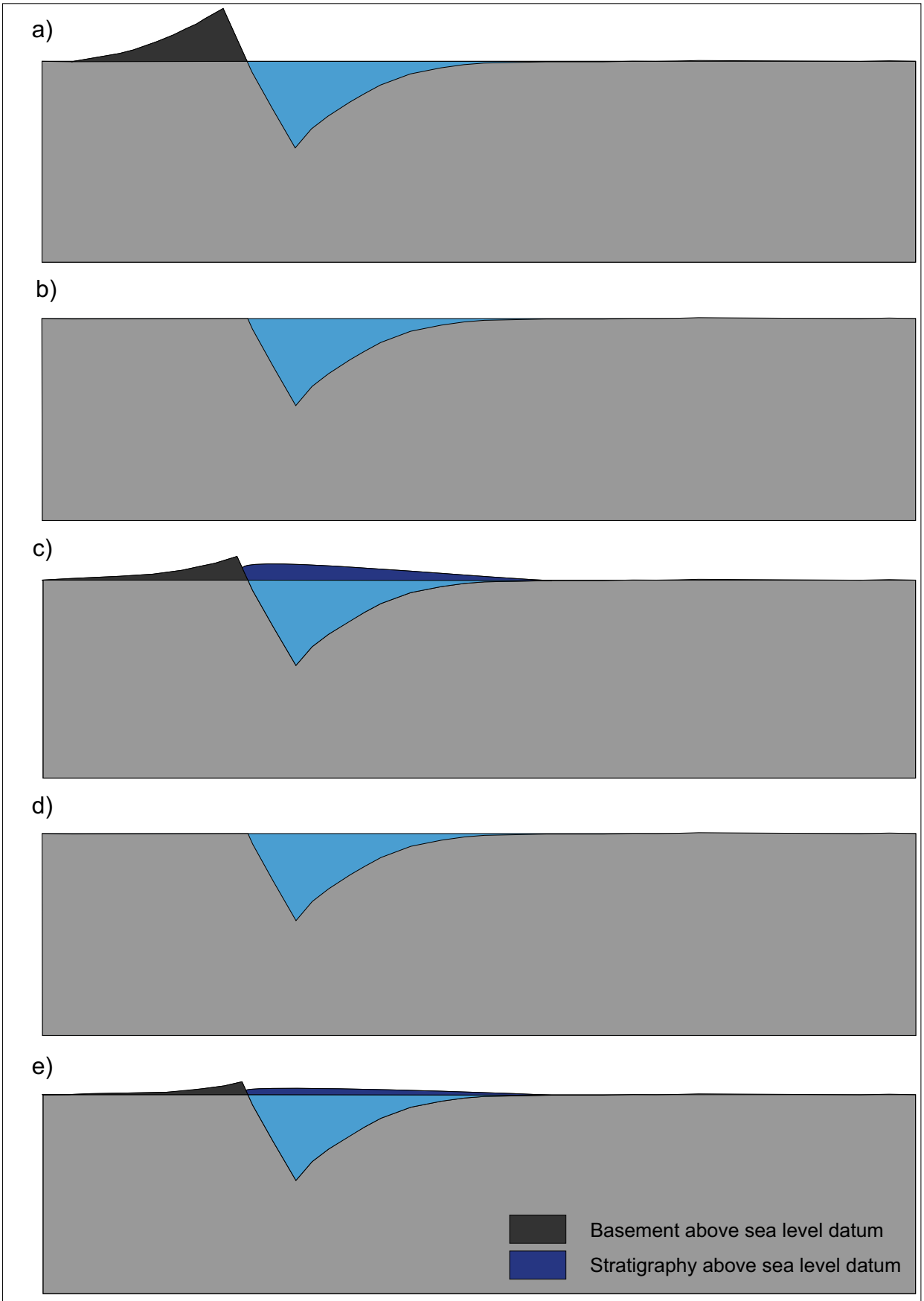


Figure 5.13. The mechanical and isostatic effect of erosion. a) Model showing footwall uplift following lithosphere extension. b) Topography elevated above sea level eroded. c) Erosion of the uplifted topography imposes a negative load upon the lithosphere and results in uplift. The uplift has a wider distribution than the eroded topography and the basin infill is also uplifted. d) Further erosion of the elevated topography. e) Isostatic uplift to compensate for erosional negative loading. The amount of uplift reduces with each subsequent iteration.

original topography, infill material within the basin may also be uplifted above the sea-level datum and subsequently eroded, and therefore should be considered in the loading and flexural response equations [5.86] to [5.88] (Figures 5.13c&e).

If the basin is infilled with water, raising the water above the sea-level datum will cause all of the water to leave the system. As such, the load generated by the iterations of erosion, $L_{er(m,x)}$, will be given by:

$$L_{er(m,x)} = \left(U_{(m,x)}\right)\rho_c g + UB_{(m,x)}\rho_w g \qquad [5.86]$$

where: $m$ is the number of the iteration

$U_{(m,x)}$ is the magnitude of the basement uplifted above the sea-level datum at each iteration

$UB_{(m,x)}$ is the magnitude of the basin infill above the sea-level datum

If the basin is infilled with sediment, the material that has been uplifted above the sea-level datum will be eroded with each iteration. As such, the load generated by the iterations of erosion, $L_{er(m,x)}$, will be given by:

$$L_{er(m,x)} = \left(U_{(m,x)}\right)\rho_c g + \left(UB_{(m,x)}\right)\rho_s g \qquad [5.87]$$

where: $\rho_s$ is the density of the sediment

The flexural response to each iteration of the erosion model, $W_{er(m,x)}$, is given by:

$$\frac{d^2}{dx^2} D \frac{d^2 W_{er(m,x)}}{dx^2} + \left[\left(\rho_m - \rho_{air}\right) g W_{er(m,x)}\right] = L_{er(m,x)} \qquad [5.88]$$

Integrated lithosphere-scale modelling of extensional basin development and the total flexural response to the erosion of the basin, $W_{er(x)}$, is given by:

$$W_{er(x)} = \sum_{m=0}^{m=n} W_{er(m,x)} \quad [5.89]$$

The total amount of erosion of the basement, $e_r B_{(x)}$, is calculated by:

$$e_r B_{(x)} = \sum_{m=0}^{m=n} U_{(m,x)} \quad [5.90]$$

The basement topography is given by:

$$B_{(x,t)} = B_{(x,t)} + W_{er(x)} - e_r B_{(x)} \quad [5.91]$$

The depth of the Moho profile, $M_{(x,t)}$, is given by:

$$M_{(x,t)} = M_{(x,t)} + W_{er(x)} \quad [5.92]$$

The geometry of the fault profile is given by:

$$F_{(x,t)} = F_{(x,t)} + W_{er(x)} - e_r F_{(x,t)} \quad [5.93]$$

where: $e_r F_{(x,t)}$ is the erosion of the fault surface and is equal to $e_r B_{(x)}$

## 5.5 An integrated tectonic, thermal, isostatic and stratigraphic model of lithosphere extension

Figure 5.14 summarises the sequential operations involved in modelling the structure and stratigraphy resulting from lithosphere extension as detailed below:

1. **Initial structural deformation due to rifting** – extension of the upper crust by faulting causes thinning of the crust. Algorithms have been

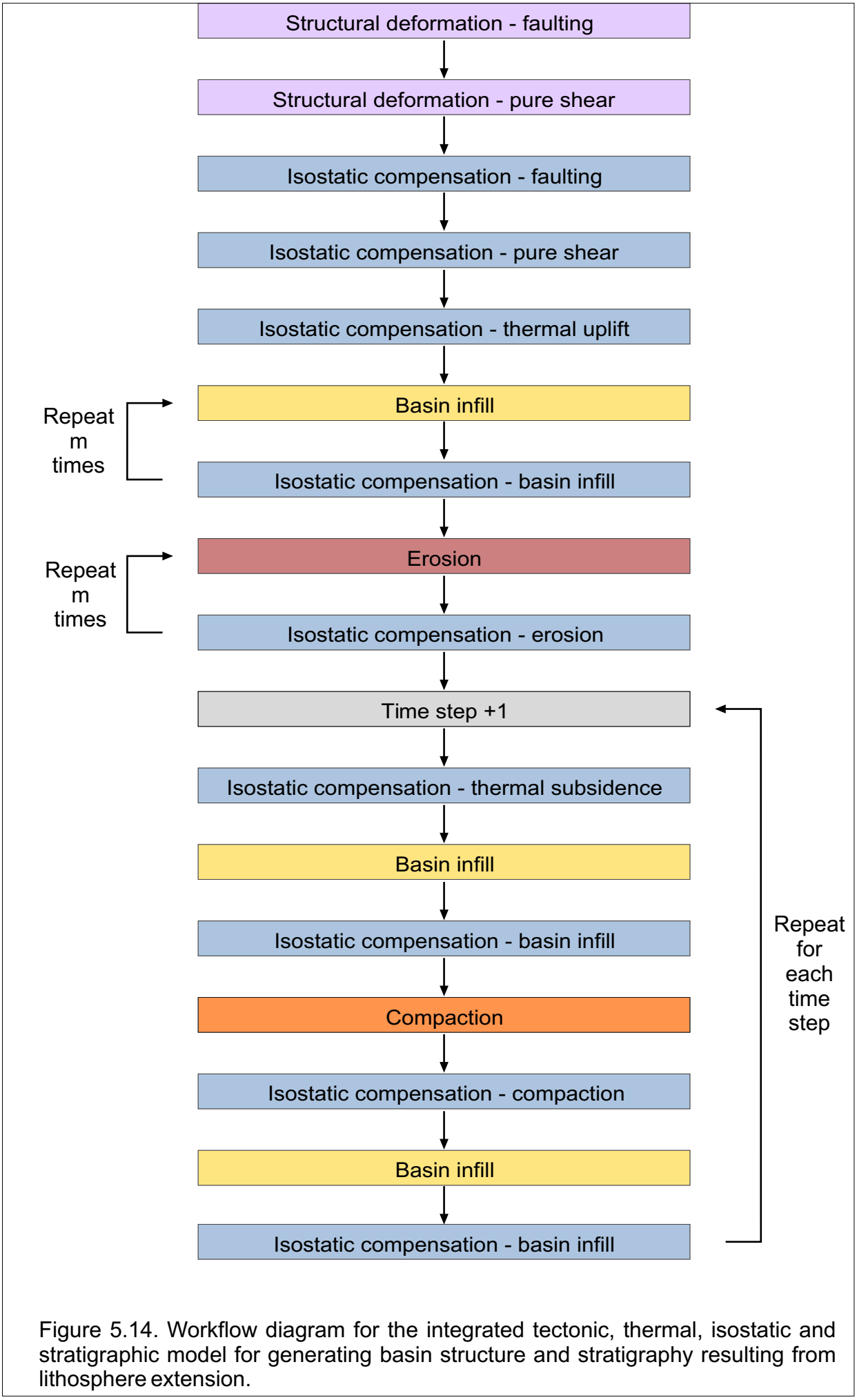


Figure 5.14. Workflow diagram for the integrated tectonic, thermal, isostatic and stratigraphic model for generating basin structure and stratigraphy resulting from lithosphere extension.

developed to model multiple faults, including the modification of footwall and hanging wall geometries to account for deformation along previous faults.

2. **Initial structural deformation due to rifting** – extension by pure shear causes thinning of the lower crust and mantle lithosphere. The magnitude of extension by pure shear can be the equivalent to or independent of the magnitude of extension by faulting in order to simulate uniform and non-uniform lithosphere extension scenarios.

3. **Isostatic compensation** – the extension of the crust by faulting negative loading of the lithosphere and results in uplift.

4. **Isostatic compensation** – thinning of the lower crust by pure shear results in positive loading of the lithosphere and generates subsidence.

5. **Isostatic compensation** –perturbations of the lithosphere temperature field raises the geotherm which represents a buoyancy load and produces isostatic uplift.

6. **Basin infill** – initial accommodation space can be infilled with water or sediment, or a combination of the two if palaeobathymetry is considered.

7. **Isostatic compensation** – loading of the lithosphere as a result of infilling the basin generates subsidence.

8. **Basin infill** – the additional subsidence generated by the isostatic response to the initial basin fill is then infilled with water or sediment.

9. **Isostatic compensation** – loading of the lithosphere as a result of the additional basin infill generates subsidence. Steps 8 and 9 are repeated a number of times until the amount of additional space generated by the isostatic compensation is negligible.

10. **Erosion** – A selected percentage of material which is raised above the sea level datum can be eroded.

11. **Isostatic compensation** – the lithosphere responds to compensate for the mass of the material that has been removed due to erosion, generating uplift. This raises additional material above the sea level datum. Steps 10 and 11 are repeated in a series of iterative steps until the amount of uplift produced is negligible.

12. **Next model time-step**

13. **Isostatic compensation** – thermal re-equilibration of the geotherm generates subsidence.

14. **Basin infill** – the additional space generated by the thermally induced subsidence is infilled. As in step 6, if the accommodation space is infilled with sediment, palaeobathymetry can be considered.

15. **Isostatic compensation** – the basin infill initiates further subsidence in response to the positive loading of the lithosphere.

16. **Compaction** – compaction of stratigraphic layers beneath the top sequence can be calculated, as required. This generates additional accommodation space within the basin.

17. **Basin infill** – the accommodation space generated by compaction of the underlying sediments is infilled.

18. **Isostatic compensation** – the additional loading resulting from infilling of the accommodation space created by compaction is isostatically compensated, producing subsidence.

19. **Next model time-step** – processes 13 – 18 are repeated for each additional time-step.

# 6 Two-dimensional modelling of the Northumberland Trough Region

The Northumberland Trough Region is an extensional basin system with a complex subsidence-uplift history. The aim of this investigation is to utilise the modelling approach outlined in chapters 4 and 5 to examine the mechanisms responsible for the structural and stratigraphic evolution of the Northumberland Trough Region.

## 6.1 Burial History Modelling

Burial history analysis has been used to quantify the amount of 'tectonic' and sediment load generated subsidence. In addition decompaction of the sediments is used to establish the thickness of sediments at deposition. These data, in addition to the subsurface data analysed in chapter 3 provide a point of comparison for the model results. The methodology used to produce burial history models for this project is well established and has been included in appendix D, in addition to annotated numerical results.

### *6.1.1 One-dimensional burial history modelling from borehole data*

The data from a number of deep boreholes are available within the Northumberland Trough Region. The boreholes that have been used as part of this study are detailed in section 3.1.2. A number of these deep boreholes penetrate a significant amount of the Carboniferous sequence within the Northumberland and Stainmore Troughs as well as the Alston

Block. The burial history modeling approach described above has been applied to these boreholes to ascertain the amount of tectonic subsidence that occurred during initial basin development.

#### 6.1.1.1 Seal Sands borehole

The Seal Sands borehole is situated on the east coast of Northern England, within the Stainmore Trough (Figure 3.2). It provides a near complete section through the Carboniferous to Triassic age strata within the basin.

The amount of strata deposited and eroded between the end of the Triassic and the end of the Miocene eras is not known. Estimates of erosion within Northern England range between 1 km and 3 km (Green, 2002) and the effect of erosion between these values is investigated. Figure 6.1 illustrates the burial history for the Seal Sands dataset with zero erosion of the Triassic to present day strata, 1 km, 2 km and 3 km erosion. Figure 6.1a exhibits the decompacted subsidence history for each unit. With increasing erosion, greater compaction of the sediments occurs as they are buried more deeply and their porosity decreases according to equation 4.50. Figure 6.1b shows the tectonic subsidence corrected for sediment loading using a flexural isostasy approach and the total subsidence of the basement for the Seal Sands dataset with increasing erosion. The palaeobathymetry was estimated from the lithology deposited within each unit. The palaeoeustatic sea level is based on the sea level curves of Haq *et al.* (1988) and Haq and Schutter, (2008). The burial history model for the Seal Sands dataset indicates that the syn-rift phase

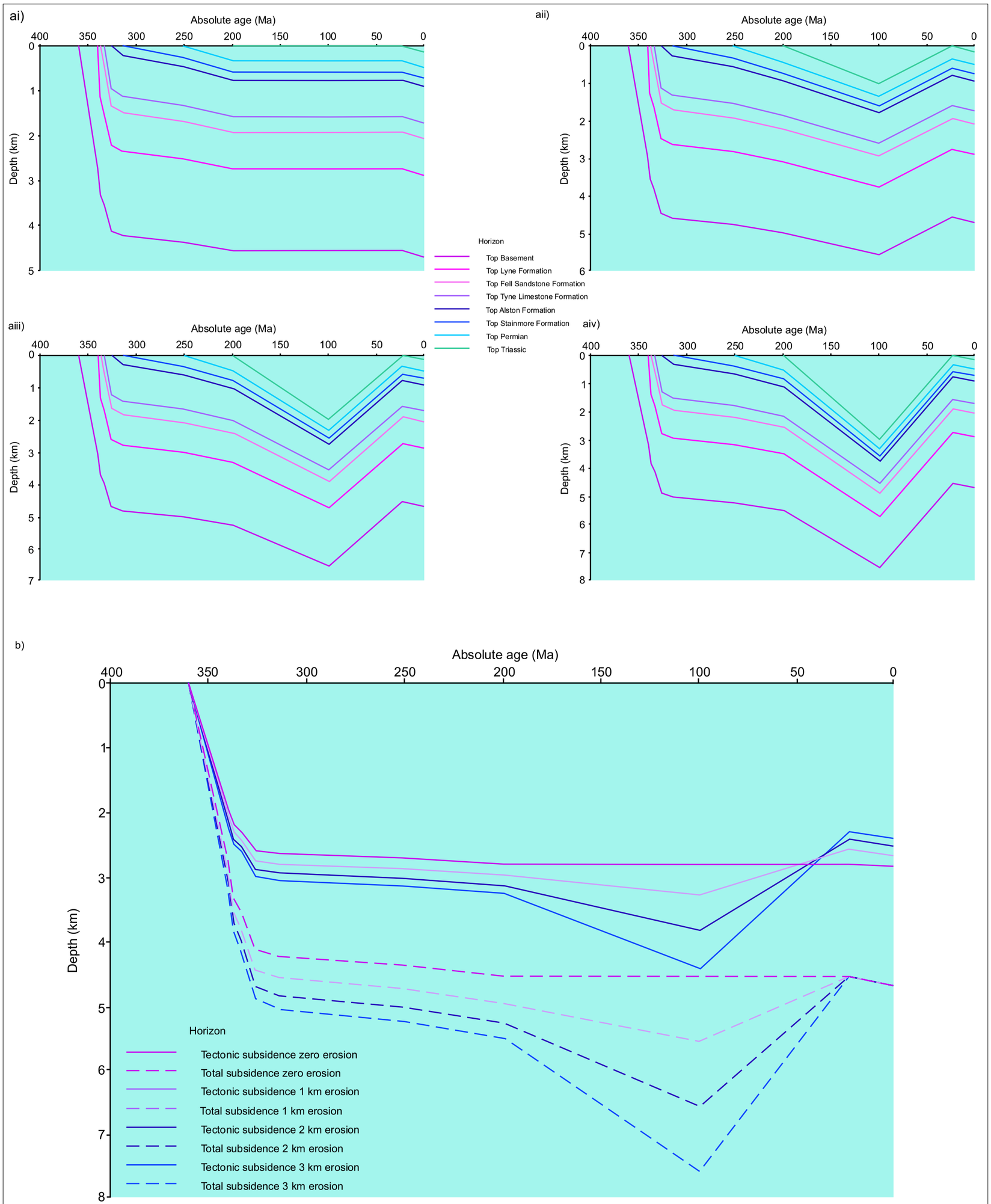


Figure 6.1. The burial history for the Seal Sands dataset with zero, 1 km, 2 km and 3 km erosion. a) Decompacted subsidence history for each unit. ai) Zero erosion. aii) 1 km erosion. aiii) 2 km erosion. aiv) 3km erosion. With increasing erosion, greater compaction of the sediments occurs as they are buried more deeply and their porosities decrease. b) Tectonic subsidence corrected for sediment loading, palaeobathymetry and palaeoeustacy and the total subsidence of the basement with increasing erosion.

of tectonic subsidence continues from 360 Ma to 326 Ma within the Stainmore Trough. This is consistent with evidence of growth sequences within the Tyne Limestone and Alston formations as well as the Fell Sandstone and Lyne formations observed within the cross-sections of the Stainmore Trough (Figures 3.16 and 3.20). The model predicts between 1.9 km and 2.2 km of tectonic subsidence between 360 Ma and 340 Ma with a further 650-800 m between 340 Ma and 326 Ma. The amount of tectonic subsidence generated between 360 and 326 Ma, during the syn-rift phase of the Carboniferous deposition is greater with increasing erosion. In addition, more extension occurs during the Jurassic subsequently followed by renewed uplift. The precise timing and rate of the tectonic subsidence that results in the deposition of the eroded strata, and the uplift that is responsible for the erosion of this strata is unknown and can only be broadly estimated from evidence from surrounding areas as there is no strata present that can be dated.

#### 6.1.1.2 Longhorsley 1 borehole

The Longhorsley 1 well is situated within the Northumberland Trough (Figure 3.2) and penetrates the Stainmore, Alston, Tyne Limestone and the Fell Sandstone formations as well as part of the Lyne Formation. The Whin Sill has intruded at two levels, within the Tyne Limestone and Alston formations.

Figure 6.2 illustrates the burial history of the Longhorsley 1 strata with varying erosion. Figure 6.2a shows the decompacted subsidence history for each unit with zero, 1 km, 2 km and 3 km erosion of the Permian to

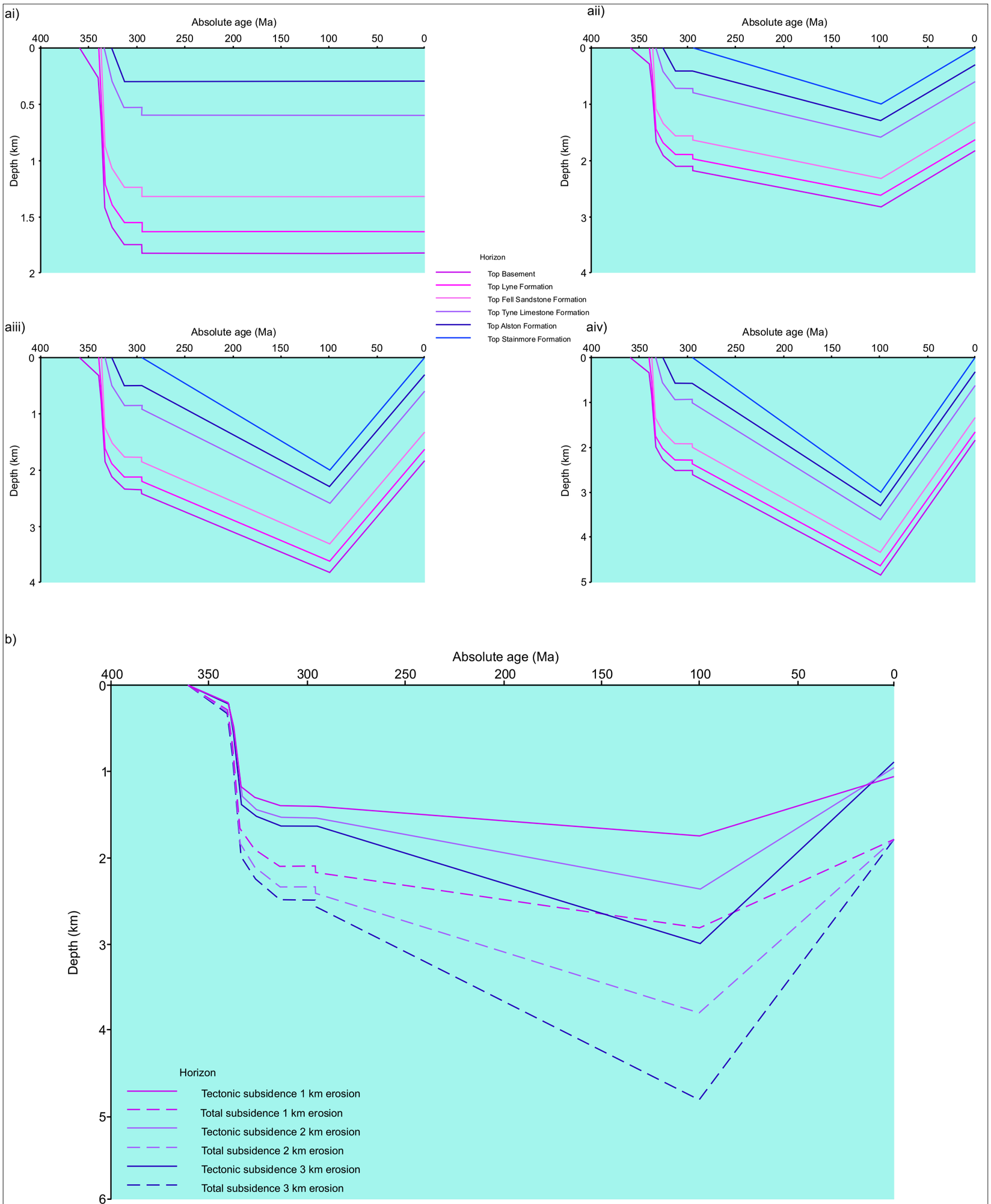


Figure 6.2. Burial history modelling based on the Longhorsley 1 dataset with zero, 1 km, 2 km and 3 km erosion. a) the decompacted subsidence history for each unit. ai) Zero erosion. aii) 1 km erosion. aiii) 2 km erosion. aiv) 3km erosion. With increasing erosion, greater compaction of the sediments occurs as they are buried more deeply and their porosities decrease. b) Tectonic subsidence corrected for sediment loading, palaeobathymetry and palaeoeustacy and the total subsidence of the basement with increasing erosion.

Pleistocene sediments. With increasing erosion, the original the original thickness of the units increases. The increase in compaction within the formations beneath the top Alston Formation horizon that occurs at 295 Ma is a result of the intrusion of the Whin Sill within the Alston and Tyne Limestone formations. The Alston Formation compacts by 0.058 km, while the Tyne Limestone Formation compacts by 0.066 km.

Figure 6.2b illustrates the tectonic subsidence calculated by assuming a flexural isostatic approach with an elastic thickness of 5 km with 1 km, 2 km and 3 km erosion of Permian to Pleistocene sediments. The initial phase of extension between 360 Ma and 340 Ma within this model predicts only 0.23 km of extension. This is interpreted as being a result of the borehole not penetrating far enough into the Lyne Formation and, therefore, not representing the full extent of the sediments that were deposited between 360 Ma and 340 Ma. The second phase of extension between 340 Ma and 333 Ma gives between 1.4 and 1.7 km of total subsidence of which, between 1 and 1.2 km is modelled as being a result of tectonic subsidence. With increasing erosion, there is an increase in the amount of subsidence generated.

#### 6.1.1.3 Errington 1 borehole

The Errington 1 borehole is situated within the Northumberland Trough and penetrates from the Alston Formation at the top through to the Lyne Formation at its base. The Whin Sill intrudes within the Tyne Limestone Formation. The results of decompaction modelling within the Errington 1 borehole are illustrated in Figure 6.3a. 1 km of sediments have been

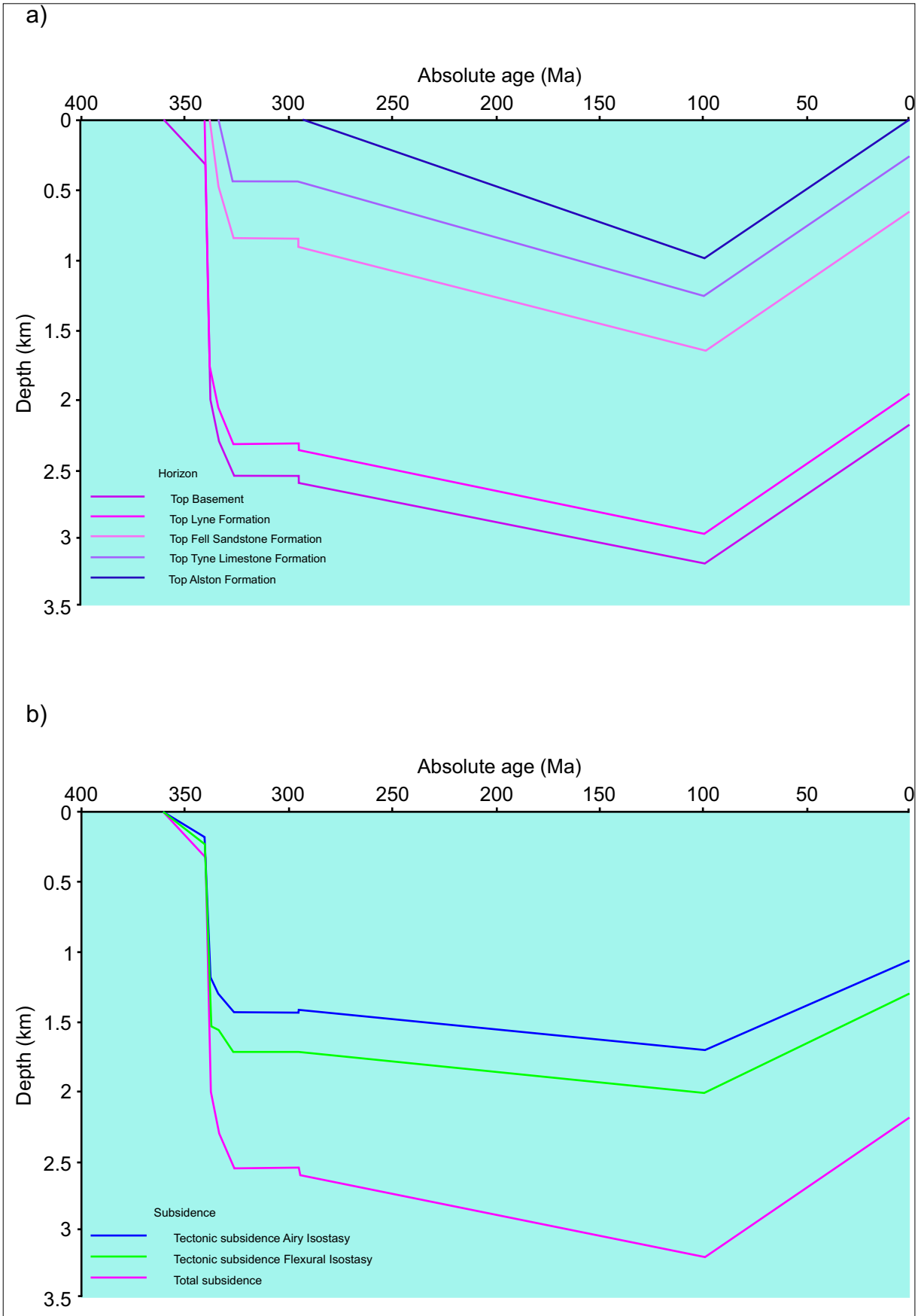


Figure 6.3. The burial history for the Errington 1 borehole dataset with 2 km erosion. a) Decompacted subsidence history for each unit. b) Tectonic subsidence corrected for sediment loading, palaeobathymetry and palaeoeustacy and the total subsidence of the basement.

assumed as being deposited and eroded within the model between the beginning of the Permian period and the present day. The exact timing of the extension, deposition, uplift and erosion are unknown, but the amount of erosion is consistent with the latest estimates of 0.7 to 1.5 km (Green, 2002). There is an increase in compaction resulting from the intrusion of the Whin Sill affecting the sediments within the Lyne and Fell Sandstone formations. Figure 6.3b presents the total subsidence and the tectonic subsidence generated using both the Airy and flexural isostatic methods for the sedimentary loading correction. The amount of tectonic subsidence generated by the flexural isostasy method is greater than that generated by the Airy isostasy method by up to 0.29 km. This is a result of the sedimentary load within the borehole being supported away from the position of the borehole. As such, a greater amount of tectonic subsidence is required to be filled and loaded with sediment to generate the same overall subsidence as when the Airy isostasy approach is used. As with the Longhorsley 1 borehole, the Errington 1 borehole does not penetrate the full extent of the Lyne Formation within the area. The amount of extension modelled between 360 Ma and 340 Ma as a result of this is 0.18 to 0.23 km, a small proportion of the expected extension. Between 340 Ma and 337 Ma there is a second phase of extension with 1.17 km of extension predicted using the flexural isostasy approach and 1.01 km predicted using the Airy isostasy approach.

### *6.1.2 Two-dimensional burial history modelling from cross-section data*

Pseudo two-dimensional burial history models are produced by carrying out one-dimensional decompaction and burial history models at regular intervals, every 1 km, along the cross-section. This modelling has been carried out for every cross-section. The results from cross-sections B-B', G-G' and I-I' (Figure 3.4) are presented here.

#### 6.1.2.1 Cross-section B-B'

This cross-section (Figure 3.6) crosses the Solway Basin from north-west to south-east. It also crosses the Vale of Eden Basin from north-north-west to south-south-east then from north-east to south west. Figure 6.4 illustrates the compaction history of the cross-section based on decompaction modelling. In order to look more closely at the burial history within the Solway Basin, the results from horizontal position x = 22 km, where the lower deposits of the Lyne Formation (Lower Border Group Lower) have a maximum thickness of 4.5 km at 345 Ma. These sediments are the earliest deposits modelled within the cross-section and have a present day thickness of 2.7 km, a decrease of 41%. The burial history data for position x = 22 km is presented in appendix D. The decompaction history of the deposits at this location, situated within the hanging wall of the Maryport Fault, with 1 km erosion shows the greatest amount of compaction occurring within the Lyne Formation between 360 Ma and 340 Ma. The amount of tectonic subsidence between 360 Ma and 340 Ma, is between 2.85 and 3.2 km tectonic subsidence, after which the tectonic subsidence represents the post-rift thermal subsidence phase.

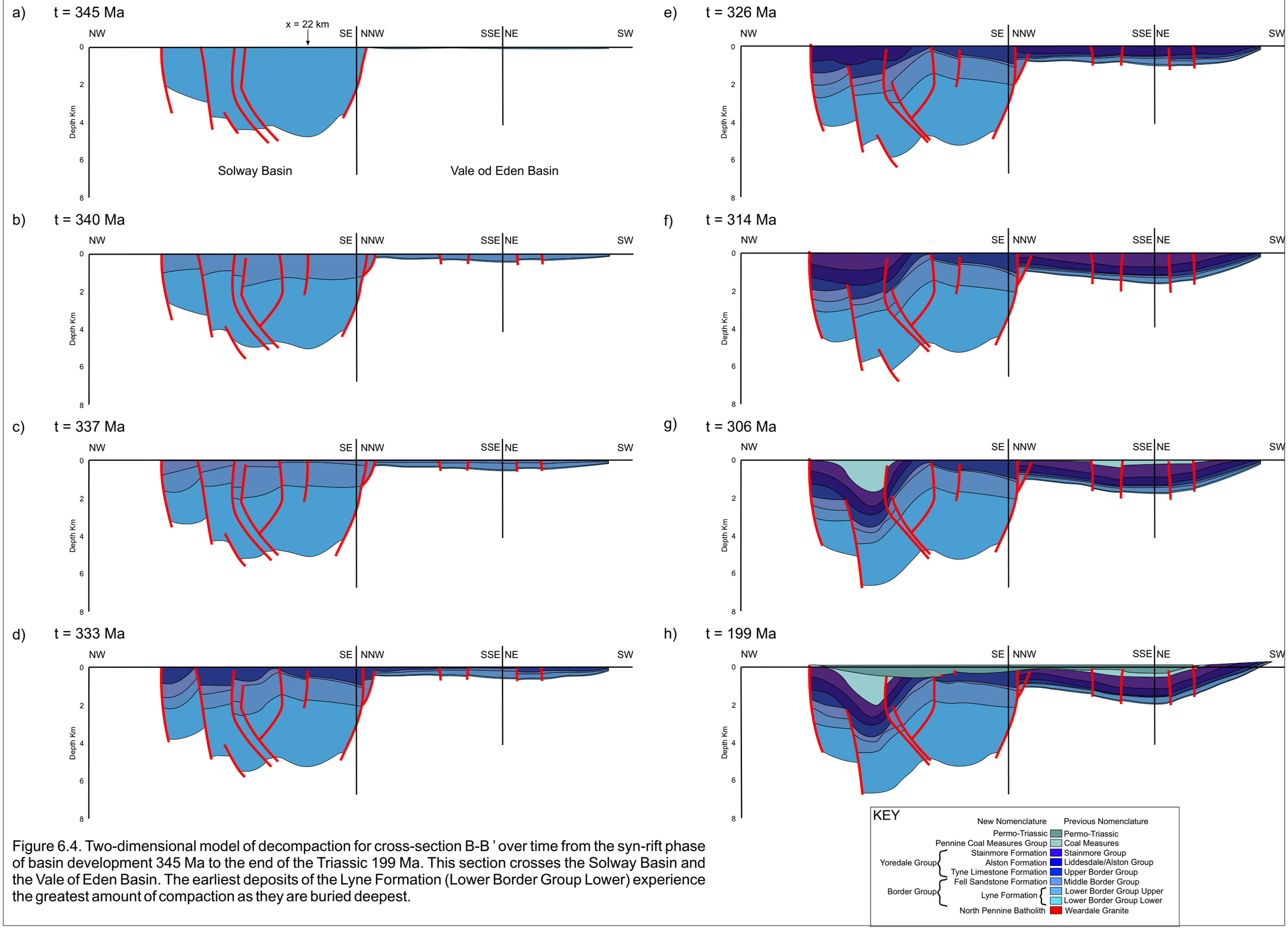


Figure 6.4. Two-dimensional model of decompaction for cross-section B-B ' over time from the syn-rift phase of basin development 345 Ma to the end of the Triassic 199 Ma. This section crosses the Solway Basin and the Vale of Eden Basin. The earliest deposits of the Lyne Formation (Lower Border Group Lower) experience the greatest amount of compaction as they are buried deepest.

#### 6.1.2.2 Cross-section G-G'

Cross-section G-G' (Figure 3.12) crosses the Northumberland Trough, the Alston Block and the northern section of the Stainmore Trough. Figure 6.5 presents the compaction history of the cross-section based on decompaction modelling between 345 Ma and 314 Ma. The syn-rift deposits, represented by the Lyne Formation have a maximum thickness of 3.17 km at 340 Ma, at x = 42 km in the hanging wall of the Stublick Fault. This unit decreases in thickness to 2.03 km at the present day, a decrease of 35.8%. The tectonic subsidence gives the amount of subsidence directly related to the extensional event between 360 Ma and 340 Ma of 2.24 km (flexural isostatic method), a rate of 0.11 $kmMa^{-1}$. This decreases to 0.04 $kmMa^{-1}$ between 340 Ma and 326 Ma, where thermal subsidence takes over as the dominant mechanism driving subsidence.

#### 6.1.2.3 Cross-section I-I'

This cross-section (Figure 3.14) crosses the Northumberland Trough, the Alston Block and the northern section of the Stainmore Trough near the east coast of Northern England. Figure 6.6 illustrates the compaction history of the cross-section. In this section, fault related subsidence occurred between 360 Ma and 326 Ma, with the greatest amount of deposition and compaction closest to the faults. Between 326 Ma and 306 Ma regional, thermal subsidence becomes the dominant mechanism of 'tectonic' subsidence with deposition at this time greatest over the Alston Block. At x = 42 km, located within the hanging wall of the Ninety Fathom Fault, the Lyne Formation is compacted by the greatest amount,

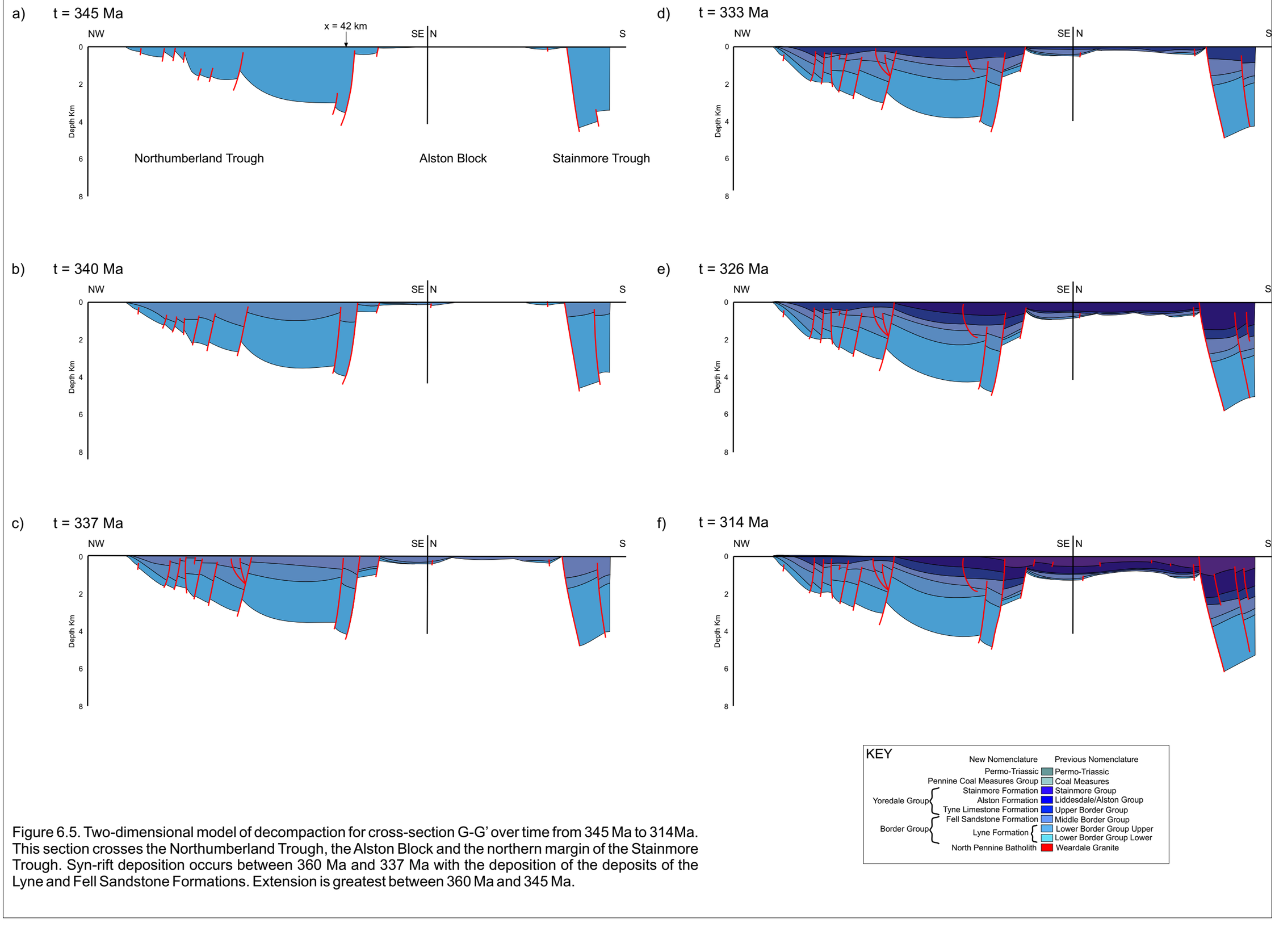


Figure 6.5. Two-dimensional model of decompaction for cross-section G-G' over time from 345 Ma to 314Ma. This section crosses the Northumberland Trough, the Alston Block and the northern margin of the Stainmore Trough. Syn-rift deposition occurs between 360 Ma and 337 Ma with the deposition of the deposits of the Lyne and Fell Sandstone Formations. Extension is greatest between 360 Ma and 345 Ma.

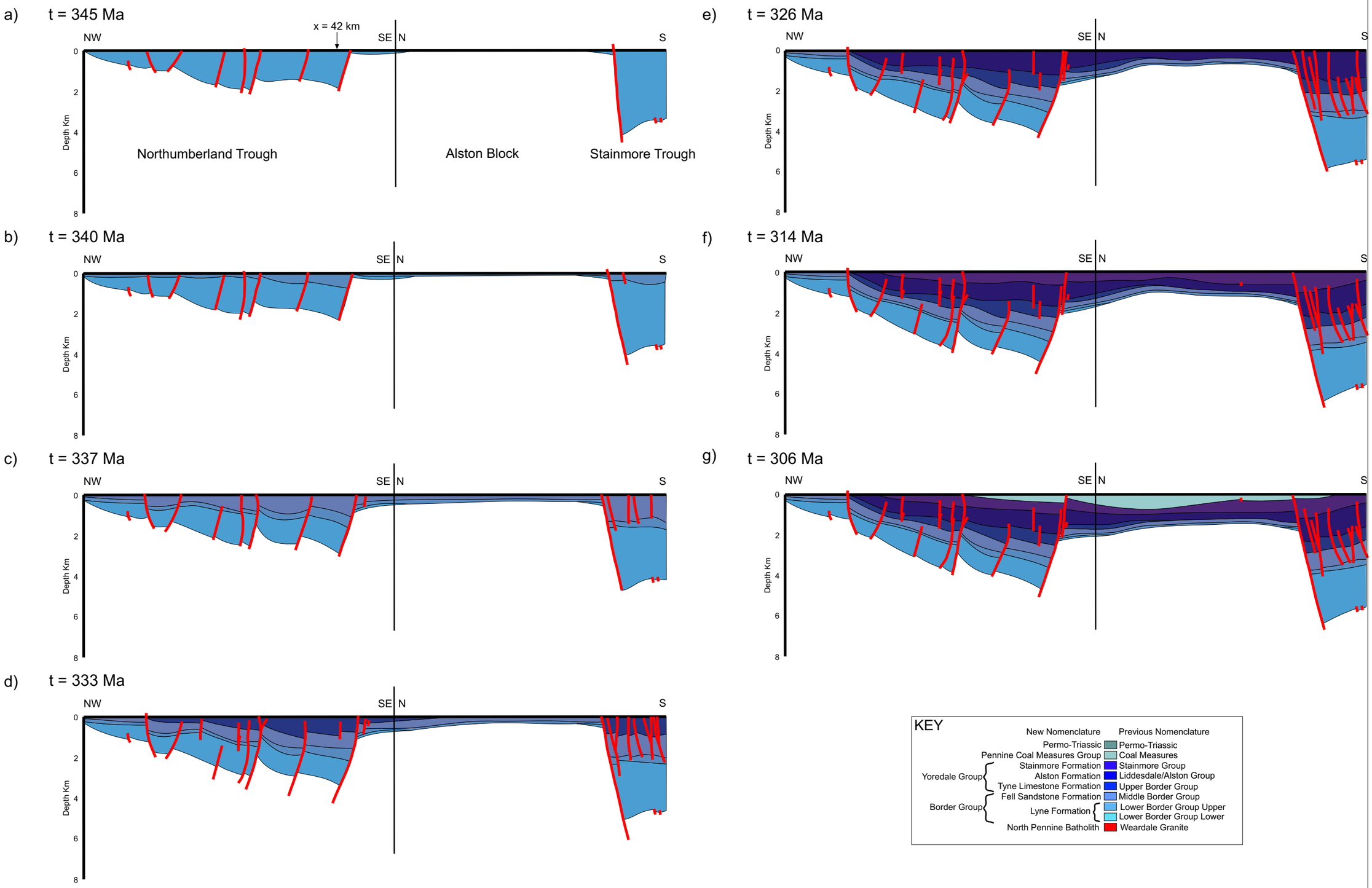


Figure 6.6. Two-dimensional model of decompaction for cross-section I-I' over time from 345 Ma to 306 Ma. This section crosses the Northumberland Trough, the Alston Block and the northern margin of the Stainmore Trough. Fault related subsidence occurred between 360 Ma and 326 Ma, with the greatest amount of deposition and compaction closest to the faults.

decreasing in thickness from 1.9 km to 1.15 km, a 40% decrease. There is an initial phase of extension-related subsidence between 360 Ma and 340 Ma of 1.35 km, followed by a second phase of extension related subsidence between 340 Ma and 326 Ma of 1.27 km. This is followed by thermal subsidence between 326 Ma and 306 Ma.

## 6.2 Integrated modelling

The integrated tectonic, thermal, isostatic and stratigraphic modelling approach developed in chapter 5 has been applied to the Northumberland Trough Region in order to investigate its structural and stratigraphical evolution. The models generated using the integrated modelling approach adopt the same pre-extensional lithosphere conditions as simulated in chapters 4 and 5, and demonstrated in Figure 6.7. An initial crustal thickness of 35 km and a lithosphere thickness of 125 km are assumed. The temperature at the base of the lithosphere is modelled as 1333°C accompanied by a co-efficient of thermal expansion of $3.28 \times 10^{-5}$ $K^{-1}$. The density of the crust and mantle are assumed to have average values of 2800 $kgm^{-3}$ and 3300 $kgm^{-3}$, respectively. Any accommodation space created in the basin is assumed to have been infilled with sediment of bulk density 2500 $kgm^{-3}$. The surface porosity of the sediment is assumed to be 49% and the porosity at depth is calculated with a compaction co-efficient of 0.27. There is no reliable dataset from which to make a precise estimate of palaeobathymetry; however, an interpretation of the sedimentology of the deposits within the Northumberland Trough Region suggests a shallow water depth of between 0.1 km and 0 km (Wells *et al.*, 2005).

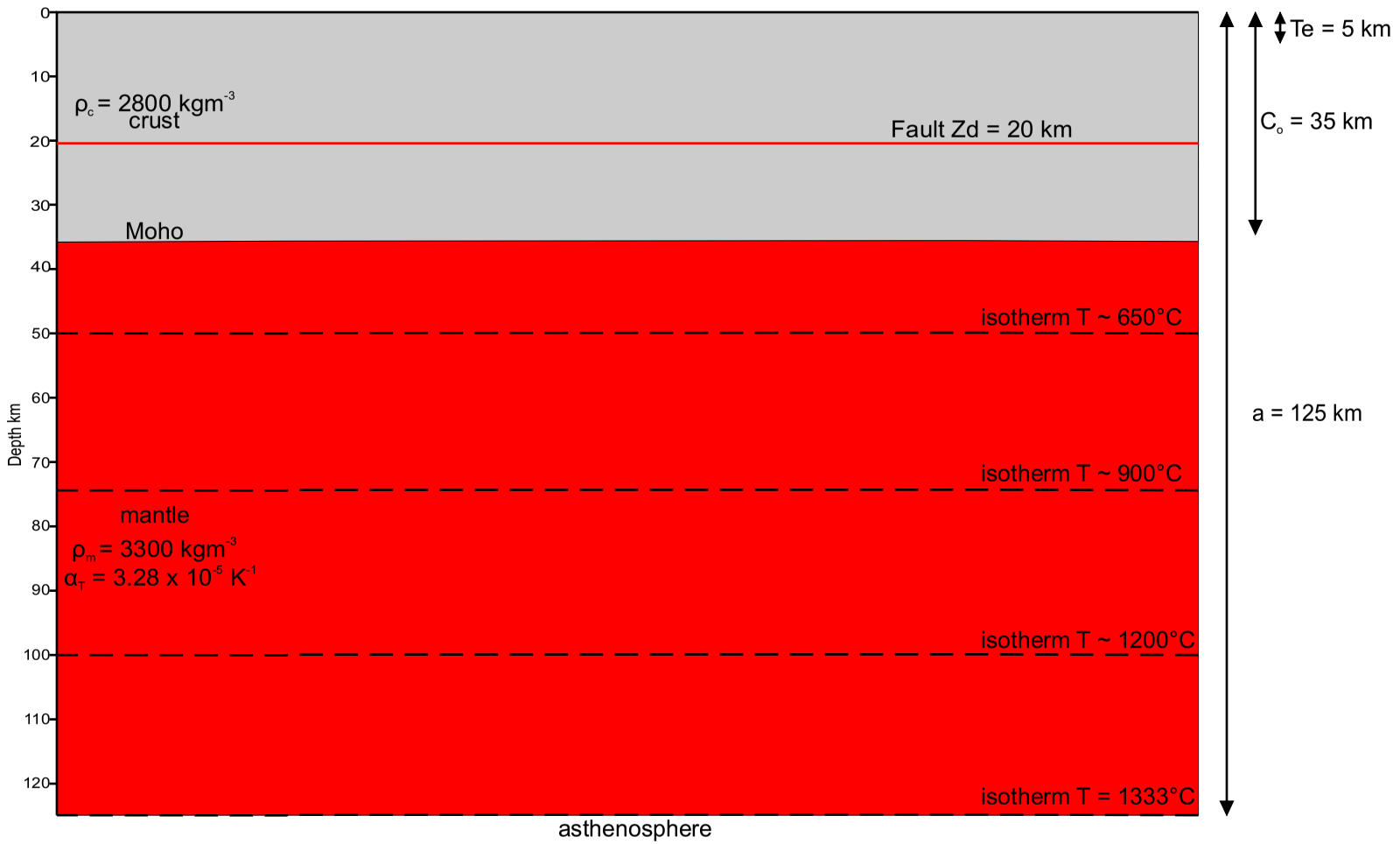


Figure 6.7. Parameters for the calculation of integrated model with flexural isostatic compensation, Model shown pre-extension. Extension of the upper crust above detachment depth, Zd occurs by faulting and is balanced by pure shear of the lower crust, which raises the lithosphere/asthenosphere boundary and perturbs the geotherm. Accommodation space created in the basin is assumed to have been filled with sediment of density $\rho_s = 2500$ kgm$^{-3}$. The effect of flexural isostasy on basin evolution is controlled by the flexural rigidity of the lithosphere, which is determined by its effective elastic thickness. The density of the mantle, $\rho_m$, and the density of the crust, $\rho_c$, also affect the flexural response.

Models have been generated in the context of both uniform and non-uniform lithosphere extension, with a detachment within the crust between the extension by faulting and the extension by pure shear occurring at a depth of 20 km based on interpretation of seismic data. The effective elastic thickness of the lithosphere, which controls the wavelength of the flexural isostatic response to loading is assumed to be 5 km during and following extension.

### *6.2.1 Cross-section I-I'*

Cross-section I-I' (Figure 3.14) crosses the Northumberland Trough, Alston Block and Stainmore Trough to the east. Figure 6.8 illustrates a uniform lithosphere extension model of cross-section I-I' at t = 0 Ma after extension and t = 360 Ma after extension. At t = 0 Ma after extension (Figure 6.8a), the maximum subsidence generated within the Northumberland Trough is 2.4 km. This is 0.5 km greater than predicted by the burial history modelling following the first phase of extension. 3.2 km of subsidence is generated within the Stainmore Trough, 0.9 km less than generated within the burial history model. At t = 360 Ma after extension (Figure 6.8b), the model generates 4 km of subsidence within the Northumberland Trough and 5.1 km of subsidence within the Stainmore Trough. This is 0.6 km and 1.2 km less than observed within the cross-section, respectively. The model predicts 13-19% less subsidence within the basins than is observed within the cross-section.

Carboniferous extension in Northern England is attributed to the slabpull force generated by subduction to the south where closure of the mid-

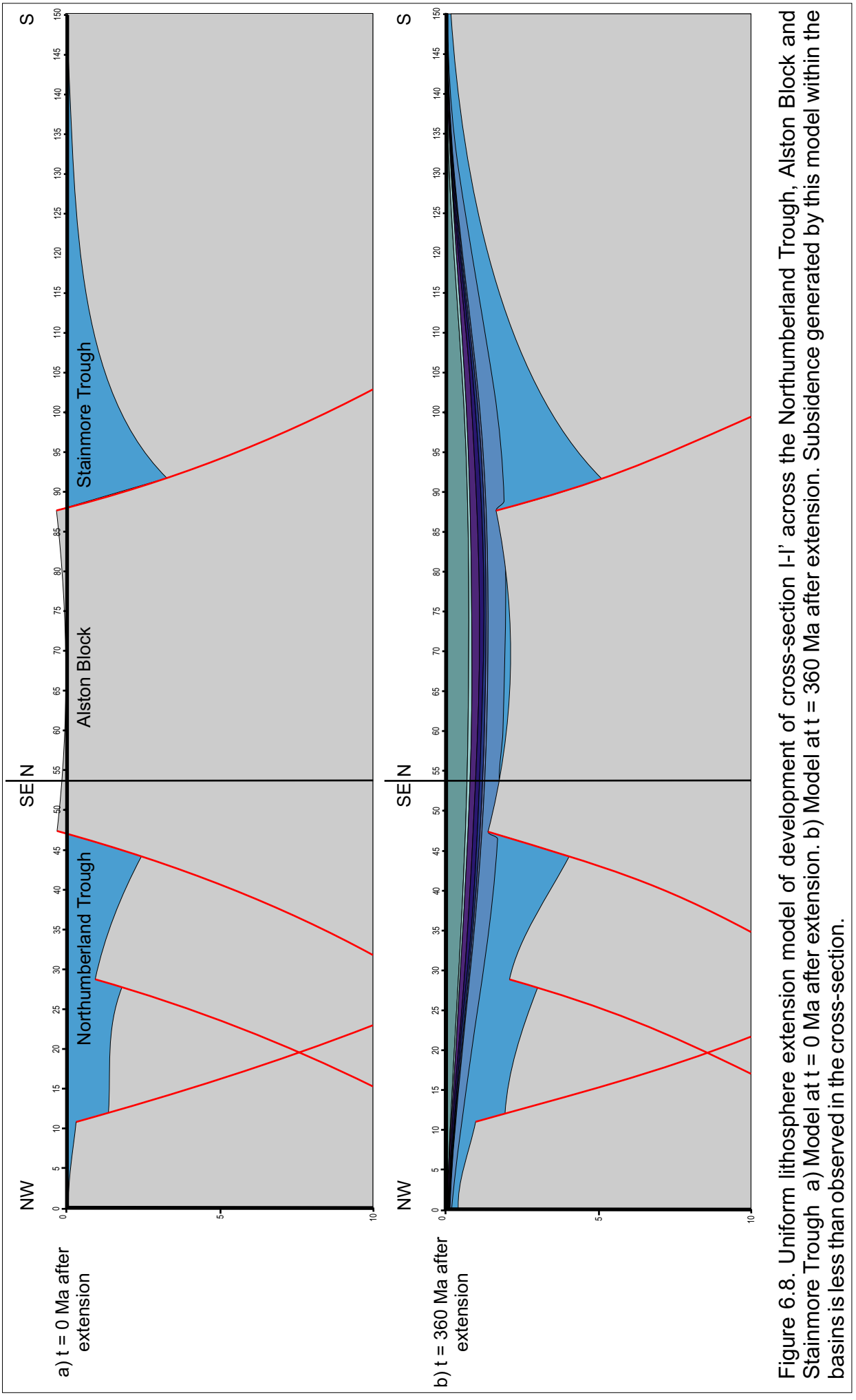


Figure 6.8. Uniform lithosphere extension model of development of cross-section I-I' across the Northumberland Trough, Alston Block and Stainmore Trough a) Model at t = 0 Ma after extension. b) Model at t = 360 Ma after extension. Subsidence generated by this model within the basins is less than observed in the cross-section.

European marginal sea was occurring (Bott, 1976; Leeder, 1976; Johnson, 1981). Bott *et al.* (1984) proposed a non-uniform lithosphere extension mechanism for the development of the Northumberland Trough Region, with the lower crust and mantle lithosphere undergoing greater stretching as a result of pure shear than faulting in the upper crust. Non-uniform extension of the lithosphere creates mass balance problems within the lithosphere. These can be avoided providing that subduction of the upper crust occurs more slowly than the ductile lower lithosphere (Bott *et al.*, 1984). Figure 6.9 illustrates a non-uniform lithosphere extension model of cross-section I-I' at t = 0 Ma and t = 360 Ma after extension. The lower crust is extended by 140% of the extension in the upper crust. At t = 360 Ma after extension (Figure 6.9), the non-uniform lithosphere extension model generates 4.7 km of subsidence in the Northumberland Trough and 5.9 km subsidence within the Stainmore Trough. The subsidence produced by the model is within 2-6% of that observed within the cross-section. This implies that the Northumberland Trough Region may have been subject to non-uniform lithosphere extension during its development.

### *6.2.2 Cross-section G-G'*

Figure 6.10 illustrates the model based on parameters from cross-section G-G' (Figure 3.12) at time, t = 0 Ma after extension, with extension by pure shear 133% greater than extension by faulting. This model chosen demonstrates the stages of basin evolution that have been modelled across the centre of the Northumberland Trough, Alston Block and Stainmore

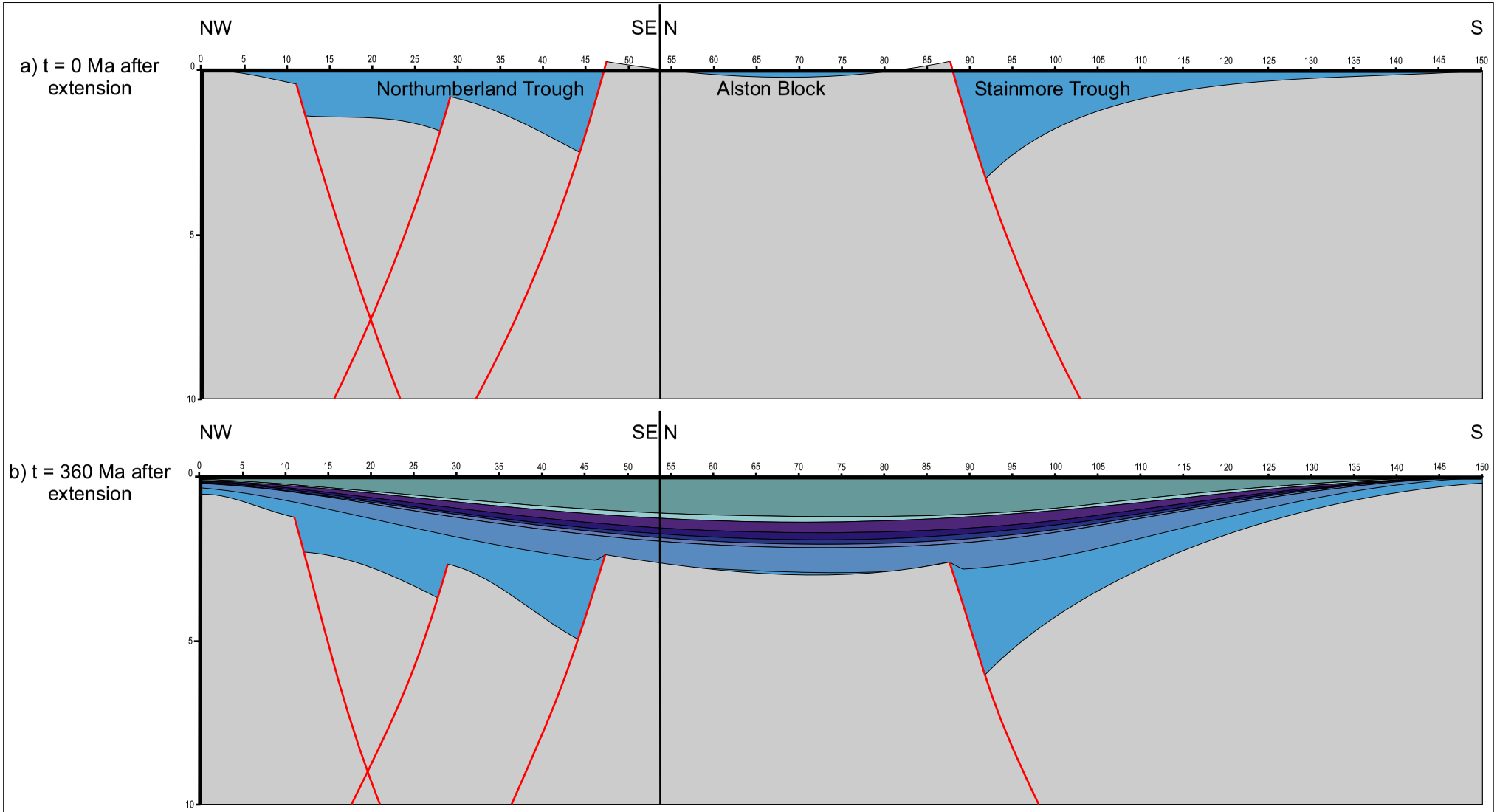


Figure 6.9. Non-uniform lithosphere extension model of development of cross-section I-I' across the Northumberland Trough, Alston Block and Stainmore Trough a) Model at t = 0 Ma after extension. b) Model at t = 360 Ma after extension. Non-uniform lithosphere extension generates greater subsidence than uniform lithosphere extension that is more compatible with the observed values within the basin.

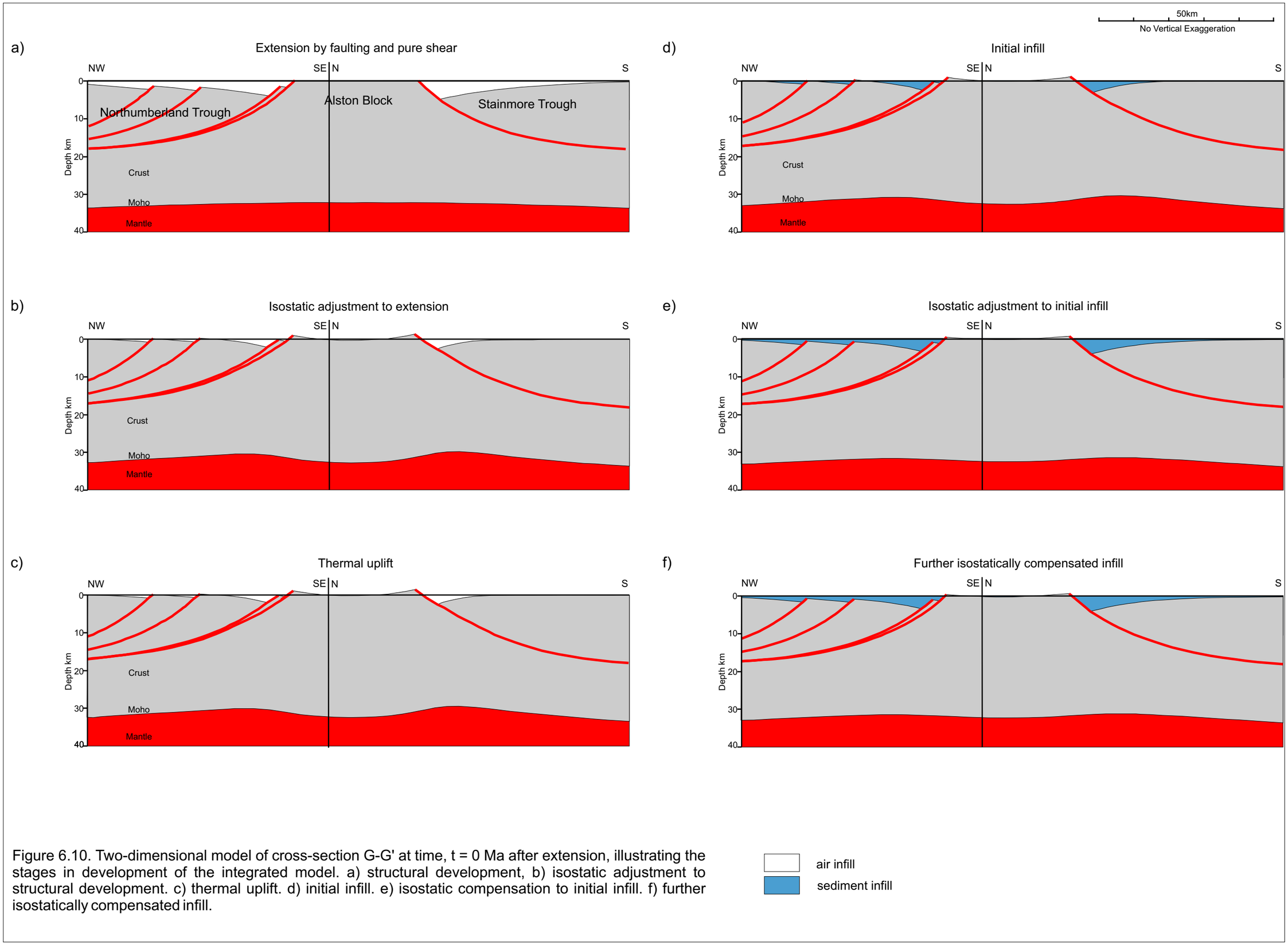


Figure 6.10. Two-dimensional model of cross-section G-G' at time, t = 0 Ma after extension, illustrating the stages in development of the integrated model. a) structural development, b) isostatic adjustment to structural development. c) thermal uplift. d) initial infill. e) isostatic compensation to initial infill. f) further isostatically compensated infill.

Trough (Figure 3.12). Initial extension occurs as the lithosphere is subjected to faulting and pure shear (Figure 6.10a). The lithosphere responds isostatically to the loads imposed on it by the extensional deformation, resulting in uplift in response to the faulting and subsidence in response to the pure shear (Figure 6.10b). Perturbation of the geotherm as a result of uplift of the lithosphere/asthenosphere boundary causes thermal uplift (Figure 6.10c). The accommodation space created by these processes is infilled by sediment (Figure 6.10d). The lithosphere responds to this basin infill isostatically, generating additional subsidence and the creation of new accommodation space, which is then infilled (Figures 6.10e & f). The maximum basin depth within the Northumberland Trough occurs next to the basin-bounding fault at x = 42 km, where a depth of 3.51 km is predicted. This corresponds well with the maximum basin depth of 3.58 km predicted by the burial history modelling. To the north, the modelled basin is 1 km deeper than predicted by the burial history modelling. This is likely to be a result of fault movement occurring later in the north of the basin. In the Stainmore Trough to the south, the maximum basin depth of 4.2 km corresponds closely with the maximum basin depth of 4.31 km proposed by the burial history modelling.

Figure 6.11 illustrates the model after t = 0 Ma at time stages corresponding to the main stratigraphic intervals described in chapter 2. At t = 20 Ma after extension (Figure 6.11a), the discrepancy between the subsidence predicted by the model results and the burial history modelling in the north of the Northumberland Trough has been reduced to 0.3 km

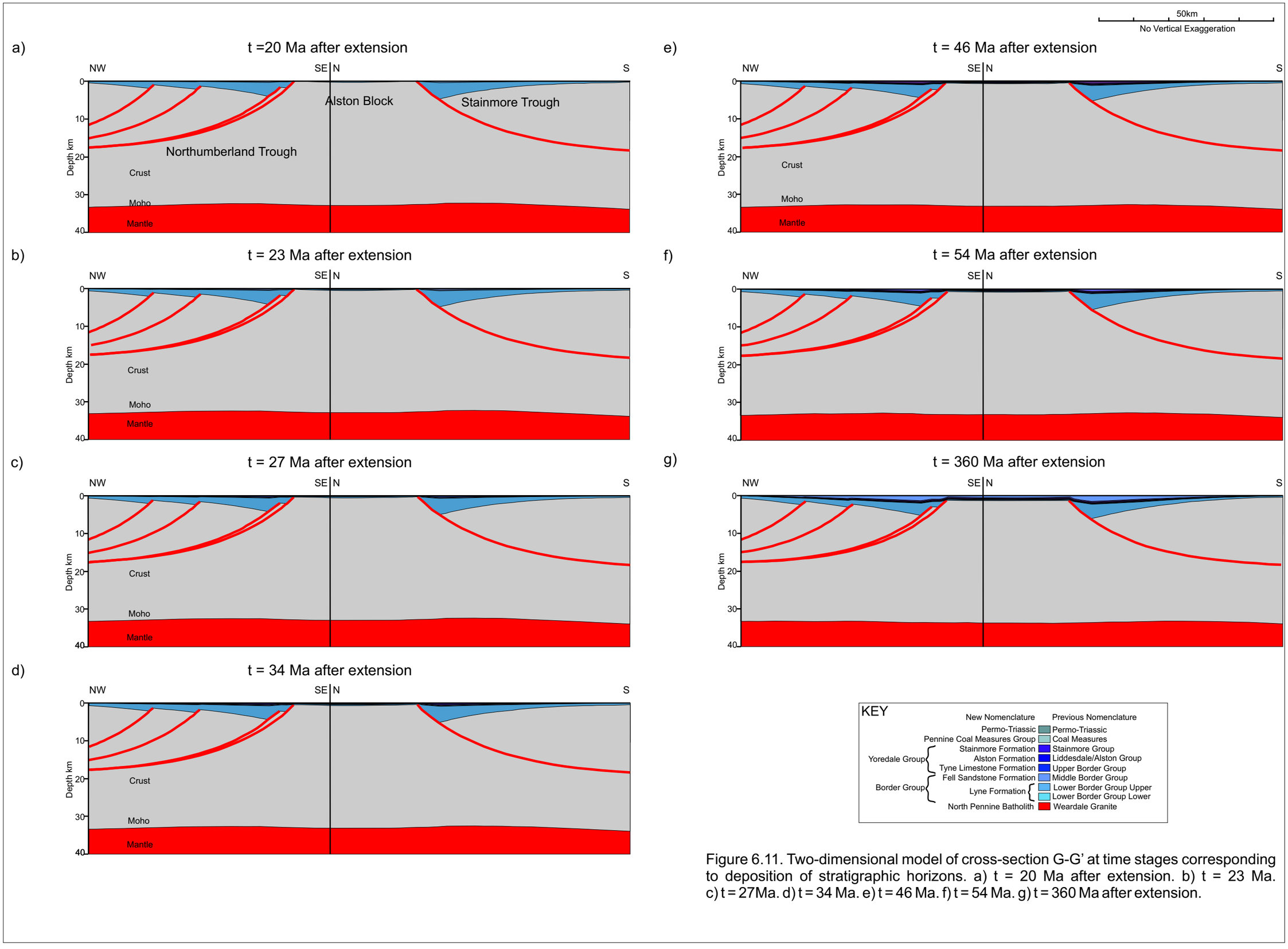


Figure 6.11. Two-dimensional model of cross-section G-G' at time stages corresponding to deposition of stratigraphic horizons. a) t = 20 Ma after extension. b) t = 23 Ma. c) t = 27Ma. d) t = 34 Ma. e) t = 46 Ma. f) t = 54 Ma. g) t = 360 Ma after extension.

implying that some fault movement has occurred within the Northumberland Trough between these two time stages. At t = 360 Ma after extension (Figure 6.11g), the model predicts maximum basin depths of 5.4 km and 6.3 km in the Northumberland Trough and Stainmore Basin, respectively. These depths are within 2 and 10% of the subsidence observed within the cross-section.

The model predicts the basement of the Alston Block to have been buried to a depth of 1.4 km. Within cross-section G-G', the basement of the Alston Block is buried to depths between 0.74 km and 1 km. Whilst there is reasonable agreement between the maximum basin depths, the amount of subsidence produced over the Alston Block is excessive. It has been suggested (Bott and Masson-Smith, 1957) that the Alston Block is structurally supported by the presence of the North Pennines Batholith, which will be investigated in section 6.4.

### *6.2.3 Cross-section C-C'*

This cross-section (Figure 3.7) crosses the Solway Basin into the Northumberland Trough, over the north-west corner of the Alston Block into the Vale of Eden Basin. Figure 6.12 illustrates the model based on cross-section C-C'. At time, t = 0 Ma after extension (Figure 6.12a) the maximum depth of the Solway Basin, at x = 32 km is 3.42 km. To the south, the maximum depth of the Vale of Eden Basin is 3.3 km. Within the Stainmore Trough, the burial history modelling predicts a maximum depth of 3.9 km for the Solway Basin and 0.6 km for the Vale of Eden Basin after the first phase of extension. At t = 360 Ma after extension

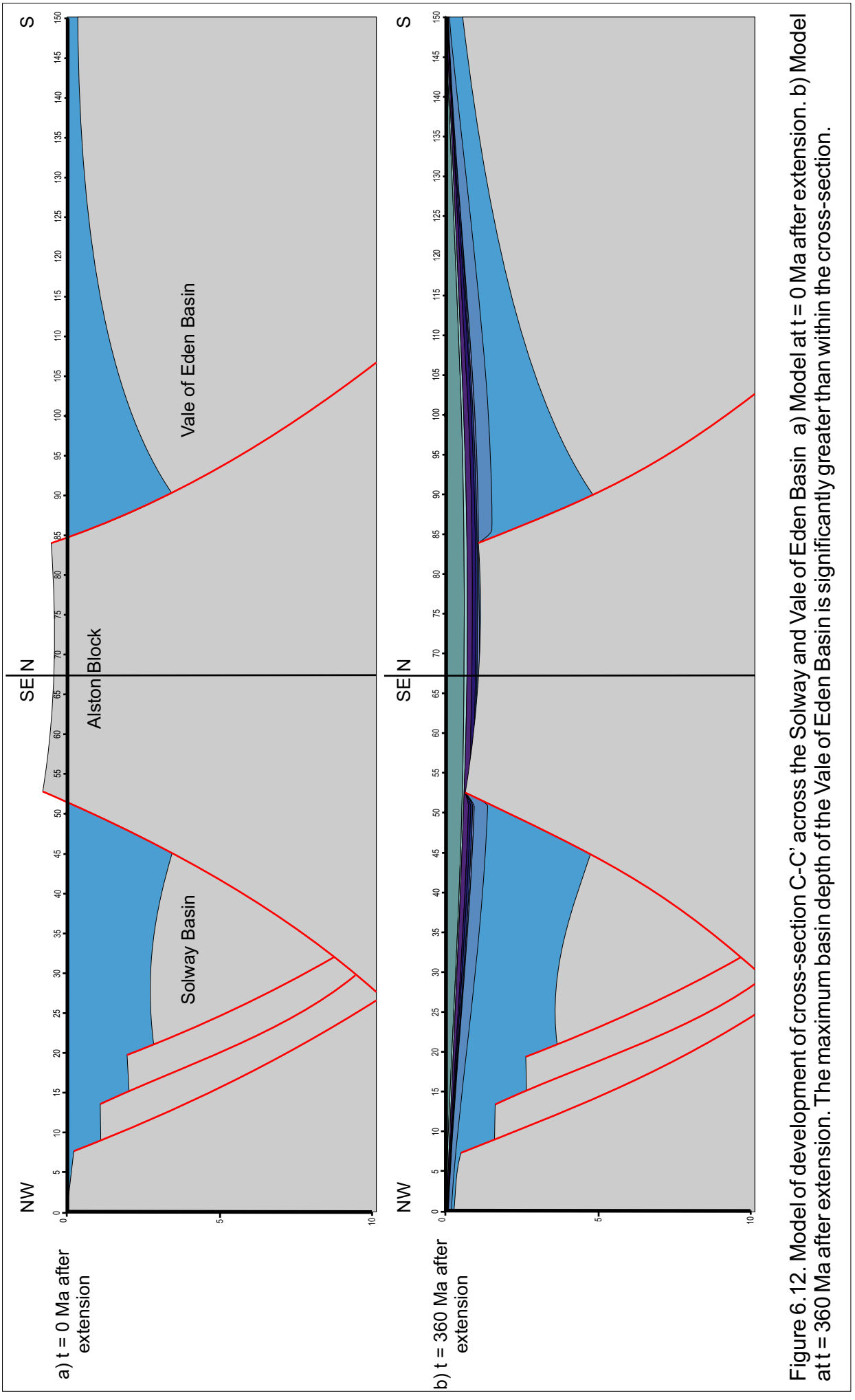


Figure 6.12. Model of development of cross-section C-C' across the Solway and Vale of Eden Basin a) Model at t = 0 Ma after extension. b) Model at t = 360 Ma after extension. The maximum basin depth of the Vale of Eden Basin is significantly greater than within the cross-section.

(Figure 6.12b), the maximum depth of the Solway Basin has increased to 4.92 km, within 3% of the 4.74 km observed within the cross-section. The basement of the Alston Block is buried to a depth of 1.14 km, which is considerably deeper than the maximum depth observed within the cross-section of 0.47 km. In addition, the Vale of Eden Basin attains a maximum depth of 4.81 km, 64% greater than the maximum observed depth of 2.94 km. Whilst there is good correlation within the Solway Basin for the maximum depth attained at t = 360 Ma, the relationship between the syn-rift deposits and the post-rift deposits does not correlate. In cross-section C-C' the thickness of post-rift deposits is greatest towards the centre/northern-margin of the basin. In the model they are thickest towards the southern margin of the basin. The excess subsidence of the Alston Block and Vale of Eden Basin also need to be considered.

Movement upon the Pennine Fault, which controls the development of the Vale of Eden Basin, did not begin until late-Carboniferous/early-Permian times. Taking this and the post-rift sediment distribution into account, it should be considered that the pure shear extension associated with the extension within the Solway Basin may not have occurred beneath the Alston Block and Vale of Eden Basin. Figure 6.13 illustrates the model of cross-section C-C' with pure shear shifted to beneath the Solway Basin between x = -30 km and x = 70 km. At t = 360 Ma after extension (Figure 6.13b) the maximum basin depth of the Solway Basin is 4.92 km. The maximum depth of burial of the Alston Block is 0.56 km and the maximum depth of the Vale of Eden Basin is 3.09 km. The Alston Block

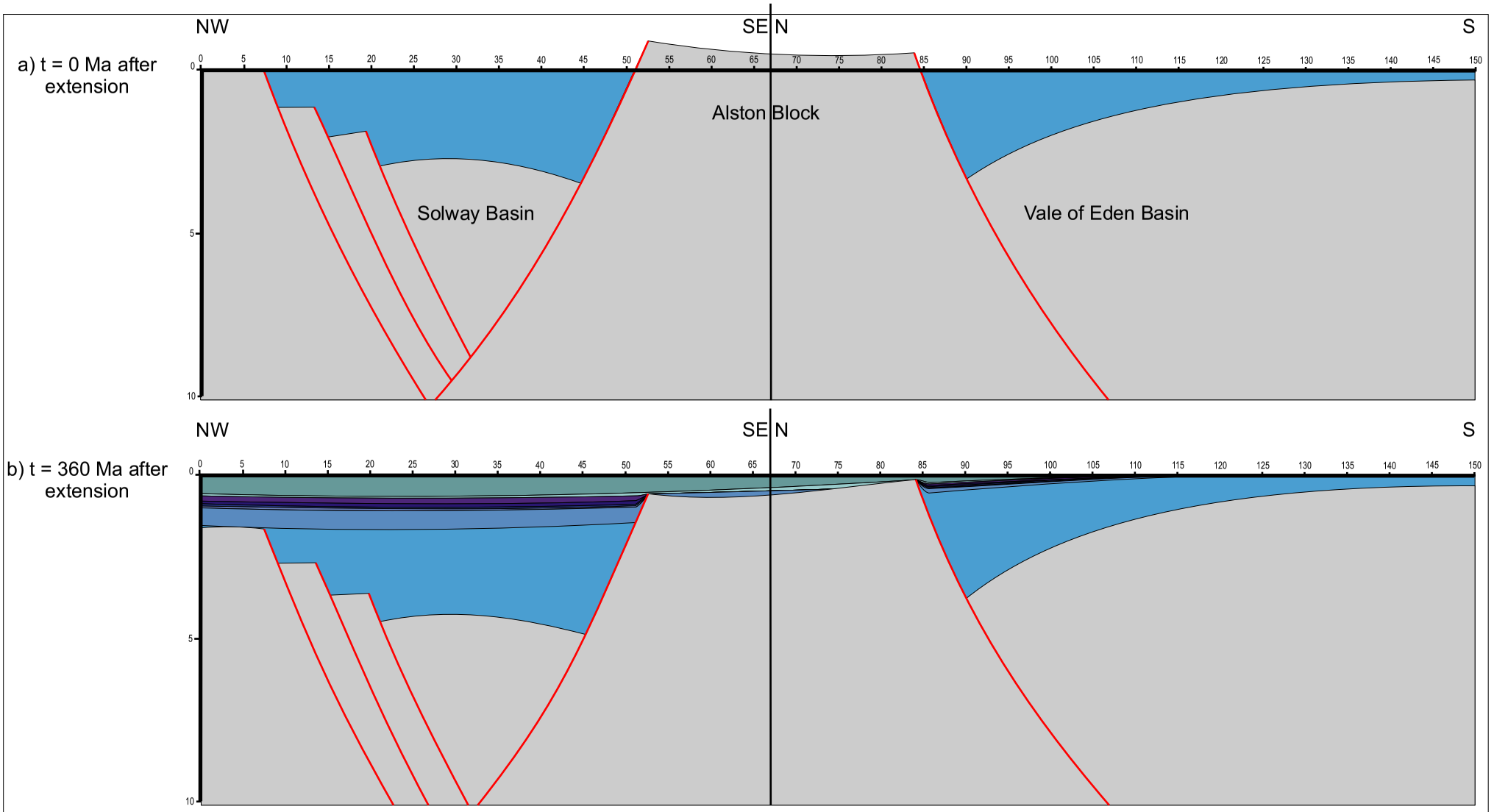


Figure 6.13. Model of development of cross-section C-C' across the Solway Basin, the Alston Block and the Vale of Eden Basin with pure shear extension situated beneath the Solway Basin. a) Model at t = 0 Ma after extension. b) Model at t = 360 Ma after extension. The maximum basin depth of the Vale of Eden Basin is consistent with that within the cross-section.

and the Vale of Eden Basin have a better correlation with the observed results from the cross-section within this model. In addition, there is a better correlation between the thicknesses of post-rift deposits towards the north-west. However, within the cross-section the Solway Basin has been subjected to uplift and erosion which cannot be replicated within the model. The Alston and Stainmore formations and the Pennine Coal Measures Group have been eroded. These represent 0.42 km of sediment at x = 22 km, where the modelled Solway Basin is 0.77 km deeper than the cross-section. An estimate of the amount of uplift required to isostatically compensate for the removal of this load predicts 0.32 km, which combined with the amount of sediment removed is 0.74 km, consistent with the discrepancy between the model and the cross-section.

### *6.2.4 Cross-section B-B'*

Figure 6.14 illustrates a model based on the parameters of cross-section B-B' across the Solway and Vale of Eden basins (Figure 3.6). This is a non-uniform lithosphere extension model, with extension by pure shear equal 133% greater than the extension by faulting. At time t = 0 Ma after extension (Figure 6.14a) the basin reaches a maximum depth of 4.2 km at x = 18 km. At x = 22 km, the basin attains a depth of 3.6 km. This is significantly less than the 4.5 km predicted by the burial history modelling. At time t = 360 Ma after extension (Figure 6.14b). The maximum basin depth within the model is 5.4 km. The maximum basin depth within the Solway Basin within the cross-section is 6.7 km.

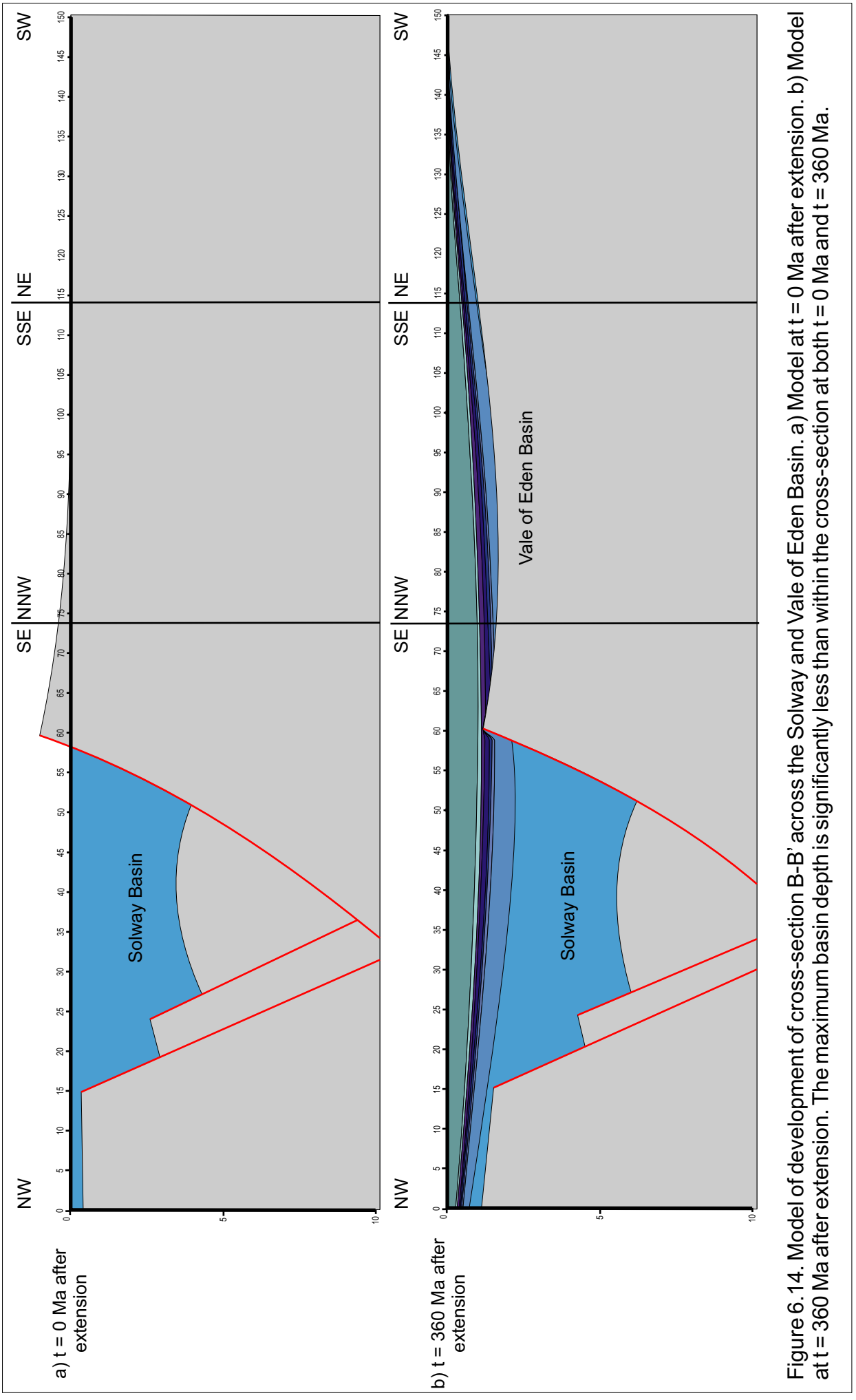


Figure 6.14. Model of development of cross-section B-B' across the Solway and Vale of Eden Basin. a) Model at t = 0 Ma after extension. b) Model at t = 360 Ma after extension. The maximum basin depth is significantly less than within the cross-section at both t = 0 Ma and t = 360 Ma.

There are two possible explanations for the discrepancy. The original interpretation of this cross-section (Figure 3.6) shows folding of the strata between faults 1 and 2 in the centre of the Solway Basin. This inversion-related folding, which cannot be included within the model, is a possible reason for the difference between the two datasets. An alternative explanation for this discrepancy could be a misinterpretation of the cross-section. The Brackenhill Fault interpreted on the cross-section as ending within the Lyne Formation, could instead be interpreted as detaching within the pre-Carboniferous basement or crust.

Figure 6.15 illustrates the model of cross-section B-B' with an additional fault within the Solway Basin at x = 16 km, synthetic to the main basin-bounding fault, with 2 km heave. At t = 0 Ma after extension (Figure 6.15a) the basin has a depth of 4.45 km at x = 22 km, which is a closer correlation to the estimate of 4.5 km total subsidence predicted by the burial history modelling. At t = 360 Ma after extension (Figure 6.15b) the basin has a maximum depth of 6.5 km, consistent with the maximum depth of the Solway Basin of 6.7 km within the cross-section.

In the south-west of both models at x = 65 km, the Vale of Eden Basin is 1.1 km deep. Within the cross-section at this point, the Vale of Eden Basin is only 0.2 km deep. At this location, the Vale of Eden Basin is beginning to onlap the Lake District Block. The additional uplift within the cross-section is possibly the result of the structural high of the Lake District Block is supporting the south western end of the Vale of Eden Basin.

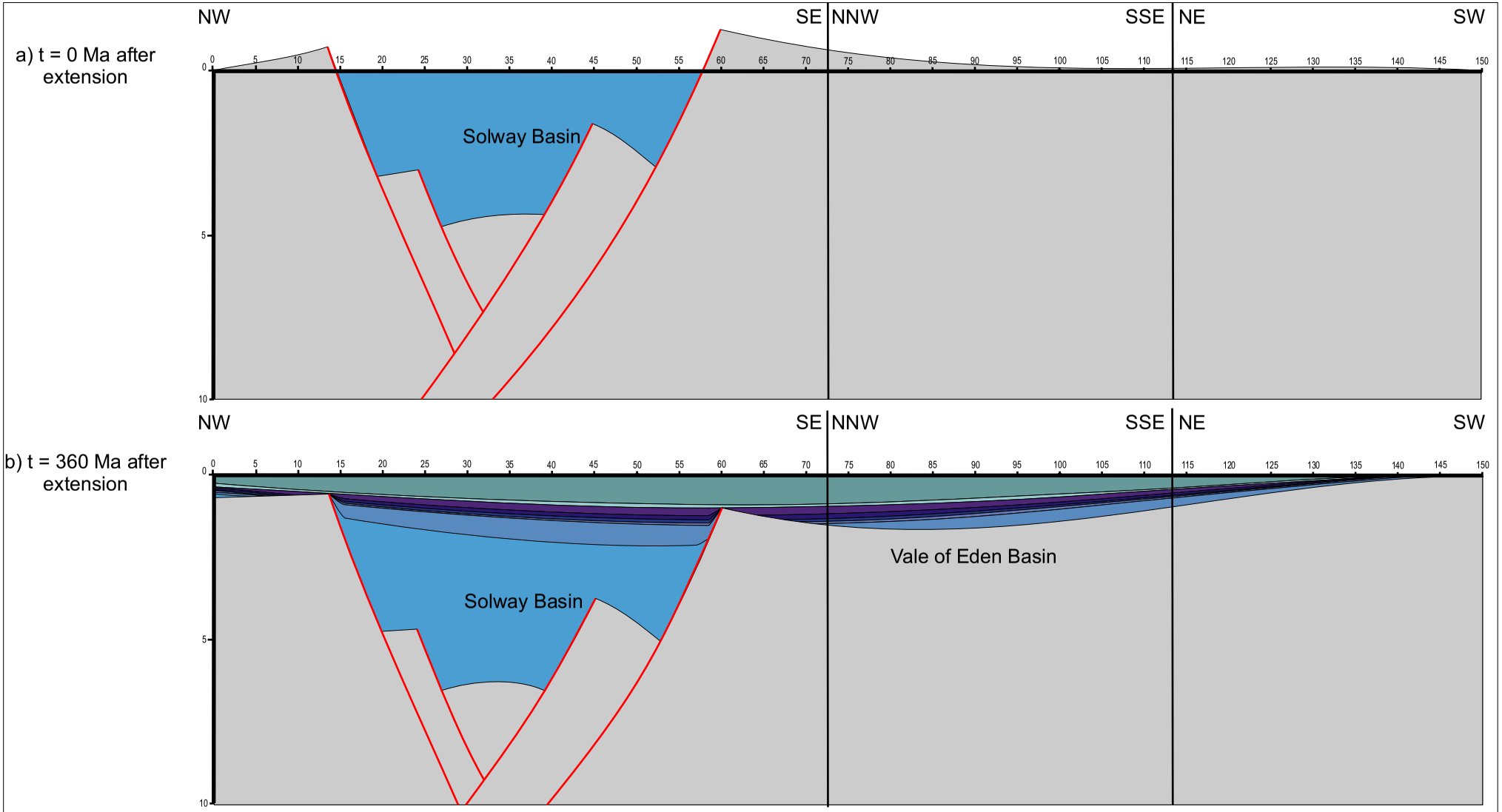


Figure 6.15. Model of development of cross-section B-B' across the Solway and Vale of Eden Basin, reinterpreted with an additional subsidiary fault within the Solway Basin synthetic to the basin-bounding fault. a) Model at t = 0 Ma after extension. b) Model at t = 360 Ma after extension. The maximum basin depth corresponds with that of the cross-section at t = 360 Ma.

## 6.3 Multiple tectonic events

The model developed as part of this research is, to date, restricted to simulating a single instantaneous extensional event. It has been demonstrated in analysis of cross-sections C-C' and G-G' that fault movement within the Northumberland Trough Region is not restricted to a single period of extension.

An alternative model, developed by Egan (Egan *et al.*, 2009) to simulate multiple episodes of extension has been used in order to consider the implications of multiple rifting on basin geometry and stratigraphy. This model has been given the same initial parameters as the integrated tectonic model (section 6.2) with the exception of the fault shear angle, which is 0° within these models, representing vertical shear. All of the models produced within this section are uniform lithosphere extension models.

### *6.3.1 Cross-section C-C'*

Evidence from analysis of the cross-section C-C', in addition to burial history modelling and the results of the instantaneous modelling carried out in section 6.2.3, suggest that extension occurred as at least three separate events.

Figure 6.16 illustrates a multiple extension model (model 1) of cross-section C-C' in which extension has been assumed to occur as three separate events

1 At t = 0 Ma – 3 km extension upon the Stublick Fault of the

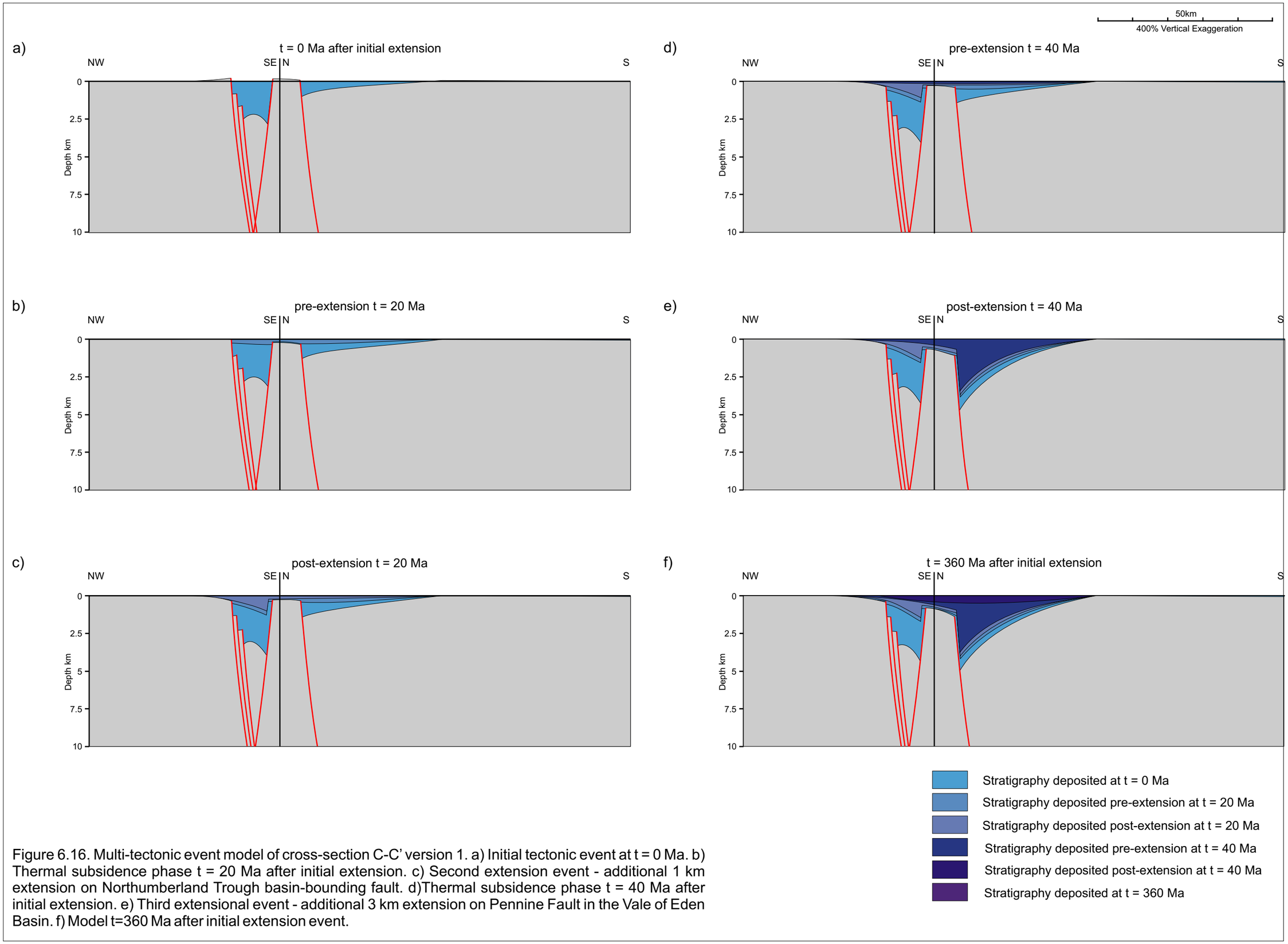


Figure 6.16. Multi-tectonic event model of cross-section C-C' version 1. a) Initial tectonic event at t = 0 Ma. b) Thermal subsidence phase t = 20 Ma after initial extension. c) Second extension event - additional 1 km extension on Northumberland Trough basin-bounding fault. d)Thermal subsidence phase t = 40 Ma after initial extension. e) Third extensional event - additional 3 km extension on Pennine Fault in the Vale of Eden Basin. f) Model t=360 Ma after initial extension event.

Northumberland Trough has been modeled with 1 km extension on each of 3 subsidiary faults in the north of the Northumberland Trough/Solway Basin, antithetic to the main basin bounding fault. 1 km extension has been modelled on the Pennine Fault of the Vale of Eden Basin. Overall this model generates 0.85 km less subsidence than the instantaneous extension model near to the Stublick Fault, and 0.05 km less subsidence to the north of the trough. Within the Vale of Eden basin there is 2.53 km less subsidence than the instantaneous extension model.

2 At t = 20 Ma after initial extension an additional 1 km extension is assumed to occur along the Stublick Fault, which s generates an additional 0.7 km subsidence.

3 At t = 40 Ma after initial extension an additional 3 km extension is assumed to occur along the Pennine Fault. This generates an additional 3.1 km subsidence in the Vale of Eden Basin.

Figure 6.17 illustrates a second multiple extension model (model 2) of cross-section C-C' in which extension occurs as three separate events:

1 At t = 0 Ma, 3 km of extension upon the Stublick Fault of the Northumberland Trough has been assumed with 1 km extension on the Pennine Fault related to the Vale of Eden Basin. This generates 1.2 km less subsidence than the

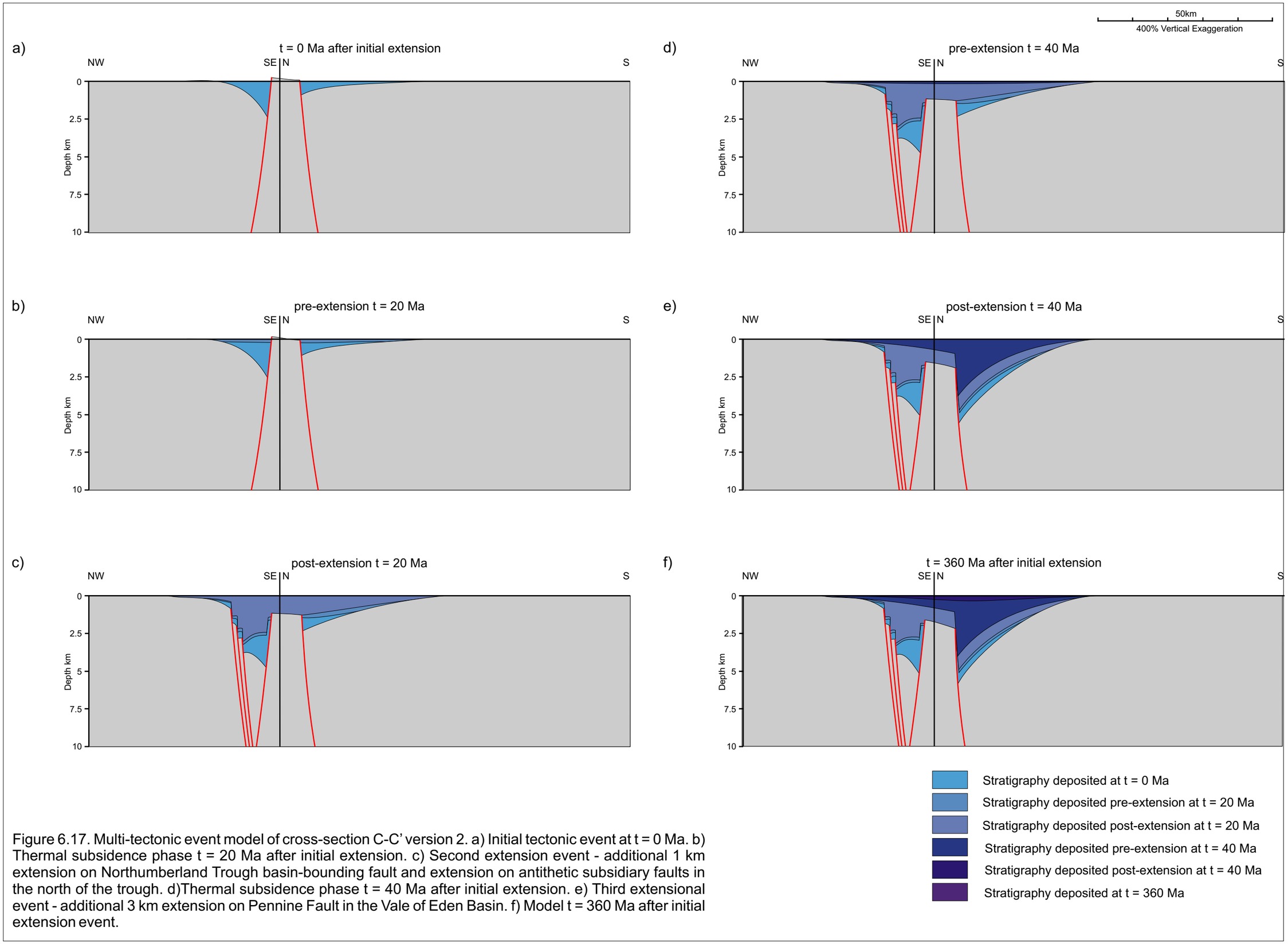


Figure 6.17. Multi-tectonic event model of cross-section C-C' version 2. a) Initial tectonic event at t = 0 Ma. b) Thermal subsidence phase t = 20 Ma after initial extension. c) Second extension event - additional 1 km extension on Northumberland Trough basin-bounding fault and extension on antithetic subsidiary faults in the north of the trough. d)Thermal subsidence phase t = 40 Ma after initial extension. e) Third extensional event - additional 3 km extension on Pennine Fault in the Vale of Eden Basin. f) Model t = 360 Ma after initial extension event.

instantaneous extension model next to the Stublick Fault, and 2.1 km less subsidence to the north of the trough, where movement on the subsidiary faults has not yet occurred. Within the Vale of Eden Basin there is 2.55 km less subsidence than the instantaneous model.

2 At t = 20 Ma after initial extension it has been assumed that 1 km extension has taken place on each of 3 subsidiary faults in the north of the Northumberland Trough/Solway Basin, antithetic to the main basin bounding fault. An additional 1 km extension has been assumed to take place upon the Stublick Fault. This faulting configuration generates an additional 2.24 km of subsidence in the vicinity of the Stublick Fault and up to 2.85 km additional subsidence in the north of the trough. There is also additional subsidence upon the Alston Block and within the Vale of Eden Basin as the model treats these areas a part of the hanging wall of the antithetic faults within the Northumberland Trough.

3 At t = 40 Ma after initial extension an additional 3 km extension has been assumed along the Pennine Fault. This late phase of extension generates an additional 3.3 km subsidence in the Vale of Eden Basin.

Figure 6.18 illustrates the results of the instantaneous extension model (Figure 6.18a) and the multi-tectonic models of cross-section C-C' at

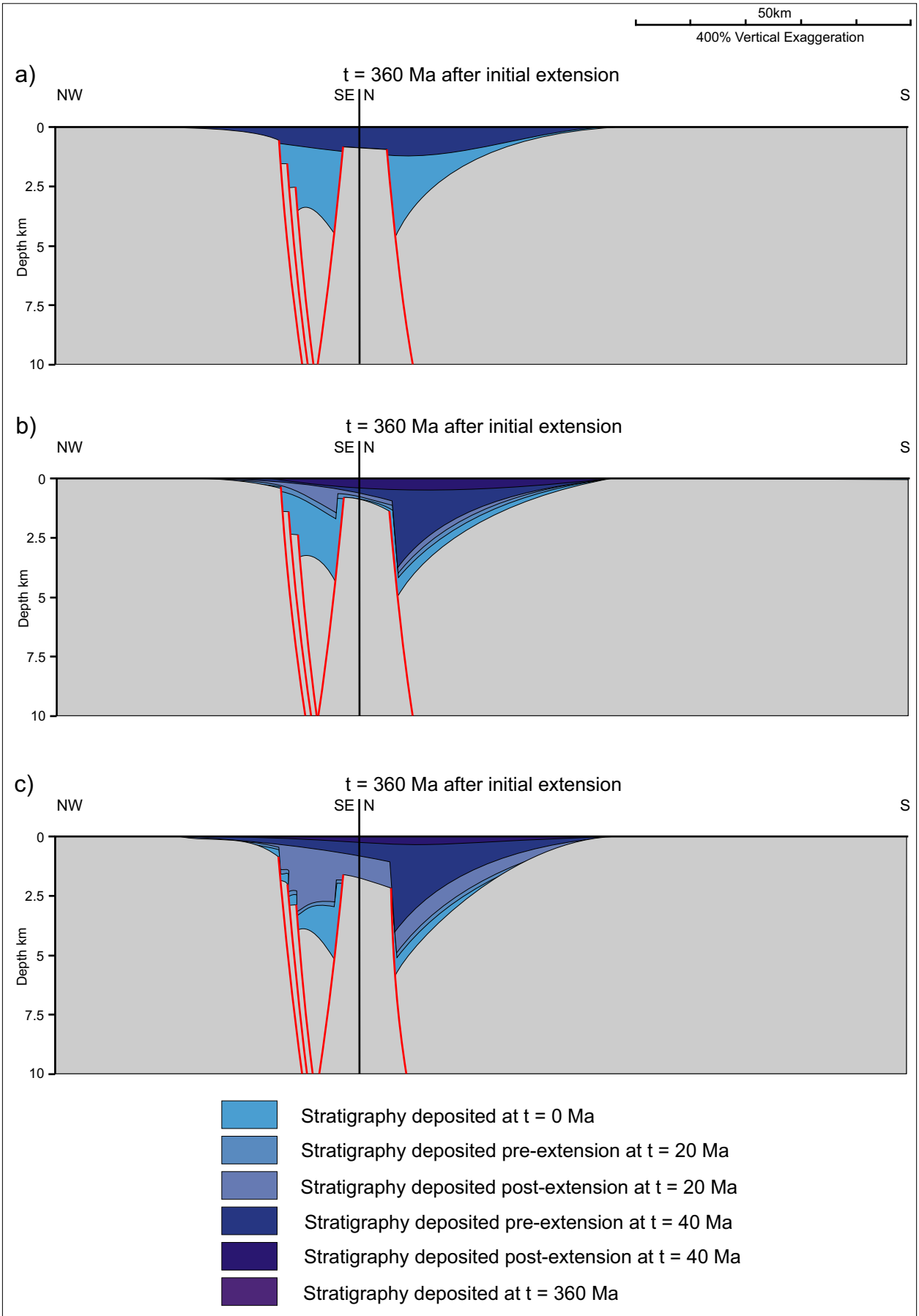


Figure 6.18. Models of cross-section C-C'with multi-stage extension at t = 360 Ma. a) Single stage extension model. b) Multi-stage model version 1 with additional extension on the basin bounding fault of the Northumberland Trough at t = 20 Ma and on the Pennine Fault at t = 40 Ma. c) Multi-stage model version 2 with additional extension on subsidiary faults in the north of the Northumberland Trough at t = 20 Ma.

t = 360 Ma after initial extension. Multi-tectonic model 1 (Figure 6.18b) generates 0.6 km less subsidence than that observed within the Northumberland Trough/Solway Basin cross-section (Figure 3.7). Across the Alston Block, it generates between 0 km (north) and 0.9 km (south) greater subsidence than observed within the cross-section. The subsidence of the Vale of Eden Basin is 2.1 km greater than observed. It was hypothesised in section 6.2.3 that the excess subsidence generated is the result of the pure shear extension not being located beneath the Vale of Eden Basin and beneath the Alston Block. The pattern of stratigraphy generated is consistent with that observed within the cross-section of the Vale of Eden Basin with the stratigraphy deposited during the t = 40 Ma after initial extension stage thickening towards the fault.

Multiple extension model 2 (Figure 6.18c) generates 0.15 km more subsidence than that observed within the Northumberland Trough/Solway Basin cross-section; this is a discrepancy of 4%. However, upon the Alston Block the model generates subsidence that is 0.8 km to 1.7 km greater than observed and within the Vale of Eden Basin the subsidence is 3 km greater. The pattern of the stratigraphy generated within the Northumberland Trough/Solway Basin in the model is comparable with that in the cross-section such that the initial syn-rift deposits of the Lyne and Fell Sandstone formations thin from the south towards the north. The deposits of the Tyne Limestone and Alston formations thicken from south to north across the basin.

*Cross-section E-E'*

Analysis of cross-section E-E' (Figure 3.10) has identified at least two stages of extension. Figure 6.19 illustrates a multi-tectonic extension model (model 1) of cross-section E-E' in which extension occurs as two separate events:

1 At t = 0 Ma, 1 km extension has been assumed upon each of the three en-echelon faults at the southern margin of the Northumberland Trough. In addition, 1 km of extension has been assumed to take place on the antithetic subsidiary fault in the north of the Northumberland Trough, which is antithetic to the main basin bounding faults. 2 km extension has been modeled on the Butterknowle Fault at the northern margin of the Stainmore Trough. This model generates 1.65 km less subsidence than the instantaneous extension model near to the Stublick Fault, the northernmost basin-bounding fault. Within the Stainmore Trough there is 0.95 km less subsidence than the instantaneous extension model. There is 0.07 km less uplift across the Alston Block.

2 At t = 20 Ma after initial extension an additional 1 km of extension has been modeled along the two northernmost basin-bounding faults as well as 1 km of additional extension upon the Butterknowle Fault. This second phase of extension generates an additional 2.2 km subsidence in the vicinity of the Stublick Fault, 1.5 km extra subsidence in the Stainmore

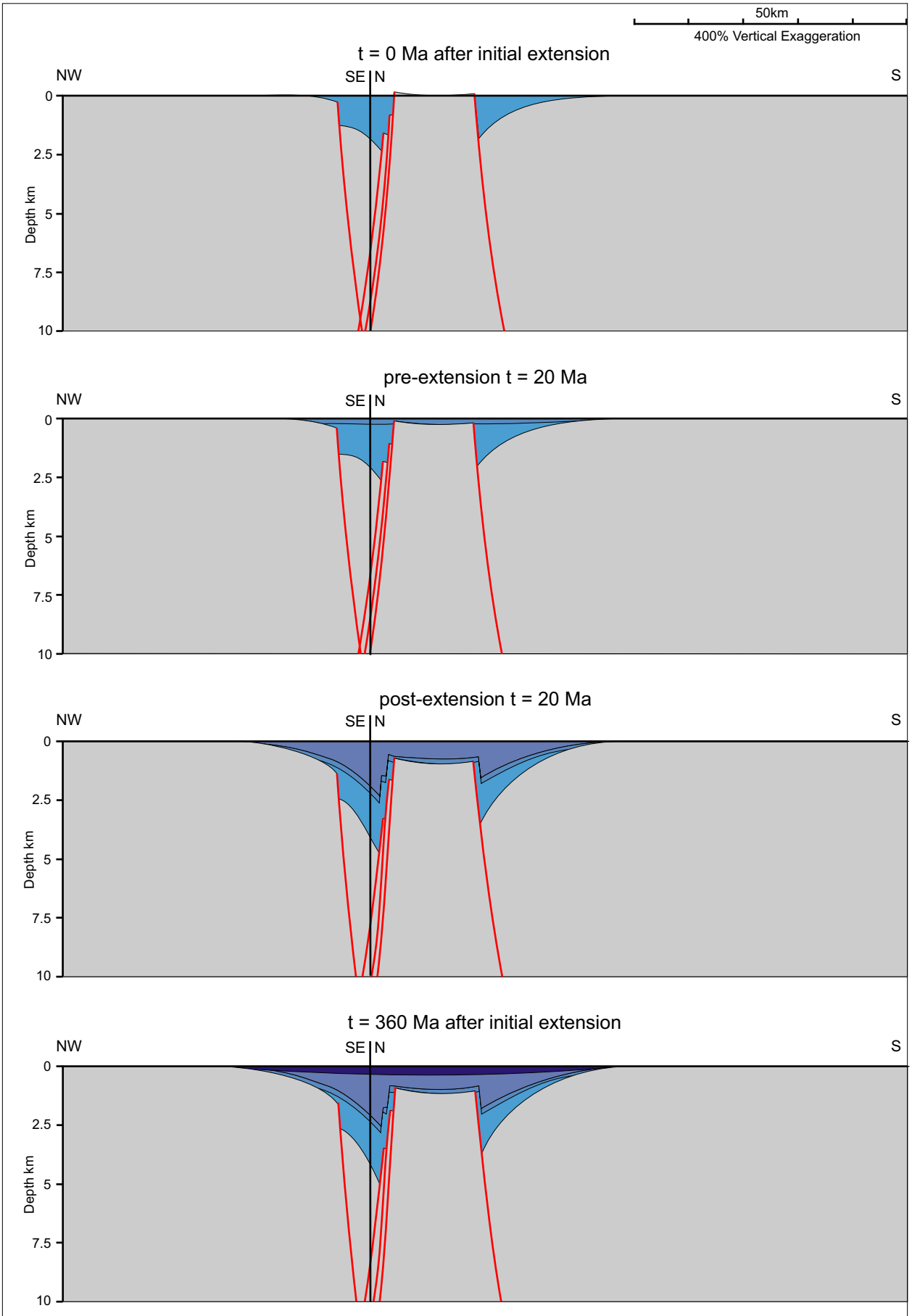


Figure 6.19. Multi-tectonic event model of cross-section E-E' version 1. a) Initial tectonic event at t = 0 Ma. b) Thermal subsidence phase t = 20 Ma after initial extension. c) Second extension event - additional 1 km extension on Northumberland Trough basin-bounding faults and additional 1 km extension on Stainmore Trough basin-bounding fault. d) Model t=360 Ma after initial extension event.

Trough adjacent to the Butterknowle Fault and 0.6 km additional subsidence of the Alston Block.

Figure 6.20 illustrates multiple extension model (model 2) of cross-section E-E' in which extension occurs as two separate events:

1 At t = 0 Ma, 1 km of extension has been assumed to occur upon each of the 3 en-echelon faults at the southern margin of the Northumberland Trough, with 2 km extension on the Butterknowle Fault at the northern margin of the Stainmore Trough. This generates 1.8 km less subsidence than the instantaneous extension model near to the Stublick Fault and 1.2 km less subsidence at the location of the subsidiary fault. There is 0.97 km less subsidence than the instantaneous model within the Stainmore Trough.

2 At t = 20 Ma after initial extension an additional 1 km of extension has been modeled upon the two northernmost basin-bounding faults. In addition, 1 km of extension has been assumed to occur on an antithetic subsidiary fault in the north of the Northumberland Trough, with 1 km additional extension upon the Butterknowle Fault. This generates an additional 2.8 km subsidence near to the Stublick Fault as well as 2.15 km of additional subsidence in the location of the subsidiary fault. Additionally, there is 1.5 km extra subsidence in the Stainmore Trough adjacent to the

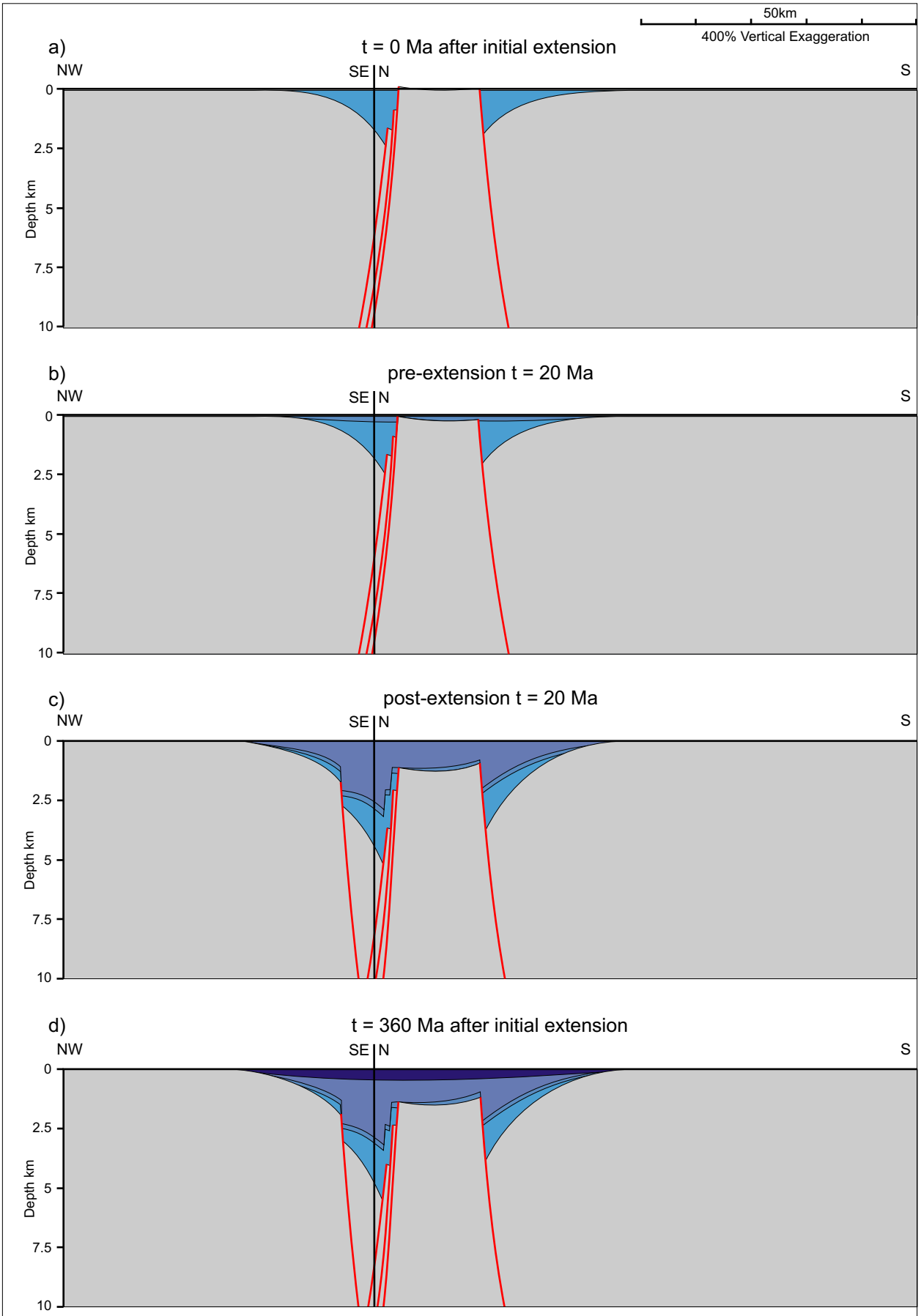


Figure 6.20. Multi-tectonic event model of cross-section E-E' version 2. a) Initial tectonic event at t = 0 Ma. b) Thermal subsidence phase t = 20 Ma after initial extension. c) Second extension event - additional 1 km extension on Northumberland Trough basin-bounding faults,extension on an antithetic subsidiary fault in the north of the basin and additional 1 km extension on Stainmore Trough basin-bounding fault. d) Model t=360 Ma after initial extension event.

Butterknowle Fault and 0.6 km additional subsidence of the Alston Block.

Figure 6.21 illustrates the results of the instantaneous extension model (Figure 6.21a) and the multi-tectonic models of cross-section E-E' at t = 360 Ma after initial extension. Multi-tectonic model 1 (Figure 6.21b) generates between 0.03 km and 0.2 km more subsidence than the instantaneous extension model. Multi-tectonic model 2 (Figure 6.21c) generates between 0.2 km and 0.7 km more subsidence than the instantaneous extension model. The stratigraphy generated by multiple extension model 1 presents 'syn-rift' deposits generated in the first phase of extension that are more uniform in thickness in the centre of the basin between the subsidiary fault and the basin-bounding faults. In addition, the t = 20 Ma post-extension deposits in the Northumberland and Stainmore troughs thicken towards the basin-bounding faults. This configuration of stratigraphy is reflected by the nature of the deposits observed within cross-section E-E' (Figure 3.10). Excessive subsidence has been generated by the model over the Alston Block. It is hypothesised that this is a result of the Alston Block being structurally supported by the presence of a buoyant granite body within the crust beneath the block.

*Cross-section H-H'*

Analysis of cross-section H-H' has identified at least two stages of extension. Figure 6.22 illustrates a multi-tectonic extension model (model 1) of cross-section H-H' in which extension occurs as two separate events:

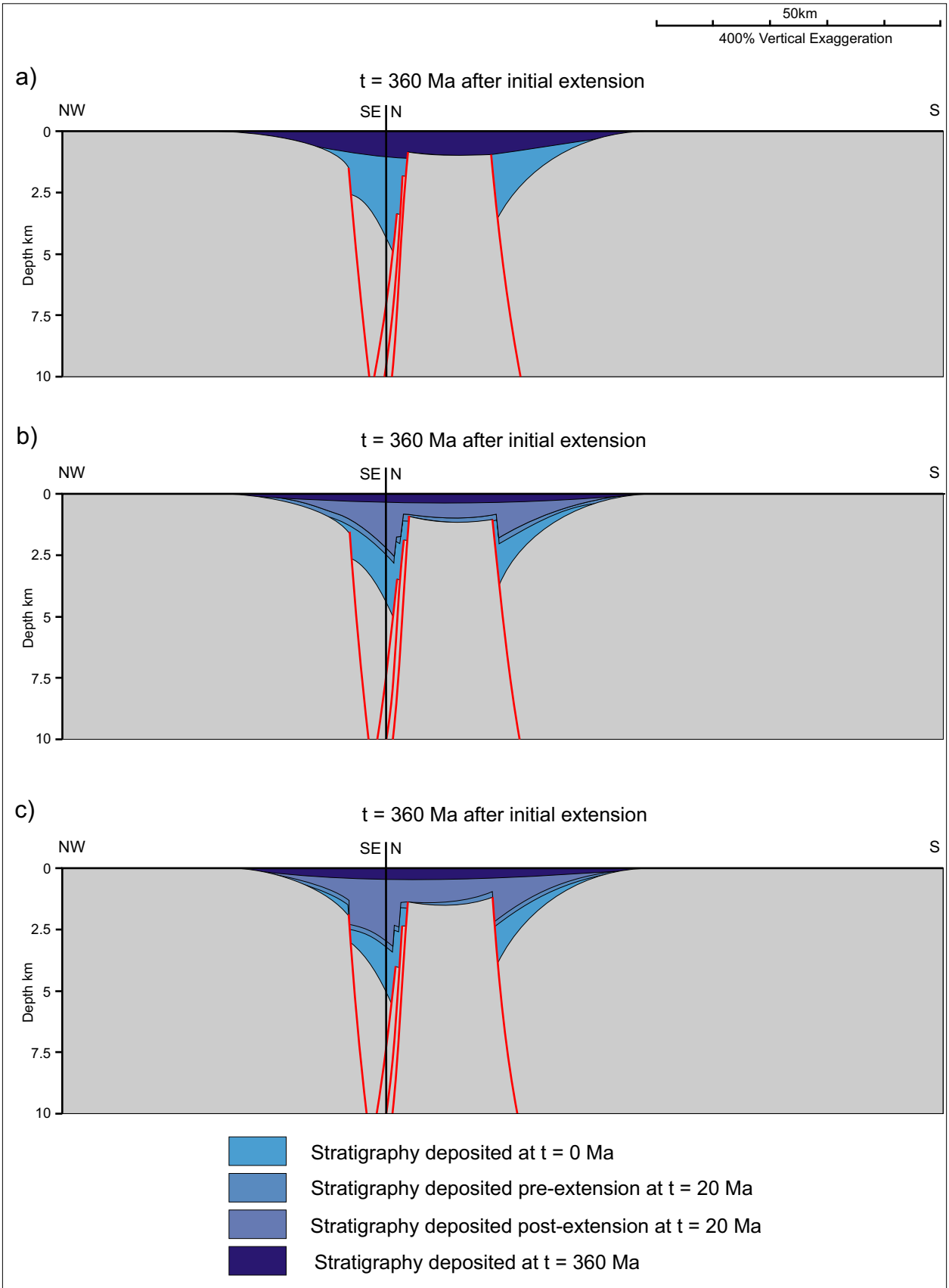


Figure 6.21. Models of cross-section E-E' with multi-stage extension at t = 360 Ma. a) Single stage extension model. b) Multi-stage model version 1 with additional extension on the basin bounding faults of the Northumberland Trough and Stainmore Trough at t = 20 Ma. c) Multi-stage model version 2 with additional extension on subsidiary fault in the north of the Northumberland Trough at t = 20 Ma.

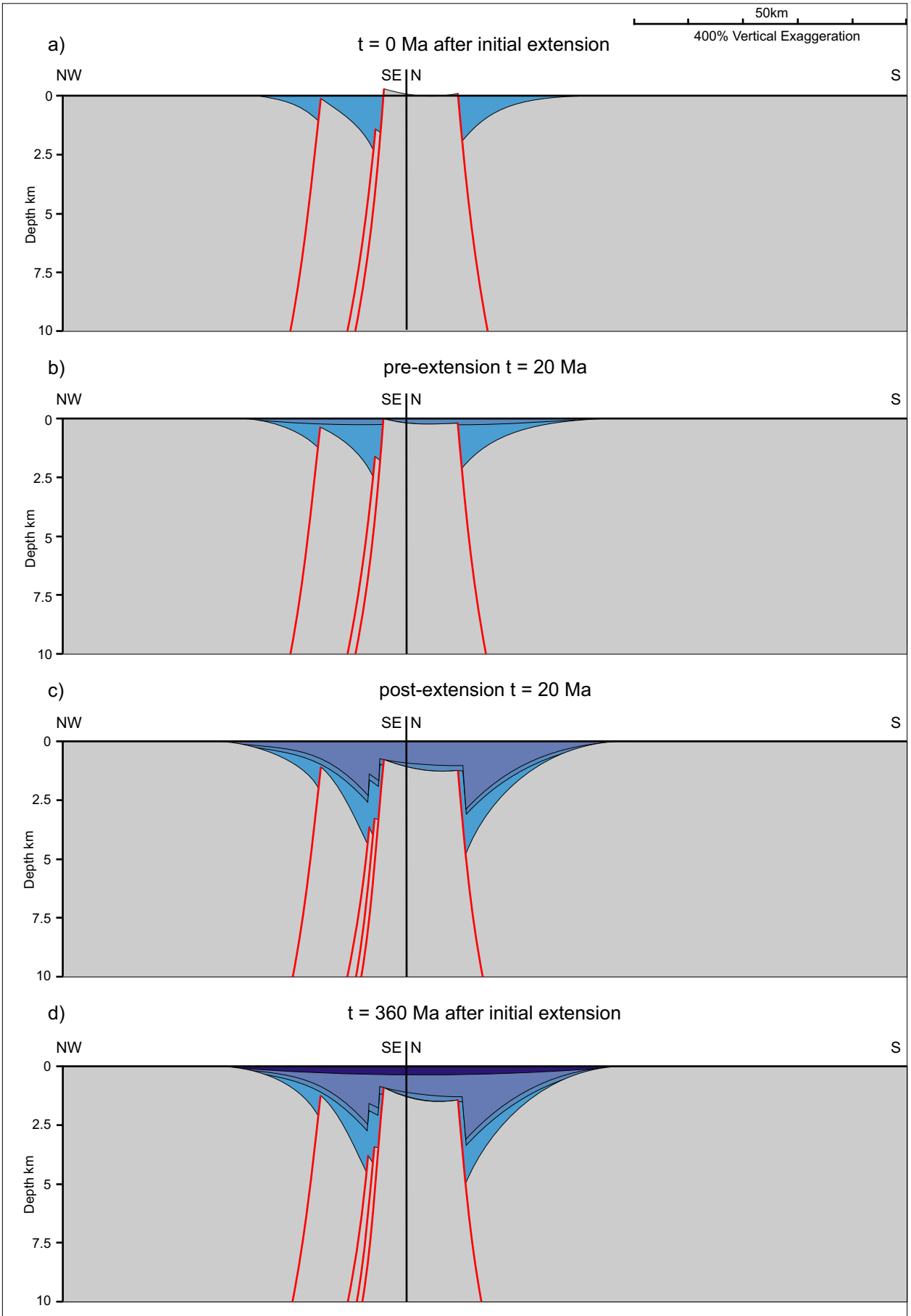


Figure 6.22. Multi-tectonic event model of cross-section H-H' version 1. a) Initial tectonic event at t = 0 Ma. b) Thermal subsidence phase t = 20 Ma after initial extension. c) Second extension event - additional 1 km extension on Northumberland Trough basin-bounding faults and additional 2 km extension on Stainmore Trough basin-bounding fault. d) Model t=360 Ma after initial extension event.

1 At t = 0 Ma, 2 km extension has been assumed to have occurred upon the Ninety Fathom Fault at the southern margin of the Northumberland Trough with 1 km extension upon the Stublick Fault to the north of the Ninety Fathom Fault. Additionally, 1 km of extension has been modeled on the subsidiary fault in the north of the Northumberland Trough, which is synthetic to the main basin bounding faults. 2 km of extension has been assumed on the Butterknowle Fault at the northern margin of the Stainmore Trough. Overall, this model generates 0.8 km less subsidence than the instantaneous extension model in the vicinity of the Ninety Fathom Fault and1.5 km less subsidence near to the Stublick Fault. Within the Stainmore Trough, there is 1.78 km less subsidence than the instantaneous extension model.

2 At t = 20 Ma after initial extension an additional 1 km of extension has been modeled upon the Ninety Fathom Fault. An additional subsidiary fault to the north of the Stublick Fault, (synthetic in orientation) has been assumed to have experienced 1 km of extension, as well as 2 km additional extension upon the Butterknowle Fault. This model generates an additional 1.53 km subsidence near to the Ninety Fathom Fault as well as 1.5 km of additional subsidence is generated in the vicinity of the Stublick Fault. There is 2.3 km of additional subsidence generated at the

position of the new subsidiary fault, and2.66 km of extra subsidence in the Stainmore Trough adjacent to the Butterknowle Fault.

Figure 6.23 illustrates multi-tectonic extension model (model 2) of cross-section H-H' in which extension occurs as two separate events:

1 At t = 0 Ma, 2 km extension has been assumed upon the Ninety Fathom Fault at the southern margin of the Northumberland Trough as well as 1 km extension upon the Stublick Fault to the north of the Ninety Fathom Fault. Additionally, 2 km of extension has been modelled on the Butterknowle Fault at the northern margin of the Stainmore Trough. At the southern margin of the Northumberland Trough, this extensional phase generates 0.8 km and 1.48 km less subsidence than the instantaneous extension model near to the Ninety Fathom and Stublick faults, respectively. There is 1.8 km less subsidence than the instantaneous extension model within the Stainmore Trough.

2 At t = 20 Ma after initial extension an additional 1 km extension upon the Ninety Fathom Fault has been modelled as well as 1km extension along two additional subsidiary faults to the north of the Stublick Fault, synthetic in orientation. In addition, 2 km of additional extension has been assumed upon the Butterknowle Fault. This extensional

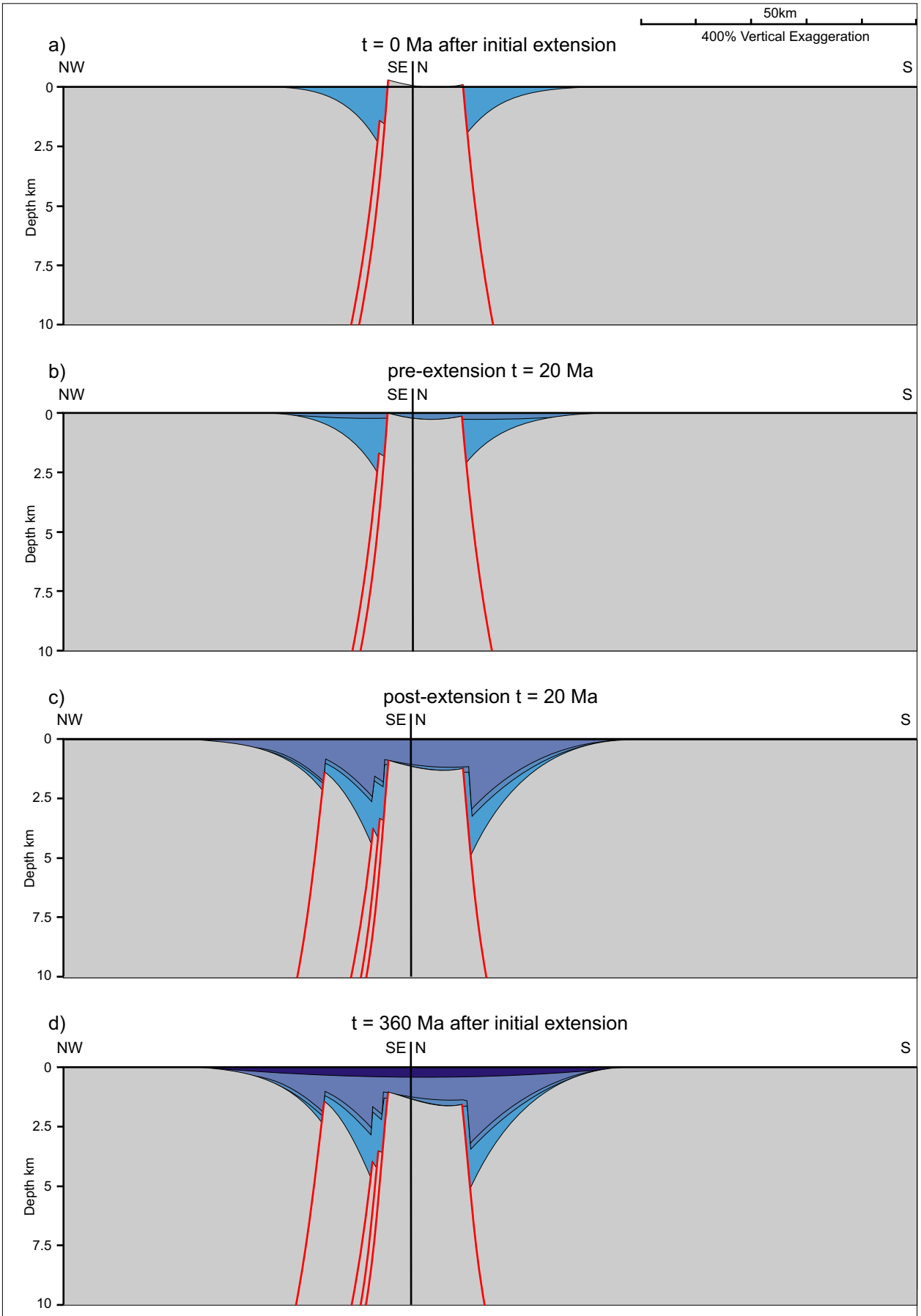


Figure 6.23. Multi-tectonic event model of cross-section H-H' version 2. a) Initial tectonic event at t = 0 Ma. b) Thermal subsidence phase t = 20 Ma after initial extension. c) Second extension event - additional 1 km extension on Northumberland Trough basin-bounding faults, new antithetic subsidiary fault in north of trough with 1km extension and additional 2 km extension on Stainmore Trough basin-bounding fault. d) Model t=360 Ma after initial extension event.

phase generates 2.43 km and 1.78 km additional subsidence at the location of the proximal and distal subsidiary faults, respectively. There is 1.65 km to 1.67 km additional subsidence in the vicinity of the basin-bounding faults of the Northumberland Trough, and 2.84 km of extra subsidence occurs in the Stainmore Trough adjacent to the Butterknowle Fault.

Figure 6.24 illustrates the results of the instantaneous extension model (Figure 6.24a) and the multi-tectonic models of cross-section H-H' at t = 360 Ma after initial extension. Multi-tectonic model 1 (Figure 6.24b) generates between 0.2 km and 0.58 km more subsidence than the instantaneous extension model. Multi-tectonic model 2 (Figure 6.24c) generates between 0.3 km and 0.7 km more subsidence than the instantaneous extension model. The configuration of the stratigraphy of multi-tectonic model 2 is consistent with the pattern of the stratigraphy in cross-section H-H' with thickening of the t = 20 post -rift deposits towards the distal synthetic fault.

## 6.4 The effect of igneous intrusion upon post-emplacement structure

Whilst some of the models produced previously generate subsidence that is comparable with that observed within the basin structures, the amount of subsidence generated on the Alston Block by these initial models is excessive. Bott and Masson-Smith (1957) and Bott (1974; 1999) suggest that local elevated topography occurs above some granite batholiths as a

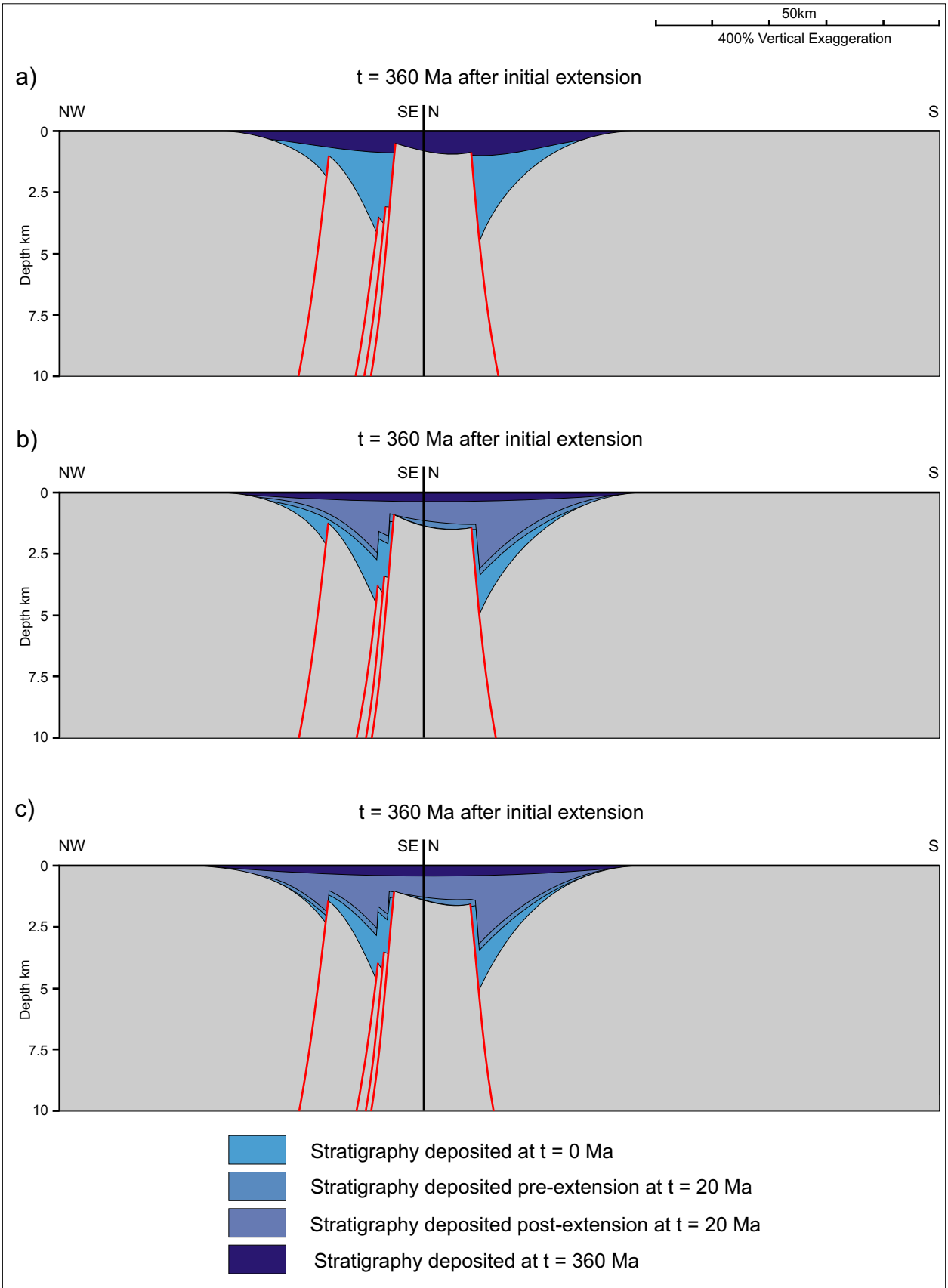


Figure 6.24. Models of cross-section H-H' with multi-stage extension at t = 360 Ma. a) Single stage extension model. b) Multi-stage model version 1 with additional extension on the basin bounding fault of the Northumberland Trough and on a synthetic subsidiary fault at t = 20 Ma. c) Multi-stage model version 2 with additional extension on antithetic subsidiary fault in the north of the Northumberland Trough at t = 20 Ma.

result of the isostatic response to their anomalously low density within the crust (Bott, 1953; 1956). It is hypothesised that the granite batholith intruded within the Northumberland Trough Region acts as a negative load upon the lithosphere and the crust responds to this negative load by isostatic uplift resulting in differential subsidence between the Alston Block and the surrounding troughs.

### *6.4.1 Modelling the isostatic response to igneous emplacement*

An algorithm to model the isostatic response of the lithosphere to the emplacement of igneous intrusions within the crust has been developed to provide insights into the influence of the North Pennines Batholith on the post-emplacement structural development of the Northumberland Trough Region.

The load arising from emplacement of an igneous intrusion within the crust ($L_{g(x)}$) is determined by the density contrast between the intrusion and the crust such that:

$$L_{g(x)} = G_{(x)} \left(\rho_g - \rho_c\right) g \qquad [6.1]$$

where: $G_{(x)}$ is the thickness of the intruded body at horizontal position x

$\rho_g$ is the density of the intrusion

$\rho_c$ is the density of the crust

$g$ is the acceleration due to gravity

When this is substituted into the flexural isostatic equation given by [4.62] the flexural response of the lithosphere to the intrusion of an igneous body ($W_{g(x)}$):

$$\frac{d^2}{dx^2} D \frac{d^2 W_{g(x)}}{dx^2} + \left(\rho_m - \rho_{air}\right) g W_{g(x)} = G_x \left(\rho_g - \rho_c\right) g \qquad [6.2]$$

where: $\rho_m$ is the density of the mantle lithosphere

$\rho_{air}$ is the density of air

This equation is then solved for $W_{g(x)}$ using a Fast Fourier Transform (FFT) and applying the response function given by equation [5.28].

The result of equation [6.2] is used to determine the geometry of the basement, Moho and faults within the model. The depths to these horizons are given by:

$$B_{(x,t)} = B_{(x,t)} + W_{g(x)} \qquad [6.3]$$

$$M_{(x,t)} = M_{(x,t)} + W_{g(x)} \qquad [6.4]$$

$$F_{(x,t)} = F_{(x,t)} + W_{g(x)} \qquad [6.5]$$

where: $B_{(x,t)}$ is the basin profile

$M_{(x,t)}$ is the Moho profile

$F_{(x,t)}$ is the fault profile

### *6.4.2 The isostatic response to igneous intrusions*

In order to study the effect of igneous intrusions upon the structural and stratigraphic evolution of a basin system, these algorithms have been incorporated into the model described in section 6.2, with the initial parameters consistent with those illustrated in Figure 6.7, as used to model the Northumberland Trough Region. A density for the granite intrusion of 2630 $kgm^{-3}$ is assumed based on the density of the North Pennines Batholith (Bott, 1967), except where the granite-crustal density

contrast is investigated. In addition to the granite-crustal density contrast, the effect of varying the elastic thickness of the lithosphere is considered. Within the initial models, a square block is used to represent the granite body; however effect of the shape and area of the batholith are also modelled.

#### 6.4.2.1 The effect of elastic thickness of the lithosphere on the isostatic response to igneous intrusions

As demonstrated in chapter 4 the larger the elastic thickness (*Te*) of the lithosphere, the broader the region over which loads are isostatically compensated. Figure 6.25 illustrates the flexural isostatic effect of increasing the *Te* on modelling of the granite intrusion. A Te of 0 km represents Airy isostatic uplift, where the response to the load imposed by the granite occurs directly above the intruded body. Figure 6.25b shows the flexural response of the lithosphere at x = 66 km, the centre of the granite body. With increasing *Te*, initially the amount of uplift increases as the width of the flexural distribution increases. At values of *Te* greater than 3 km, the amount of uplift generated decreases in an almost linear manner with a decrease of 0.01 km for every 1 km increase in *Te*.

#### 6.4.2.2 The effect of the intrusion density on the isostatic response to igneous intrusions

The effects of varying the density of the crust and mantle have been considered in appendix C. The density contrast between the crust and the igneous intrusion determines the value of the negative load that is

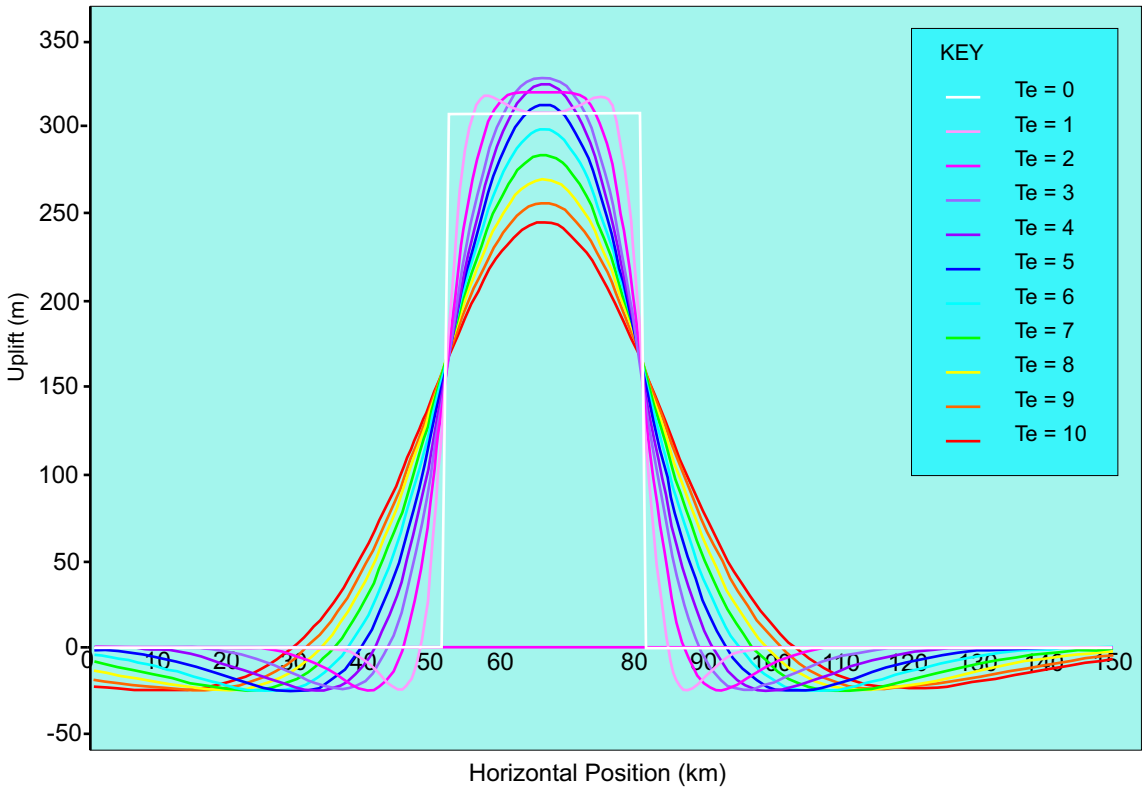


A Te of 0 km represents an Airy isostatic approach, with the compensation for the load occurring directly above the load. In general, the larger the elastic thickness, the broader the region over which loads are isostatically compensated. Uplift at the centre of the model decreases and uplift at the margins of the batholith increases.

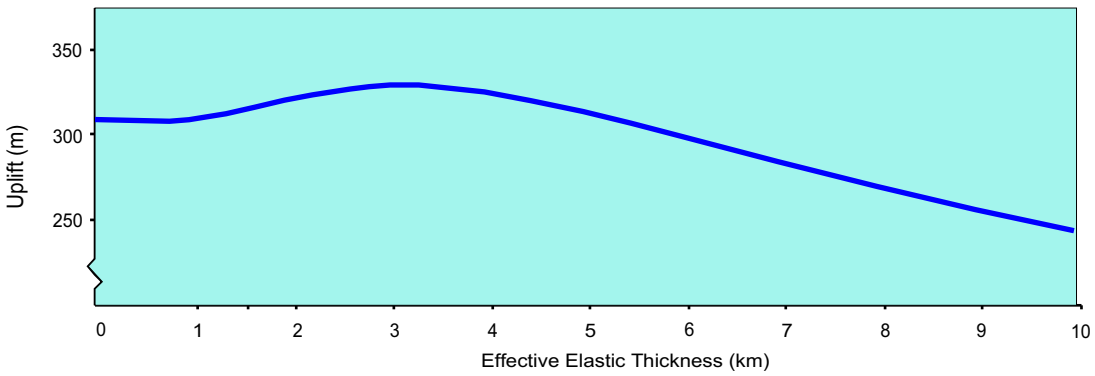


Initially the amount of uplift increases with increasing Te. At Te values greater than 3 km, uplift decreases with increasing Te.

Figure 6.25. The effect of effective elastic thickness (Te) upon the flexural isostatic response to an igneous intrusion. a) The profile of the flexural response at emplacement, t = 0 Ma. b) Isostatic response to intrusion with varying effective elastic thickness of the lithosphere at x = 66 km.

imposed upon the lithosphere and proportion of mantle material that is required to compensate for the load. The effect of varying the density contrast between the intrusion and the crust is achieved by varying the density of the igneous intrusion with a fixed crustal density of 2800 $kgm^{-3}$ and is shown in Figure 6.26. The result of increasing the density of the igneous intrusion leads to a reduction in the amount of uplift produced. At x = 66 km (Figure 6.26b), there is a decrease in uplift of 0.0018 km for every 1 $kgm^{-3}$ increase in intrusion density or for every 1 $kgm^{-3}$ decrease in density contrast between the crust and the intrusion.

#### 6.4.2.3 The effect of intrusion shape and area upon the isostatic response to igneous intrusions

Increasing the area of the igneous intrusion, results in an increase in the amount of negative loading on the lithosphere that results from emplacement of the intrusion and a corresponding increase in uplift. Figure 6.27 illustrates the results from modelling the effect of increasing the area of the batholith. This is achieved by increasing the height of the square, increasing the thickness of the batholith at any position of x. At the centre of the batholith, x = 66 km (Figure 6.27b), there is an increase of 0.051 km per 1 km increase in batholith thickness. At the edge of the batholith, x = 52 km, this effect is reduced to an increase of 0.025 km per 1 km increase in batholith thickness.

The shape of the batholith is responsible for the distribution of the lower density material of the intrusion within the crust and may determine where the effect of the batholith is greatest. Figures 6.28-6.30 illustrate

a)

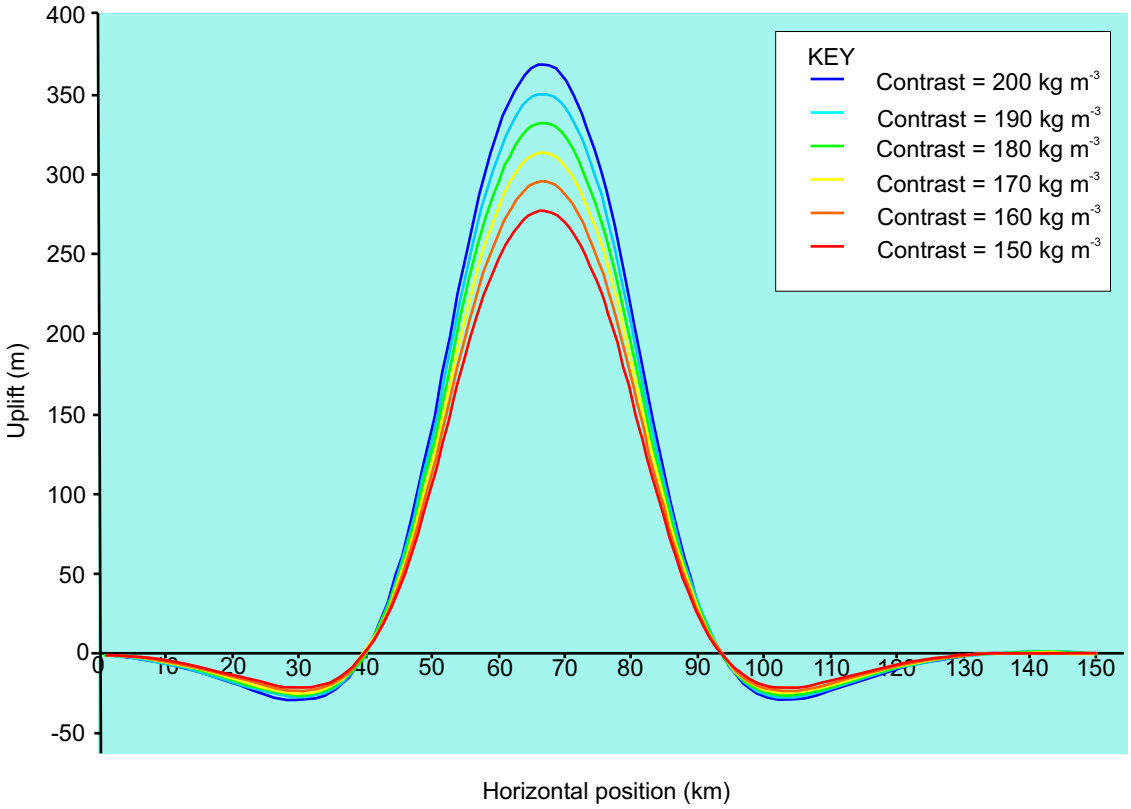


With increasing density contrast, the amount of uplift generated in response to the negative load imposed upon the lithosphere by the granite increases.

b)

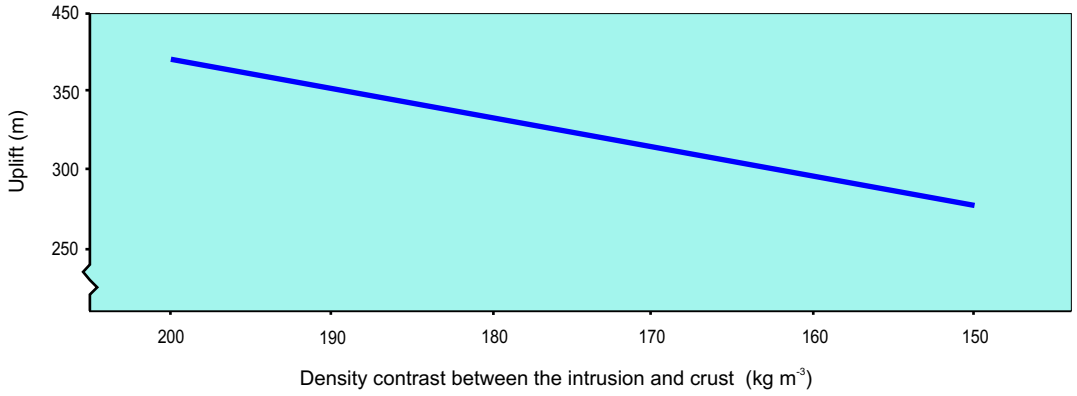


There is a linear relationship between the crust-intrusion density contrast and the amount of uplift generated in response to the intrusion. At x = 66 km, there is an increase in uplift of 0.0018 km for every 1 kgm$^{-3}$ increase in density contrast.

Figure 6.26. The effect of the density contrast between the granite intrusion and the crustal density ($\rho_c$- $\rho_g$) upon the flexural isostatic response to an igneous intrusion. a) The profile of the flexural response at emplacement, t = 0 Ma. b) Isostatic response to intrusion with varying density contrast at x = 66 km.

a)

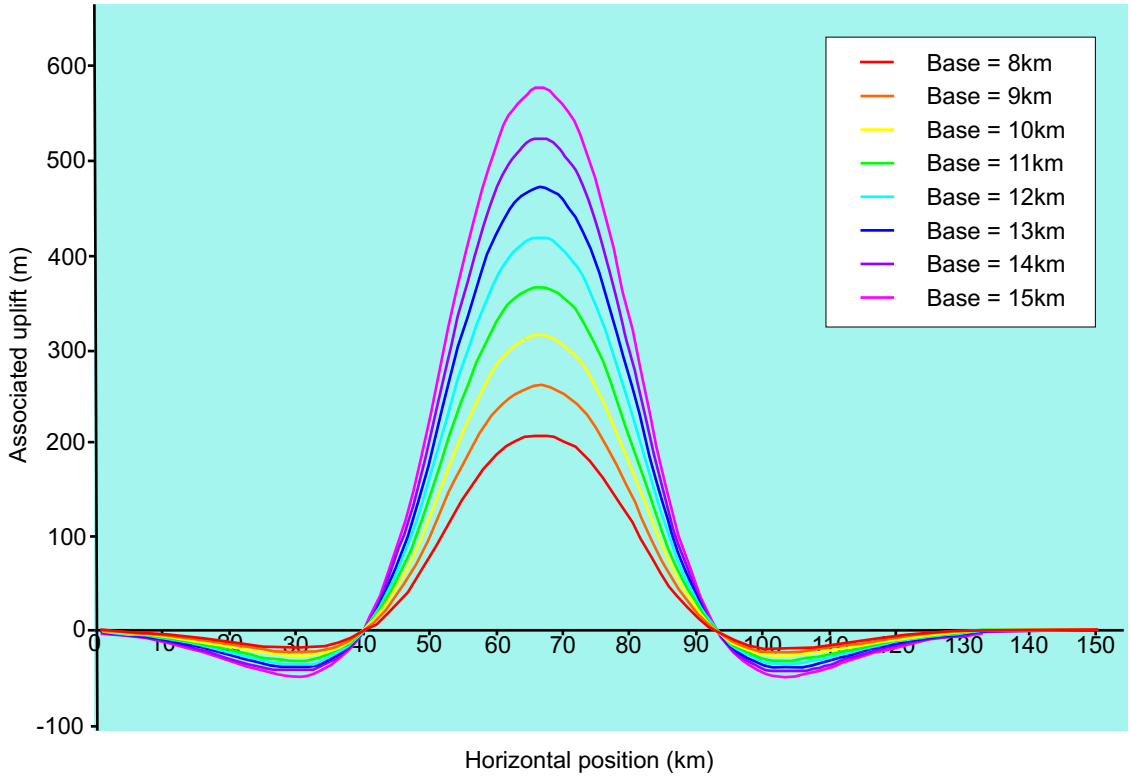


With increasing granite area (thickness), the amount of uplift generated in response to the negative load imposed upon the lithosphere by the granite increases.

b)

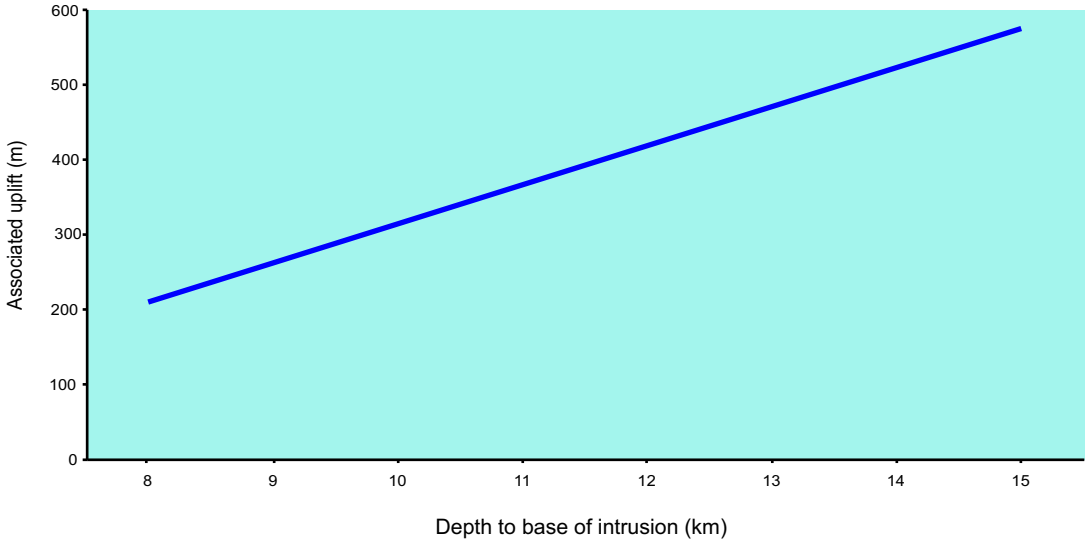


There is a linear relationship between the thickness of the granite body and the amount of uplift generated in response to the intrusion. At x = 66 km, there is an increase in uplift of 0.051 km for every 1 km increase in granite thickness.

Figure 6.27. The effect of the size of the granite intrusion upon the flexural isostatic response to an igneous intrusion. a) The profile of the flexural response at emplacement, t = 0 Ma with increasing thickness. b) Isostatic response to intrusion with varying thickness of intrusion at x = 66 km.

the results from modelling the influence of the varying shape of the batholith.

Figure 6.28 shows the isostatic response to an intrusion whose top surface slopes from one edge to the other. The distribution of the flexural response has a smaller wavelength and greater amplitude than the average box shaped intrusion of the same total area (Figure 6.28b). The peak is also skewed towards the thickest part of the batholith, where the area of the column is greatest. The deviation from the average (Figure 6.28c) is greatest where the thickness of the batholith is reduced to the greatest extent (i.e. x = 80 km).

Figure 6.29 illustrates the isostatic response to varying the shape of the intrusion such that it is narrowest in the centre and thickest towards the margins. This results in a flexural response distribution that has a greater amplitude and slightly smaller wavelength than the average box shaped intrusion of equal total area (Figure 6.29b). The deviation from the average is greatest at the centre of the batholith, where the response is greater (Figure 6.29c).

Figure 6.30 illustrates the effect of an intrusion with a variable surface modelled from gravity data over the Alston Block. The shape of the batholith is taken from cross-section G-G'. The resultant distribution has a smaller wavelength and greater amplitude than the average boxed shaped granite of the same total area. Additionally the peak in the distribution of the flexural response is skewed towards the area where the batholith is thickest (Figure 6.30b). The greatest deviation from the average occurs

a)

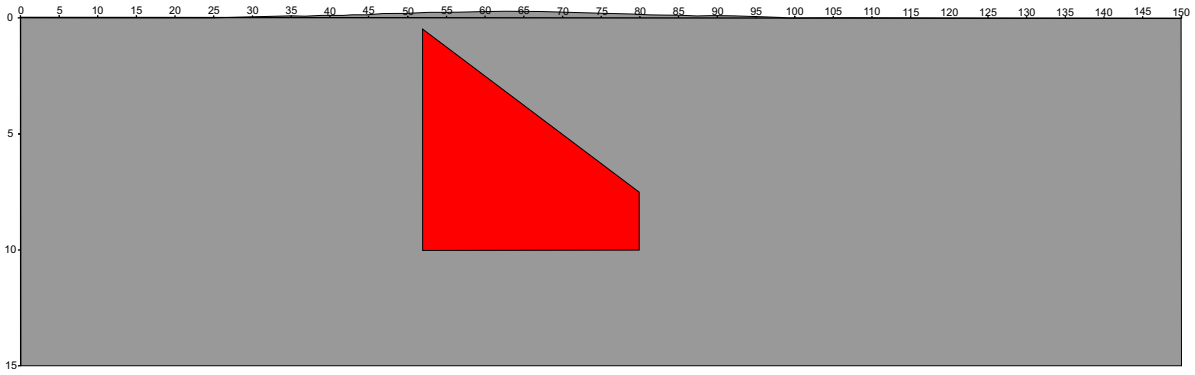

b)

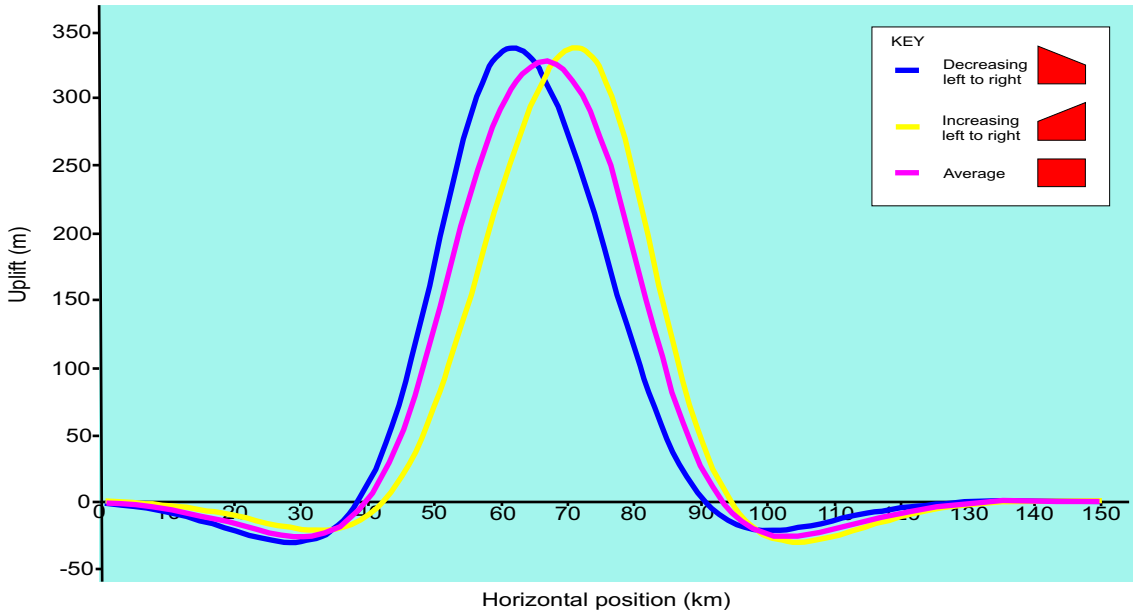


c)

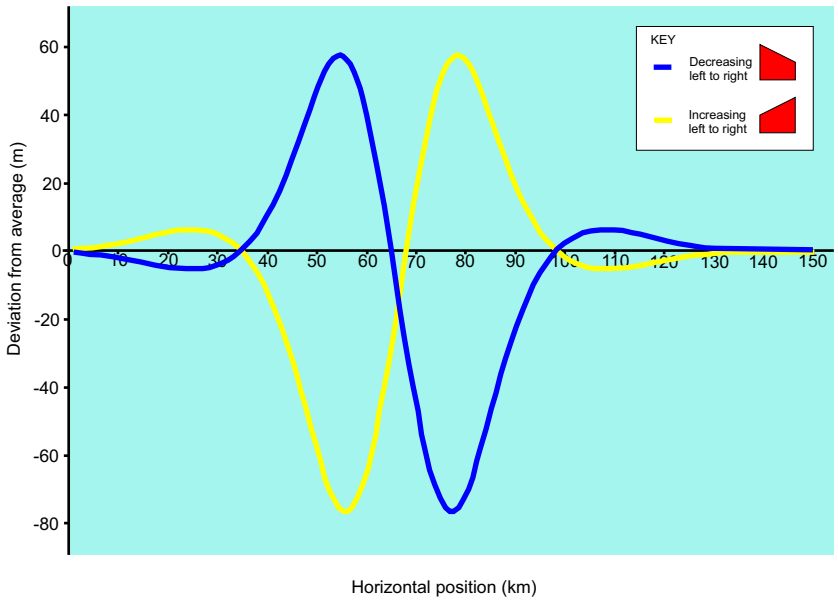


Figure 6.28. The effect of varying the shape of the top of the batholith on the flexural isostatic response to igneous intrusion. a) Model of granite intrusion with top that slopes from left to right. b) The flexural response to a batholith with a sloping top. c) Deviation of flexural response from average box shaped granite.

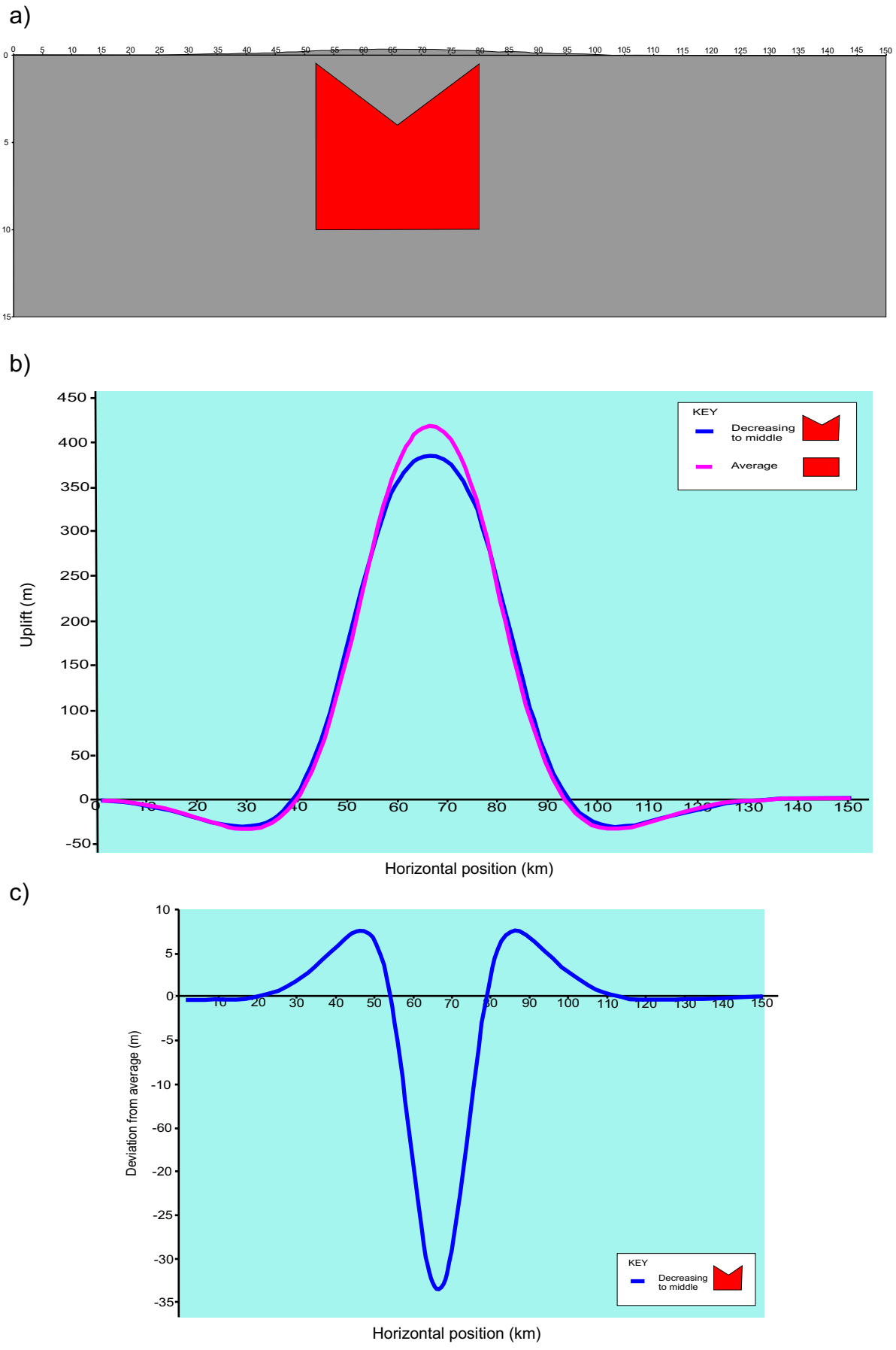


Figure 6.29. The effect of varying the shape of the top of the batholith on the flexural isostatic response to igneous intrusion. a) Model of granite intrusion that thins from the margins to the centre in both directions. b) The flexural response to a batholith with a sloping top. c) Deviation of flexural response from average box shaped granite.

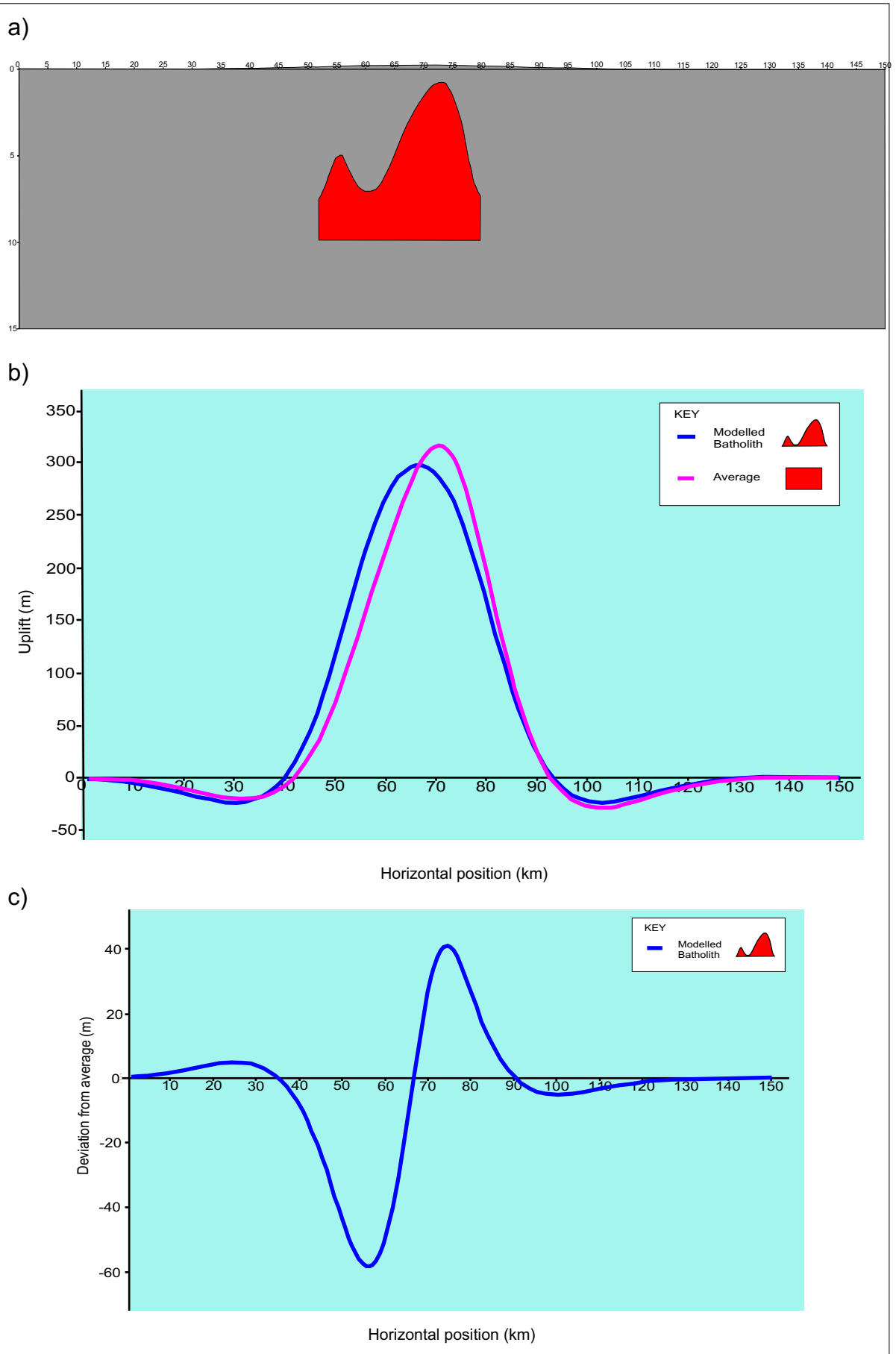


Figure 6.30. The effect of varying the shape of the top of the batholith on the flexural isostatic response to igneous intrusion. a) Model of granite with shape of top granite in cross-section G-G'. b) The flexural response to a batholith with a varying shape top. c) Deviation of flexural response from average box shaped granite.

where the thickness of the batholith is less than the average (Figure 6.30c).

### *6.4.3 Implications for the Northumberland Trough Region*

The modelling approach detailed in section 6.4.1 has been applied to the Northumberland Trough Region in order to provide insights into the influence of the North Pennines Batholith on the structural development of the region post-emplacement. Analysis of the initial model of cross-section G-G' (section 6.2.2) indicates that the model reconciled the amount of extensional deformation generated with the amount of subsidence observed within the basin structures of the cross-section. However, over the Alston Block the amount of subsidence generated by the model exceeded the amount of subsidence observed in the cross-section by a considerable amount. It is hypothesised that incorporating the effect of the North Pennines Batholith into the model of the Northumberland Trough Region will allow for the production of models that reconcile the amount of subsidence across the Alston Block as well as within the basin structures.

The shape and position of the top of the North Pennines Batholith is well constrained by gravity and seismic data interpretations (chapter 3). The base of the intrusion is less well constrained. Estimates have been made based on the available subsurface data. Seismic data provides the best insights into the position of the base of the granite with reflective lower crust present at between 5 and 6 seconds two way travel time, indicating a depth to the base of the batholith of approximately 10 km (Chadwick and Evans, 2005) which has been adopted as the base of the granite within the

model. The pattern of density variation across the batholith is inferred from the density of samples, which show small variations around the average value of 2630 $kgm^{-3}$ (Bott, 1967), which is assumed within the model.

#### 6.4.3.1 Cross-section D-D'

Cross-section D-D' (Figure 3.8) crosses the Northumberland Trough, Alston Block and Vale of Eden Basin on its western margin. This cross-section passes over 3 cupolas of the North Pennines Batholith, these are the western extent of the main cupola to the north of the section, the Tynehead cupola in the centre and the Scoredale cupola to the south. The top of the batholith reaches a minimum depth of 2 km beneath the basement of the Alston Block. Figure 6.31 illustrates model profiles of cross-section D-D', both with and without the granite intrusion at t = 0 Ma after extension. Within the Northumberland Trough, both models produce a maximum basin depth of 3.1 km.

Without the presence of the North Pennines Batholith, the basement of the Alston Block attains its maximum uplift at the margins where footwall uplift has the greatest influence. The northern margin is uplifted to 0.29 km above sea level, whereas uplift on the southern margin is slightly greater at 0.32 km above sea level. In the centre of the block, the basement is at sea level.

When the North Pennines Batholith is introduced into the model, between x = 45 km and x = 76 km, uplift of the Alston Block above sea level is

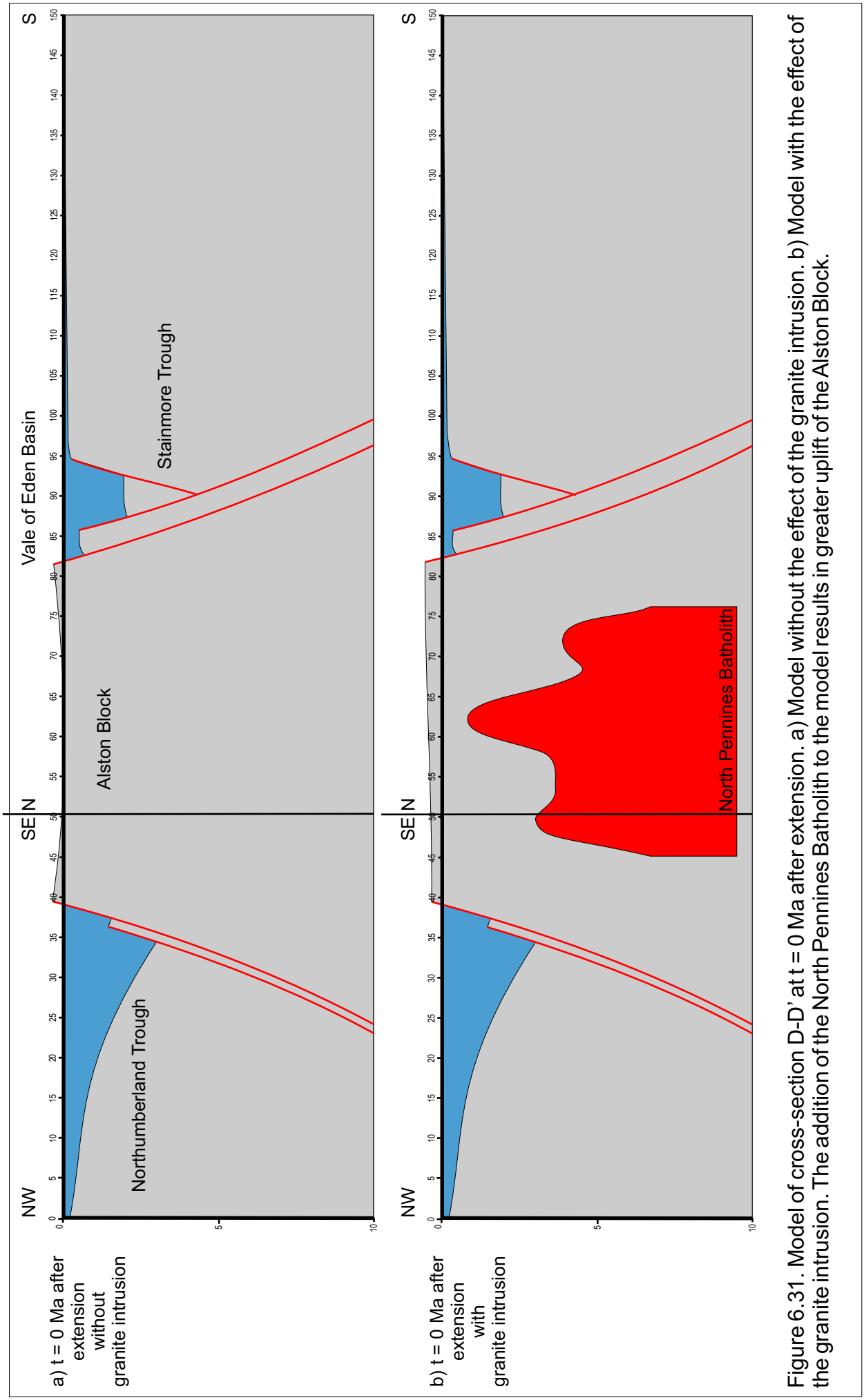


Figure 6.31. Model of cross-section D-D' at t = 0 Ma after extension. a) Model without the effect of the granite intrusion. b) Model with the effect of the granite intrusion. The addition of the North Pennines Batholith to the model results in greater uplift of the Alston Block.

increased. The height of the Alston Block varies between 0.37 km (at x = 39 km) and 0.54 km (at x = 67 km).

Figure 6.32 illustrates the results of modelling cross-section D-D' at t = 360 Ma after extension both with and without the effect of the North Pennines Batholith. The maximum depth of the Northumberland Trough in the cross-section is 5.2 km. In the model without the intrusion, the Northumberland Trough has a maximum depth of 5.7 km. In the model with the intrusion, the maximum depth is 5.5 km. These values are within 10% and 7% of the cross-section data respectively. Within the Stainmore Trough/Vale of Eden Basin, the cross-section has a maximum depth of 2.39 km (within the Vale of Eden Basin).

The model without the granite intrusion has a maximum depth of 3 km within the Vale of Eden Basin, 30% greater than the observed maximum depth. In the granite model, the maximum depth is 2.6 km, within 9% of the observed depth. Over the Alston Block, the basement of the non-granite model reaches a maximum depth of 2.2 km at x = 58 km. This is 665% greater than the 0.28 km subsidence observed within the cross-section.

In the granite model, the basement of the Alston Block reaches a maximum depth of 1.84 km at the northern margin of the block. This is 6% greater than observed. Between x = 58 km and x = 80 km the subsidence produced within the model is between 2 and 12% greater than the observed subsidence. In the observed data the basement of the Alston Block decreases in depth from 1.84 at x = 58 km to 0.34 km at x = 52 km.

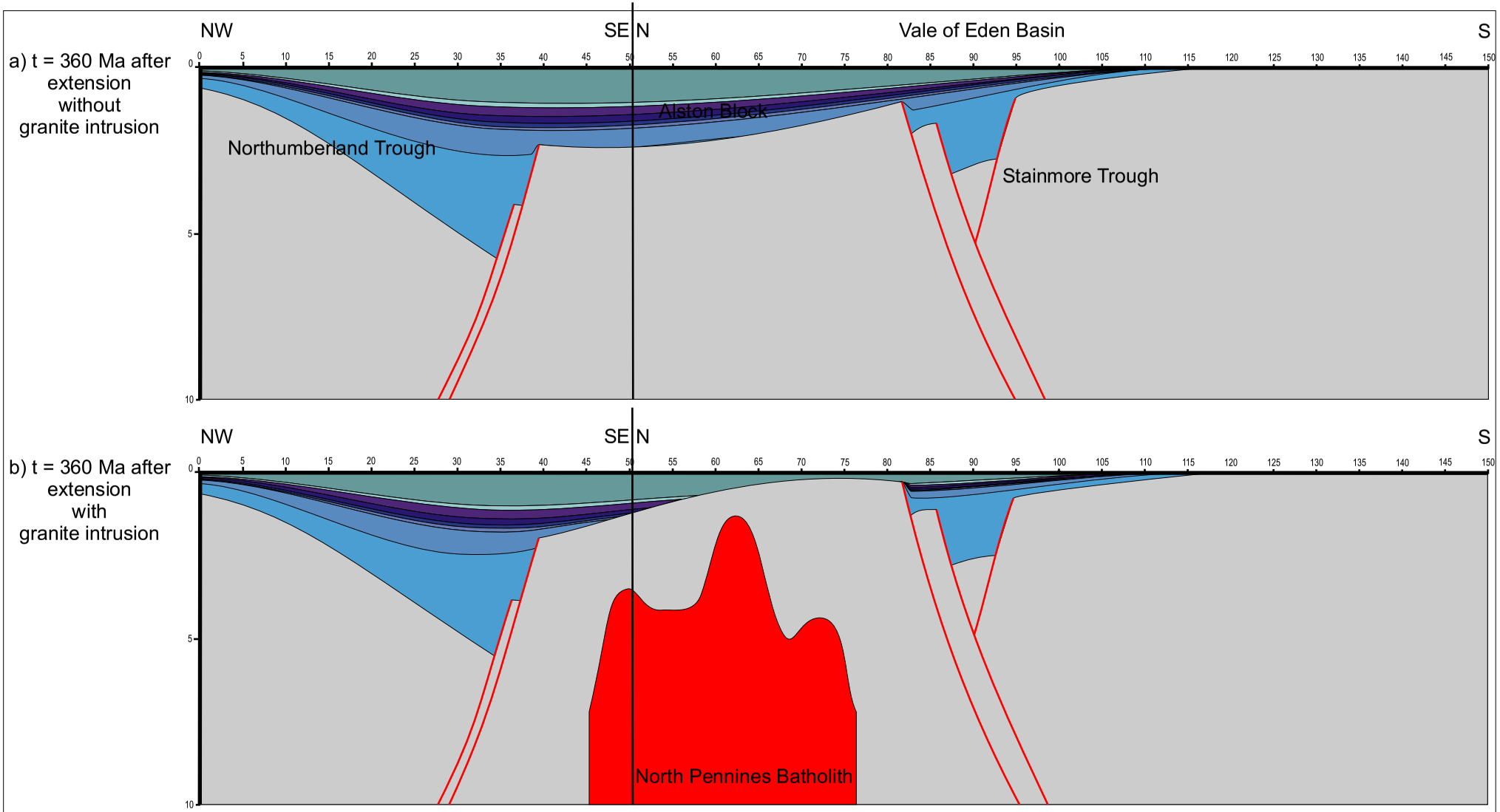


Figure 6.32. Model of cross-section D-D' at t = 360 Ma after extension. a) Model without the effect of the granite intrusion. b) Model with the effect of the granite intrusion. The presence of the North Pennines Batholith results in greater uplift across the Alston Block, resulting in a better correlation between the observed and modelled depths to the basement.

At this point the depth of the basement within the granite model is 1 km, 200% greater than the observed depth. These results suggest that the granite may have a greater influence between x = 45 and x = 58 km than that produced by the model.

#### 6.4.3.2 Cross-section F-F'

This cross-section (Figure 3.11) concentrates upon the Alston Block and its margins with the Northumberland Trough to the north and the Stainmore Trough to the South. This section crosses the centre of the Alston Block from North to South and contains the main cupola of the North Pennines Batholith. The depth to the top of the batholith varies from 1.5 km to 0.2 km beneath the basement of the Alston Block. Figure 6.33 illustrates the model at t = 0 Ma after extension. With the presence of the North Pennines Batholith beneath the basement (Figure 6.33b) the model generates 0.41 km of uplift in the centre of the block, 0.25 km at the northern margin and 0.8 km at the southern margin. Figure 6.34 illustrates the model of cross-section F-F' at t = 360 Ma after extension. The model containing the granite batholith (Figure 6.34b) produces 0.9 km less subsidence at the centre of the Alston Block than the model without the granite batholith (Figure 6.34a), resulting in a basement depth of 0.04 km at x = 25 km, within 5% of the observed basement depth of 0.46 km at x = 25 km within the cross-section F-F'.

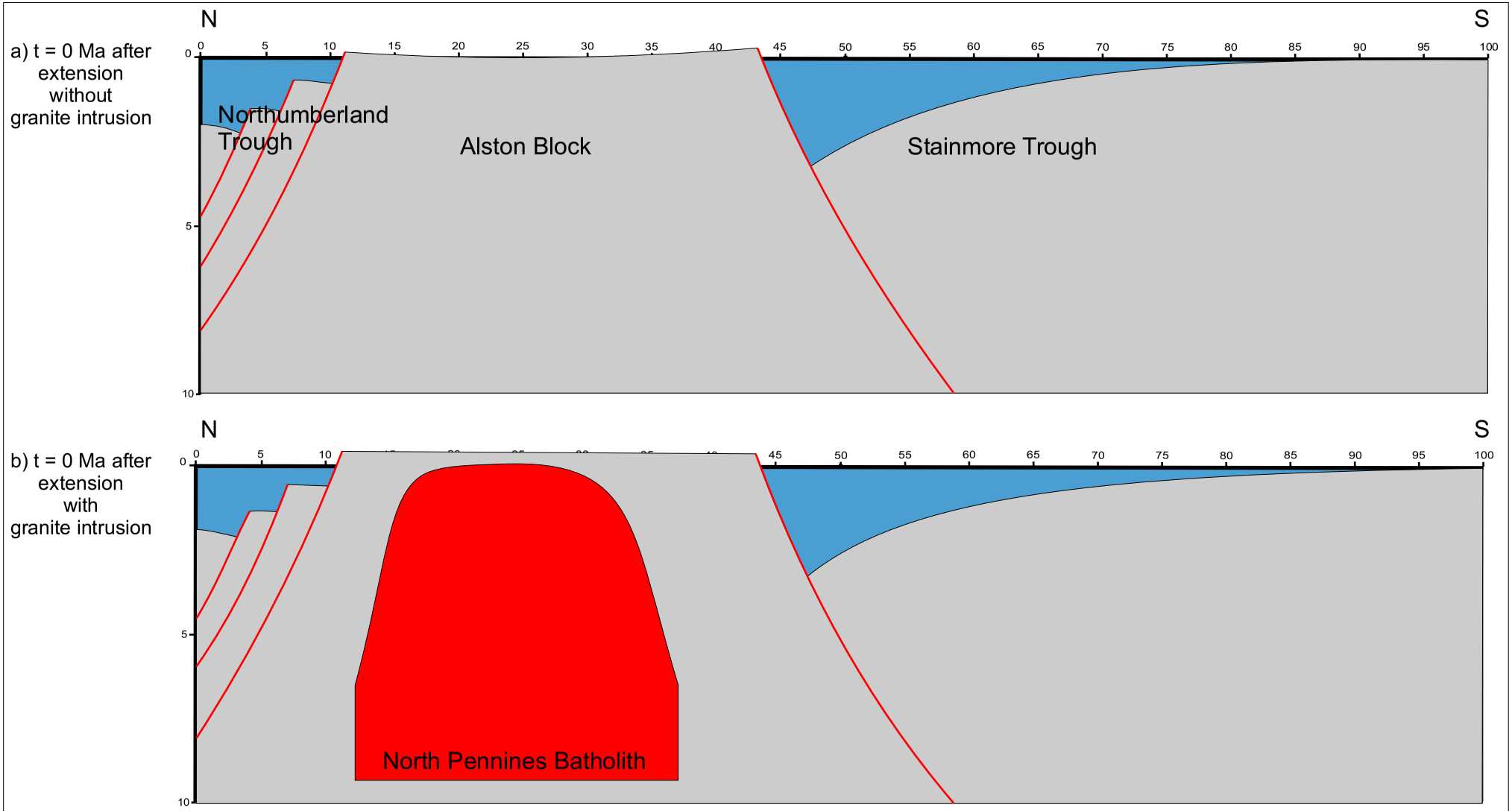


Figure 6.33. Model of cross-section F-F' at t = 0 Ma after extension. a) Model without the effect of the granite intrusion. b) Model with the effect of the granite intrusion. The addition of the North Pennines Batholith to the model results in greater uplift, concentrated in the centre of the Alston Block.

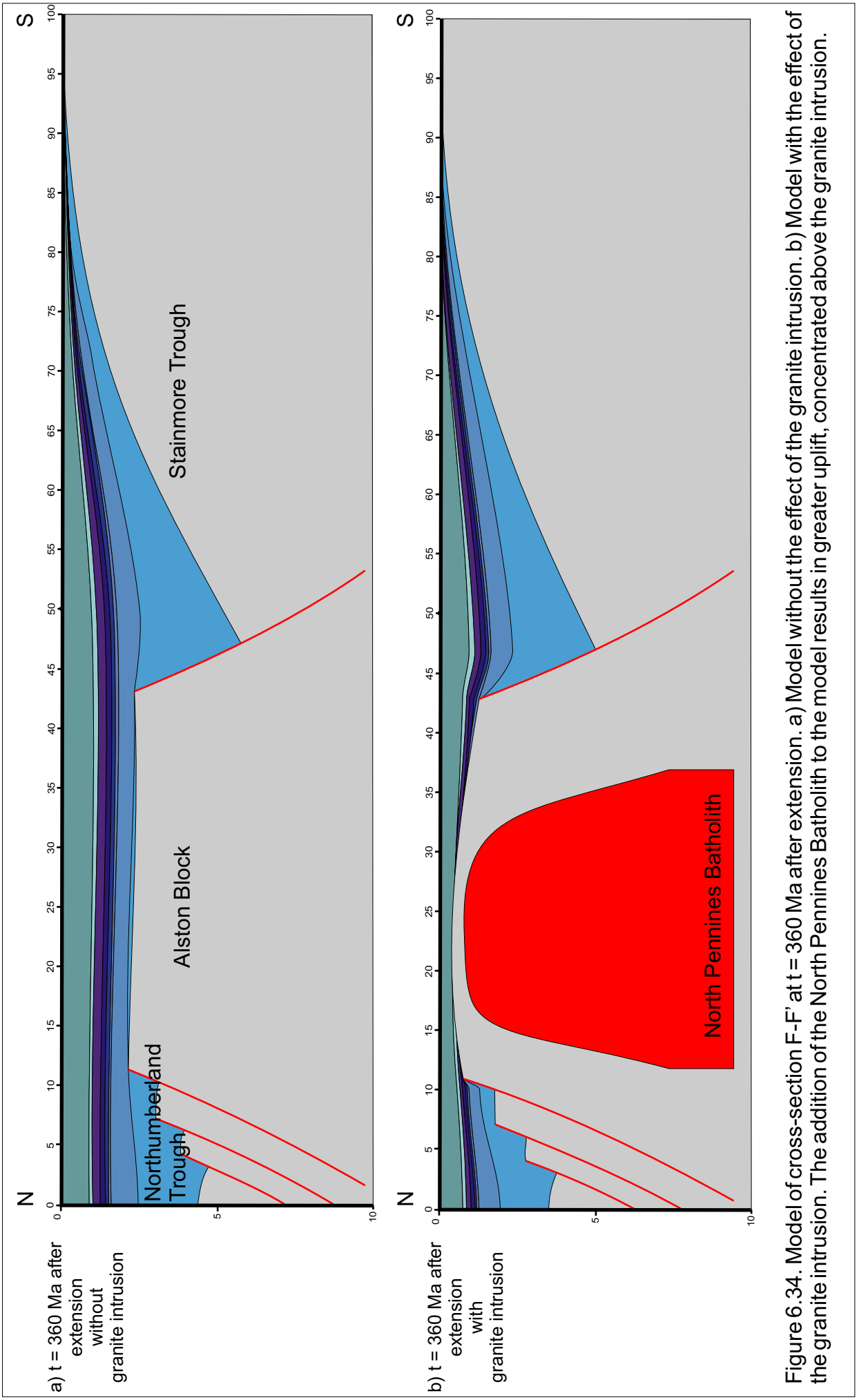


Figure 6.34. Model of cross-section F-F' at t = 360 Ma after extension. a) Model without the effect of the granite intrusion. b) Model with the effect of the granite intrusion. The addition of the North Pennines Batholith to the model results in greater uplift, concentrated above the granite intrusion.

#### 6.4.3.3 Cross-section G-G'

Analysis of the initial model of this cross-section produced subsidence of the block that was 0.5 km greater than observed within the cross-section. This section crosses the western edge of the Rowlands Gill cupola to the north and the centre of the Cornsay cupola to the south. The top of the northern cupola has a minimum depth of 5 km beneath the basement and the southern cupola has a minimum depth of 1.5 km beneath the basement. Figure 6.35 illustrates the model of cross-section G-G' at t = 0 Ma after extension. The addition of the batholith uplifts the block above sea level across its entire extent (Figure 6.35b). The uplift of the block is greatest towards the south where the greater area of batholith is present.

Figure 6.36 illustrates the model of cross-section G-G' at t = 360 Ma after extension. The presence of the batholith generates a significant amount of uplift to produce an uplift-subsidence pattern across the Alston Block that is comparable to that observed within the cross-section. This is demonstrated by the configuration of stratigraphy of which the earliest deposits are of the Tyne Limestone Formation and occur upon the north of the block.

#### 6.4.3.4 Cross-section H-H'

This cross-section (Figure 3.13) crosses the eastern edge of the Alston Block. The North Pennines Batholith beneath this cross-section represents the eastern edge of the Rowlands Gill and Cornsay cupolas. The two cupolas are of roughly equal size beneath this cross-section with a

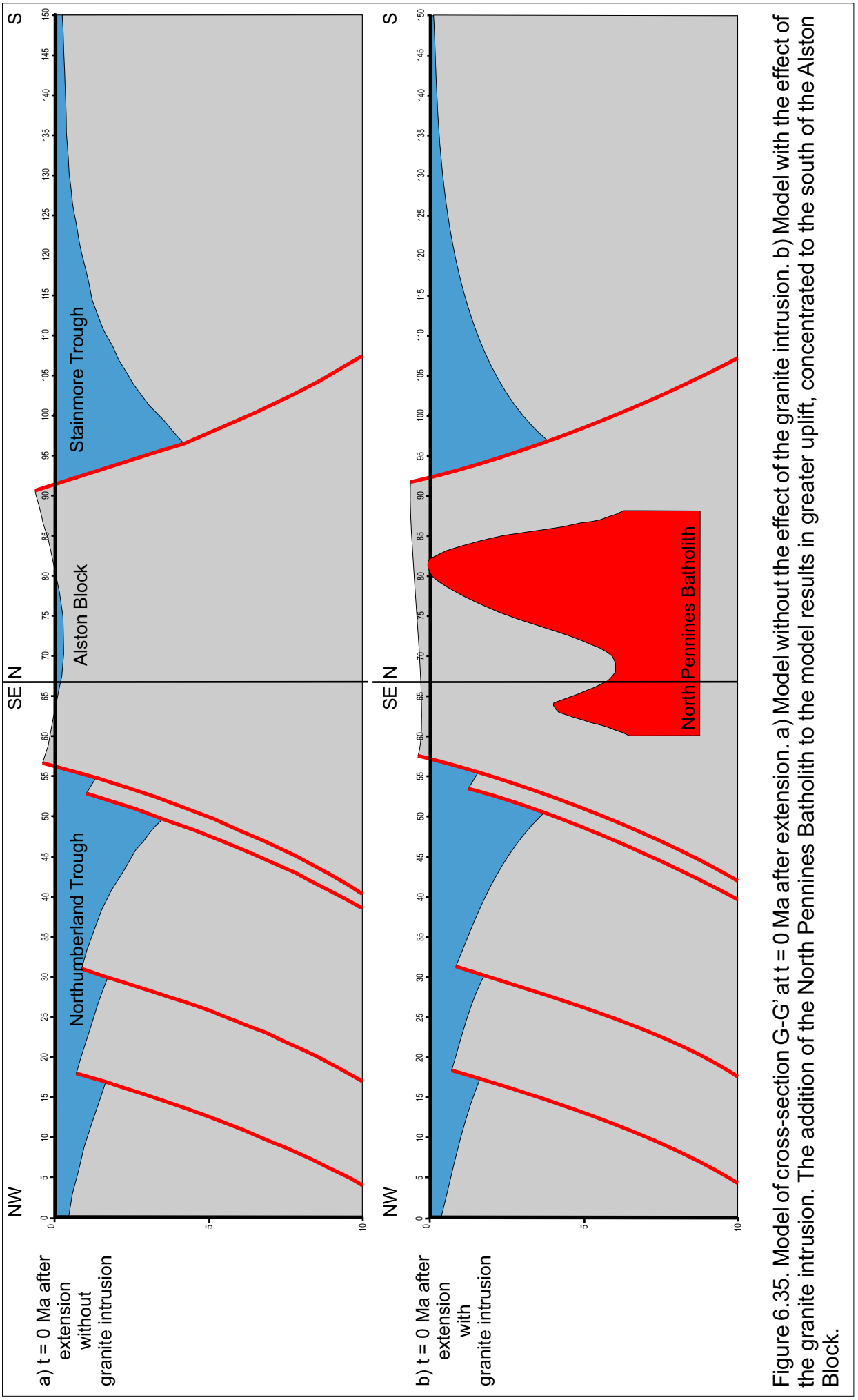


Figure 6.35. Model of cross-section G-G' at t = 0 Ma after extension. a) Model without the effect of the granite intrusion. b) Model with the effect of the granite intrusion. The addition of the North Pennines Batholith to the model results in greater uplift, concentrated to the south of the Alston Block.

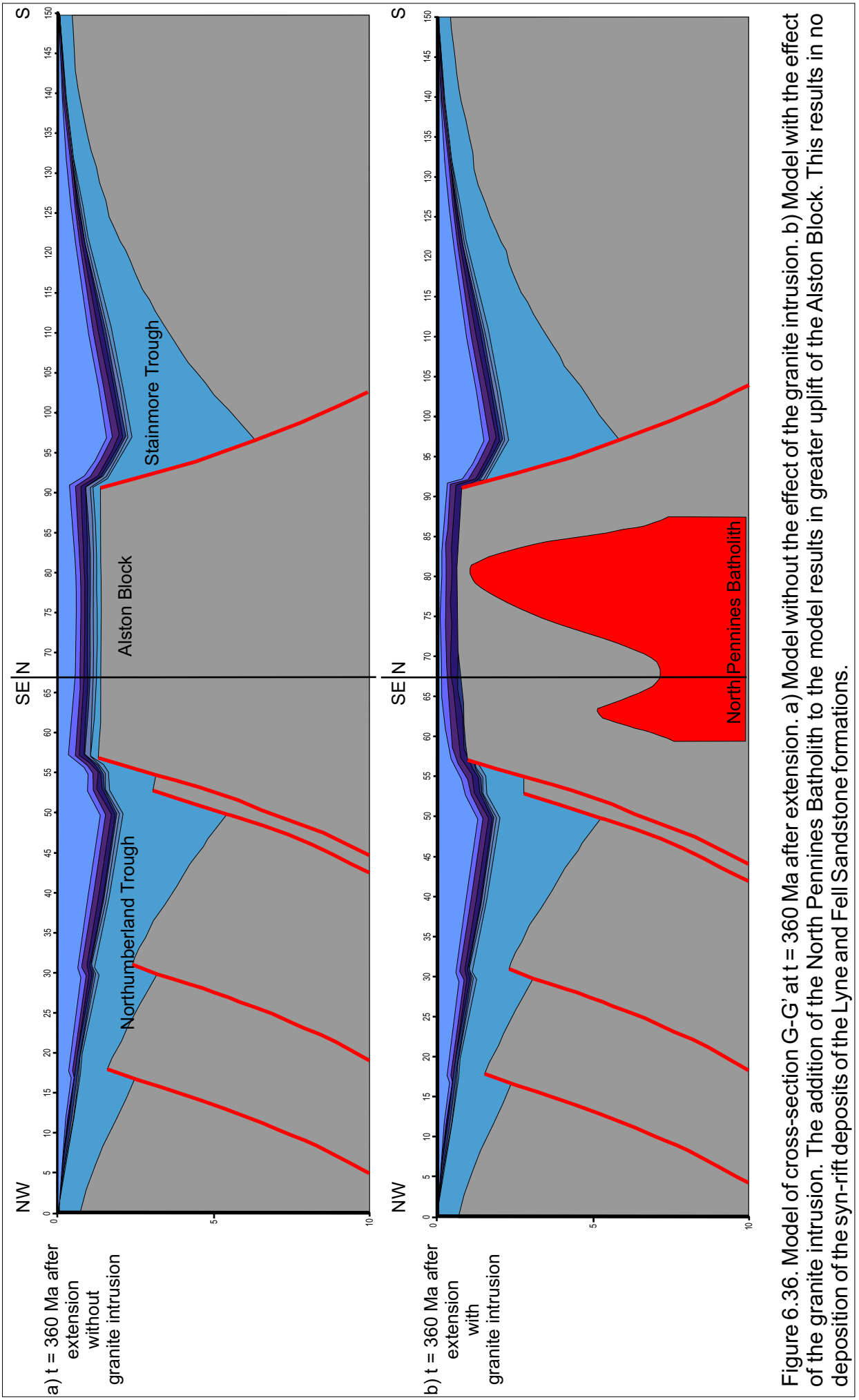


Figure 6.36. Model of cross-section G-G' at t = 360 Ma after extension. a) Model without the effect of the granite intrusion. b) Model with the effect of the granite intrusion. The addition of the North Pennines Batholith to the model results in greater uplift of the Alston Block. This results in no deposition of the syn-rift deposits of the Lyne and Fell Sandstone formations.

minimum depth to the top of the batholith of 5 km, separated by a small dip. Figure 6.37 illustrates the model of cross-section H-H' at t = 0 Ma after extension. The North Pennines Batholith uplifts Alston Block by 0.26 km at the centre (x = 62 km), where its effect is greatest. Figure 6.38 illustrates the model of cross-section H-H' at t = 360 Ma after extension. The granite model (Figure 6.38a) produces 1 km less subsidence at x = 62 km than the non-granite model (Figure 6.38b). However, this is still 0.4 km greater than the subsidence observed in cross-section H-H' at this locality. From the syn-rift deposits upon the Alston Block within the H-H' cross-section, it can be deduced that the effect of the North Pennines Batholith upon the Alston Block is starting to be reduced as the volume of granite is reduced. However the effect is not as reduced as the model results suggest. This could be a result of the rest of the granite body to the west, out of the plane of this section, having a flexural isostatic effect upon this section that is not modelled.

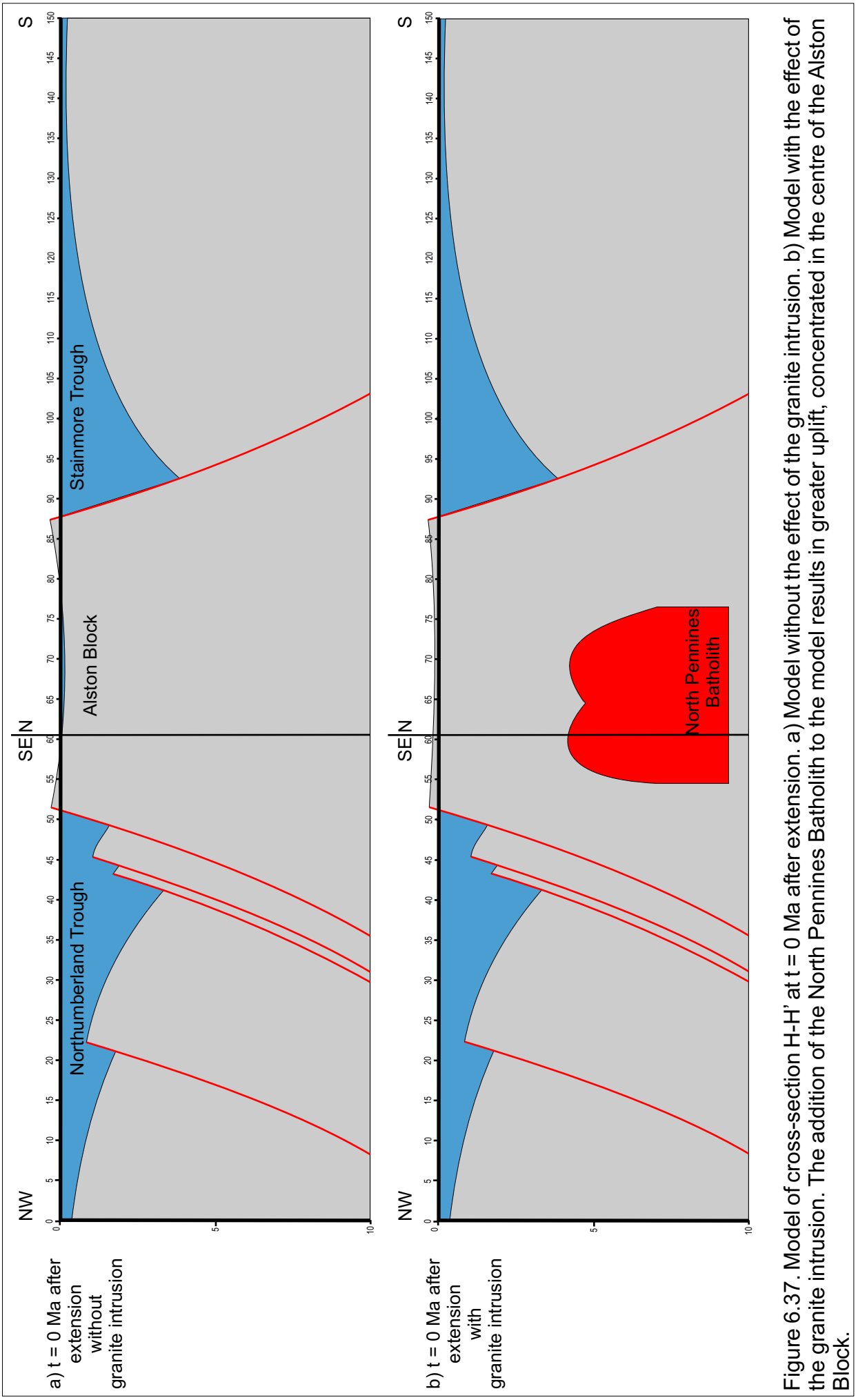


Figure 6.37. Model of cross-section H-H' at t = 0 Ma after extension. a) Model without the effect of the granite intrusion. b) Model with the effect of the granite intrusion. The addition of the North Pennines Batholith to the model results in greater uplift, concentrated in the centre of the Alston Block.

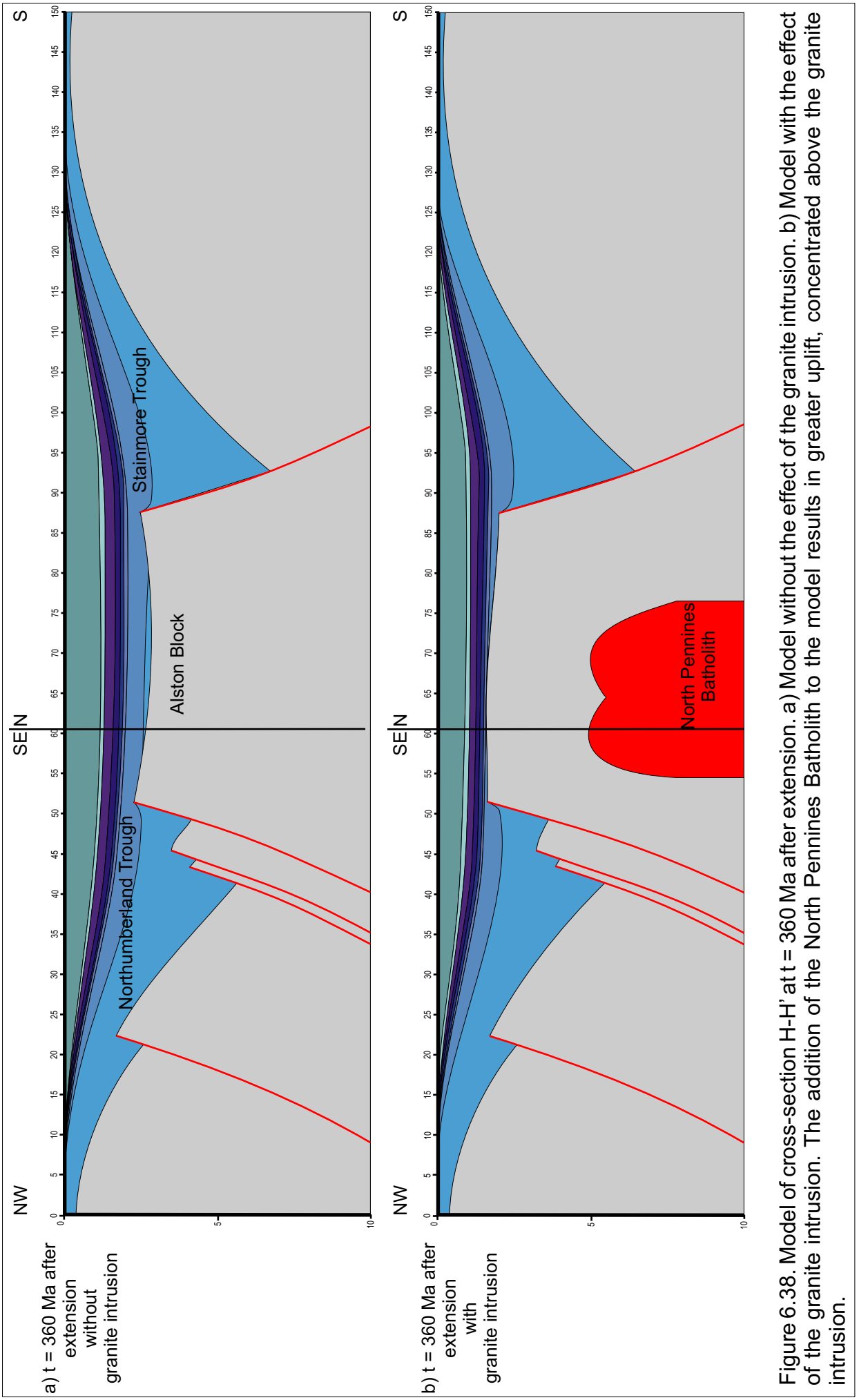


Figure 6.38. Model of cross-section H-H' at t = 360 Ma after extension. a) Model without the effect of the granite intrusion. b) Model with the effect of the granite intrusion. The addition of the North Pennines Batholith to the model results in greater uplift, concentrated above the granite intrusion.

# 7 Three-dimensional modelling of the Northumberland Trough Region

It is an inherent weakness of the two-dimensional approach to modelling flexural isostasy that the model assumes that the lithosphere perpendicular to the plane of section is infinite with constant physical properties that do not influence the flexural response to loading within the section.

The regional nature of the flexure of the lithosphere in response to loading ensures that, at any point within the lithosphere, loading imposed by the processes associated with extension will have an effect upon the basement surrounding it in three-dimensions. As a result, two-dimensional models tend to result in greater uplift in response to extension than three-dimensional models (Hodgetts *et al.*, 1998).

The data within this project, described in chapter 3, has been analysed within a three-dimensional co-ordinate frame such that the data can be interpolated to provide input parameters for the three-dimensional aspect of the research. A representative three-dimensional model has been produced from the seismic and borehole data using GoCAD, a computer aided design application. This allows for a regional interpretation of the data to be carried out. This research also employs an integrated three-dimensional lithosphere modelling technique developed by Meredith (2003) to consider the implications of a three-dimensional flexural response on the evolution of the Northumberland Trough Region.

## 7.1 Summary of the regional geology of the Northumberland Trough Region in three-dimensions

GoCAD is a geological object computer aided design program that has been used in this project to produce a three-dimensional model representative of the present day structure of the Northumberland Trough region. Data from the seismic interpretation, boreholes and cross-sections have been included in the form of point data with x, y and z attributes applied to them, where x and y are Cartesian co-ordinates and z is depth.

Surfaces were produced from the data by selecting the outline profile of the surface and densifying the data within. A homogeneous triangles method was used to densify the data. This is achieved by constructing triangles that are homogeneous in size between the data points with known value. In some cases it was necessary to apply enforced adding points to add interpolated point data between the triangle borders in order to produce representative triangles.

Figure 7.1 illustrates each stratigraphical horizon within the model and how they combine in three-dimensions. The Northumberland Trough Region represents a system with a block and basin architecture. With this model it is possible to consider the evolution of each basin individually as well as in the context if the region as a whole.

### *7.1.1 Solway Basin*

Figure 7.2 demonstrates the Solway basin in three-dimensions. The development of the Solway Basin occurred as a result of displacement

a)

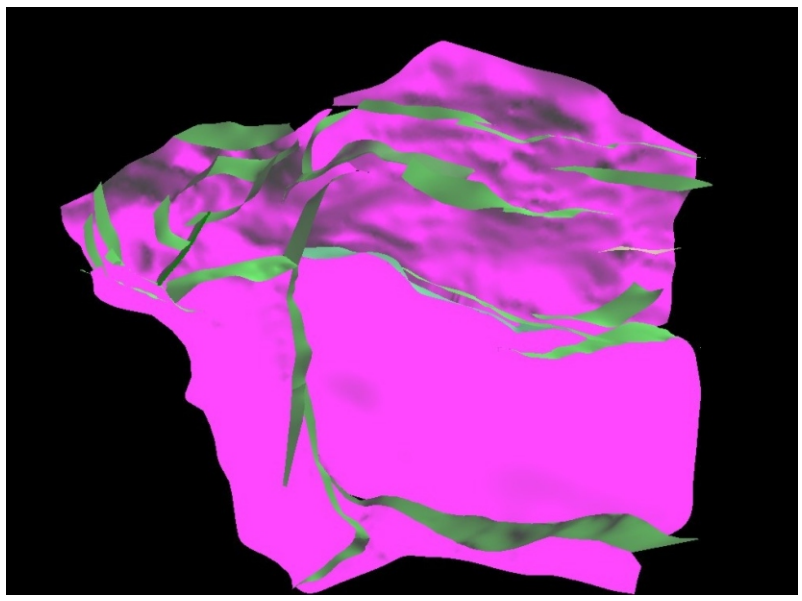

e)

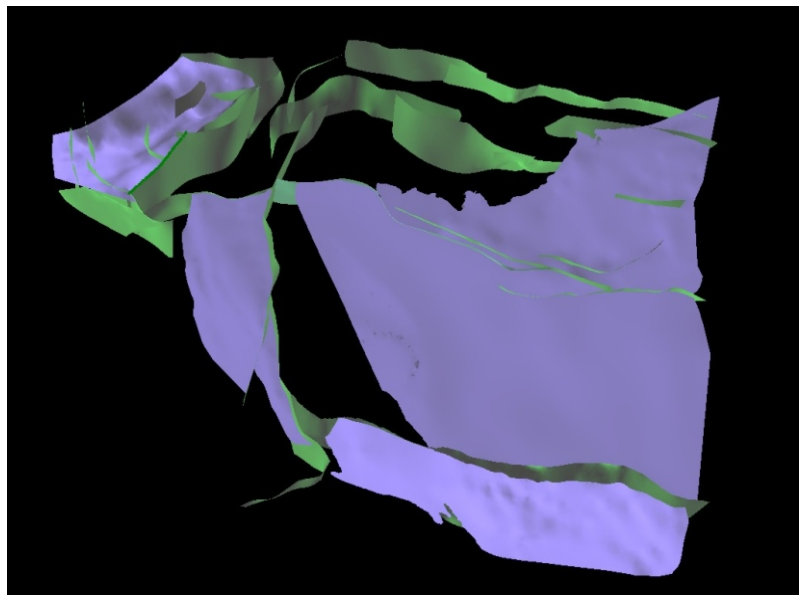

b)

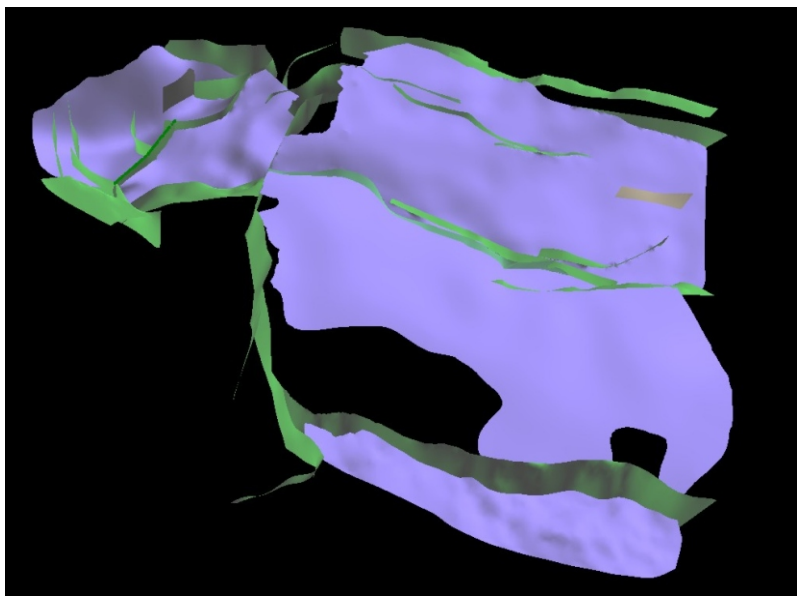

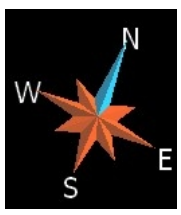


f)

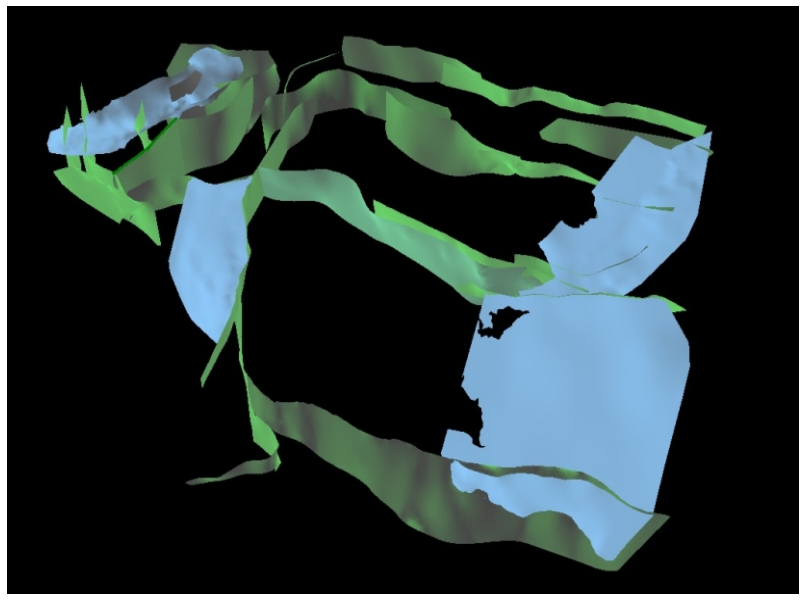

c)

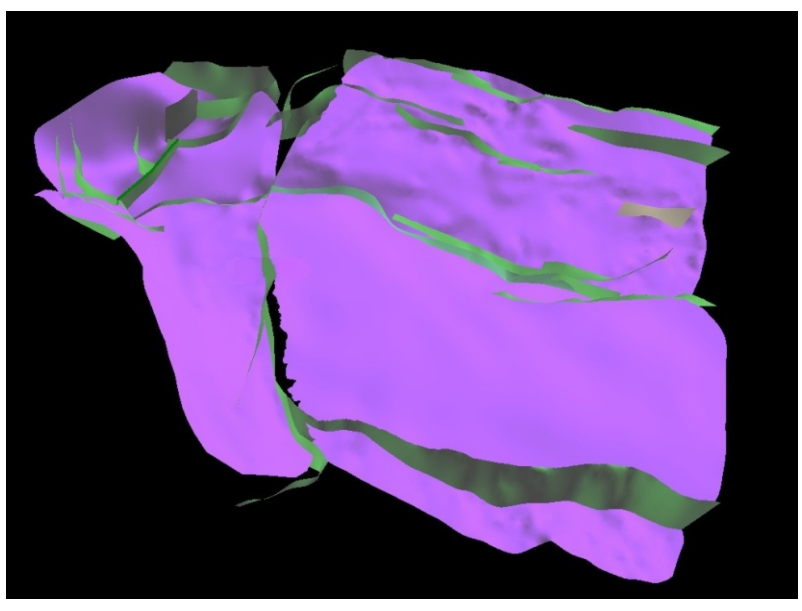

g)

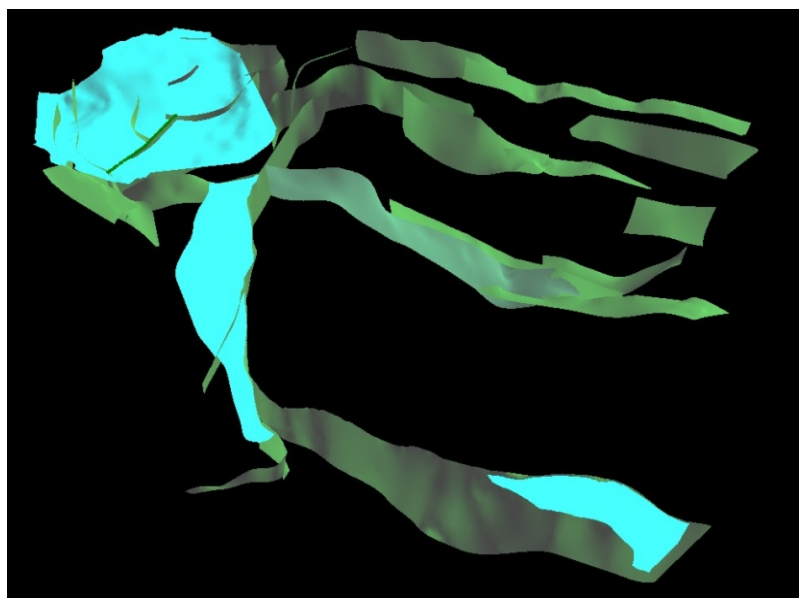

d)

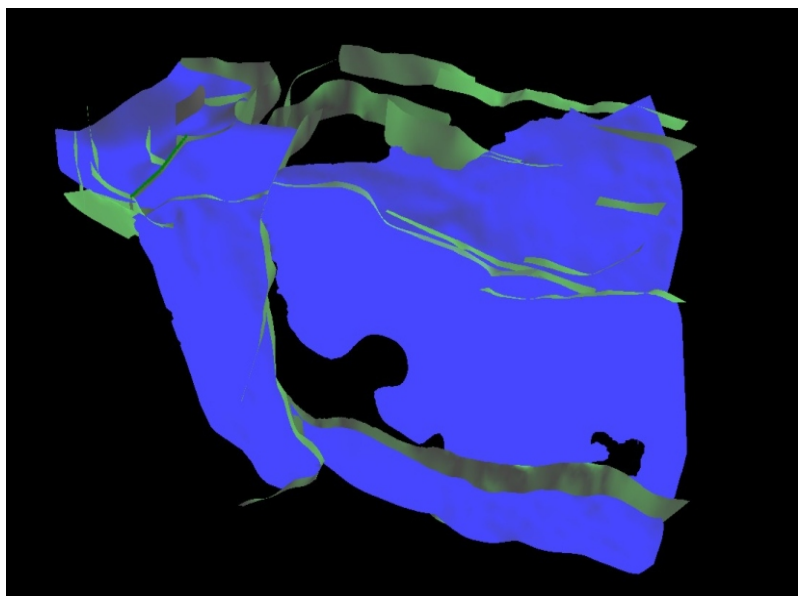

h)

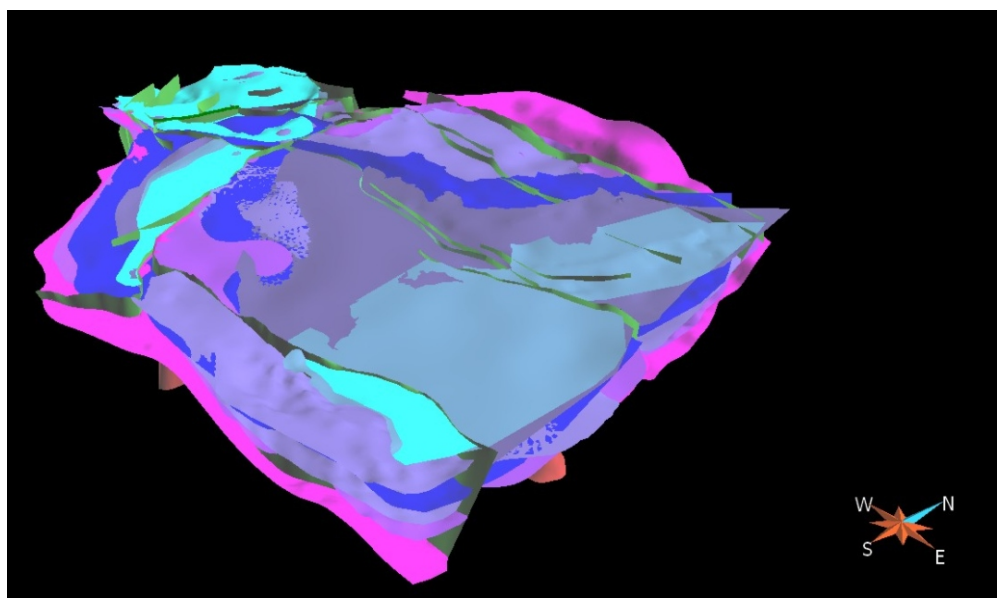


Figure 7.1. 3D representation of the Northumberland Trough Region. a) Pre-Carboniferous Basement b) Base Fell Sandstone Formation c) Base Tyne Limestone Formation d) Base Alston Formation e) Base Stainmore Formation f) Base Coal Formation g) Base Permo-Triassic h) Combined model of the Northumberland Trough Region.

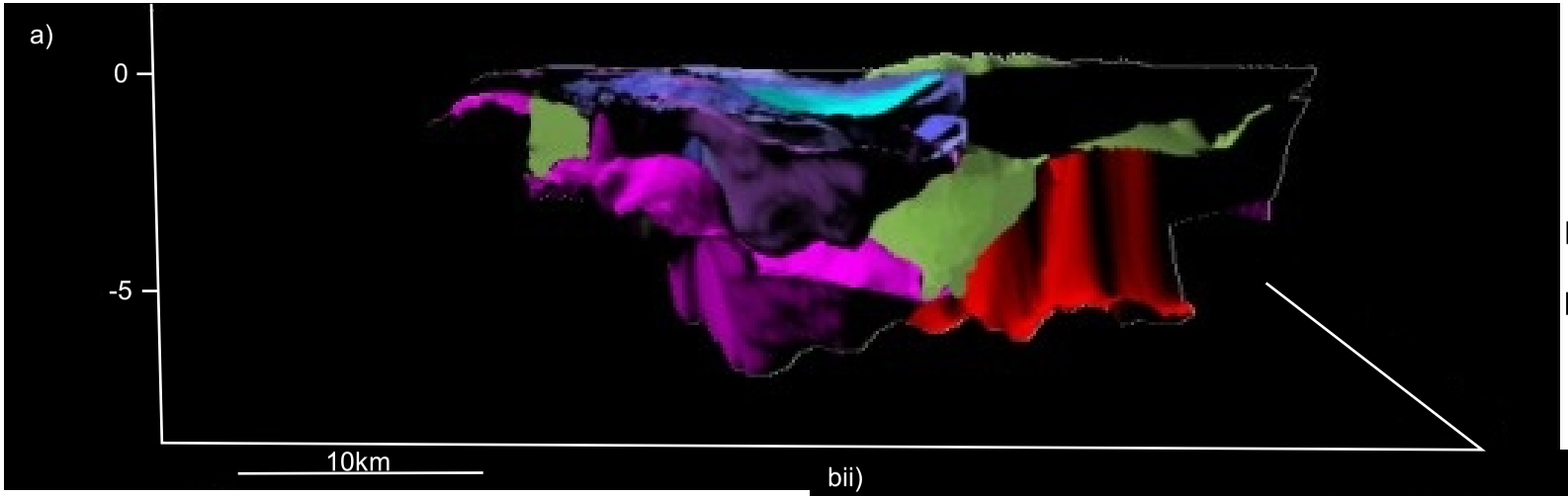


Figure 7.2. 3D representation of the Solway Basin. a) shows the Solway basin in the wider context of the Northumberland Trough Region. bi) contour map of the pre-Carboniferous basement with cut line. bii) slice through the 3D structure of the Solway basin.

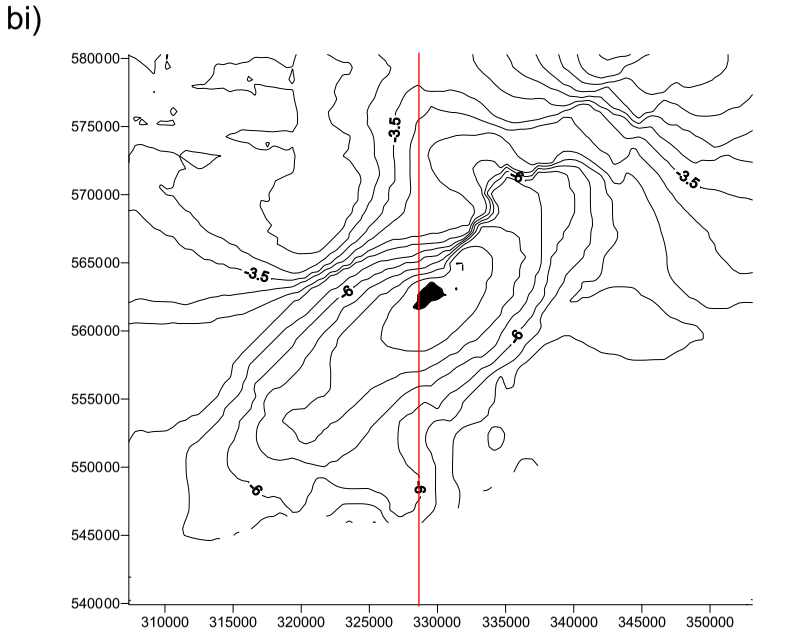


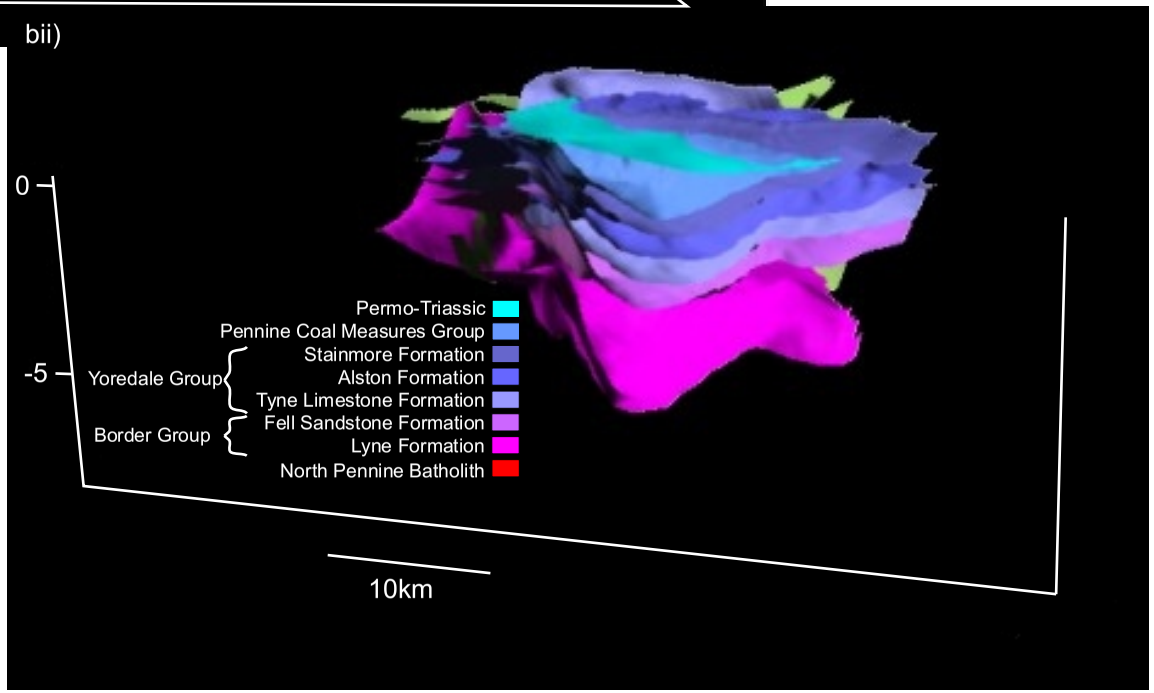

upon the Maryport Fault and its en-echelon continuations, the Waver-Warnall Fault and the Thornthwaite Fault, generating an asymmetrical half-graben. Extension of the northern margin of the basin occurs on faults with dips that are antithetic to the main northwards-dipping basin-bounding faults, for example the Gilknockie Fault. These faults accommodate less extension than the faults at the southern margin and generate an asymmetrical graben structure. The syn-rift deposits of the Lyne Formation and the Fell Sandstone Formation thicken towards the Maryport Fault system. This can be seen in Figure 7.2bii. The early post-rift deposits of the Yoredale Group thicken towards the Gilknockie Fault in the north, implying that they are contemporaneous with movement on the fault and as such, movement on the Gilknockie Fault occurred later than the movement on the Maryport Fault at the southern margin of the basin. The syn-rift deposits and throw on the Maryport Fault system are reduced from east to west across the basin.

The Solway basin was subjected to inversion resulting in large scale folding and some fault reactivation with a reverse sense of movement, as a result of the Variscan orogeny. The Solway Basin reaches a maximum sediment thickness of 8 km in the centre of the basin, within the Solway Syncline, where Variscan folding has steepened the inclination of the beds.

### *7.1.2 Northumberland Trough*

The Solway Basin passes eastwards into the Northumberland Trough via the Bewcastle Anticline. The Northumberland Trough is an asymmetrical

half-graben, whose development is controlled by the Stublick-Ninety Fathom Fault system (Figure 7.3) In the west of the basin, extension is taken up on two en-echelon branches of the Stublick Fault that pass east onto the Ninety Fathom Fault. Evidence suggests the extension within the Northumberland Trough began on one main fault, with the extension subsequently being taken up on a second fault within the system located further north in a more distal position within the basin compared to the original fault. The amount of extension accommodated by the basin-bounding faults decreases from west to east. Throw on the basin-bounding faults decreases from 5.5 km to 3.5 km across the basin. The thickness of syn-rift deposits likewise decreases from west to east and corresponds with the amount of throw on the faults, implying that sedimentation kept pace with extension.

### *7.1.3 Alston Block*

The Alston Block is a structural high supported by the presence of a buoyant granite intrusion, the North Pennines Batholith, within the crust, this is illustrated in Figure 7.4. The Alston Block is structurally stable with very little apparent extensional faulting. The North Pennines Batholith has a complex structure beneath the Alston Block, with a main central cupola and several smaller cupolas branching off from it. There is little evidence of syn-rift deposition on the Alston Block as the uplift generated by the granite intrusion kept it emergent prior to deposition of the Alston Formation. There are some syn-rift deposits on the flanks of the Alston Block, where they onlap the margin of the block from the

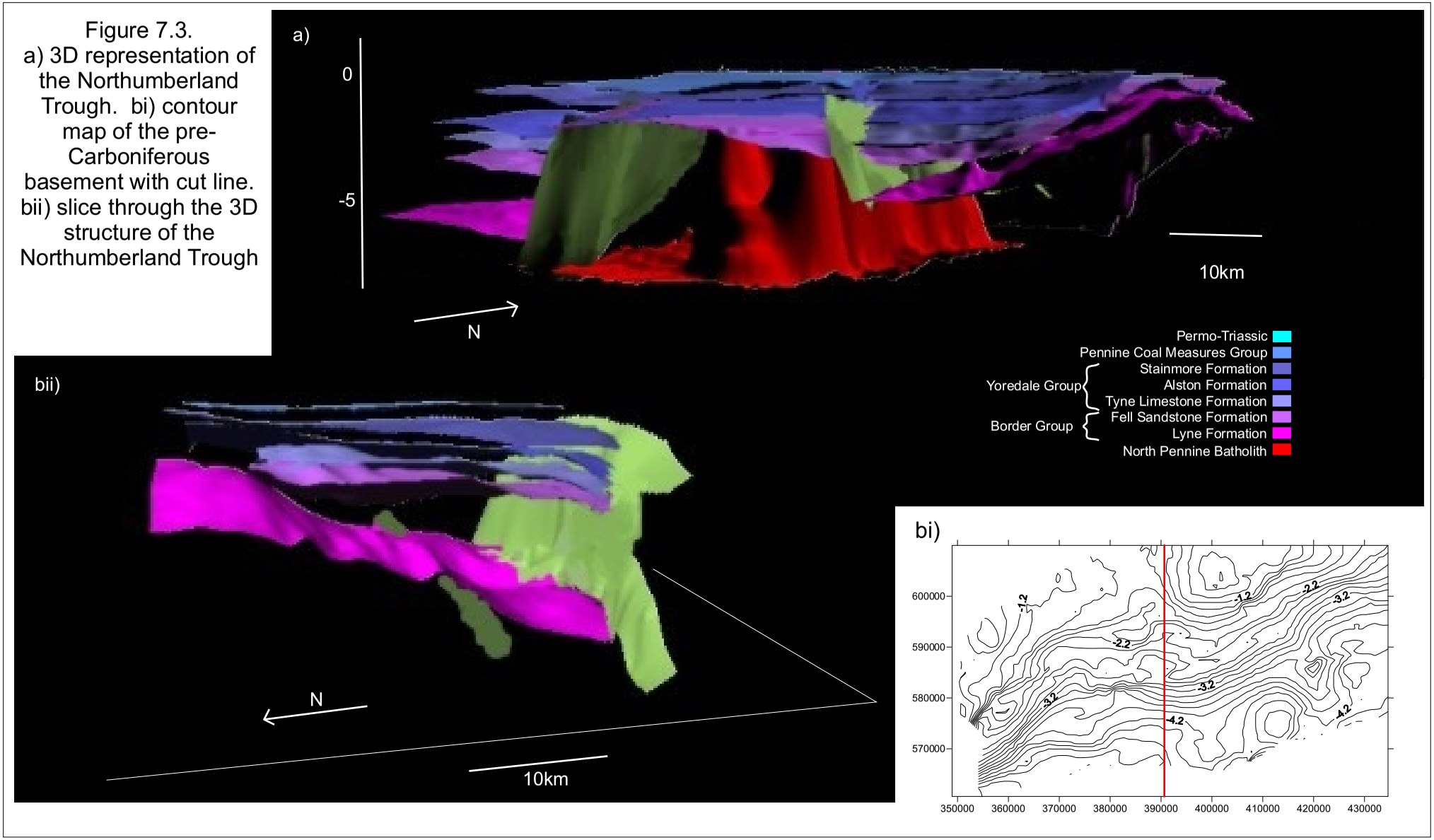


Figure 7.3.
a) 3D representation of the Northumberland Trough. bi) contour map of the pre-Carboniferous basement with cut line. bii) slice through the 3D structure of the Northumberland Trough

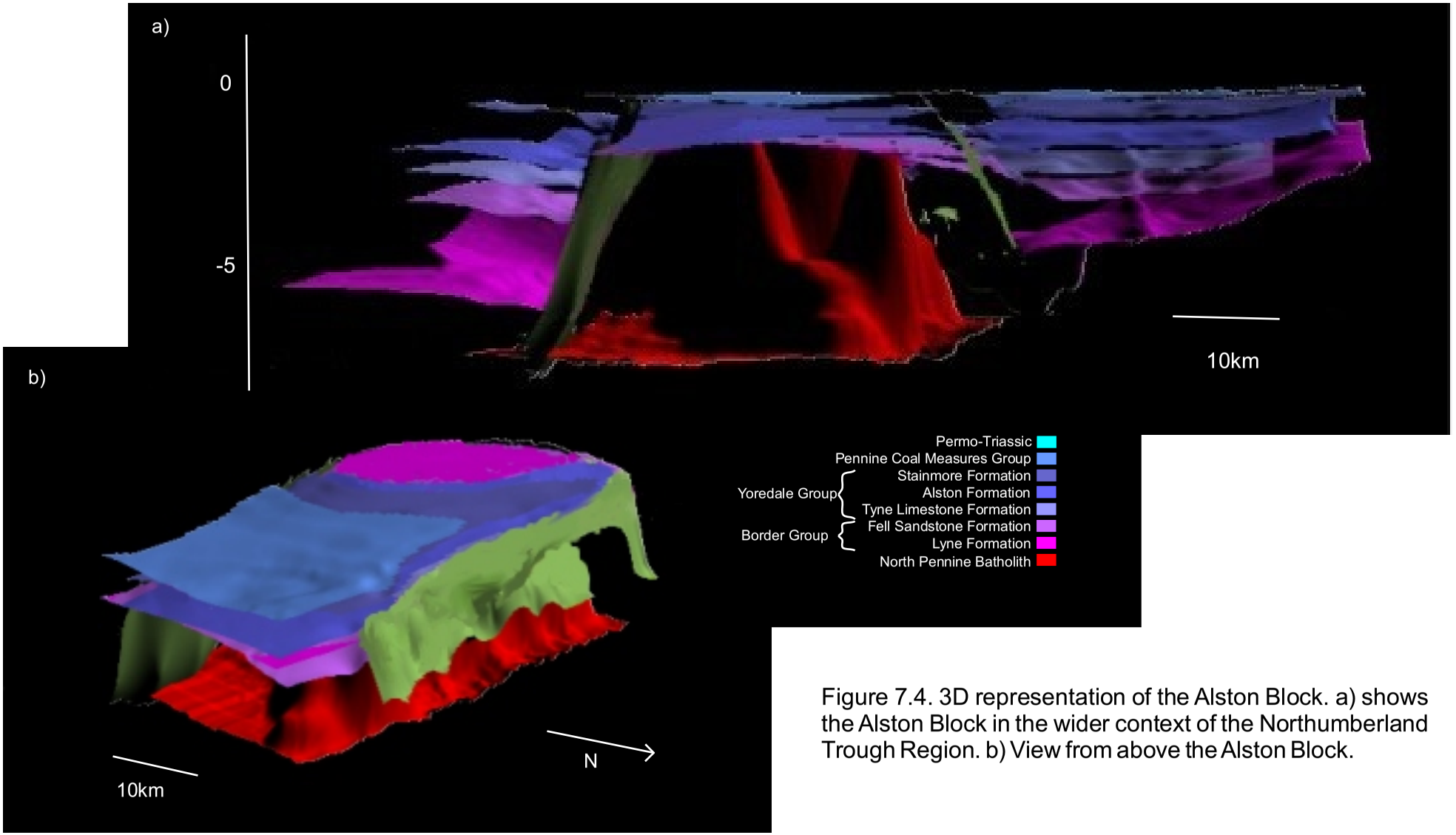


Figure 7.4. 3D representation of the Alston Block. a) shows the Alston Block in the wider context of the Northumberland Trough Region. b) View from above the Alston Block.

Northumberland Trough to the north and the Stainmore Trough to the South. On the east of the Alston Block, where the effect of the North Pennines Batholith is diminished, a thicker succession of sediments is present. In the west, the Alston Block is uplifted towards the Pennine Fault as a result of footwall uplift, causing some deposits of the Yoredale Group to be uplifted and eroded (Figure 7.4b).

### *7.1.4 Vale of Eden Basin*

The Vale of Eden Basin is an asymmetrical half-graben that is oblique to the main east-north-east, west-south-west trend of the Solway basin, Northumberland Trough and Stainmore Trough (Figure 7.5). Development of the Vale of Eden Basin occurred as a result of displacement upon the north-north-west trending, westerly-dipping Pennine Fault. Movement along the fault commenced during the late Carboniferous/early Permian times, as such the Stainmore Formation forms the main syn-rift sequence in the Vale of Eden Basin (Figure 7.5biii). Prior to extension on the Pennine Fault, the Vale of Eden Basin was an area of low topography, surrounded by the Alston Block to the east and the Lake District Block to the west. The early-mid Carboniferous age sediments were deposited in a depocentre created by regional subsidence. The syn-rift deposits of the Vale of Eden Bain thin towards the Lake District Block where the basin is not fault controlled (Figure 7.5bii).

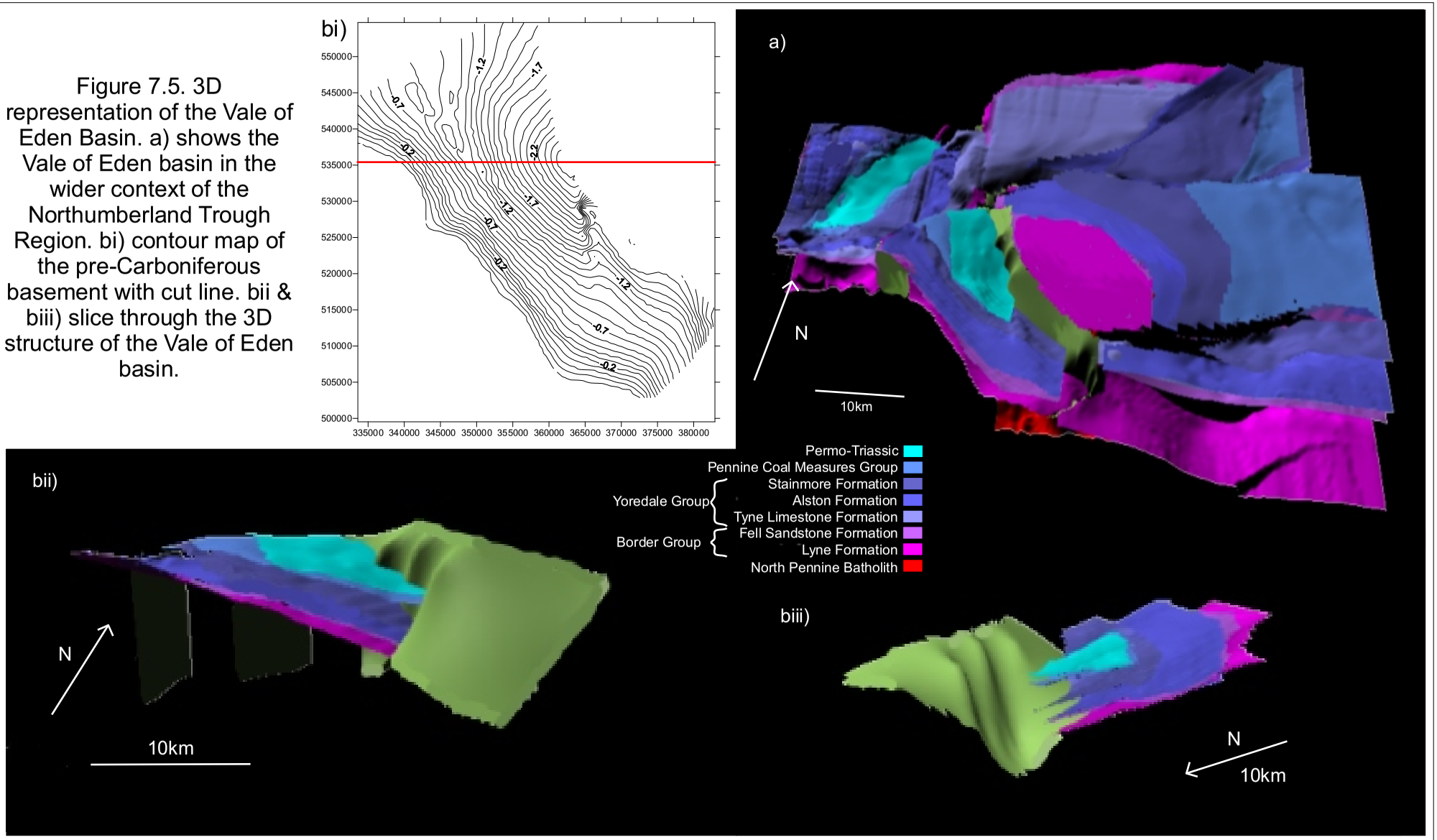


Figure 7.5. 3D representation of the Vale of Eden Basin. a) shows the Vale of Eden basin in the wider context of the Northumberland Trough Region. bi) contour map of the pre-Carboniferous basement with cut line. bii & biii) slice through the 3D structure of the Vale of Eden basin.

### *7.1.5 Stainmore Trough*

The Stainmore Trough is an asymmetrical half-graben controlled by extension on the southerly-dipping Closehouse-Lunedale-Butterknowle Fault system at the northern margin of the basin. Extension on the Closehouse-Lunedale-Butterknowle Fault system increases from west to east (Figure 7.6a). Thickening of deposits in the post-rift Yoredale Group towards the fault system implies that a second phase of fault movement occurred (Figure 7.6b).

## 7.2 Modelling flexural isostasy in three-dimensions.

This project utilises a computer program by Meredith (2003) to model flexural isostasy in three-dimensions. In this model deformation is assumed to occur by a pure shear mechanism and loading is compensated for using a three-dimensional flexural algorithm modelled from the two-dimensional approach defined in chapter 5, after Hodgetts *et al.* (1998).

The pressure exerted by an applied load that varies in the x-direction is given by:

$$\frac{d^2}{dx^2} D \frac{d^2 W_{(x)}}{dx^2} + \left[ \left( \rho_m - \rho_i \right) g W_{(x)} \right] = L_{(x)} \qquad [7.1]$$

Similarly, for a load that varied in the y-direction:

$$\frac{d^2}{dy^2} D \frac{d^2 W_{(y)}}{dy^2} + \left[ \left( \rho_m - \rho_i \right) g W_{(y)} \right] = L_{(y)} \qquad [7.2]$$

To account for loading variations in both the x and y directions, equations [7.1] and [7.2] can be combined:

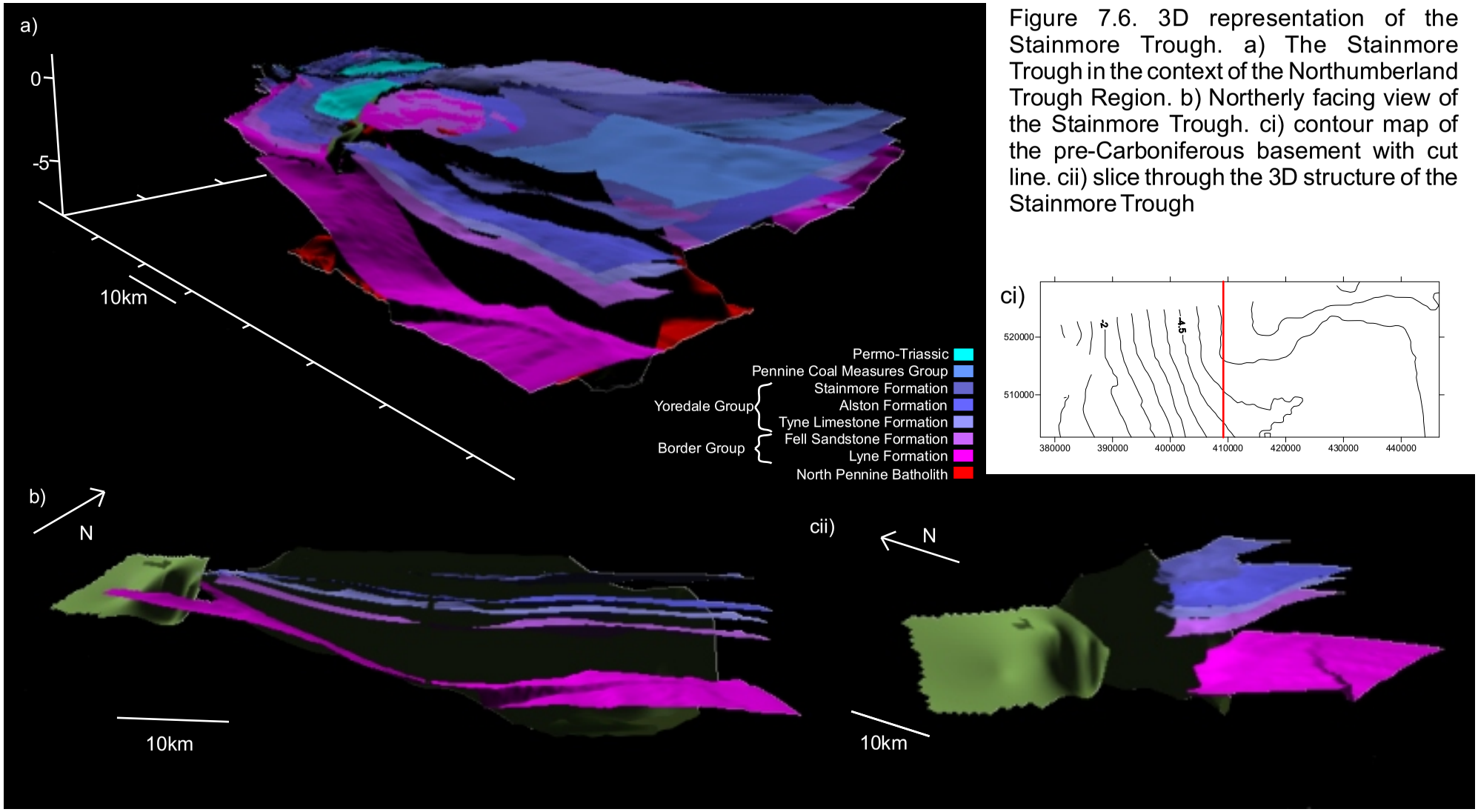


Figure 7.6. 3D representation of the Stainmore Trough. a) The Stainmore Trough in the context of the Northumberland Trough Region. b) Northerly facing view of the Stainmore Trough. ci) contour map of the pre-Carboniferous basement with cut line. cii) slice through the 3D structure of the Stainmore Trough

$$\left(\frac{d^2}{dx^2}+\frac{d^2}{dy^2}\right)D\left(\frac{d^2W_{(xy)}}{dx^2}+2\frac{d^2W_{(xy)}}{\left(dx^2\right)\left(dy^2\right)}+\frac{d^2W_{(xy)}}{dy^2}\right)+\left[\left(\rho_m-\rho_i\right)gW_{(xy)}\right]=L_{(xy)}$$

[7.3]

where: $L_{(xy)}$ is the pressure exerted by the applied load which may vary with the horizontal x co-ordinate.

$W_{(xy)}$ is the flexural response as a function of x and y

As with the two-dimensional approach, equation [7.3] is solved using a Fast Fourier Transform. In this case a three-dimensional FFT routine is used. Once the data has passed through the FFT routine, it is filtered using the response function:

$$Resp_3=\left(\frac{2\pi x}{N\times 1000}\right)^2+\left(\frac{2\pi y}{N\times 1000}\right)^2 \qquad [7.4]$$

$$Resp_4=\frac{1}{\left(\rho_m g\right)+\left(D\times Resp_3\right)} \qquad [7.5]$$

The isostatic response in then calculated:

$$W_{(xy)}=L_{(xy)}\times Resp_4 \qquad [7.6]$$

Once the data have been filtered and the isostatic response calculated, it is passed through the reverse FFT.

The model incorporates extension by pure shear, with the magnitude of extension determined by beta values calculated from extimates of crustal thinning. The thermal consequences of lithosphere extension are incorporated using a modification of the McKenzie (1978) analytical approach. At each time step within the model accommodation space

generated tectonically by the mechanical stretching and thermal processes is flexural compensated for basin infill (Meredith, 2003).

In order to simulate extension in three-dimensions, a three-dimensional dataset is required. The cross-sections produced as part of this study have been constructed within a three-dimensional co-ordinate frame with two sections parallel to the strike of the structural features and perpendicular to the other cross-sections. Figure 7.7 illustrates several of the cross-sections previously described in chapter 3 within a three-dimensional co-ordinate system. Relationships between faults and/or stratigraphy can be observed. The three-dimensional model requires beta values to define the magnitude of extension. These data are calculated from crustal thinning interpreted from the cross-sections.

$$\beta = \frac{C_0}{C_1} \qquad [7.7]$$

where: $C_0$ is the original crustal thickness
$C_1$ is the final crustal thickness

The data interpreted from the cross-sections results in randomly spaced data that must be converted into an evenly spaced grid. Figure 7.8 illustrates the distribution of the data points before interpolation. A krigging gridding method has been used applied to the data to interpolate between the lines of data generated from the cross-sections. Krigging uses a semivariogram, a measure of the degree of special continuity, to estimate the value for a surface at any unsampled data point (Davis, 1986). The 997 data points collected from the cross-sections are converted

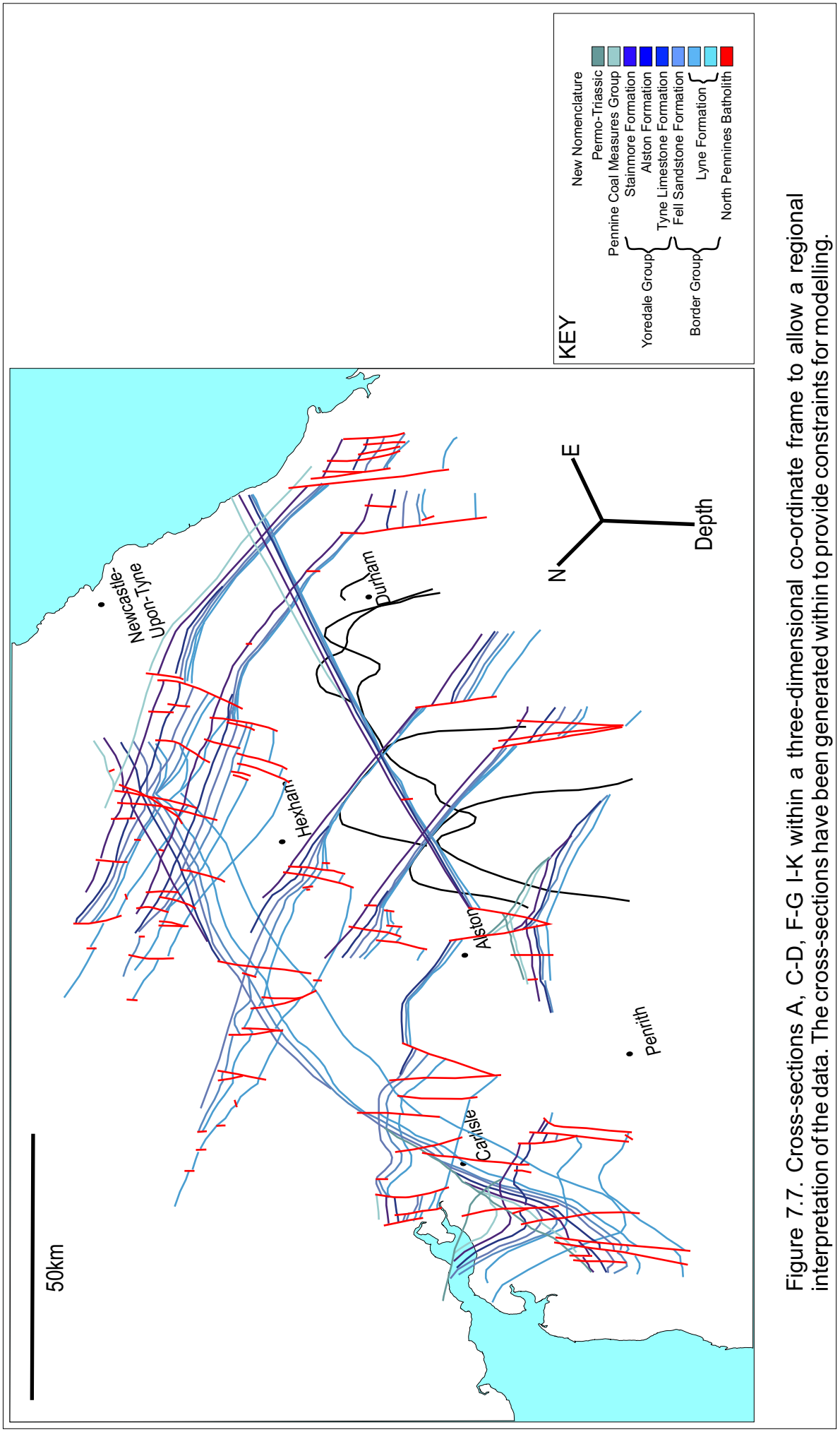


Figure 7.7. Cross-sections A, C-D, F-G I-K within a three-dimensional co-ordinate frame to allow a regional interpretation of the data. The cross-sections have been generated within to provide constraints for modelling.

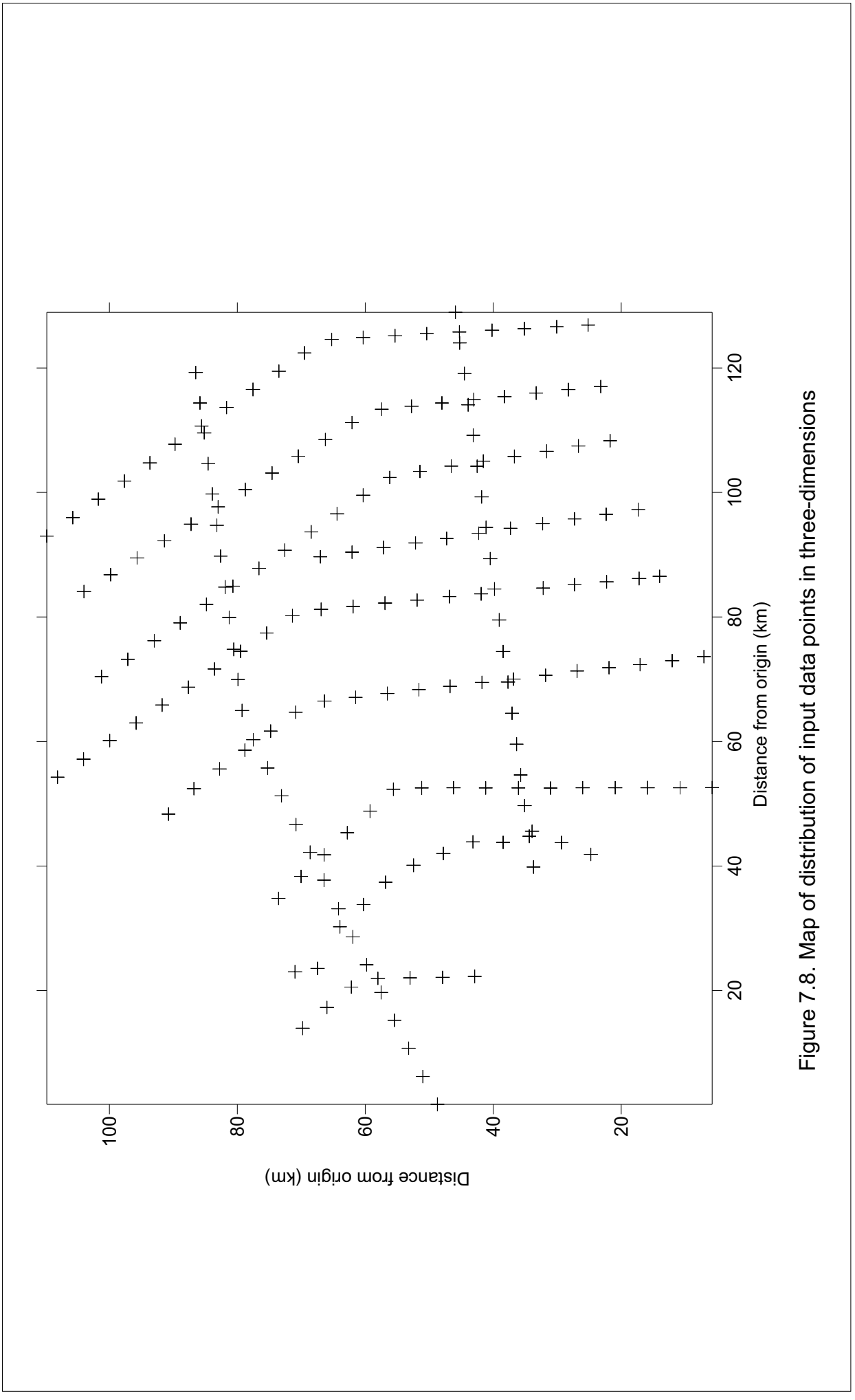


Figure 7.8. Map of distribution of input data points in three-dimensions

into a grid 80 rows by 100 columns with a separation of 1.333 km between x co-ordinates and 1.325 km between y co-ordinates.

Breaklines, three-dimensional blanking files that define a line in x, y and z co-ordinates can be applied to the data during the gridding process to control the flow of information during the interpolation. When the algorithm encounters a breakline, it calculates the z value of the nearest grid node using a combination of the data from the surrounding data points and the breakline (Bresnahan and Dickenson, 2002). This method of interpolation is used to define breaks in slope, for example those generated by faulting. A number of breaklines have been applied to the gridding method used in this study to define the position of the major faults within the model to improve the accuracy of the interpolation. Figure 7.9 illustrates the beta distribution generated by gridding the data with and without the application of breaklines representing the faulting. The addition of the breaklines generates a north-west to south-east oriented trend in the beta data beneath between the Alston Block and Stainmore Trough, this may influence the response to the boundary between the block and the trough in the modelling. Figure 7.10 illustrates several sections orientated N-S across the beta distribution map. The greatest beta values, and therefore the greatest extension occurs within the Solway Basin (Figure 7.10a). Beta increases across the Alston Block and Stainmore Trough from west to east (Figures 7.10c-f).

Figure 7.11 illustrates the results from three-dimensional modelling of the Northumberland Trough region at t=0Ma after extension. The same initial

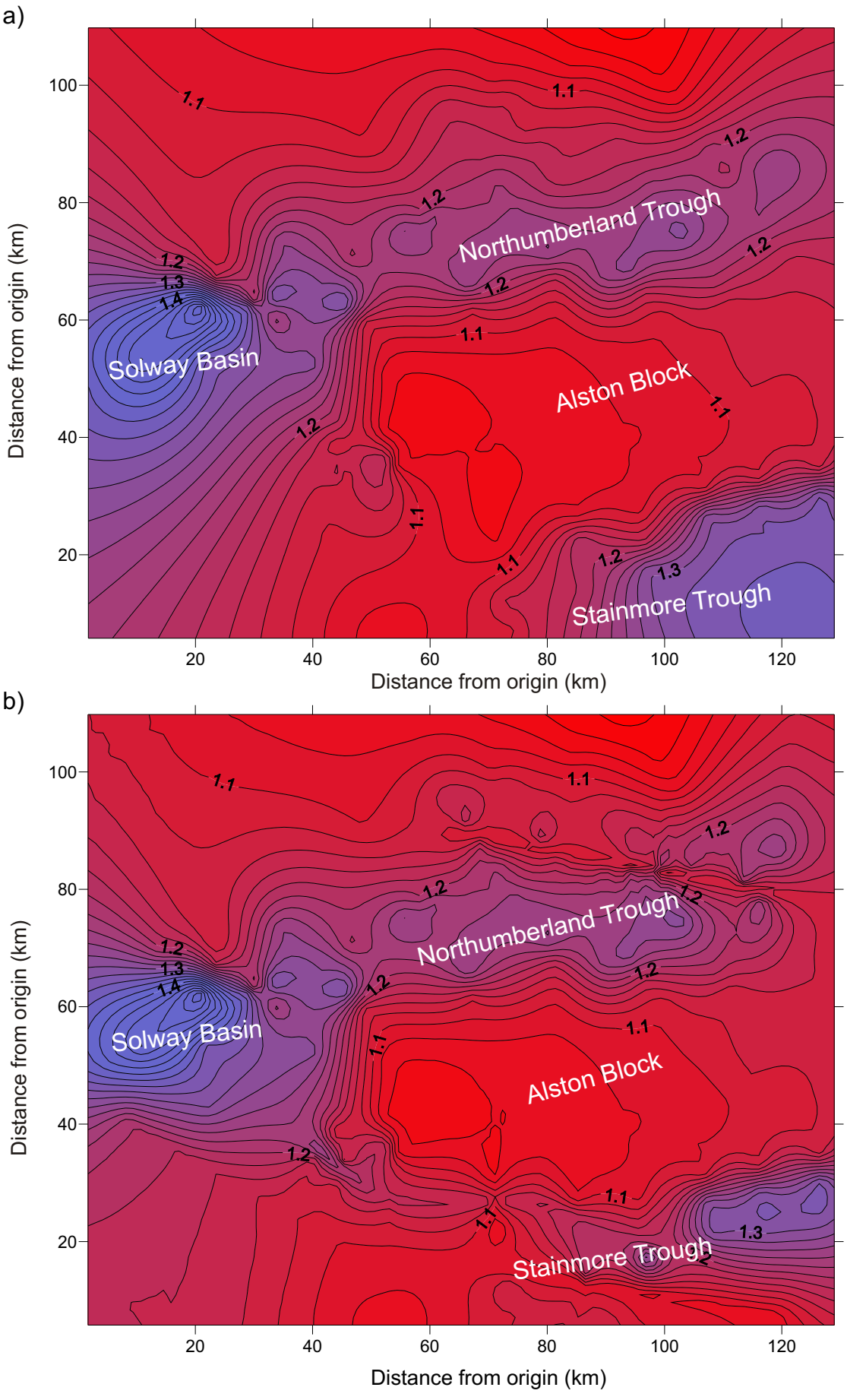


Figure 7.9. Beta distribution map to quantify extension of the Northumberland Trough Region interpolated from crustal thinning/thickness data from cross-sections. a) Interpolation without blanking files. b) interpolation with blanking files.

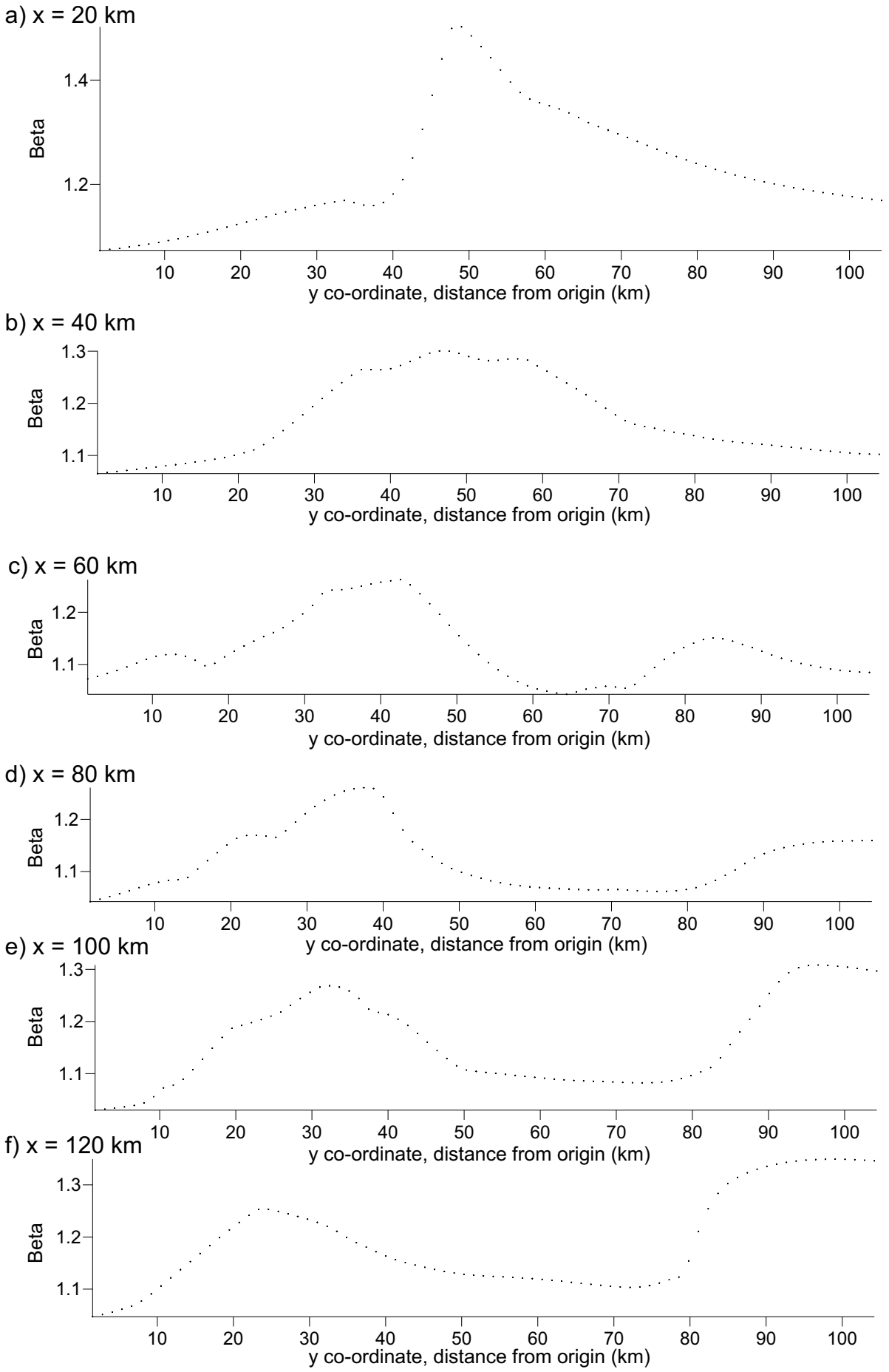


Figure 7.10. Cross-sections orientated N-S through the beta distribution map. a) x = 20 km. b) x = 40 km. c) x = 60 km. d) x = 80 km. e) x = 100 km. f) x = 120 km.

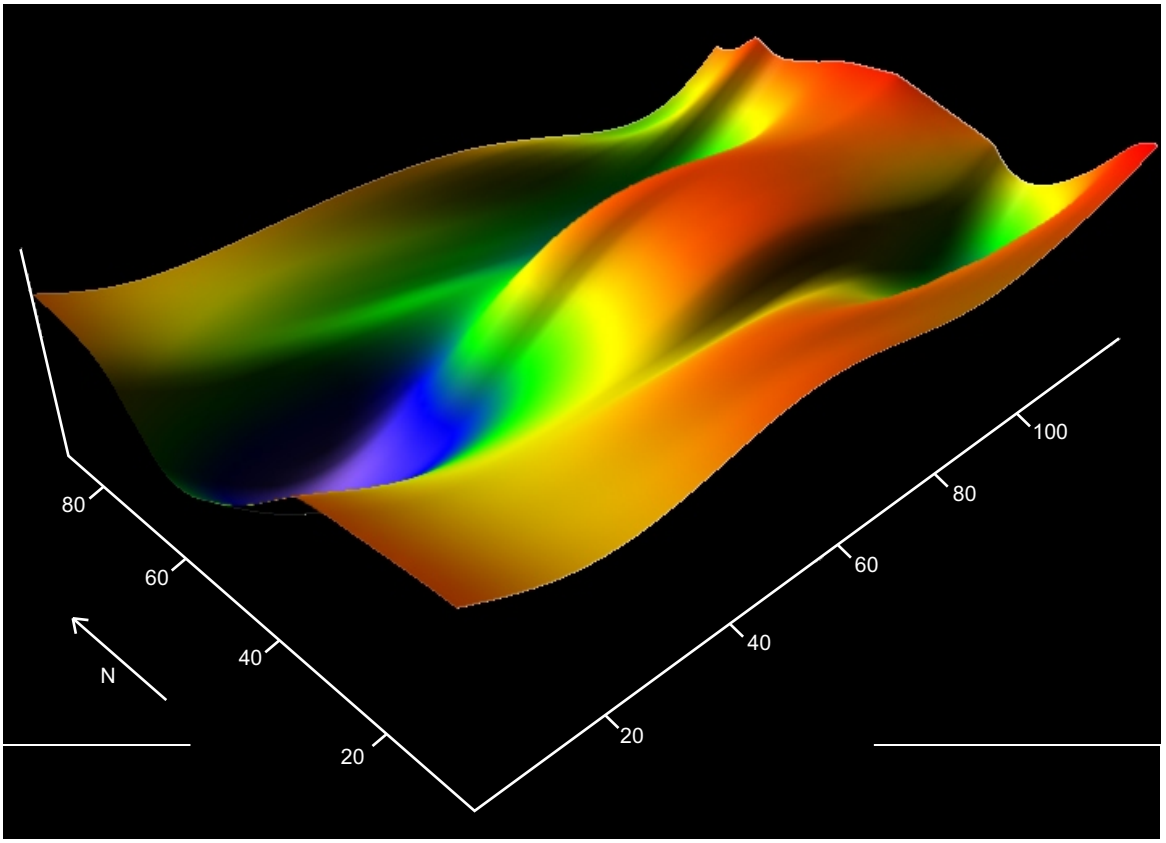


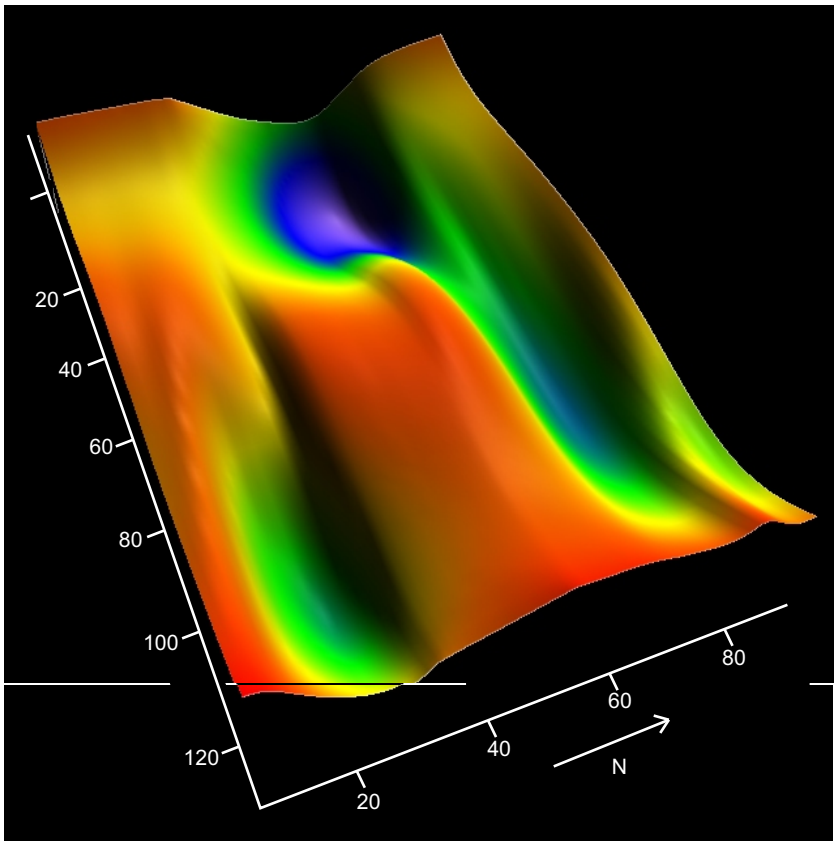


Figure 7.11. 3D model of the subsidence resulting from pure shear extension of the lithosphere. The Northumberland Trough deepens from east to west. The Stainmore Trough deepens from west to east. The subsidence is greatest in the Solway basin.

pre-extension lithosphere parameters have been used as in the two-dimensional modelling to allow for a comparison between the results (Figure 6.7). The greatest amount of extension has occurred beneath the Solway Basin. Extension within the Northumberland Trough is greatest in the west and decreases to the east. The extension within the Stainmore Trough to the south is the opposite with the greatest extension in the eastern part of the basin.

Figure 7.12 provides a comparison between the three-dimensional modelling results and the two-dimensional approach from chapters 4&5. The two dimensional approach generates greater uplift over the Alston Block and deeper subsidence in the basins. The two-dimensional modelling approach does not take into account any loading out of the plane of the section, as a result this generates greater uplift in response to extension and greater subsidence in response to loading. In this case the effect of basin infill generated subsidence has a greater influence than the extension related uplift in the basins and vice versa on the block which may well have been uplifted above sea level and therefore not loaded by sediment following the initial extension phase.

## 7.3 Modelling the flexural effect of the batholith intrusion in three-dimensions

The three-dimensional flexural isostasy algorithm described here has been used to model the effect of the imposition of the granite batholith beneath the Alston Block in three-dimensions. It has already been established in

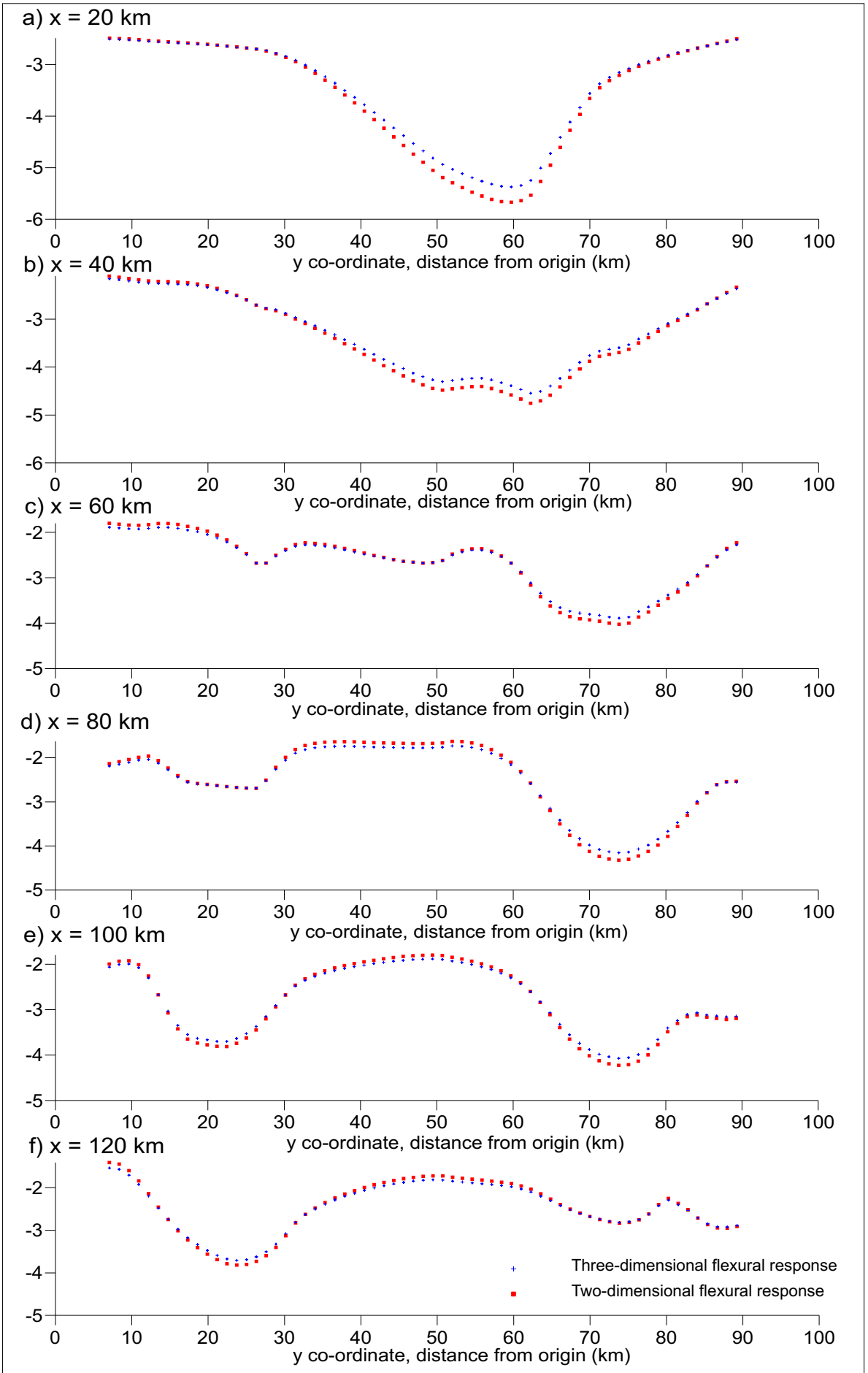


Figure 7.12. Comparison between the two-dimension and three-dimensional flexural response to crustal thinning. Cross-sections orientated N-S a) x = 20 km. b) x = 40 km. c) x = 60 km. d) x = 80 km. e) x = 100 km. f) x = 120 km.

chapter 6 that when the lower density granite replaces higher density crustal material, there is a flexural uplift in order to isostatically compensate for the reduction in loading.

The flexural isostatic response to rifting within the Meredith (2003) model is calculated from a set of three-dimensional structural thickness geometries that are produced prior to the onset of modelling. These are used to determine the amount of crustal thinning by pure shear, which can be expressed as β values. These can then be used to calculate the tectonically induced subsidence/uplift resulting from the initial rifting phase and its isostatic compensation.

In the case of the batholith, which occurred prior to the main rifting phase, the 'crustal thinning' and subsequently calculated β values need to represent the change in density brought about by the batholith emplacement.

$$G_{t(x,y)} = G_{o(x,y)}\left(1 - \frac{\rho_g}{\rho_c}\right) \qquad [7.8]$$

where: $G_{t(x,y)}$ is the crustal thinning value that represents the equivalent amount of crustal density material

$G_{o(x,y)}$ is the thickness of the granite.

If equation [7.8] is used to calculate the beta value, then assuming no infill, results for the modelling of pure shear with flexural compensation can be used to calculate the uplift generated by the presence of the batholith.

However the crust is not thinned by the presence of the batholith. It is therefore necessary to remove the effect of the pure shear related thinning from the results to leave just the flexural uplift response $W_{(x,y)}$.

$$W_{(x,y)} = G_{t(x,y)} + B_{(x,y,0)}$$

where $B_{(x,y,0)}$ is the basement at position x,y at time t=0Ma after extension

Figure 7.13 illustrates the results of modelling of the North Pennines Batholith based on gravity data. The main cupola is surrounded by two cupolas to the west, the Tynehead and Scoredale cupolas, and two cupolas to the east, the Rowlands Gill and Cornsay cupolas. This data in the form of depth to the top granite surface has been interpolated using the krigging method described previously to produce a grid that can be used for the three-dimensional modelling of the response to the North Pennines Batholith.

Figure 7.14 illustrates the results of three-dimensional modelling of the flexural response to the North Pennines Batholith. This figure has been vertically exaggerated to demonstrate that the overall effect of the flexure mirrors the shape of the batholith. Figure 7.15 compares the results of the three-dimensional modelling with those of the two-dimensional approach discussed in chapter 6. The two-dimensional modelling approach generates additional uplift across the main batholith structure, whereas the three-dimensional response is shallower and broader, generating greater uplift at the edges of the batholith.

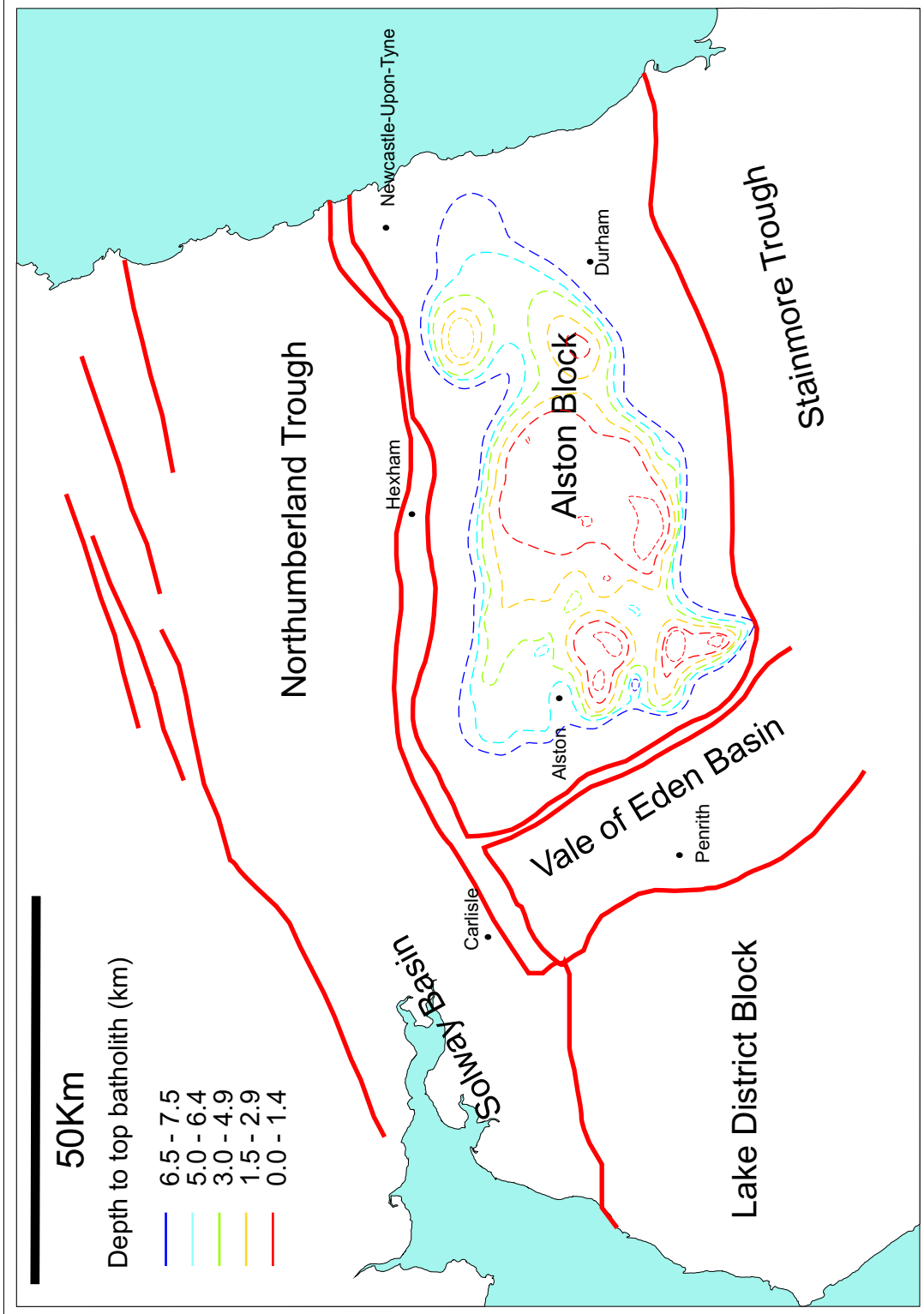


Figure 7.13. Contours for the depth to the top of the batholith, results of three-dimensional modelling of the North Pennines Batholith based on gravity data ( North Pennines Batholith data reproduced by permission of the British Geological Survey. ©NERC. All rights reserved).

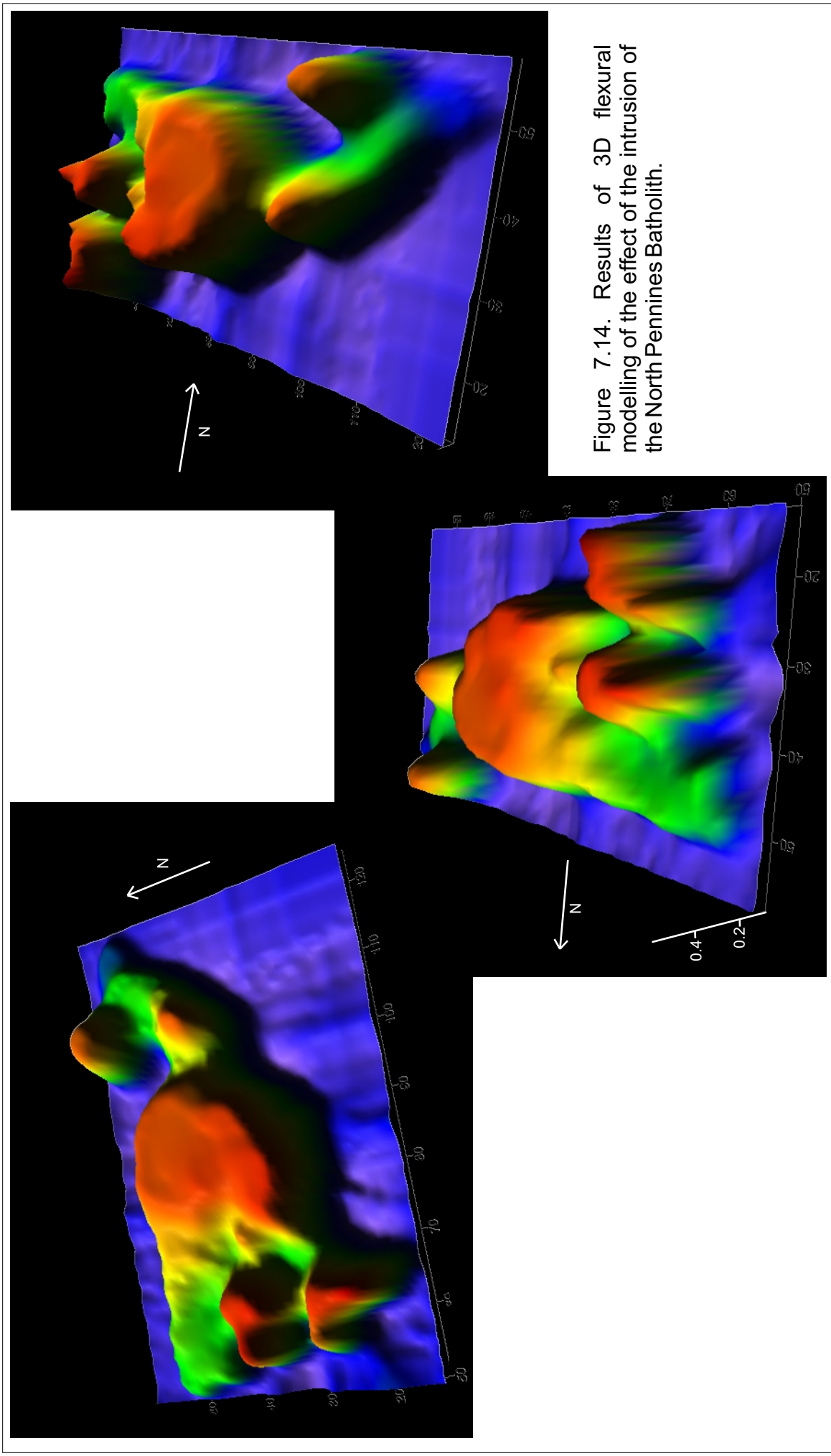


Figure 7.14. Results of 3D flexural modelling of the effect of the intrusion of the North Pennines Batholith.

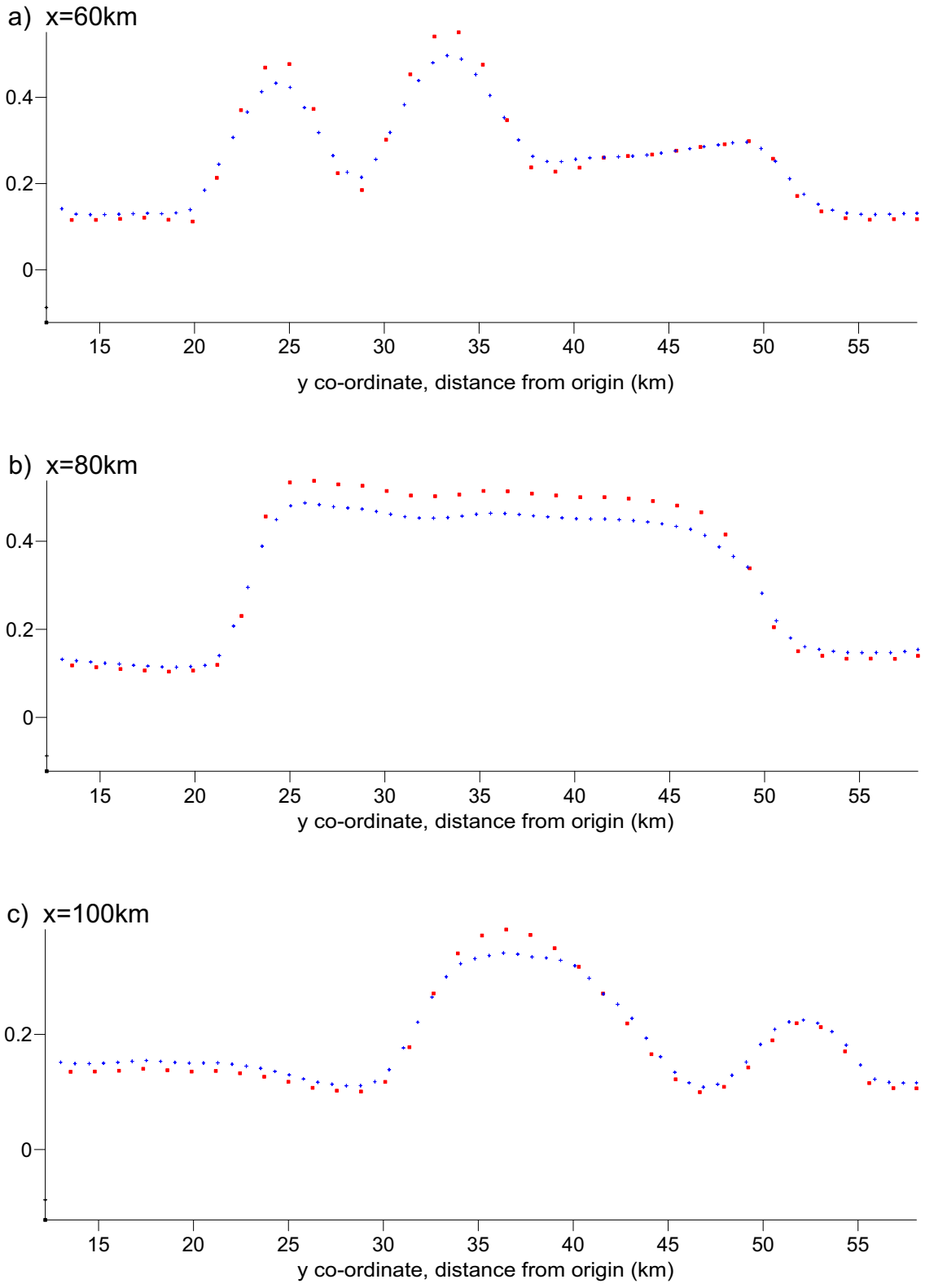


Figure 7.15. Comparison between the two-dimension and three-dimensional flexural response to batholith emplacement. Cross-sections orientated N-S through the uplifted basement. a) x = 60 km. b) x = 80 km. c) x = 100 km.

Figure 7.16 compares the three-dimensional modelling of the extension of the Northumberland Trough Region with and without the emplacement of the North Pennines Batholith at time t=0Ma after extension. The presence of the batholith greater uplift across the region, but this is concentrated upon the Alston Block beneath which the batholith lies directly. At x = 120km the influence of the batholith is reduced as this is beyond the edge of the main intrusion.

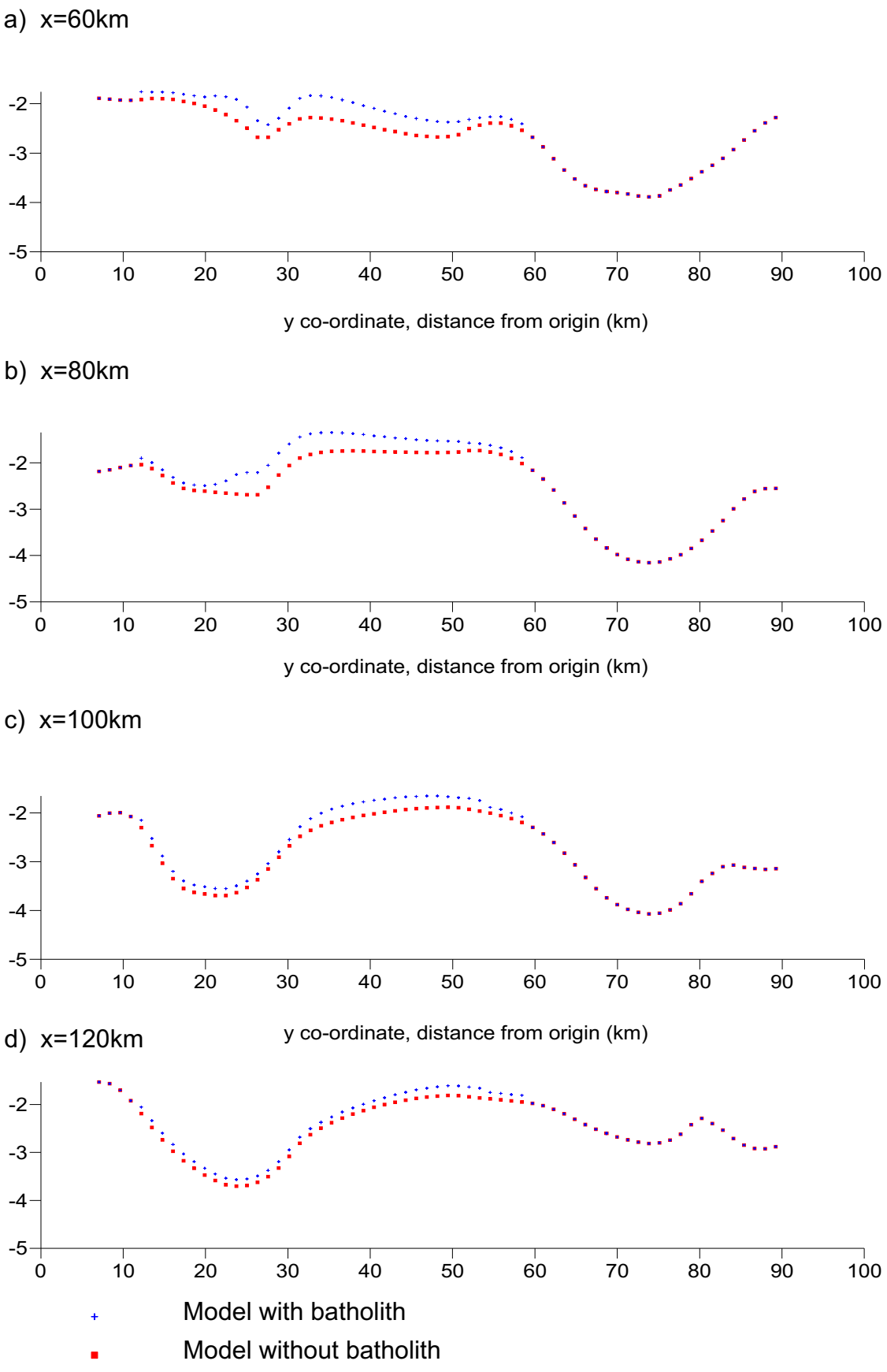


Figure 7.16. Comparison between the three-dimensional flexural response to pure shear with and without batholith emplacement. Cross-sections orientated N-S through the uplifted basement. a) x = 60 km. b) x = 80 km. c) x = 100 km. d) x=120km.

# 8 Conclusions and Further Work

## 8.1 Model and algorithm development

An integrated tectonic, thermal, isostatic and stratigraphic modellling approach has been developed and used to investigate the evolution of the Northumberland Trough Region in NE England. The tectonic processes responsible for lithosphere extension are investigated in a coupled simple-shear/pure-shear model. In addition, the thermal and flexural isostatic consequences of lithosphere extension that influence post-extensional basin structure are simulated.

At the low temperatures and pressures encountered within the upper crust, rock behaves elastically with the application of stress until the stresses become sufficiently large such that failure occurs by faulting. Normal faults with listric geometry are simulated with hanging wall deformation occurring by simple shear, along shear planes that are either vertical or inclined. Extensional faulting tends to occur within structural provinces in which the majority of displacement is accommodated on a small number of major faults, with a number of smaller subsidiary faults. The deformation of the hanging wall is controlled by the fault detachment depth, the magnitude of extension, the sense and extent of inclination of the shear, and the interaction between the major faults and their subsidiary faults.

At higher temperatures and pressures the lithosphere behaves in a ductile manner and extension occurs by pure shear. Lithosphere extension may be

uniform, with the magnitude of extension by faulting matched by the magnitude of extension by pure shear, or non-uniform, with, for example, enhanced extension in the lower lithosphere. The amount of crustal thinning by pure shear is quantified by the extension factor β and is dependent on the magnitude of extension, the thickness of the lower lithosphere undergoing deformation and the width over which the pure shear deformation is distributed.

Extension of the lithosphere perturbs the geotherm. Over time, these perturbations decay exponentially to restore the geotherm to a state of equilibrium. These thermal processes influence basin evolution by generating uplift during rifting followed by subsidence during post-rift basin evolution. The thermal perturbation of the lithosphere is modelled using an analytical approach (McKenzie 1978) modified to include the effects of flexural isostasy. Simulations of thermal processes highlight the importance of the magnitude of extension in controlling the extent of the perturbation of the geotherm.

A regional, flexural approach to modelling the isostatic response of the lithosphere to loading has been utilised in which variations in loading produce complex deflections of the basement and underlying crustal structure. The flexural isostatic compensation of loads induced by extensional tectonics have significant implications in controlling the creation and destruction of accommodation space, and in controlling the resultant stratigraphy and basement geometry. The effective elastic thickness of the lithosphere has the most important control on the amount

by which the lithosphere flexes in response to loading and as such it controls the lateral effect of any load.

A stratigraphic model to reconstruct sedimentary sequences has been developed to simulate sedimentary infill constrained by palaeobathymetry, as well as compaction of sediment, in order to produce a pattern of basin infill that is consistent with the observed stratigraphy. The accuracy of the model reconstruction depends upon generating adequate accommodation space at the right time intervals.

Development of an algorithm to model the effect of igneous intrusions upon the structural development of the region has allowed the buoyant influence of the granite North Pennines Batholith to be studied in greater detail.

This project also employed an integrated three-dimensional modelling technique developed by Meredith (2003) to consider the implications of a three-dimensional flexural response on the evolution of the Northumberland Trough Region. The three-dimensional flexural algorithm has also been used to model the effect of the emplacement of the North Pennines Batholith in three dimensions.

## 8.2 Application of modelling to the Northumberland Trough

Two-dimensional and three-dimensional models have been used in conjunction with burial history analysis and subsurface data to investigate the structural and geodynamic processes responsible for the evolution of the Northumberland Trough Region.

Burial history modelling, constrained by borehole and subsurface data, provides a quantitative analysis of trends in subsidence and uplift across the Northumberland Trough Region.

The burial history modelling studies allow for consideration of the amount of uplift and erosion that occurs within the Northumberland Trough Region during Mesozoic and Cenozoic times. The tectonic subsidence is counteracted by the uplift and erosion. As such the precise timing and rate of Mesozoic tectonic subsidence and the uplift responsible for erosion of the strata deposited during the subsidence has been estimated at between 1.5 and 2 km in coastal areas (Green, 2002). Analysis of borehole data has provided estimates of between 0.55 km and 0.74 km of tectonic subsidence with 2 km erosion.

The burial history modelling also provides some constraints on the timing of tectonic events. Extension within the Northumberland Trough Region is not restricted to a singular extensional event 360 Ma ago. Results from burial history modelling provide evidence of 'syn-rift' deposition up to 326 Ma, during the deposition of the Alston Formation in some areas within the region.

The modelling technique developed in chapters 4 and 5 have been utilised in this study of the Northumberland Trough Region. The amount of extension has been quantified according to the extension observed on faults within the cross-section and from burial history results.

Previous studies have suggested that extension of the Northumberland Trough Region is non-uniform, with greater extension by pure shear within the lower crust and lithosphere mantle than by faulting in the upper crust (Bott *et al.*, 1984). Model results incorporating non-uniform lithosphere extension produce greater subsidence than uniform lithosphere extension models. The outcome of modelling the Northumberland Trough supports a non-uniform mode of lithosphere extension.

Initial models generate subsidence comparable to that observed within the basin structures. However, the composition of the stratigraphy produced within the basins does not accurately reflect the pattern of 'syn-rift' and 'post-rift" sedimentation. An approach that utilises multiple tectonic events has been applied to the Northumberland Trough Region in order to simulate the evolution of the structure and the stratigraphy. The multi-tectonic modelling technique provides results that resolve the timing of movement upon faults that is reflected in the stratigraphy.

The amount of subsidence generated upon the Alston Block by the initial models is excessive. This is attributed to the effect of the North Pennines Batholith, a granite intrusion with a low density relative to the surrounding crust, situated beneath the basement of the Alston Block. The intrusion represents a negative load within the lithosphere which responds by uplift. Models incorporating the effect of the batholith generate uplift across the Alston Block. The resultant uplift within the models generate profiles for the basement of the Alston Block that are

comparable with the observed basement across the block, with the exception of the eastern edge of the block, where the subsidence produced within the model is greater than the observed basement depth. This is likely the result of a limitation of the two-dimensional modelling approach in that the influence of the granite out of the plane of the section cannot be considered within the model.

Results from modelling that assumes uniform-lithosphere extension do not reproduce the amount of basement subsidence which is observed within the basins. A non-uniform approach to lithosphere extension, based on the estimates of Bott *et al.* (1984), yields subsidence of the basement that is comparable to that observed within the subsurface data within the basin structures. It has been suggested that the extension within the ductile lower crust may be slower than faulting in the upper crust.

Where the model is applied to the Alston Block, it is not possible to reconcile the amount of subsidence generated with that observed by either the uniform or non-uniform method of lithosphere extension; a greater amount of subsidence is generated than observed upon the block. Results from modelling that incorporates the flexural response to the intrusion of the North Pennines Batholith generate uplift that influences the structure of the block. Across the centre of the block, where the batholith is concentrated, the subsidence of the basement generated by the model is comparable with the observed subsidence. At the margins of the block, where the influence of the batholith is reduced, the subsidence of the basement within the model is greater than the observed subsidence.

Consequently, while the models account for the observed subsidence directly above the batholith, across the areas of Alston Block that is not directly underlain by the batholith, or the batholith is reduced in size, the observed subsidence is not attained within the model. It is a limitation of the two-dimensional model that the flexural effect of the granite outside of the plane of the section is not considered. Additionally, Bott and Masson-Smith (1956) suggest that igneous intrusions may be accompanied by thickening of the crust beneath them. Investigation into these processes will involve further work, which is discussed in the section 8.3.

Extension within the Northumberland Trough Region has not been restricted to a single extensional event. Results generated using a modelling approach that utilises multiple tectonic events, developed by Egan et al. (2009), generate stratigraphic patterns of syn-rift and post-rift deposition that support extension at multiple time stages within the early-Carboniferous of the Northumberland Trough Region. At least two stages of extension, and in some cases more have been identified in all of the sections analysed. Modelling with multiple phases of extension produce less initial subsidence in the basins. Models in which subsidiary faulting occurred later than the extension on the basin bounding faults produce subsidence 'patterns' that mirror the observed subsidence.

In summary, the Northumberland Trough Region is an extensional system that has been subjected to non-uniform lithosphere extension during multiple episodes of extension. The presence of the North Pennines Batholith has influenced the structure of the region by enhancing the

basin and block architecture that resulted from extension. The integrated modelling approach utilised by this study constrains the timing, magnitude and geodynamic consequences of extension.

## 8.3 Modelling limitations and potential future work

There are a number of aspects resulting from this research that could form the basis of further investigation. A number of additional key processes have been identified to be integrated into the modelling approach used, as well development of three-dimensional algorithms to simulate the isostatic effect of igneous intrusions (and other significant crustal density anomalies) in order to understand their influence on the basement structure. There are also several weaknesses to the modelling approach used that may be worthy of investigation.

The two-dimensional kinematic model, like all models is dependent on the accuracy of the initial parameters and the data input. By taking an iterative approach to the modelling, it is possible to create the same outcome using different starting parameters. In which case it is important to have a good understanding of the starting conditions and it may be necessary to judge the results on the basis of the geological understanding of the situation. One such situation where the input data may not be accurate is that of the amount of extension. The amount of extension used is constrained only by the magnitude of observed fault controlled deformation. It is impossible to ignore the possibility that the data sections analysed do not show all of the extensional deformation that occurred, or have been subject to reactivation and inversion. Also it is

possible that there has been significantly greater extension within the lower-crust and mantle, as suspected in the Northumberland Trough Region, than by faulting that can be observed in the cross-sections.

Bott and Masson-Smith (1956) suggest that the emplacement of igneous intrusions within the crust may be accompanied by crustal thickening. Thickening of the crust will be accompanied by flexural isostatic uplift as mantle material is replaced by less dense crustal material. Development of an algorithm to simulate the crustal thickening combined with its flexural isostatic response will allow the extent of this mechanism, and its effect on the structure of the region, to be explored.

In addition, the crustal density within the model is assumed to be constant, when in reality it increases with depth. This will have an effect on the influence of batholith emplacement as it may increase the reduction in the load generated by the crust that contains the batholith. I would expect a study of the effect of increasing the density of the crust with depth to show the replacement of the lower crustal material with lower density granite material to have a greater isostatic effect.

Also as a result of variation in crustal density with depth, the positive load imposed by the mantle replacement of the lower crust as a result of pure shear may be subject to overestimation. In reality lower crustal density values would more closely approximate the density of the upper mantle resulting in less of a positive load and therefore less subsidence.

A major weakness with two-dimensional basin models is that the coordinates that extend perpendicular to the plane of the section are

assumed to be constant and infinite in extent in terms of their physical properties (Hodgetts *et al.*, 1998). As a result, the effects of lateral discontinuities in the size and structure of the igneous intrusion are ignored, which has important implications when considering the flexural response to the negative load imposed upon the lithosphere by the presence of the batholith. Development of an algorithm to model the isostatic effect of the igneous intrusions would allow the regional flexural response to the intrusion to be investigated.

Within the model a bulk density, surface porosity and compaction coefficient are assumed for the sediment infilling the basin. This assumption does not account for any lateral or vertical variations in sediment density as a result of changes in lithology that occur spatially and between stratigraphical units. In addition to variations of density with lithology, as sediment is buried and compacted it increases in density. This increase in density is reflected by the use of a larger bulk sediment density than recorded in sediments at the surface. However, this will cause greater subsidence when the sediment is first deposited within the basin and reduced subsidence as the sediment is buried compared to a more realistic value of sediment density that varies with depth. Development of algorithms that allow the physical properties of the sediment to vary laterally and between units, as well as with depth of burial, would allow for densities and porosities to be more representative of the stratigraphy within the basin under investigation.

The model developed by Egan et al. (2009) employing multiple tectonic events generate a stratigraphic model that better reconciles stratigraphy and fault movement. Adapting the two dimensional model created as part of this research to model multiple tectonic events, in addition to the modifications to the modelling of stratigraphy proposed above, would allow for the generation of a stratigraphic model in which the effects of palaeobathymetry, compaction and the variations in sediment properties can be combined with the subsidence generated by fault movement. This combined structural and stratigraphic model would be effective in constraining the timing of fault movement and in determining the processes which influence the distribution of the basin depocentre over time, particularly in regions that have a complex structural history with multiple tectonic events.

# References

Ahnert, F., 1970. Functional relationships between denudation, relief, and uplift in large, mid-latitude drainage basins. *American Journal of Science,* **268**, 3, 243-263.

Airy, G.B., 1855. On the computation of the effect of the attraction of mountain-masses, as disturbing the apparent astronomical latitude of stations in geodetic surveys. *Philosophical Transactions of the Royal Society of London,* **145** 101-104.

Allen, P.A. and Allen, J.R., 1990. Basin analysis principles and applications. Blackwell Scientific, Oxford.

Alvarez, F., Virieux, J. and Le Pichon, X., 1984. Thermal consequences of lithosphere extension over continental margins: the initial stretching phase. *Geophysical Journal of the Royal Astronomical Society,* **78**, 2, 389-411.

Anderson, T.B., Parnell, J. and Ruffell, A.H., 1995. Influence of basement on the geometry of Permo-Triassic basins in the northwest British Isles. In: S.A.R. Boldy (Ed) *Permian and Triassic Rifting in Northwest Europe.* Geological Society of London Special Publication No. 91, 103-122.

Anderson, D.L., 1990. Geophysics of the continental mantle: An historical perspective. In: M.A. Menzies (Ed) *Continental Mantle.* Clarendon Press, Oxford, 1-30.

Andréasson, P.G., Gee, D.G., Whitehouse, M.J. and Schöberg, H., 2003. Subduction-flip during Iapetus Ocean closure and Baltica–Laurentia collision, Scandinavian Caledonides. *Terra Nova,* **15**, 6, 362-369.

Aplin, A.C., Yang, Y. and Hansen, S., 1995. Assessment of [beta] the compression coefficient of mudstones and its relationship with detailed lithology. *Marine and Petroleum Geology,* **12**, 8, 955-963.

Armstrong, H.A., Pearson, D.G. and Griselin, M., 2001. Thermal effects on rare earth element and strontium isotope chemistry in single conodont elements. *Geochimica et Cosmochimica Acta,* **65**, 3, 435-441.

Artemjev, M.E. and Artyushkov, E.V., 1971. Structure and isostasy of the Baikal rift and the mechanism of rifting. *Journal of Geophysical Research,* **76**, 5, 1197-1211.

Arthurton, R.S. and Wadge, A.J., 1981. Geology of the country around Penrith memoir for 1:50,000 geological sheet 24. H.M.S.O, London.

Arthurton, R.S., Burgess, I.C. and Holliday, D.W., 1978. Permian and Triassic. In: F. Moseley (Ed) *The geology of the Lake District.* Yorkshire Geological Society, Leeds, 189-206.

Artyushkov, E.V., 1980. Lithosphere and Asthenosphere Rheology. In: N.A. Mörner (Ed) *Earth Rheology, Isostasy and Eustasy.* John Wiley and Sons, Chichester, 89.

Athy, L.F., 1930. Density, porosity, and compaction of sedimentary rocks. *Bulletin American Association of Petroleum Geologists,* **14**, 1, 1-24.

Bahr, D.B., 1997. Global distributions of glacier properties: a stochastic scaling paradigm. *Water Resources Research,* **33**, 7, 1669-1679.

Bahr, D.B., Hutton, E.W.H., Syvitski, J.P.M. and Pratson, L.F., 2001. Exponential approximations to compacted sediment porosity profiles. *Computers & Geosciences,* **27**, 6, 691-700.

Baldwin, B. and Butler, C.O., 1985. Compaction curves. *Bulletin American Association of Petroleum Geologists,* **69**, 4, 622-626.

Banks, R.J., Francis, S.C. and Hipkin, R.G., 2001. Effects of loads in the upper crust on estimates of the elastic thickness of the lithosphere. *Geophysical Journal International,* **145**, 1, 291-299.

Barrett, P.A., 1988. Early Carboniferous of the Solway Basin: a tectonostratigraphic model and its bearing on hydrocarbon potential. *Marine and Petroleum Geology,* **5**, 3, 271-281.

Beamish, D. and Smythe, D.K., 1986, Geophysical images of the deep crust: the Iapetus suture. *Journal of the Geological Society of London,* **143**, 489-497.

Beaumont, C., Keen, C.E. and Boutilier, R., 1982. A comparison of foreland and rift margin sedimentary basins. *Philosophical Transactions of the Royal Society of London.Series A, Mathematical and Physical Sciences,* **305** 295-317.

Besly, B.M., 1988. Palaeogeographic implications of late Westphalian to early Permian red-beds, Central England. In: B.M. Besly and G. Kelling (Eds) *Sedimentation in a synorogenic basin complex: the Upper Carboniferous of northwest Europe.* 200-221.

Bosence, D. and Waltham, D., 1990. Computer modeling the internal architecture of carbonate platforms. *Geology,* **18**, 1, 26-30.

Bott, M.H.P., 1953. Negative Gravity Anomalies over Acid “Intrusions” and their Relation to the Structure of the Earth's Crust. *Geological Magazine,* **90**, 4, 257-267.

Bott, M.H.P., 1956. A geophysical study of the granite problem. *Quarterly Journal of the Geological Society,* **112**, 1-4, 45-67.

Bott, M.H.P., 1967. Geophysical investigations of the northern Pennine basement rocks. *Proceedings of the Yorkshire Geological Society,* **36**, 2, 139-168.

Bott, M.H.P., 1971. Evolution of young continental margins and formation of shelf basins. *Tectonophysics,* **11**, 5, 319-327.

Bott, M.H.P., 1974. The geological interpretation of a gravity survey of the English Lake District and the Vale of Eden. *Journal of Geological Society,* **130**, 4, 309-331.

Bott, M.H.P., 1976. Formation of sedimentary basins of graben type by extension of the continental crust. *Tectonophysics,* **36**, 1-3, 77-86.

Bott, M.H.P., 1980. Mechanisms of subsidence at passive continental margins. In: A.W. Bally (Ed) *Dynamics of Plate Interiors.* American Geophysical Union, Washington, D.C., 27-35.

Bott, M.H.P., 1982a. Origin of the lithospheric tension causing basin formation. *Philosophical Transactions of the Royal Society of London.Series A, Mathematical and Physical Sciences,* **305** 319-324.

Bott, M.H.P., 1982b. Interior of the earth: its structure, constitution and evolution. 2nd Edn. Edward Arnold, London.

Bott, M.H.P., 1999. Modeling local crustal isostasy caused by ductile flow in the lower crust. *Journal of Geophysical Research-Solid Earth,* **104**, 9, 20349-20359.

Bott, M.H.P., Swinburn, P.M. and Long, R.E., 1984. Deep structure and origin of the Northumberland and Stainmore troughs. *Proceedings of the Yorkshire Geological Society,* **44**, 32, 479-495.

Bott, M.H.P. and Masson-Smith, D., 1957. The geological interpretation of a gravity survey of the Alston Block and the Durham Coalfield. *Quarterly Journal of the Geological Society,* **113**, 1-4, 93-116.

Bouch, J.E., Naden, J., Shepherd, T.J., McKervey, J.A., Young, B., Benham, A.J. and Sloane, H.J., 2006. Direct evidence of fluid mixing in the formation of stratabound Pb–Zn–Ba–F mineralisation in the Alston Block, North Pennine Orefield (England). *Mineralium Deposita,* **41**, 8, 821-835.

Bracewell, R.N., 1986. The fourier transform and its applications. 2nd Edn. McGraw-Hill, New York.

Braun, J. and Beaumont, C., 1989. A physical explanation of the relation between flank uplifts and the breakup unconformity at rifted continental margins. *Geology,* **17**, 8, 760-764.

Bredehoeft, J.D. and Hanshaw, B.B., 1968. On the maintenance of anomalous fluid pressures: I. Thick sedimentary sequences. *Geological Society of America Bulletin,* **79**, 9, 1097-1106.

Bresnahan, T. and Dickensen, K., 2002, Surfer 8 Self-Paced Training Guide. Golden Software Inc.

Brewer, J.A., Matthews, D.H., Warner, M.R., Hall, J., Smythe, D.K. and Whittington, R.J., 1983. BIRPS deep seismic reflection studies of the British Caledonides. *Nature,* **305**, 5931, 206-210.

Brown, P.E., Ryan, P.D., Soper, N.J. and Woodcock, N.H., 2008. The Newer Granite problem revisited: a transtensional origin for the Early Devonian trans-suture suite. *Geological Magazine,* **145**, 2, 235-256.

Bruce, C.H., 1973. Pressured Shale and Related Sediment Deformation; mechanism for Development of Regional Contemporaneous Faults. *Bulletin American Association of Petroleum Geologists,* **57**, 5, 878-886.

Buck, W.R., Martinez, F., Steckler, M.S. and Cochran, J.R., 1988. Thermal consequences of lithospheric extension: pure and simple. *Tectonics,* **7**, 2, 213-234.

Burgess, I.C., 1971. *Synopses of logs of Allenheads No 1 Borehole ([8604 4539]; OD 406.76m) and No 2 Borehole ([8715 4505]; OD 536.45m).* Annual Report for the Institute of Geological Sciences for 1970.

Burgess, I.C. and Harrison, R.K., 1967. Carboniferous basement beds in the Roman Fell district, Westmorland. *Proceedings of the Yorkshire Geological Society,* **36**, 2, 203-225.

Burgess, I.C. and Holliday, D.W., 1979. Geology of the country around Brough-under-Stainmore. H.M.S.O, London.

Burov, E. and Cloetingh, S., 1997. Erosion and rift dynamics: new thermomechanical aspects of post-rift evolution of extensional basins. *Earth and Planetary Science Letters,* **150**, 1-2, 7-26.

Burov, E.B. and Diament, M., 1995. The effective elastic thickness (T e) of continental lithosphere: What does it really mean? *Journal of Geophysical Research-Solid Earth,* **100**, 3, 3905-3927.

Burov, E. and Poliakov, A., 2003. Erosional forcing of basin dynamics: new aspects of syn-and post-rift evolution. In: D.A. Nieuwland (Ed) *New insights into structural interpretation and mapping.* Geological Society of London Special Publication No. 212, London, 209-223.

Busby, J.P., 1987. An interactive FORTRAN 77 program using GKS graphics for 2.5 D modeling of gravity and magnetic data. *Computers & Geosciences,* **13**, 6, 639-644.

Caldwell, J. and Turcotte, D., 1979. Dependence of the thickness of the elastic oceanic lithosphere on age. *Journal of Geophysical Research,* **84** 7572-7576.

Cann, J.R. and Banks, D.A., 2001. Constraints on the genesis of the mineralization of the Alston Block, Northern Pennine Orefield, northern England. *Proceedings of the Yorkshire Geological Society,* **53**, 3, 187-196.

Chadwick, R.A. and Evans, D.J., 2005. A seismic atlas of southern Britain: images of subsurface structure. British Geological Survey, Keyworth, Nottingham.

Chadwick, R.A., Evans, D.J. and Holliday, D.W., 1993. The Maryport fault: the post-Caledonian tectonic history of southern Britain in microcosm. *Journal of the Geological Society,* **150**, 2, 247-250.

Chadwick, R.A. and Holliday, D.W., 1991. Deep Crustal Structure and Carboniferous Basin Development Within the Iapetus Convergence Zone, Northern England. *Journal of the Geological Society,* **148**, 1, 41-53.

Chadwick, R.A., Holliday, D.W., Holloway, S. and Hulbert, A.G., 1995. The structure and evolution of the Northumberland-Solway Basin and adjacent areas, Subsurface memoir. H.M.S.O for the British Geological Survey, London.

Champagnac, J.D., Schlunegger, F., Norton, K., von Blanckenburg, F., Abbühl, L.M. and Schwab, M., 2009. Erosion-driven uplift of the modern Central Alps. *Tectonophysics,* **474**, 1-2, 236-249.

Clarke, S.M., 2002. Faulting, fault zone processes and hydrocarbon flow through three-dimensional basin models. 2 vols. PhD Edn. Keele. University. Department of Earth Sciences and Geography.

Clarke, S.M., 2007. *The geology of NY76NW (S), Cawfields, Northumberland.* Keyworth, Nottingham: British Geological Survey Open Report OR/07/034.

Cocks, L.R.M., 2000. The early Palaeozoic geography of Europe. *Journal of the Geological Society,* **157**, 1, 1-10.

Cocks, L.R.M. and Fortey, R.A., 1982. Faunal evidence for oceanic separations in the Palaeozoic of Britain. *Journal of the Geological Society,* **139**, 4, 465-478.

Collier, R.E.L., 1989. Tectonic evolution of the Northumberland Basin; the effects of renewed extension upon an inverted extensional basin. *Journal of the Geological Society,* **146**, 6, 981-989.

Collier, R.E.L., 1991. The Lower Carboniferous Stainmore Basin, N. England; extensional basin tectonics and sedimentation. *Journal of the Geological Society,* **148**, 2, 379-390.

Cooley, J.W. and Tukey, J.W., 1965. An algorithm for the machine calculation of complex Fourier series. *Mathematics of computation,* **19**, 90, 297-301.

Cope, J.C.W., Guion, P.D., Sevastopulo, G.D. and Swan, A.R.H., 1992. Carboniferous. In: J.C.W. Cope, J.K. Ingham and P.F. Rawson (Eds) *Atlas of palaeogeography and lithofacies.* Geological Society of London Memoirs, 13, 67-86.

Corex UK, 2002. *Petrographic Study of the Stonehaugh and Longhorsley-1 Wells.*

Cormen, T.H., Rivest, R.L., Stein, C. and Leiserson, C., 2001. Introduction to algorithms. The MIT press, New York.

Coward, M.P., 1986. Heterogeneous stretching, simple shear and basin development. *Earth and Planetary Science Letters,* **80**, 3-4, 325-336.

Cox, R.A., Dempster, T.J., Bell, B.R. and Rogers, G., 1996. Crystallization of the Shap Granite: evidence from zoned K-feldspar megacrysts. *Journal of the Geological Society,* **153**, 4, 625-635.

Dabek, Z.K. and Williamson, J.P., 1999. *Forward and inverse wavenumber formulae for the gravity and magnetic responses of layered models.* British Geological Survey, Technical Report WK/99/03C.

Das, B.M., 1983. Advanced soil mechanics. McGraw-Hill, New York.

Davis, J.C., 1986, Statistics and Data Analysis in Geology. John Wiley, New York.

Davis, G. and Reynolds, S.J., 1996. Structural geology of rocks and regions. 2nd Edn. Wiley, New York.

Dawson, J.B., Carswell, D.A., Hall, J. and Wedepohl, K.H., 1986. Introduction. In: J.B. Dawson, D.A. Carswell, J. Hall and K.H. Wedepohl (Eds) *The Nature of the Lower Continental Crust.* Geological Society of London Special Publication No. 24, London, vii-viii.

De Paola, N., Holdsworth, R.E., McCaffrey, K.J.W. and Barchi, M.R., 2005. Partitioned transtension: an alternative to basin inversion models. *Journal of Structural Geology,* **27**, 4, 607-625.

Dewey, J.F. and Strachan, R.A., 2003. Changing Silurian-Devonian relative plate motion in the Caledonides: sinistral transpression to sinistral transtension. *Journal of the Geological Society,* **160**, 2, 219-229.

Dula, W.F., 1991. Geometric models of listric normal faults and rollover folds. *Bulletin American Association of Petroleum Geologists,* **75**, 10, 1609-1625.

Dunham, A.C. and Kaye, M.J., 1965. The petrology of the Little Whin Sill, County Durham. *Proceedings of the Yorkshire Geological Society,* **35** 229-276.

Dunham, K.C. and Johnson, G.A.L., 1962. Sub-Surface Data on the Namurian Strata of Allenheads, South Northumberland. *Proceedings of the Yorkshire Geological Society,* **33**, 3, 235-254.

Dunham, K.C., Dunham, A.C., Hodge, B.L. and Johnson, G.A.L., 1965. Granite beneath Viean sediments with mineralization at Rookhope, northern Pennines. *Quarterly Journal of the Geological Society,* **121**, 1-4, 383-417.

Eastwood, T., 1930. The geology of the Maryport district. H.M.S.O, London.

Egan, S.S., 1992. The Flexural Isostatic Response of the Lithosphere to Extensional Tectonics. *Tectonophysics,* **202**, 2-4, 291-308.

Egan, S.S., Kane, S., Buddin, T.S., Williams, G.D. and Hodgetts, D., 1999. Computer modelling and visualisation of the structural deformation caused by movement along geological faults. *Computers & Geosciences,* **25**, 3, 283-297.

Egan, S.S., Mosar, J., Brunet, M.F. and Kangarli, T., 2009. Subsidence and uplift mechanisms within the South Caspian Basin: insights from the onshore and offshore Azerbaijan region. In: M.F. Brunet, M. Wilmsen and J.W. Granarth (Eds) *South Caspian to Central Iran Basins.* Geological Society of London Special Publication No. 312, London, 219-240.

Elliott, D.F. and Rao, K.R., 1982. Fast transforms: algorithms, analyses, applications. Academic Press, Inc, New York.

Elliott, T., 1974. Abandonment facies of high-constructive lobate deltas, with an example from the Yoredale Series. *Proceedings of the Geologists' Association,* **85**, 3, 359-365.

Elliott, T., 1975. The sedimentary history of a delta lobe from a Yoredale (Carboniferous) cyclothem. *Proceedings of the Yorkshire Geological Society,* **40**, 4, 505-536.

Enos, P., 1991. Sedimentary parameters for computer modeling. In: E.K. Franseen, W.L. Watney, C.G.S.C. Kendall and W. Ross (Eds) *Sedimentary modelling computer simulations and methods for improved parameter definition.* Kansas Geological Society Bulletin No. 233, 63-99.

Evans, C.J., Kimbell, G.S. and Rollin, K.E., 1988. Hot dry rock potential in urban areas. Investigation of the geothermal potential of the UK. British Geological Survey, Keyworth, Nottingham.

Falvey, D.A. and Middleton, M.F., 1981. Passive continental margins: Evidence for a prebreakup deep crustal metamorphic subsidence mechanism. In: R. Blanchet and L. Montadert (Eds) *Proceedings of 26th International Geological Congress, Geology of Continental Margins Symposium, Paris, 7–17 July 1980.* Oceanologica Acta, 103-114.

Fernāndez, M. and Ranalli, G., 1997. The role of rheology in extensional basin formation modelling. *Tectonophysics,* **282**, 1-4, 129-145.

Fielding, C.R., 1984a. Upper delta plain lacustrine and fluviolacustrine facies from the Westphalian of the Durham coalfield, NE England. *Sedimentology,* **31**, 4, 547-567.

Fielding, C.R., 1984b. A coal depositional model for the Durham Coal Measures of NE England. *Journal of the Geological Society,* **141**, 5, 919-931.

Fitch, F.J. and Miller, J.A., 1965. Age of the Weardale granite. *Nature,* **208** 743-745.

Fitch, F.J. and Miller, J.A., 1967. The age of the Whin Sill. *Geological Journal,* **5**, 2, 233-250.

Fleischer, R.L. and Price, P.B., 1964. Techniques for geological dating of minerals by chemical etching of fission fragment tracks. *Geochimica et Cosmochimica Acta,* **28**, 10-11, 1705-1714.

Forsyth, D.W., 1985. Subsurface loading and estimates of the flexural rigidity of continental lithosphere. *Journal of Geophysical Research-Solid Earth,* **90**, 14, 12623-12632.

Francis, E.H., 1982. Magma and sediment-I Emplacement mechanism of late Carboniferous tholeiite sills in northern Britain: President's anniversary address 1981. *Journal of the Geological Society,* **139**, 1, 1-20.

Fraser, A.J. and Gawthorpe, R.L., 1990. Tectono-stratigraphic development and hydrocarbon habitat of the Carboniferous in northern England. In: R.F.P. Hardman and J. Brooks (Eds) *Tectonic Events Responsible for Britain's Oil and Gas Reserves.* Geological Society of London Special Publication No. 55, London, 49-86.

Freeman, B., Klemperer, S.L. and Hobbs, R.W., 1988. The deep structure of northern England and the Iapetus Suture zone from BIRPS deep seismic reflection profiles. *Journal of the Geological Society,* **145**, 5, 727-740.

Frost, D.V. and Holliday, D.W., 1980. Geology of the country around Bellingham: Memoir for 1:50,000 geological sheet 13. H.M.S.O, London.

Galloway, W.E., 1989. Genetic stratigraphic sequences in basin analysis I: architecture and genesis of flooding-surface bounded depositional units. *Bulletin American Association of Petroleum Geologists,* **73**, 2, 125-142.

Garland, G.D., 1971. Introduction to geophysics mantle, core and crust. W.B. Saunders Company, Philadelphia.

Gayer, R., Hathaway, T. and Nemcok, M., 1998. Transpressionally driven rotation in the external orogenic zones of the Western Carpathians and the SW British Variscides. In: R.E. Holdsworth, R.A. Strachen and J.F. Dewey (Eds) *Continental Transpression and Transtensional Tectonics.* Geological Society of London Special Publication No. 135, London, 253-266.

George, T.N., Johnson, G.A.L., Mitchell, M., Prentice, J.E., Ramsbottom, W.H.C., Sevastopulo, G.D. and Wilson, R.B., 1976. A correlation of Dinantian rocks in the British Isles. Geological Society of London, Special Report 7, .

Gibbs, A.D., 1983. Balanced cross-section construction from seismic sections in areas of extensional tectonics. *Journal of Structural Geology,* **5**, 2, 153-160.

Gibbs, A.D., 1984. Structural evolution of extensional basin margins. *Journal of the Geological Society,* **141**, 4, 609-620.

Gilchrist, A.R., Summerfield, M.A. and Cockburn, H.A.P., 1994. Landscape dissection, isostatic uplift, and the morphologic development of orogens. *Geology,* **22**, 11, 963-966.

Glennie, K.W., 1998. Lower Permian–Rotliegend. In: K.W. Glennie (Ed) *Petroleum Geology of the North Sea.* 4th Edn. Blackwell Science, 137-173.

Green, P.F., 1986. On the Thermo-Tectonic Evolution of Northern England - Evidence from Fission-Track Analysis. *Geological Magazine,* **123**, 5, 493-506.

Green, P.F., 2002. Early Tertiary paleo-thermal effects in Northern England: reconciling results from apatite fission track analysis with geological evidence. *Tectonophysics,* **349**, 1-4, 131-144.

Green, P.F., Duddy, I.R., Laslett, G.M., Hegarty, K.A., Gleadow, A.J.W. and Lovering, J.F., 1989. Thermal annealing of fission tracks in apatite 4. Quantitative modelling techniques and extension to geological timescales. *Chemical Geology: Isotope Geoscience section,* **79**, 2, 155-182.

Gunn, R., 1949. Isostasy: Extended. *The Journal of Geology,* **57**, 3, 263-279.

Hall, J., Brewer, J.A., Matthews , D.H. and Warner, M.R., 1984. Crustal structure across the Caledonides from the 'WINCH' seismic reflection profile:

influences on the evolution of the Midland Valley of Scotland. *Transactions of the Royal Society of Edinburgh-Earth Sciences,* **75** 97-109.

Halliday, A.N., Aftalion, M., Van Breemen, O. and Jocelyn, J., 1979. Petrogenetic significance of Rb-Sr and U-Pb isotopic systems in the 400 Ma old British Isles granitoids and their hosts. In: A.L. Harris, C.H. Holland and B.E. Leake (Eds) *Caledonides of the British Isles - Reviewed.* Geological Society of London Special Publication No. 8, London, 653-661.

Hamblin, W.K., 1965. Origin of "Reverse Drag" on the Downthrown Side of Normal Faults. *Geological Society of America Bulletin,* **76**, 10, 1145-1164.

Hampson, G.J., Elliott, T. and Davies, S.J., 1997. The application of sequence stratigraphy to Upper Carboniferous fluvio-deltaic strata of the onshore UK and Ireland: implications for the southern North Sea. *Journal of the Geological Society,* **154**, 4, 719-733.

Haq, B.U. and Schutter, S.R., 2008. A chronology of Paleozoic sea-level changes. *Science,* **322**, 5898, 64-68.

Haq, B.U., Hardenbol, J. and Vail, P.R., 1988. Mesozoic and Cenozoic chronostratigraphy and cycles of sea-level change. In: C.K. Wilgus (Ed) *Sea-level changes: an integrated approach.* Society of Economic Paleontologists and Mineralogists Special Publication 42, 71-108.

Hess, H.H., 1962. History of Ocean Basins. In: A.E.J. Engel, H.L. James and B.F. Leonard (Eds) *Petrologic studies: a volume in honor of A. F. Buddington.* Scripps Institution of Oceanography Library, San Diego, 599-620.

Higgins, A.C. and Varker, W.J., 1982. Lower Carboniferous conodont faunas from Ravenstonedale, Cumbria. *Palaeontology,* **25**, 1, 145-166.

Hodgetts, D., Egan, S.S. and Williams, G.D., 1998. Flexural modelling of continental lithosphere deformation: a comparison of 2D and 3D techniques. *Tectonophysics,* **294**, 1-2, 1-20.

Holland, J.G., 1967. Rapid analysis of the Weardale granite. *Proceedings of the Yorkshire Geological Society,* **36**, 1, 91-113.

Holland, J.G. and Lambert, R.S.J., 1970. Weardale Granite. In: G.A.L. Johnson and G. Hickling (Eds) *Geology of Durham County.* Transactions of the Natural History Society of Northumberland, Durham and Newcastle upon Tyne, 41, Newcastle Upon Tyne, 103-118.

Holliday, D.W., 1993a. Mesozoic cover over northern England: interpretation of apatite fission track data. *Journal of the Geological Society,* **150**, 4, 657-660.

Holliday, D.W., 1993b. Geophysical log signatures in the Eden Shales (Permo-Triassic) of Cumbria and their regional significance. *Proceedings of the Yorkshire Geological Society,* **49**, 4, 345-354.

Holliday, D.W., Holloway, S., McMillan, A.A., Jones, N.S., Warrington, G. and Akhurst, M.C., 2004. The evolution of the Carlisle Basin, NW England and SW Scotland. *Proceedings of the Yorkshire Geological Society,* **55**, 1, 1-20.

Holliday, D.W., Neves, R. and Owens, B., 1979. Stratigraphy and palynology of early Dinantian (Carboniferous) strata in shallow boreholes near Ravenstonedale, Cumbria. *Proceedings of the Yorkshire Geological Society,* **42**, 3, 343-356.

Holliday, D.W., Warrington, G., Brookfield, M.E., McMillan, A.A. and Holloway, S., 2001. Permo–Triassic rocks in boreholes in the Annan-Canonbie area, Dumfries and Galloway, southern Scotland. *Scottish Journal of Geology,* **37**, 2, 97-113.

Holloway, S., 1985. Triassic. In: A. Whittaker (Ed) *Atlas of onshore sedimentary basins in England and Wales.* Blackie, Glasgow, 31-36.

Holmes, A. and Harwood, H.F., 1928. The age and composition of the Whin Sill and the related dykes of the north of England. *Mineralogical Magazine,* **21** 493-542.

Hounslow, M.W. and Ruffell, A.H., 2006. Triassic: seasonal rivers, dusty deserts and saline lakes. In: P.J. Brenchley and P.F. Rawson (Eds) *Geology of England and Wales.* Geological Society of London, London, 295-324.

Hu, S., O'Sullivan, P.B., Raza, A. and Kohn, B.P., 2001. Thermal history and tectonic subsidence of the Bohai Basin, northern China: a Cenozoic rifted and local pull-apart basin. *Physics of the Earth and Planetary Interiors,* **126**, 3-4, 221-235.

Hubbert, M.K. and Rubey, W.W., 1959. Role of fluid pressure in mechanics of overthrust faulting, 1: Mechanics of fluid-filled porous solids and its application to overthrust faulting. *Geological Society of America Bulletin,* **70**, 2, 115-167.

Hughes, R.A., Evans, J.A., Noble, S.R. and Rundle, C.C., 1996. U-Pb chronology of the Ennerdale and Eskdale intrusions supports sub-volcanic relationships with the Borrowdale Volcanic Group (Ordovician, English Lake District). *Journal of Geological Society,* **153**, 1, 33-38.

Jackson, D.I., Jackson, A.A., Evans, D., Wingfield, R.T.R., Barnes, R.P. and Arthur, M.J., 1995. United Kingdom offshore regional report: the geology of the Irish Sea. H.M.S.O for the British Geological Survey, London.

Jackson, J. and McKenzie, D., 1983. The geometrical evolution of normal fault systems. *Journal of Structural Geology,* **5**, 5, 471-482.

Jaeger, J.C., 1969. Elasticity, fracture and flow, with engineering and geological applications. 3rd Edn. Methuen, London.

Johnson, G.A.L., 1959. The Carboniferous stratigraphy of the Roman Wall district in western Northumberland. *Proceedings of the Yorkshire Geological Society,* **32**, 1, 83-130.

Johnson, G.A.L., 1967. Basement control of Carboniferous sedimentation in northern England. *Proceedings of the Yorkshire Geological Society,* **36**, 2, 175-194.

Johnson, G.A.L., 1981. Geographical evolution from Laurasia to Pangaea. *Proceedings of the Yorkshire Geological Society,* **43**, 3, 221-252.

Johnson, G.A.L., 1984. Subsidence and sedimentation in the Northumberland Trough. *Proceedings of the Yorkshire Geological Society,* **45**, 1-2, 71-83.

Johnson, G.A.L. and Nudds, J.R., 1995. Carboniferous biostratigraphy of the Rookhope Borehole, Co. Durham. *Transactions of the Royal Society of Edinburgh-Earth Sciences,* **86**, 3, 181-226.

Jones, N.S. and Holliday, D.W., 2006. *The stratigraphy and sedimentology of Upper Carboniferous Warwickshire Group red-bed facies in the Canonbie area of S.W. Scotland.* British Geological Survey Internal Report, IR/06/043.

Karner, G.D. and Watts, A.B., 1982. On isostasy at Atlantic-type continental margins. *Journal of Geophysical Research-Solid Earth,* **87**, 4, 2923-2948.

Kearey, P. and Vine, F.J., 1990. Global Tectonics. Blackwell Scientific Publications, Oxford.

Keary, P., Brooks, M. and Hill, I., 2002. An introduction to geophysical exploration. 3rd Edn. Blackwell Science, Oxford.

Keen, C.E., 1985. The dynamics of rifting: deformation of the lithosphere by active and passive driving forces. *Geophysical Journal of the Royal Astronomical Society,* **80**, 1, 95-120.

Keen, C.E., 1987. Some important consequences of lithospheric extension. In: M.P. Coward, J.F. Dewey and P.L. Hancock (Eds) *Continental Extensional Tectonics.* Geological Society of London Special Publication No. 28, 67-73.

Kendall, A.C., 1992. Evaporites. In: R.G. Walker and N.P. James (Eds) *Facies Models: Response to Sea Level Changes.* Geological Association of Canada, 375-409.

Kimbell, G.S., Chadwick, R.A., Holliday, D.W. and Werngren, O.C., 1989. The structure and evolution of the Northumberland Trough from new seismic reflection data and its bearing on modes of continental extension. *Journal of the Geological Society,* **146**, 5, 775-787.

Kimbell, G.S., Young, B., Millward, D. and Crowley, Q.G., 2010. The North Pennine batholith (Weardale Granite) of northern England - new data on its age and form. *Proceedings of the Yorkshire Geological Society,* **In Press**.

Kington, J.D. and Goodliffe, A.M., 2008. Plate motions and continental extension at the rifting to spreading transition in Woodlark Basin, Papua New Guinea: Can oceanic plate kinematics be extended into continental rifts? *Tectonophysics,* **458**, 1-4, 82-95.

Kirby, S.H., 1983. Rheology of the lithosphere. *Reviews of Geophysics,* **21**, 6, 1458-1487.

Klemperer, S.L., 1988. Crustal thinning and nature of extension in the northern North Sea from deep seismic reflection profiling. *Tectonics,* **7**, 4, 803-821.

Kohlstedt, D.L., Evans, B. and Mackwell, S.J., 1995. Strength of the lithosphere: Constraints imposed by laboratory experiments. *Journal of Geophysical Research-Solid Earth,* **100**, 9, 17587-17602.

Kusznir, N.J. and Bott, M.H.P., 1977. Stress concentration in the upper lithosphere caused by underlying visco-elastic creep. *Tectonophysics,* **43**, 3-4, 247-256.

Kusznir, N.J. and Egan, S.S., 1989. Simple-Shear and Pure-Shear Models of Extensional Sedimentary Basin Formation: Application to the Jeanne d'Arc Basin, Grand Banks of Newfoundland. In: A.J. Tankard and H.R. Balkwill (Eds) *Extensional Tectonics and Stratigraphy of the North Atlantic Margin.* American Association of Petroleum Geologists Memoir No.46, 305-322.

Kusznir, N.J., Karner, G.D. and Egan, S., 1987. Geometric, thermal and isostatic consequences of detachments in continental lithosphere extension and basin formation. In: C. Beaumont and A.J. Tankard (Eds) *Sedimentary Basins and Basin-Forming Mechanisms.* Canadian Society of Petroleum Geologists Memoir No.12, 185-203.

Kusznir, N.J. and Matthews, D.H., 1988. Deep seismic reflections and the deformational mechanics of the continental lithosphere. *Journal of Petrology,* **29**, Special Lithosphere Issue, 63-87.

Kusznir, N.J. and Park, G., 1987. The extensional strength of the continental lithosphere: its dependence on geothermal gradient, crustal composition and thickness. In: M.P. Coward, J.F. Dewey and P.L. Hancock (Eds) *Continental Extensional Tectonics.* Geological Society of London Special Publication No.28, 35-52.

Kusznir, N.J. and Karner, G., 1985. Dependence of the flexural rigidity of the continental lithosphere on rheology and temperature. *Nature,* **316** 138-142.

Langseth, M.G., Le Pichon, X. and Ewing, M., 1966. Crustal structure of the mid-ocean ridges, 5, Heat flow through the Atlantic Ocean floor and convection currents. *Journal of Geophysical Research,* **71** 5321-5355.

Lawrence, D.J.D., Arkley, S.L.B., Everest, J.D., Clarke, S.M., Millward, D., Hyslop, E.K., Thompson, G.L. and Young, B., 2007. Northumberland National Park: Geodiversity Audit and Action Plan. British Geological Survey, Natural Environment Research Council, Northumberland National Park, Nottingham.

Le Pichon, X., Angelier, J. and Sibuet, J., 1982. Plate boundaries and extensional tectonics. *Tectonophysics,* **81**, 3-4, 239-256.

Leeder, M.R., 1974a. Lower Border Group (Tournaisian) fluvio-deltaic sedimentation and palaeogeography of the Northumberland Basin. *Proceedings of the Yorkshire Geological Society,* **40**, 2, 129-180.

Leeder, M.R., 1974b. Origin of the Northumberland basin. *Scottish Journal of Geology,* **10**, 4, 283-296.

Leeder, M.R., 1976. Sedimentary facies and the origins of basin subsidence along the northern margin of the supposed hercynian ocean. *Tectonophysics,* **36**, 1-3, 167-179.

Leeder, M.R., 1982. Upper Palaeozoic basins of the British Isles--Caledonide inheritance versus Hercynian plate margin processes. *Journal of the Geological Society,* **139**, 4, 479-491.

Leeder, M.R., Fairhead, D., Lee, A., Stuart, G., Clemmey, H., Al-Haddeh, B. and Green, B., 1989. Sedimentary and tectonic evolution of the Northumberland Basin. In: R.S. Arthurton, P. Gutteridge and S.C. Nolan (Eds) *The Role of Tectonics in Devonian and Carboniferous Sedimentation in the British Isles.* Yorkshire Geological Society Occasional Publication No. 6, 207-223.

Leggett, J.K., McKerrow, W.S. and Soper, N.J., 1983. A model for the crustal evolution of southern Scotland. *Tectonics,* **2**, 2, 187-210.

Lerche, I., 1990. Basin analysis: Quantitative Methods. Academic Press, San Diego.

Lewis, C.L.E., Green, P.F., Carter, A. and Hurford, A.J., 1992. Elevated K/T palaeotemperatures throughout Nortwest England: three kilometres of Tertiary erosion? *Earth and Planetary Science Letters,* **112**, 1-4, 131-145.

Liss, D., Owens, W.H. and Hutton, D.H.W., 2004. New palaeomagnetic results from the Whin Sill complex: evidence for a multiple intrusion event and revised virtual geomagnetic poles for the late Carboniferous for the British Isles. *Journal of the Geological Society,* **161**, 6, 927-938.

Love, A.E.H., 1944. A treatise on the mathematical theory of elasticity. 4th Edn. Dover Publications, New York.

Lowrie, W., 1997. Fundamentals of geophysics. Cambridge University Press, Cambridge.

Lubimova, E.A. and Nikitina, V.N., 1975. On heat flow singularities over mid-ocean ridges. *Journal of Geophysical Research,* **80**, 2, 232-243.

Macdonald, R., Millward, D., Beddoe-Stephens, B. and Laybourn-Parry, J., 1988. The role of tholeiitic magmatism in the English Lake District: evidence from dykes in Eskdale. *Mineralogical Magazine,* **52** 459-472.

Manning, D.A.C., Younger, P.L., Smith, F.W., Jones, J.M., Dufton, D.J. and Diskin, S., 2007. A deep geothermal exploration well at Eastgate, Weardale, UK: a novel exploration concept for low-enthalpy resources. *Journal of the Geological Society, London,* **164**, 2, 371-382.

Mareschal, J.C., 1981. Uplift by thermal expansion of the lithosphere. *Geophysical Journal of the Royal Astronomical Society,* **66**, 3, 535-552.

McCann, T., Pascal, C., Timmerman, M.J., Krzywiec, P., López-Gómez, J., Wetzel, A., Krawczyk, C.M., Rieke, H. and Lamarche, J., 2006. Post-Variscan (end Carboniferous-Early Permian) basin evolution in Western and Central Europe. In: D.G. Gee and R.A. Stephenson (Eds) *European Lithosphere Dynamics.* Geological Society of London Memoirs, 32, London, 355-388.

McKenzie, D.P., 1967. Some remarks on heat flow and gravity anomalies. *Journal of Geophysical Research,* **72**, 24, 6261-6273.

McKenzie, D., 1978. Some remarks on the development of sedimentary basins. *Earth and Planetary Science Letters,* **40**, 1, 25-32.

McKenzie, D. and Fairhead, D., 1997. Estimates of the effective elastic thickness of the continental lithosphere from Bouguer and free air gravity anomalies. *Journal of Geophysical Research-Solid Earth,* **102**, 12, 27523-27552.

McKerrow, W.S. and Soper, N.J., 1989. The Iapetus Suture in the British Isles. *Geological Magazine,* **126**, 1, 1-8.

McNutt, M.K., Diament, M. and Kogan, M.G., 1988. Variations of elastic plate thickness at continental thrust belts. *Journal of Geophysical Research-Solid Earth,* **93**, 8, 8825-8838.

Meissner, R., 1986. The continental crust: A geophysical approach. Academic Press, Inc, London.

Menzies, M.A., 1990. Petrology and Geochemistry of the Continental Mantle: An historical Perspective. In: M.A. Menzies (Ed) *Continental Mantle.* 31-54.

Meredith, D.J., 2003. *2-D and 3-D computer modelling of lithosphere dynamics and sedimentary basin formation*, Keele University, PhD.

Meredith, D.J. and Egan, S.S., 2002. The geological and geodynamic evolution of the eastern Black Sea basin: insights from 2-D and 3-D tectonic modelling. *Tectonophysics,* **350**, 2, 157-179.

Merriman, R.J., Rex, D.C., Soper, N.J. and Peacor, D.R., 1995. The age of Acadian cleavage in northern England, UK: K–Ar and TEM analysis of a Silurian metabentonite. *Proceedings of the Yorkshire Geological Society,* **50**, 3, 255-265.

Miller, J.A. and Mussett, A.E., 1963. Dating basic rocks by the potassium-argon method: the Whin Sill. *Geophysical Journal of the Royal Astronomical Society,* **7**, 5, 547-553.

Millward, D., 2002. Early Palaeozoic magmatism in the English Lake District. *Proceedings of the Yorkshire Geological Society,* **54** 65-93.

Millward, D., 2004. The Caradoc volcanoes of the English Lake District. *Proceedings of the Yorkshire Geological Society,* **55**, 2, 73-105.

Millward, D. and Evans, J.A., 2003. U-Pb chronology and duration of late Ordovician magmatism in the English Lake District. *Journal of the Geological Society,* **160**, 5, 773-781.

Millward, D., Marriner, G.F. and Beddoe-Stephens, B., 2000. The Eycott Volcanic Group, an Ordovician continental margin andesite suite in the English Lake District. *Proceedings of the Yorkshire Geological Society,* **53**, 2, 81-96.

Morgan, P., 1984. The thermal structure and thermal evolution of the continental lithosphere. *Physics and Chemistry of the Earth,* **15** 107-193.

Morton, A., Fanning, M. and Jones, N., 2010. Variscan sourcing of Westphalian (Pennsylvanian) sandstones in the Canonbie Coalfield, UK. *Geological Magazine,* **147**, 5, 718-727.

Murchison, R.I. and Harkness, R., 1864. On the Permian rocks of the north-west of England, and their extension into Scotland. *Quarterly Journal of the Geological Society,* **20**, 1-2, 144-165.

Murrell, S.A.F., 1976. Rheology of the lithosphere--Experimental indications. *Tectonophysics,* **36**, 1-3, 5-24.

Negredo, A.M., Fernāndez, M. and Zeyen, H., 1995. Thermo-mechanical constraints on kinematic models of lithospheric extension. *Earth and Planetary Science Letters,* **134**, 1-2, 87-98.

O'Brien, C., Plant, J.A., Simpson, P.R. and Tarney, J., 1985. The geochemistry, metasomatism and petrogenesis of the granites of the English Lake District. *Journal of the Geological Society,* **142**, 6, 1139-1157.

Özişik, M.N., 1980. Heat conduction. Wiley, Chichester.

Park, R.G., 1989. Foundations of structural geology. 2nd Edn. Blackie, London.

Parsons, B. and Sclater, J.G., 1977. An analysis of the variation of ocean floor bathymetry and heat flow with age. *Journal of Geophysical Research,* **82**, 5, 803-827.

Peacock, D.C.P., Knipe, R.J. and Sanderson, D.J., 2000. Glossary of normal faults. *Journal of Structural Geology,* **22**, 3, 291-305.

Pedley, R.C., 1991. *GRAVMAG user manual: interactive 2.5 D gravity and magnetic modeling.* Keyworth, Nottingham: British Geological Survey, Technical Report WK/93/26/R.

Picken, G.S., 1988. The concealed coalfield at Canonbie: an interpretation based on boreholes and seismic surveys. *Scottish Journal of Geology,* **24**, 1, 61-71.

Piper, J.D.A., McArdle, N.J. and Almaskeri, Y., 2007. Palaeomagnetic study of the cairnsmoor of fleet granite and criffel-dalbeattie granodiorite contact aureoles: Caledonian tectonics of the southern uplands of Scotland and devonian palaeogeography. *Geological Magazine,* **144**, 5, 811-835.

Pollack, H.N. and Chapman, D.S., 1977. On the regional variation of heat flow, geotherms, and lithospheric thickness. *Tectonophysics,* **38**, 3-4, 279-296.

Posamentier, H.W. and Vail, P.R., 1988. Eustatic controls on clastic deposition II—sequence and systems tract models. In: C.K. Wilgnus, C.G.S.C. Hastings, H.W. Kendall, H.W. Posamentier, C.A. Ross and J.C. Van Wagoner (Eds) *Sea-Level Changes: An Integrated Approach.* SEPM, Special Publication, 125–154.

Pratt, J.H., 1859. On the Influence of the Ocean on the Plumb-Line in India. *Philosophical Transactions of the Royal Society of London,* **149** 779-796.

Purdy, E.G., 1974. Reef configurations; cause and effect. In: L.F. Laporte (Ed) *Reefs in Time and Space: Selected examples from the recent and ancient.* SEPM, Special Publication No. 18, Tulsa, Oklahoma, 9-76.

Putnam, G.R., 1930. Isostatic Compensation in Relation to Geological Problems. *The Journal of Geology,* **38**, 7, 590-599.

Quinlan, G., Walsh, J., Skogseid, J., Sassi, W., Cloetingh, S., Lobkovsky, L., Bois, C., Stel, H. and Banda, E., 1993. Relationship between deeper lithospheric processes and near-surface tectonics of sedimentary basins. *Tectonophysics,* **226**, 1-4, 217-225.

Ramsay, J.G., 1980. Shear zone geometry: a review. *Journal of Structural Geology,* **2**, 1-2, 83-99.

Ramsbottom, W.H.C., 1973. Transgressions and regressions in the Dinantian: a new synthesis of British Dinantian stratigraphy. *Proceedings of the Yorkshire Geological Society,* **39**, 4, 567-607.

Ramsbottom, W.H.C., 1977. Major cycles of transgression and regression (mesothems) in the Namurian. *Proceedings of the Yorkshire Geological Society,* **41**, 3, 261-291.

Reston, T.J., 1988. Evidence for shear zones in the lower crust offshore Britain. *Tectonics,* **7**, 5, 929-945.

Reston, T.J., 1990a. Shear in the lower crust during extension: not so pure and simple. *Tectonophysics,* **173**, 1-4, 175-183.

Reston, T.J., 1990b. Mantle shear zones and the evolution of the northern North Sea basin. *Geology,* **18**, 3, 272-275.

Reynolds, D.J., Steckler, M.S. and Coakley, B.J., 1991. The role of the sediment load in sequence stratigraphy: the influence of flexural isostasy and compaction. *Journal of Geophysical Research-Solid Earth,* **96**, 4, 6931-6949.

Robson, D.A., 1981. The geology of North East England. Special Publication of the Natural History Society of Northumbria, .

Rollin, K.E., 1988. *GM3D: forward and interactive 3-D gravity and magnetic modelling using vertical square prisms.* British Geological Survey, Technical Report WK/88/17.

Rosenbaum, G., Weinberg, R.F. and Regenauer-Lieb, K., 2008. The geodynamics of lithospheric extension. *Tectonophysics,* **458**, 1-4, 1-8.

Rowley, D.B. and Sahagian, D., 1986. Depth-dependent stretching: a different approach. *Geology,* **14**, 1, 32-35.

Royden, L. and Keen, C.E., 1980. Rifting process and thermal evolution of the continental margin of Eastern Canada determined from subsidence curves. *Earth and Planetary Science Letters,* **51**, 2, 343-361.

Rubey, W.W. and Hubbert, M.K., 1959. Role of fluid pressure in mechanics of overthrust faulting, 2: Overthrust belt in geosynclinal area of western Wyoming in light of fluid-pressure hypothesis. *Geological Society of America Bulletin,* **70**, 2, 167-205.

Ruffell, A.H., Holliday, D.W. and Smith, D.B., 2006. Permian : arid basins and hypersaline seas. In: P.J. Brenchley and P.F. Rawson (Eds) *The Geology of England and Wales.* 269-293.

Rutter, E.H., 1986. On the nomenclature of mode of failure transitions in rocks. *Tectonophysics,* **122**, 3-4, 381-387.

Schumm, S.A., 1963. The disparity between present rates of denudation and orogeny. *US Geological Survey, Professional Paper,* **454** 1-13.

Sclater, J.G. and Christie, P.A.F., 1980. Continental stretching: an explanation of the post-mid-Cretaceous subsidence of the central North Sea basin. *Journal of Geophysical Research-Solid Earth,* **85**, 7, 3711-3739.

Scotese, C.R. and McKerrow, W.S., 1990. Revised world maps and introduction. In: W.S. McKerrow and C.R. Scotese (Eds) *Palaeozoic Palaeogeography and Biogeography.* Geological Society of London Memoirs, 12, London, 1-24.

Selby, D., Conliffe, J., Crowley, Q.,G and Feely, M., 2008. Geochronology (ReOs and UPb) and fluid inclusion studies of molybdenite mineralisation associated with the Shap, Skiddaw and Weardale granites, UK. *Applied Earth Science: IMM Transactions section B,* **117**, 1, 11-28.

Sherlock, S.C., Kelley, S.P., Zalasiewicz, J.A., Schofield, D.I., Evans, J.A., Merriman, R.J. and Kemp, S.J., 2003. Precise dating of low-temperature deformation: Strain-fringe analysis by 40Ar-39Ar laser microprobe. *Geology,* **31**, 3, 219-222.

Sibson, R.H., 1977. Fault rocks and fault mechanisms. *Journal of Geological Society,* **133**, 3, 191-213.

Sleep, N.H., 1969. Sensitivity of heat flow and gravity to the mechanism of sea-floor spreading. *Journal of Geophysical Research,* **74**, 2, 542-549.

Sleep, N.H., 1971. Thermal effects of the formation of Atlantic continental margins by continental break up. *Geophysical Journal of the Royal Astronomical Society,* **24**, 4, 325-350.

Sleep, N.H. and Snell, N.S., 1976. Thermal contraction and flexure of mid-continent and Atlantic marginal basins. *Geophysical Journal of the Royal Astronomical Society,* **45**, 1, 125-154.

Sloss, L.L., 1963. Sequences in the cratonic interior of North America. *Bulletin of the Geological Society of America,* **74**, 2, 93-114.

Smith, D.B., 1970. Permian and Trias. In: G.A.L. Johnson and G. Hickling (Eds) *Geology of Durham County.* Transactions of the Natural History Society of Northumberland, Durham and Newcastle upon Tyne, 41, 66-91.

Smith, D.B., 1992. Permian. In: P.M.D. Duff and A.J. Smith (Eds) *Geology of England and Wales.* 1st Edn. Geological Society, London, 275-306.

Smith, D.B., Harwood, G.M., Pattison, J. and Pettigrew , T.H., 1986. A revised nomenclature for Upper Permian strata in eastern England. In: G.M. Harwood and D.B. Smith (Eds) *The English Zechstein and Related Topics.* Geological Society of London Special Publication No. 22, 9-17.

Smith, D.B., Jackson, D.I. and Holliday, D.W., 1994. Discussion of "Geophysical log signatures in the Eden Shales (Permo–Triassic) of Cumbria and their regional significance" Proceedings, Vol. 49, part 4, pp. 345–354, 1993. *Proceedings of the Yorkshire Geological Society,* **50**, 2, 173-184.

Smith, J.E., 1971. The dynamics of shale compaction and evolution of pore-fluid pressures. *Mathematical Geology,* **3**, 3, 239-263.

Smith, S.A. and Holliday, D.W., 1991. The sedimentology of the Middle and Upper Border groups (Viséan) in the Stonehaugh Borehole, Northumberland. *Proceedings of the Yorkshire Geological Society,* **48**, 4, 435-446.

Soper, N.J., 1986, The Newer Granite problem: a geotectionic view. *Geological Magazine*, **123**, 227-236

Soper, N.J., England, R.W., Snyder, D.B. and Ryan, P.D., 1992b. The Iapetus suture zone in England, Scotland, and eastern Ireland; a reconciliation of geological and deep seismic data. *Journal of the Geological Society,* **149**, 5, 697-700.

Soper, N.J., Strachan, R.A., Holdsworth, R.E., Gayer, R.A. and Greiling, R.O., 1992a. Sinistral transpression and the Silurian closure of Iapetus. *Journal of Geological Society,* **149**, 6, 871-880.

Steckler, M.S., Watts, A.B. and Thorne, J.A., 1988. Subsidence and basin modeling at the U.S. Atlantic passive margin. In: R.E. Sheridan and J.A. Grow (Eds) *The Atlantic Continental Margin.* The Geological Society of America, 399-416.

Stephens, W.E. and Halliday, A.N., Geochemical contrasts between late Caledonian granitoid plutons of northern, central and southern Scotland. *Transactions of the Royal Society of Edinburgh-Earth Sciences,* **75**, 2, 259-273.

Stephenson, D., Bevins, R.E., Millward, D., Highton, A.J., Parsons, I., Stone, P. and Wadsworth, W.J., 1999. *Caledonian Igneous Rocks of Great Britain*. Geological Conservation Review Series, No. 17, Joint Nature Conservation Committee, Peterborough.

Stephenson, M.H., Millward, D., Leng, M.J. and Vane, C.H., 2008. Palaeoecological and possible evolutionary effects of early Namurian (Serpukhovian, Carboniferous) glacioeustatic cyclicity. *Journal of Geological Society,* **165**, 6, 993-1005.

Stone, P., Millward, D., Young, B., Merritt, J.W., Clarke, S.M., McCormac, M. and Lawrence, D.J.D., 2010. Northern England. 5th Edn. British Geological Survey, Keyworth, Nottingham.

Taylor, B.J., Burgess, I.C., Land, D.H., Mills, D.A.C., Smith, D.B. and Warren, P.T., 1971. Northern England. 4th Edn. British Geological Survey, H.M.S.O, London.

Terzaghi, K. and Peck, R.B., 1948. Soil mechanics in engineering practice. John Wiley & Sons, New York.

Thompson, D.B., 1970. Sedimentation of the Triassic (Scythian) red pebbly sandstones in the Cheshire Basin and its margins. *Geological Journal,* **7**, 1, 183-216.

Thorne, J.A. and Swift, D.J.P., 1991. Sedimentation on continental margins, II: application of the regime concept. In: D.J.T. Swift, G.F. Oertel and R.W. Tillman (Eds) *Shelf Sand and Sandstone Bodies: Geometry, Facies and Distribution.* International Association of Sedimentologists, Special Publication No. 14, 33-58.

Thorpe, R.S. and MacDonald, R., 1985. Geochemical evidence for the emplacement of the Whin Sill complex of northern England. *Geological Magazine,* **122**, 4, 389-396.

Timmerman, M.J., Heeremans, M., Kirstein, L.A., Larsen, B.T., Spencer-Dunworth, E.A. and Sundvoll, B., 2009. Linking changes in tectonic style with magmatism in northern Europe during the late Carboniferous to latest Permian. *Tectonophysics,* **473**, 3-4, 375-390.

Timoshenko, S.P., 1958. Strength of Materials. Part 1. Elementary Theory and Problems. D Van Norstrand Company, New York.

Torsvik, T.H. and Rehnström, E.F., 2003. The Tornquist Sea and Baltica-Avalonia docking. *Tectonophysics,* **362**, 1-4, 67-82.

Tucker, M.E., Gallagher, J., Lemon, K. and Leng, M., 2003, The Yoredale Cycles of Northumbria: High-Frequency Clastic-Carbonate Sequences of the Mid-Carboniferous Icehouse World. *Open University Geological Society Journal*, **24**, 5-10.

Turcotte, D.L. and Emerman, S.H., 1983. Mechanisms of active and passive rifting. *Tectonophysics,* **94**, 1-4, 39-50.

Turcotte, D.L. and Oxburgh, E.R., 1967. Finite amplitude convective cells and continental drift. *Journal of Fluid Mechanics,* **28**, 1, 29-42.

Turcotte, D.L. and Schubert, G., 1982. Geodynamics applications of continuum physics to geological problems. John Wiley & Sons, New York.

Turner, B.R., Dewey, C. and Fordham, C.E., 1997. Marine ostracods in the Lower Carboniferous fluviatile Fell Sandstone Group: evidence for base level change and marine flooding of the central graben, Northumberland Basin. *Proceedings of the Yorkshire Geological Society,* **51**, 4, 297-306.

Twiss, R.J. and Moores, E.M., 1992. Structural geology. Freeman, New York.

van der Beek, P., Andriessen, P. and Cloetingh, S., 1995. Morphotectonic evolution of rifted continental margins: Inferences from a coupled tectonic-surface processes model and fission track thermochronology. *Tectonics,* **14**, 2, 406-421.

Van Wagoner, J.C., 1985. Reservoir facies distribution as controlled by sea-level change, *Abstract and poster session, SEPM mid-year meeting, Golden, CO. SEPM, Tulsa, OK,* 1985, pp91-92.

Van Wagoner, J.C., Posamentier, H.W., Mitchum, R.M., Vail, P.R., Sarg, J.F., Loutit, T.S. and Hardenbol, J., 1988. An overview of the fundamentals of sequence stratigraphy and key definitions. In: C.K. Wilgnus, C.G.S.C. Hastings, H.W. Kendall, H.W. Posamentier, C.A. Ross and J.C. Van Wagoner (Eds) *Sea-Level Changes: An Integrated Approach.* SEPM, Special Publication No. 42, 39-45.

Vening Meinesz, F.A., 1937. The determination of the earth's plasticity from the postglacial uplift of Scandinavia; Isostatic adjustment. *Proceedings of the Netherlands Academy, Wetensch,* **40** 654-662.

Vening Meinesz, F.A., 1941. Gravity over the Hawaiian Archipelago and over the Madeira area. *Proceedings of the Netherlands Academy, Wetensch,* **44** 1-12.

Verrall, P., 1981. Structural interpretation with applications to North Sea problems. Joint Association for Petroleum Exploration Courses (UK).

Vogt, P.R. and Ostenso, N.A., 1967. Steady state crustal spreading. *Nature,* **215**, 5102, 810-817.

Wadge, A.J., Harrison, R.K. and Snelling, N.J., 1972. Olivine-dolerite intrusions near Melmerby, Cumberland, and their age-determination by the potassium–argon method. *Proceedings of the Yorkshire Geological Society,* **39** 59-70.

Walcott, R.I., 1970. Flexural rigidity, thickness, and viscosity of the lithosphere. *Journal of Geophysical Research-Solid Earth,* **75**, 20, 3941-3954.

Walcott, R.I., 1972. Gravity, flexure, and the growth of sedimentary basins at a continental edge. *Geological Society of America Bulletin,* **83**, 6, 1845-1848.

Waples, D.W. and Kamata, H., 1993. Modelling porosity reduction as a series of chemical and physical processes. In: A.G. Doré, J.H. Augustson, C. Hermanrud,

D.J. Stewart and Ø. Sylta (Eds) *Basin Modelling: Advances and Applications: Proceedings of the Norwegian Petroleum Society Conference, 13-15 March, 1991, Stavanger, Norway.* Elsevier Science, 303-320.

Ward, J., 1997. Early Dinantian evaporites of the Easton-1 well, Solway Basin, onshore, Cumbria, England. In: N.S. Meadows, S.R. Trueblood, M. Hardman and G. Cowan (Eds) *Petroleum Geology of the Irish Sea and Adjacent Areas.* Geological Society of London Special Publication No. 124, London, 277-296.

Warren, J.K. and Kendall, C.G.S.C., 1985. Comparison of sequences formed in marine sabkha (subaerial) and salina (subaqueous) settings modern and ancient. *Bulletin American Association of Petroleum Geologists,* **69**, 6, 1013-1023.

Warrington, G. and Ivimey-Cook, H.C., 1992. Triassic. In: J.C. Cope, J.K. Ingham and P.F. Rawson (Eds) *Atlas of paleaogeography and Lithofacies.* Geological Society of London Memoirs, 13, London, 97-106.

Waters, C.N., Browne, M.A.E., Dean, M.T. and Powell, J.H., 2007. *Lithostratigraphical framework for Carboniferous successions of Great Britain (Onshore).* British Geological Survey Research Report, RR/07/01.

Waters, C.N. and Davies, S.J., 2006. Carboniferous: extensional basins, advancing deltas and coal swamps. In: P.J. Brenchley and P.F. Rawson (Eds) *The Geology of England and Wales.* 2nd Edn. 173-223.

Watts, A.B., 1992. The effective elastic thickness of the lithosphere and the evolution of foreland basins. *Basin research,* **4**, 3 - 4, 169-178.

Watts, A.B., 2001. Isostasy and Flexure of the Lithosphere. Cambridge University Press, Cambridge.

Watts, A.B., Bodine, J.H. and Ribe, N.M., 1980. Observations of flexure and the geological evolution of the Pacific Ocean basin. *Nature,* **283**, 5754, 532-537.

Watts, A.B. and Burov, E.B., 2003. Lithospheric strength and its relationship to the elastic and seismogenic layer thickness. *Earth and Planetary Science Letters,* **213**, 1-2, 113-131.

Watts, A.B., Karner, G.D. and Steckler, M.S., 1982. Lithospheric flexure and the evolution of sedimentary basins. *Philosophical Transactions of the Royal Society of London A,* **305** 249-281.

Waugh, B., 1965. A preliminary electron microscope study of the development of authigenic silica in the Penrith Sandstone. *Proceedings of the Yorkshire Geological Society,* **35**, 1, 59-69.

Waugh, B., 1970. Petrology, provenance and silica diagenesis of the Penrith Sandstone (Lower Permian) of northwest England. *Journal of Sedimentary Petrology,* **40** 1226-1240.

Wells, M.R., Allison, P.A., Hampson, G.J., Piggott, M.D. and Pain, C.C., 2005. Modelling ancient tides: the Upper Carboniferous epi - continental seaway of Northwest Europe. *Sedimentology,* **52**, 4, 715-735.

Wernicke, B., 1985. Uniform normal sense simple shear of the continental lithosphere. *Canadian Journal Earth Sciences,* **22**, 1, 108-125.

Wernicke, B. and Burchfiel, B.C., 1982. Modes of extensional tectonics. *Journal of Structural Geology,* **4**, 2, 105-115.

Wessel, P. and Smith, W.H.F., 1991, Free Software helps Map and Display Data, *EOS Trans. American Geophysical Union*, **72**, 441, 445-446.

Wills, L.J., 1956. Concealed coalfields. Blackie, London.

Wilson, J.T., 1966. Did the Atlantic close and then re-open? *Nature,* **211**, 5050, 676-681.

Woodcock, N.H. and Rickards, B., 2003. Transpressive duplex and flower structure: Dent Fault System, NW England. *Journal of Structural Geology,* **25**, 12, 1981-1992.

Woodcock, N.H., Soper, N.J. and Strachan, R.A., 2007. A Rheic cause for the Acadian deformation in Europe. *Journal of Geological Society,* **164**, 5, 1023-1036.

Xiao, H. and Suppe, J., 1992. Origin of rollover. *Bulletin American Association of Petroleum Geologists,* **76**, 4, 509-529.

Young, B., 2006. *Geology of 1:10 000 sheet NY86SW and the southern parts of NY86NW and NY76NE.* Keyworth, Nottingham: British Geological Survey Internal Report, IR/06/053.

Zharkov, V.N., 1998. On the dependence of the coefficient of thermal expansion on density. *Physics of the Earth and Planetary Interiors,* **109**, 1-2, 79-89.

# 3 Appendix A

## 3.1 Gravity data: Profile 1

Figure A3.1 illustrates the gravity data and model for profile 1, which crosses the Solway Basin in a north-south orientation. The observed gravity profile across the Solway Basin is interpreted as a local gravity low over the basin superimposed on a longer wavelength gravity high. In this case, the observed gravity measurement is considerably higher than would be expected for a sedimentary basin of this size (Kimbell *et al.*, 2006). There are two explanations to explain the observed gravity profile. A large wavelength gravity high results from an area of relatively high density basement located beneath the Solway Basin. Where there is high density anhydrite present within the Lyne Formation a gravity low is superimposed upon the gravity high, which is a result of a reduced density contrast between the basement and the basin infill. The Lake District Batholith, to the south of the Solway Basin, and Criffel Complex to the north produce gravity lows as a result of the low density of the intrusions generating a large density contrast with the surrounding basement.

## 3.2 Gravity data: Profile 3

Figure A3.2 illustrates the gravity data and model for profile 3. This profile crosses the Northumberland Trough, Alston Block and Stainmore Trough perpendicular to the main east-west trend of the basins. The Northumberland Trough appears to exhibit little effect upon the gravity

field. This can be explained by a combination of high density anhydrite within the Lyne Formation and a southwards thinning wedge of Lower Palaeozoic strata including relatively dense Skiddaw Group rocks, which reduces the density contrast (Lee, 1989).

### 3.3 Seismic Data

Figure A3.3 illustrates the interpretation of seismic line TOC86-V103, which crosses the Northumberland Trough from north to south, perpendicular to the main basin-bounding faults (Figure 3.2). Line TOC86-V103 is situated 2 km to the east of cross-section G-G' along a roughly parallel route. Extension is first taken up on the Ninety Fathom Fault. The extension is then accommodated on a series of faults that are en-echelon and synthetic to the Ninety Fathom Fault, including two branches of the Stublick Fault. In addition, there are a number of smaller antithetic faults within the syn-rift Border Group formation. Within the north of the basin extension is accommodated over a number of faults that are antithetic to the main basin-bounding fault.

### 3.4 Gravity data: Profile 4

Figure A3.4 presents the gravity anomaly data and model for profile 4. This profile extends from the Lake District Block, across the Vale of Eden Basin in a direction perpendicular to the Pennine Fault and across the Alston Block from south-west to north-east. The profile crosses three cupolas of the North Pennines Batholith, the Scordale cupola in the south-west, the main central cupola, and the Rowlands Gill cupola in the north-

east. Collectively these three granite cupolas reduce the Bouger anomaly across the whole of the Alston Block, with the greatest effect over the central cupola.

### 3.5 Gravity data: Profile 6

Figure A3.5 presents a north-south section across the eastern end of the North Pennines Batholith. The profile crosses two cupolas of the North Pennines Batholith, the Rowlands Gill cupola to the north and the Cornsay cupola to the south. Both cupolas are modelled as having the same depth, but the Corsay cupola has a greater thickness and width than the Rowlands Gill cupola and as such a greater cross-sectional area. As a result of this, the Corsay cupola has a greater effect on the gravity profile, creating a deeper and larger wavelength gravity low.

### 3.6 Seiesmic data

Section BGS-86-05 (Figure A3.6) crosses the Alston Block from south-west to north-east and crosses over the north-eastern edge of the main cupola and the Rowlands Gill cupola. The top of the Rowlands Gill cupola is located deeper within the crust than the main cupola or the Cornsay cupola in section BGS-86-04. The Rowlands Gill cupola is also a greater distance from the main cupola and the top of the batholith is reflected at 2.9 s twtt (~ 8 km depth) between the main cupola and the Rowland Gill cupola.

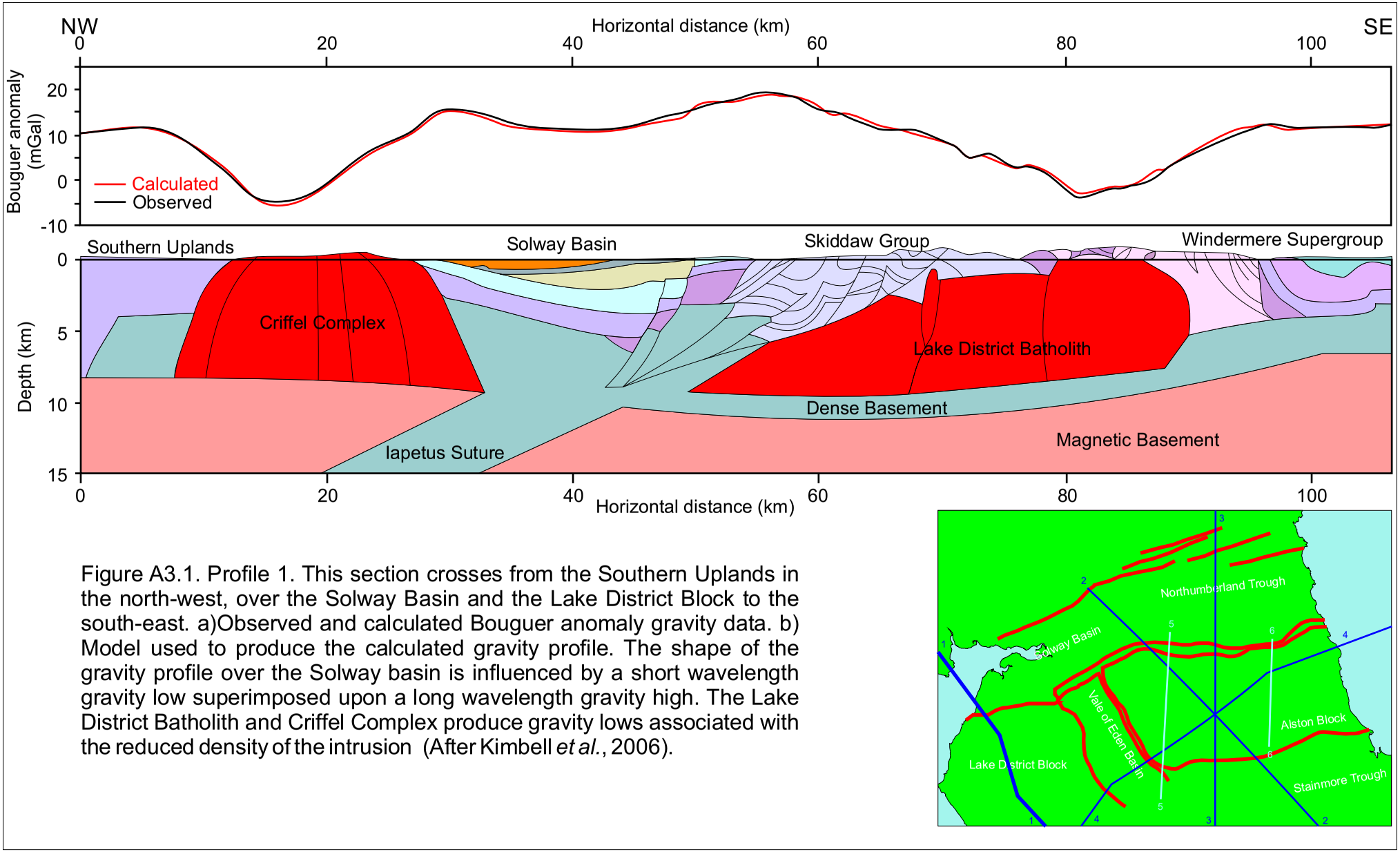


Figure A3.1. Profile 1. This section crosses from the Southern Uplands in the north-west, over the Solway Basin and the Lake District Block to the south-east. a)Observed and calculated Bouguer anomaly gravity data. b) Model used to produce the calculated gravity profile. The shape of the gravity profile over the Solway basin is influenced by a short wavelength gravity low superimposed upon a long wavelength gravity high. The Lake District Batholith and Criffel Complex produce gravity lows associated with the reduced density of the intrusion (After Kimbell *et al.*, 2006).

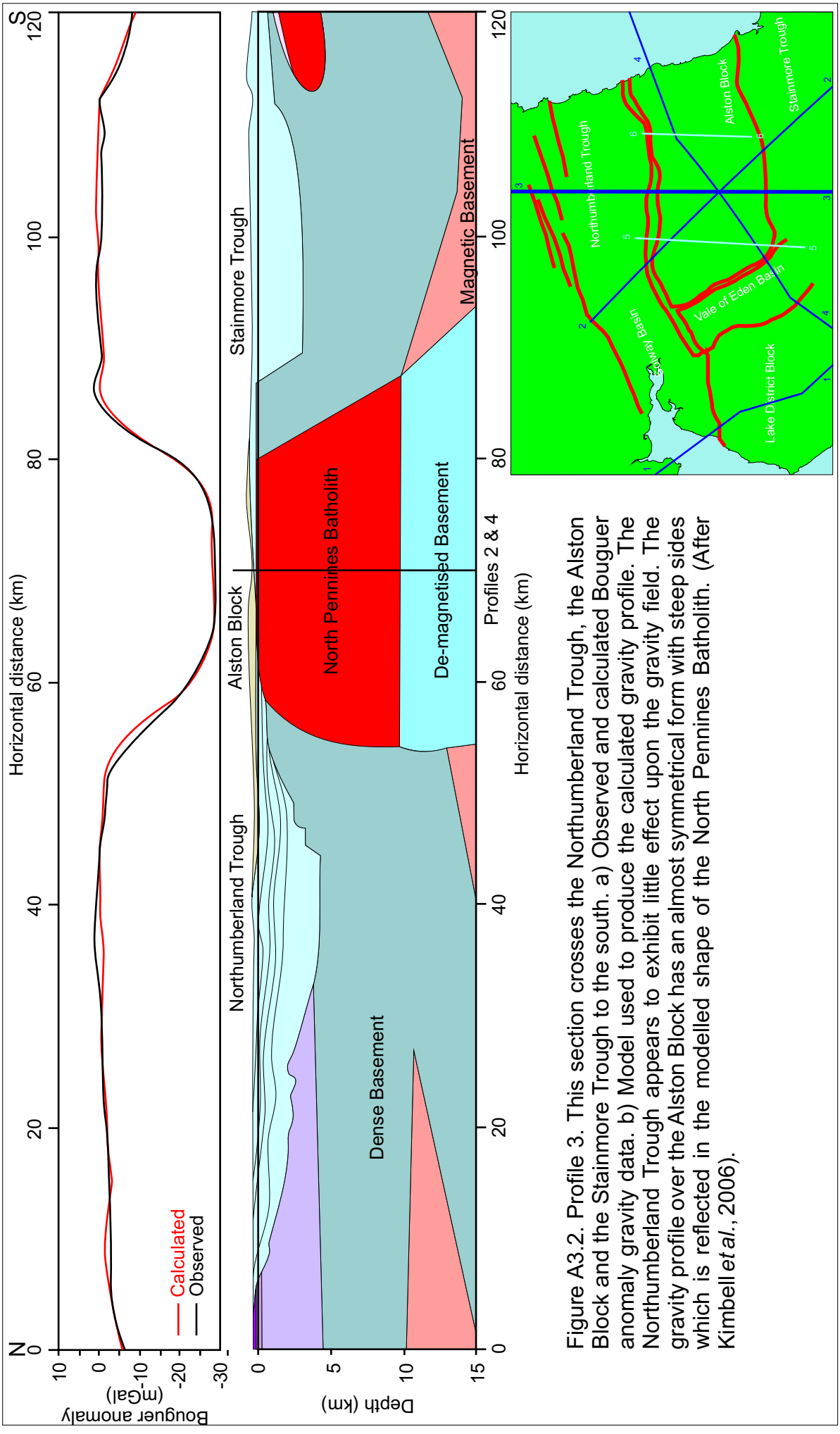


Figure A3.2. Profile 3. This section crosses the Northumberland Trough, the Alston Block and the Stainmore Trough to the south. a) Observed and calculated Bouguer anomaly gravity data. b) Model used to produce the calculated gravity profile. The Northumberland Trough appears to exhibit little effect upon the gravity field. The gravity profile over the Alston Block has an almost symmetrical form with steep sides which is reflected in the modelled shape of the North Pennines Batholith. (After Kimbell *et al.*, 2006).

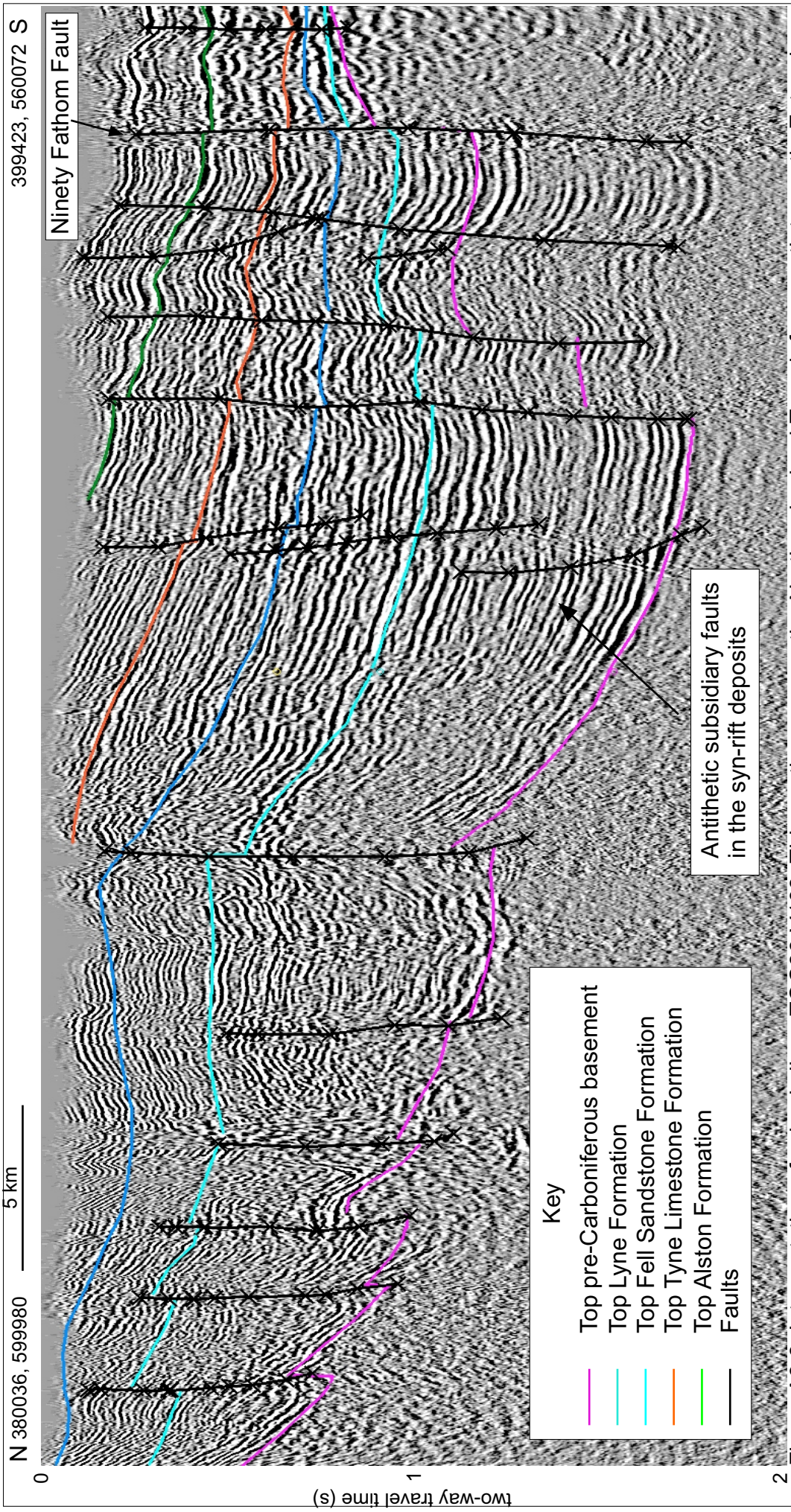


Figure A3.3. Interpretation of seismic lines TOC86-V103. This section crosses the Northumberland Trough from north to south. Extension is accommodated by several north-dipping faults at the southern margin of the basin. This is accompanied by several antithetic subsidiary faults in the syn-rift deposits.

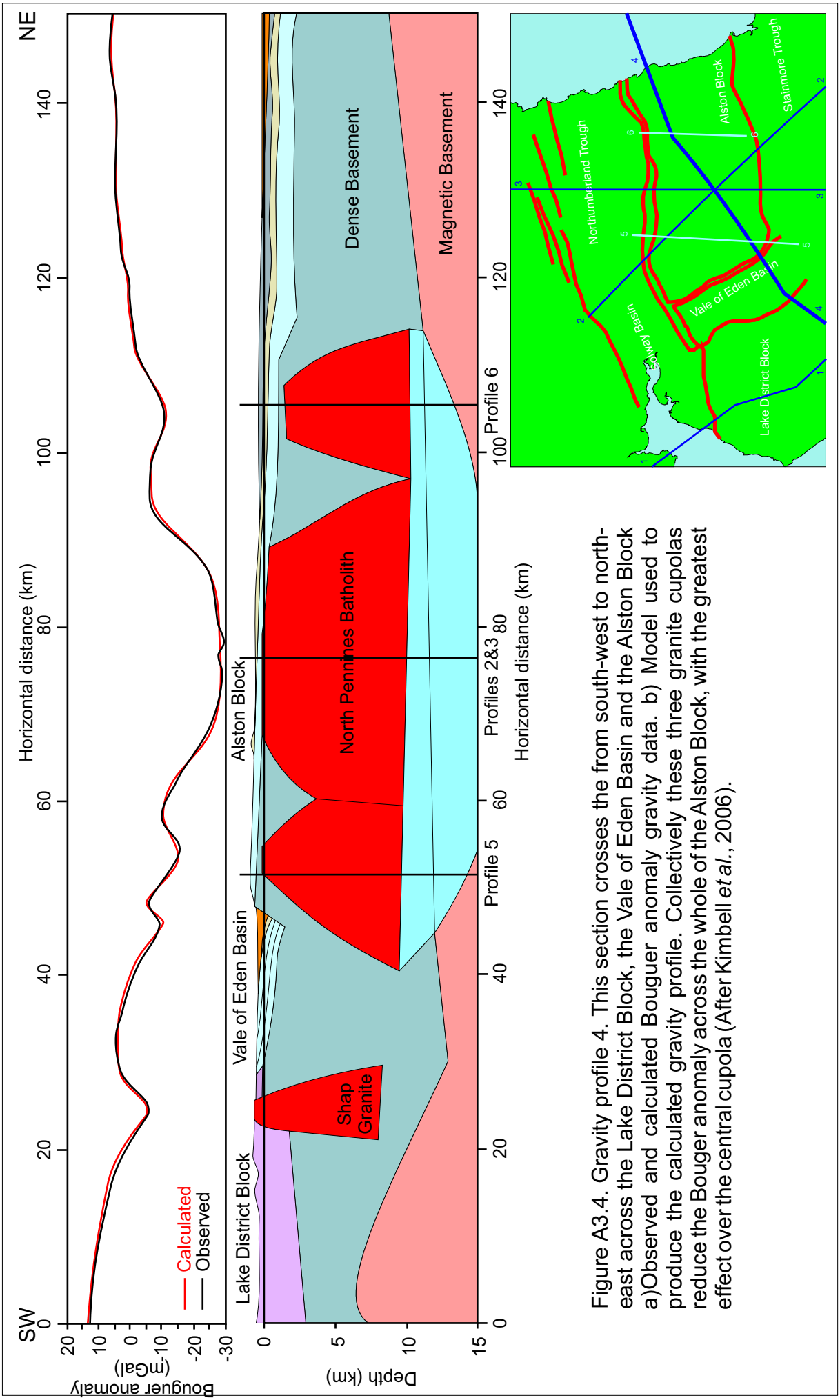


Figure A3.4. Gravity profile 4. This section crosses the from south-west to north-east across the Lake District Block, the Vale of Eden Basin and the Alston Block a)Observed and calculated Bouguer anomaly gravity data. b) Model used to produce the calculated gravity profile. Collectively these three granite cupolas reduce the Bouger anomaly across the whole of the Alston Block, with the greatest effect over the central cupola (After Kimbell *et al.*, 2006).

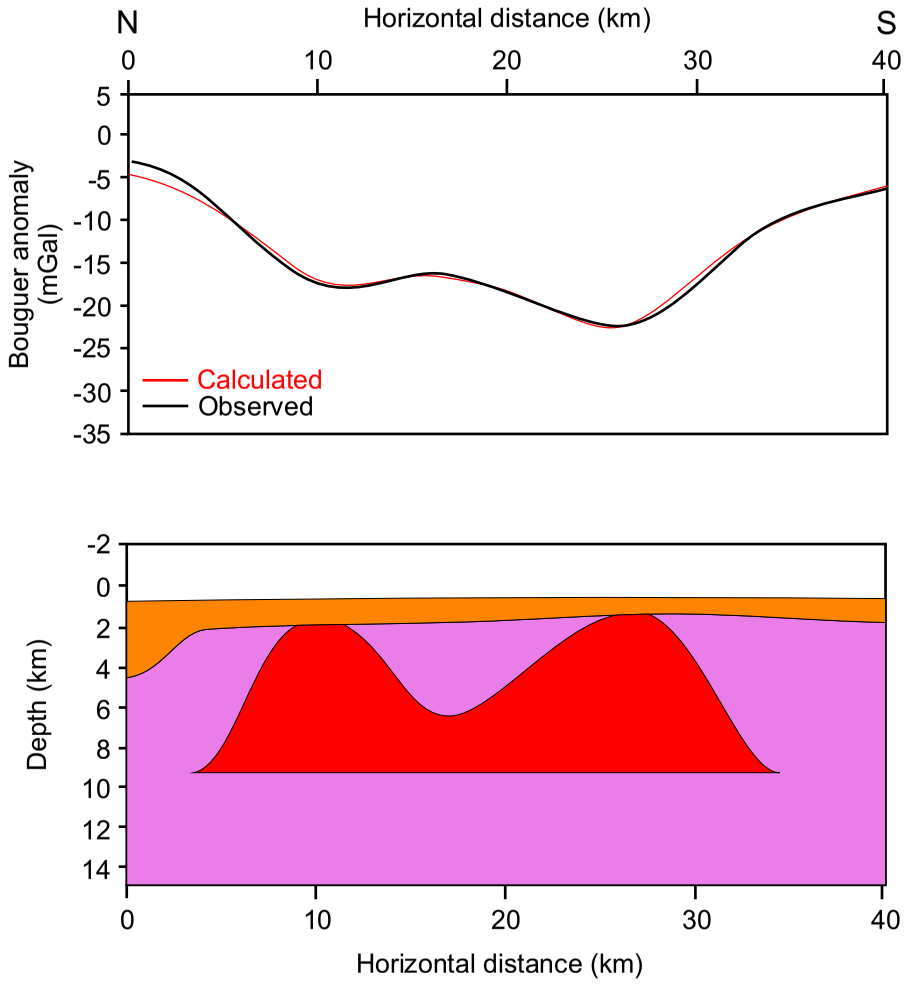


Figure A3.5. Profile 6. This section crosses the Alston Block from north to south a) Observed and calculated Bouguer anomaly gravity data. b) Model of the North Pennines Batholith used to produce the calculated gravity profile. The profile contains two cupolas of the North Pennines Batholith, the Rowlands Gill cupola to the north and the Cornsay cupola to the south (After Kimbell *et al.*, 2006).

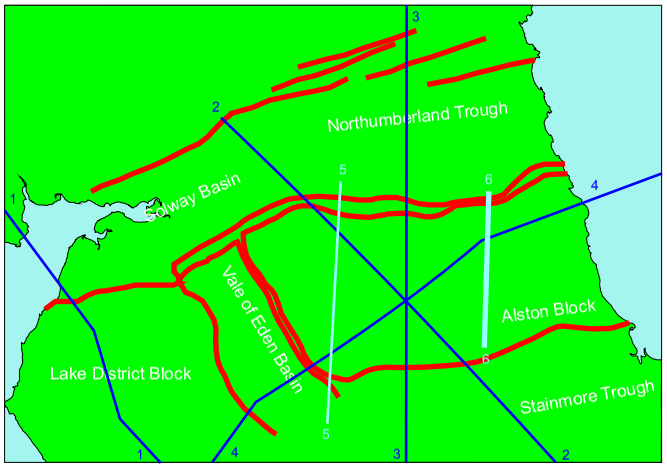

Figure A3.6. Interpretation of seismic lines BGS-86-05 across the Alston Block. The North Pennines Batholith can be identified in the crust by its poor reflective nature. BGS-86-05 The main cupola deepens towards the north-east. The top of the Rowlands Gill cupola is separated from the Carboniferous sequence by pre-Carboniferous basement.

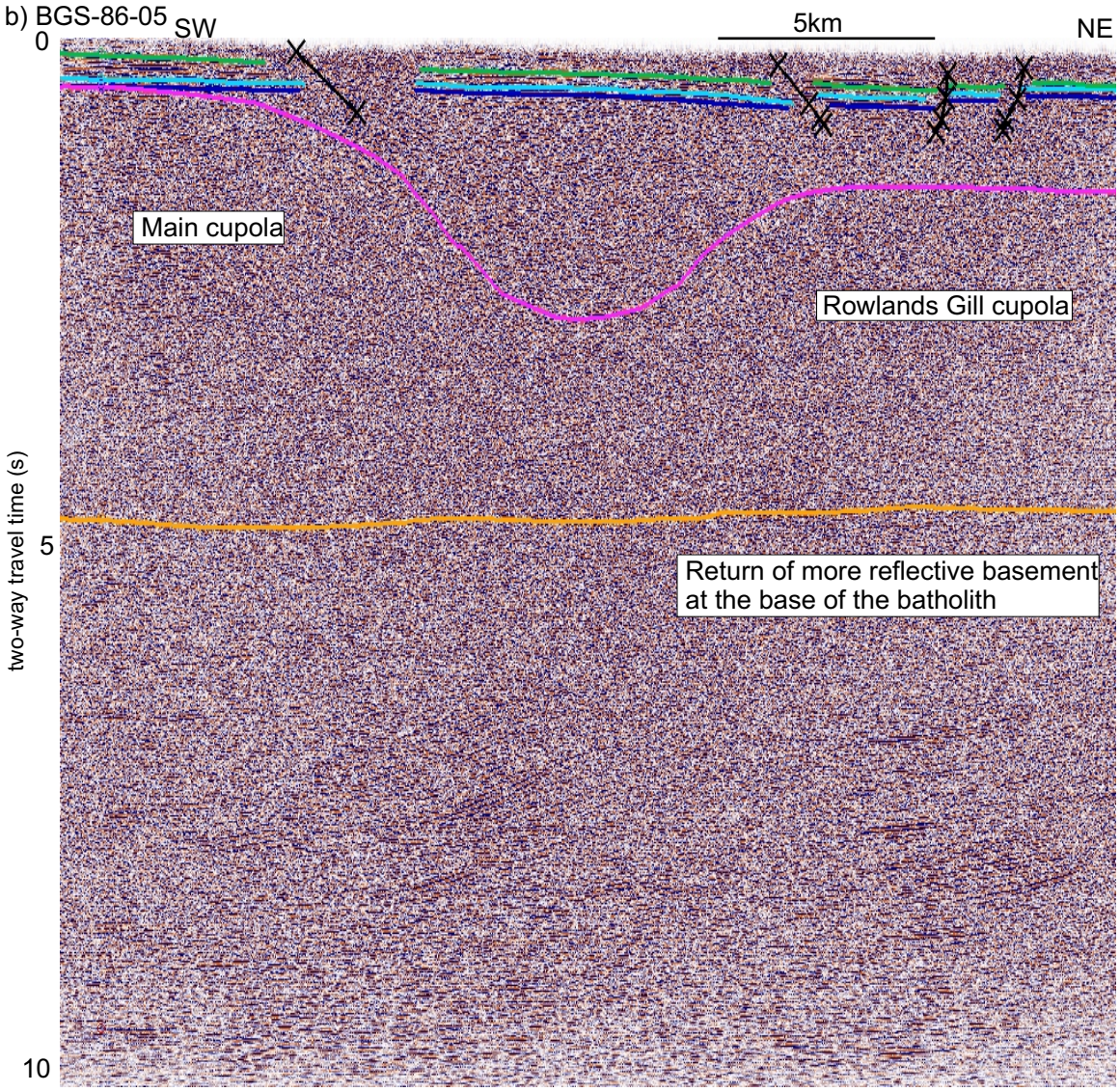


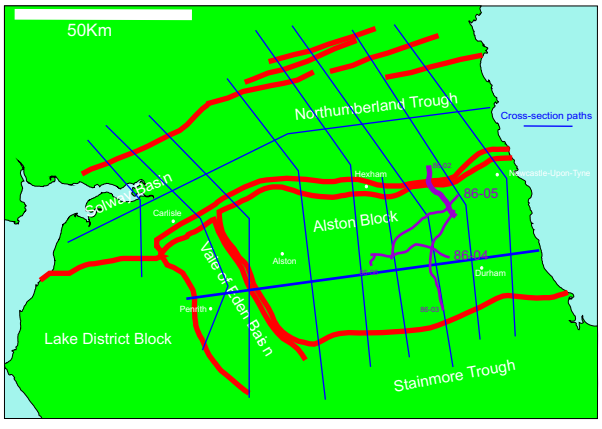


Key

- Top pre-Carboniferous basement
- Top batholith
- Base Batholith
- Top Alston Formation
- Top Stainmore Formation
- Faults
- Moho

# 4 Appendix B: Two dimensional modelling of the deformation resulting from extension.

## 4.1 The vertical shear construction and derivatives

The vertical shear construction (Verrall, 1981) can, for a given fault geometry and value of heave, predict the resulting deformation of the hanging wall following normal or reverse fault movement. In two-dimensions the method assumes that, with no change in rock density, any cross-sectional area 'created' during deformation must be accounted for elsewhere in a section parallel to the mass movement direction (Gibbs, 1983; Bosworth, 1985). This is a two-dimensional simplification of the three-dimensional law of conservation of volume (Goguel, 1962; Dahlstrom, 1969) and is valid only in a section parallel to the mass movement direction. In order to conserve cross-sectional area, vertical thinning of the rollover strata and bed-parallel extension in the rollover of the hanging wall must occur often leading to the formation of subsidiary faults (Gibbs, 1984).

The vertical shear construction (Figure B4.1) assumes that during deformation the hanging wall is displaced laterally by an amount of heave ($h$), where heave is defined as the horizontal component of extension in the mass movement direction. In two dimensions, the horizontal component of extension normal to the fault surface may not occur in the mass movement direction. (Geikie, 1882; Peacock *et al.*, 2000). This leaves part of the hanging wall unsupported. The void beneath the hanging wall is

gravitationally unstable and it is assumed that the hanging wall collapses vertically onto the underlying footwall, which is assumed to be rigid. In order to accommodate this collapse, the strata of the hanging wall are deformed by simple shear on an infinite number of vertical shear planes generating a rollover anticline, the form of which is related to the underlying fault surface. This process can be modelled graphically (Figure B4.1) by superimposing a vertical grid across the section with a horizontal spacing equal to the value of heave (Williams and Vann, 1987). Each point in the hanging wall that corresponds with a vertical shear line is displaced along a displacement vector ($d$) determined from the average dip of the fault profile between its position and the next shear line (Clarke, 2002) (Figure B4.1). Deformation as a result of simple shear on vertical and parallel planes is a reasonable assumption as it allows finite motion on fault planes that do not intersect, and is equivalent to implying that the hanging wall deforms by motion on small parallel faults (White *et al.*, 1986).

The vertical shear construction can be modelled numerically in order to simulate deformation caused by fault movement. The radius of curvature of a listric fault is dependent on its detachment depth such that the geometry of a listric fault can be modelled as a mathematical function $F$ of lateral distance x as follows (Egan *et al.*, 1999):

$$F_{(x)} = 0 \quad \text{for} \quad x < x_f$$

$$F_{(x)} = Zd\left[1 - \exp\left(-\frac{x - x_f}{Zd}\right)\right] \quad \text{for} \quad x \geq x_f \qquad \text{[B4.1]}$$

where: $x_f$ is the horizontal position of the surface outcrop of the fault.

$Zd$ is the detachment depth of the fault.

The profile of the hanging wall is assumed it to have been at zero elevation prior to deformation. It is defined as the function $HW$ and is given by:

$$HW_{(x)} = F_{(x)} - F_{(x-e)} \qquad \text{[B4.2]}$$

where: $HW_{(x)}$ is the depth to the hanging wall at position x.

$F_{(x)}$ is the depth to the fault at position x.

$e$ is amount of horizontal extension.

The vertical shear construction is a 'constant heave' model, such that as the listric fault develops, the horizontal displacement is the only constant factor in the movement of the hanging wall along the fault (Williams and Vann, 1987; Dula, 1991). If the heave is conserved, the vertical component of displacement, throw ($t_f$), and the displacement ($d$) will vary with the angle of dip of the fault surface ($\theta$) such that:

$$t_f = e \tan\theta \qquad \text{[B4.3]}$$

$$d = \frac{e}{\cos\theta} \qquad \text{[B4.4]}$$

where: $t_f$ is the throw of the fault

$e$ is horizontal extension (heave)

$d$ is fault displacement

$\theta$ is the angle of fault dip

As the dip of the fault decreases the amount of displacement decreases until fault dip reaches zero.

Williams and Vann (1987) proposed a modification to the vertical shear construction that preserves displacement along the fault, with throw and heave varying with the angle of dip of the fault (Figure B4.2). Their method is referred to as the 'modified chevron construction' and is similar to the vertical shear construction except that the vertical grid superimposed across the section divides the cross-section into areas of equal displacement rather than heave. However, if lines within the vertical grid change their relative spacing, the area of rock bounded by the lines will increase or decrease if the lines move further apart or closer together, respectively. As such, this model does not conserve cross-sectional area within the hanging wall. Wheeler (1987) further developed the model such that changes in the relative spacing between the vertical grid lines is accompanied by changes in height of the hanging wall blocks between the grid lines.

### 4.2 The slip-line construction and derivatives

The slip-line construction (Williams and Vann, 1987) is an alternative method of modelling hanging wall deformation from the profile of a fault. Williams and Vann (1987) suggested that instead of considering displacement in vertical segments it is reasonable to consider movement of the hanging wall material along lines parallel to the fault known as slip lines (Figure B4.3a). This method is based on conservation of displacement along the fault profile. Hanging wall displacement is considered in terms of segments that are perpendicular to the fault displacement, rather than vertical heave segments (Williams and Vann, 1987) (Figure B4.3b). Each

segment has a unique position where it touches the regional, and also the deformed hanging wall. In this position it represents a slip line parallel to the fault.

Like the 'modified chevron construction', which is also dependent on conservation of displacement, area is not balanced. Wheeler (1987) proposed a modification of the slip-line construction to conserve area locally by changing the length of the slip lines such that they converge on the fault plane (Figure B4.3c).

Fault Parallel Flow is a method of modelling hanging wall deformation based upon the slip-line construction, with the addition of an angular shear component in order to balance area and bed length (Williams *et al.*, 1999). This method relies on flow-line equations rather than geometrical construction techniques to model the hanging wall deformation (Egan *et al.*, 1999).

### 4.3 Review of two-dimensional modelling techniques

The methods presented here for modelling deformation in response to extension, predict significantly different hanging wall geometries depending on the mechanism by which the hanging wall is deformed. The vertical shear and inclined shear construction methods deform the hanging wall by a constant heave. The modified chevron construction, slip-line construction and fault parallel flow methods deform the hanging wall by a constant amount of displacement. The inclined shear construction is particularly suitable for the modelling being carried out as part of this

research as it allows the geometry of the hanging wall away from the fault surface to be established (Clarke, 2002) and in many cases it approximates hanging wall deformation more realistically than the vertical shear and modified chevron construction models (Dula, 1991). The assumption that hanging wall deformation occurs along a shear plane that is at an inclined angle is supported by evidence of subsidiary faulting within the hanging wall block of the Northumberland Trough that can be observed in the cross-sections shown in chapter 3 and in the interpreted seismic data (Figure 3.22).

### 4.4 Method for determining $x - e'$

Within the computer model the output from equations [4.3]-[4.7] are stored as elements within arrays. The position of each element within the array is determined by the variable $i$.

$$i = \frac{x}{d} \qquad \text{[B4.5]}$$

where: $d$ is the distance between $x$ co-ordinates

However, following rotation into the $(x', y')$ co-ordinate system, the distance $(d)$ between the $x$ co-ordinates is no longer fixed, it varies between each $x$ co-ordinate. Within the computer model, the value of $i$ for $x - e'$ must be represented by an integer as it indicates the position of the fault $(F')$ or hanging wall $(HW')$ geometry element within an array that requires accessing. As the value of $i$ for $x - e'$ is not automatically an

integer, it is necessary to determine the position of the element in the array that represents $x - e'$ ($X_e$).

It is first necessary to determine the distance between each $x'$ co-ordinate, $dNew_x$ for each value of $i$ between $i = 0$ and $i = i_{max} - 1$ [B4.6].

$$dNew_i = x_{(i+1)}' - x_i' \qquad \text{[B4.6]}$$

where: $i_{max}$ is the final position in the array.

The value of $e'$ must be converted into an array position $e_A$ that represents $e'$ in terms of the number of increments, represented by $dNew_x$, that $x - e'$ is from the value of $x$ (Figure A4.4). This is achieved using equations [B4.7]-[B4.11] for each value of x between $i = 1$ and $i = i_{max} - 1$. A variable, $xInc$, is established to consider the increments in $x$. For each value of $x$, $xInc$ is reset to 0 [A4.3]. A variable, $Inc$, to measure the number of increments between $x$ and $x - e'$ is set up and reset to 0 for each value of x [A4.4].

$$xInc = 0 \qquad \text{[B4.7]}$$

$$Inc = 0 \qquad \text{[B4.8]}$$

To determine the number of increments between $x$ and $x - e'$, $xInc$ is increased from 0 at the $x$ position by increments of $dNew_x$ [B4.9].

$$xInc = x\,Inc + dNew_k \qquad \text{[B4.9]}$$

where $k$ decreases incrementally by 1 between $x - 1$ and 1

After each increment, if $xInc < e'$ then $Inc$ is incremented by 1, [B4.10], if $xInc > e'$ then $e_A$ is set at the current value of $Inc$ [B4.11] and the loop is broken, moving on to repeat the process for the next value of $x$.

$$Inc = Inc + 1 \qquad \text{[B4.10]}$$

$$e_A = Inc \qquad \text{[B4.11]}$$

The value that represents $x - e'$ as an array position ($X_e$) is then calculated using equation [B4.12].

$$X_e = x - e_A \text{ for values of } x \text{ between 0 and } x_{max} \qquad \text{[B4.12]}$$

Inserting this into equation [4.7] gives:

$$HT_{x'} = \left(F_{x'} - HW_{x'}\right) - \left(F_{X_e'} - HW_{X_e'}\right) \qquad \text{[B4.13]}$$

### 4.5 Rheology

Analyses of the mechanical properties of rocks have divided the lithosphere into three rheological regions (Kholstedt *et al.*, 1995). These are the upper crust, the lower crust and the lithospheric mantle. In this model, the upper crust is usually assumed to have a granodioritic composition, in which the most abundant element is silica (Shaw *et al.*, 1967; Wedephol, 1995). It follows, therefore, that extension of the upper crust is mainly controlled by the deformation characteristics of quartz (White, 1976; Kusznir and Park, 1986; 1987). There is more uncertainty with regard to the composition of the lower crust, with research based on seismic data and laboratory experiments. This research predicts a model for lower crustal composition that consists of mafic rocks that have been

metamorphosed to granulite facies (Kern and Shenk, 1988; Rudnick and Fountain, 1995; Wedephol, 1995) and in which plagioclase feldspar is the dominant mineral affecting deformation. The mantle lithosphere has a dominantly peridotite composition (Menzies, 1990) whose deformation is usually considered to be controlled by the characteristics of olivine.

Kusznir and Park (1987) present yield strength envelopes for the lithosphere based on numerical modelling of lithosphere rheology; examples of some of their results are presented in Figure B4.5. The effect of varying the proportions of quartz-dominated and feldspar-dominated crustal compositions on the stress in the lithosphere, including some affects of water in the system, are shown in Figure B4.5a. The rheology of the crust, dominated by quartz and plagioclase feldspar, is weaker than the olivine-dominated rheology of the mantle for the same temperature (Kusznir and Park, 1984). The strength of the lithosphere is therefore dependent on the proportions of crustal and mantle material, which, in turn, is determined by the thickness of the crust. With increasing crustal thickness, stress is concentrated higher into the crust (Figure B4.5b) (Kusznir, 1991; Watts and Burov, 2003; Gueydan *et al.*, 2008).

For cool lithosphere with a low geothermal gradient, the stress resulting from an applied force is transmitted deep into the lithosphere mantle. With increasing geothermal gradient, the largest yield stresses focus higher in the mantle and crust producing low-strength regions in other layers (Figure B4.5c). Therefore, the strength of the lithosphere is controlled by the olivine rheology of the mantle for low geothermal

gradients and the quartz-dominated rheology of the upper crust for high geothermal gradients (Kusznir and Park, 1982; 1987).

With the application of stress over time, or with an increase in geothermal gradient, the overall strength of the lithosphere is reduced. This eventually enables whole lithosphere failure (WLF) to occur resulting in extension (Figure B4.6) (Kusznir and Park, 1987; Kusznir, 1991). The materials that make up the lithosphere exhibit elastic behaviour, which is recoverable upon removal of the stress; however, once the yield stress is reached then WLF occurs, at which point the material begins to deform plastically (Artemjev and Artyushkov, 1971; Bott, 1976; Turcotte and Schubert, 2002).

These models of lithosphere strength tend to present a three-layer model with a weaker lower crust sandwiched between relatively strong upper crust and mantle. This representation of lithosphere rheology has been dubbed the 'jelly sandwich' model (Jackson, 2002) and has been opposed by those researchers who believe that the strength of the lithosphere lies entirely within the seismogenic layer of the crust and that the lithosphere mantle is relatively weak, on the basis of earthquake depths (Maggi *et al.*, 2000; Jackson, 2002; McKenzie and Jackson, 2002). McKenzie and Jackson (2002) propose that lower crustal flow can occur due to the presence of igneous intrusions or water, and is, in fact, necessary to explain regions where variable amounts of stretching have occurred, but where the Moho remains flat, for example north of Scotland (Brewer and Smythe, 1984). Afonso and Ranalli (2004) suggest that in regions of

subduction, metasomatism or collision, the lower crust is stronger than the upper mantle and the strength of the lithosphere lies entirely within the seismogenic upper crust. In early Palaeozoic lithosphere they suggest that the mantle is stronger than the lower crust, which is felsic in composition.

### 4.6 Heat transfer within the Earth

Heat within the Earth comes from a combination of short-lived and long-lived radioactive isotopes and the residual heat from accretion of the Earth and core formation (Bott, 1982b). The transfer of heat energy within the Earth occurs predominantly by conduction and convection. Conduction is the dominant mechanism of heat transfer in the lithosphere, the lowermost asthenospheric mantle and the core. Elsewhere, conduction is subordinate to convection (Bott, 1982b).

Heat transfer by conduction occurs when energy is exchanged, in the presence of a temperature gradient, from an area of high temperature to an area of low temperature (Ozisik, 1980). Heat is transferred in the form of kinetic energy from vibrations of molecules within a lattice as they collide (lattice conduction) or by collisions between electrons (electronic conduction) (Poirier, 1991). Heat transfer by convection occurs as mass movement is induced by thermal buoyancy in a layer of fluid-like material heated from beneath or internally (Busse, 1989). Although the mantle is solid, it can be considered as having fluid-like properties such as a very high viscosity ($10^{21}$ – $10^{22}$ kg(sm)$^{-1}$) and as such can transfer heat by convection (Poirier, 1991). In the convecting mantle, the mean

temperature increases with depth according to the adiabatic temperature gradient that results from the overlying pressure (Turcotte and Schubert, 2002).

### *4.6.1 Heat transfer by conduction*

Fourier's Law describes heat transfer by conduction. The heat flux is directly proportional to the temperature gradient that exists between two points. In one dimension, Fourier's Law (Fourier, 1878) is given by:

$$q = -K\frac{\delta T}{\delta y} \qquad \text{[B4.14]}$$

where: $q$ is the heat flux, measured in $mWm^{-2}$ or $calcm^{-2}s^{-1}$

$K$ is the co-efficient of thermal conductivity

$T$ is the temperature

$y$ is the Cartesian co-ordinate in the direction of temperature variation (i.e. depth)

Heat flows in the direction of decreasing temperature. As $\delta T/\delta y > 0$, $T$ increases in the positive $y$ direction. Heat must therefore flow in the negative $y$ direction (Turcotte and Schubert, 2002).

Heat flux at the Earth's surface can be used to infer processes within the Earth's interior. Heat flux can be calculated from measurements of surface temperature as long as the thermal conductivity, $K$, is known (Allen and Allen, 1990). Table B4.1 summarises heat flux data for several continental settings and indicates that regions of extensional tectonics (e.g. Basin and Range) are characterised by high magnitudes of heat flow.

| Province | Examples | Heat Flow ($mWm^{-2}$) |
|---|---|---|
| Bulk Continental Crust | | 47 - 49[1,2,3,4] |
| | | 76 at age 0 - 250 Ma[5] |
| | | 46 at age >1700 Ma[5] |
| Proterozoic Continental Crust | | 54 - 58[6,7] |
| | North America | 54[5] |
| | South America | 53[5] |
| | Europe and Asia | 60[5] |
| | UK | 59[5,8] |
| Archean Craton | | 41 - 42[4,9,10,11] |
| | Canadian Shield | 39±7[12,13] |
| | Western Australia | 39±8[14] |
| | Baltic Shield | 36±8[12,13,14] |
| Tectonic Continental Crust | | 70 - 81[7] |
| | Basin and Range | 92±33[4,15] |
| | Zambia | 67±7[9,14] |
| | Eastern Australia | 72±27[9] |
| | Indian Shield | 71±11[14] |

Table B4.1. Estimates of continental heat flow

[1]Shaw *et al*., 1986; [2]Christensen and Mooney, 1995; [3]Wedephol, 1995; [4]Rudnick *et al*., 1998; [5]Sclater *et al*., 1980; [6]Nyblade and Pollack, 1993; [7]Röhm *et al*., 2000; [8]Richardson and Oxburgh, 1978; [9]Taylor and McLennon, 1985; [10]Rudnick and Fountain, 1995; [11]McLennon and Taylor, 1996; [12]Rao and Jessop, 1975; [13]Pollack and Chapman, 1977; [14]Morgan, 1984; [15]Sass et al, 1971

Assuming heat transfer is solely a result of conduction and that it occurs only in one direction and does not vary with time (steady state), the variation of temperature with depth (geotherm) can be calculated. The time-dependent effects of conductive heat transport are disregarded due to the age of the lithosphere (Turcotte and Schubert, 2002). Under these conditions, the temperature, $T$, at any depth in the crust can be calculated (Allen and Allen, 1990).

$$T = T_s + \frac{q_s}{K} y - \frac{\rho_c H}{2K} y^2 \qquad \text{[B4.15]}$$

where: $T_s$ is the surface temperature

$q_s$ is the surface heat flux

$H$ is the radiogenic heat production rate per unit mass

$\rho_c$ is the density of the crust

Radiogenic heat production ($H$) decreases exponentially with depth (Allen and Allen, 1980; Turcotte and Schubert, 2002).

$$H = H_s \exp^{-\frac{y}{h_r}} \qquad [B4.16]$$

where: $H_s$ is the surface radiogenic heat production per unit mass

$h_r$ is a length scale for the decrease in $H$ with depth

Figure B4.7 represents the geotherm calculated for continental crust with respect to radiogenic heat production and conductive heat transfer. If the steep geothermal gradient predicted by equation [B4.15] continued beneath 100 km depth, temperatures would be in excess of 2700 K and extensive melting would be expected. Therefore, the geothermal gradient that is generated by this method must be significantly reduced before a depth of 100 km is reached (Bott, 1982b).

| Depth (km) | Temperature (K) | | | | | |
|---|---|---|---|---|---|---|
| | A82 | BS81 | BM86 | P86 | dS2000 Perovskite | dS2000 Pyrolite |
| 100 | 1450 | | | | | |
| 171 | 1508 | | | | | |
| 421 | 1699 | | | | | |
| 671- | 1830 | 1873 | | | 2060 | 1700 |
| 671+ | 1980 | | | | 2410 | |
| 2571 | 2814 | | | | | |
| 2886- | 2937 | 2773 | | | | |
| 2886+ | 3637 | 3573 | 3800 | 3800 | 4600 | 4000 |
| 5156 | 4676 | | 5000 | 5000 | | |
| 6371 | 4805 | | 5000 | | | |

Table B4.2 The Earth's geotherm; variation in temperature with depth.

A82 - Anderson, 1982; Bs81 - Brown and Shankland, 1981; Bm86 - Brown and McQueen, 1986; P86 - Poirier, 1986; dS2000 - daSilva *et al.*, 2000

Figure B4.8 represents approximations of the Earth's geotherm based on the data presented in Table B4.2. This table presents results from both theoretical calculations and practical experiments. Studies of the shock melting of iron provide data for the lower mantle and core (Brown and McQueen, 1986; Poirier, 1986; Anderson, 1982). Calculations based on adiabatic gradients also provide lower mantle data (Brown and Shankland, 1981; daSilva *et al.*, 2000).

The time taken for conductive heat flow in a body is related to its thermal conductivity, $K$, and its size. The amount of time required for this thermal conduction to take place can be determined from the one-dimensional time-dependent (unsteady) equation for heat flux [B4.17] (Davies, 1999).

$$\frac{\delta T}{\delta t} = \kappa \frac{\delta^2 T}{\delta y^2} + H \qquad \text{[B4.17]}$$

where: $t$ is time

$\kappa$ is the thermal diffusivity and:

$$\kappa = \frac{K}{\rho C_p} \qquad \text{[B4.18]}$$

where: $\rho$ is the density per unit mass of material

$C_p$ is the specific heat at a constant pressure

Assuming that there is no heat generation, $H = 0$, then the cooling time can be estimated by approximating the differentials in equation [B4.17] (Davies, 1999). $T/t$ is a measure of the rate of change of T, $\delta T/\delta t$.

$$\frac{T}{t} = \kappa \frac{T}{y^2} \qquad \text{[B4.19]}$$

Therefore the cooling time is given by equation [B4.20]:

$$t = \frac{y^2}{\kappa} \qquad \text{[B4.20]}$$

Or alternatively, by rearranging equation [B4.20], the distance over which the heat has been transferred can be calculated if $\kappa$ and $t$ are known.

$$y = \sqrt{\kappa t} \qquad \text{[B4.21]}$$

It is important to understand the time-dependent nature of the process of heat conduction in order to calculate the thermal effects of lithospheric extension.

#### 4.6.1.1 Airy isostasy

Airy isostasy (Airy, 1855) assumes that the Earth has a thin crust that overlies a fluid substratum and that the original crustal thickness is uniform. In addition the theory also assumes that the density of the crust, $\rho_c$, and the density of the mantle, $\rho_m$, are constant, and that the density of the mantle is greater than the density of the crust such that, $\rho_m > \rho_c$ (Watts, 2001).

The Airy isostasy hypothesis achieves isostatic equilibrium by varying the thickness of the crustal and mantle layers to restore hydrostatic equilibrium according to the Archimedes' principle such that; 'Any solid lighter than a fluid will, if placed in the fluid, be so far immersed that the weight of the solid will be equal to the weight of the fluid displaced.' (Archimedes c.f. Heath, 1897 p. 257).

In regions of topography elevated above sea level, additional mass is compensated for by a thickening of the lower density crust, replacing denser mantle material, forming a 'root'. In regions of topography below sea level, the crust is thinned with denser mantle material compensating for the reduced crustal mass, creating an 'anti-root'. A mathematical model for the Airy isostatic hypothesis was developed by Heiskanen, which became known as the Airy-Heiskanen model (Heiskanen, 1931) Figure B4.9 demonstrates the Airy-Heiskanen model.

The pressure, $P$, applied to the compensation level by a column of rock is determined by equation [B4.22]:

$$P = \frac{mass}{unit\ area} g \qquad [B4.22]$$

such that the pressure applied by an elevated region, $P_E$, is given by:

$$P_E = \left(C_o + h + r\right) \rho_c g \qquad [B4.23]$$

where: $C_o$ is the original crustal thickness
$h$ is the height of the land elevated above sea level
$r$ is the thickness of the crustal 'root'
$\rho_c$ is the density of the crust
$g$ is the acceleration due to gravity

Assuming isostatic equilibrium, the thickness of the root, r, the amount by which the crust has been thickened is calculated by:

$$r = \frac{\rho_c}{\rho_m - \rho_c} h \qquad [B4.24]$$

and the crustal thickness, $C_{th}$ is:

$$C_{th} = C_o + r \qquad \text{[B4.25]}$$

The pressure applied to the compensation level by a column of rock, whose topography lies below sea level, $P_s$, is established by equation [B4.26]:

$$P_s = C_o \rho_c g + r \rho_m g \qquad \text{[B4.26]}$$

where: $\rho_m$ is the density of the mantle

Assuming the lithosphere to be in isostatic equilibrium, the thickness of the 'anti-root' of mantle material, $r_a$, is given by:

$$r_a = \frac{\rho_c - \rho_w}{\rho_m - \rho_c} d \qquad \text{[B4.27]}$$

where: $\rho_w$ is the density of water

$d$ is the water depth

the thickness of the crust can be calculated from:

$$C_{th} = C_o - d - r_a \qquad \text{[B4.28]}$$

Given that the isostatic compensation occurs directly beneath the anomalous masses, the lower surface of the crust (i.e. the Moho) is a vertically exaggerated mirror image of the upper surface of the crust (Lyustikh, 1960). Figure B4.10 shows a lithosphere extension model illustrating the Airy isostatic compensation resulting from faulting, pure shear and thermal uplift at time, t = 0 Ma after rifting. Extension by faulting thins the upper crust and generates a region of low topography, imposing a negative load upon the lithosphere. The amount of thinning is greatest at $x_f + e$ (Figure B4.10a). The Airy isostatic response to extension by faulting generates uplift that is greatest at $x_f + e$ where the negative

load is greatest (Figure B4.10b). Extension by pure shear thins the lower crust, which causes the Moho to rise and imposes a positive load upon the lithosphere. The Airy isostatic response generates subsidence directly above the region of pure shear creating additional accommodation space in a more distal position within the basin (Figure B4.10c).

#### 4.6.1.2 Pratt isostasy

Pratt isostasy (Pratt, 1859), assumes that the depth of compensation occurs at the base of the crust, which is at a uniform level. Isostatic equilibrium is achieved by varying the density of the crust laterally (Figure B4.11) such that regions of elevated topography are underlain by low density crust, whereas areas of reduced topography are underlain by higher density crust (Lowrie, 1997).

A mathematical model of the Pratt isostatic hypothesis was derived by Hayfield to form the Pratt-Hayfield model (Hayfield, 1909). The model assumes that the density of the crust above sea level is the same as the density of crust, whose topography is undisturbed, and the density of the crust below sea level varies laterally (Figure B4.11).

The pressure at the base of the crust (the compensation depth) beneath an area of elevated topography, $P_E$, can be derived from equation [B4.29]:

$$P_E = C_o \rho_a g + h \rho_c g \qquad \text{[B4.29]}$$

where: $\rho_a$ is the density of the crust beneath sea level under the elevated region

The pressure an undisturbed column of rock at sea level, $P_U$, exerts upon the compensation depth is given by:

$$P_U = C_o \rho_c \, g \qquad \text{[B4.30]}$$

If the system is in isostatic equilibrium, the pressure exerted upon the compensation depth is equal, such that, $P_E = P_U$:

$$C_o \rho_a \, g + h \rho_c \, g = C_o \rho_c \, g \qquad \text{[B4.31]}$$

The density of the rock in the crust beneath the elevated region is therefore calculated by:

$$\rho_a = \left( \frac{C_o - h}{C_o} \right) \rho_c \qquad \text{[B4.32]}$$

The pressure exerted by an area of reduced topography, $P_s$, is calculated by:

$$P_s = \left( C_o - d \right) \rho_b \, g + d \rho_w \, g \qquad \text{[B4.33]}$$

Under isostatic equilibrium, the density of the crust beneath sea level is given by:

$$\rho_b = \frac{C_o \rho_c - d \rho_w}{C_o - d} \qquad \text{[B4.34]}$$

Evidence from geophysical investigations lends greater support to the Airy isostasy model. The Pratt isostasy model requires large lateral variations in densities that are not observed in the crust. In addition, variations in

the depth of the Moho across compressional and extensional tectonic regimes are incompatible with the Pratt hypothesis, which has a uniform crustal base level (Kearey *et al.*, 2009).

Both the Airy and Pratt models have a major deficiency, in that compensation occurs only directly beneath variations in topographic loading and as such, assumes the lithosphere to have no lateral strength (Lowrie, 1997). The Pratt theory of isostasy is not considered further in this study.

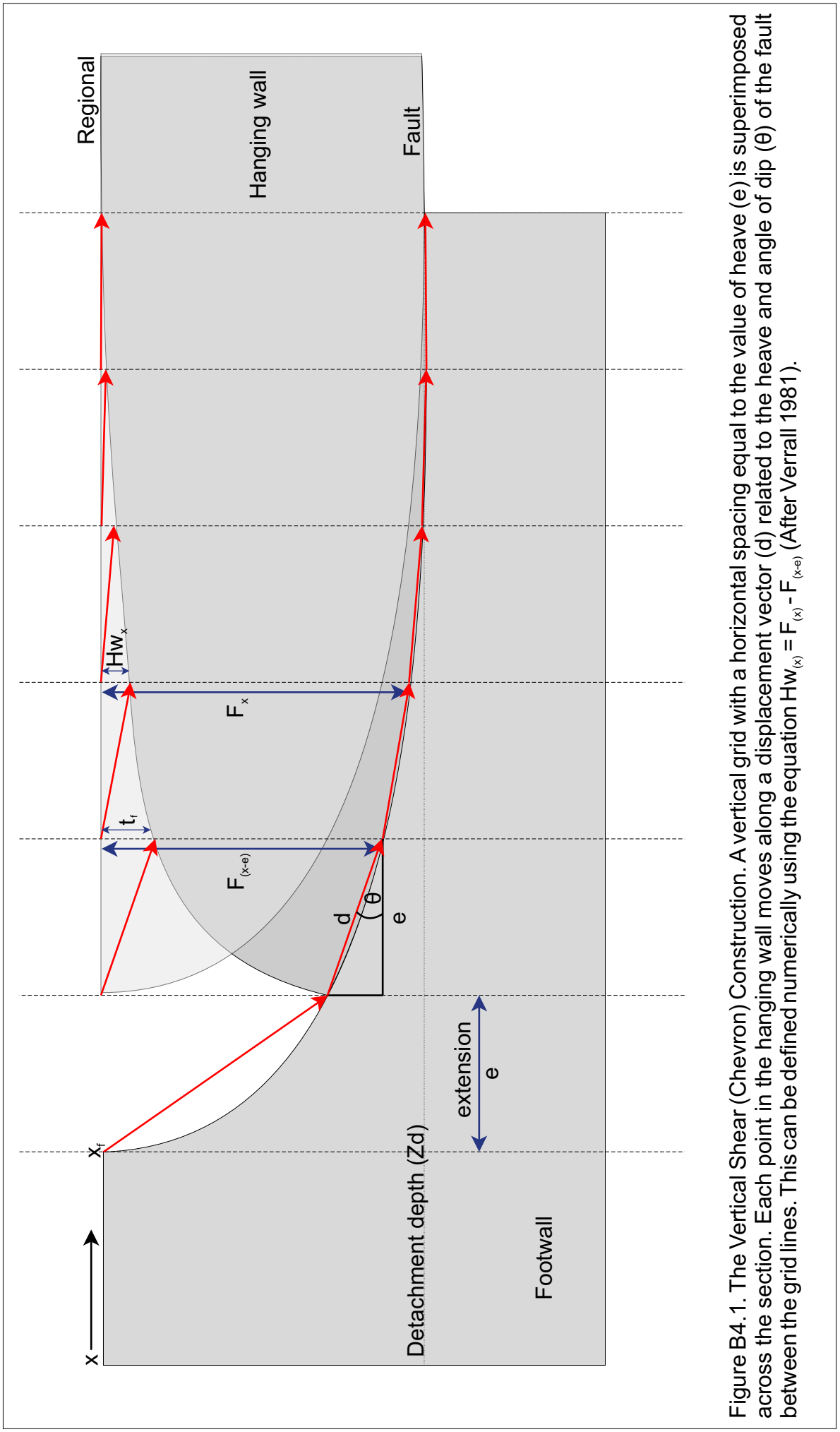


Figure B4.1. The Vertical Shear (Chevron) Construction. A vertical grid with a horizontal spacing equal to the value of heave (e) is superimposed across the section. Each point in the hanging wall moves along a displacement vector (d) related to the heave and angle of dip (θ) of the fault between the grid lines. This can be defined numerically using the equation $Hw_{(x)} = F_{(x)} - F_{(x-e)}$ (After Verrall 1981).

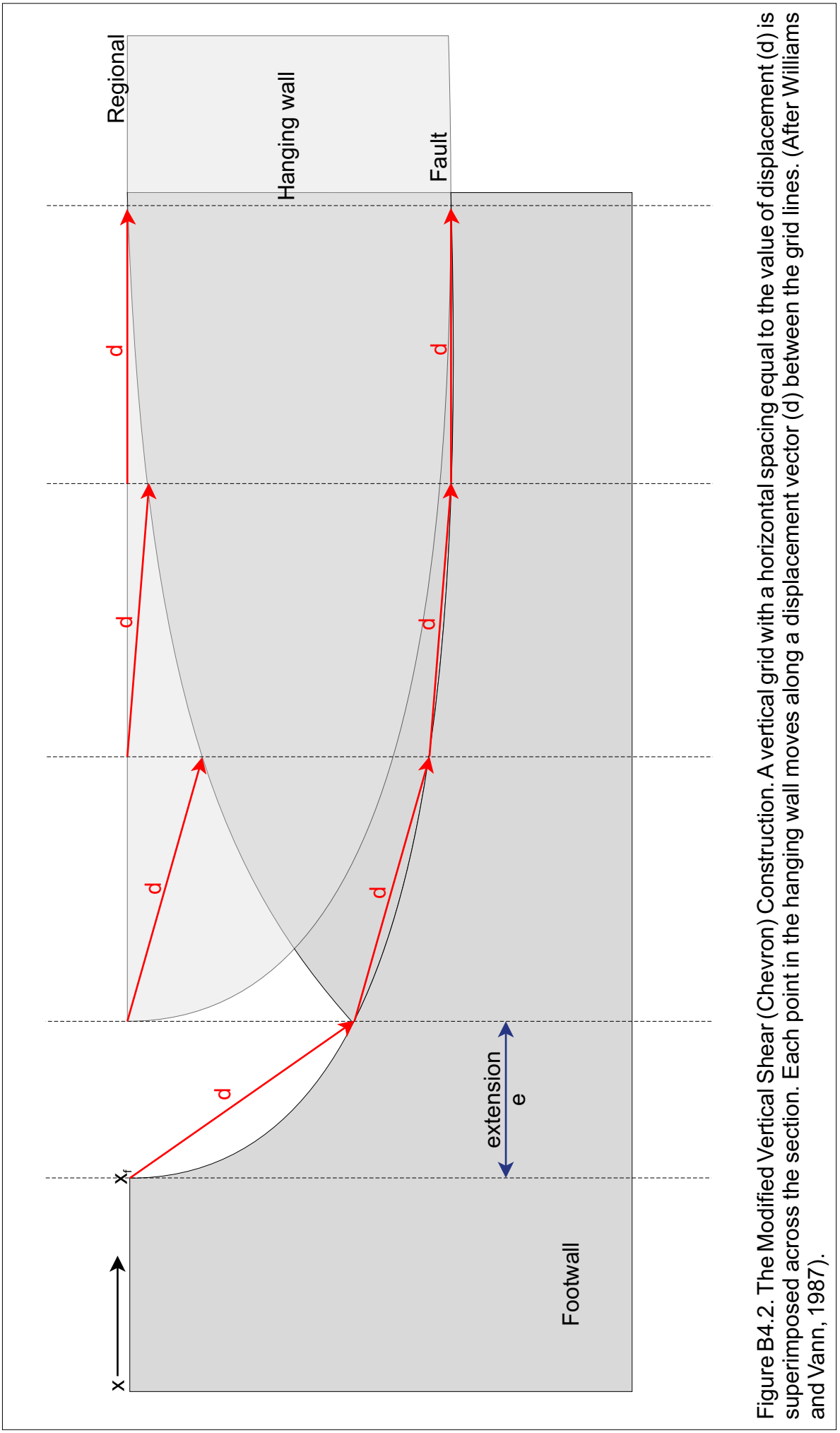


Figure B4.2. The Modified Vertical Shear (Chevron) Construction. A vertical grid with a horizontal spacing equal to the value of displacement (d) is superimposed across the section. Each point in the hanging wall moves along a displacement vector (d) between the grid lines. (After Williams and Vann, 1987).

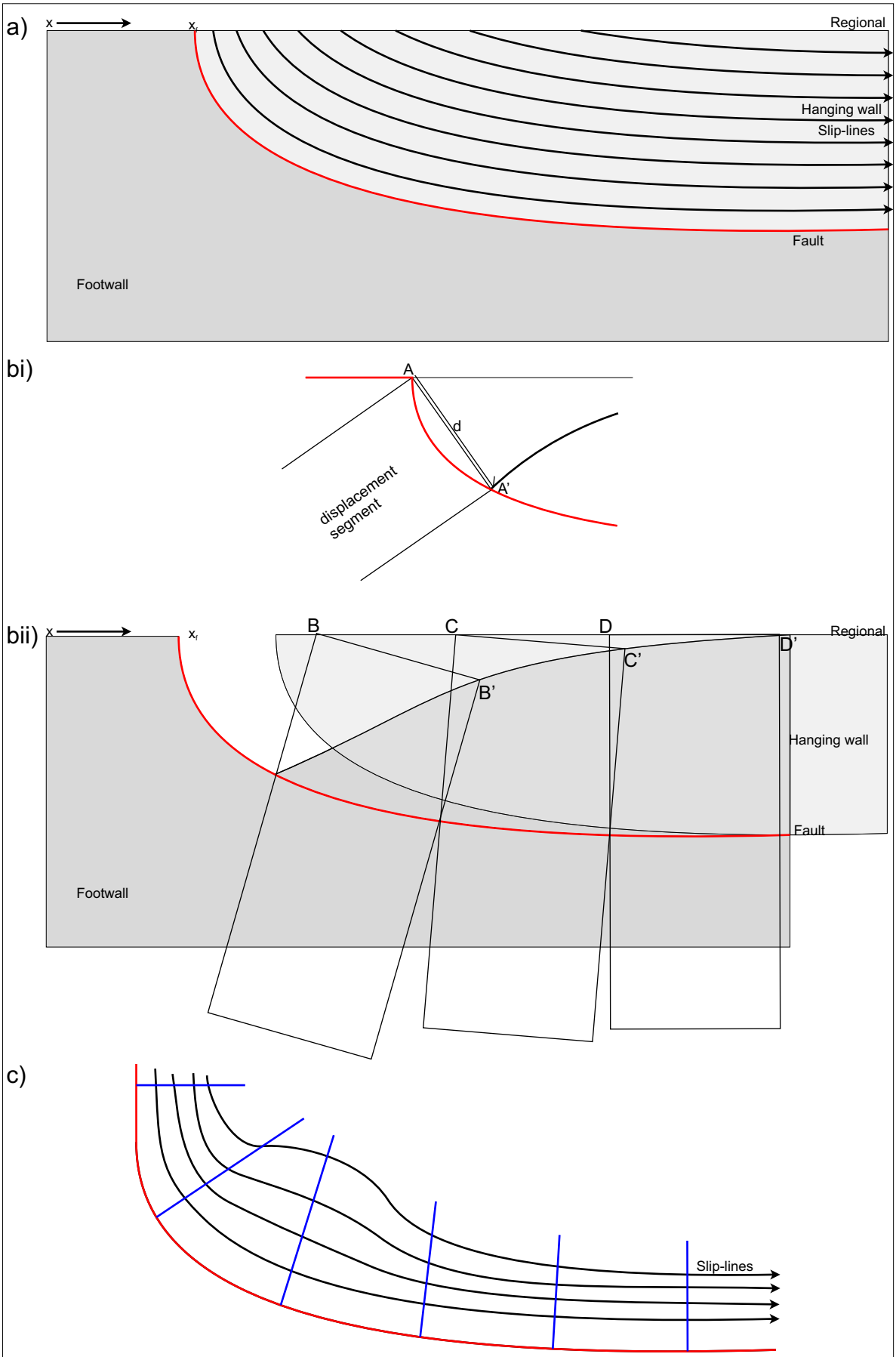


Figure B4.3. Slip-Line Construction a) Slip-lines on a normal listric fault (After Williams and Vann, 1987). bi) Slip-line construction, the amount of displacement, d, calculated from the distance A-A'. bii) Slip-line construction method using fault profile to predict hanging wall geometry, displacement conserved (A-A' = B-B' = d). c) Area corrected slip-lines, lines converge on straighter portions of the fault (After Wheeler, 1987).

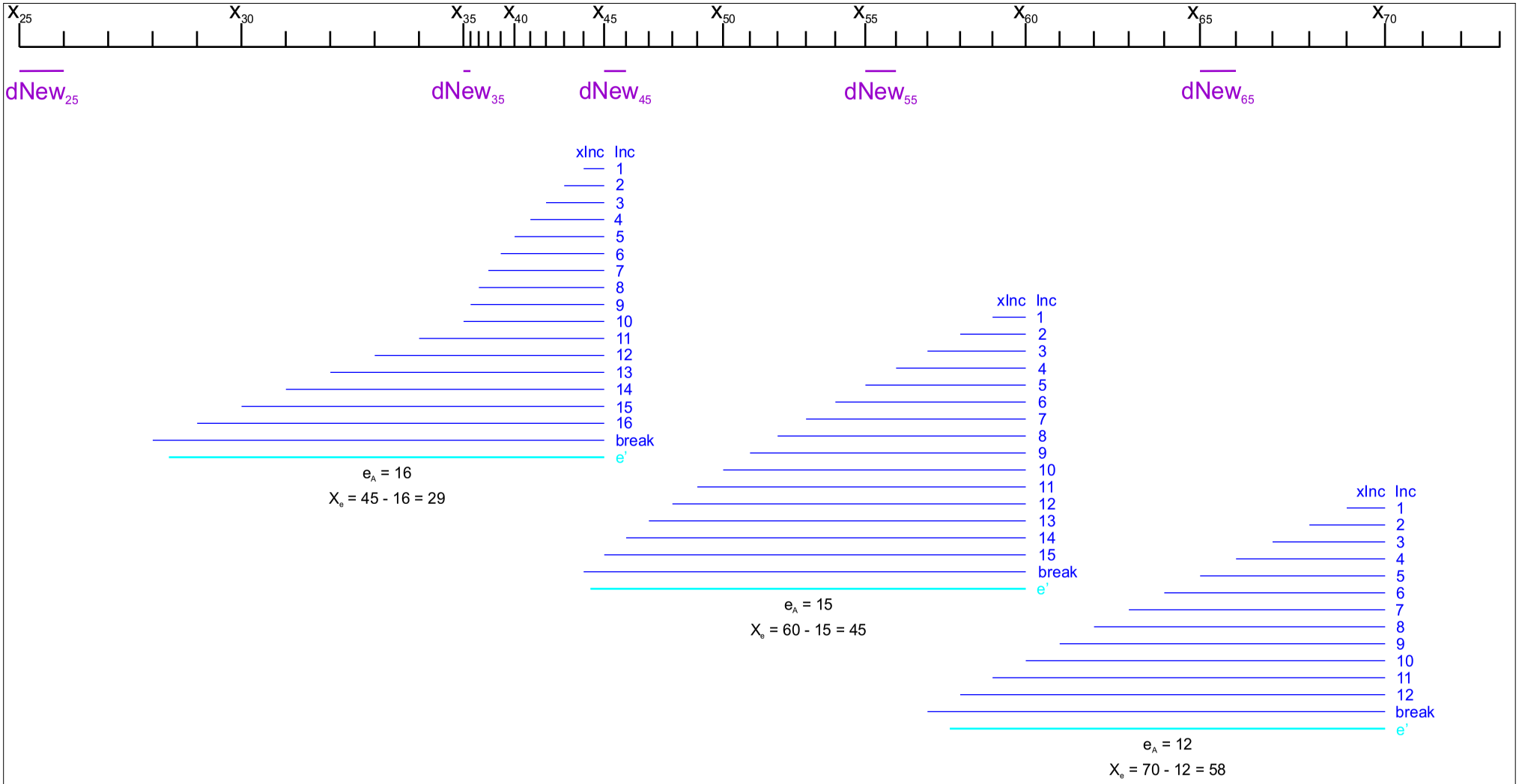


Figure B4.4. Calculating the array position of the element that represents x-e'. $dNew_x$ represents the distance between x co-ordinates. Due to the rotation of the co-ordinate system this is no longer a fixed distance (d). $e_A$ is the number of increments in $dNew_x$ that represents e' at any point and $X_e$ is the array position that represents x-e' for any position of x

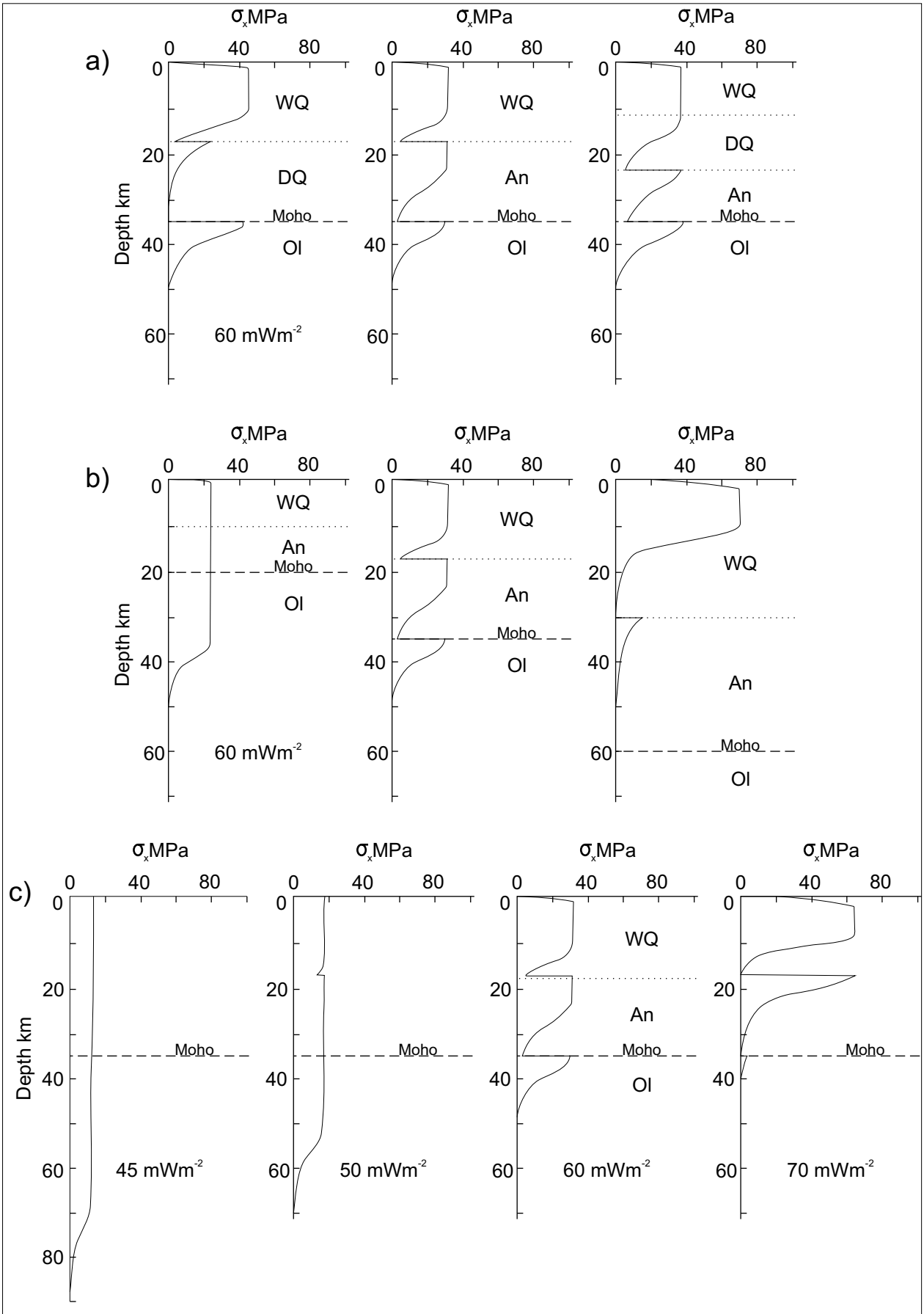


Figure B4.5. Yield stress envelopes for the continental lithosphere. a) Stress plotted against depth for a range of crustal compositions, WQ = Wet Quartz; DQ = Dry Quartz; An = Anorthosite (Plagioclase); Ol = Olivine. b) Stress plotted against depth for a range of crustal thicknesses, 20 km; 35 km; 60 km. c)Stress plotted against depth for a range of geothermal gradients giving surface heat flows between 45 and 70 $mWm^{-2}$ (After Kusznir and Park, 1987).

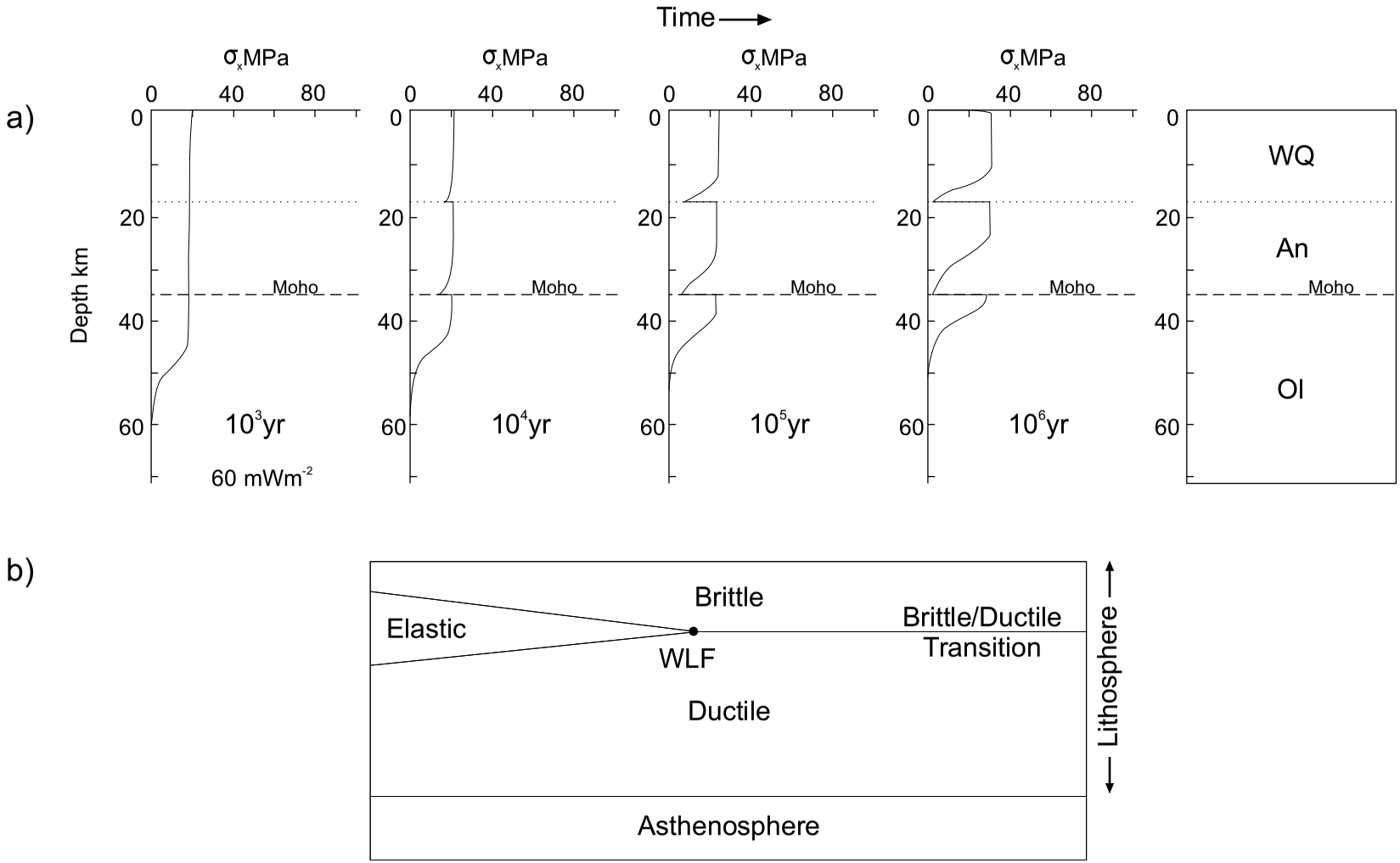


Figure B4.6. a) Stress plotted against depth at various times after application of a tensile force. Low strength regions develop above rheological boundaries. b) A representative diagram of the brittle-ductile transition leading to whole lithosphere failure (WLF) resulting in geologically significant strain (After Kusznir and Park, 1987).

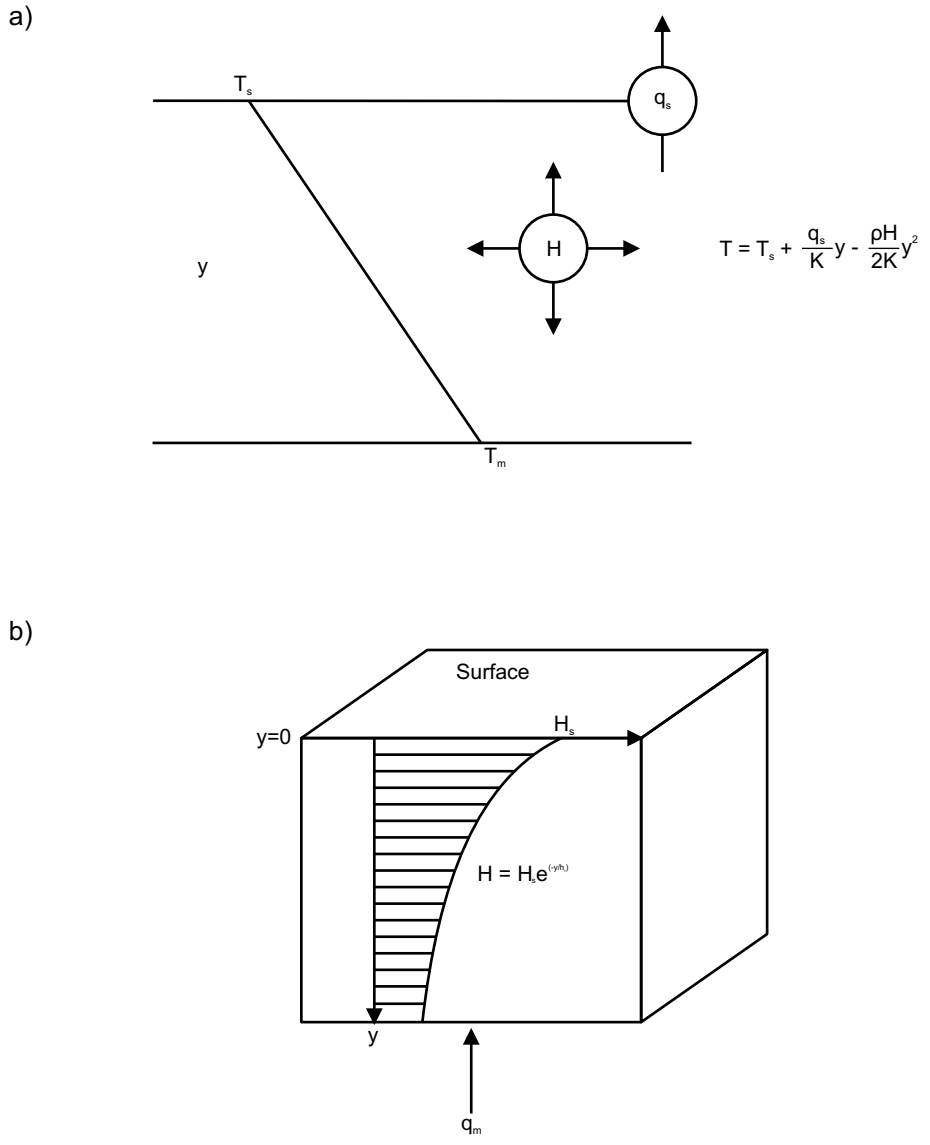


Figure B4.7. a) Heat conduction geotherm. H is the rate of internal heat generation, $q_s$ is the surface heat flow, K is the thermal conductivity and $T_s$ and $T_m$ are the surface and mantle temperatures respectively. b) Model of the continental crust with exponential radiogenic heat production with depth. c) Model of the continental geotherm that results from the exponential heat production demonstrated in (b) (After Allen and Allen, 1990).

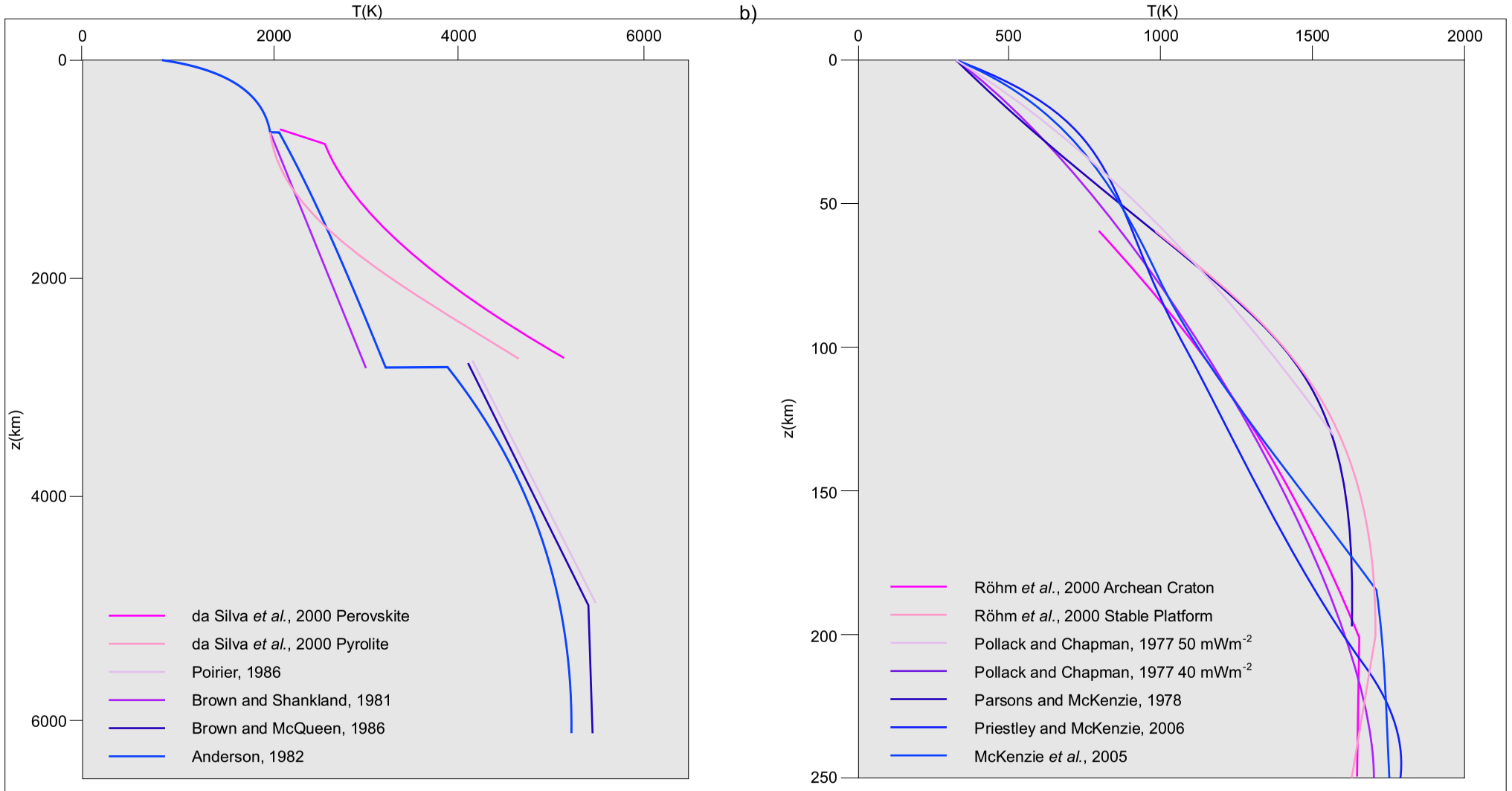


Figure B4.8. a) The Earth's geotherm (After Brown and Shackland, 1981; Anderson, 1982; Brown and McQueen, 1986; Poirier, 1986; Poirier, 1991; da Silva *et al*., 2000) b) The geotherm of the continental lithosphere (After Pollack and Chapman, 1977; Parsons and McKenzie, 1978; Röhm *et al.,* 2000; McKenzie, 2005; Priestley and McKenzie, 2006)

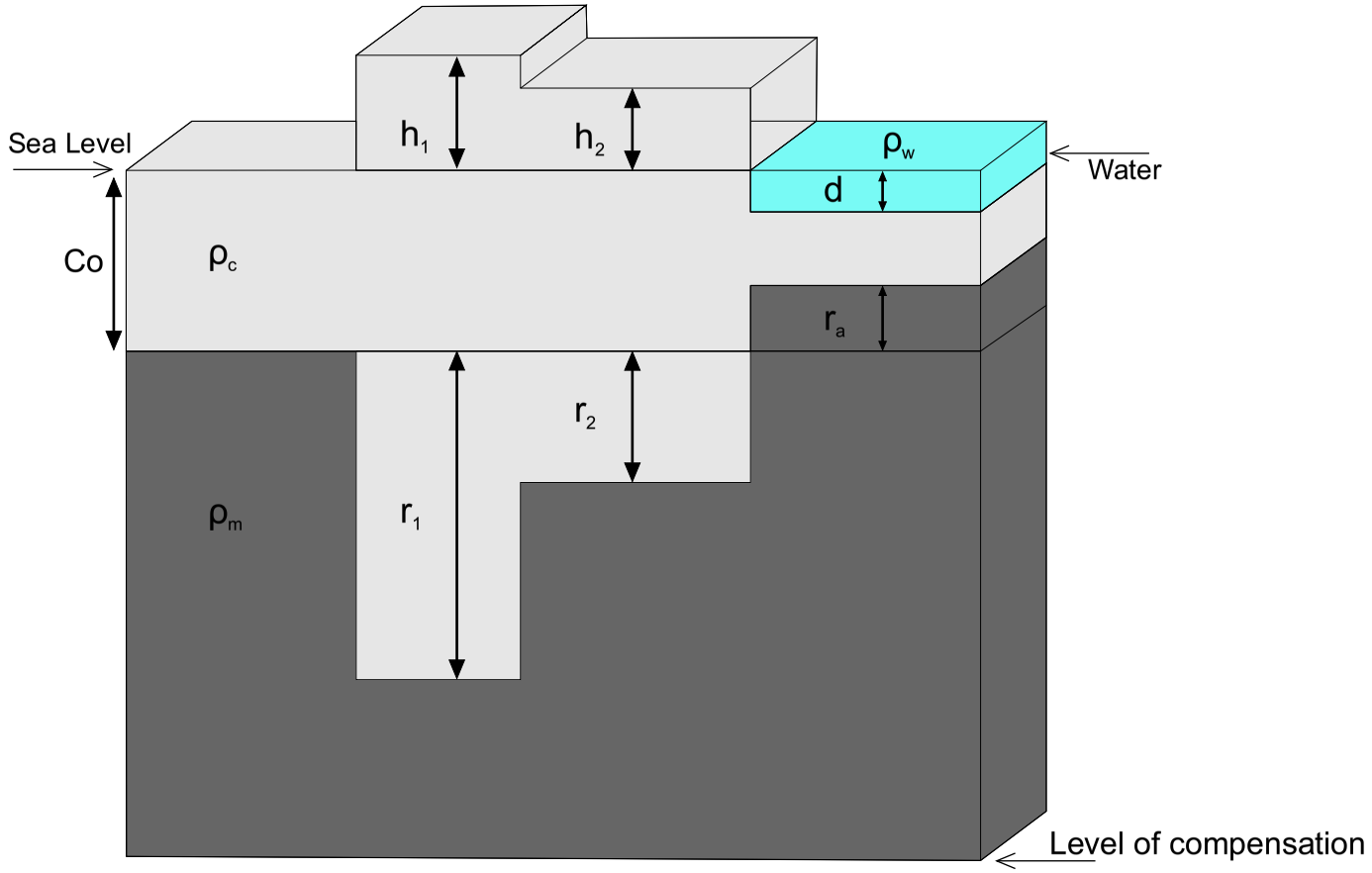


Figure B4.9. The Airy-Heiskanen model of isostasy. Compensation for changes in topography are achieved by alterations in the thickness of the underlying crust. $h_1$ and $h_2$ represents the height of the mountain belt and $r_1$ and $r_2$ the depth of the root required to reach hydrostatic equilibrium for $h_1$ and $h_2$ respectively. d represents a negative topography, a basin, $r_a$ represents the anti-root, or mantle uplift required to retain equilibrium. (After Watts, 2001; Allen and Allen, 2005).

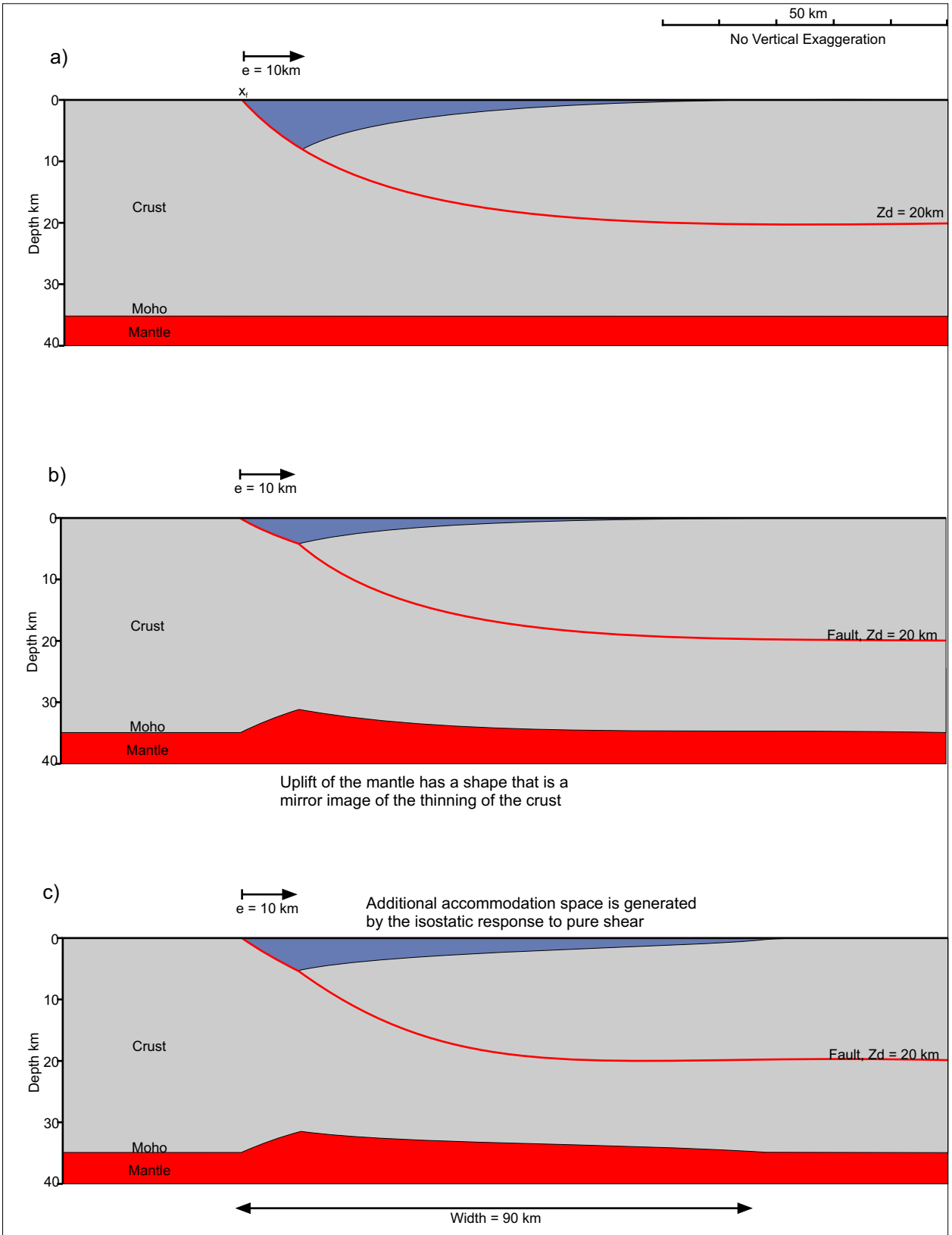


Figure B4.10 Model of lithosphere extension at time, t = 0 Ma after rifting assuming isostatic compensation using the Airy isostatic hypothesis. Extension by faulting in the upper crust with a magnitude of 10 km is balanced by extension by pure shear in the lower crust, with an intercrustal detachment between the two extension mechanisms at a depth of 20 km. a) Fault model with no isostatic compensation. b) Isostatically compensated fault and basin assuming no pure shear. c) Model of faulting and pure shear isostatically compensated.

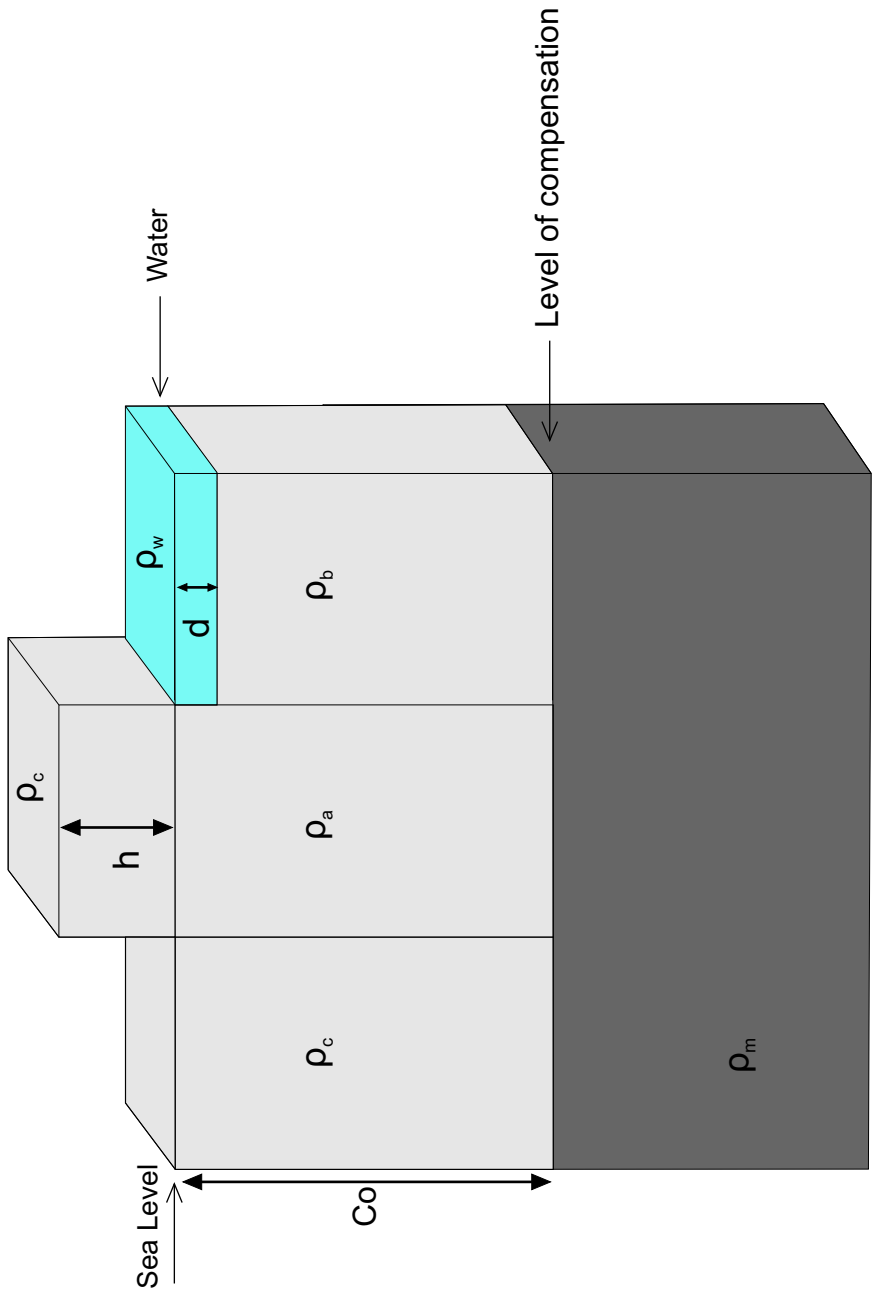


Figure B4.11. The Pratt-Hayfield isostatic model. The model assumes that the depth of compensation occurs at the base of the crust, which is at a uniform level. The model also assumes that the density of the crust above sea level is the same as the density of crust, whose topography is undisturbed. Isostatic equilibrium is achieved by varying the density of the crust below sea level laterally, such that $\rho_a < \rho_c$ and $\rho_b > \rho_c$ . (After Watts, 2001; Allen and Allen, 2005).

# 5 Appendix C: Integrated lithosphere-scale modelling of basin development in two-dimensions; model testing and code.

## 5.1 Effects of faulting on basin geometry

Sensitivity analysis has been carried out in order to determine how variation in the value of independent variables affect the model of fault deformation. By implementing the model repeatedly, whilst altering the values for the input parameters, it is possible to observe the effect that individual parameters have on the model results and identify those parameters to which the result is sensitive. Within the model, extension occurs as a result of faulting within the upper crust and the magnitude of fault-related extension remains at 10 km except when the effect of varying the magnitude of extension is investigated. An initial crustal thickness ($C_o$) of 35 km and a fault detachment depth ($Zd$) of 20 km are assumed. The behaviour of the model in response to varying the magnitude of extension ($e$), the fault detachment depth ($Zd$), and angle of shear ($\alpha_s$) are investigated.

### *5.1.1 Effect of magnitude of extension on fault-related basin geometry*

Figure C5.1 shows the effect of increasing the magnitude of extension on basin geometry. The geometry of the fault is unaffected by variations in the magnitude of extension. The effect of extension on basin geometry is determined solely by the variation in hanging wall geometry that results

from changes in the amount of extension, e. With increasing magnitude of extension, the resultant basin becomes deeper and wider. The basin has a maximum depth, which equals $Zd$, as this defines the depth at which the fault detaches.

Figure C5.2 illustrates how increasing the magnitude of fault-controlled extension influences the hanging wall profile. The resultant basin is deepest where the hanging wall cuts off against the fault at $x = x_f + e$. The maximum depth of the basin increases with increasing heave (Figure C5.2b). As extension increases, the rate of increase in maximum depth decreases progressively towards the maximum possible depth, Zd. For values of *e* between 0 and 25 km, the average increase in depth is 0.57 km per 1 km increase in *e*. For values of *e* between 25 km and 50 km, the average increase in depth is 0.16 km per 1 km increase in *e*. Figure C5.2c illustrates the effect of increasing *e* on a more distal position in the basin (x = 100 km). The increase in depth with increasing extension is characterised by larger increases in depth with higher values of *e*; for values of extension between 0 and 25 km, the average increase in depth is 0.05 km or 50m per 1 km increase in *e*. For values of extension between 25 km and 50 km, the average increase in depth is 0.21 km per 1 km increase in *e*. Figure C5.2d examines the effect of varying the magnitude of extension on the width of the basin. Basin width increases with increasing extension. At a depth of 2.5 km, the magnitude of increase in basin width is greatest at lower values of extension. Between 0 and 15 km there is an average increase in width of 2.93 km for every 1 km increase in

*e*. After 15 km there is an almost linear relationship between extension and basin width, which increases by 1.31 km for every 1 km in *e*.

### *5.1.2 Effect of fault detachment depth on fault-related basin geometry*

The fault detachment depth, $Zd$, is the level within the crust at which the fault angle of a listric fault is reduced to zero and is the maximum depth that the fault profile will reach. Variations in $Zd$ affect both the fault and hanging wall profiles. Figure C5.3 shows fault deformation models with increasing $Zd$. The depth of the fault profile, at any value of $x > x_f$, increases with increasing $Zd$. The hanging wall rollover becomes shallower with the fault profile steepening as $Zd$ increases.

Figure C5.4 examines the effect of $Zd$ on the fault profile. With increasing distance from the surface position of the fault, $x_f$, the fault angle starts at 70° at $x = x_f$ and becomes shallower until it reaches 0°. The rate of change of the fault angle varies with $Zd$ (Figure C5.4b). For example, for a $Zd$ of 5 km between x = 30 km ($x_f$) and x = 40 km the rate of change in fault angle with increasing x position was 5.3° per km. This decreases to an average change of 1.15° per km between x = 40 km and x = 60 km where the fault becomes horizontal and the fault angle is 0°. In contrast, for a $Zd$ of 30 km, the rate of change of fault angle is 0.78° per km between x = 30 km ($x_f$) and x = 100 km. At x = 100 km the fault is dipping at 15° whilst any fault whose $Zd$ is less than 15 km has reached its detachment level and is horizontal. These variations in rate of change of fault angle result in a steepening of the fault at any position of x with increasing $Zd$

(Figure C5.4c). For example at x = 40 km, a fault with $Zd$ = 5 km is dipping at 23° whilst a fault with $Zd$ = 30 km is dipping at 63°.

Figure C5.5 illustrates the effect of increasing $Zd$ on the hanging wall profile. The maximum depth of the basin increases with increasing $Zd$ (Figure C5.5b). As $Zd$ increases, the rate of increase of basin depth diminishes; for values of $Zd$ between 5 and 15 km, the average increase in depth is 0.30 km per 1 km increase in $Zd$. For values of $Zd$ between 15 km and 30 km, the average increase in depth is 0.08 km. Figure C5.5c illustrates the effect of $Zd$ in a more distal position in the basin (x = 75 km). The increase in depth with increasing $Zd$ is characterised by larger increases in depth with higher values of $Zd$. For values of $Zd$ between 0 and 15 km, the average increase in depth is 0.07 km per 1 km increase in $Zd$. For values of $Zd$ between 15 km and 30 km, the average increase in depth is 0.13 km per 1 km increase in $Zd$. Figure C5.6d examines the effect of varying detachment depths on the width of the basin. Basin width increases with increasing $Zd$. At a depth of 1 km, there is an almost linear relationship between $Zd$ and basin width, which increases by 2.3 km for every 1 km in $Zd$.

### *5.1.3 Effect of the sense and inclination of shear on fault-related basin geometry*

The deformation of a fault using the inclined shear construction does not alter the profile of the fault but does influence the deformation of the hanging wall. Faults modelled using the inclined shear construction can

be deformed using a shear angle, $\alpha_s$, whose sense is either synthetic to the fault, or antithetic to the fault. Figure C5.6 shows inclined shear models whose sense of shear is synthetic to the fault. With increasing angle of shear, the position at which the hanging wall cuts off against the fault becomes more distal to the surface position of the fault, $x_f$. This results in a deeper and wider basin.

Figure C5.7 further examines the effect of increasing shear angle with a synthetic sense of shear on the deformation of the hanging wall. The position of the hanging wall cut-off against the fault can be considered as the value of $x_f$ + 'apparent heave' as this appears to show the amount of horizontal extension if $\alpha_s = 0°$. The 'apparent heave' rises at an increasing rate with increasing values of $\alpha_s$ (Figure C5.7b). Between $\alpha_s = 0°$ and $\alpha_s = 30°$, for a true heave value of 10 km, the increase in 'apparent heave' with shear angle has an average gradient of 0.24 km per 1° increase in shear angle. Between $\alpha_s = 30°$ and $\alpha_s = 60°$, this rises to 0.6 km per 1° increase in shear angle. The maximum basin depth is related to the value of 'apparent heave' and increases with increasing values of $\alpha_s$ (Figure C5.7c). The magnitude of basin depth increase follows a similar pattern to that of 'apparent heave' with an average gradient of 0.1 km per 1° increase in shear angle between $\alpha_s = 0°$ and $\alpha_s = 30°$, and a gradient of 0.18 km per 1° increase in shear angle between $\alpha_s = 30°$ and $\alpha_s = 60°$.

Figure C5.8 exhibits inclined shear models whose sense of shear is antithetic to the fault. In this case, with increasing shear angle the position at which the hanging wall is cut-off against the fault becomes

more proximal to the surface position of the fault, $x_f$, creating a shallower basin. Figure C5.9 illustrates the effect of increasing shear angle with an antithetic sense of shear on the deformation of the hanging wall. The 'apparent heave' decreases with increasing values of $\alpha_s$ (Figure C5.9b). Between $\alpha_s = 0°$ and $\alpha_s = 10°$, for a true heave value of 10 km, the gradient of the 'apparent heave' is -0.2 km per 1° increase in shear angle. There is a linear relationship between 'apparent heave' and $\alpha_s$ between $\alpha_s = 10°$ and $\alpha_s = 60°$, with the 'apparent heave' decreasing by 0.1 km per 1° increase in shear angle. This linear relationship is in contrast to the relationship between synthetic shear angle and 'apparent heave' for synthetic shear which exhibits a curved geometry with the magnitude of increase in 'apparent heave' rising with increasing angle of shear. This is a result of the shape of the listric fault surface; antithetic shear angles direct the hanging wall onto a section of the fault that is almost straight and synthetic shear angles direct the hanging wall onto a section of the fault that is more curved. The maximum basin depth decreases with increasing $\alpha_s$ (Figure C5.9c). As with the 'apparent heave', the maximum depth of the basin resulting from deformation of the hanging wall has a linear relationship. Between $\alpha_s = 0°$ and $\alpha_s = 10°$ the maximum basin depth decreases at a rate of 0.13 km per 1° increase in shear angle. Between $\alpha_s = 10°$ and $\alpha_s = 60$, the maximum basin depth decreases at a rate of 0.08 km per 1° increase in shear angle.

Model results indicate that basin depth and width, as well as faut geometry, are controlled by the magnitude of extension ($e$), the fault

detachment depth ($Zd$), and angle of shear ($\alpha_s$). The geometry of the fault is unaffected by variations in the amount of horizontal extension, heave, that it is subjected to; however variations in the amount of heave do effect the deformation of the hanging wall and therefore the size of the resultant basin. With increasing heave, the basin becomes deeper and wider. Variations in $Zd$ affect both the fault and hanging wall profiles. The depth of the fault profile, at any point basinward of the surface position of the fault, increases with increasing $Zd$, as does the angle of the fault. The depth and width of the basin increases, with increasing $Zd$, as a result of hanging wall deformation. The deformation of a fault using the inclined shear construction does not alter the profile of the fault but does influence the deformation of the hanging wall. With increasing angle of shear and when the sense of shear is synthetic, the position of the hanging wall cut-off against the fault becomes more distal to the surface position of the fault. In contrast, the hanging wall cut-off becomes more proximal when the sense of shear is antithetic. This results in a deeper and wider basin with increasing synthetic shear and a shallower basin with increasing antithetic shear.

### 5.2 The effects of pure shear on basin geometry

A number of models have been produced with varying parameters in order to establish the effect that pure shear has on basin geometry and subsidence. Figure 4.7 provides an overview of the model and its variables. An initial crustal thickness ($C_o$) of 35 km is assumed. Extension in the upper crust occurs as a result of faulting. The magnitude of fault-related

extension remains at 10 km except when the effect of varying the magnitude of extension is investigated. The fault detachment depth (*Zd*) is 20 km. Accommodation space created within the basin is infilled by sediment with density of 2500 $kgm^{-3}$. The crust and mantle density remain fixed at 2800 $kgm^{-3}$ and 3300 $kgm^{-3}$, respectively. The behaviour of the model in response to varying the magnitude of extension and the distribution of the pure shear, as well as the thickness of the lower crust that is being subjected to pure shear (by varying the fault detachment depth and initial crustal thickness), are investigated.

### *5.2.1 The effects of the magnitude and distribution of pure shear*

Figure C5.10 shows the effect of pure shear with varying amounts of total extension. With increasing magnitudes of pure shear deformation distributed over a constant width, the resultant sag basin created by the isostatic compensation gets deeper in response to greater thinning of the lower crust. Changes in the depth to the Moho are controlled by thinning of the lower crust by pure shear and the isostatic subsidence that occurs subsequently. Increasing the magnitude of pure shear deformation results in greater thinning of the crust with increasing uplift of the Moho.

Assuming that the magnitude of fault-controlled simple shear deformation of the upper crust balances thinning of the lower crust by pure shear, Figure C5.11 illustrates how increasing the magnitude of fault-controlled extension also enhances the subsidence due to pure shear deformation. This deepening is greatest at the centre of the sag basin (x=75 km) where

it has an average gradient of 0.116 or 116 m per 1 km extension (Figure C5.11b). Decreasing the width of the lithosphere over which the pure shear deformation is distributed whilst maintaining the magnitude of extension, illustrated in Figures C5.12 and C5.13, also results in a deepening of the sag basin created. However, decreasing the width of the pure shear distribution also leads to a narrowing of the resultant sag basin. The width over which the thinning of the crust is apportioned controls the profile of the Moho, with it being raised by a greater amount but over a narrower lateral extent with decreasing width of pure shear. At the centre of the basin (x=75 km) increasing the width of the pure shear distribution results in a shallowing of the basin. The relationship between width of pure shear distribution and subsidence is exemplified by an average gradient of -0.032 or -32 m subsidence per 1 km width of distribution (Figure C5.13b).

The lateral position of the pure shear distribution within the lower crust is difficult to constrain from geological and geophysical data (Rudnick and Fountain, 1995). Whilst it can be expected to occur in a position that is related to the overlying brittle deformation in the upper crust, it could conceivably be influenced by other structures outside the extent of the model. It is therefore necessary to consider the effect of varying the lateral position of the pure shear with respect to the simple shear. In Figure C5.14, models are shown in which the width of the pure shear distribution remains constant at 90 km, but it has been moved laterally with respect to the fault. The variation in the lateral position of the pure shear with

respect to the simple shear demonstrates its importance in relation to basin subsidence. In Figure C5.14b, the lateral position of the pure shear deformation coincides approximately with fault-controlled extension of the upper crust. This configuration results to increased subsidence across the whole basin as subsidence due to both simple shear and pure shear are superimposed upon each other. In Figure C5.14c-d, the pure shear is displaced in a more distal position with respect to the overlying faulting. As a result, the pure shear deformation deepens the distal portion of the basin, such that the fault-related depocentre and the pure shear-related depocentre are offset. Additionally, the profile of the Moho in Figure C5.14 is controlled by fault-related isostatic uplift as well as crustal thinning and subsidence related to the pure shear deformation. Isostatic adjustments related to crustal thinning due to faulting raises the Moho directly beneath the fault (Figure C5.14a), but the thinning of the lower crust by pure shear raises the Moho over a broader area and the resulting isostatic subsidence depresses the profile over a similarly broad expanse. This effect can be seen in Figure C5.14b where the Moho is raised by a greater amount immediately below the fault but then gradually deepens towards the distal part of the basin. The increased offset between simple shear and pure shear causes the Moho profile to be broader such that in Figures C5.14c and C5.14d there are two separate regions where the Moho has been raised.

### *5.2.2 The effects of lower crustal thickness on pure shear*

The thickness of the lower crust that undergoes extension by pure shear is controlled by the fault detachment depth ($Zd$) and the original crustal thickness ($C_o$). The effect of varying depth of detachment is investigated in Figure C5.15, and the effect of varying crustal thickness is considered in Figure C5.16. Both of these factors have a significant effect on the geometry of the resultant basin. Although varying $Zd$ and $C_o$ does not change the values of β, these parameters do vary the thickness of the lower crust over which the pure shear is distributed, so they affect the amount of crustal thinning. Increasing $Zd$ decreases the thickness of the lower crust with lower amounts of thinning due to pure shear and, as a result, a reduction in the amount of subsidence. Conversely increasing $C_o$, increases the thickness of the lower crust and therefore the amount of thinning due to pure shear and hence increases the amount of subsidence. The ratio of the thickness of crust that is affected by deformation as a result of simple shear to the thickness of crust thinned by pure shear deformation is determined by the 'necking depth' of the lithosphere. The depth of necking of the lithosphere is defined as the level in the lithosphere that does not move vertically during deformation before isostatic adjustments are implemented (Braun and Beaumont, 1989; Weissel and Karner, 1989; Kooi *et al.*, 1992). The necking depth is set at a constant level in most numerical models, either implicitly or as a variable model parameter (Fjeldskaar *et al.*, 2004). In the McKenzie model, the necking depth is implicitly set at 0 km. In coupled simple-shear/pure-

shear models the necking depth is often set at the level where major faults detach ($Zd$) (Ter Voorde and Cloetingh, 1996; Fjeldskaar *et al.*, 2004). Increasing the necking depth has two opposing effects that work to counteract each other; a structural effect and an isostatic effect. The structural effect of increasing the necking depth flattens the Moho as the contribution from thinning of the lower crust decreases. The isostatic effect of increasing necking depth is to reduce the amount of isostatic subsidence as the amount of crustal material replaced by higher density mantle material is reduced (Kooi and Cloetingh, 1992; Fjeldskaar *et al.*, 2004). The thickness of the lower crust, $C_L$, is given by:

$$C_L = C_o - Zd \qquad \text{[C5.1]}$$

A model of pure shear geometry with parameters $C_o$ = 35 km and $Zd$ = 5 km (Figure C5.13a) produces the same amount of subsidence as a model with parameters $C_o$ = 50 km and $Zd$ = 20 km (Figure C5.16a); in both cases the thickness of the lower crust, $C_L$, is 30 km. Figure C5.17a illustrates the subsidence generated due to pure shear with increasing lower crustal thickness. There is a linear relationship between lower crustal thickness and the subsidence exhibited by the overlying basin to extension by pure shear (Figure C5.17b). In the centre of the basin where subsidence is at a maximum, there is a gradient of 0.0989 or 98.9 m of subsidence per 1 km of lower crustal thickness.

## 5.3 Effect of thermal processes on basin evolution

A model has been produced incorporating extension by faulting and pure shear as well as thermal uplift at time t = 0Ma after rifting followed by thermal subsidence. Several models have been produced at time intervals, 0, 5, 25, 50, 75 and 100Ma after extension to illustrate the effect of thermal subsidence over time. Figure 4.9 exhibits the model used showing the parameters that are involved in the calculation of the thermal response to lithosphere extension. The behaviour of the model is examined in the following sections in response to varying the parameters that influence the thermal response to lithosphere extension. The magnitude of extension is an important factor affecting the thermal response as it dictates the amount of thinning of the lower crust and mantle lithosphere, and therefore the amount by which the lithosphere/asthenosphere boundary is raised, including the geotherm. The thickness of the lithosphere, the co-efficient of thermal expansion and the density of the mantle are also parameters whose effects on the thermal processes are investigated. The sag basins that result from thermal subsidence are subjected to infilling by sediment, which has an additional isostatic effect that will be examined in section C5.5.

### *5.3.1 The effect of magnitude of extension on the thermal response to extensional deformation*

A balanced deformation model is being used such that the amount of extension by faulting is balanced by the amount of extension by pure

shear. The extension factor, $\beta_{(x)}$, and the width of the pure shear determine the distribution of thinning of the lower crust and mantle lithosphere. $\beta_{Max}$ represents the extension factor at the peak of the pure shear which is modelled using a sinusoidal distribution. Figure C5.18 illustrates the thermal uplift at time (t) = 0Ma after extension, with $\beta_{Max}$ values of 1.19, 1.45, 1.79 and 2.26, representing an equivalent extension by faulting of 10, 20, 30 and 40 km, respectively. Increasing the magnitude of extension, results in an increase in the amount of thermal uplift of the lithosphere generated in response to extension, as the lithosphere is thinned by a greater amount bringing the hotter material of the asthenosphere closer to the surface, thus raising the geotherm by a greater amount. The amount of uplift generated increases by 0.035 km or 35 m for every 1 km increase in magnitude of extension.

Figure C5.19 displays the cumulative amount of subsidence generated after 100 Ma. With increasing magnitude of extension, the amount of thermal subsidence generated increases, with an increase in subsidence of 0.115 km for every 1 km increase in extension. The initial rise in the geotherm is greater with increased extension, as such there is more heat to be transferred in order to re-establish the geothermal equilibrium within the lithosphere, resulting in greater thermal subsidence. In addition, the amount of subsidence generated is cumulative and as time passes, despite the amount of subsidence generated diminishing, at larger magnitudes of extension, greater amounts of subsidence are generated than at smaller magnitudes of extension over the same time periods

(Figure C5.20a). For example, the ratio between the cumulative amount of subsidence and magnitude of extension at t = 25 Ma is a 0.045 km increase in subsidence to a 1 km increase in extension, and at t = 50Ma the ratio is 0.078 km subsidence to 1 km extension. As time since extension increases, the rate of thermal subsidence decreases (Figure C5.20c), resulting in a leveling of the cumulative subsidence, which can be observed in Figure C5.20b; however, the rate of subsidence slows more quickly when the magnitude of extension is lower. Models of thermal uplift and subsidence for increasing magnitude of extension at time intervals 0, 5, 25, 50, 75 and 100Ma after extension are presented in Figure C5.21.

### *5.3.2 The effect of lithosphere thickness on the thermal response to extensional deformation*

The thickness of the lithosphere affects thermal uplift and subsidence processes following extension by determining the distance over which heat is transferred by conduction. It influences the heat flux by spreading the heat within the lithosphere over a smaller or larger distance, controlling the $\delta y$ component in the equation for heat flux of the lithosphere [6.1].

Figure C5.22 presents models of thermal uplift with increasing lithosphere thickness. Increasing lithosphere thickness results in increased thermal uplift. Within these models, there is 0.0036 km of extra uplift for every 1 km increase in lithosphere thickness.

The effect of lithosphere thickness on thermal subsidence is illustrated by Figure c5.23, which presents the cumulative thermal subsidence at t = 100Ma since extension. Model results show that there is an increase in subsidence of 0.012 km for every 1 km increase in lithosphere thickness.

Figure C5.24 shows the effect of thermal processes on basin development over time with varying thicknesses of lithosphere. The rate of subsidence decreases more rapidly for greater thicknesses of lithosphere (Figure C5.24c). The greatest decrease in rate of subsidence occurs in the first 5Ma after extension where the average rate of subsidence is 0.032 $kmMa^{-1}$ for $a$ = 100 km, and 0.048 $kmMa^{-1}$ for $a$ = 150 km. The rate of subsidence at t = 25Ma is 0.02 $kmMa^{-1}$ for $a$ = 100 km, and 0.03 $kmMa^{-1}$ for $a$ = 150 km. At t = 100Ma the rate of subsidence has been reduced to 0.006 $kmMa^{-1}$ for $a$ = 100 km, and 0.008 $kmMa^{-1}$ for $a$ = 150 km. The cumulative amount of subsidence has begun to reach asymptotic values at t = 100Ma (Figure C5.24b). Models of thermal uplift and subsidence for increasing lithosphere thickness at time intervals 0, 5, 25, 50, 75 and 100Ma after extension are presented in Figure C5.25.

### *5.3.3 The effect of thermal expansion co-efficient on the thermal response to extensional deformation*

The co-efficient of thermal expansion, $\alpha_T$, is a measure of a material's ability change volume with temperature. An average value for the co-efficient of thermal expansion of $3.28 \pm 1.19 \times 10^{-5}\ K^{-1}$ for the lithosphere has been proposed in Parsons and Sclater, (1977) and McKenzie(1978);

however, there is much scope for variation in the possible value for this parameter in the context of the lithosphere. These variations depend upon the type of lithosphere, continental or oceanic, and the age of the lithosphere; for example, a value of $3.04 \times 10^{-5}$ $K^{-1}$ has been proposed for Archaean continental lithosphere and $3.25 \times 10^{-5}$ $K^{-1}$ proposed for younger Phanerozoic lithosphere (Afonso *et al.*, 2005). These variations in the value of the co-efficient of thermal expansion range from $1.6 \times 10^{-5}$ $K^{-1}$ (Stacey 1992; 1995) to $4.2 \times 10^{-5}$ $K^{-1}$ (Doin and Fleitout, 1996). Figure C5.26 illustrates models of thermal uplift for these two extreme values as well as a more average value of $3.28 \times 10^{-5}$ $K^{-1}$. With increasing co-efficient of thermal expansion there is a greater amount of expansion due to the increased heat from raising of the asthenosphere. This results in increased thermal uplift, with 0.2 km uplift at x = 75 km (i.e. the centre of model) for $\alpha_T = 1.6 \times 10^{-5}$ $K^{-1}$, 0.45 km uplift at x = 75 km for $\alpha_T = 3.28 \times 10^{-5}$ $K^{-1}$, and 0.57 km uplift at x = 75 km for $\alpha_T = 4.2 \times 10^{-5}$ $K^{-1}$. There is a linear relationship between thermal uplift and the co-efficient of thermal expansion with 0.0136 km uplift per $0.1 \times 10^{-5}$ $K^{-1}$ increase in thermal expansion.

The effect of the thermal expansion co-efficient on thermal subsidence is considered in Figure C5.27, which demonstrates the cumulative thermal subsidence at t = 100Ma after extension. The higher the value of the thermal expansion co-efficient, the greater the amount of contraction, and therefore density increase, as the geotherm re-equilibrates, resulting in increased subsidence. At t = 100Ma the cumulative amount of subsidence

at the centre of the basin (x = 75 km) is 0.73 km at $\alpha_T$ = 1.6 x $10^{-5}$ $K^{-1}$, 1.5 km at $\alpha_T$ = 3.28 x $10^{-5}$ $K^{-1}$, and 1.92 km at $\alpha_T$ = 4.2 x $10^{-5}$ $K^{-1}$. There is a linear relationship between the co-efficient of thermal expansion and thermal subsidence, with a gradient of 0.046 km per 0.1 x $10^{-5}$ $K^{-1}$ or a rate of 0.00046 km per 0.1 x $10^{-5}$ $K^{-1}Ma^{-1}$. The increased subsidence associated with an increase in the co-efficient of thermal expansion is greatest between 0 and 25Ma after extension where it increases by 0.021 km for every 0.1 x $10^{-5}$ $K^{-1}$ increase in the co-efficient of thermal expansion, a rate of 0.00084 km per 0.1 x $10^{-5}$ $K^{-1}Ma^{-1}$.

Figure C5.28 shows the effect of thermal processes on basin development over time with varying the magnitude of the co-efficient of thermal expansion. The rate of subsidence decreases over time (Figure C5.28c), with the sharpest fall in the rate of subsidence occurring between 0 and 25 Ma after extension. During this time period the rate of subsidence decreases from 0.040 $kmMa^{-1}$, for a co-efficient of thermal expansion of 3.3 x $10^{-5}$ $K^{-1}$, to 0.024 $kmMa^{-1}$, a reduction of 0.016 $kmMa^{-1}$ over 25Ma during which the average rate of subsidence is 0.027 $kmMa^{-1}$. By 100Ma after extension, the rate of subsidence has been reduced to 0.0069 $kmMa^{-1}$ for a co-efficient of thermal expansion of 3.3 x $10^{-5}$ $K^{-1}$, a reduction of 0.017 $kmMa^{-1}$ over 75 Ma. This reduction in rate of subsidence results in a leveling in the amount of cumulative subsidence as the amount of additional subsidence is minimised (Figure C5.28b). Models of thermal uplift and subsidence for increasing co-efficient of thermal expansion at

time intervals 0, 5, 25, 50, 75 and 100Ma after extension are presented in Figure C5.29.

### *5.3.4 The effect of the density of the lithospheric mantle on the thermal response to extensional deformation*

In the mantle, density is non-linear and discontinuous as a result of phase transitions, and temperature variations (Ringwood, 1975; Simon and Podladchikov, 2008). An estimate of the density of the lithosphere at 0°C is required to model thermal processes. An average value for the sub-continental lithospheric mantle is generally assumed to be 3300 $kgm^{-3}$ (Parsons and Sclater, 1977; McKenzie, 1978). Density heterogeneities produce gravity anomalies reaching amplitudes of a few hundred $10^{-5}$ $ms^{-2}$, corresponding to density variations in the region of 30 $kgm^{-3}$ and 100 $kgm^{-3}$. (Artemjev *et al.*, 1994; Yegorova *et al.*, 1995; 1997; Yegorova and Starostenko, 2002). Estimates of mantle densities ranging from 3310±160 $kgm^{-3}$ for Archaean mantle to 3360±2 $kgm^{-3}$ for Phanerozoic mantle have been calculated from data on mantle composition, thermal state and thickness (Poudjom Djomani *et al.*, 2001). In areas where melt extraction has depleted the mantle, the density is reduced; for example, estimates for the mantle density beneath Iceland range from 3170 $kgm^{-3}$ to 3260 $kgm^{-3}$ (Derbyshire *et al.*, 2000). Models have been produced to study the effect of varying mantle density using values of mantle density between 3200 $kgm^{-3}$ and 3400 $kgm^{-3}$.

Figure C5.30 illustrates thermal uplift at t = 0Ma after extension with increasing lithospheric mantle density. The mantle density is a controlling factor in determining the Airy isostatic response to thermal perturbations, $\rho_m/(\rho_m - \rho_i)$, such that increasing the density of the mantle, increases the density contrast between the mantle and the basin infill, which, in turn, reduces the amount of mantle material that is necessary for isostatic adjustment. As a result, at t = 0Ma there is a reduction in thermal uplift with increasing mantle density. The amount of thermal uplift generated at t = 0Ma is 0.652 km when mantle density is 3200 $kgm^{-3}$ and 0.635 km when mantle density is 3400 $kgm^{-3}$ a reduction of 0.006 km in uplift per 100 $kgm^{-3}$ increase in mantle density. At t = 100Ma, illustrated in Figure C5.31, the cumulative amount of subsidence decreases with increasing mantle density. The total thermal subsidence at t = 100Ma is 1.66 km when mantle density is 3200 $kgm^{-3}$ and 1.37 km when mantle density is 3400 $kgm^{-3}$, a gradient of -0.00145 km per 1 $kgm^{-3}$ increase in mantle density. Figure C5.32 shows the effect of thermal processes on the basin development over time with varying mantle density. The rate of subsidence is greatest in the first 25Ma after extension when it has an average rate of 0.031 $kmMa^{-1}$ at $\rho_m$ = 3200 $kgm^{-3}$ and 0.025 $kgMa^{-1}$ at $\rho_m$ = 3400 $kgm^{-3}$ (Figure C5.32c). By t = 100Ma the rate of subsidence has been reduced to 0.0076 $kmMa^{-1}$ at $\rho_m$ = 3200 $kgm^{-3}$ and 0.0062 $kgMa^{-1}$ at $\rho_m$ = 3400 $kgm^{-3}$. The cumulative amount of subsidence is negligible as the geotherm approaches equilibrium (Figure C5.32b). Models of thermal

uplift and subsidence for increasing mantle density at time intervals 0, 5, 25, 50, 75 and 100Ma after extension are presented in Figure C5.33.

Varying the magnitude of extension has the greatest effect on the response of the lithosphere to thermal processes with increased thermal uplift and subsequent thermal subsidence generated by increasing magnitudes of extension. Increasing the thickness of the lithosphere and the thermal expansion co-efficient also increases the amount of thermal uplift and subsidence, but to a lesser extent than varying the magnitude of extension. Varying the density of the mantle affects the isostatic response of the lithosphere to thermal processes, such that an increase in mantle density results in a reduction in the magnitude of the thermal uplift and thermal subsidence.

## 5.4 The effect of flexural isostasy on basin evolution

A model has been produced incorporating extension by faulting and pure shear and thermal uplift at time, t = 0 Ma after rifting, with isostatic equilibrium maintained by applying the principles of flexural isostasy. Following the initial extension phase, a post-extensional thermal subsidence is applied to the model, also compensated using flexural isostasy. Models have been produced to examine the effect of applying flexural isostasy, by comparing the flexural isostatic response to the Airy isostatic response at each stage in the process. Several models have been produced at time intervals of 0, 5, 25, 50, 75 and 100 Ma after extension has occurred.

Figure 5.6 provides an overview of the model and the input parameters assumed, including an original crustal thickness of 35 km and a lithosphere thickness of 125 km. Extension by faulting in the upper crust with a magnitude of 10 km is balanced by extension by pure shear in the lower crust, with an intercrustal detachment between the two extension mechanisms at 20 km. The co-efficient of thermal expansion is assumed to be $3.28 \times 10^{-5}$ $K^{-1}$ and the temperature at the base of the lithosphere is 1333°C. Any accommodation space created in the basin is assumed to have been infilled by sediment with a density of 2500 $kgm^{-3}$. A Te of 5 km has been assumed. The effect of filling the basin is addressed in section C5.5. The model has been recalculated in order to observe the effect of individual variables on the isostatic response to lithosphere extension. In particular, the effects of varying the elastic thickness of the lithosphere, the density of the mantle, and the density crust have been investigated.

### *5.4.1 The effect of the elastic thickness of the lithosphere on the isostatic response to extensional deformation*

The flexural rigidity, and therefore the amount by which the lithosphere flexes in response to loading is determined by its elastic thickness, $Te$. The larger the elastic thickness, the broader the region over which loads are isostatically compensated. Figure C5.34 illustrates the effect of increasing the elastic thickness of the lithosphere at time, t = 0 Ma after extension. The model incorporates extension of 10 km magnitude by faulting and pure shear and thermal uplift, with the basin assumed to be infilled by sediment. In addition, Figure C5.35 summarises the effects of $Te$ on basin

evolution, including the flexural response of the basin at selected locations. Figure C5.34a represents an elastic thickness of zero, and as a result the lithosphere has no flexural strength; this is equivalent to Airy isostasy. The lithosphere with a flexural rigidity of zero acts in a slightly anomalous fashion as the isostatic response is laterally coincident with the load generating it. With increasing elastic thickness, the maximum basin depth increases. For example, at the x = 40 km position along the model profiles, which corresponds to the central part of the basin, there is an increase in depth of 0.079 km for every 1 km increase in $Te$ (Figure C5.35e). This occurs as the flexural uplift is extended over a broader area but its amplitude decreases. The flexural response of the basin at t = 0 Ma after extension can be observed in Figure C5.35a. At low values of $Te$, the amount of footwall uplift increases with increasing flexural rigidity; averaging an increase of 0.026 km per 1 km increase in $Te$ at location x = 30 km, reaching a peak uplift at a $Te$ of 7.5 km. The maximum amount of footwall uplift generated decreases as flexural rigidity continues to increase; decreasing by 0.012 km for a 1 km increase in $Te$ at location x = 30 km (Figure C5.35D). The lateral extent of the footwall uplift increases with increasing flexural rigidity as the wavelength of the flexural rebound increases (Figure C5.35a&c). At low values of $Te$ (<8 km) the flexural response to the processes that occur at t = 0 Ma after rifting generates subsidence in the footwall, in front of the uplift, creating a basin. This basin deepens with decreasing $Te$ until a maximum depth is reached at a $Te$ of 5 km (Figure C5.35c). The profile of the Moho becomes

subdued as flexural rigidity increases as the maximum amount of uplift is reduced and the flexural rebound becomes more laterally distributed.

Figure C5.36 illustrates the effect of increasing the elastic thickness of the lithosphere at t = 100 Ma after rifting. In addition, the overall flexural response of the basin can be observed in Figure C5.35b. The maximum amount of thermal subsidence generated decreases with increasing $Te$. As a result, the depth of the distal part of the basin (locations x = 70-100 km), where thermal subsidence has a greater influence than the fault related uplift, decreases with increasing $Te$. The depth of the basin at location x = 90 km decreases by an average of 0.028 km for every 1 km increase in $Te$ (Figure C5.35f). At a greater horizontal distance from the fault, x = 130 km, the basin deepens with increasing flexural rigidity; a 1 km increase in $Te$ corresponds to an increase in basin depth of 0.022 km. This arises as the width over which the flexural response is distributed is increased and consequently, towards the limits of the isostatic response, the amount of thermal subsidence increases with increasing $Te$. The same process also affects the amount of footwall uplift, which, with increasing flexural rigidity is reduced and broadened. Footwall uplift adjacent to the fault(ie at location x = 30 km) decreases by an average of 0.0295 km for every 1 km increase in $Te$ (Figure C5.35d). Models showing the effect of increasing the elastic thickness of the lithosphere at time intervals 0, 5, 25, 50, 75 and 100Ma after extension are presented in Figure C3.37.

### *5.4.2 The effect of the density of the lithospheric mantle on the isostatic response to extensional deformation*

The lithosphere responds to counteract the imposition or removal of loads, such than a constant pressure is maintained upon the base of the lithosphere. This is achieved by the flow of mantle material, which is denser than the overlying crustal material; increasing its thickness beneath areas of negative loading and decreasing its thickness beneath areas of positive loading. Varying the density of the lithospheric mantle, $\rho_m$, alters the quantity of mantle material that is required to compensate for anomalous loads. Figure C5.38 demonstrates the effect of increasing the mantle density at time, t = 0 Ma after rifting. Figure C5.39 provides a summary of the effect of mantle density on basin evolution, including the flexural response of selected locations along the basin profile. With increasing mantle density, less material is required to replace the negative load associated with thinning of the crust by faulting and the basin deepens as there is less flexural rebound following rifting. The flexural response that acts upon the lithosphere in response to rifting at t = 0 Ma is displayed in Figure C5.39a. At its deepest, at location x = 40 km, the basin increases in depth by 0.0026 km per 1 $kgm^{-3}$ increase in mantle density (Figure C5.39e). In a more proximal position within the basin, the influence of thermal uplift increases the amount by which mantle density affects basin evolution. The amount of thermal uplift generated is reduced by increasing the density of the mantle as less mantle material needs to be added to the system to compensate for the decrease in density associated

with thermal expansion. As such the basin deepens with increasing mantle density, averaging 0.0042 km per 1 $kgm^{-3}$ increase in mantle density at x = 75 km (Figure C5.39f). The amount of footwall uplift generated decreases with increasing mantle density, with an average decrease of 0.0011 km for every 1 $kgm^{-3}$ increase in mantle density adjacent to the fault at x = 30 km (Figure C5.39d). The flexural response to the processes that occur at t = 0 Ma after rifting generates subsidence in the footwall before the uplift, creating a basin. This basin is deeper at lower values of mantle density, increasing 0.00025 km per 1 $kgm^{-3}$ decrease in mantle density at x = 15 km (Figure C5.39c).

Figure C5.40 illustrates the effect of increasing the density of the lithospheric mantle at t = 100 Ma after extension. Increasing the mantle density increases the depth of the basin. In a position proximal to the fault, the increase in subsidence from time t = 0 Ma is less than the increase in subsidence in a distal position. For example, at a mantle density of 3200 $kgm^{-3}$, there is 0.61 km of subsidence between 0 and 100 Ma at location x = 40 km, this corresponds to a rate of 0.0061 $kmMa^{-1}$. At x = 75 km, there is 1.64 km of subsidence or 0.0164 $kmMa^{-1}$ (Figures C5.39e&f). This is a result of an offset between the lateral position of the fault-controlled deformation and the pure shear extension within the model. Thermal uplift and subsidence occur where the lithosphere has been thinned by pure shear, raising the geotherm. The rate of subsidence decreases with increasing mantle density. At a mantle density of 3400 $kgm^{-3}$, the rate of subsidence decreases from the rate at 3200 $kgm^{-3}$

by ~27% such that, at x = 40 km the rate is reduced to 0.0051 $kmMa^{-1}$. At x = 75 km, the rate of subsidence is reduced to 0.0136 $kmMa^{-1}$ (Figures C5.39e&f). This decrease in subsidence with increasing mantle density is due to less mantle material being required to leave the system to compensate for the increase in the density of the lithosphere associated with thermal contraction and to restore isostatic equilibrium. At times greater than t = 0 Ma, increasing the mantle density decreases the amount of subsidence generated by thermal processes. When this reduced subsidence is combined with the reduced uplift generated at t = 0 Ma, the overall effect of varying the density of the mantle on basin development is reduced from that demonstrated at t = 0 Ma (Figure C5.39b). Within the deepest part of the basin near to location x = 40 km (Figure C5.39e) the relationship between mantle density and basin depth is indicated by an increase in basin depth of 0.0021 km per 1 $kgm^{-3}$ increase in density. In comparison, the distal part of the basin, at x = 75 km, (Figure C5.39f) exhibits an increase in depth of 0.0015 km for every 1 $kgm^{-3}$ increase in mantle density; this is significantly less than the 0.0042 km increase in depth per 1 $kgm^{-3}$ at t = 0 Ma after extension. Models showing the effect of increasing the density of the lithospheric mantle at time intervals 0, 5, 25, 50, 75 and 100Ma after extension are presented in Figure C5.41.

### *5.4.3 The effect of the density of the crust on the isostatic response to extensional deformation*

The quantity of mantle material that is required to compensate for any volume of crustal material is determined by the contrast in density

between the crust and the mantle. Increasing the density of the crust reduces the density contrast between the crust and mantle, therefore the density of the crust determines the value of the load removed from the lithosphere as a result of extension. Increasing the density of the crust leads to a larger load being removed which results in an increase in the flexural uplift response to faulting. As the crust is thinned by pure shear, it is replaced by mantle material. With increasing crustal density, the contrast between the mantle and crust is reduced and less subsidence is required to restore isostatic equilibrium. The isostatic responses to thermal perturbations of the lithosphere resulting from extension are not affected by the crustal density.

Figure C5.42 displays models of lithosphere extension at time, t = 0 Ma after extension, with varying crustal density. As a result of increasing crustal density, there is increased uplift in response to faulting and decreased subsidence in response to pure shear. At any point in the resultant basin, increasing the crustal density causes the depth of the basin to be reduced. The difference in basin depth as a result of increasing crustal density is greatest in a position adjacent to the fault, where the flexural response to faulting is greatest. Figure C5.43 illustrates the effect of varying the density of the crust upon the flexural response to extension and upon the basin development over time at selected locations. At location x = 40 km there is a decrease in basin depth of 0.0069 km for every 1 $kgm^{-3}$ increase in crustal density (Figures C5.43a&e). At x = 75 km, this decrease in basin depth is reduced to 0.0041 km for every

1 $kgm^{-3}$ increase in crustal density (Figure C5.43a&f). The region of subsidence of the hanging wall before the footwall uplift decreases with increasing crustal density, with an increase of 0.0004 km per 1 $kgm^{-3}$ increase in density at location x = 15 km (Figure C5.43c). The amount of footwall uplift generated in response to the crustal thinning caused by faulting increases with increasing crustal density, with an increase of 0.0024 km per 1 $kgm^{-3}$ increase in crustal density adjacent to the fault at x = 30 km (Figure C5.43d).

Figure C5.44 illustrates the effect of varying the density of the crust at t = 100 Ma after rifting. Because the crustal density does not influence the flexural response to thermal subsidence, the relationship between crustal density and basin evolution does not vary over time. The basin generated at t = 100 Ma after rifting is widened by the maximum thermal subsidence occurring in a position that is offset from the fault. In this position the total subsidence is greater than the total uplift (Figure C5.43b). Models showing the effect of increasing the density of the crust at time intervals 0, 5, 25, 50, 75 and 100Ma after extension are presented in Figure C5.45.

## 5.5 The effect of infilling a basin and its control on its evolution and stratigraphy

The effect of infilling a basin is investigated by simulating the effects of both water and sediment infill materials. The model, based on that described in section 5.2 with the addition of basin infill algorithms, is run with a fixed *Te* of 5 km, $\rho_m$ of 3300 $kgm^{-3}$ and $\rho_c$ of 2800 $kgm^{-3}$. The basin

is created by movement along a single fault with extension of 10 km magnitude. Pure shear extension of the lower crust with $\beta$ equivalent to 10 km extension takes place below the faulting between x = 30 km and x = 120 km. The density of the infill, $\rho_i$, is varied to reflect a water infill, $\rho_i$ = 1000 kgm$^{-3}$ and a sediment infill, $\rho_i$ = 2500 kgm$^{-3}$. The effect of varying the sediment density is also investigated.

Figure C5.46 illustrates the effect of basin infill at time, t = 0 Ma after extension. Figure C5.46a shows the basin with only air infill ($\rho_i$ = 1 kgm$^{-3}$.), resulting in no additional loading relating to the basin infill. As such, the basin reflects the dominant flexural response; the large amount of uplift resulting from the thinning of the upper crust by faulting. Figure C5.46b demonstrates water infill of the basin, which creates additional loading, enhancing basin subsidence. As a result, the basin is deeper across its lateral extent and the footwall uplift is reduced. Figure C5.46c illustrates a sediment filled basin. The load generated by the sediment is 2.5 times greater than the load generated by the water infill which results in overall subsidence that is 1.5 times greater than that produced by the water infill.

Figure C5.47 illustrates the effect of basin infill at time, t = 100 Ma after extension whereby the subsidence due to thermal re-equilibration of the geotherm has also been infilled. This intensifies the effect of infilling the basin, generating additional subsidence. The amount of subsidence generated by sediment infill of the basin between 0 and 100 Ma after rifting is 2.75 times greater than that generated by water infill. Models

showing the effect of varying the basin infill at time intervals 0, 5, 25, 50, 75 and 100Ma after extension are presented in Figure C5.48.

When the basin is infilled with sediment, it is also possible to examine how the basin stratigraphy develops over time, as illustrated in Figure C5.49. At time, t = 0 Ma after extension, the first stratigraphic unit fills the basin created by extension of the lithosphere (Figure C5.49a). Between t = 0 Ma and t = 5 Ma, the main basin depocentre moves to a more proximal position in the basin with the onset of post-rift thermal subsidence that mainly overlies the thinning of the lower crust and mantle lithosphere by pure shear (Figure C5.49b). As time since rifting increases, additional thermal subsidence and loading is generated. However, the amount of subsidence generated decreases and the stratigraphic units become thinner with each subsequent unit of stratigraphy onlapping the underlying unit (Figure C5.49c,d&e). The stratigraphical thickness of each unit is maintained over time such that the stratigraphic unit created at t = 0 Ma is as thick at t = 100 Ma after rifting as it was at t = 0 Ma (Figures C5.49a&b); however, the effects of compaction are considered in section 5.4.3.

### *5.5.1 The effect of sediment density on basin evolution*

Several factors interact to determine the density of sediment deposited within a basin. Sediment density varies laterally and horizontally across the basin as the type of sediment varies by environment of deposition. Sediment density also varies as a result of depth, with density increasing

as compaction reduces pore space, such that at the bottom of the basin, the sediment density eventually increases to reflect a crustal-like density of ~ 2800 $kgm^{-3}$. At the surface, the unconsolidated sediment will have a reduced density of ~ 2000 – 2200 $kgm^{-3}$ (Sclater and Christie, 1980). In addition, the density of sediment is time dependent, increasing as sedimentation within post-rift subsidence generates additional compaction of the sediments beneath. The model developed uses a bulk density that represents the average sediment density within the basin.

Figure C5.50 illustrates the effect of varying the bulk density of the sediment, $\rho_s$, infilling the basin in terms of its control on the flexural response of the lithosphere and, in turn, on the basement depth laterally across the section. With increasing $\rho_s$, the maximum depth of the basin, adjacent to the fault, increases (Figure C5.50a&b). At location x = 40 km, the maximum basin depth increases from 5.01 km, at time, t = 100 Ma after rifting when $\rho_s$ = 1750 $kgm^{-3}$ to 8.07 km when $\rho_s$ = 2750 $kgm^{-3}$, an average increase of 0.003 km per 1 $kgm^{-3}$ increase in sediment density (Figure C5.50e). The rate of increase in basin depth with increasing $\rho_s$ is greatest in the distal region of the basin, where the effect of thermal subsidence is greatest (Figure C5.50b). At x = 75 km, the rate of increase in basin depth is 0.0078 $kmMa^{-1}$ at $\rho_s$ = 1750 $kgm^{-3}$ and 0.0216 $kmMa^{-1}$ at $\rho_s$ = 2750 $kgm^{-3}$ (Figure C5.50f). The amount of footwall uplift is reduced with increasing $\rho_s$ as additional subsidence is generated. Adjacent to the fault, at x = 30 km, where footwall uplift is greatest, there is an average decrease in footwall uplift of 0.001 km per 1 $kgm^{-3}$ increase in $\rho_s$

(Figure C5.50d). The region of flexurally-generated subsidence on the footwall next to the footwall uplift decreases with increasing $\rho_s$ (Figure C5.50c). This is a flexural effect due to the increasing influence of the sedimentary loading on the overall flexural response shifting the position of the flexural response into a more distal position in the basin.

## 5.6 The effect of varying palaeobathymetry on basin and stratigraphy evolution

In order to investigate the effect of palaeobathymetry on basin evolution and stratigraphy, a model developed as described by Figure 5.6, with the addition of a maximum palaeobathymetry level that determines the maximum water depth within the basin, has been produced. The level of maximum palaeobathymetry is altered to consider the effect of varying palaeobathymetry. Extension within the model is balanced with equal amounts of extension in the upper crust, faulting, and lower crust, pure shear. Unless otherwise stated the magnitude of extension is 10 km. The effects of varying the magnitude of extension and the sediment infill density and the mantle density with varying palaeobathymetry are examined. The sediment density is 2500 $kgm^{-3}$ unless otherwise stated.

Figure C5.51 illustrates the effect of varying the palaeobathymetry on basin evolution at time, t = 0 Ma after extension. With increasing depth of maximum palaeobathymetry, the maximum basin depth is reduced. This is a result of increased water infilling part of the basin. The density contrast between the sediment and water ($\rho_s - \rho_w$) results in a reduced

load being applied when the palaeobathymetry is increased, generating less flexural subsidence in response to basin infill. Figure C5.52 examines the effect of varying palaeobathymetry on the flexural response to lithosphere extension and basin development. Figure C5.52a shows the profile of the flexural response at time, t = 0 Ma after extension, where the cumulative isostatic response to lithosphere extension at t = 0 Ma is flexural uplift. The amount of uplift increases with increasing palaeobathymetry in a proximal position within the basin. At x = 40 km, where the basin is deepest, there is a decrease in basin depth of 0.119 km per 0.1 km increase in the depth of the maximum palaeobathymetry (Figure C5.52e). There is also an increase in footwall uplift adjacent to the fault as a result of the reduction in subsidence associated with increasing palaeobathymetry. At x = 30 km, where footwall uplift is greatest, there is an increase in footwall uplift of 0.051 km per 0.1 km increase in maximum palaeobathymetry (Figure C5.52d). In a position before the footwall uplift, the flexural response to extension generates subsidence. The amount of subsidence generated decreases with an increasing maximum level of palaeobathymetry, such that there is a decrease of 0.003 km per 0.1 km increase in maximum palaeobathymetry (Figure C5.52c). In a more proximal position within the basin, the effect of increasing the maximum palaeobathymetry is reduced at greater depths of palaeobathymetry. At x = 75 km, maximum palaeobathymetry depths up to 0.5 km, there is an average decrease in basin depth of 0.049 km per 0.1 km increase in palaeobathymetry. At palaeobathymetry depths greater than 0.5 km, the

basin depth at this proximal position is less than 0.5 km and therefore increasing the maximum palaeobathymetry has little effect as in this case the actual palaeobathymetry is equal to the basin depth (Figure C5.52f).

Figure C5.53 illustrates the basin at time, t = 100 Ma after extension. If the basin depth is greater than the maximum palaeobathymetry level, the basin is infilled with sediment. As such, the maximum palaeobathymetry level has an important influence on the development of stratigraphy within the basin. With increasing maximum palaeobathymetry the deposits become narrower and their maximum thickness is reduced. Models showing the effect of increasing the maximum depth of palaeobathymetry at time intervals 0, 5, 25, 50, 75 and 100Ma after extension are presented in Figure C5.54.

### *5.6.1 The effect of magnitude of extension and varying palaeobathymetry*

Figure C5.55 illustrates the effect of varying the magnitude of extension with varying depths of maximum palaeobathymetry. Figure C5.55a presents the effect of increasing the magnitude of extension upon the basin with a maximum palaeobathymetry depth of 0.5 km. With increasing magnitude of extension, the basin depth increases across the whole basin. The maximum basin depth, at position x = 30 km + magnitude of extension, increases by a greater amount at lower values of extension, such that there is an average increase in basin depth of 0.337 km per 1 km increase in extension, when the magnitude of extension is less than 20 km, and an average increase in basin depth of

0.104 km when the magnitude of extension is between 20 and 50 km. In a more distal position within the basin, x = 90 km, the depth of the basin increases a greater amount with increasing magnitude of extension. Between 5 and 20 km extension, there is an average increase in basin depth of 0.021 km per 1 km increase in extension. Between 20 and 35 km extension this gradient increases to 0.093 km and between 35 and 50 km extension there is an increase in basin depth of 0.295 km per 1 km increase in extension. The maximum amount of footwall uplift, at x = 30 km, initially increases with increasing magnitude of extension, until a maximum footwall uplift is achieved at ~ 25 km extension, after which, the maximum amount of footwall uplift begins to decrease. At magnitudes of extension less than 25 km there is an average increase in footwall uplift of 0.021 km per 1 km increase in extension. At magnitudes of extension greater than 25 km, there is an average decrease in footwall uplift of 0.003 km per 1 km increase in extension.

Figure C5.55b exhibits the effect of increasing the magnitude of extension upon the basin with a maximum palaeobathymetry depth of 0.5 km at time, t = 100 Ma after extension. The increase in basin depth over time is greater with increasing magnitude of extension. At the position of maximum basin depth, at 5 km extension the rate of subsidence over time between 0 and 100 Ma is 0.004 $kmMa^{-1}$, and at 50 km extension the rate of subsidence is 0.015 $kmMa^{-1}$, an average increase of 0.0003 $kmMa^{-1}$ per 1 km extension. Figures C5.55c-e consider the effect of magnitude of extension with maximum palaeobathymetry depths of 0, 0.5 and 1 km at

time, t = 100 Ma. The relationship between magnitude of extension and footwall uplift at x = 30 km (Figure C5.55c) takes the same form with varying palaeobathymetry. The amount of footwall uplift however, is greater at greater values of maximum palaeobathymetry depth. In each case the footwall uplift increases with increasing magnitude of extension when the magnitude of extension is less than 20 km, an increase of 0.025 km per 1 km increase in extension. At magnitudes of extension greater than 20 km there is a decrease in footwall uplift of 0.008 km per 1 km increase in extension.

Figure C5.55d considers the effect of magnitude of extension with varying palaeobathymetry on maximum basin depth at time, t = 100 Ma. Increasing the magnitude of extension increases the effect of the maximum palaeobathymetry depth. It has already been established that the basin depth decreases with increasing maximum palaeobathymetry depth. The basin depth decreases by 0.079 km per 0.1 km increase in palaeobathymetry when the magnitude of extension is 5 km. This increases to a reduction in basin depth of 0.18 km per 0.1 km increase in palaeobathymetry when the magnitude of extension is 50 km. Figure C5.55e considers the effect of magnitude of extension with varying palaeobathymetry on basin depth in a more distal position within the basin, at x = 90 km, at t = 100 Ma. At x = 90 km, if the maximum palaeobathymetry level is greater than the basin depth, varying the maximum palaeobathymetry does not affect the basin depth as the actual palaeobathymetry is equal to the basin depth. As such, when the

magnitude of extension is less than 10 km, basin depth remains constant at palaeobathymetry levels between 0.5 km and 1 km, basin depth increases when the maximum palaeobathymetry level is between 0.5 km and 0 km. Increasing the magnitude of extension increases the effect of the maximum palaeobathymetry depth by deepening the basin. The basin depth decreases by 0.024 km per 0.1 km increase in palaeobathymetry when palaeobathymetry is between 0 and 0.5 km and the magnitude of extension is 5 km. This increases to a decrease in basin depth of 0.17 km per 0.1 km increase in palaeobathymetry when the magnitude of extension is 50 km.

### *5.6.2 The effect of sediment density and palaeobathymetry*

Figure C5.56 illustrates the effect of varying the sediment density and maximum palaeobathymetry. Figure C5.56a shows the basin profile with varying sediment density at t = 0 Ma after extension when the maximum palaeobathymetry is 0.5 km. The basin deepens with increasing sediment density. In a proximal position, at x = 40 km, where the basin is deepest, there is an increase in basin depth of 0.0018 km per 1 $kgm^{-3}$ increase in sediment density. In a more distal position, where the depth of the basin is less than the maximum palaeobathymetry level, the effect of sediment density is reduced such that at x = 75 km, there is an increase in basin depth of 0.0002 km per 1 $kgm^{-3}$ increase in sediment density. The amount of footwall uplift is reduced by increasing sediment density such that, at x = 30 km, there is a decrease in footwall uplift of 0.00081 km per 1 $kgm^{-3}$ increase in sediment density.

Figure C5.56b illustrates the effect of increasing sediment density at time, t = 100 Ma after extension when the maximum palaeobathymetry depth is 0.5 Km. The basin deepens with increasing sediment density. The basin deepens in the centre, where the effect of thermal subsidence is greatest. Figures C5.56c-e consider the effect of varying the sediment density with varying palaeobathymetry at time, t = 100 Ma after extension. Figure C5.56c illustrates the effect of varying sediment density and palaeobathymetry upon footwall uplift. The maximum footwall uplift decreases with increasing sediment infill density and increases with increasing palaeobathymetry. Increasing the density of the sediment increases the effect of the maximum palaeobathymetry depth. The amount of footwall uplift increases by 0.014 km per 0.1 km increase in palaeobathymetry when the density of the sediment is 1750 $kgm^{-3}$. This increases to 0.077 km per 0.1 km increase in palaeobathymetry when the sediment density is 2750 $kgm^{-3}$. This is a result of the flexural effect of the isostatic compensation to a reduced load resulting from infilling the basin by a greater amount of water instead of the more dense sediment when palaeobathymetry is greater.

Figure C5.56d illustrates the effect of varying sediment density and palaeobathymetry upon the maximum basin depth at x = 40 km and t = 100 Ma after extension. The maximum basin depth decreases with increasing palaeobathymetry. Increasing the density of the sediment infill increases the effect of the maximum palaeobathymetry depth. The basin depth decreases by 0.034 km per 0.1 km increase in palaeobathymetry

when the density of the sediment is 1750 $kgm^{-3}$. This decrease in basin depth increases to 0.177 km per 0.1 km increase in palaeobathymetry when the sediment density is 2750 $kgm^{-3}$. Figure C5.56e illustrates the effect of varying sediment density and palaeobathymetry upon the basin depth in a more distal position within the basin x = 65 km at t = 100 Ma after extension. The amount by which the basin deepens with increasing sediment density is reduced with increasing maximum palaeobathymetry. Increasing the density of the sediment infill increases the effect of the maximum palaeobathymetry depth. The affect of this increase in sediment density is greater at lower values of palaeobathymetry. When palaeobathymetry is between 0 and 0.5 km, the basin depth decreases by 0.036 km per 0.1 km increase in palaeobathymetry when the density of the sediment is 1750 $kgm^{-3}$, which increases to 0.213 km per 0.1 km increase in palaeobathymetry when the sediment density is 2750 $kgm^{-3}$. When palaeobathymetry is between 0.5 and 1 km, the basin depth decreases by 0.004 km per 0.1 km increase in palaeobathymetry when the density of the sediment is 1750 $kgm^{-3}$, which increases to 0.065 km per 0.1 km increase in palaeobathymetry when the sediment density is 2750 $kgm^{-3}$. The increase is greater at lower values of palaeobathymetry because a greater amount of sediment is deposited.

### *5.6.3 The effect of mantle density and palaeobathymetry*

Figure C5.57 illustrates the effect of varying the mantle density upon the basin considering palaeobathymetry. Figure C5.57a shows the basin at time, t = 0 Ma, when the maximum palaeobathymetry depth is set to

0.5 km. With increasing mantle density, the basin deepens. At x = 40 km, where the basin is deepest, there is an increase in basin depth of 0.0027 km per 1 $kgm^{-3}$ increase in mantle density. In a more distal position within the basin, x = 75 km, the increase in basin depth with increasing mantle density is reduced to 0.0017 km per 1 $kgm^{-3}$ increase in mantle density. The amount of footwall uplift is also reduced with increasing mantle density, with a reduction of 0.001 km per 1 $kgm^{-3}$ increase in mantle density.

Figure C5.57b presents the profiles of the basin with increasing mantle density and a maximum palaeobathymetry depth of 0.5 km at time, t = 100 Ma after extension. Increasing the mantle density increases the depth of the basin. Figures C5.57c-e consider the effect of varying the mantle density with varying palaeobathymetry at time, t = 100 Ma after extension. Figure C5.57c investigates the effect of varying mantle density and palaeobathymetry upon footwall uplift at x = 30 km. Increasing the density of the mantle reduces the effect of the maximum palaeobathymetry depth. This is because the density contrast between the water infill and the mantle material, is greater than the density contrast between the sediment infill and the mantle material $(\rho_m - \rho_w) > (\rho_m - \rho_s)$. The amount of footwall uplift increases by 0.055 km per 0.1 km increase in palaeobathymetry when the mantle density is 3200 $kgm^{-3}$. This is reduced to 0.048 km per 0.1 km increase in palaeobathymetry when the mantle density is 3400 $kgm^{-3}$. At x = 40 km, illustrated by Figure C5.57d, the maximum basin depth decreases with increasing palaeobathymetry.

Increasing the density of the mantle reduces the effect of the maximum palaeobathymetry depth. The basin depth decreases by 0.12 km per 0.1 km increase in palaeobathymetry when the mantle density is 3200 $kgm^{-3}$. This is reduced to 0.11 km per 0.1 km increase in palaeobathymetry when the mantle density is 3400 $kgm^{-3}$. At a distal position within the basin, Figure C5.57e, increasing the palaeobathymetry decreases basin depth. Increasing the density of the mantle increases the effect of the maximum palaeobathymetry depth. This is because as mantle density increases, the basin deepens and at lower values of palaeobathymetry, the basin is deeper than the palaeobathymetry and sediment is deposited. At greater values of maximum palaeobathymetry, the basin depth at a distal position will be less than the maximum palaeobathymetry level, and therefore the actual palaeobathymetry will be equal to the basin depth and the load upon the lithosphere is less than of there were sediment deposited within the basin.

## 5.7 The effect of compaction on basin and stratigraphic evolution

A model including the algorithms examined in section 5.4.3 has been developed in order to study the effect of compaction of sediment over time upon basin and stratigraphic evolution. The parameters of the model have been set as described in Figure 5.6 and remain fixed unless otherwise stated. A sandstone lithology with surface porosity 49% and compaction co-efficient of 0.27 have been assumed. In reality, compaction of sediment has two effects upon basin evolution; increasing the sediment density with increasing depth of burial and generation of additional accommodation

space. Increasing sediment density with depth results in positive loading of the lithosphere the deeper the sediments are buried. This is accounted for in the model by the use of a bulk sediment density that represents the average sediment density within the basin. The implications of studying this further are discussed in chapter 8. Compaction of the sediments also creates new accommodation space within the basin, which is consequently infilled by sediment and loads the lithosphere resulting in subsidence and further loading. It is this effect of compaction that the algorithms in section 5.4.3 take into account. In addition to the effect of compaction upon basin evolution, the effect of compaction on stratigraphy over time is examined by measuring the development of the thickness of each stratigraphic unit over time. The effect of varying the bulk sediment density upon compaction is examined. Further, changes in porosity of the deposits, affected by the surface porosity and the co-efficient of compaction using the Sclater and Christie (1980) model are observed.

Figure C5.58 illustrates the development of the basin and stratigraphy over time including compaction with a bulk sediment density, $\rho_s$, of 2500 $kgm^{-3}$. At time, t = 0 Ma after rifting (Figure C5.58a), the basin is the same as that produced by the basin model without compaction, as the compaction has not yet occurred. As time since extension increases, the basin depth increases when compared to the model with no compaction (Figure C5.58). The maximum thickness of the stratigraphy deposited at t = 0 Ma after rifting, decreases from 6.40 km to 5.64 km over 100Ma. Unlike in the non-compacted model, in which the subsequent deposits are

thickest in the centre of the basin where thermal subsidence dominates the generation of accommodation space, in the compacted model, the subsequent deposits are thickest where the basin is deepest and the maximum amount of compaction takes place.

The amount of compaction decreases over time. This is a result of a combination of the exponential nature of the relationship between porosity and depth and a decrease in the rate of thermal subsidence over time. As a result of the relationship between porosity and depth, Figure 5.12, the rate of decrease in porosity with increasing depth is reduced as the depth of burial of the sediments increases. Additionally, as the rate of thermal subsidence decreases, the rate at which the sediments are buried decreases over time.

The additional loading of the basin generates subsidence of the footwall uplift such that between t = 25 Ma and t = 50 Ma after rifting (Figures C5.58c-d), it is subsided beneath the sea level datum and then forms part of the basin with the stratigraphy deposited between t = 25 Ma and t = 50 Ma after rifting onlapping the sediments that were deposited in the small basin generated by flexure in the footwall in front of the uplift.

### *5.7.1 The effect of sediment density upon the effect of compaction*

Figure C5.59 illustrates the effect of increasing the bulk sediment density, $\rho_s$, upon basin and stratigraphical development with compaction, whilst keeping all other parameters the same. The basin profiles at t = 0 Ma after rifting, Figure C5.59a, are the same as the basin profiles with varying

sediment density at time, t = 0 Ma after rifting with no compaction, Figure C5.50a. It was demonstrated in section C5.5 that increasing the sediment density increases the basin depth across the entire basin and reduces footwall uplift. The effect of increasing the sediment density upon basin development with compaction at time, t = 100 Ma after extension is illustrated in Figure C5.59b. Compacting the sediment deepens the basin and eliminates the footwall uplift when compared to the effect of increasing sediment density without compaction (Figure C5.59b).

At x = 30 km and t = 100 Ma after extension, Figure C5.59c, the basement remains uplifted above the sea level datum at values of $\rho_s$ less than 2375 $kgm^{-3}$, after which the footwall subsides beneath the sea level datum to form part of the basin. The rate of decrease in preserved footwall uplift at t = 100 Ma after extension increases with increasing sediment density. This variation is due to the fact that once the footwall subsides beneath the sea level datum, it is loaded with sediment which in turn generates additional subsidence.

At x = 40 km, Figure C5.59d, the rate of increase in basin depth increases with increasing sediment density. With increasing sediment density, the load resulting from infilling the accommodation space generated by thermal subsidence is greater, in turn generating additional subsidence. This increases the burial depth of the sediments producing greater amounts of compaction and therefore accommodation space, which, in turn, is loaded with the denser sediment resulting in greater subsidence to isostatically compensate for the load.

In a more distal position within the basin, x = 75 km (Figure C5.59e), the effect of increasing the sediment density upon the increasing basin depth is greater than in the distal positions within the basin. Table C5.1 summarises the effect of increasing sediment density upon the depth of the basin at t = 100 Ma.

| | Variation in basement depth per 1 kgm$^{-3}$ increase in $\rho_s$ | |
|---|---|---|
| x | $\rho_s$ 1750-2250 kgm$^{-3}$ | $\rho_s$ 2250-2750 kgm$^{-3}$ |
| 30 km | -0.0013 km | -0.0052 km |
| 40 km | +0.03 km | +0.01 km |
| 75 km | +0.0018 km | +0.0087 km |

Table C5.1. A summary of the effect of increasing sediment density upon basement depth at t = 100 Ma after extension.

Figure C5.59f illustrates the effect of increasing sediment density upon the thickness over time since extension of the stratigraphic sequence deposited at t = 0Ma after extension. The change in thickness of this layer has been tracked at x = 40 km where the deposit is thickest. As time since extension increases, the thickness of the sequence decreases. The rate of decrease in thickness is greater with increasing sediment density. The rate of decrease in thickness is greatest between 0 and 25 Ma after extension. Table C5.2 summarises the effect of increasing sediment density upon the thickness of the stratigraphy over time.

| $\rho_s$ | Rate of decrease in thickness of unit 1 | | |
|---|---|---|---|
| | t = 0 to t = 25 Ma | t = 25 to t = 100 Ma | decrease in rate |
| 1750 kgm$^{-3}$ | +0.068 kmMa$^{-1}$ | +0.002 kmMa$^{-1}$ | 0.066 kmMa$^{-1}$ |
| 2250 kgm$^{-3}$ | +0.012 kmMa$^{-1}$ | + 0.0033 kmMa$^{-1}$ | 0.0087 kmMa$^{-1}$ |
| 2750 kgm$^{-3}$ | +0.028 kmMa$^{-1}$ | +0.0064 kmMa$^{-1}$ | 0.0216 kmMa$^{-1}$ |

Table C5.2. A summary of the effect of increasing sediment density upon the thickness of sediment unit 1 over time

The thickness of sediment decreases at a greater rate when sediment density is higher because it is buried deeper and therefore compacted more. The rate of compaction of the sediment decreases by a greater amount over time because as the depth of burial increases, the decease in porosity with additional burial is reduced.

### *5.7.2 The effect of varying porosity with depth upon compaction*

As shown in section 5.4.3.1 the relationship between porosity and depth is determined by the surface porosity, $\phi_s$, and the compaction co-efficient, *c*. Figure C5.60 illustrates the effect of varying the surface porosity and the compaction co-efficient on basin development. Figure C5.60ai presents basin profiles at t = 100 Ma after extension with varying surface porosity. With increasing surface porosity, the basin deepens across the whole basin, with the increase in basin depth greater in the proximal and central areas of the basin. In addition, with increasing surface porosity, the rate of decrease in porosity with depth increases, and, as a result, when the sediment is buried to the same depth, greater compaction occurs,

generating more accommodation space that is loaded and isostatically compensated for.

At t = 100Ma the footwall has been subsided beneath the sea level datum. The amount of subsidence increases with increasing surface porosity. At x = 30 km, Figure C5.60aii, the increase in subsidence with increasing surface porosity gets greater as time since extension increases. At t = 0 Ma after extension, there is no change in the footwall with increasing surface porosity as compaction has not yet occurred. At t = 25 Ma after extension, there is an increase in the depth of the footwall of 0.016 km per 1% increase in $\phi_s$. At t = 100 Ma after extension, there is an increase in the depth of the footwall of 0.027 km per 1% increase in $\phi_s$.

At x = 40 km, Figure C5.60aiii, there is an increase in basin depth with increasing surface porosity. At t = 100 Ma after extension, there is an increase in basin depth of 0.054 km per 1% increase in $\phi_s$. In a more distal position, x = 75 km (Figure C5.60aiv), there is an increase in basin 0.038 km per 1% increase in $\phi_s$ at t = 100 Ma.

Figure C5.60bi presents profiles of the basin at t = 100 Ma after extension with varying compaction co-efficient. With increasing compaction co-efficient, the basin deepens across the whole basin and the footwall subsides beneath the sea level datum. As the compaction co-efficient increases, the rate of decrease in porosity with depth increases at depths less than 5 km. At depths greater than 5 km, the rate of decrease in porosity with depth decreases with increasing compaction co-efficient.

Figure C5.60bii shows the effect of varying the compaction co-efficient on the footwall at x = 30 km over time. As time since extension increases, the depth of the footwall increases. At x = 40 km, presented in Figure C5.60biii, the maximum basin depth increases with increasing compaction co-efficient. At x = 75 km, in a more distal position within the basin, (Figure C5.60biv), there is an increase in basin depth of 0.012 km per 0.1 increase in *c* at t = 25 Ma after extension. This increases by 0.01 km to 0.022 km per 0.1 increase in *c* at t = 100 Ma after extension. This increase in basin depth between 25 and 100Ma after extension per 0.1 increase in *c* is similar to that at x = 40 km. The effect of increasing the compaction co-efficient on basin depth is summarised in Table C5.3.

| | Variation in basement depth per 0.1 increase in compaction-coeficient | |
|---|---|---|
| x | t = 0 to t = 25 Ma | t = 25 to t = 100 Ma |
| 30 km | +0.0011 km | +0.0018 km |
| 40 km | +0.022 km | +0.034 km |
| 75 km | +0.0012 km | +0.0022 km |

Table C5.3. A summary of the effect of increasing compaction co-efficient upon basement depth over time.

This is a result of the reduced rate of decrease in porosity with depth at depths greater than 5 km with increasing compaction co-efficient, reducing the overall effect of the compaction co-efficient at x = 40 km where the sediment within the basin are buried deeper than 5 km.

## 5.8 The effect of subaerial erosion on basin evolution

In order to study the effect of erosion on basin evolution, a model was developed as described in Figure 5.6, with the addition of a percentage erosion parameter. The parameters within the model are fixed except when their effects are under investigation. The effects of varying the percentage of erosion and the effect of varying mantle, crustal and sediment density parameters on the effect of erosion are considered.

### *5.8.1 The effect of percentage erosion on basin evolution*

Figure C5.61 illustrates the model at t = 0 Ma after extension following 0, 50 and 100% erosion. With increasing percentage of erosion, the amount of footwall uplift is reduced. At 50% erosion, the maximum footwall uplift at x = 30 km is reduced from 0.57 km to 0.29 km, which is 50% of the original maximum footwall uplift without erosion.

Figure C5.62 displays the effect of increasing the percentage of erosion upon the development of the basin across the model. Figure 7.37a shows the profile of the basin at t = 0 Ma after extension, where the greatest effect of increasing the percentage of erosion can be seen to be in the footwall of the fault. Subsidence in front of the footwall uplift, at x = 15 km, decreases with increasing percentage of erosion when the percentage of erosion is less than 60%. This is a result of isostatic uplift following production of a negative load, generated by erosion. The amount of subsidence decreases by 0.021 km for every 10% increase in erosion. At percentages of erosion greater than 60%, the decrease in subsidence is

reduced to 0.001 km per 10% increase in erosion. This is due to the fact that the basement has been uplifted to the extent that it has been raised above the sea level datum and is therefore subject to erosion (Figure C5.62c). The amount of footwall uplift has a linear relationship with erosion and decreases by 0.056 km for every 10% increase in erosion (Figure C5.62d). Within the basin, the effect of increasing erosion is greatest in a proximal position. At x = 40 km, where the maximum basin depth is achieved, there is a decrease in basin depth of 0.02 km for every 10% increase in erosion (Figure C5.62e). In a more distal position within the basin, x = 75 km, the amount of erosion has little effect on the basin depth. This is due to the distance from the erosion of the footwall uplift and uplifted basin, which are much greater than the flexural wavelength (Figure C5.62f).

Figure C5.62b illustrates the basin profile at t = 100 Ma after extension with increasing percentage of erosion. Erosion takes place during the t = 0 Ma after rifting time step. As such, its effect is only active during this time step. The basin then continues to develop in the same manner regardless of the percentage of erosion. The differences in basin and footwall geometry at t = 100 Ma after extension are the same as the differences in the geometry at t = 0 Ma after extension.

### *5.8.2 The effect of mantle density on erosion*

Figure C5.63 illustrates the effect of increasing the mantle density, $\rho_m$, upon the basin development with varying percentage of erosion.

Figure C5.63a shows the profile of the basin at t = 0 Ma after extension with 100% erosion, leading to complete removal of any footwall uplift. The basin depth increases with increasing mantle density with the greatest increase in the distal position within the basin where there is an increase of 0.0035 km per 1 $kgm^{-3}$ increase in mantle density. Figure C5.63b presents the profile of the basin at t = 100 Ma after extension with 100% erosion. Due to the subsidence that has occurred within the model after 100 Ma, the eroded footwall uplift now forms part of the basin. The increase in basin depth over time is greatest in the centre of the basin, where the effect of thermal subsidence is dominant. Increased mantle density generates less thermal subsidence, reducing the overall effect of varying the mantle density on basin development at times greater than 0 Ma after extension.

Figures C5.63c-e show the effect of varying the density of the mantle upon the effect of erosion on basin development at time, t = 0 Ma after extension. Figure C5.63c illustrates the effect on the maximum footwall uplift at x = 30 km. With increasing mantle density, the effect of erosion is reduced. When mantle density is 3200 $kgm^{-3}$, there is a decrease in footwall uplift of 0.065 km per 10% increase in erosion. When mantle density is 3400 $kgm^{-3}$, this is reduced to 0.049 km per 10% increase in erosion. Figure C5.63d illustrates the effect of varying the mantle density upon the effect of erosion at x = 40 km, where the basin is deepest. Due to its proximity to the erosion, increasing the mantle density reduces the effect of erosion. Greater amounts of uplift are required to restore isostatic

equilibrium at lower values of mantle density. There is a decrease in basin depth of 0.026 km per 10% increase in erosion at a mantle density of 3200 $kgm^{-3}$. This is reduced to 0.015 km when mantle density is 3400 $kgm^{-3}$. At a more distal position within the basin, x = 75 km, illustrated by Figure C5.63e, the basin deepens with increasing mantle density. However, it is not affected by varying the percentage of erosion due to its distance from the position of the eroded uplift.

### *5.8.3 The effect of crustal density on erosion*

Figure C5.64 illustrates the effect of increasing the crustal density, $\rho_c$, upon the basin development with varying percentage of erosion. Figure C5.64a presents the profile of the basin at t = 0 Ma after extension with 100% erosion such that footwall uplift has been removed by erosion. The basin depth decreases with increasing crustal density. Figure C5.64b shows the profile of the basin at t = 100 Ma after extension with 100% erosion. The footwall has subsidence to form part of the basin. The increase in subsidence is greatest in the centre of the basin, where the effect of thermal subsidence controls the generation of accommodation space. After the isostatic response to thinning of the crust and erosion of the crustal material at time, t = 0 Ma, the density of the crust does not influence the isostatic response and the relationship between crustal density and subsidence remains unchanged.

Figures C5.64c-e demonstrate the effect of varying the density of the crust upon the effect of erosion on basin evolution at time, t = 0 Ma after

extension. Figure C5.64c shows the effect on the maximum footwall uplift at x = 30 km. With increasing crustal density, the effect of erosion upon footwall uplift is increased. At a crustal density of 2700 $kgm^{-3}$, there is a decrease in footwall uplift of 0.035 km per 10% increase in erosion. This is increased to 0.082 km per 10% increase in erosion when crustal density is 2900 $kgm^{-3}$. This is because a greater amount of uplift of mantle material is required to isostatically compensate for the increased negative load associated with erosion when crustal density is increased. Figure C5.64d illustrates the effect on maximum basin depth, at x = 40 km, where increasing the crustal density increases the effect of erosion. The basin gets shallower with increasing erosion. This decrease in basin depth with increasing erosion increases from 0.011 km per 10% increase in erosion when crustal density is 2700 $kgm^{-3}$, to 0.033 km when crustal density is 2900 $kgm^{-3}$. Figure C5.64e illustrates the effect at a more distal position within the basin, x = 75 km. The basin gets shallower with increasing crustal density. The percentage of erosion has little effect in this position due to its distance from the erosion.

### *5.8.4 The effect of sediment density on erosion*

Figure C5.65 illustrates the effect of increasing the density of the basin infill, $\rho_i$, upon the basin development with varying percentage of erosion. Figure C7.4a shows the profile of the basin at t = 0 Ma after extension with varying sediment density and 100% erosion which has led to complete removal of the footwall uplift. The basin depth increases with increasing sediment density, due to the increased loading resulting in

increased subsidence. The increase in basin depth is greatest at x = 40 km, where the load is greatest. Figure C5.65b illustrates the profile of the basin at t = 100 Ma after extension with increasing sediment density and 100% erosion. The amount by which the footwall subsides to form part of the basin increases with increasing sediment density. The increase in subsidence is greatest in the centre of the basin, where thermal subsidence generates accommodation space that is subsequently loaded by sediment.

Figures C5.65c-e demonstrate the effect of varying the density of the basin infill upon the effect of erosion on basin evolution at time, t = 0 Ma after extension. Figure C5.65c illustrates the effect on the maximum footwall uplift at x = 30 km. Increasing the sediment density, decreases the effect of erosion. There is a decrease in footwall uplift of 0.127 km per 10% increase in erosion, when sediment density is 1750 $kgm^{-3}$. This is reduced to 0.014 km per 10% increase in erosion when sediment density is 2750 $kgm^{-3}$. This is due to sediment loading reducing the amount of basement uplifted above the sea level datum to be eroded. Figure C5.65d presents the effect of varying the sediment density upon the effect of erosion on maximum basin depth, at x = 40 km. Increasing the sediment density decreases the effect of erosion. There is a decrease in basin depth of 0.035 km per 10% increase in erosion when sediment density is 1750 $kgm^{-3}$. This is reduced to 0.002 km when sediment density is 2750 $kgm^{-3}$. Sediment loading reducing the amount of basement uplifted above the sea level datum to be eroded, as a result the negative load

associated with erosion is decreased and there is less isostatic uplift. Figure C5.65e shows the effect at $x = 75$ km, where the basin depth increases with increasing sediment density. Due to its distal position within the basin and therefore its distance from the erosion, varying the percentage of erosion has little effect in this position.

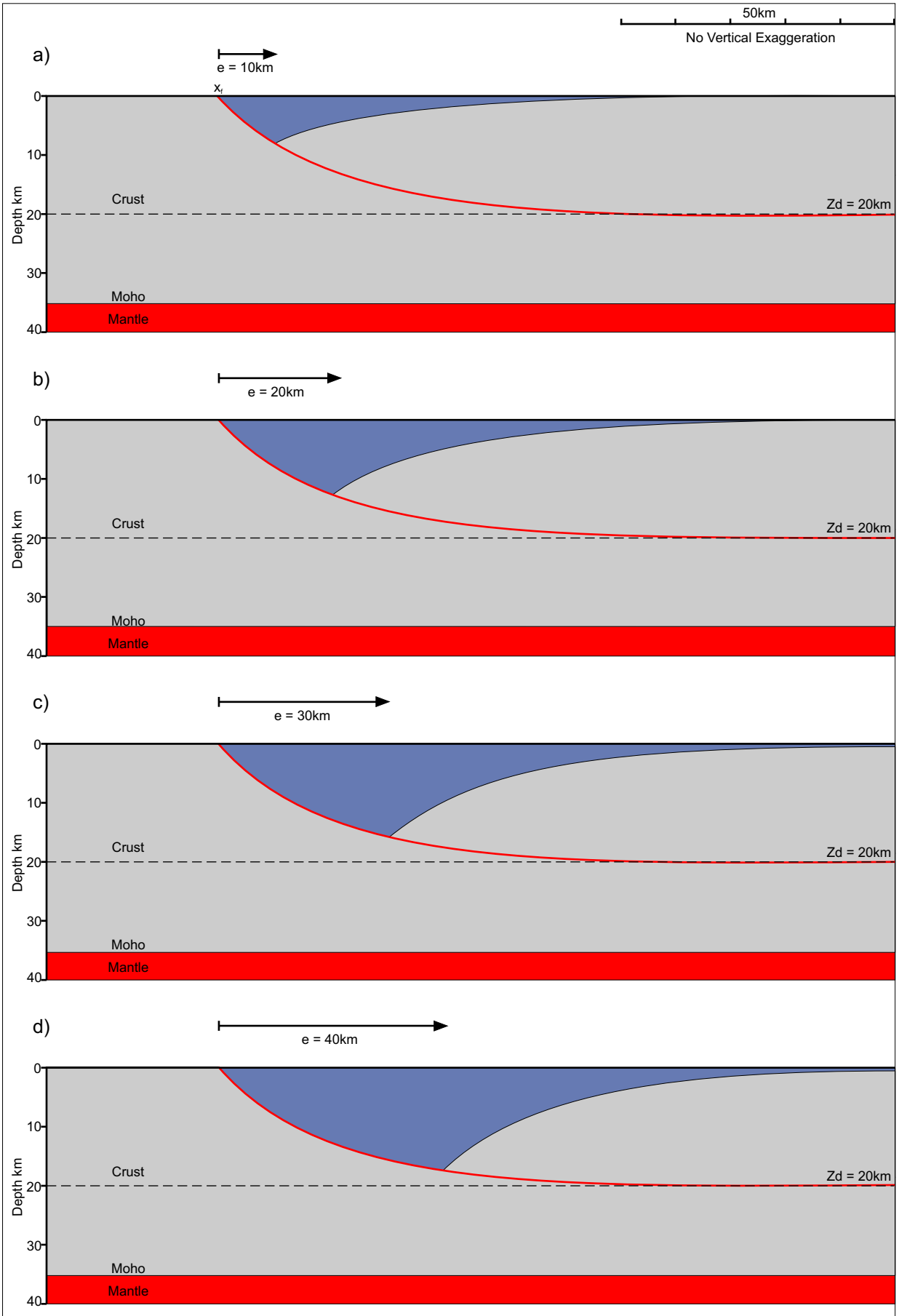


Figure C5.1 Models showing the effect of increasing the magnitude of extension. Increasing extension (e) results in a deepening and widening of the basin. The basin is deepest at $x = x_f + e$.

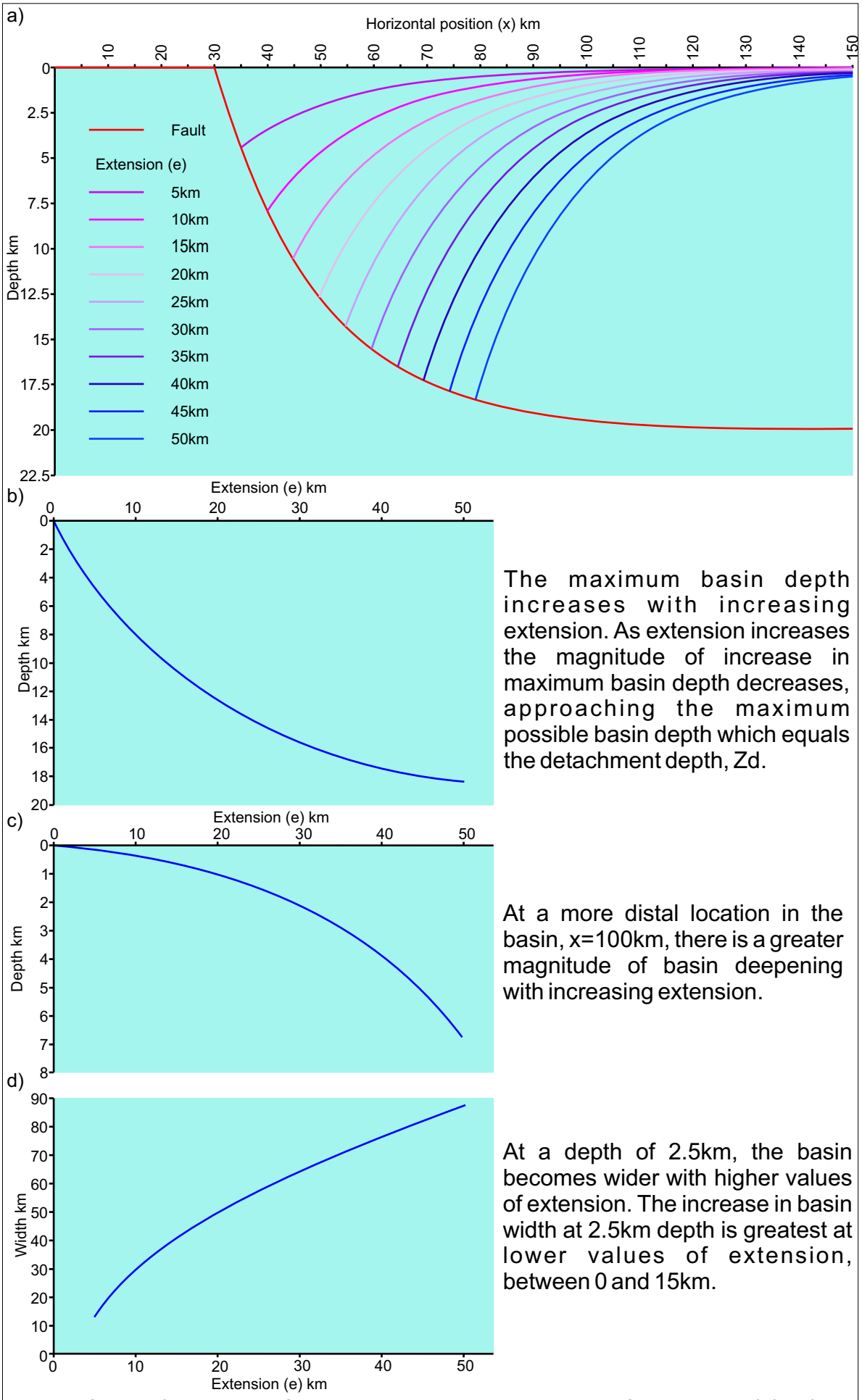


The maximum basin depth increases with increasing extension. As extension increases the magnitude of increase in maximum basin depth decreases, approaching the maximum possible basin depth which equals the detachment depth, Zd.

At a more distal location in the basin, x=100km, there is a greater magnitude of basin deepening with increasing extension.

At a depth of 2.5km, the basin becomes wider with higher values of extension. The increase in basin width at 2.5km depth is greatest at lower values of extension, between 0 and 15km.

Figure C5.2. a) Basin profile with increasing magnitude of extension (e). b)The maximum basin depth. c) Depth of the basin at x = 100km. d) Basin width at 2.5km depth.

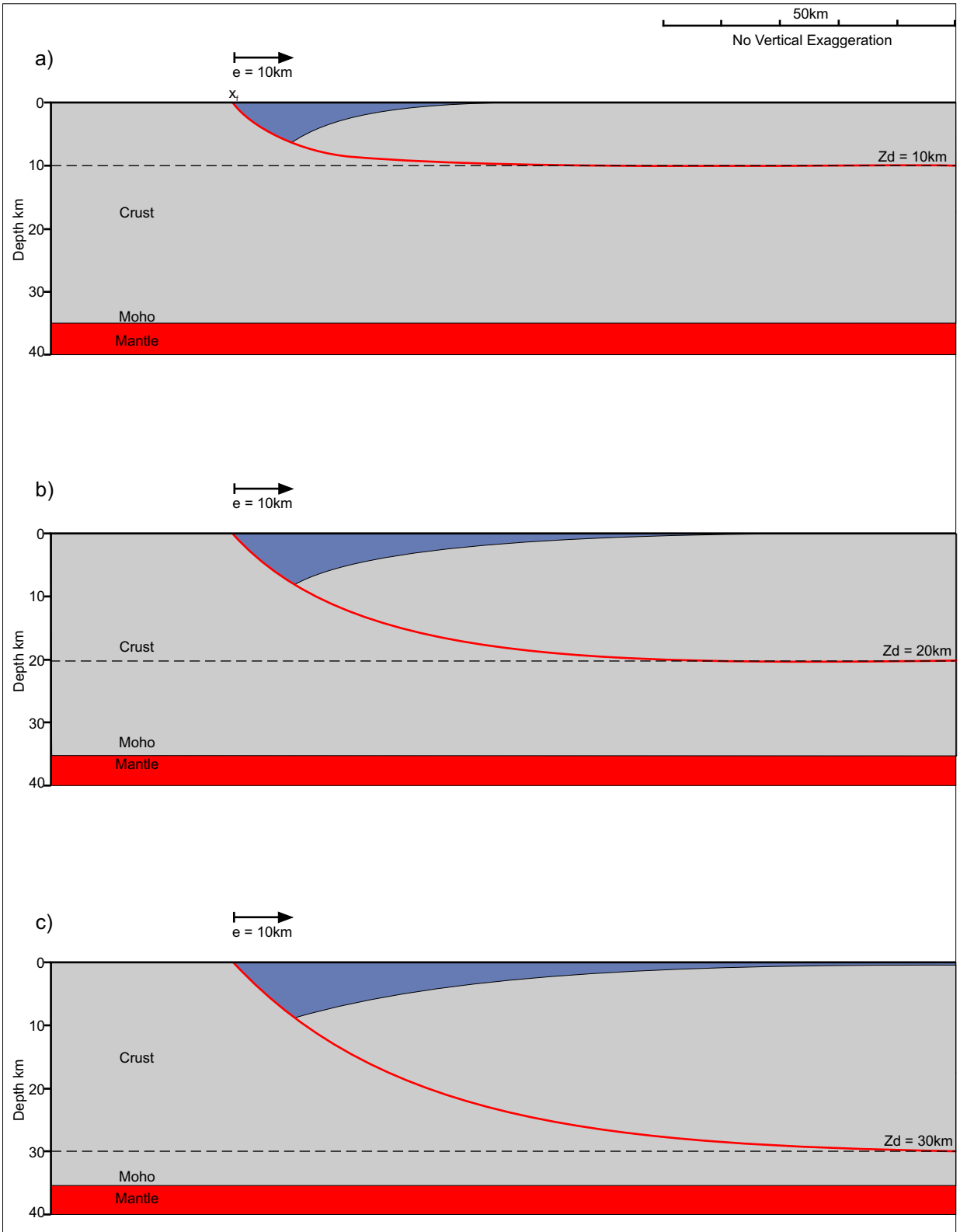


Figure C5.3. The effect of increasing the depth to detachment of the fault (Zd). Both the fault and hanging wall profiles are affected by increasing Zd. The resultant basin is deeper and wider as Zd is increased.

a)

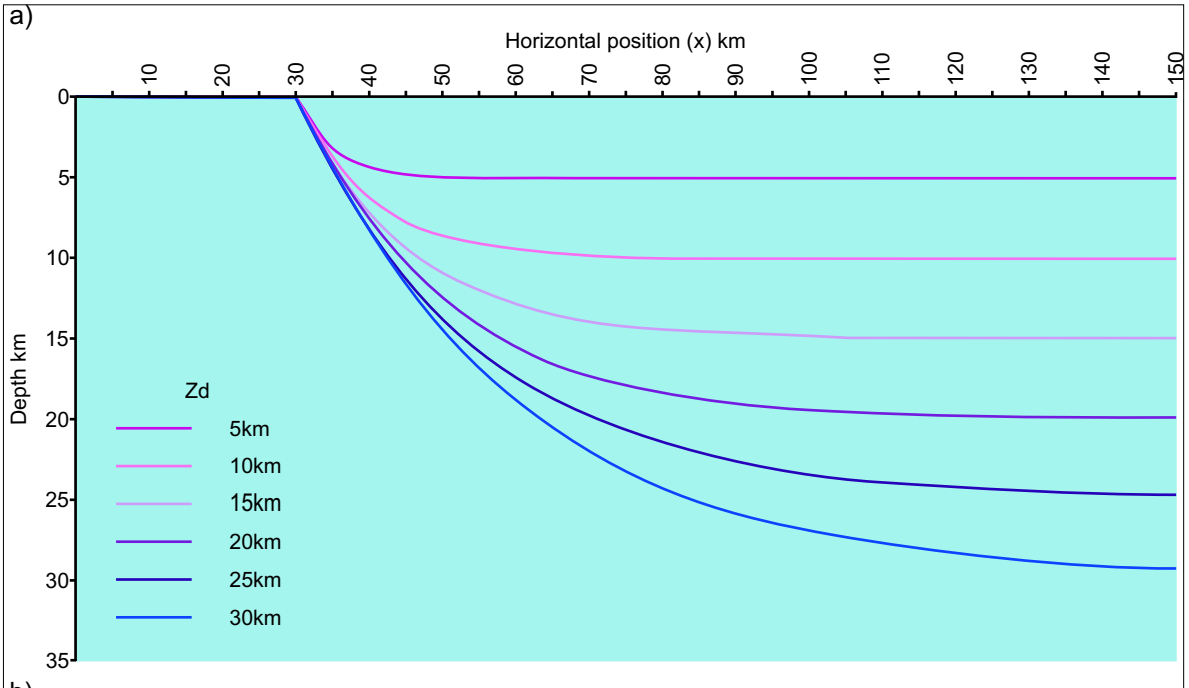


b)

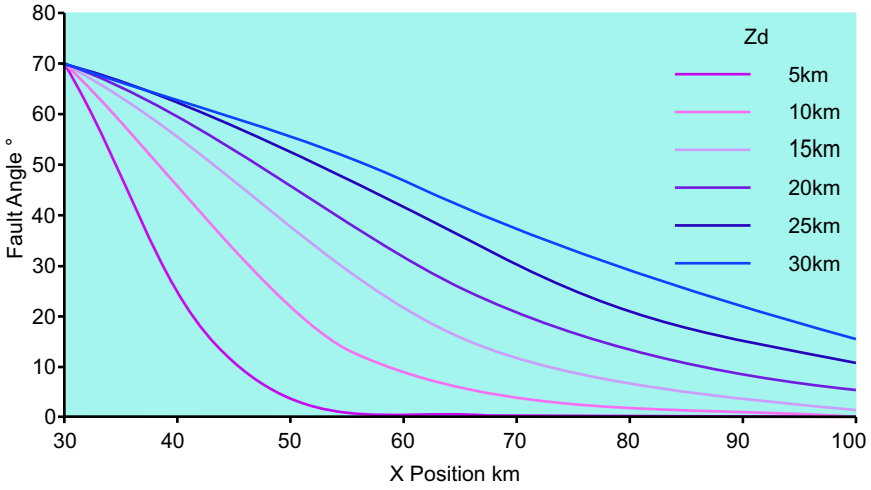


With increasing distance from the surface position of the fault, $x_f$, the fault angle decreases until it reaches 0° at the detachment.

c)

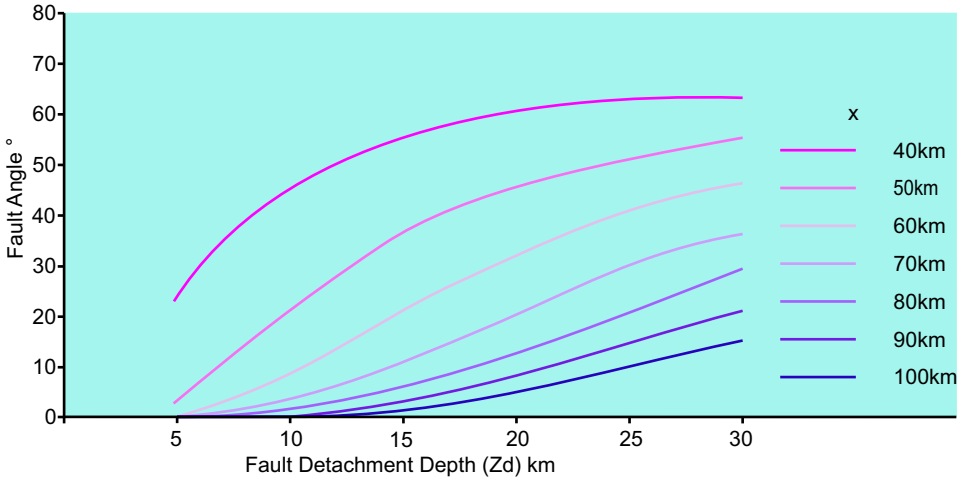


There is a steepening of the fault at any position of x with increasing Zd.

Figure C5.4. a) Profile of a listric fault with increasing detachment depth (Zd). b) The variation in fault angle across the profile between x = 30km ($x_f$) and x = 100km for varying detachment depths. c) The affect on fault angle with increasing Zd at various positions of x.

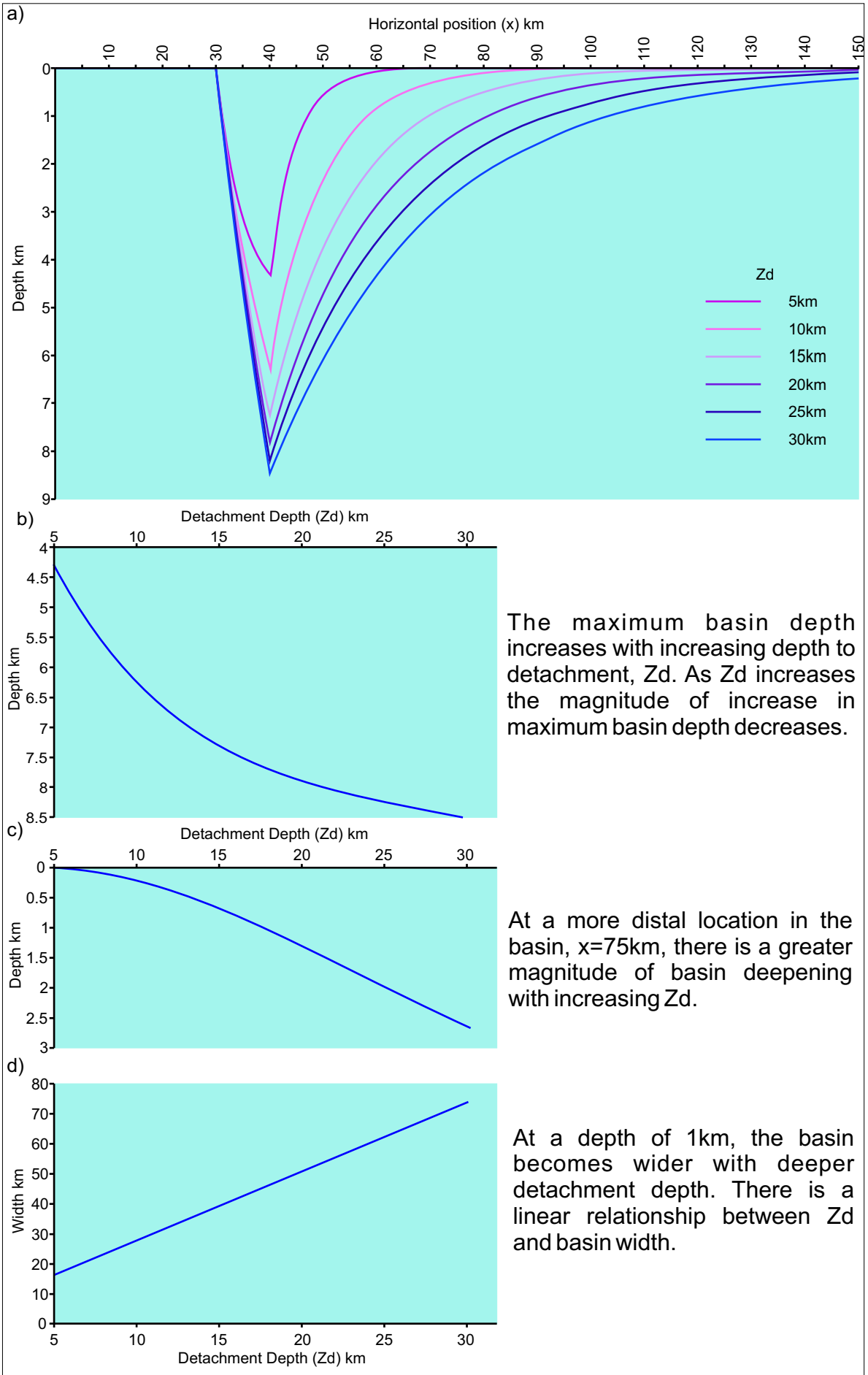


The maximum basin depth increases with increasing depth to detachment, Zd. As Zd increases the magnitude of increase in maximum basin depth decreases.

At a more distal location in the basin, x=75km, there is a greater magnitude of basin deepening with increasing Zd.

At a depth of 1km, the basin becomes wider with deeper detachment depth. There is a linear relationship between Zd and basin width.

Figure C5.5. a) Basin profile with increasing fault detachment depth (Zd). b) The maximum basin depth with increasing Zd. c) Depth of the basin at x = 75km. d) Basin width at 1km depth.

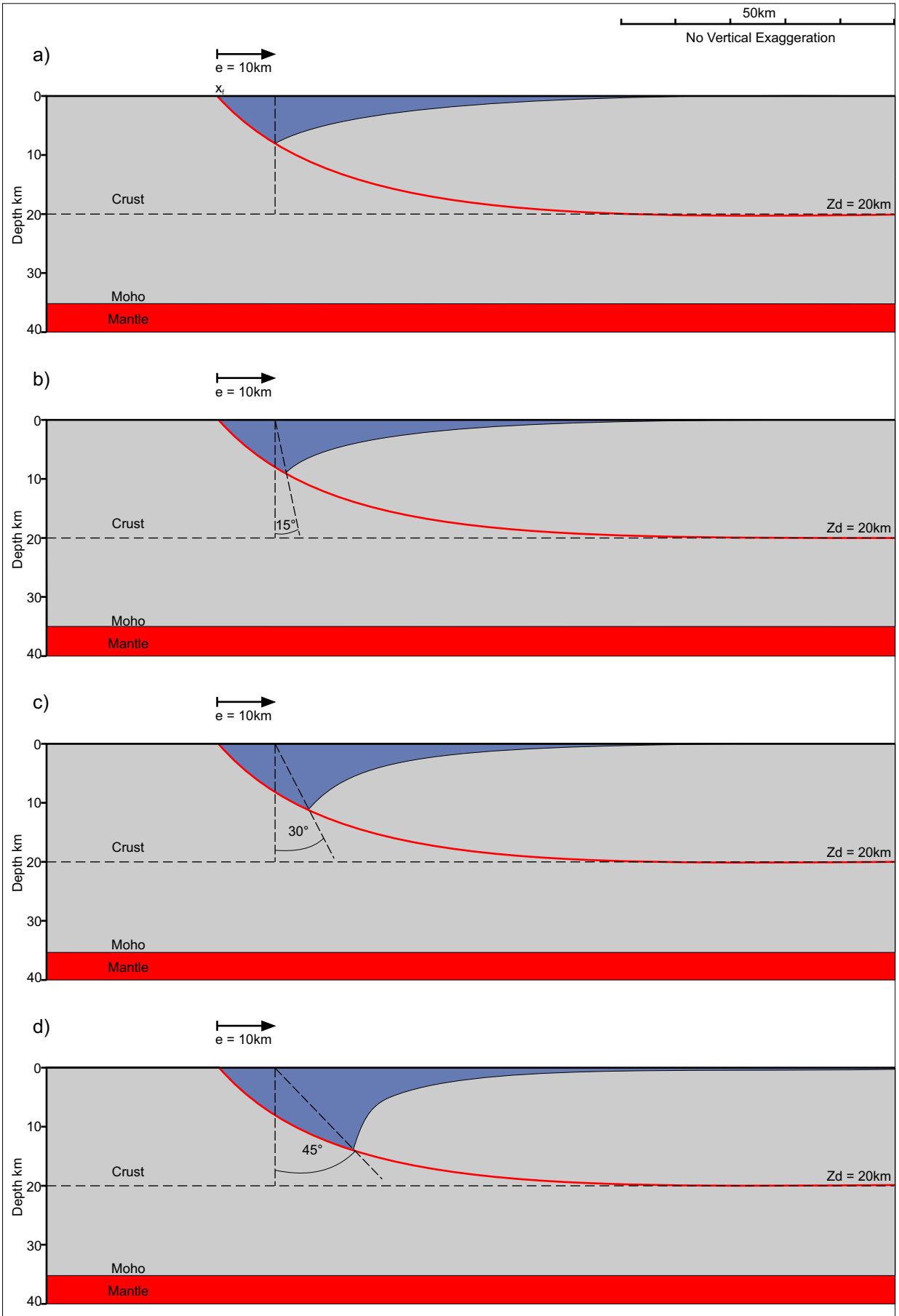


Figure C5.6. Models showing deformation of the hanging wall along inclined shear planes whose sense of shear is synthetic to the fault. Increasing the angle of shear, $\alpha_s$, deepens the basin. The 'apparent' heave, where the hanging wall cuts off against the footwall and where the basin is deepest, increases with increasing angle of shear.

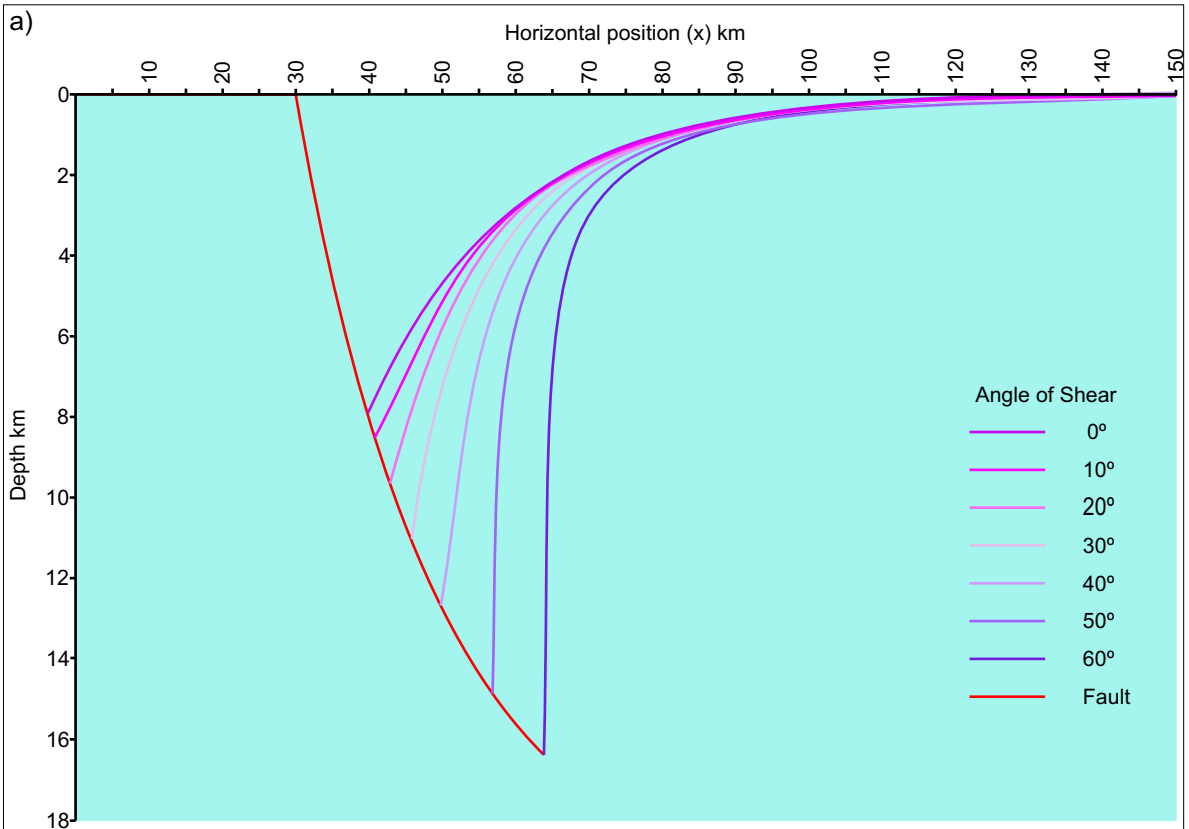


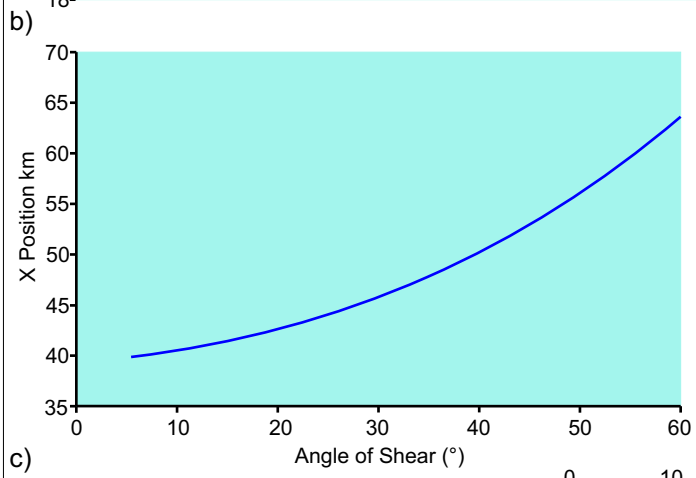


The position of the hanging wall cut-off against the fault increases with increasing values of $\alpha_s$. The magnitude by which this increases, is amplified with rising values of $\alpha_s$.

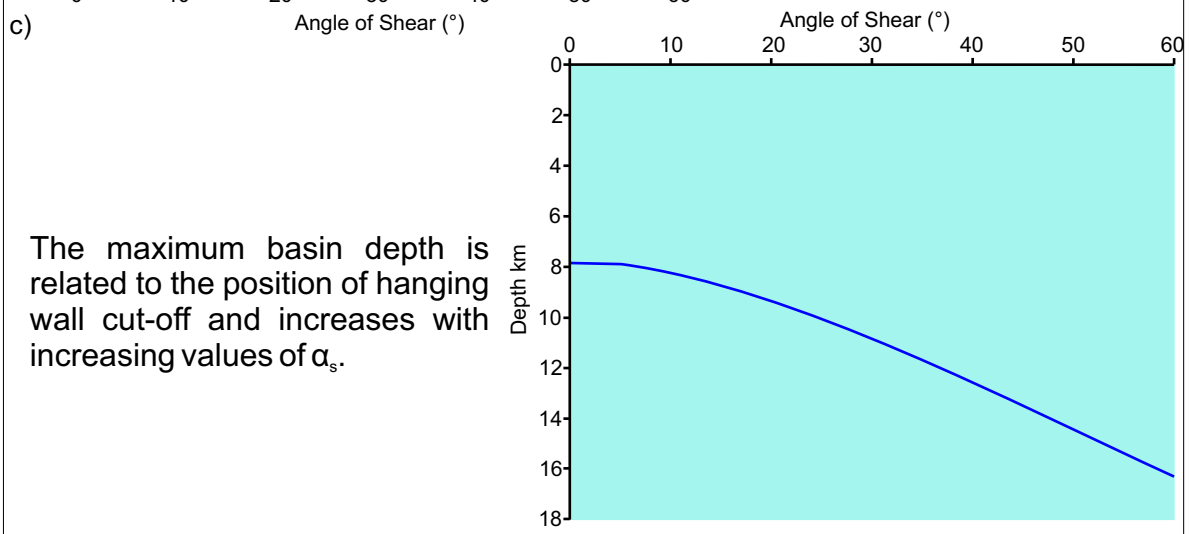


The maximum basin depth is related to the position of hanging wall cut-off and increases with increasing values of $\alpha_s$.

Figure C5.7. a) Deformation of the hanging wall along inclined shear planes whose sense of shear is synthetic to the fault. b) The position of the hanging wall cut-off against the fault with increasing synthetic shear. c) The maximum basin depth with increasing synthetic shear.

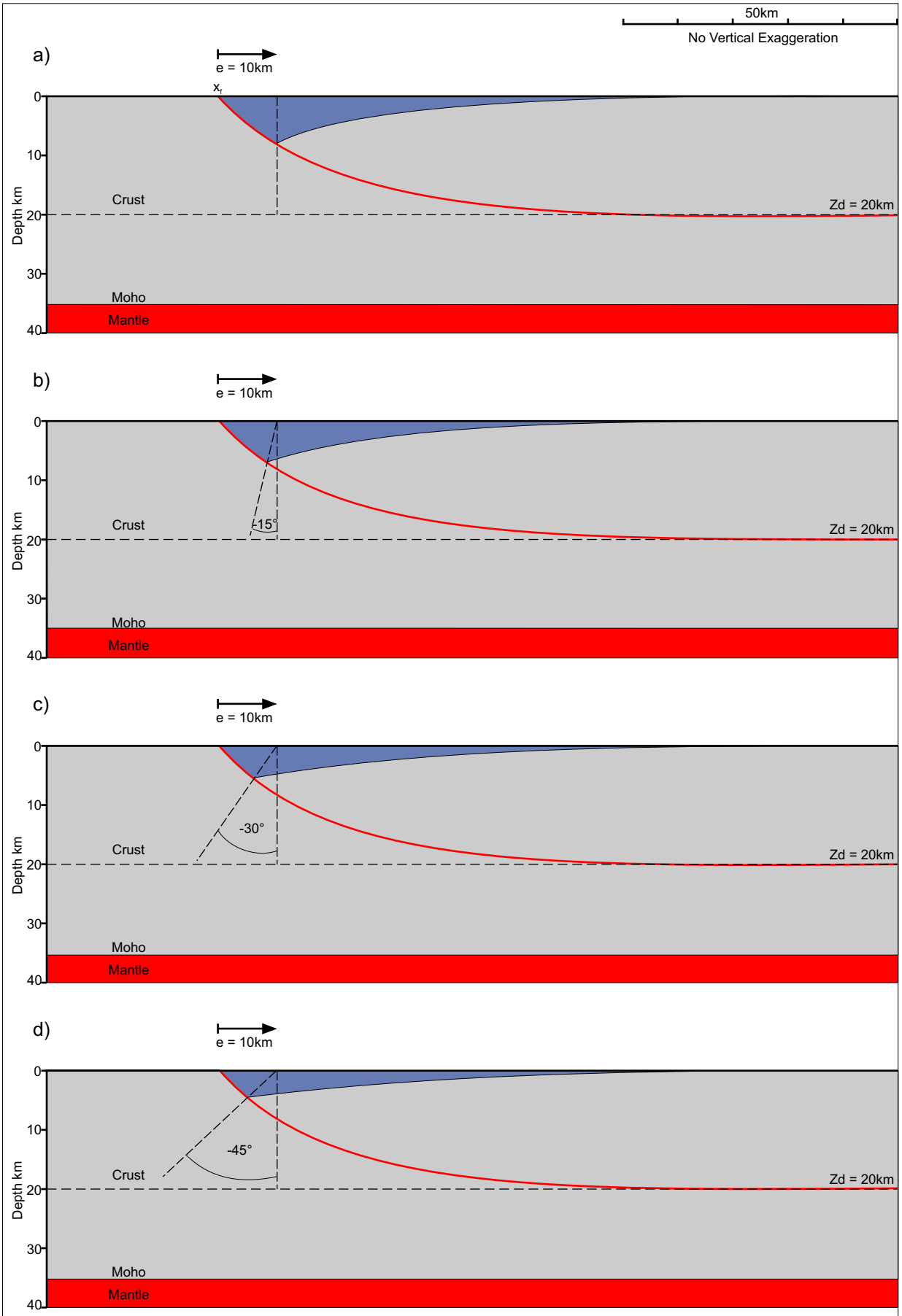


Figure C5.8. Models showing deformation of the hanging wall along inclined shear planes whose sense of shear is antithetic to the fault. Increasing the angle of shear, $\alpha_s$, causes the basin to shallow. The 'apparent' heave, where the hanging wall cuts off against the footwall and where the basin is deepest, decreases with increasing angle of shear.

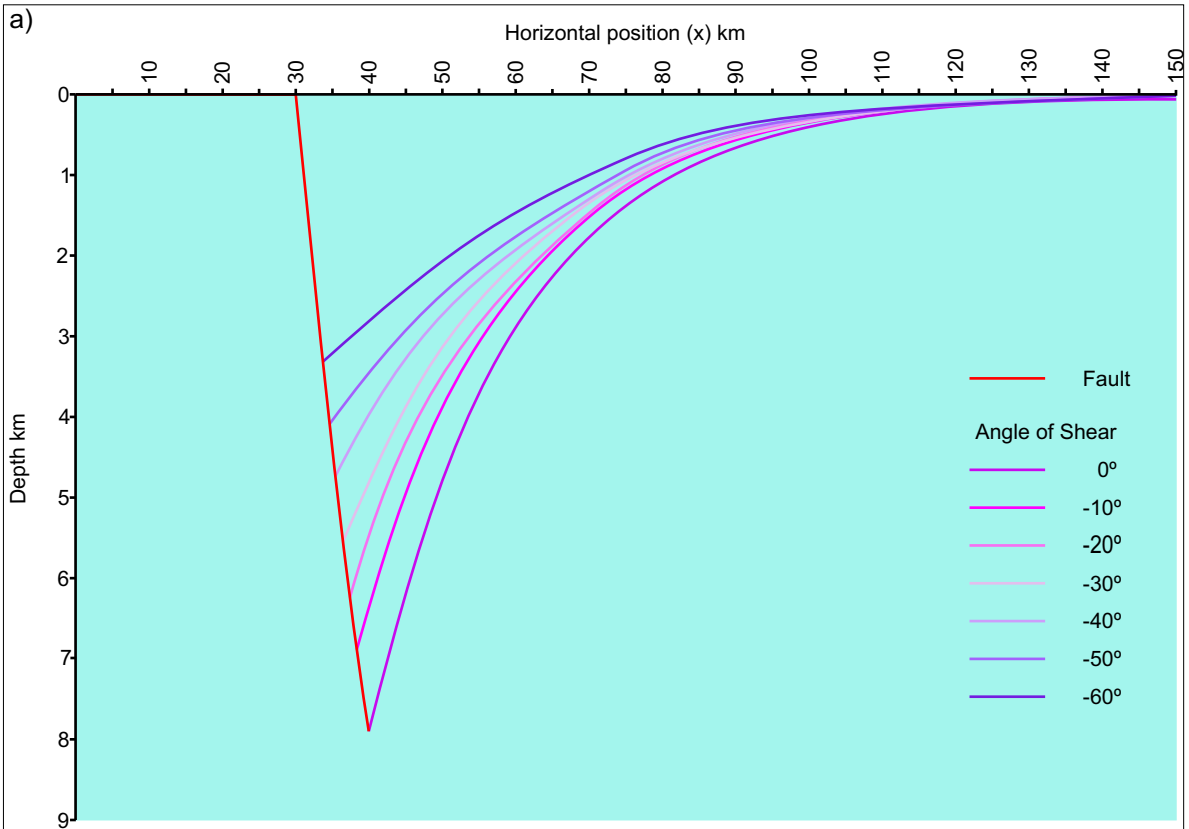


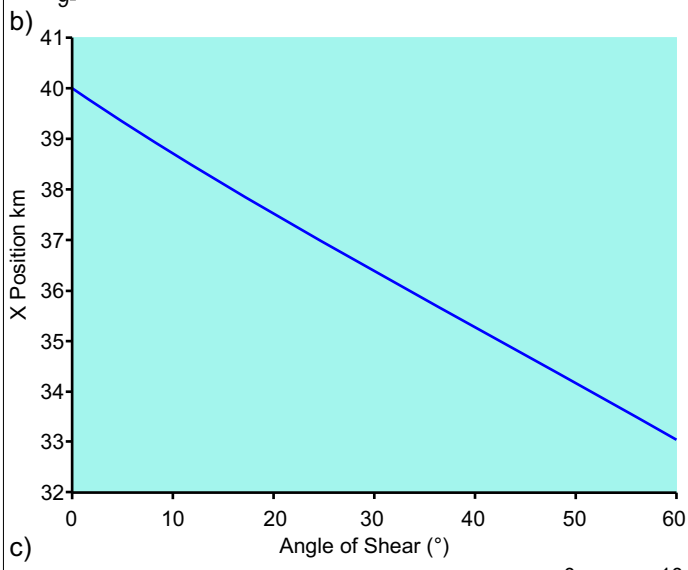


The position of the hanging wall cut-off against the fault decreases with increasing values of $\alpha_s$. The magnitude by which this decreases has a linear relationship with $\alpha_s$.

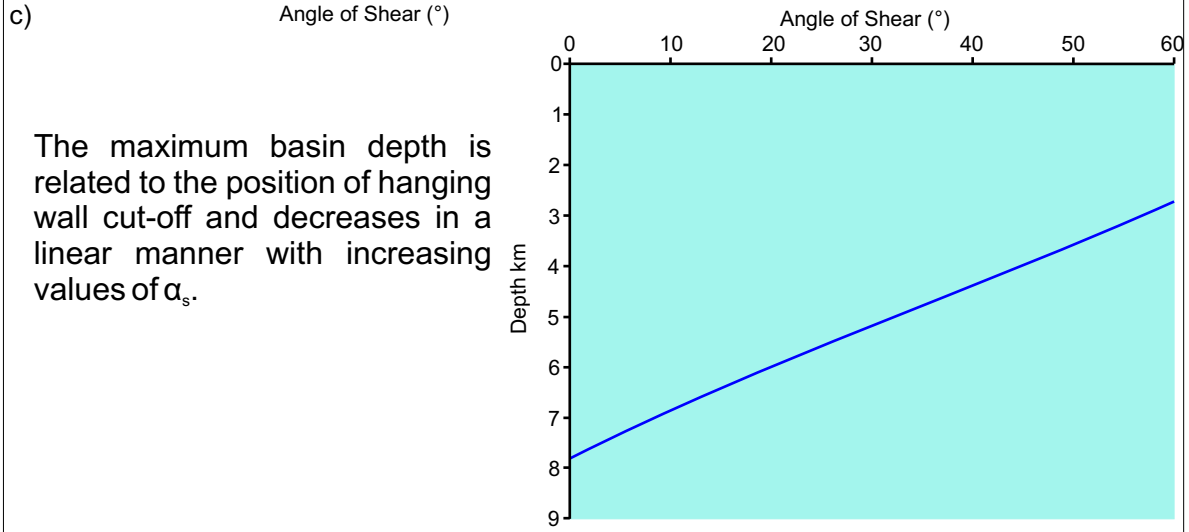


The maximum basin depth is related to the position of hanging wall cut-off and decreases in a linear manner with increasing values of $\alpha_s$.

Figure C5.9. a) Deformation of the hanging wall along inclined shear planes whose sense of shear is antithetic to the fault. b) The position of the hanging wall cut-off against the fault with increasing antithetic shear. c) The maximum basin depth with increasing antithetic shear.

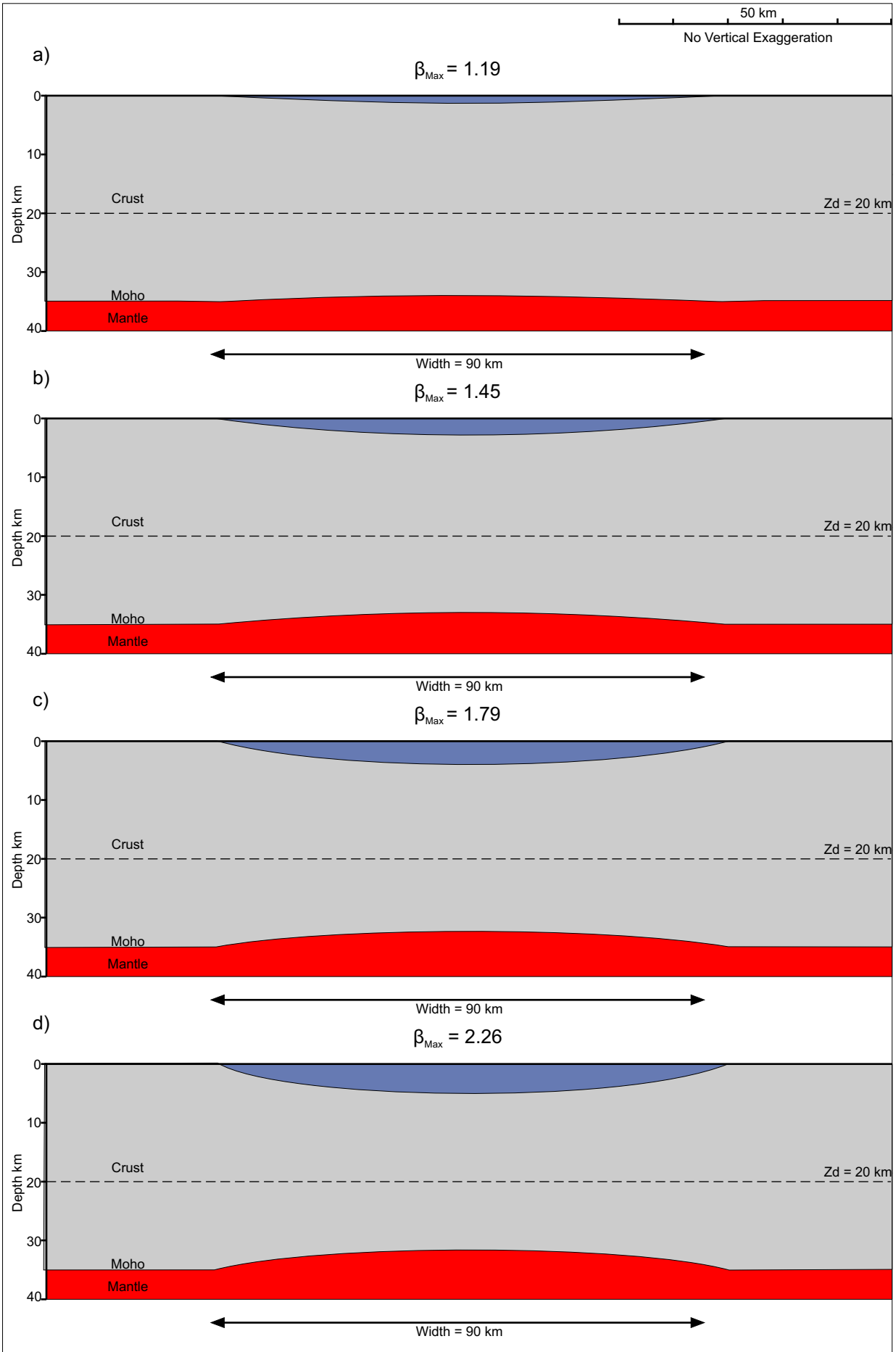


Figure C5.10. The effect of increasing the magnitude of pure shear deformation. An increase in $\beta_{Max}$ results in a deeper sag basin being developed. a) $\beta_{Max}$=1.19. b) $\beta_{Max}$=1.45. c) $\beta_{Max}$=1.79. d) $\beta_{Max}$=2.26.

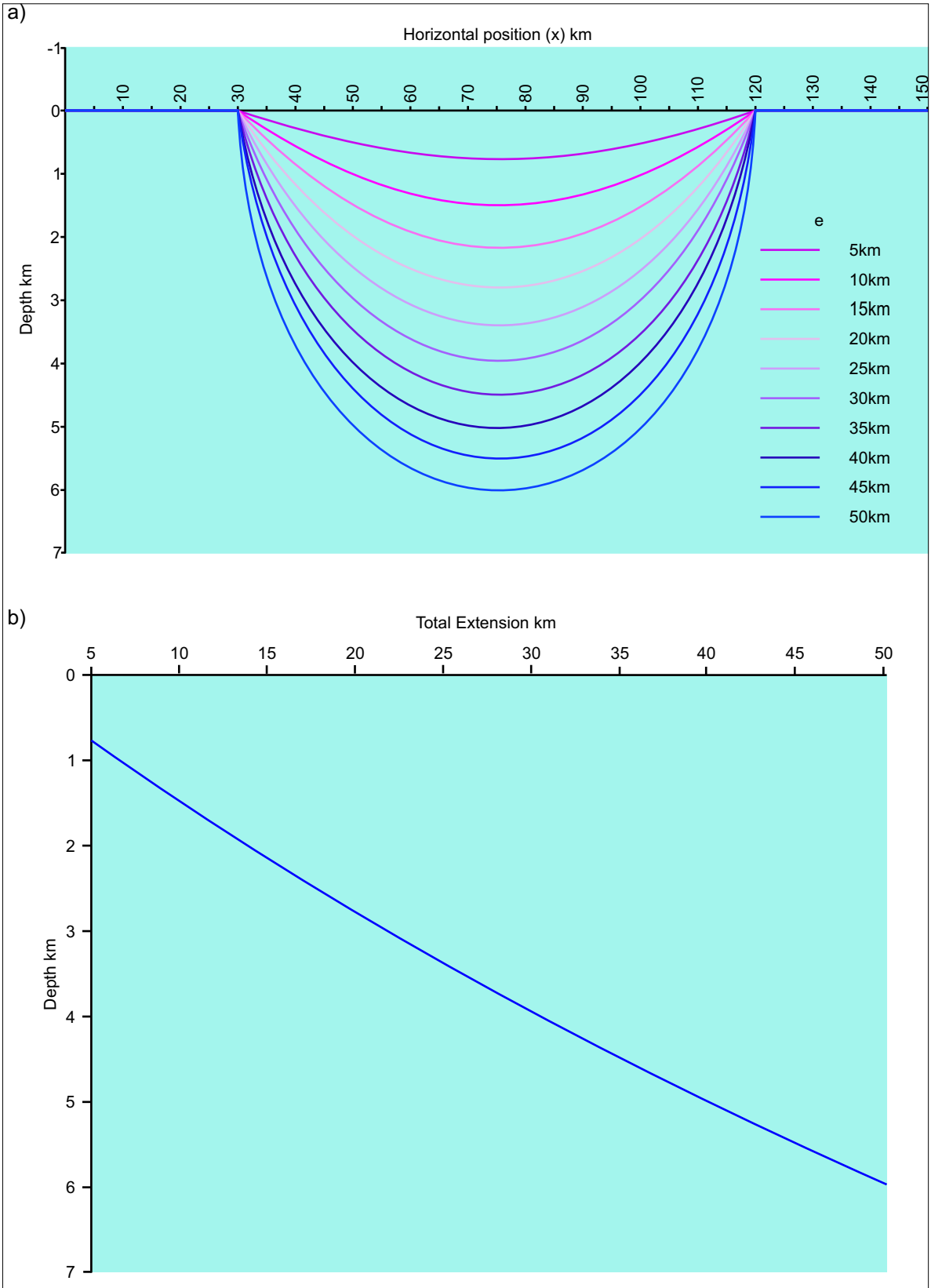


Figure C5.11. a) Basin depth due to pure shear across the profile with increasing total extension in the upper crust. b) The relationship between total horizontal extension and pure shear related subsidence at x=75 km. Increasing the magnitude of horizontal extension applied to the upper lithosphere deepens the sag basin produced by pure shear deformation. This deepening is greatest at the centre of the basin, x=75 km, where it has an average gradient of 0.116 or 116 m per 1 km increase in extension.

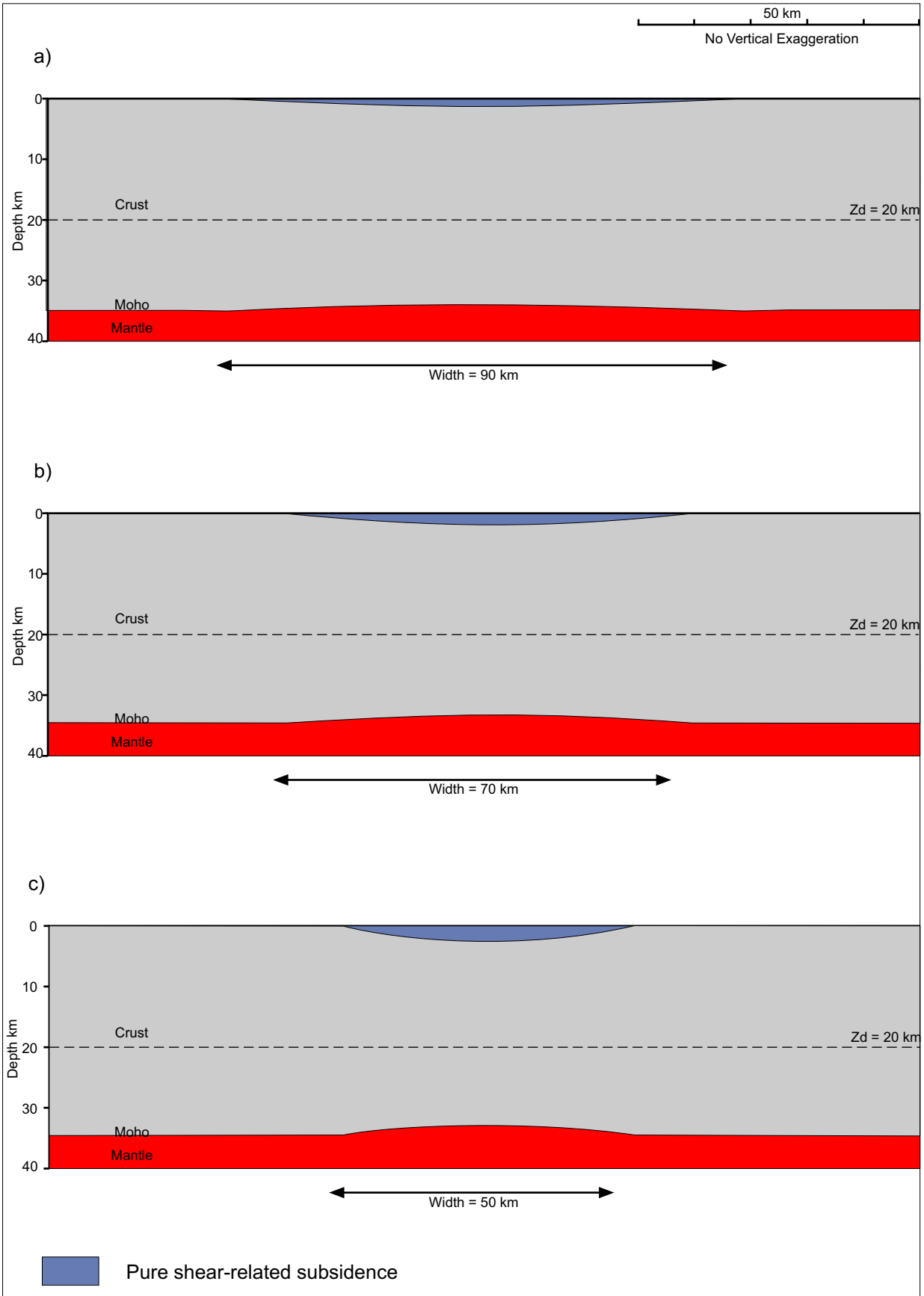


Figure C5.12. Effect of pure shear deformation with varying width of distribution. Decreasing the width over which extension, with a constant magnitude (e = 10km), takes place results in a narrowing and deepening of the pure shear related subsidence. a) Width of pure shear distribution = 90 km. b) Width of pure shear distribution = 70 km. c) Width of pure shear distribution = 50 km.

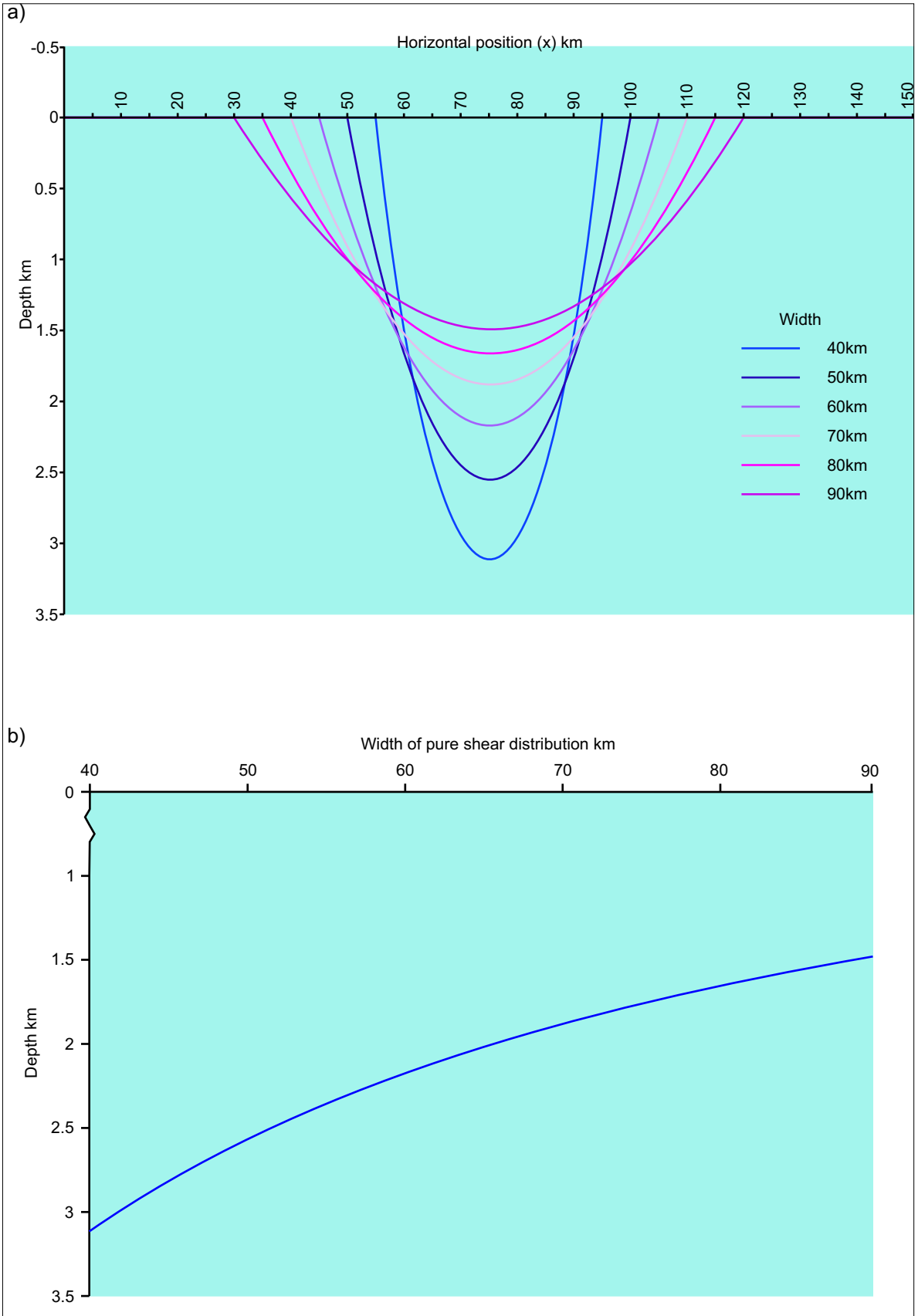


Figure C5.13. a) Basin depth across the profile with increasing width of pure shear distribution. b) The relationship between width of distribution and pure shear related subsidence at x=75 km. Increasing the width of distribution results in a shallower sag basin. The decrease in basin depth with increasing width of pure shear distribution has a gradient of 0.047km per 1km increase in width between widths of 40 and 60km this decreases to 0.023km between widths of 60 to 90 km.

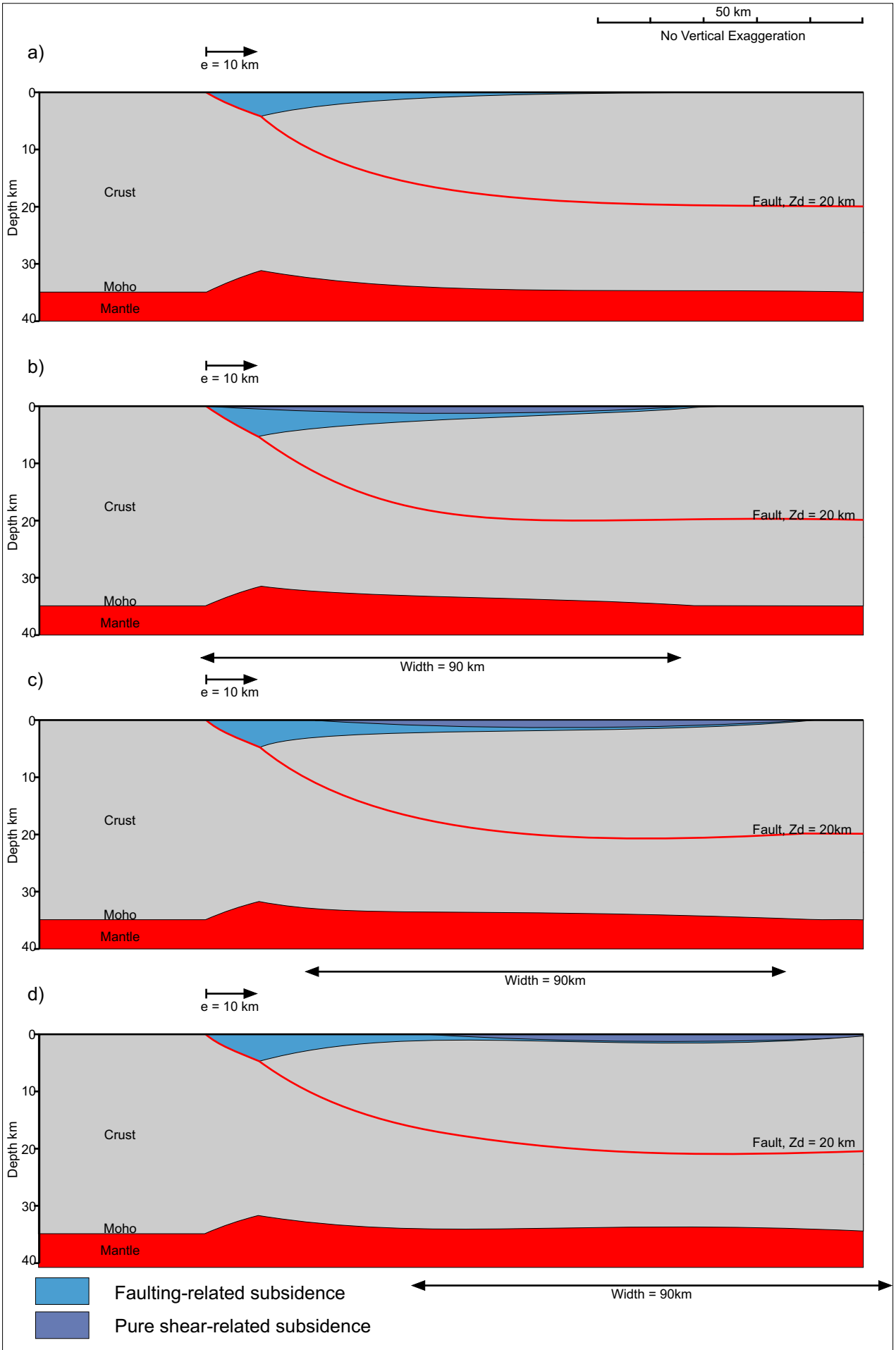


Figure C5.14. a) Isostatically compensated fault without the effect of pure shear. b, c and d) Isostatically compensated fault with pure shear of fixed width distribution but with its lateral position becoming increasingly distal in relation to the fault position. As extension by pure shear becomes more distal, the depth in the distal position of the basin increases.

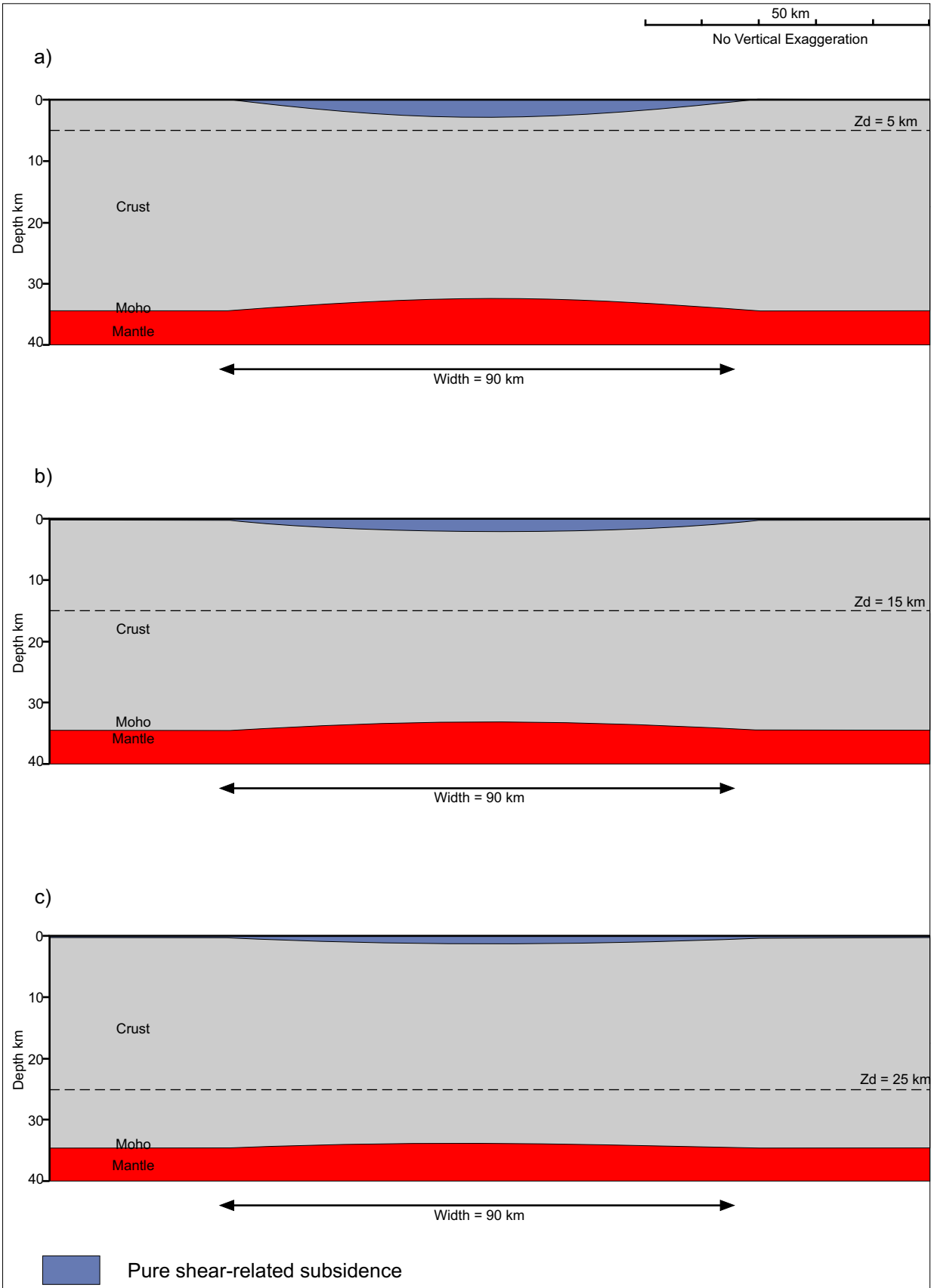


Figure C5.15. Effect of pure shear extension with varying depth to detachment. Increasing the depth to the detachment, reduces the thickness of lower crust extended by pure shear and results in a decrease in the amount of pure shear-related subsidence. a) Zd = 5 km. b) Zd = 15 km. c) Zd = 25 km.

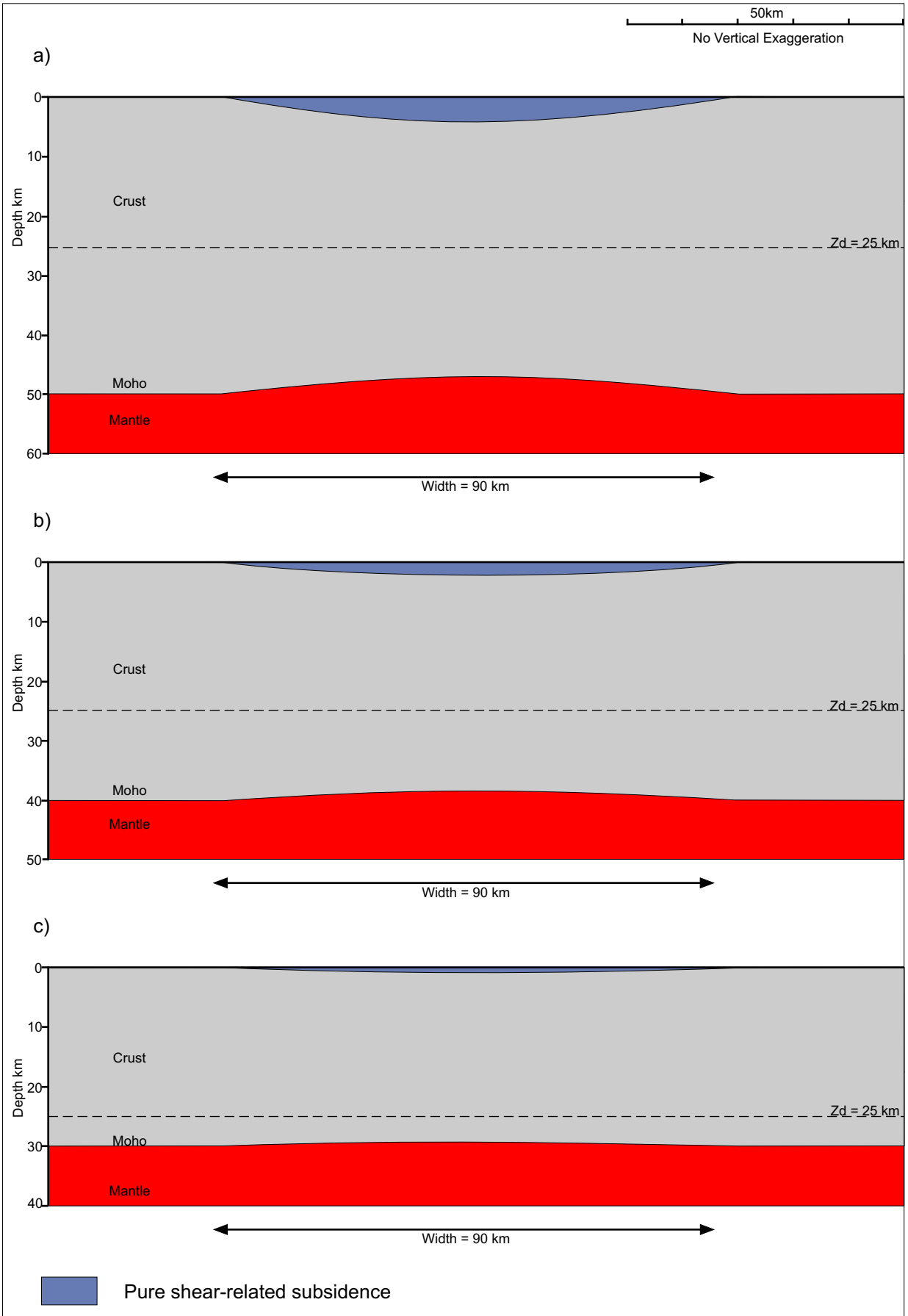


Figure C5.16. Effect of pure shear extension with varying original crustal thickness. Decreasing the original crustal thickness, reduces the thickness of lower crust extended by pure shear and results in a decrease in the amount of pure shear-related subsidence. a) $C_o = 50$ km. b) $C_o = 40$ km. c) $C_o = 30$ km.

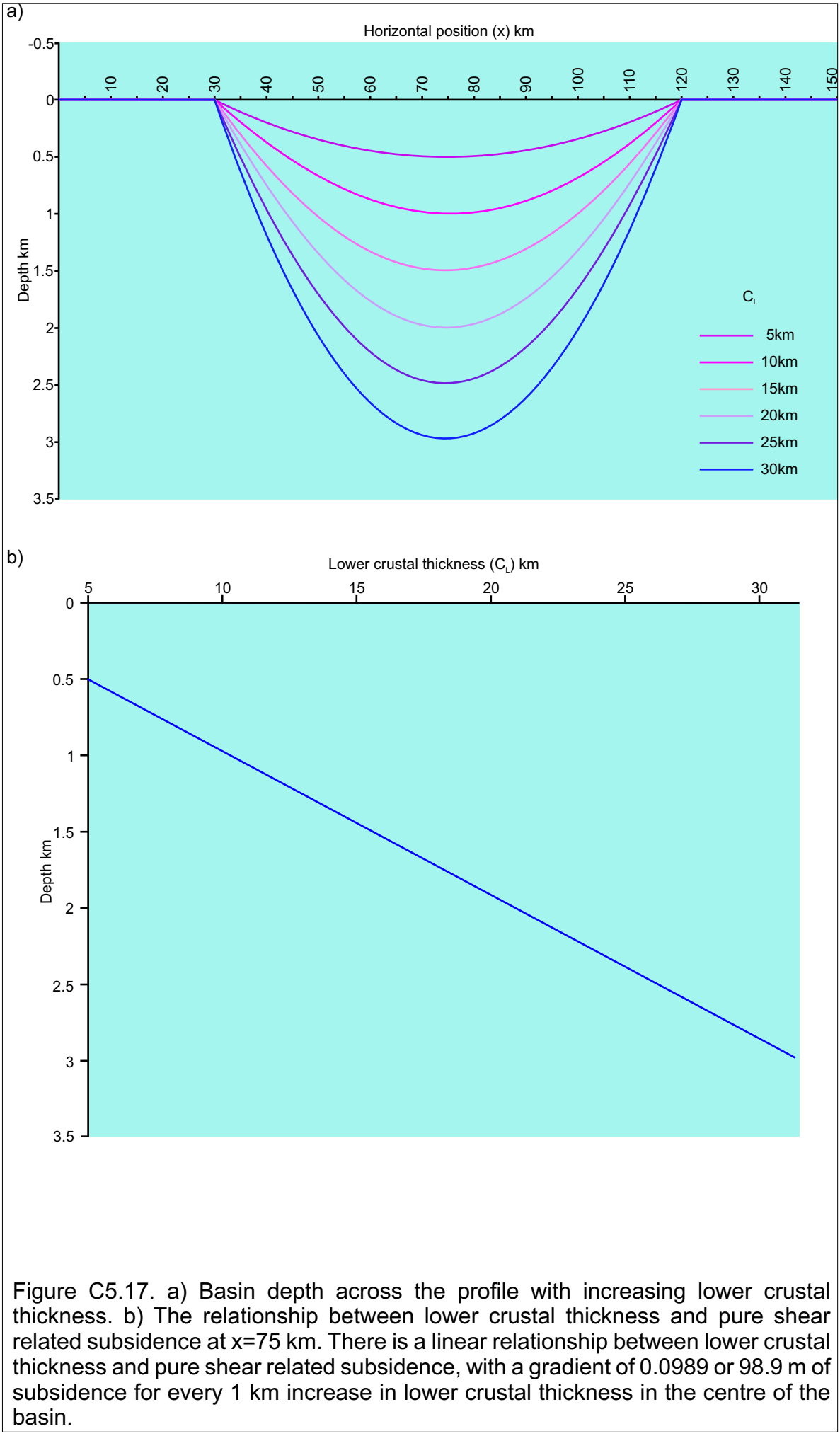


Figure C5.17. a) Basin depth across the profile with increasing lower crustal thickness. b) The relationship between lower crustal thickness and pure shear related subsidence at x=75 km. There is a linear relationship between lower crustal thickness and pure shear related subsidence, with a gradient of 0.0989 or 98.9 m of subsidence for every 1 km increase in lower crustal thickness in the centre of the basin.

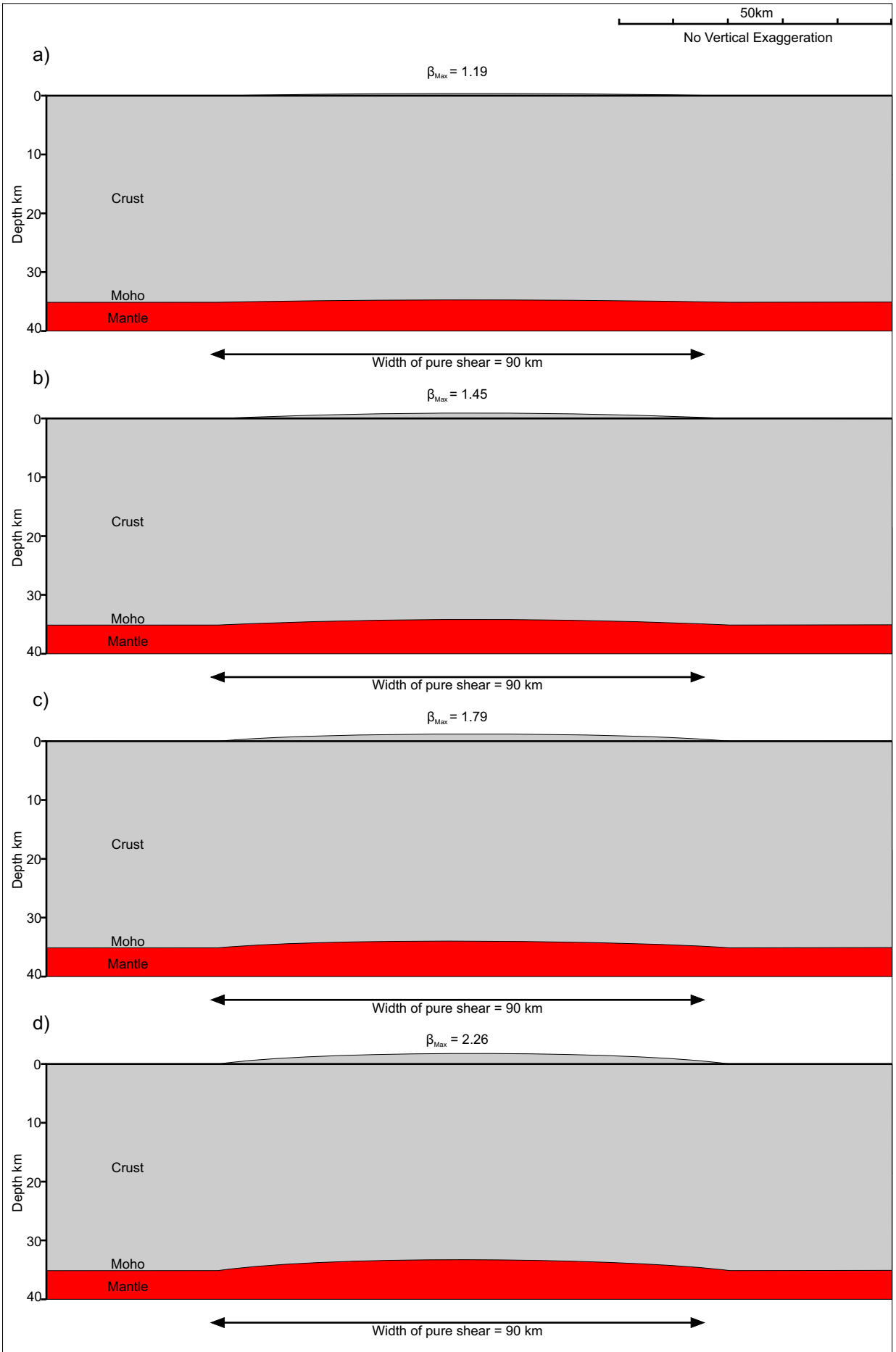


Figure C5.18. The effect of increasing the magnitude of extension at time t=0Ma after extension. An increase in $\beta_{Max}$ results in a greater amount of thermal uplift being generated. a) $\beta_{Max}$=1.19. b) $\beta_{Max}$=1.45. c) $\beta_{Max}$=1.79. d) $\beta_{Max}$=2.26.

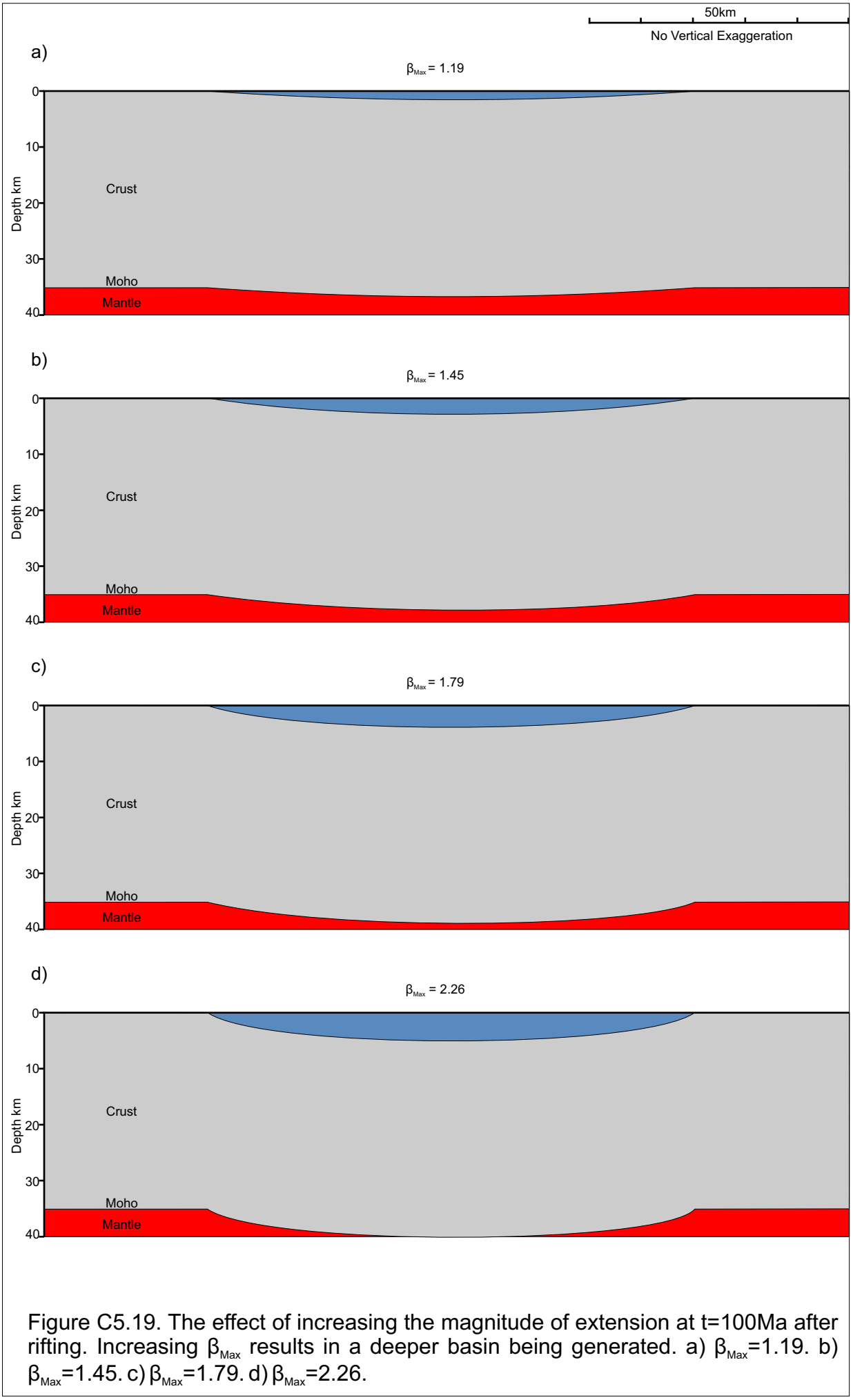


Figure C5.19. The effect of increasing the magnitude of extension at t=100Ma after rifting. Increasing $\beta_{Max}$ results in a deeper basin being generated. a) $\beta_{Max}$=1.19. b) $\beta_{Max}$=1.45. c) $\beta_{Max}$=1.79. d) $\beta_{Max}$=2.26.

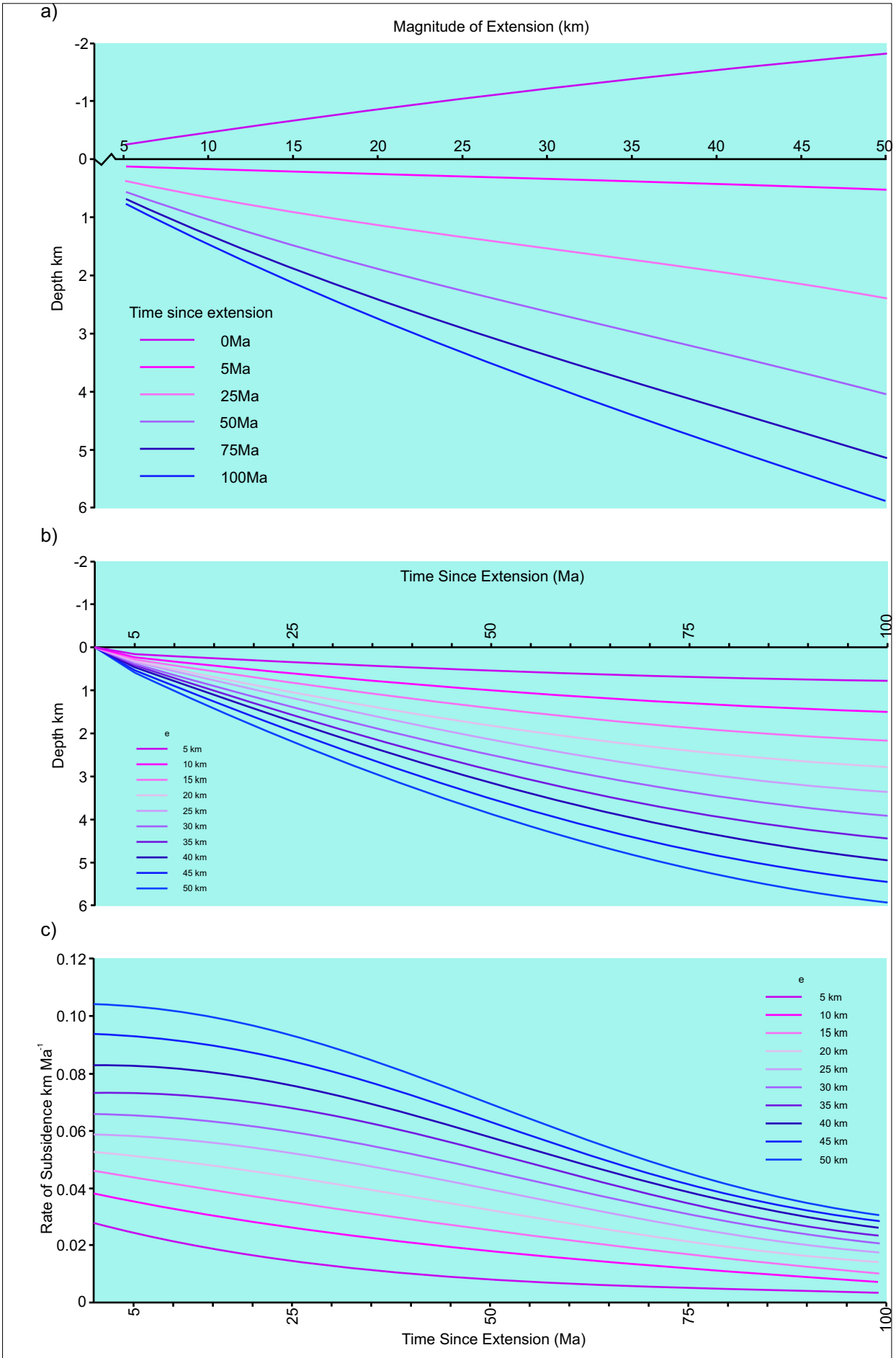


Figure C5.20. a) The effect of thermal processes on the basin over time with increasing magnitude of extension resulting in greater amounts of uplift followed by increased subsidence. Subsidence is assumed to be sediment loaded. b) The amount of thermal subsidence over time for varying magnitude of extension. c) The rate of subsidence over time for varying magnitude of extension.

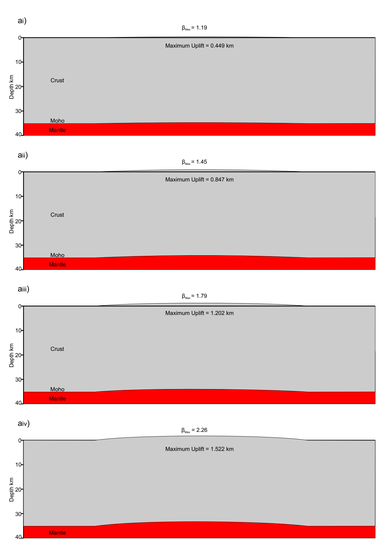


Figure C5.21a. The effect of increasing the magnitude of extension at time t=0Ma after extension. An increase in $\beta_{max}$ results in a greater amount of thermal uplift being generated.

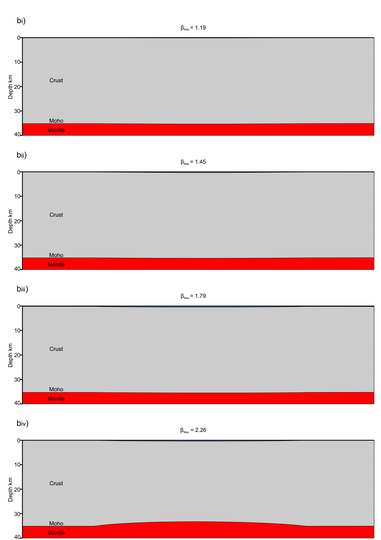


Figure C5.21b. The effect of increasing the magnitude of extension at time t=5Ma after extension. The basin generated as a result of thermal subsidence is loaded by sediment.

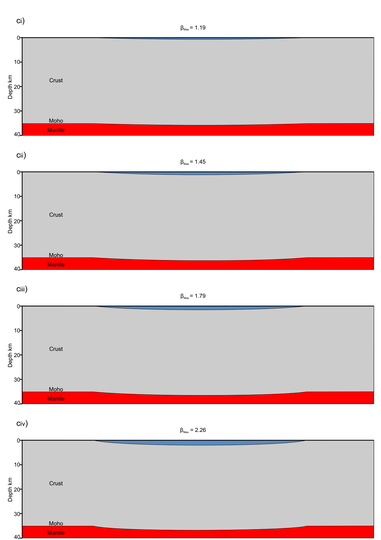


Figure C5.21c. The effect of increasing the magnitude of extension at t=25Ma after extension. The cumulative effect of thermal subsidence deepens the basin. An increase in $\beta_{max}$ results in a deeper basin being generated as a result of greater subsidence.

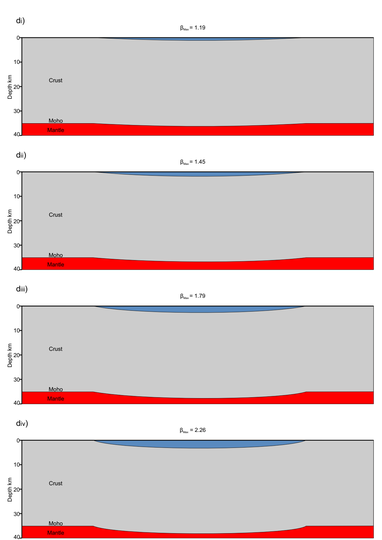


Figure C5.21d. The effect of increasing the magnitude of extension at time t=50Ma after extension. The basin continues to deepen with increasing $\beta_{max}$ resulting in a deeper basin being developed.

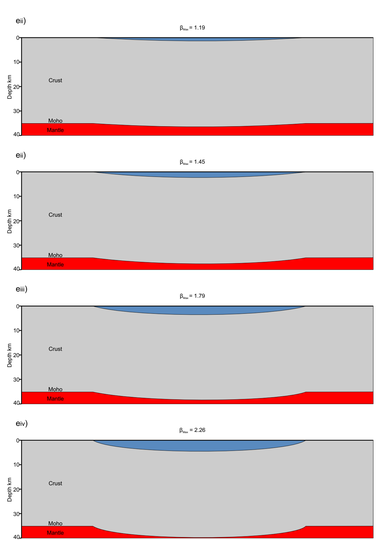


Figure C5.21e The effect of increasing the magnitude of extension at t=75Ma after extension. The rate of subsidence of the basin begins to reduce.

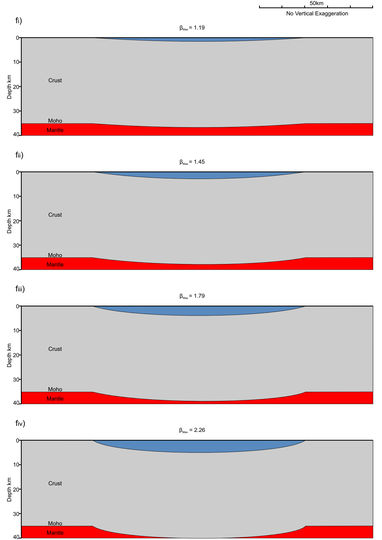


Figure C5.21f. The effect of increasing the magnitude of extension at t=100Ma after extension. The rate of basin subsidence is significantly reduced. Increasing $\beta_{max}$ results in a deeper basin being generated.

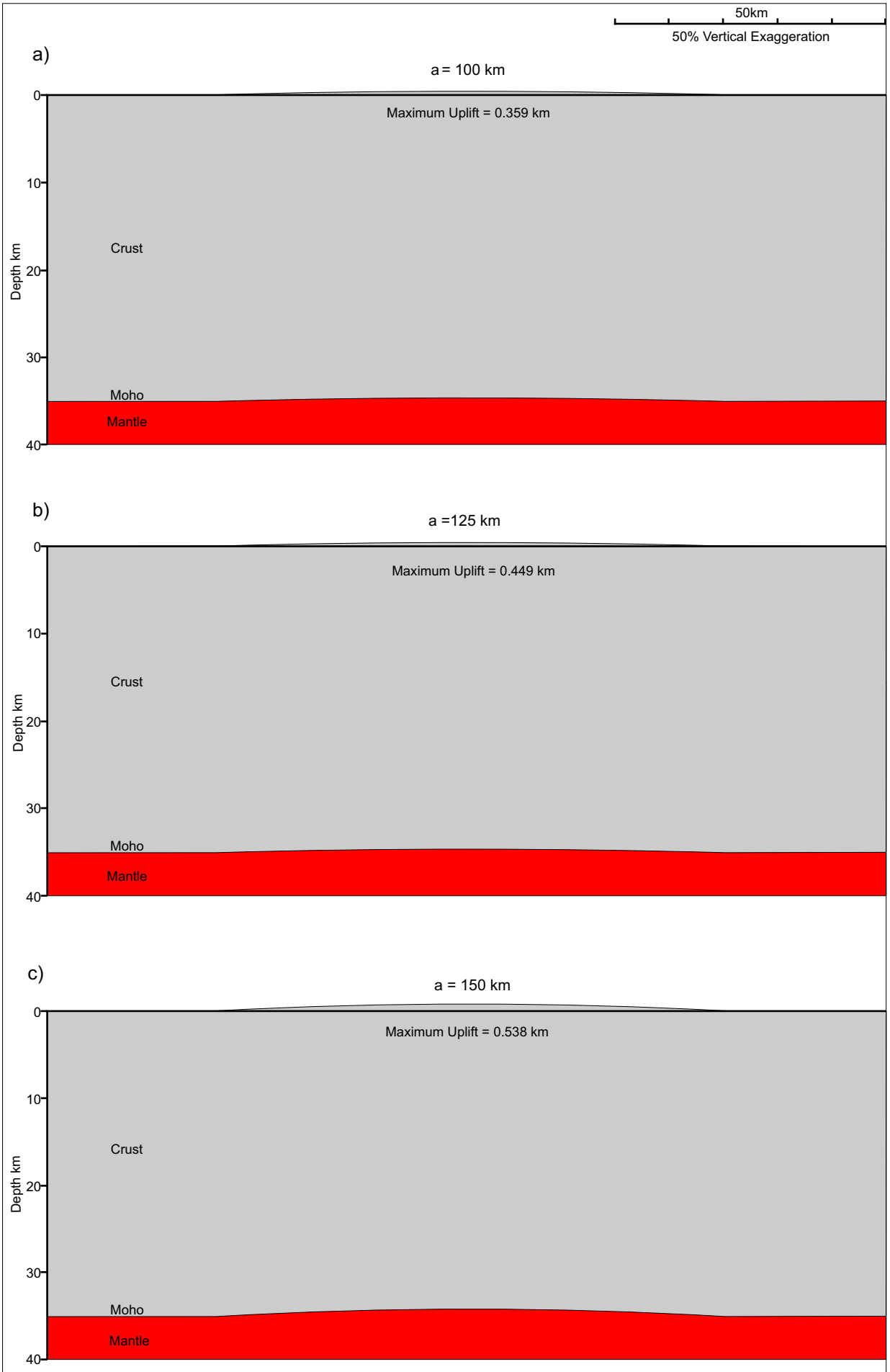


Figure C5.22. The effect of increasing the thickness of the lithosphere, a, at time t=0Ma after extension. An increase in lithosphere thickness results in a greater amount of thermal uplift being generated. a) a = 100 km. b) a = 125 km. c) a = 150 km.

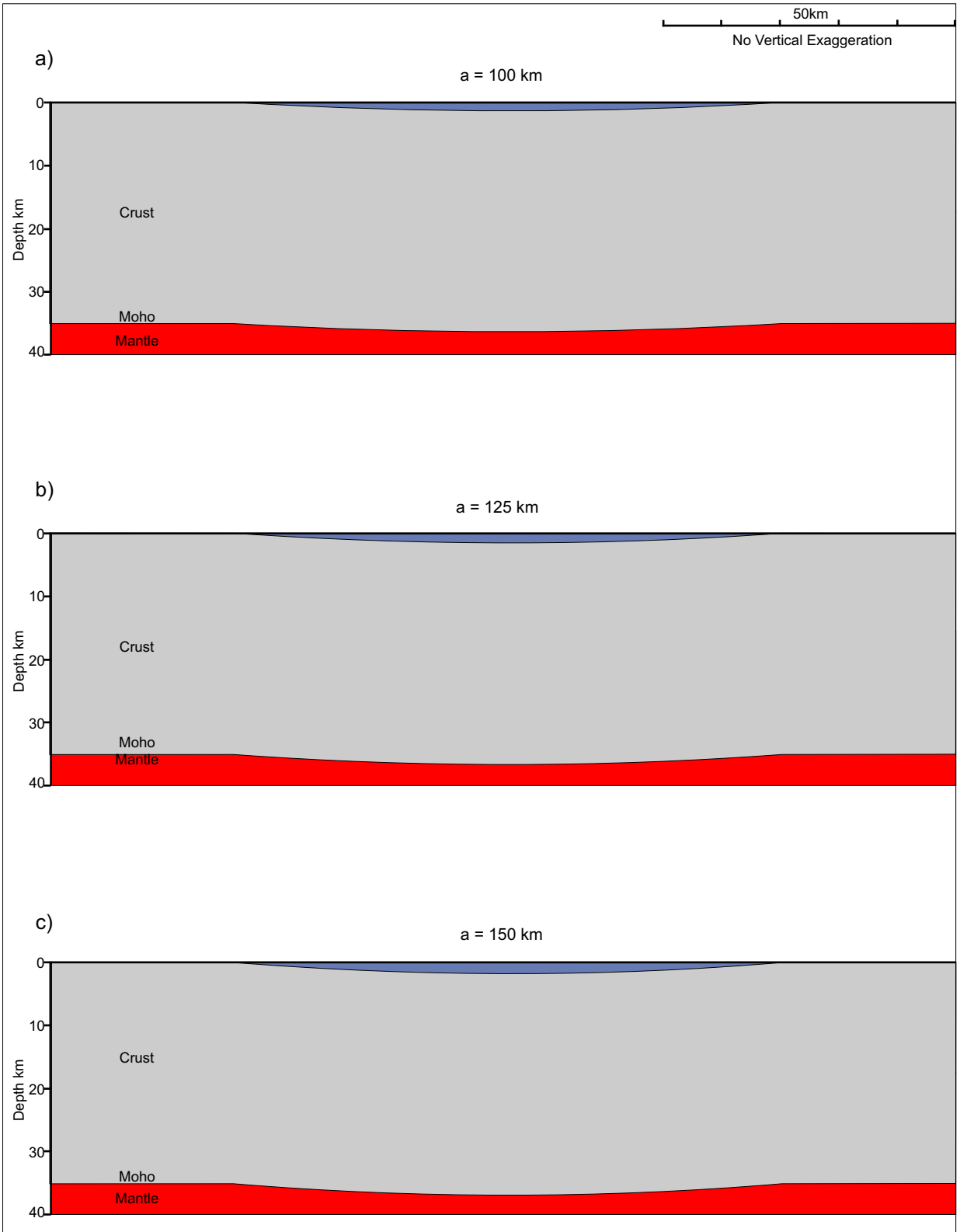


Figure C5.23. The effect of increasing the thickness of the lithosphere, a, at t=100Ma after extension. Increasing lithosphere thickness results in a deeper thermal subsidence sub-basin being generated. a) a = 100 km. b) a = 125 km. c) a = 150 km.

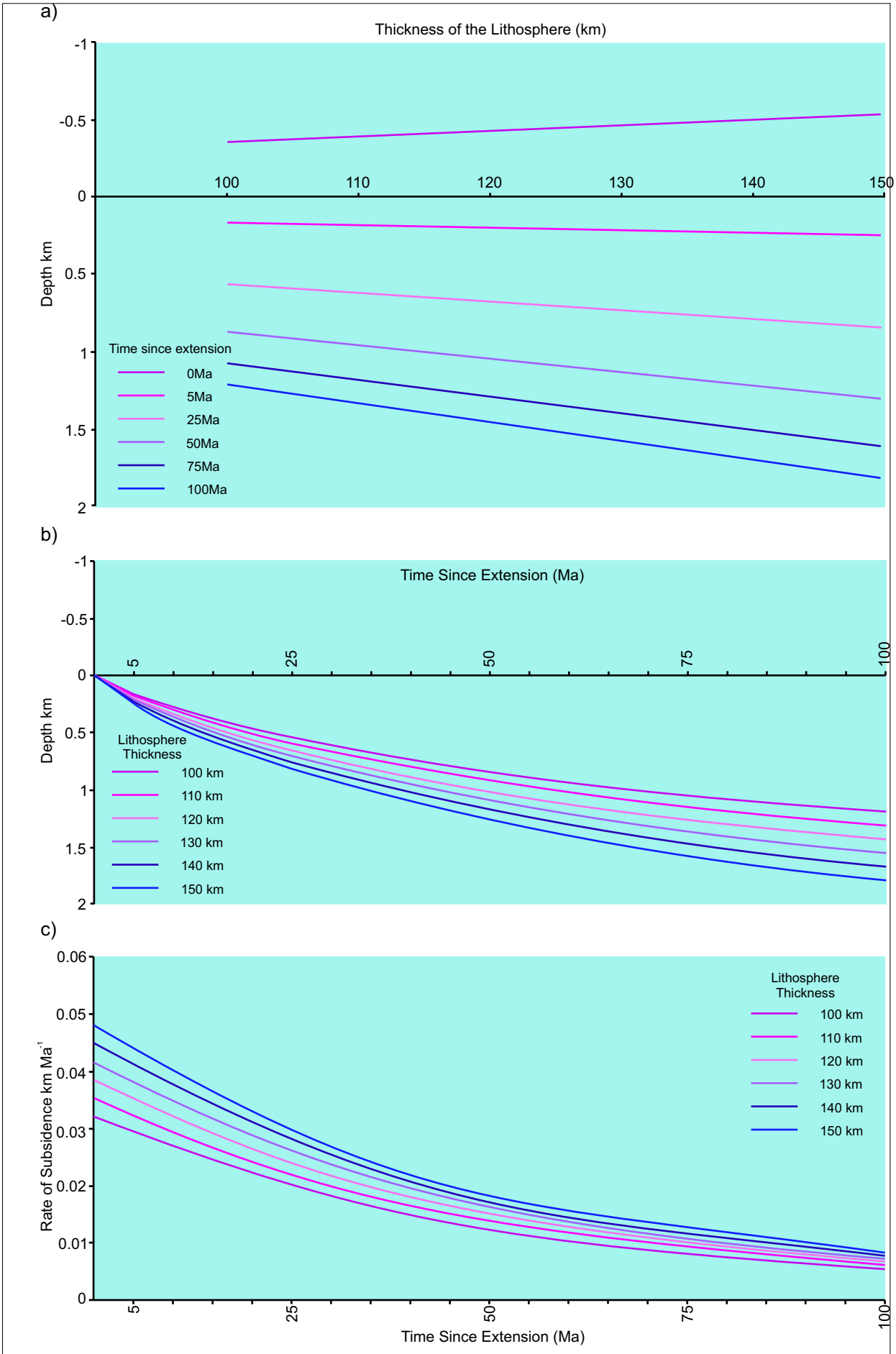


Figure C5.24. a) The effect of thermal processes on the basin over time with increasing lithosphere thickness resulting in greater amounts of uplift at rifting followed by increased post-rift, thermal subsidence. b) The amount of thermal subsidence over time for varying lithosphere thickness. c) The rate of subsidence over time for varying lithosphere thickness.

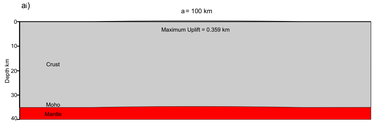


Figure C5.25a. The effect of increasing the thickness of the lithosphere, a, at time t=0Ma after extension. An increase in lithosphere thickness results in a greater amount of thermal uplift being generated.


Figure C5.25b. The effect of increasing the thickness of the lithosphere, a, at time t=5Ma after extension. Thermal subsidence generates a basin that is sediment loaded.

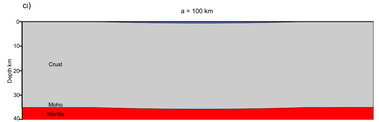


Figure C5.25c. The effect of increasing the thickness of the lithosphere, a, at t=25Ma after extension. The cumulative effect of thermal subsidence deepens the basin. An increase in lithosphere thickness results in a deeper basin being generated as a result of greater subsidence.


Figure C5.25d. The effect of increasing the thickness of the lithosphere, a, at time t=50Ma after extension. The basin continues to deepen with increasing lithosphere thickness.

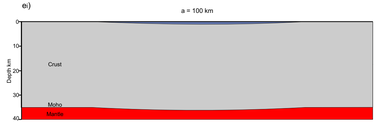


Figure C5.25e The effect of increasing the thickness of the lithosphere, a, at t=75Ma after extension. The rate of subsidence of the basin begins to reduce.

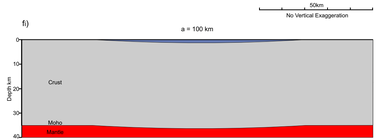


Figure C5.25f. The effect of increasing the thickness of the lithosphere, a, at t=100Ma after extension. The rate of basin subsidence is significantly reduced. Increasing lithosphere thickness results in a deeper basin being generated.

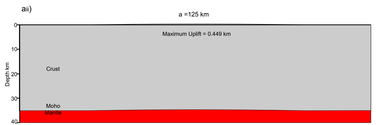


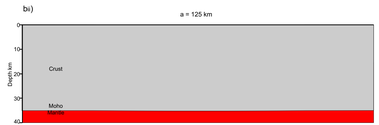



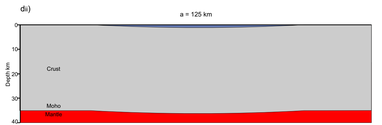


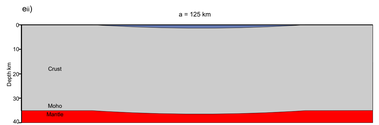


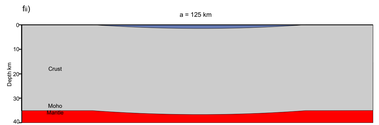



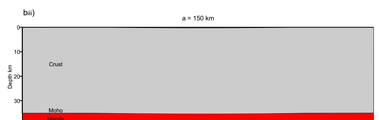



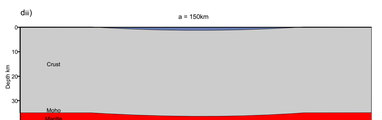


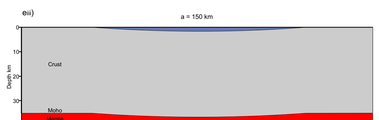


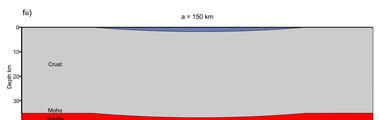

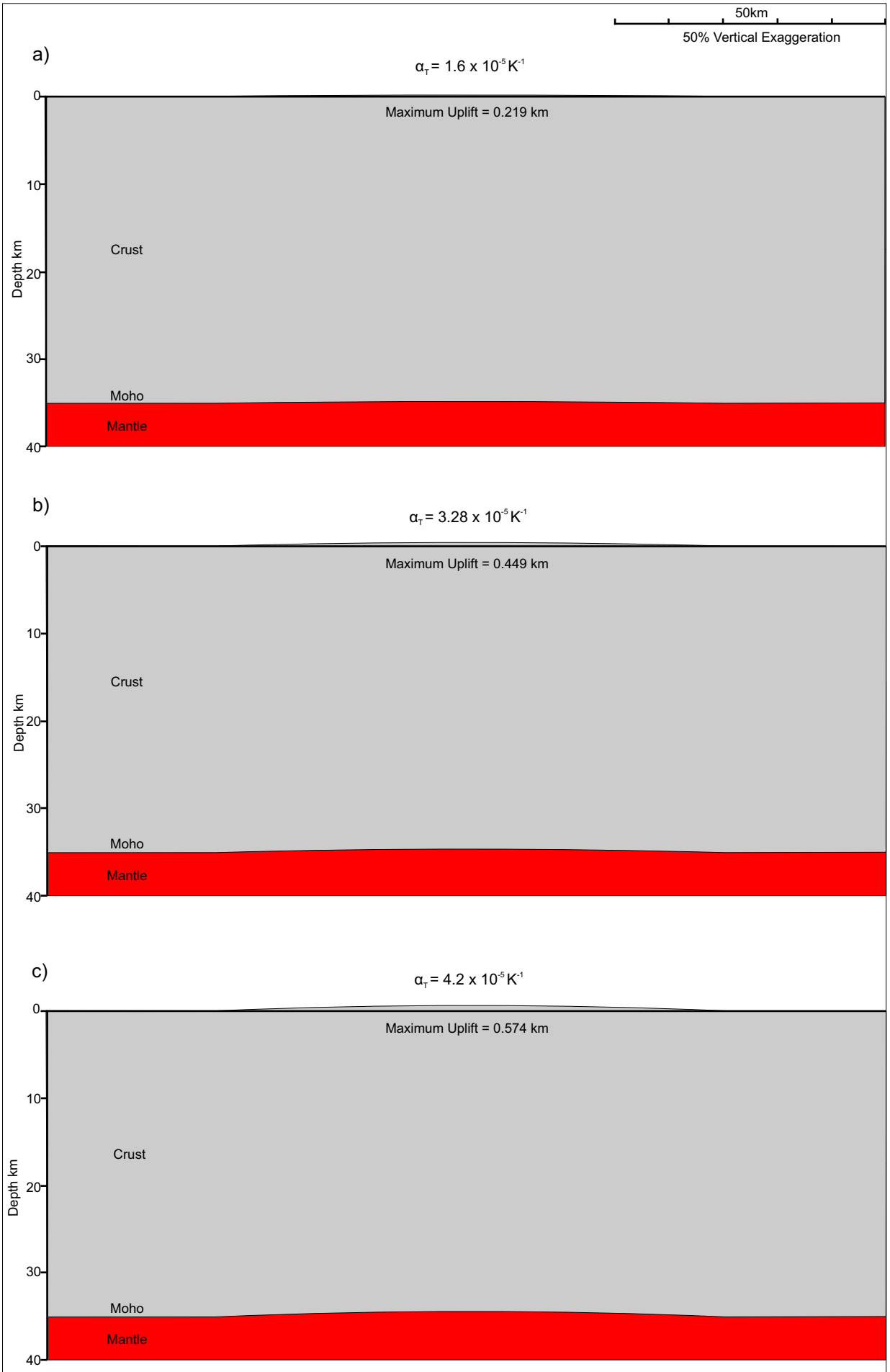


Figure C5.26. The effect of increasing the co-efficient of thermal expansion, $\alpha_T$, at time t=0Ma after extension. An increase in $\alpha_T$ results in a greater amount of thermal uplift being generated. a) $\alpha_T = 1.6 \times 10^{-5} K^{-1}$. b) $\alpha_T = 3.28 \times 10^{-5} K^{-1}$. c) $\alpha_T = 4.2 \times 10^{-5} K^{-1}$.

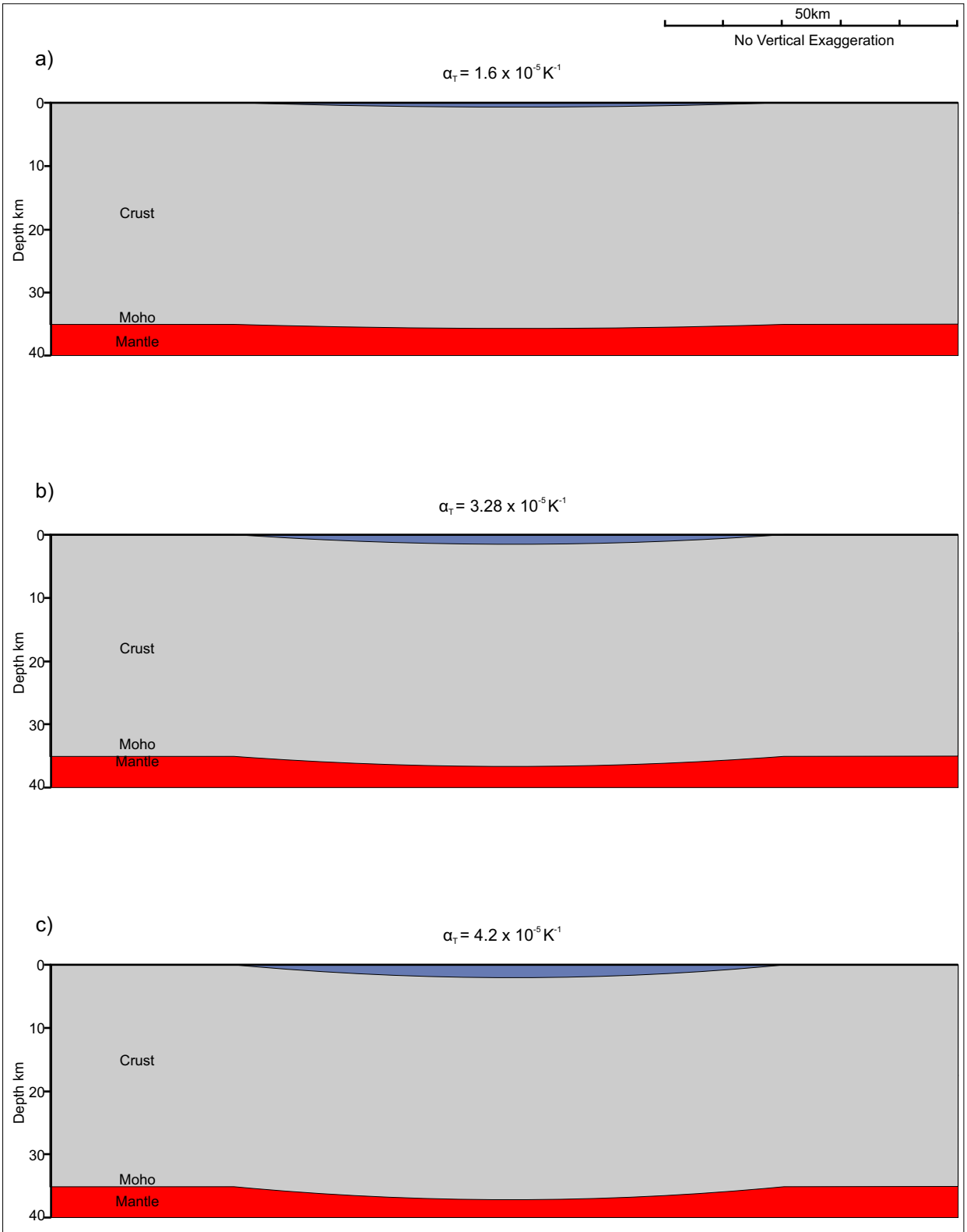


Figure C5.27. The effect of increasing the co-efficient of thermal expansion, $\alpha_T$, at t=100Ma after extension. Increasing $\alpha_T$ results in a deeper thermal subsidence sub-basin being generated.

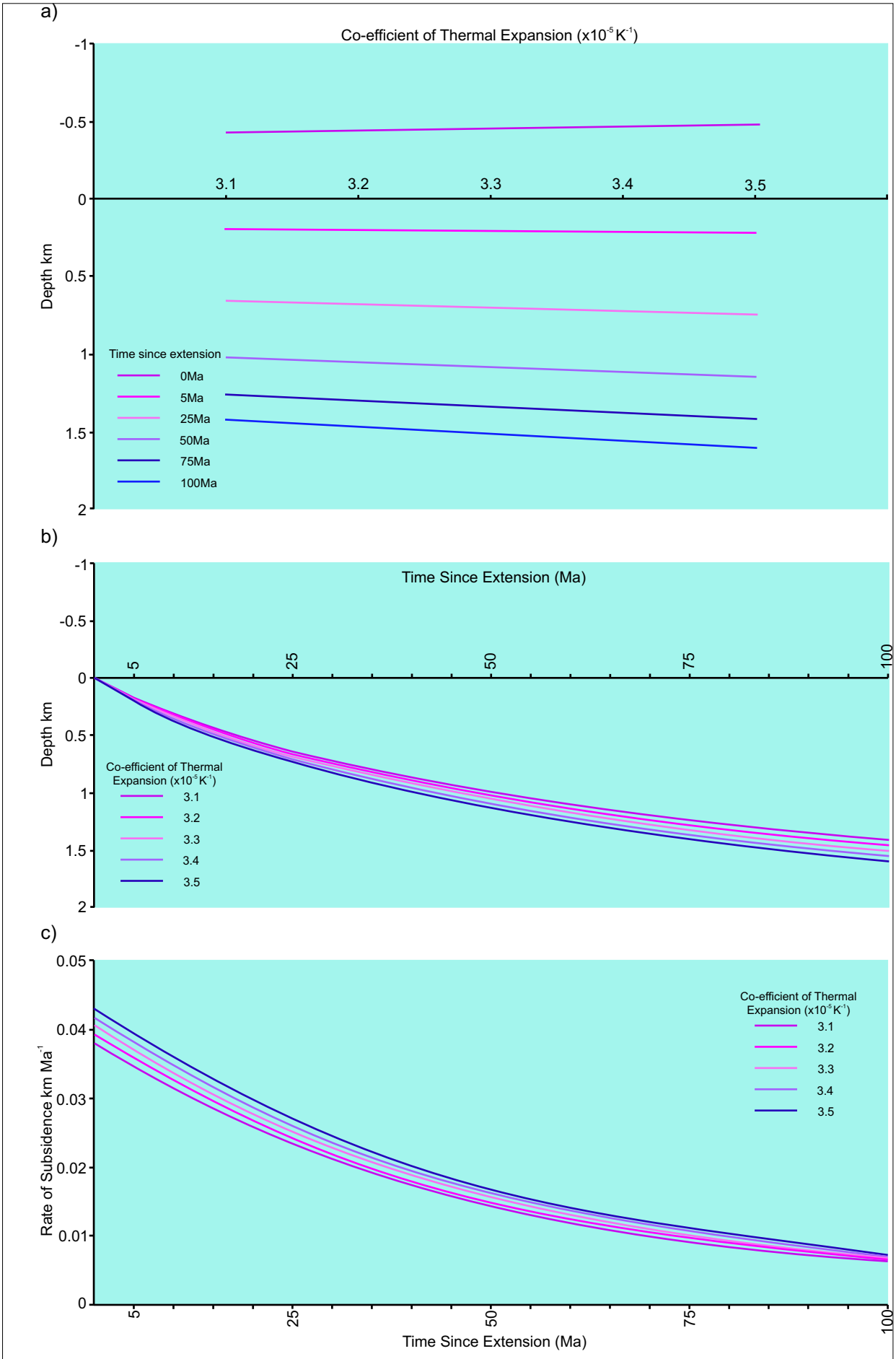


Figure C5.28. a) The effect of thermal processes on the basin over time with increasing co-efficient of thermal expansion resulting in greater amounts of uplift followed by increased subsidence. b) The amount of thermal subsidence over time for varying co-efficient of thermal expansion. c) The rate of subsidence over time for varying co-efficient of thermal expansion.

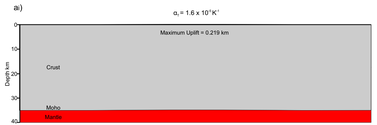


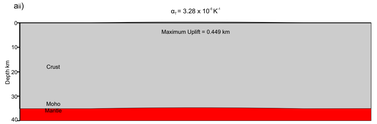


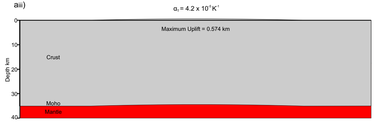


Figure C5.29a. The effect of increasing the co-efficient of thermal expansion, $\alpha_v$, at time t=0Ma after extension. An increase in $\alpha_v$ results in a greater amount of thermal uplift being generated.

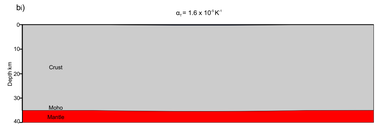


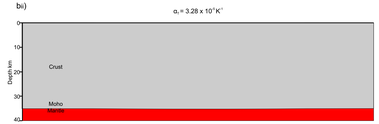


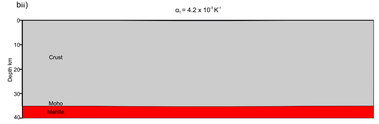


Figure C5.29b. The effect of increasing the co-efficient of thermal expansion, $\alpha_v$, at time t=5Ma after extension. Thermal subsidence produces a basin that is subsequently sediment loaded.

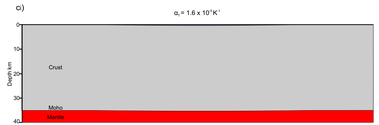


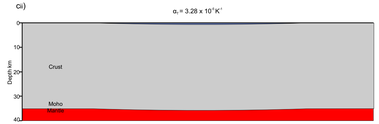


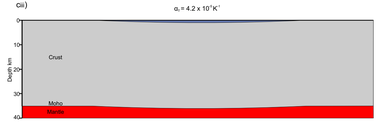


Figure C5.29c. The effect of increasing the co-efficient of thermal expansion, $\alpha_v$, at t=25Ma after extension. The cumulative effect of thermal subsidence deepens the basin. An increase in $\alpha_v$ results in a deeper basin being generated as a result of greater subsidence.

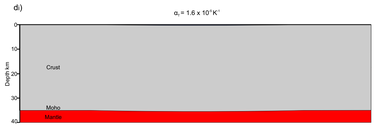


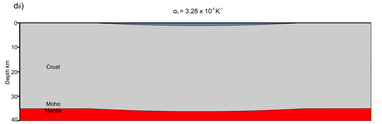


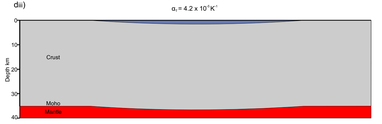


Figure C5.29d. The effect of increasing the co-efficient of thermal expansion, $\alpha_v$, at time t=50Ma after extension. The basin continues to deepen with increasing $\alpha_v$ resulting in a deeper basin being developed.

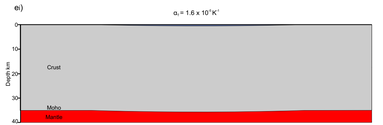


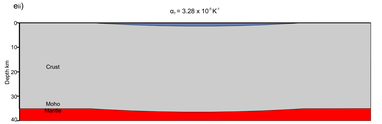


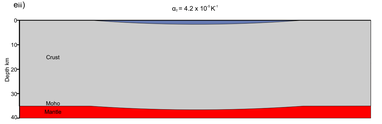


Figure C5.29e The effect of increasing the co-efficient of thermal expansion, $\alpha_v$, at t=75Ma after extension. The rate of subsidence of the basin begins to reduce.

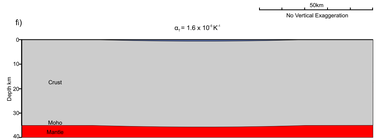


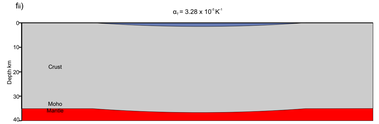


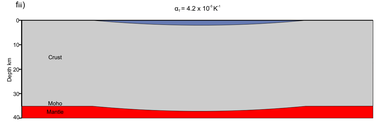


Figure 5.29f. The effect of increasing the co-efficient of thermal expansion, $\alpha_v$, at t=100Ma after extension. The rate of basin subsidence is significantly reduced. Increasing $\alpha_v$ results in a deeper basin being generated.

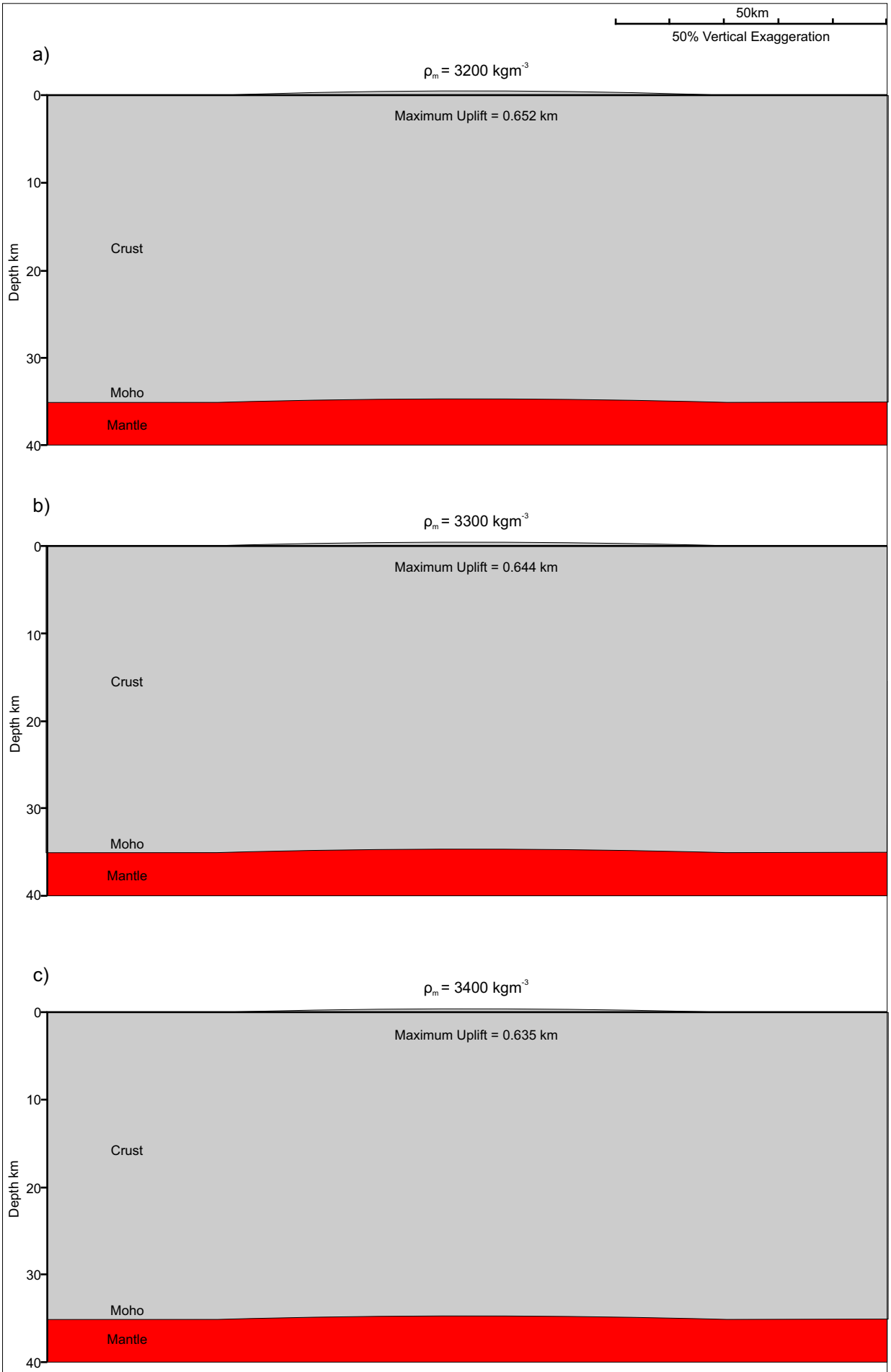


Figure C5.30. The effect of increasing the density of the mantle, $\rho_m$, at time t=0Ma after extension. An increase in mantle density results in a smaller amount of thermal uplift being generated. a) $\rho_m = 3200$ kgm$^{-3}$. b) $\rho_m = 3300$ kgm$^{-3}$. c) $\rho_m = 3400$ kgm$^{-3}$.

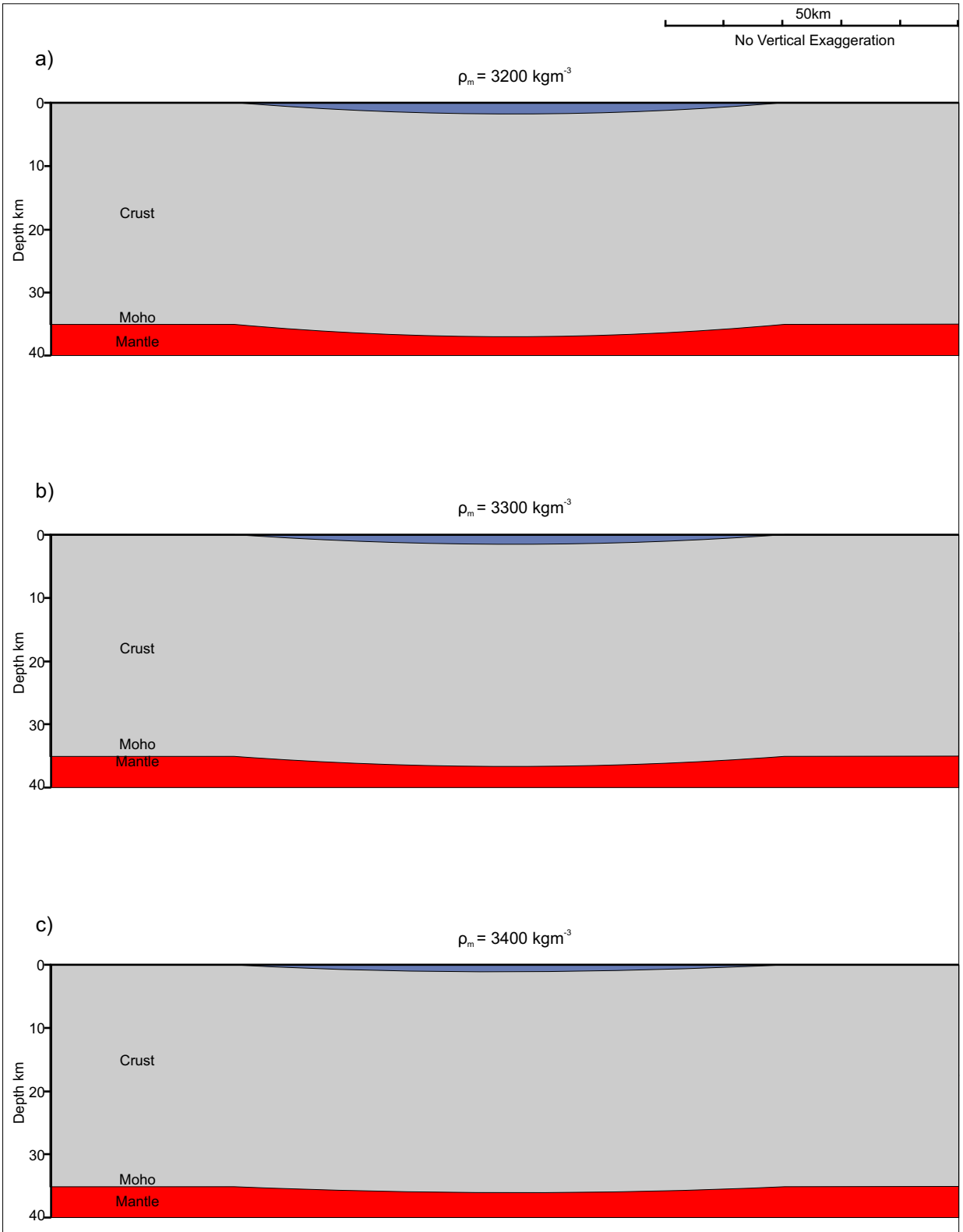


Figure C5.31. The effect of increasing the density of the mantle, $\rho_m$, at t=100Ma after extension. The rate of basin subsidence is significantly reduced. Increasing mantle density results in a shallower sub-basin being generated as a consequence of a reduced amount of thermal subsidence. a) $\rho_m$ = 3200 kgm$^{-3}$. b) $\rho_m$ = 3300 kgm$^{-3}$. c) $\rho_m$ = 3400 kgm$^{-3}$.

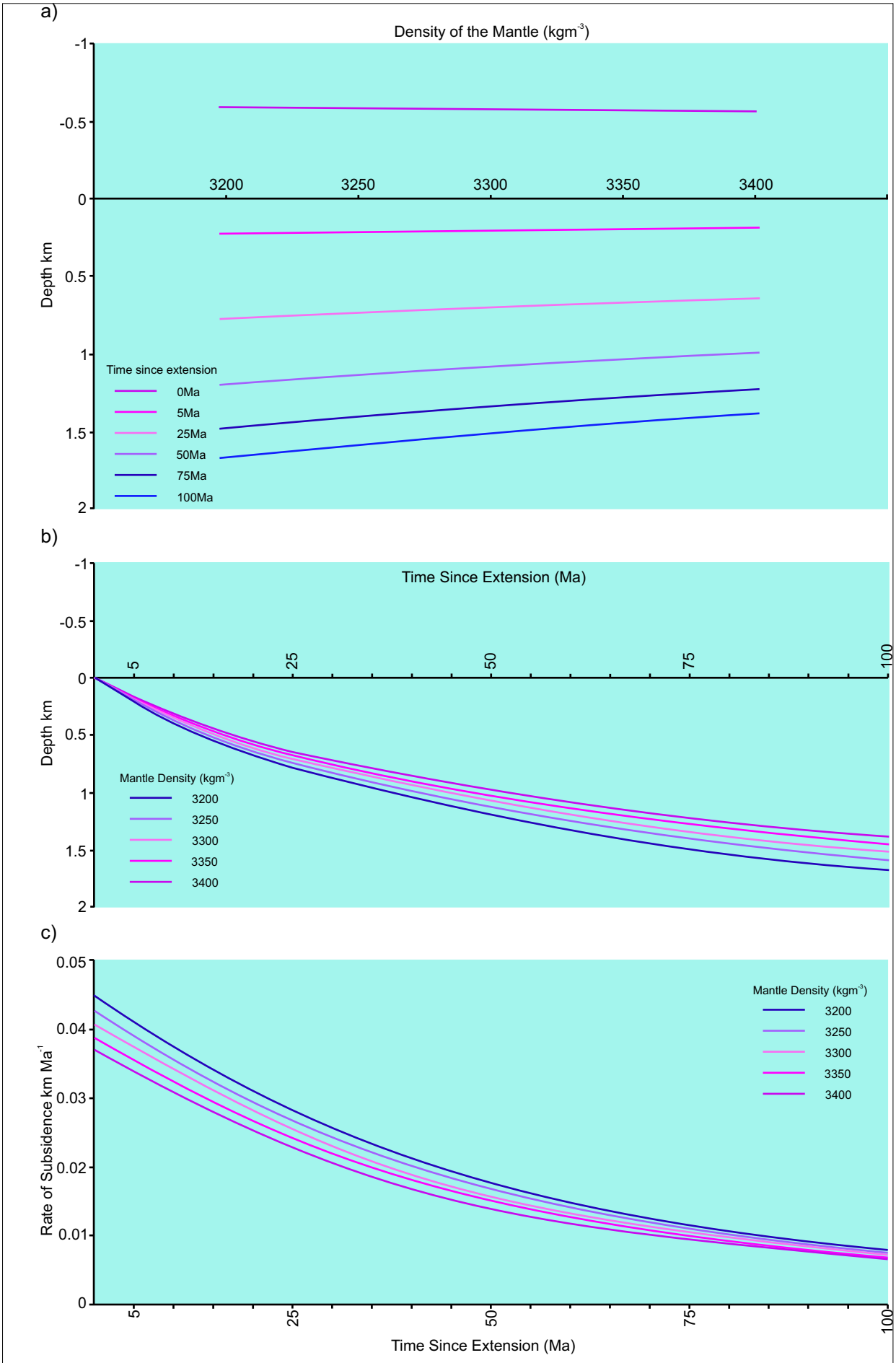


Figure C5.32. a) The effect of thermal processes on the basin over time with increasing mantle density resulting in smaller amounts of uplift followed by reduced subsidence. b) The amount of thermal subsidence over time for varying mantle density. c) The rate of subsidence over time for varying mantle density.

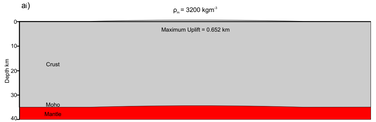


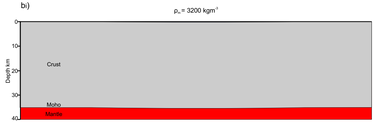


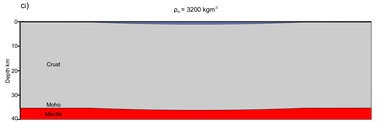


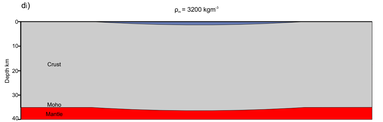


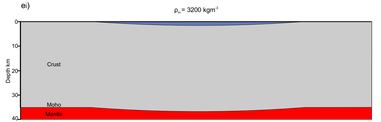


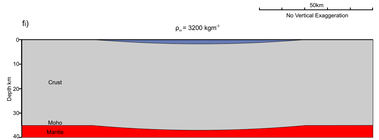


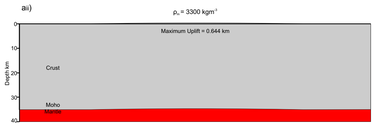


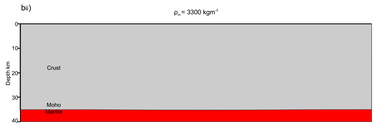


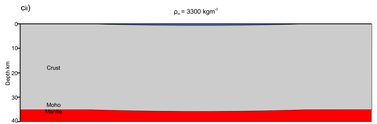


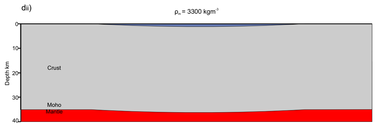


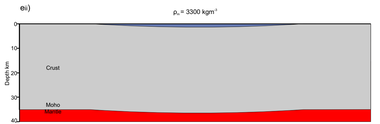


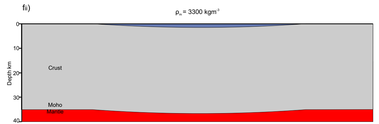


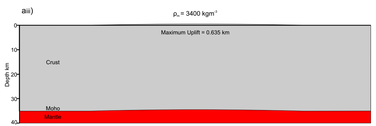


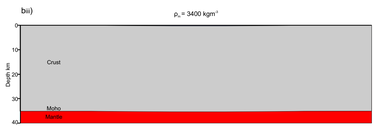


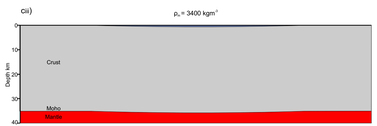


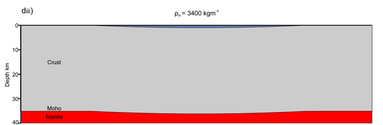


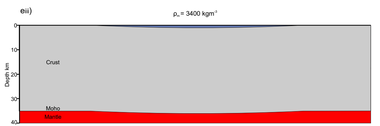


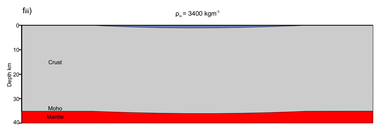


Figure C5.33a. The effect of increasing the density of the mantle, $\rho_m$, at time t=0Ma after extension. An increase in mantle density results in a smaller amount of thermal uplift being generated.

Figure C5.33b. The effect of increasing the density of the mantle, $\rho_m$, at time t=5Ma after extension. The basin generated by thermal subsidence is sediment loaded.

Figure C5.33c. The effect of increasing the density of the mantle, $\rho_m$, at t=25Ma after extension. The cumulative effect of thermal subsidence deepens the basin. An increase in mantle density results in a shallower basin being generated as a result of reduced subsidence.

Figure C5.33d. The effect of increasing the density of the mantle, $\rho_m$, at time t=50Ma after extension. Increasing mantle density results in a shallower basin being developed.

Figure C5.33e The effect of increasing the density of the mantle, $\rho_m$, at t=75Ma after extension. The rate of subsidence of the basin begins to reduce.

Figure C5.33f. The effect of increasing the density of the mantle, $\rho_m$, at t=100Ma after extension. The rate of basin subsidence is significantly reduced. Increasing mantle density results in a shallower basin being generated.

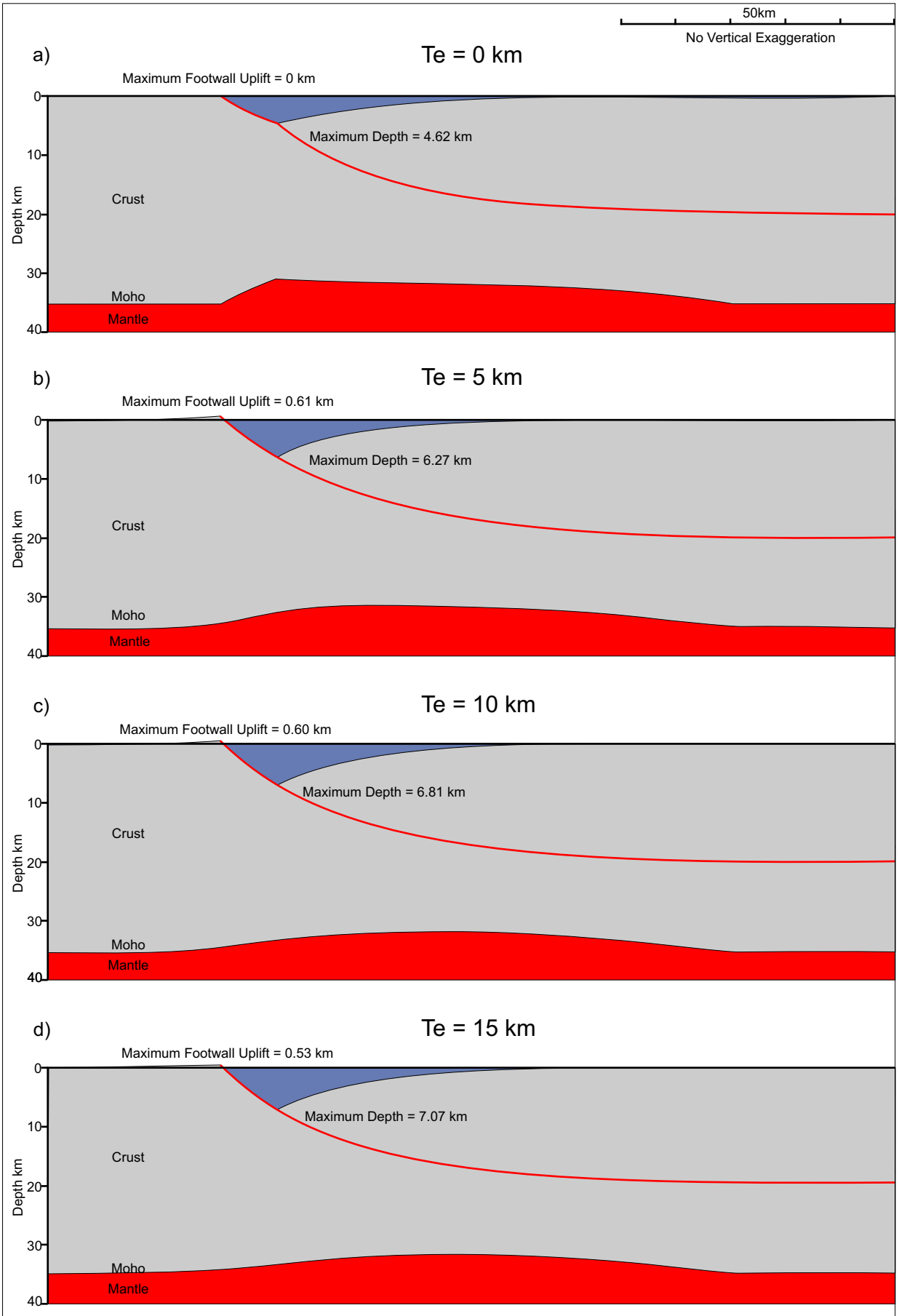


Figure C5.34. The effect of increasing the elastic thickness of the lithosphere, Te, at t=0 Ma after rifting. With increasing Te, the maximum basin depth increases as a result of a reduced maximum uplift in response to the negative load generated by faulting.

a)

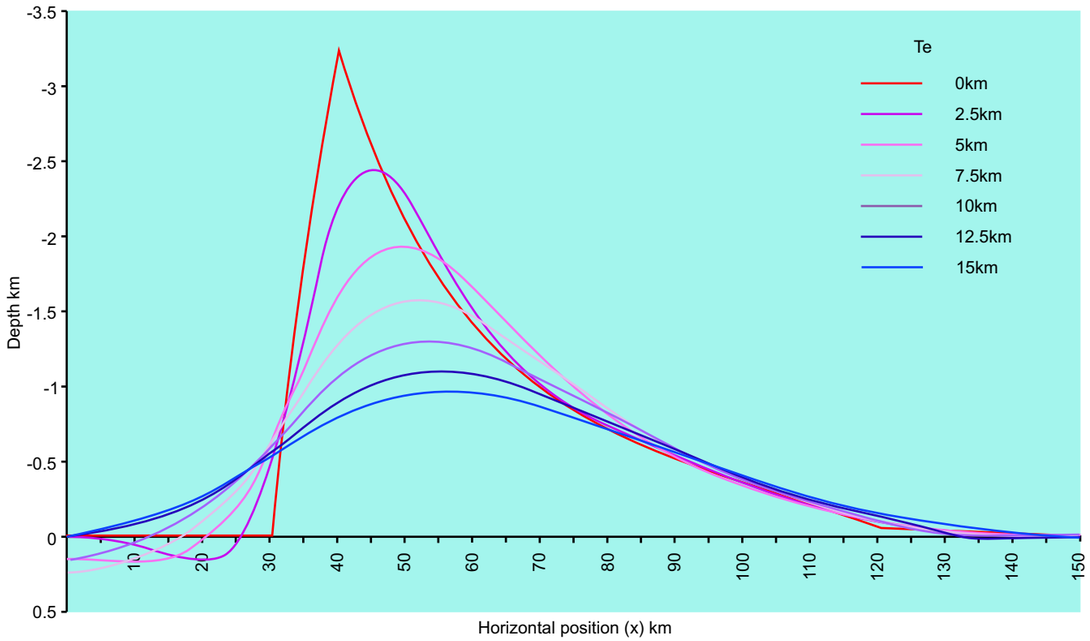


b)

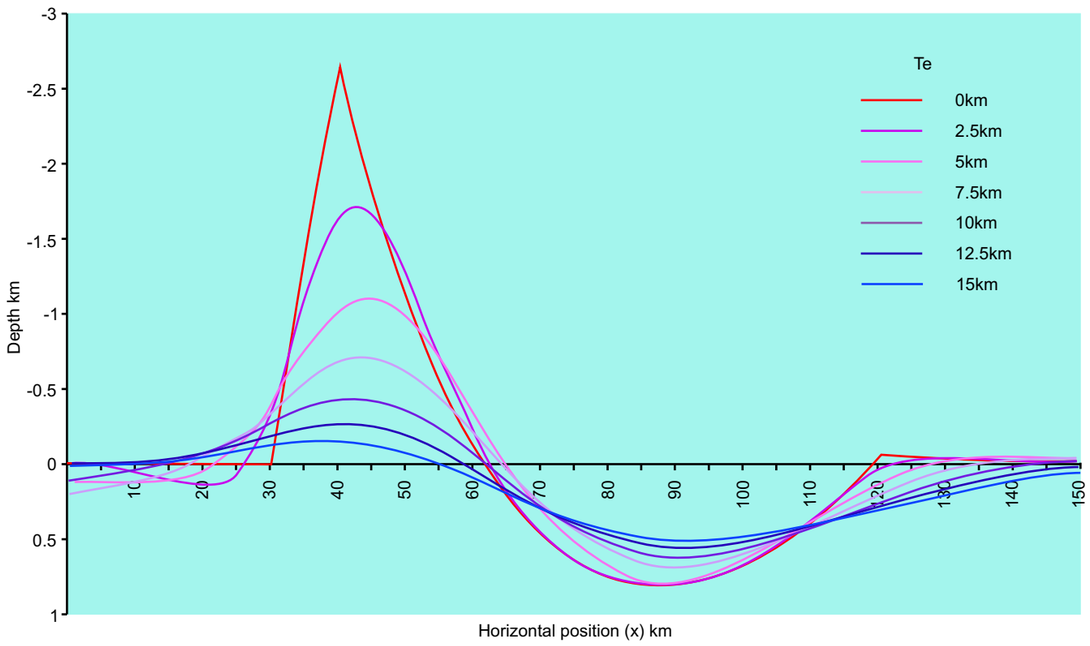


c)

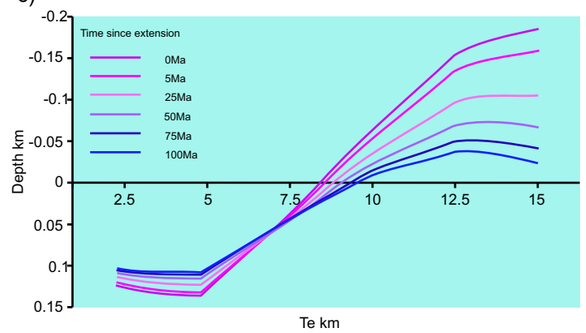


x = 15 km - The lateral extent of the footwall uplift increases with increasing flexural rigidity as the wavelength of the flexural rebound increases. There is evidence of footwall uplift at Te>8km. At values of Te<8km, the flexural response to the processes that occur at t = 0 Ma after rifting generates subsidence in the footwall, in front of the uplift, creating a basin.

d)

x = 30 km - At low values of Te, the amount of footwall uplift increases with increasing flexural rigidity, reaching a peak uplift at a of 7.5 km. The maximum amount of footwall uplift generated decreases as flexural rigidity continues to increase. Over time, with increasing flexural rigidity, the footwall uplift is flattened and broadened.

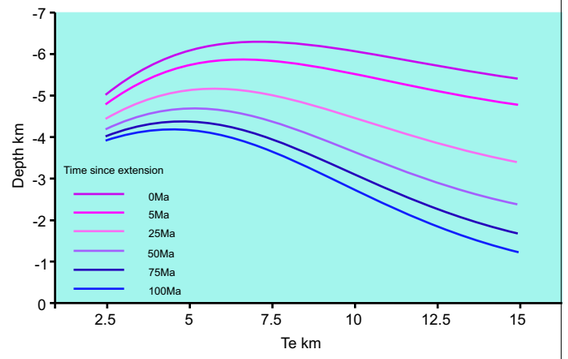


e)

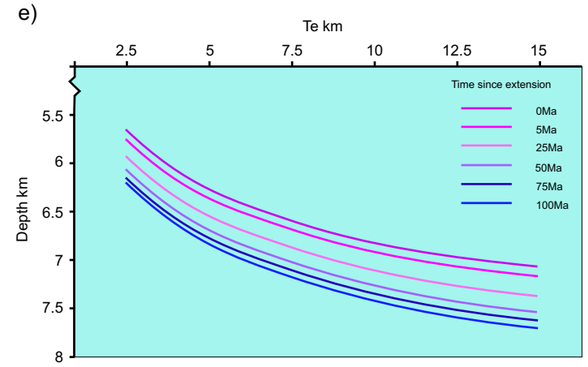


x = 40 km - With increasing elastic thickness, the maximum basin depth increases, with an increase in depth of 0.079 km for every 1 km increase in Te at t = 0Ma after rifting. This occurs as the wavelength of the flexural uplift increases and its amplitude decreases with increasing Te.

f)

The maximum amount of thermal subsidence generated decreases with increasing . As a result, the depth of the basin in a position proximal to the fault, where thermal subsidence has a greater influence than the fault related uplift, decreases with increasing Te. The depth of the basin at x = 90 km decreases by an average of 0.028 km for every 1 km increase in Te.

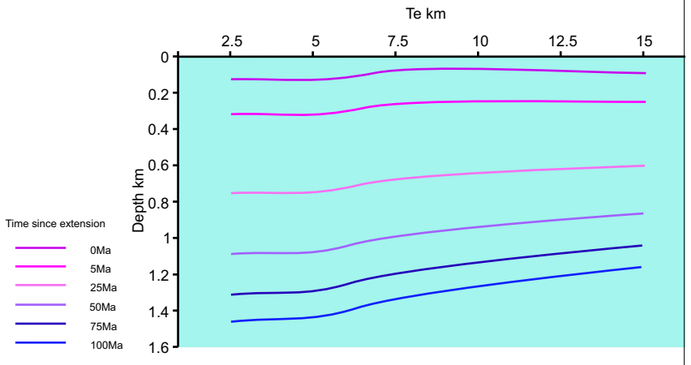


Figure C5.35. The effect of increasing the elastic thickness of the lithosphere, Te, upon the flexural isostatic response to extension and basin development. a) The profile of the flexural response at t = 0 Ma. b) The profile of the cumulative flexural response at t = 100 Ma. c) The depth to the basement with increasing Te over time at horizontal position x = 15 km. d) The footwall uplift generated adjacent to the fault at x = 30 km. e) The depth of the basin at x = 40 km over time with varying Te. f) The depth of the basin over time at x = 90 km.

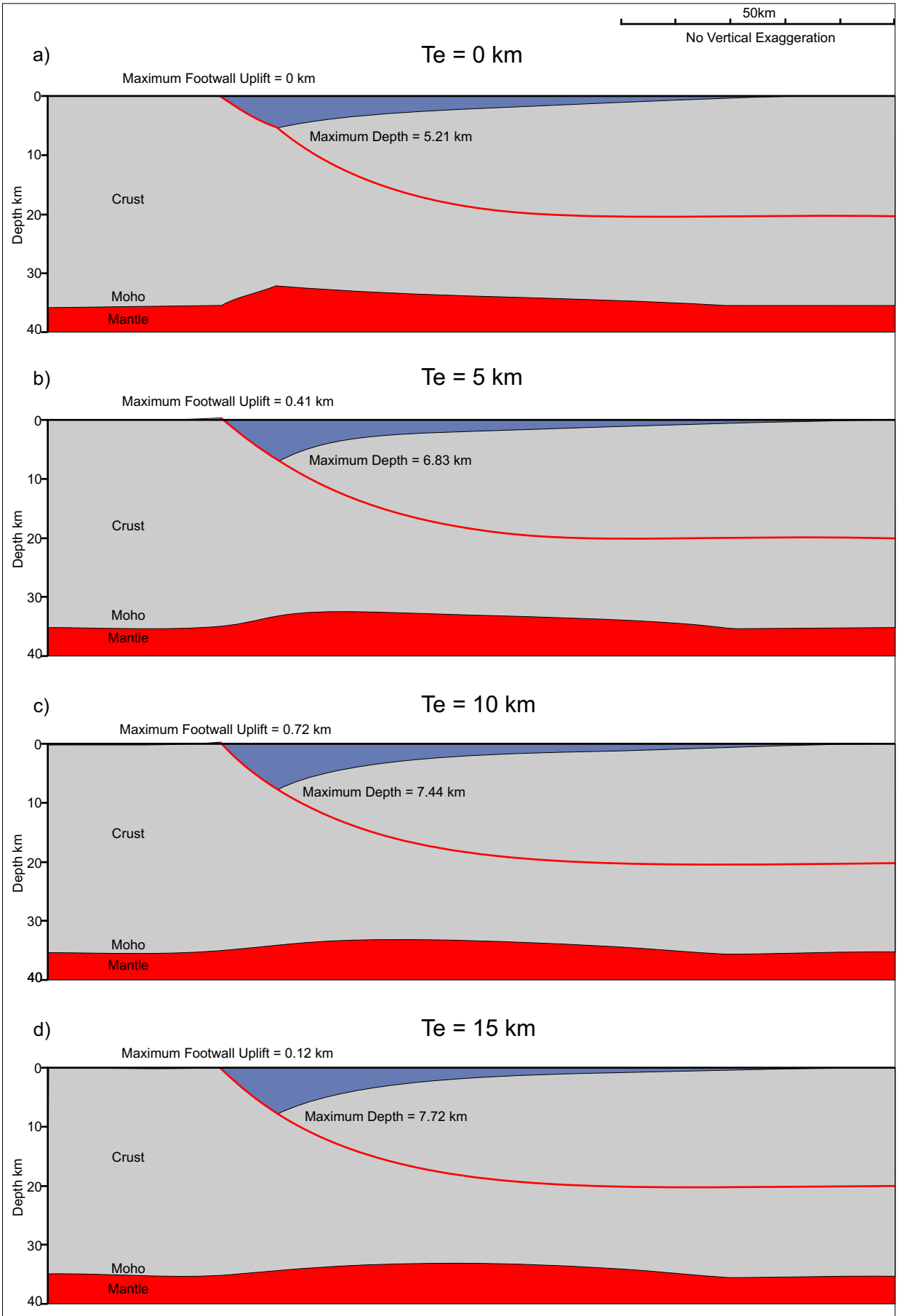


Figure C5.36. The effect of increasing the elastic thickness of the lithosphere, Te, at t=100 Ma after rifting. The maximum amount of thermal subsidence generated decreases with increasing Te.

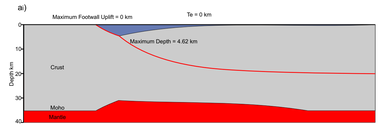


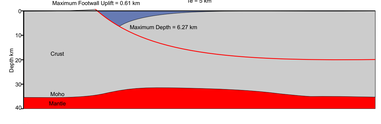


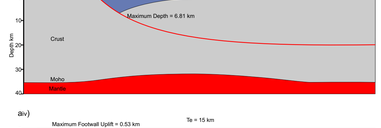


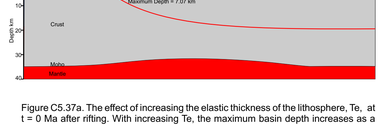


Figure C5.37a. The effect of increasing the elastic thickness of the lithosphere, Te, at t = 0 Ma after rifting. With increasing Te, the maximum basin depth increases as a result of a reduced maximum uplift in response to the -ve load generated by faulting.

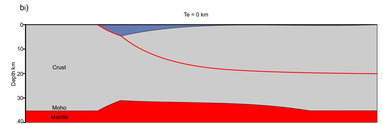


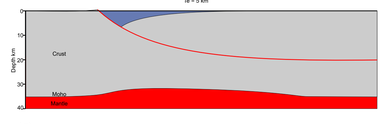


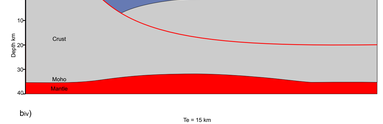


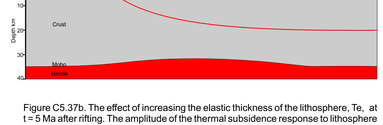


Figure C5.37b. The effect of increasing the elastic thickness of the lithosphere, Te, at t = 5 Ma after rifting. The amplitude of the thermal subsidence response to lithosphere extension decreases with increasing Te.

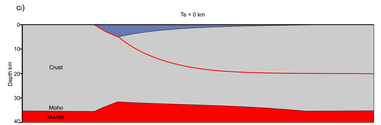


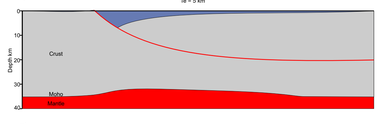


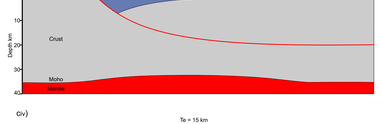


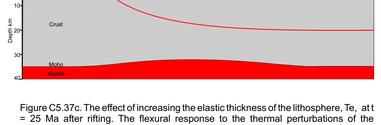


Figure C5.37c. The effect of increasing the elastic thickness of the lithosphere, Te, at t = 25 Ma after rifting. The flexural response to the thermal perturbations of the lithosphere is offset from the faulting related basin, this results in increased deepening of the basin in a more distal position from the fault.

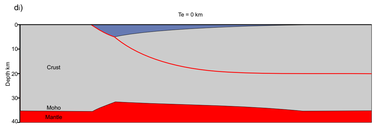


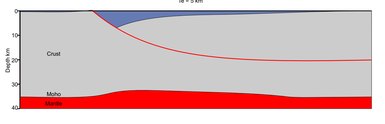


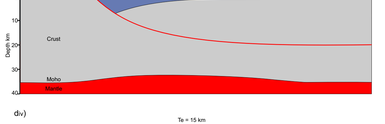


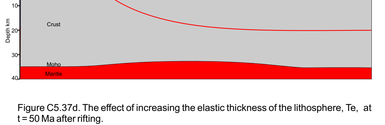


Figure C5.37d. The effect of increasing the elastic thickness of the lithosphere, Te, at t = 50 Ma after rifting.

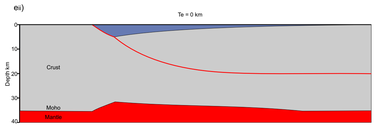


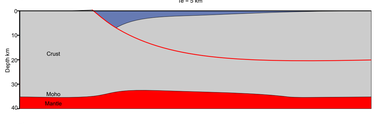


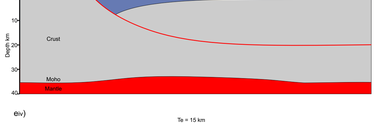


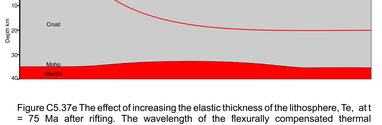


Figure C5.37e The effect of increasing the elastic thickness of the lithosphere, Te, at t = 75 Ma after rifting. The wavelength of the flexurally compensated thermal subsidence increases with increasing Te, generating greater amounts of subsidence towards the limits of the flexural response.

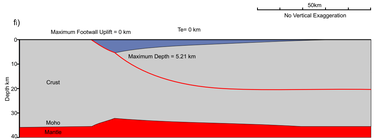


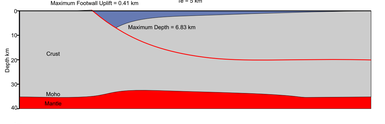


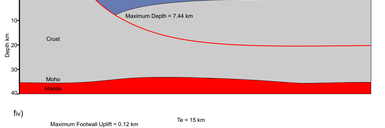


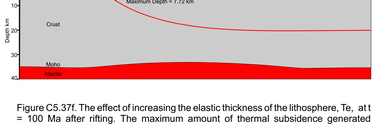


Figure C5.37f. The effect of increasing the elastic thickness of the lithosphere, Te, at t = 100 Ma after rifting. The maximum amount of thermal subsidence generated decreases with increasing Te.

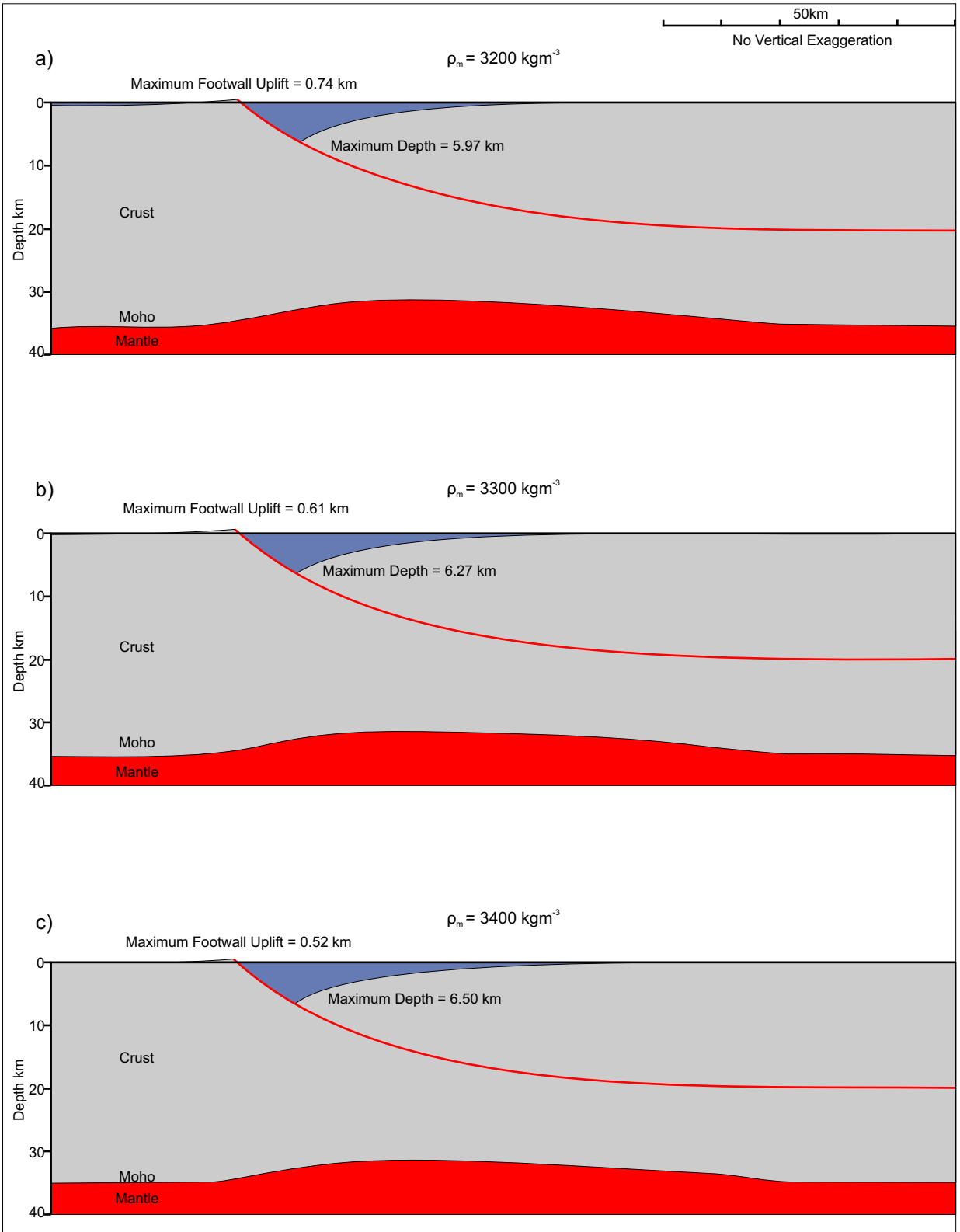


Figure C5.38. The effect of increasing the density of the mantle, $\rho_m$, at time t=0Ma after extension. An increase in mantle density results in a smaller amount of flexural uplift being generated resulting in a deeper basin.

a)

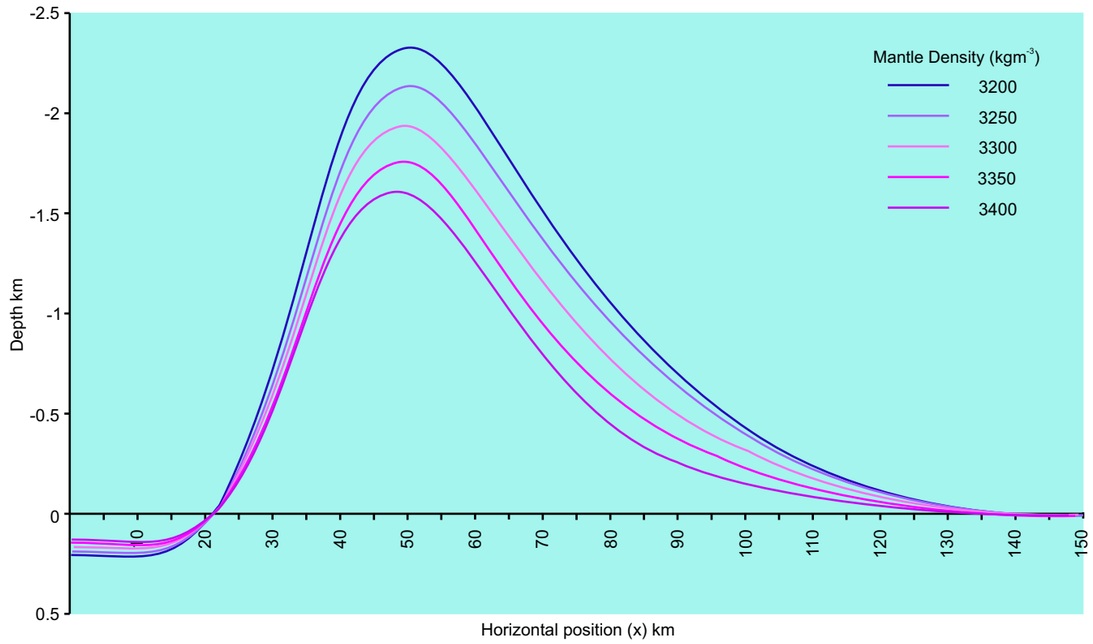


b)

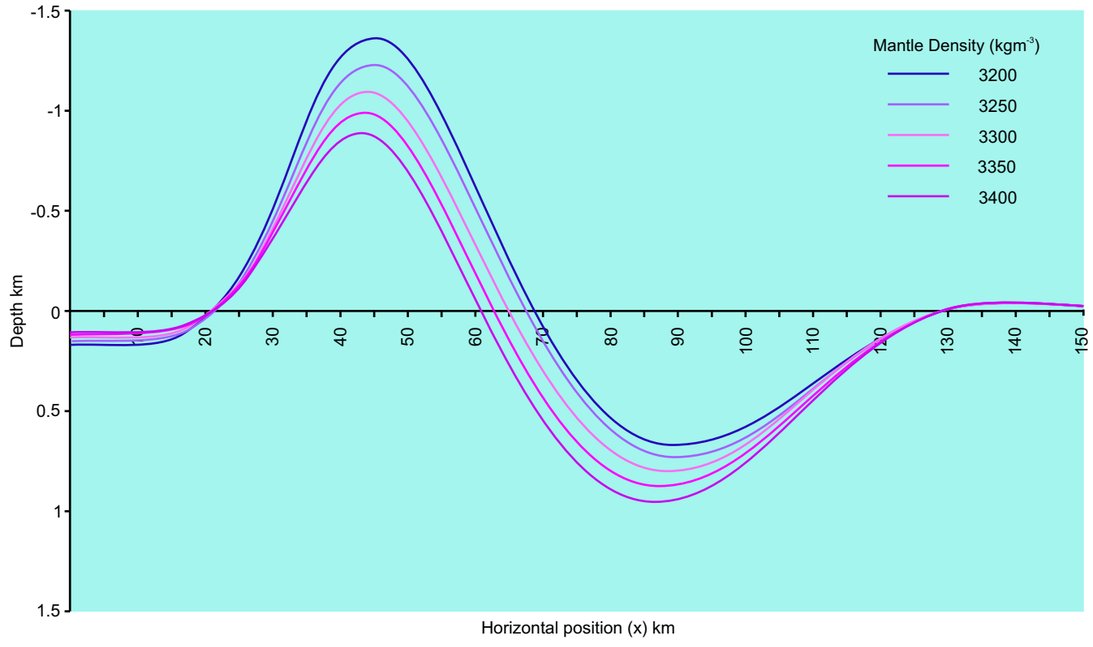


c)

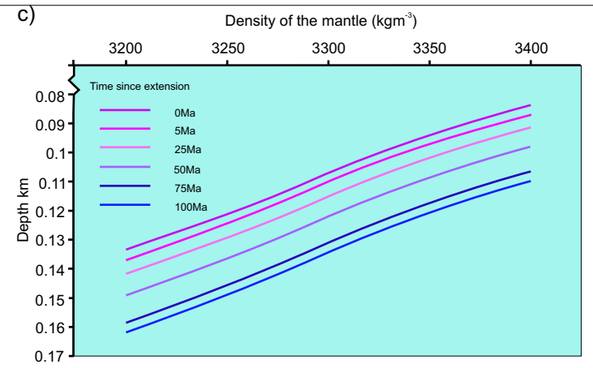


At x = 15 km, the flexural response to rifting generates subsidence in the footwall, creating a basin. The amount of subsidence generated increases with decreasing mantle density, such that the amount of subsidence increases by 0.00025 km per 1 $kgm^{-3}$ decrease in mantle density.

d)

The amount of footwall uplift generated decreases with increasing mantle density. At x=30km there is an average decrease of 0.0011 km for every 1$kgm^{-3}$ increase in mantle density adjacent to the fault.

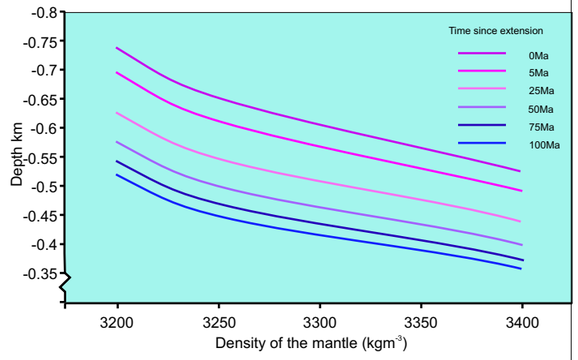


e)

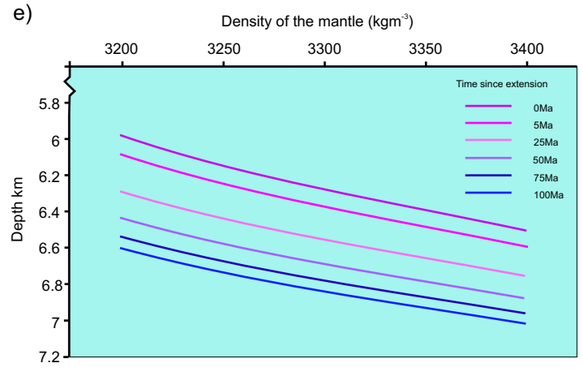


At its deepest, adjacent to the fault at x = 40 km, the basin increases in depth by 0.0026 km per 1 $kgm^{-3}$ increase in mantle density at time t=0Ma after rifting.
The rate of subsidence deceases with increasing mantle density. At a mantle density of 3200 $kgm^{-3}$, the rate of subsidence between 0 and 100 Ma is 0.0061 $kmMa^{-1}$. This is reduced to 0.0051 $kmMa^{-1}$ at a mantle density of 3400 $kgm^{-3}$ .

f)

In a distal part of the basin, at x = 75 km, the rate of subsidence deceases with increasing mantle density. At a mantle density of 3200 $kgm^{-3}$, the rate of subsidence between 0 and 100 Ma is 0.0164 $kmMa^{-1}$. This is reduced to 0.0136 $kmMa^{-1}$ at a mantle density of 3400 $kgm^{-3}$ .

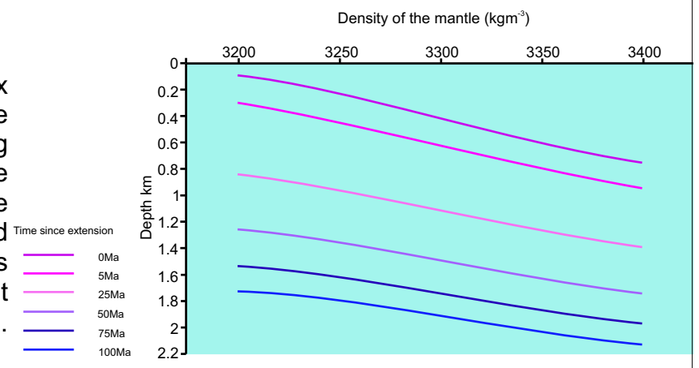


Figure C5.39. The effect of increasing the density of the mantle, $\rho_m$, upon the flexural isostatic response to lithosphere extension and basin development. a) Profiles for varying $\rho_m$ at t = 0 Ma. b) Profiles showing the cumulative flexural response at t = 100 Ma. c) The depth to the basement with increasing mantle density over time at horizontal position x = 15 km. d) The footwall uplift generated adjacent to the fault at x = 30 km. e) The depth of the basin at x = 40 km over time with varying mantle density. f) The depth of the basin over time at x = 75 km.

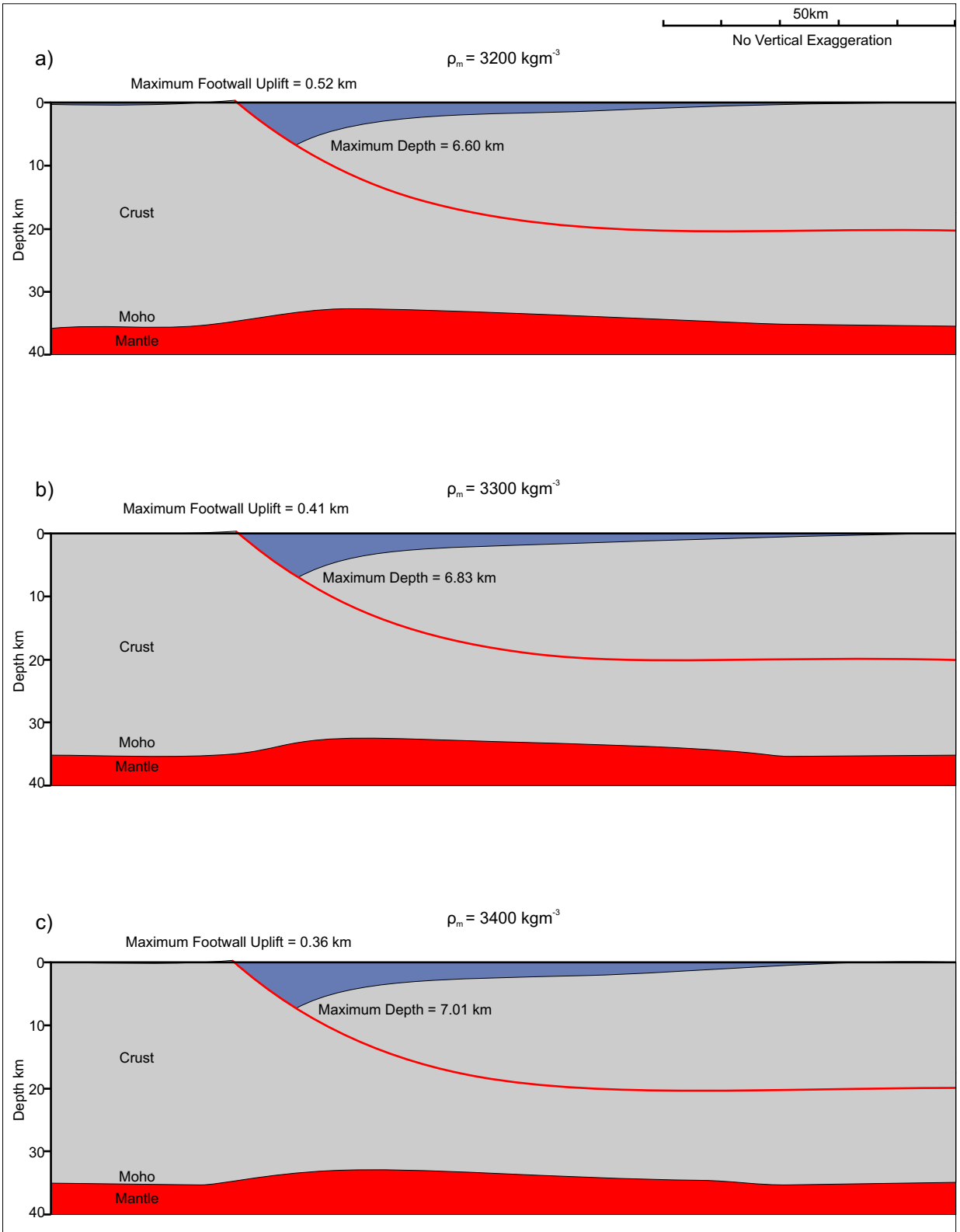


Figure C5.40. The effect of increasing the density of the mantle, $\rho_m$, at time t=100Ma after extension. An increase in mantle density results in a smaller amount of flexural subsidence being generated reducing the effect of mantle density on basin evolution.

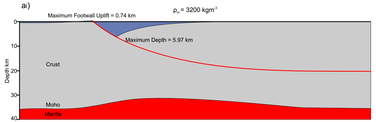


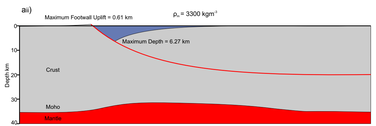


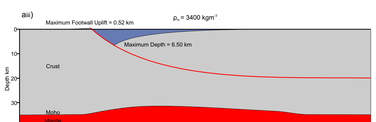


Figure C5.41a. The effect of increasing the density of the mantle, $\rho_m$, at t=0Ma after extension. An increase in mantle density results in a smaller amount of flexural uplift being generated resulting in a deeper basin.

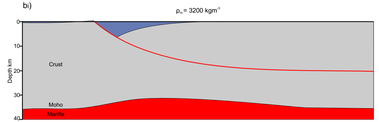


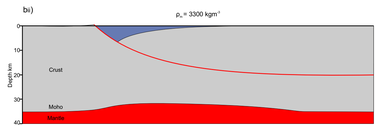


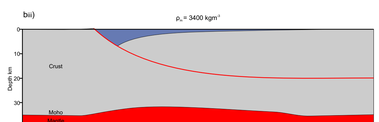


Figure C5.41b. The effect of increasing the density of the mantle, $\rho_m$, at t=5Ma after extension. An increase in mantle density results in a smaller amount of flexural subsidence being generated.

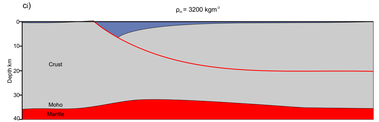


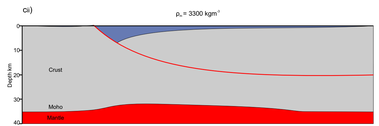


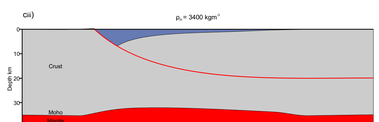


Figure C5.41c.The effect of increasing the density of the mantle, $\rho_m$, at t=25Ma after extension. The sag basin resulting from thermal subsidence is offset from the main faulting related depocentre, this results in increased subsidence in distal parts of the basin.

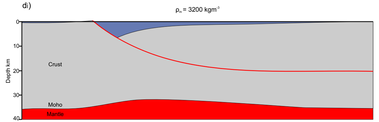


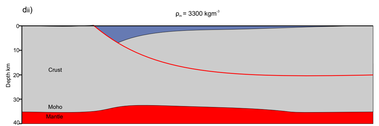


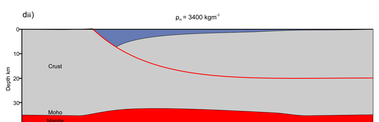


Figure C5.41d. The effect of increasing the density of the mantle, $\rho_m$, at t=50Ma after extension.

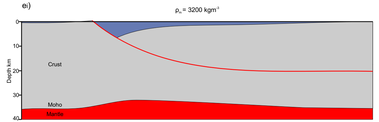


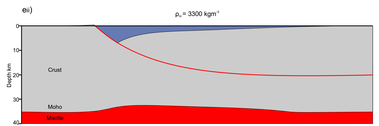


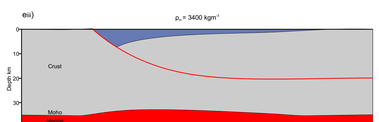


Figure C5.41e. The effect of increasing the density of the mantle, $\rho_m$, at t=75Ma after extension. The amount of thermal subsidence generated decreases over time.

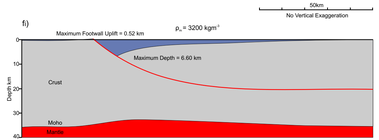


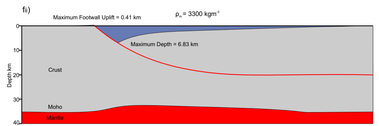


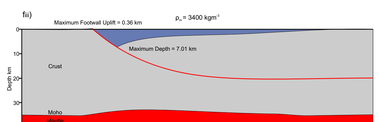


Figure C5.41f. The effect of increasing the density of the mantle, $\rho_m$, at t=100Ma after extension. The reduction in the amount of flexural subsidence being generated with increasing mantle density reduces the overall effect of mantle density on basin evolution.

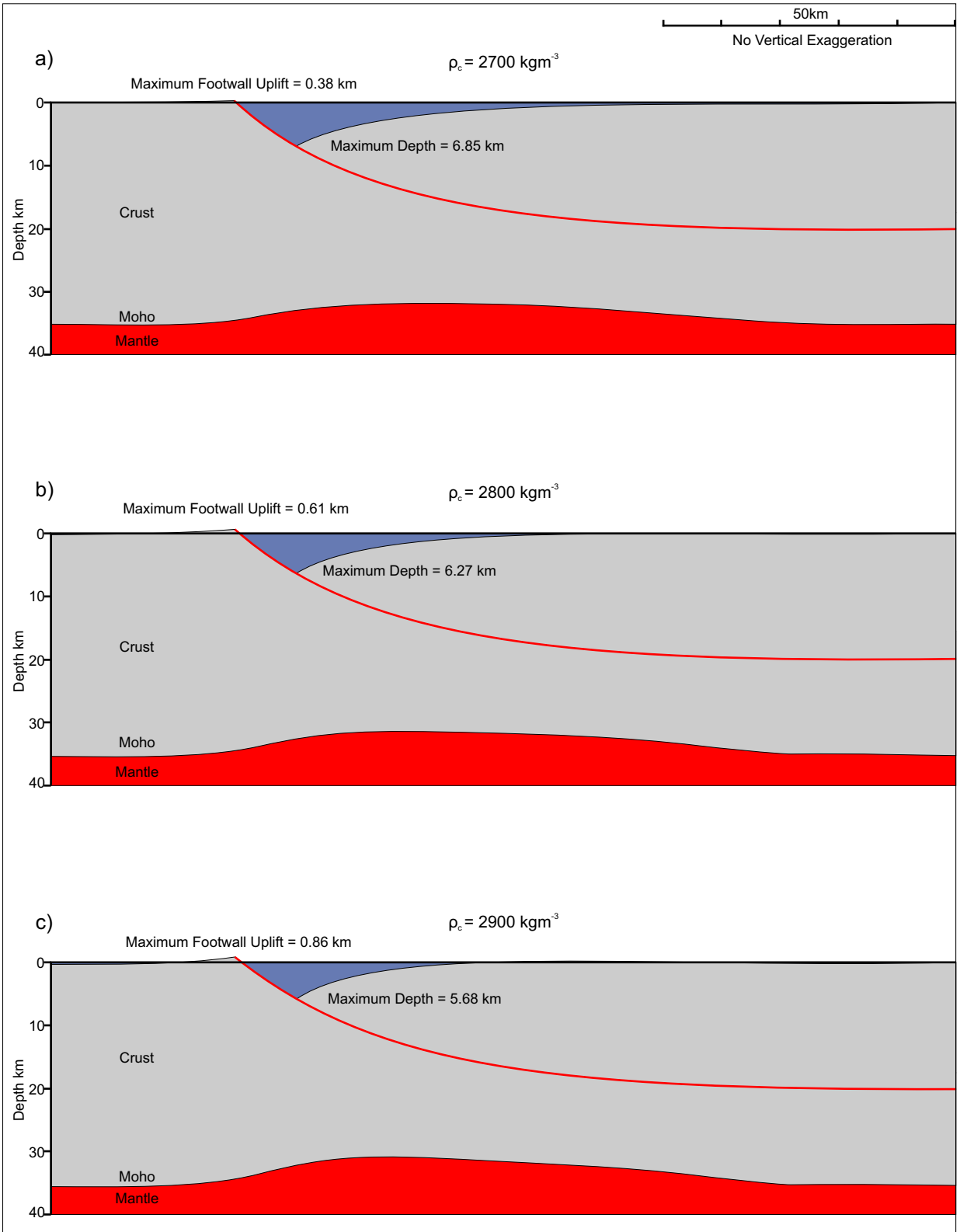


Figure C5.42. The effect of increasing the density of the crust, $\rho_c$, at time t=0Ma after extension. An increase in crustal density results in a greater amount of flexural uplift being generated, resulting in a shallower basin.

a)

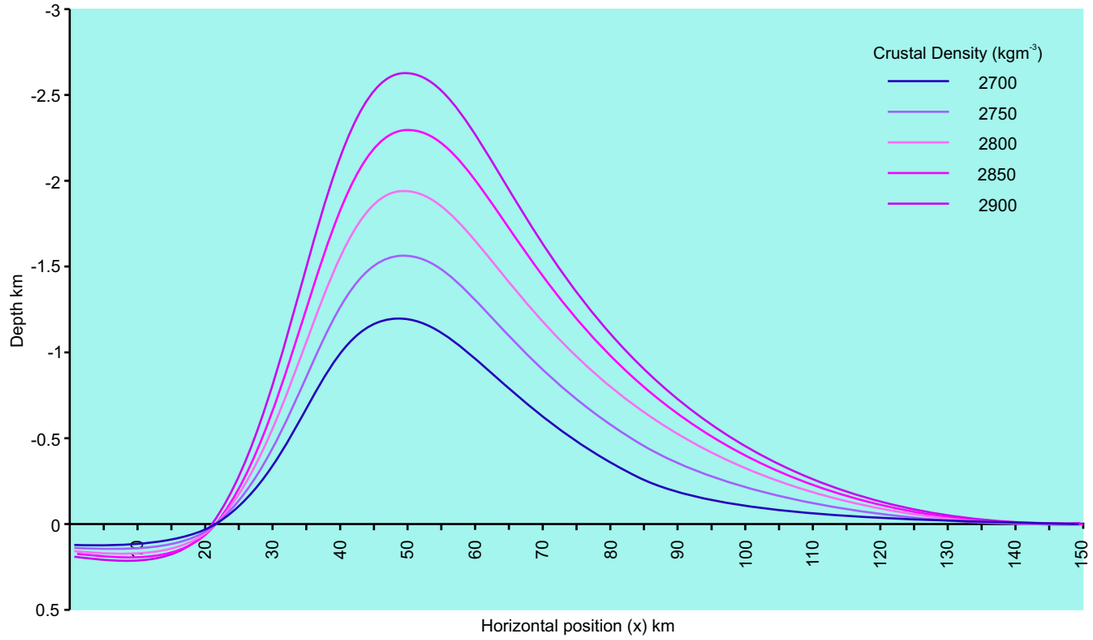


b)

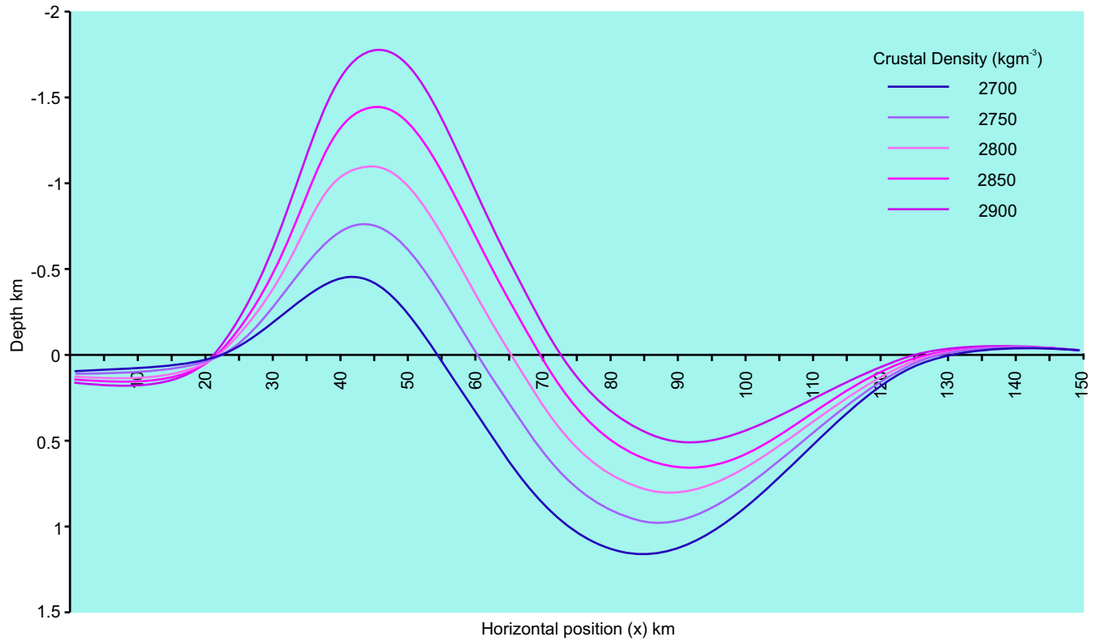


c)

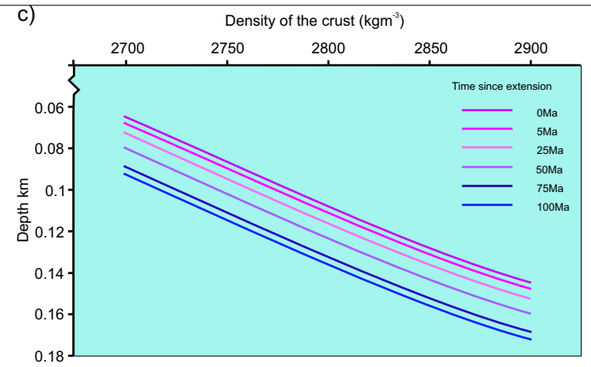


At location x = 15 km in the footwall, subsidence in front of the fault, before the footwall uplift, decreases with increasing crustal density, with an increase of 0.0004 km per 1 kgm$^{-3}$ increase in density.

d)

At x = 30 km, the amount of footwall uplift generated in response to faulting increases with increasing crustal density, with an increase of 0.0024 km per 1 kgm$^{-3}$ increase in crustal density.

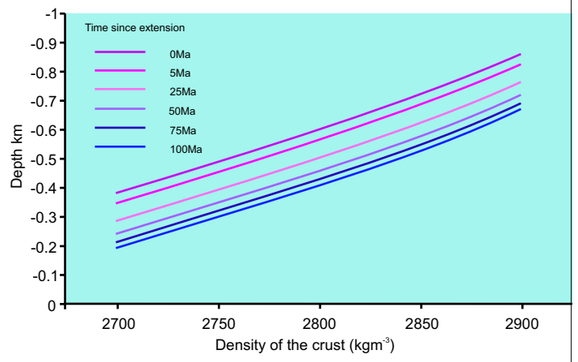


e)

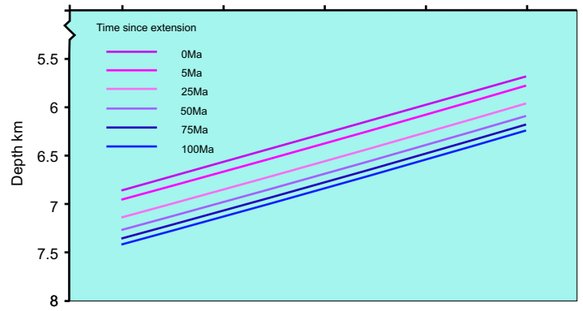


At x = 40 km, where the maximum basin depth is achieved, there is a decrease in basin depth of 0.0069 km for every 1 kgm$^{-3}$ increase in crustal density.

f)

At x = 75 km, in a more distal position within the basin, there is a decrease in basin depth of 0.0041 km for every 1 kmg$^{-3}$ increase in crustal density.

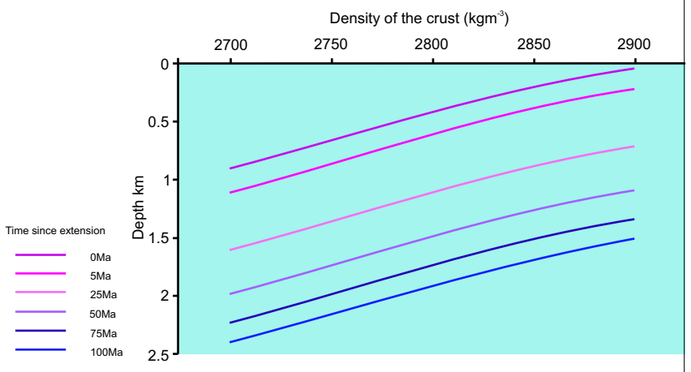


Figure C5.43. The effect of increasing the density of the crust, $\rho_c$, upon the flexural isostatic response to extension and basin development. a) Profiles showing the overall flexural response at t = 0 Ma. b) Profiles showing the cumulative flexural response at t = 100 Ma. c) The depth to the basement with increasing crustal density over time at horizontal position x = 15 km. d) The footwall uplift generated adjacent to the fault at x = 30 km. e) The depth of the basin at x = 40 km over time with varying crustal density. f) The depth of the basin over time at x = 75 km.

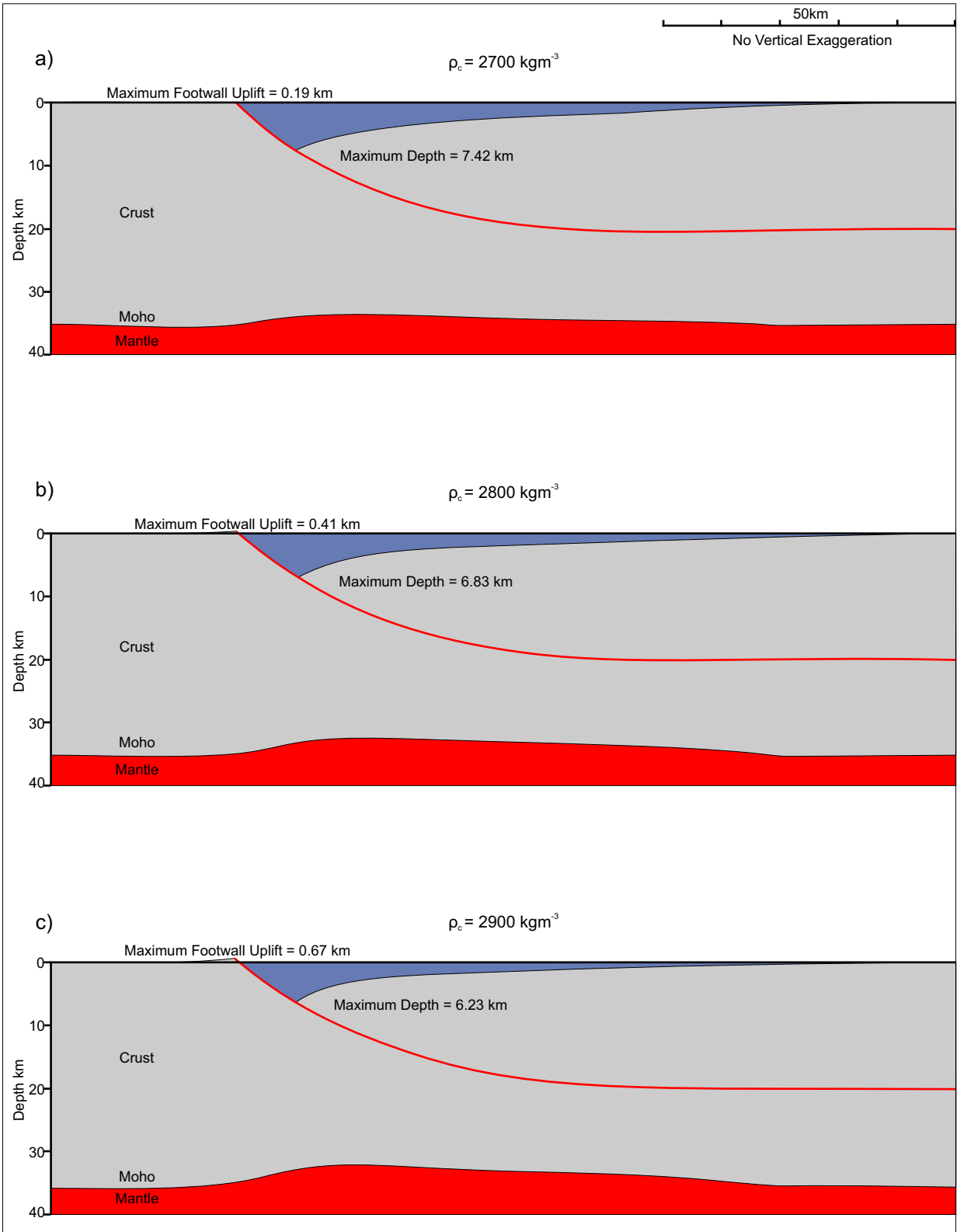


Figure C5.44. The effect of increasing the density of the crust, $\rho_c$, at time t=100Ma after extension. Increasing the crustal density, decreases basin depth as a result of the flexural response to extension at t=0Ma. Varying crustal density does not influence the amount of thermal subsidence being generated.

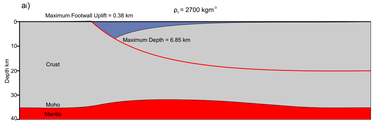


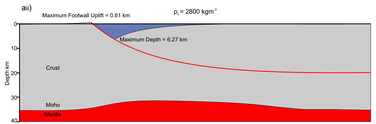


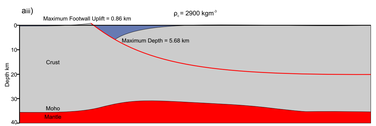


Figure C5.45a. The effect of increasing the density of the crust, $\rho_c$, at t=0Ma after extension. An increase in mantle density results in a greater amount of flexural uplift being generated resulting in a shallower basin.

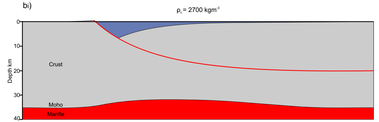


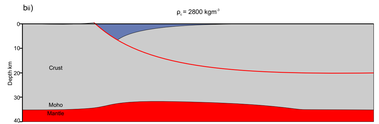


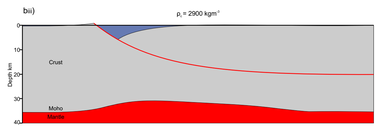


Figure C5.45b. The effect of increasing the density of the crust, $\rho_c$, at t=5Ma after extension. Increasing the crustal density, increases basin depth as a result of the flexural response to extension at t=0Ma. Varying crustal density does not influence the amount of thermal subsidence being generated.

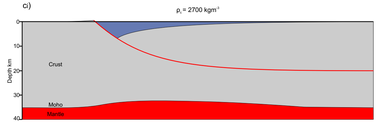


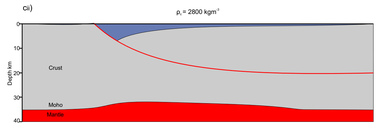


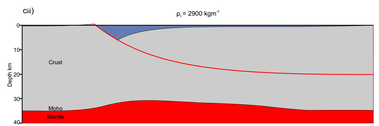


Figure C5.45c.The effect of increasing the density of the crust, $\rho_c$, at t=25Ma after extension. Thermal subsidence deepens the basin by the same amount as it is independent of crustal density.

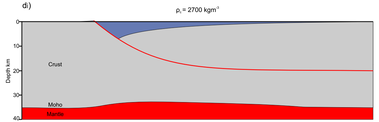


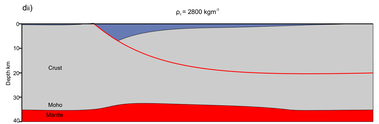


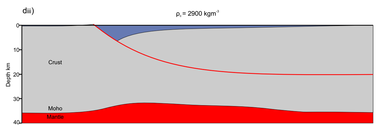


Figure C5.45d. The effect of increasing the density of the crust, $\rho_c$, at t=50Ma after extension. The thermal subsidence sag basin is offset from the fault induced subsidence.

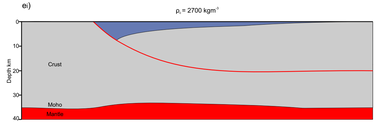


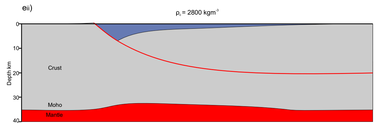


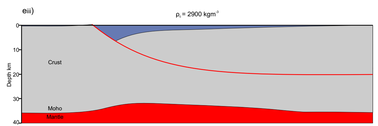


Figure C5.45e. The effect of increasing the density of the crust, $\rho_c$, at t=75Ma after extension. The amount of thermal subsidence generated reduces over time.

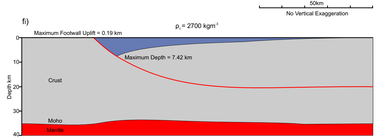


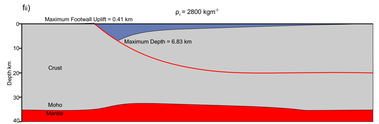


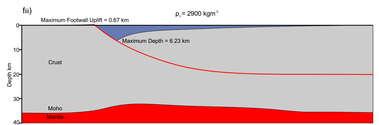


Figure C5.45f. The effect of increasing the density of the crust, $\rho_c$, at t=100Ma after extension. The difference in basin depth at t=100Ma, as a result of increasing the crustal density, is the same as the difference in basin depth at t=0Ma.

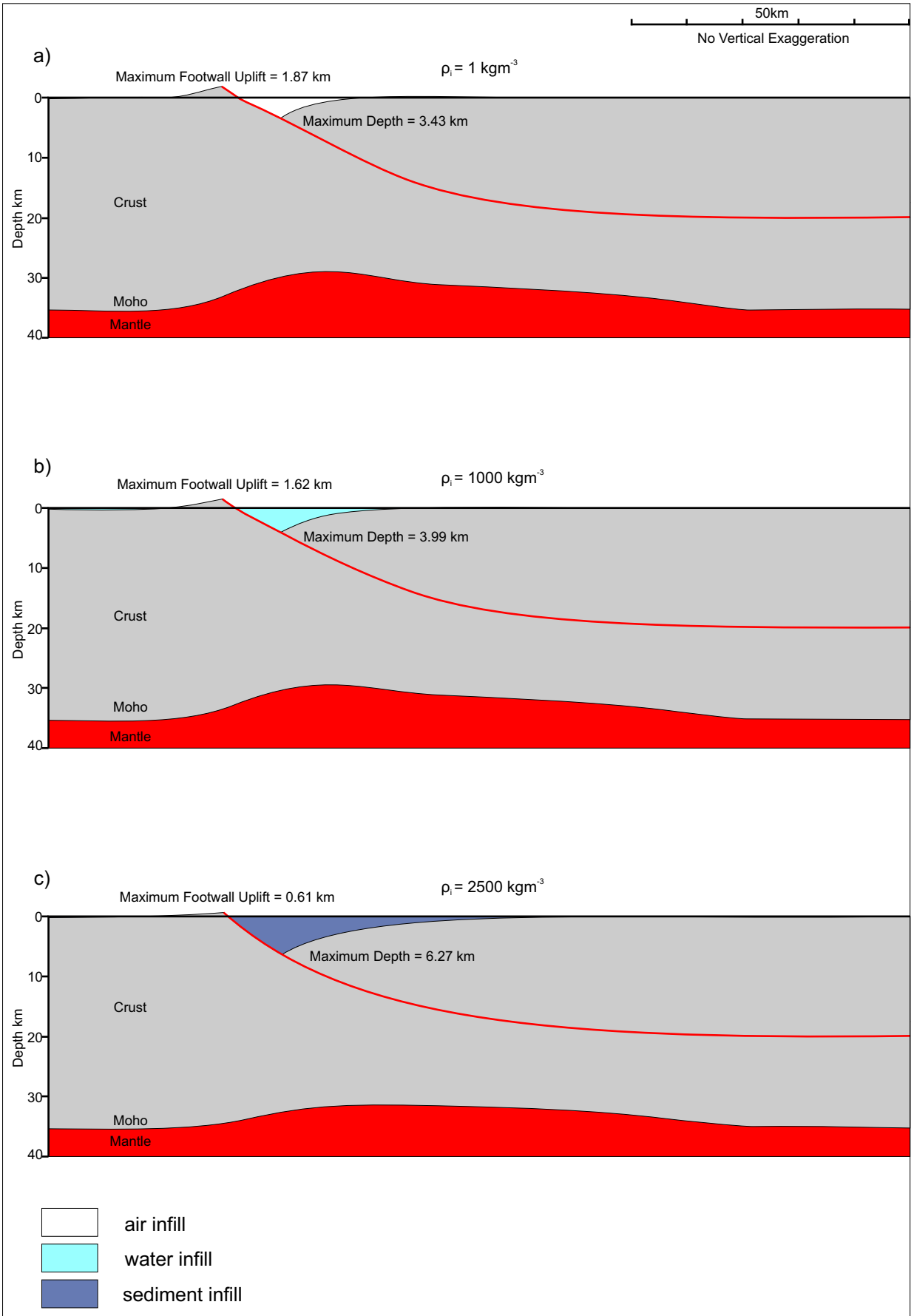


Figure C5.46.The effect of increasing the density of the basin infill, $\rho_i$, at time t=0Ma after extension. An increase in infill density results in a greater amount of flexural subsidence being generated resulting in a deeper basin.

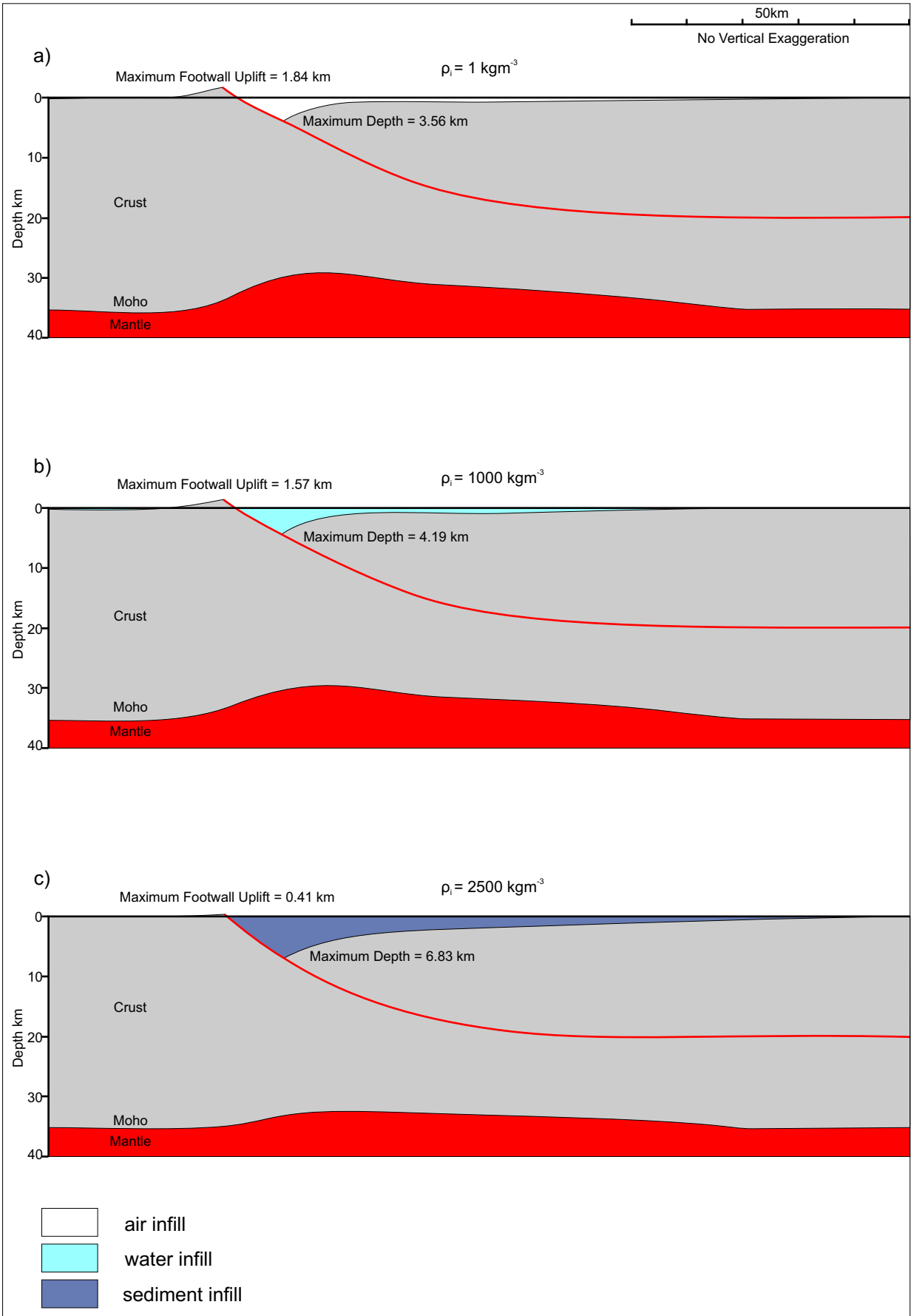


Figure C5.47.The effect of increasing the density of the basin infill, $\rho_i$, at time t=100Ma after extension. An increase in infill density results in a greater amount of flexural subsidence being generated, resulting in a deeper basin.

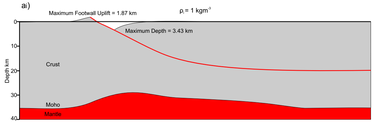


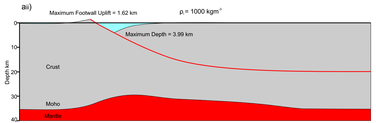


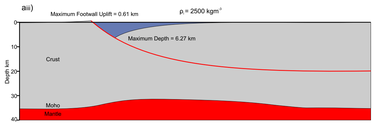



Figure C5.48a. The effect of increasing the density of the basin infill, $\rho_i$, at t=0Ma after extension. ai) air infill $\rho_i$ =1kgm$^{-3}$. b) water infill $\rho_i$ = 1000kgm$^{-3}$. c) sediment infill $\rho_i$ = 2500kgm$^{-3}$. With increasing infill density the basin becomes deeper and footwall uplift is reduced.

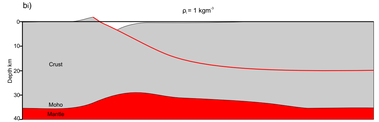


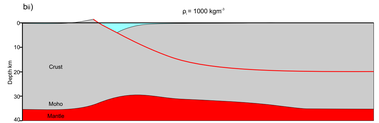


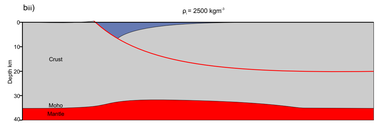


Figure C5.48b. The effect of increasing the density of the basin infill, $\rho_i$, at t=5Ma after extension. Infilling the basin with water or sediment increases the flexural response to thermal subsidence as it imposes an additional load.

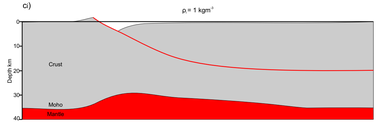


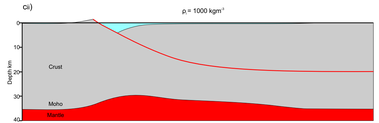


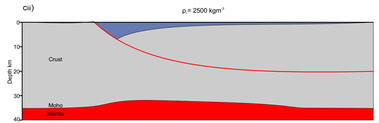


Figure C5.48c.The effect of increasing the density of the basin infill, $\rho_i$, at t=25Ma after extension. The effect of increasing the infill density increases over time as the thermal subsidence is loaded and isostatically compensated for.

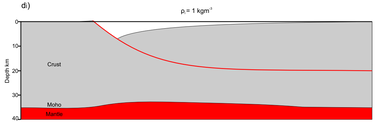


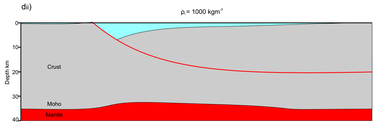


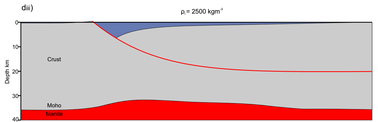


Figure C5.48d. The effect of increasing the density of the basin infill, $\rho_i$, at t=50Ma after extension.

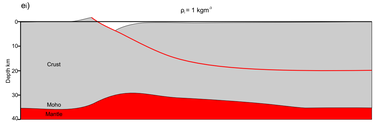


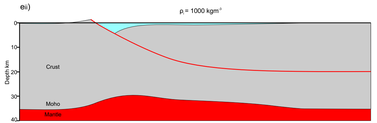


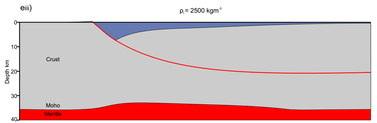


Figure C5.48e. The effect of increasing the density of the basin infill, $\rho_i$, at t=75Ma after extension.

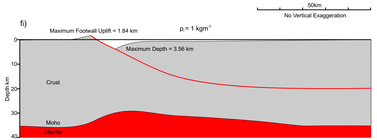


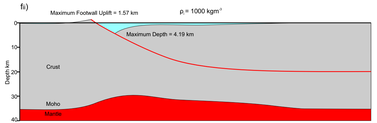


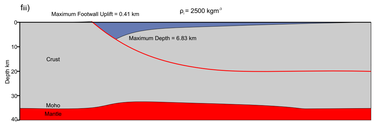


Figure C5.48f. The effect of increasing the density of the basin infill, $\rho_i$, at time t=100Ma after extension. The distal basin depth increases with increasing infill density as the thermal subsidence is loaded by the infill and compensated for.

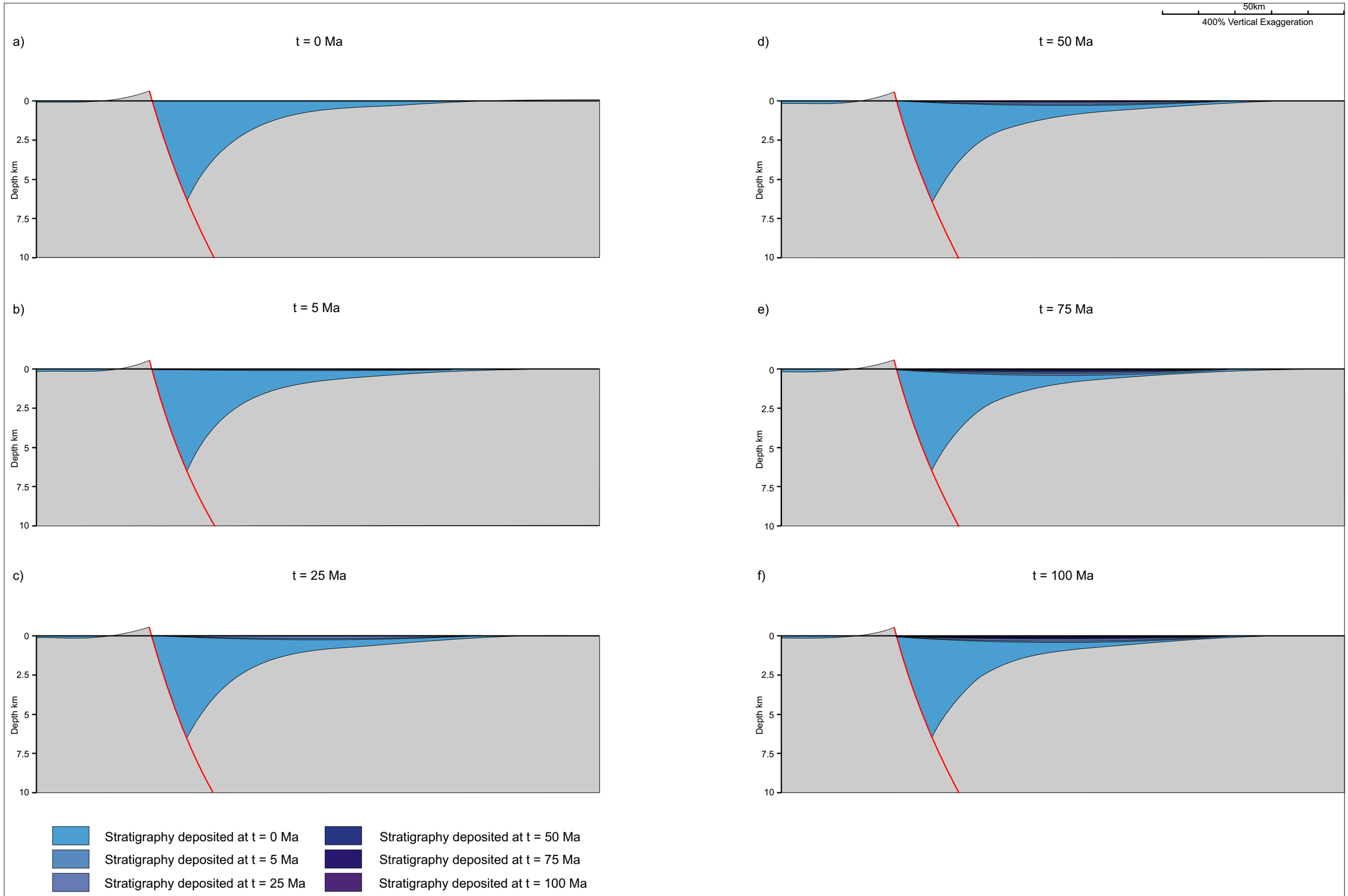


Figure C5.49. Development of basin stratigraphy over time. a) t = 0 Ma after rifting. b) t = 5 Ma after rifting. c) t = 25 Ma after rifting. d) t = 50 Ma after rifting. e) t = 75 Ma after rifting. f) t = 100 Ma after rifting. The basin is assumed to be filled to the sea level datum after each period of subsidence and the effects of compaction are ignored. The amount of subsidence produced decreases over time, as such the thickness of the stratigraphic units decreases over time.

a)

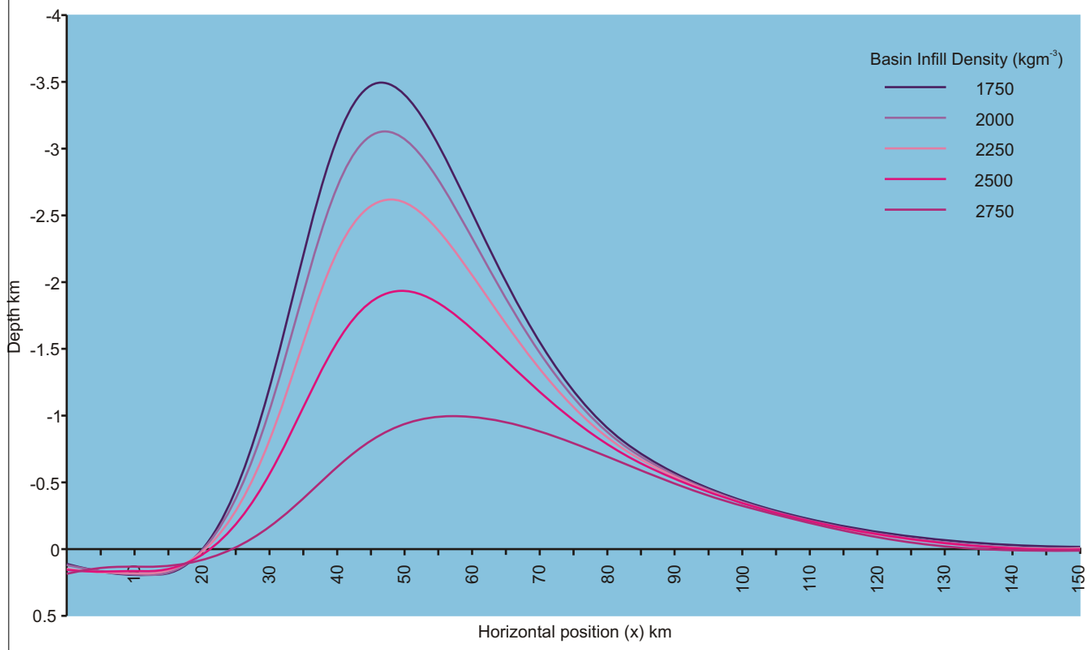


b)

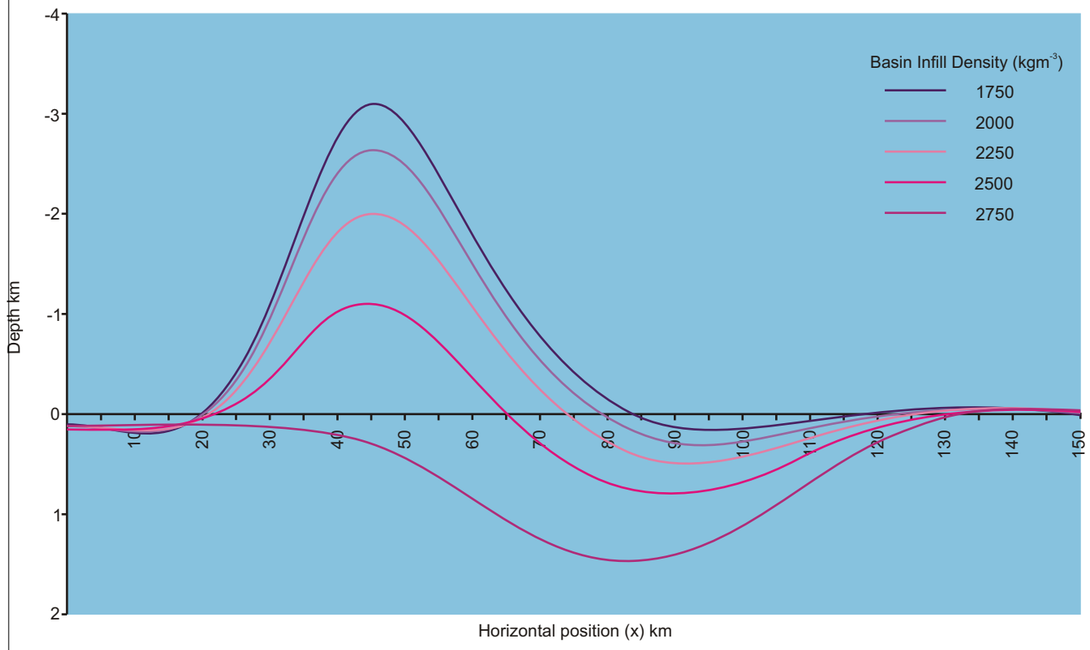


c)

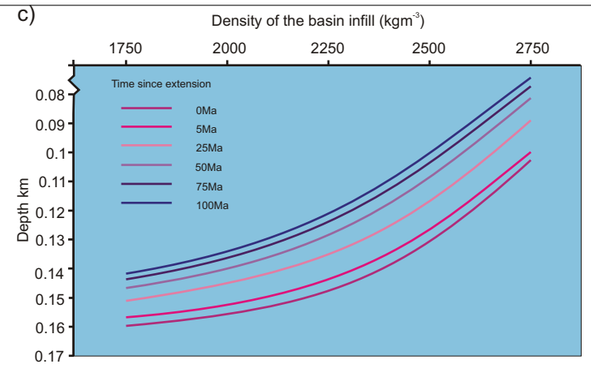


Subsidence in the footwall, before the footwall uplift, decreases with increasing sediment density, with an decrease of 0.00006 km per 1 kgm$^{-3}$ increase in density at x = 15 km.

d)

At x = 30 km, the amount of footwall uplift generated in response to faulting decreases with increasing sediment density, with a decrease of 0.001km per 1 kgm$^{-3}$ increase in sediment density adjacent to the fault.

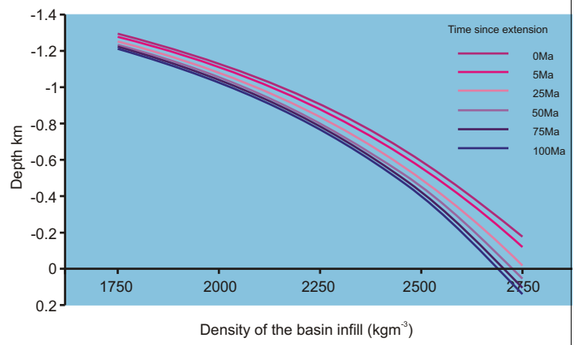


e)

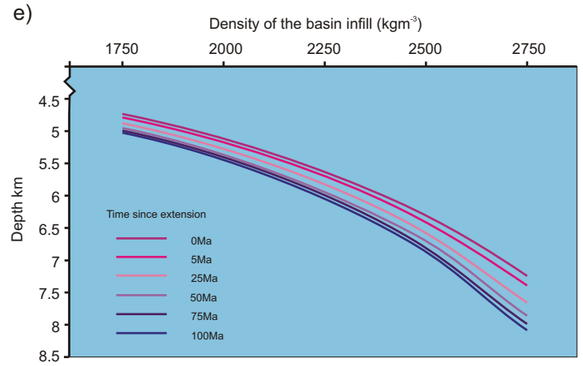


At x = 40 km, where the maximum basin depth is achieved, there is an increase in basin depth of 0.003km for every 1 kgm$^{-3}$ increase in sediment density.

f)

At x = 75 km, in a more distal position within the basin, there is an increase in basin depth of 0.0017 km for every 1 kgm$^{-3}$ increase in sediment density.

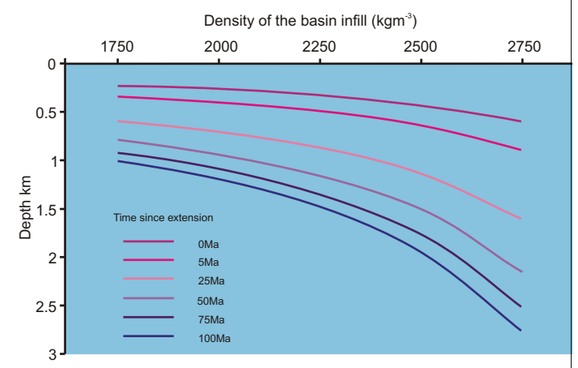


Figure C5.50. The effect of increasing the density of the sediment, $\rho_s$, upon the flexural isostatic response to extension and basin development. a) Profiles showing the flexural response at t = 0 Ma. b) Profiles showing the cumulative flexural response at t = 100 Ma. c) The depth to the basement with increasing sediment density over time at horizontal position x = 15 km. d) The footwall uplift generated adjacent to the fault at x = 30 km. e) The depth of the basin at x = 40 km, the deepest part of the basin, over time with varying sediment density. f) The depth of the distal part of the basin over time at x = 75

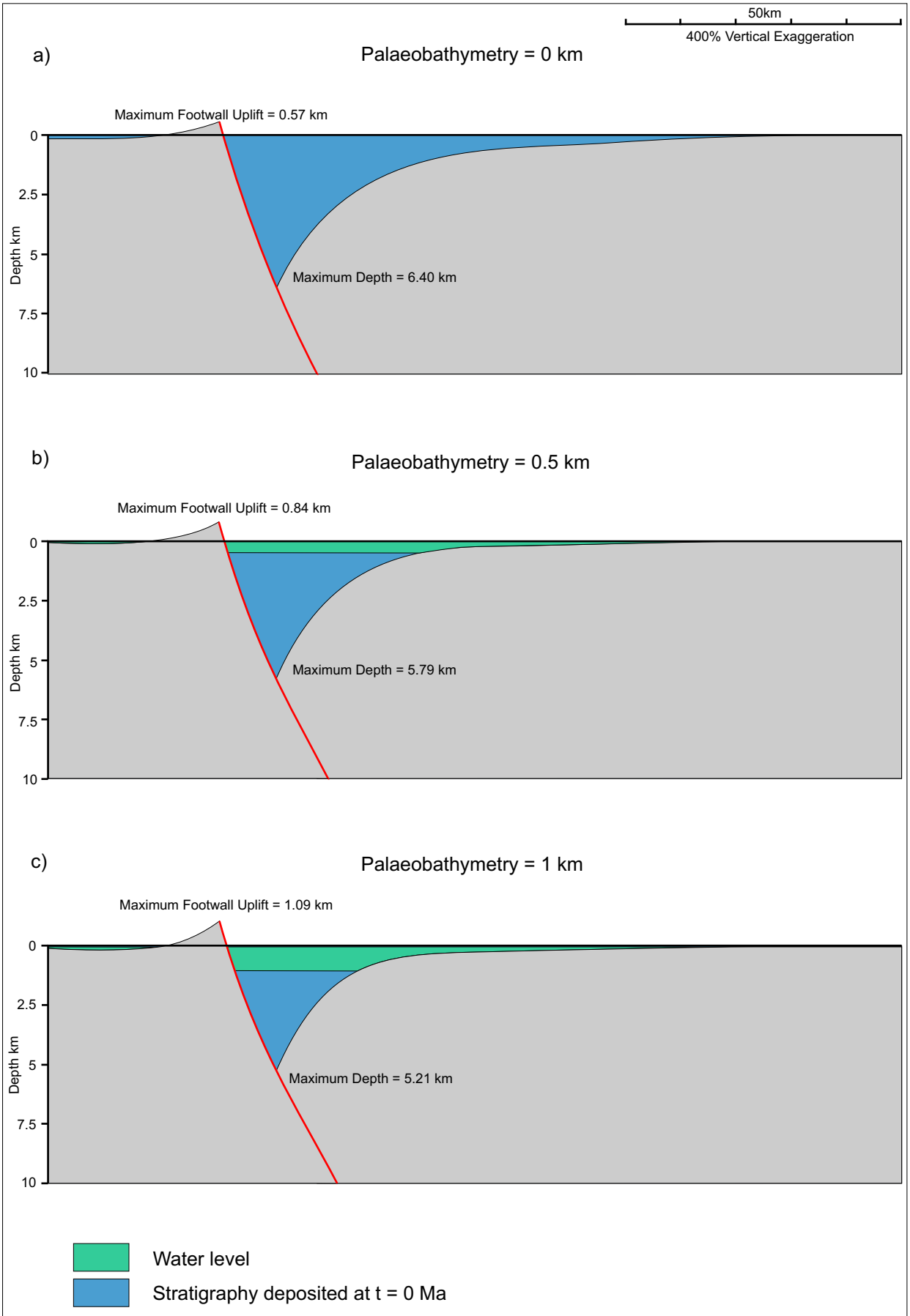


Figure 5.51. The effect of increasing the palaeobathymetry on basin development at time, t = 0 Ma after extension. With increasing palaeobathymetry, the basin depth decreases and footwall uplift increases as less subsidence is generated by infilling of the basin. The width of the sedimentary infill within the basin also decrease with increasing palaeo-bathymetry.

a)

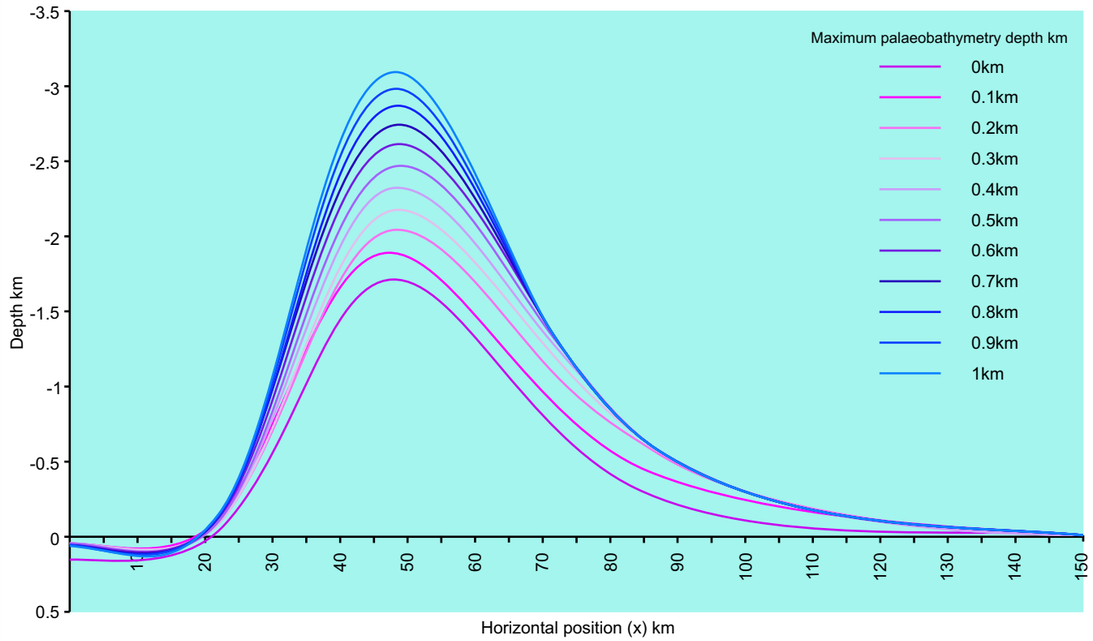


b)

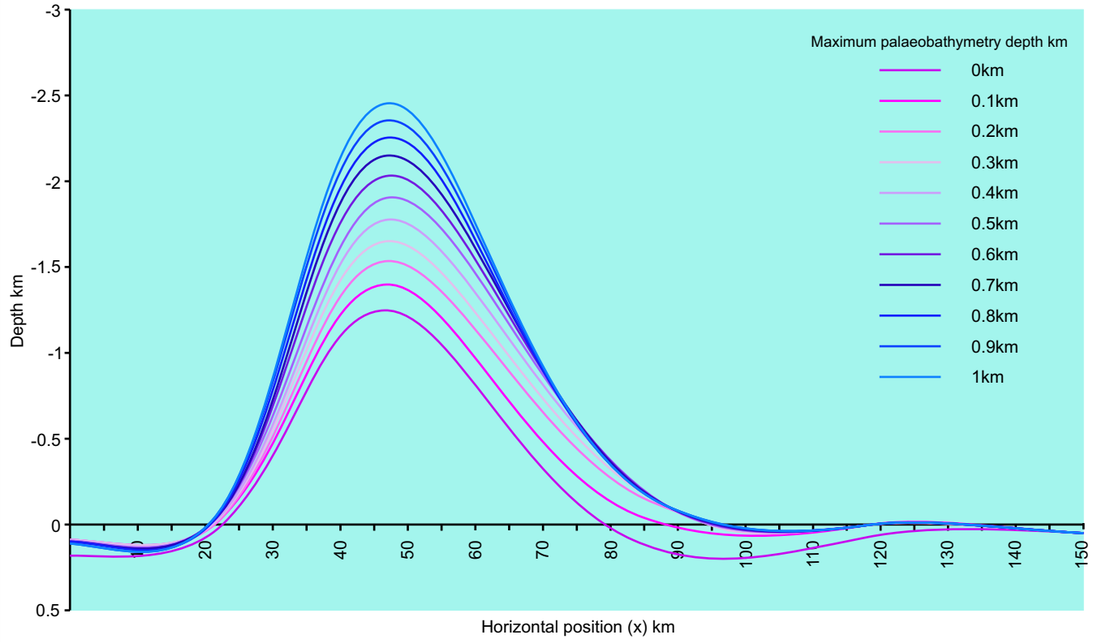


c)

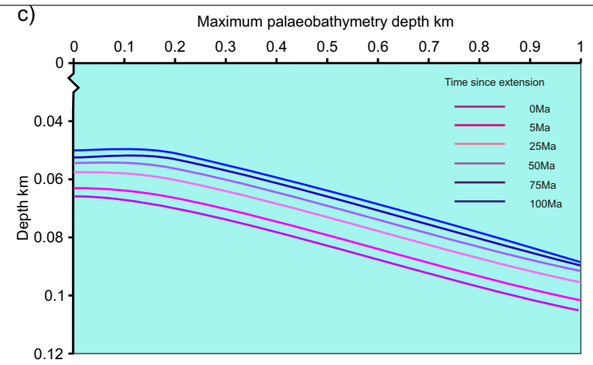


At x = 15 km, the flexural response to rifting generates subsidence in the footwall, creating a basin. The amount of subsidence generated decreases with increasing depth of palaeobathymetry, such that the amount of subsidence decreases by 0.003 km per 100m increase in palaeobathymetry depth.

d)

The amount of footwall uplift increases with increasing palaeobathymetry depth as a result of reduced subsidence. At x=30km there is an average increase of 0.051 km for every 100m increase in palaeobathymetry adjacent to the fault.

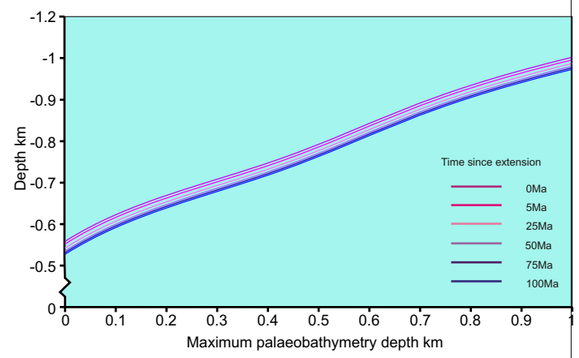


e)

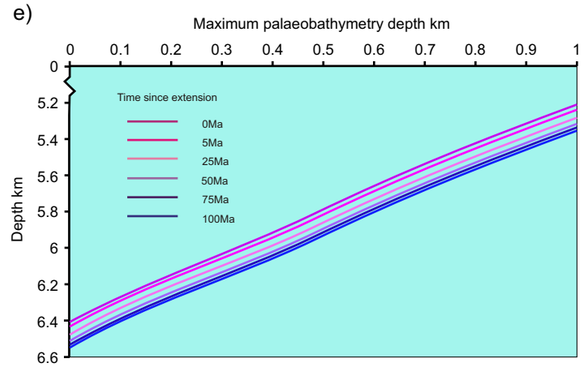


At its deepest, adjacent to the fault at x = 40 km, the basin decreases in depth by 0.119 km per 100m increase in the palaeobathymetry depth.

f)

In a distal part of the basin, at x=75 km, the amount of subsidence deceases with palaeobathymetry at low values of palaeobathymetry depth, of up to 500m. The basin depth decreases by 0.049 km for every 100m increases in palaeo-bathyetry. At greater palaeobathymerty depths, the effect on the basin is diminished, with little affect in the basin depth at this point in the basin.

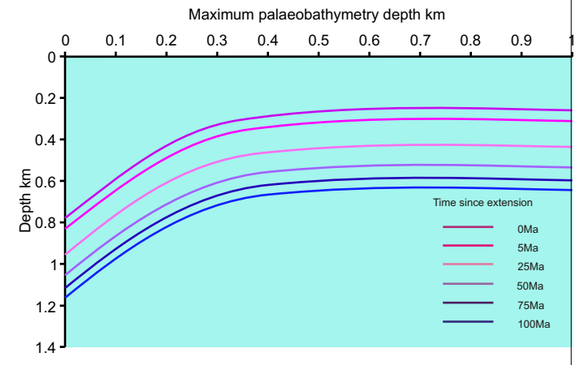


Figure 5.52. The effect of increasing the maximum palaeobathymetry upon the flexural isostatic response to extension and basin development. a) Profiles showing the flexural response at t = 0 Ma. b) Profiles showing the cumulative flexural response at t = 100 Ma. c) The depth to the basement with increasing palaeobathymetry over time at horizontal position x = 15 km. d) The footwall uplift generated adjacent to the fault at x = 30 km. e) The depth of the basin at x = 40 km over time with varying palaeobathymetry. f) The depth of the basin over time at x = 75 km.

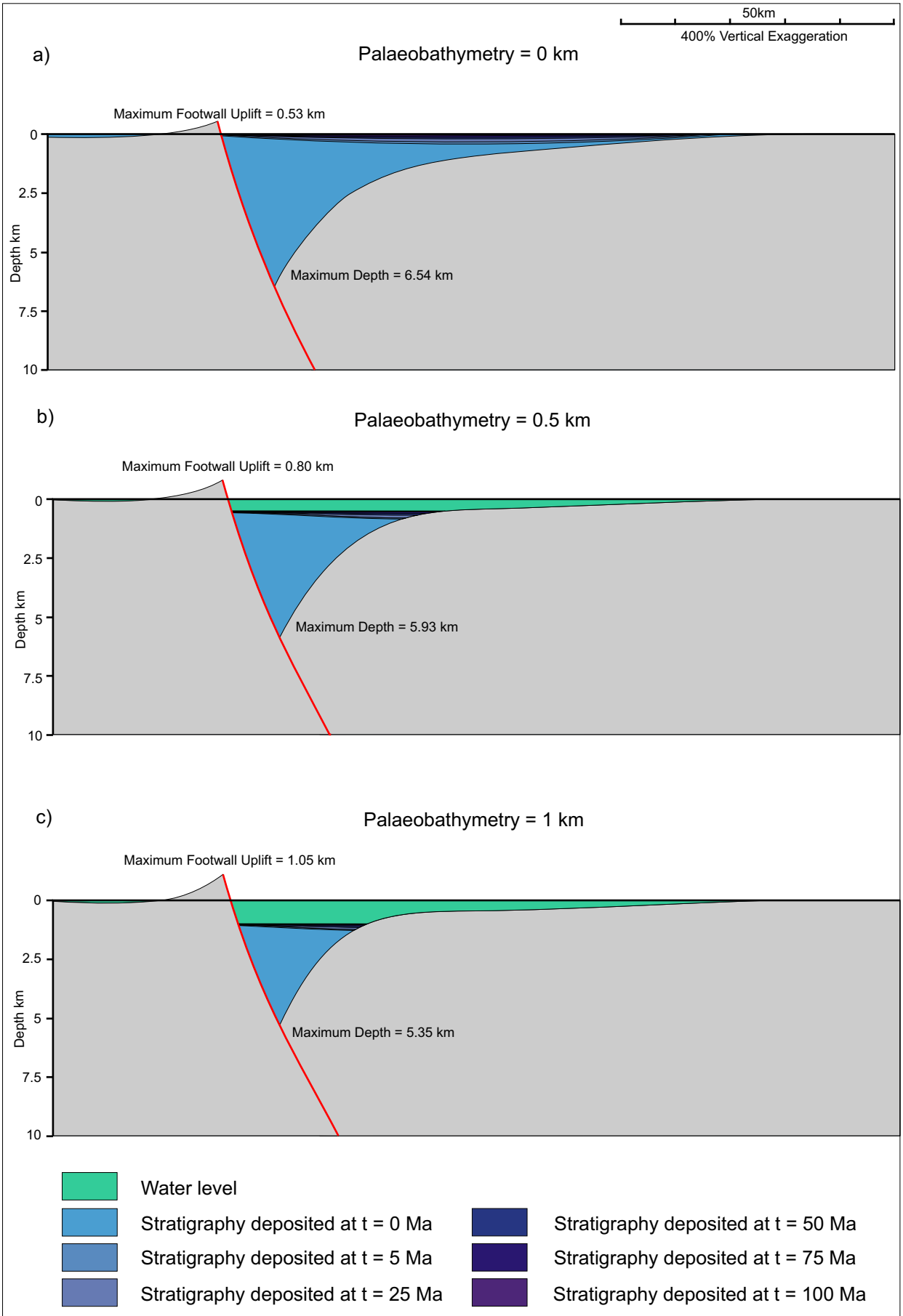


Figure C5.53. The effect of increasing palaeobathymetry on basin development at time, t = 100 Ma after extension. With increasing palaeobathymetry, the basin depth decreases. The width of the sediment deposits within the basin decrease with increasing palaeo-bathymetry as the thermal subsidence is infilled by water in the distal part of the basin.

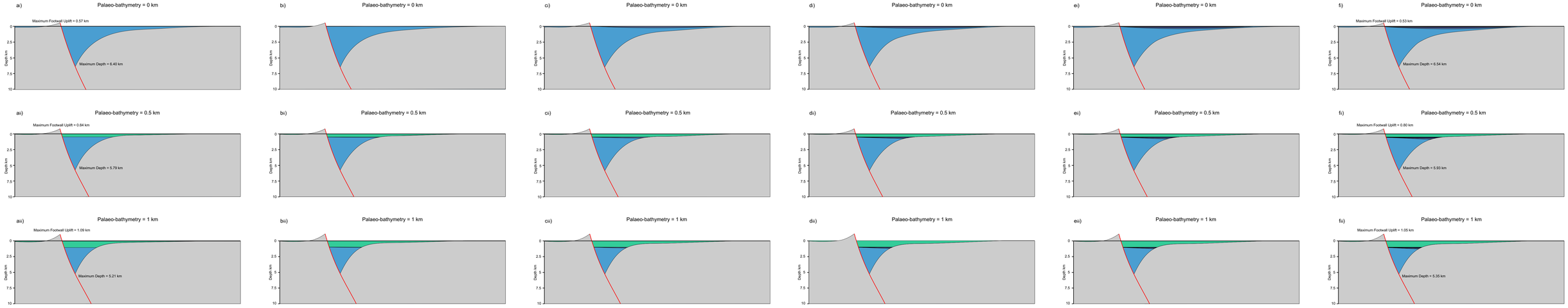


Figure C5.54a. The effect of increasing the depth of palaeo-bathymetry on basin development at time, t = 0 Ma after extension. With increasing palaeo-bathymetry, the basin depth decreases and footwall uplift increases as less subsidence is generated by infilling of the basin. The width of the sediment deposits within the basin also decrease with increasing palaeo-bathymetry.

Figure C5.54b. The effect of increasing the depth of palaeo-bathymetry on basin development at time, t = 5 Ma after extension. Once the maximum palaeo-bathymetry is achieved, additional subsidence is infilled with sediment.

Figure C5.54c.The effect of increasing the depth of palaeo-bathymetry on basin development at time, t = 25 Ma after extension. The width of the sediment deposits within the basin decrease with increasing palaeo-bathymetry as the thermal subsidence is infilled by water in the distal part of the basin.

Figure C5.54d. The effect of increasing the depth of palaeo-bathymetry on basin development at time, t = 50 Ma after extension.

Figure C5.54e. The effect of increasing the depth of palaeo-bathymetry on basin development at time, t = 75 Ma after extension.

Figure C5.54f. The effect of increasing the depth of palaeo-bathymetry on basin development at time, t = 100 Ma after extension. With increasing palaeo-bathymetry, the basin depth decreases.

a)

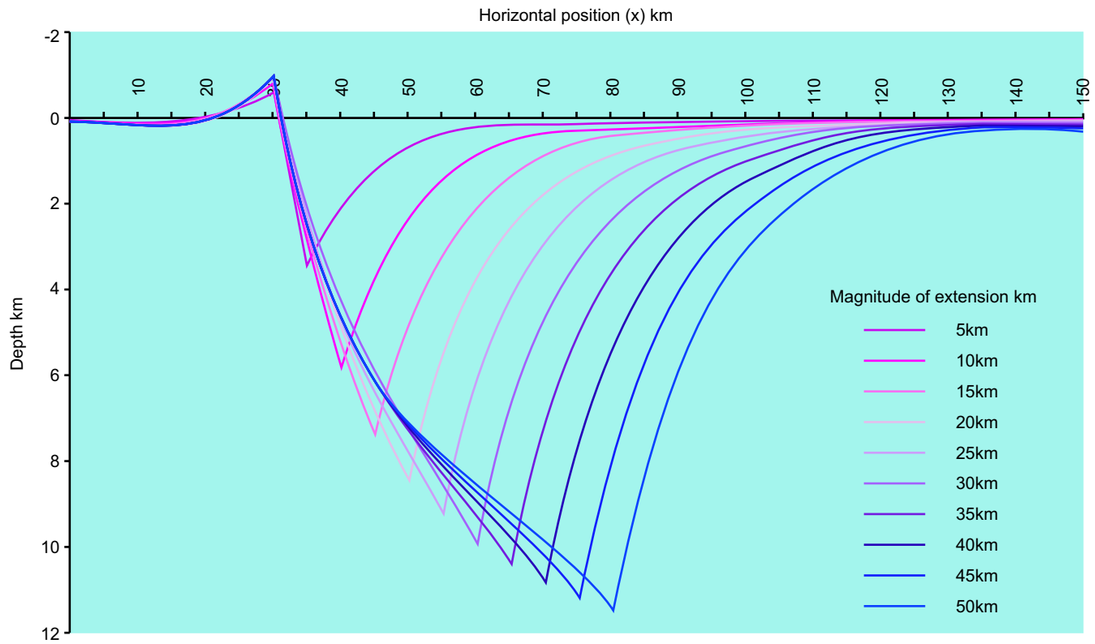


b)

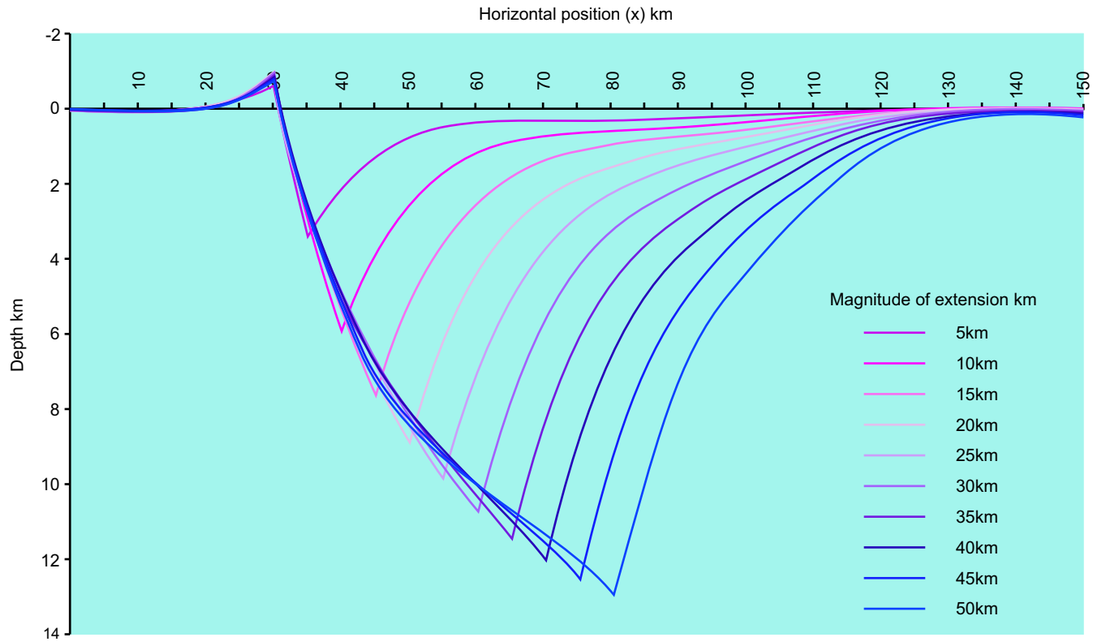


c)

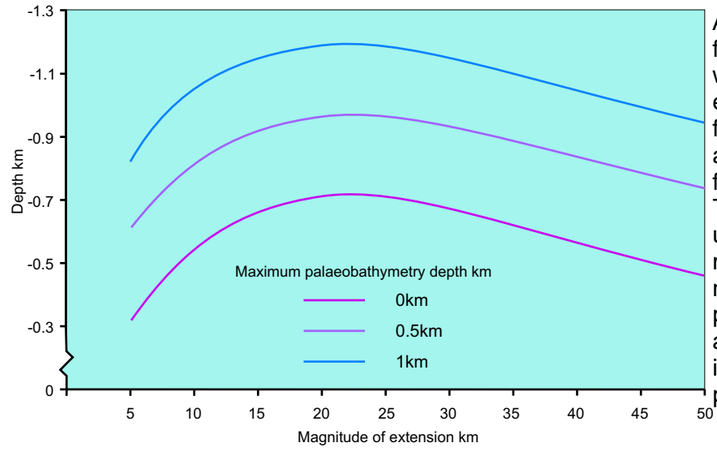


At x = 30 km, the maximum footwall uplift, initially increases with increasing magnitude of extension, after a maximum footwall uplift has been achieved at ~20km extension, the amount of footwall uplift begins to decrease. This relationship between footwall uplift and magnitude of extension remains the same with varying the maximum depth of the palaeobathymetry, however the amount of footwall uplift generated increases with increasing palaeobathymetry.

d)

The maximum basin depth increases with increasing magnitude of extension. This increase in basin depth is greater with decreasing palaeobathymetry. There is an average increase in basin depth of 0.222km per 1 km increase in extension at a palaeobathymetry of 0 km, whilst the increase in basin depth decreases to 0.198km per 1 km increase in extension when palaeobathymetry = 1 km.

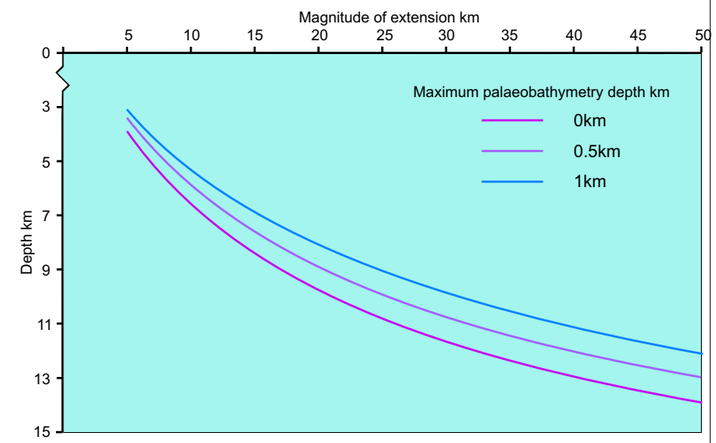


e)

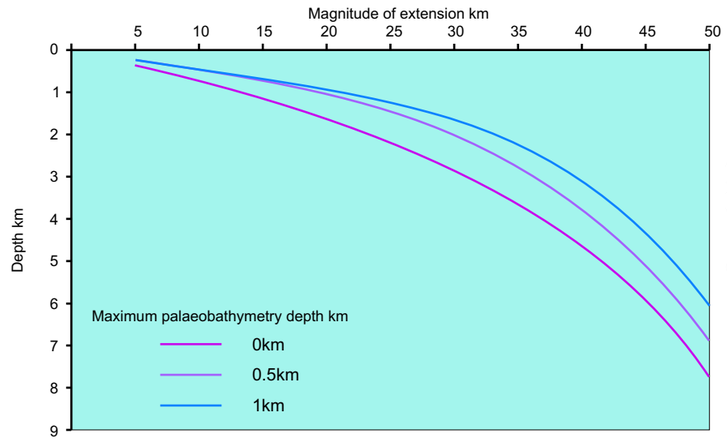


At a distal position in the basin, x=90km, the basin deepens with varying magnitude of extension. Increasing the palaeobathymetry decreases basin depth.

Figure 5.55. The effect of increasing the magnitude of extension with varying maximum palaeobathymetry upon the basin development. a) Profiles of the basin at t = 0 Ma with a maximum palaeobathymetry of 500m. b) Profiles of the basin at t = 100 Ma, with a maximum palaeobathymetry of 500m. c) The footwall uplift with increasing magnitude of extension and varying palaeobathymetry, at time, t = 100 Ma, at horizontal position x = 30 km. d) The maximum basin depth with increasing magnitude of extension and varying palaeobathymetry (x = 30 + magnitude of extension). e) The depth of the basin at x = 90 km at time, t = 100 Ma, with increasing magnitude of extension and varying palaeobathymetry.

a)

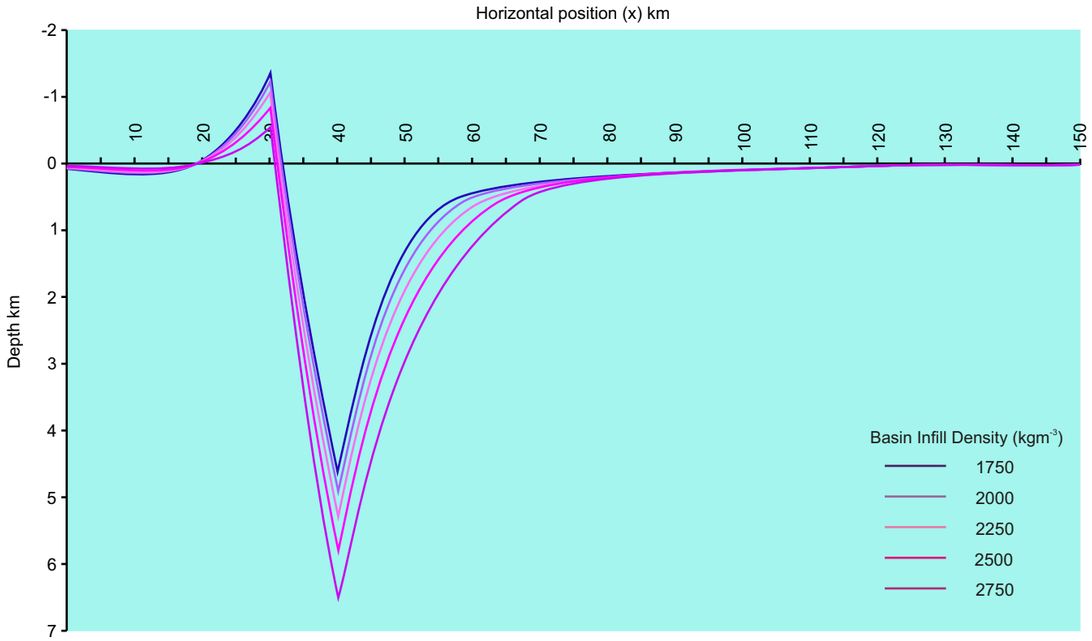


b)

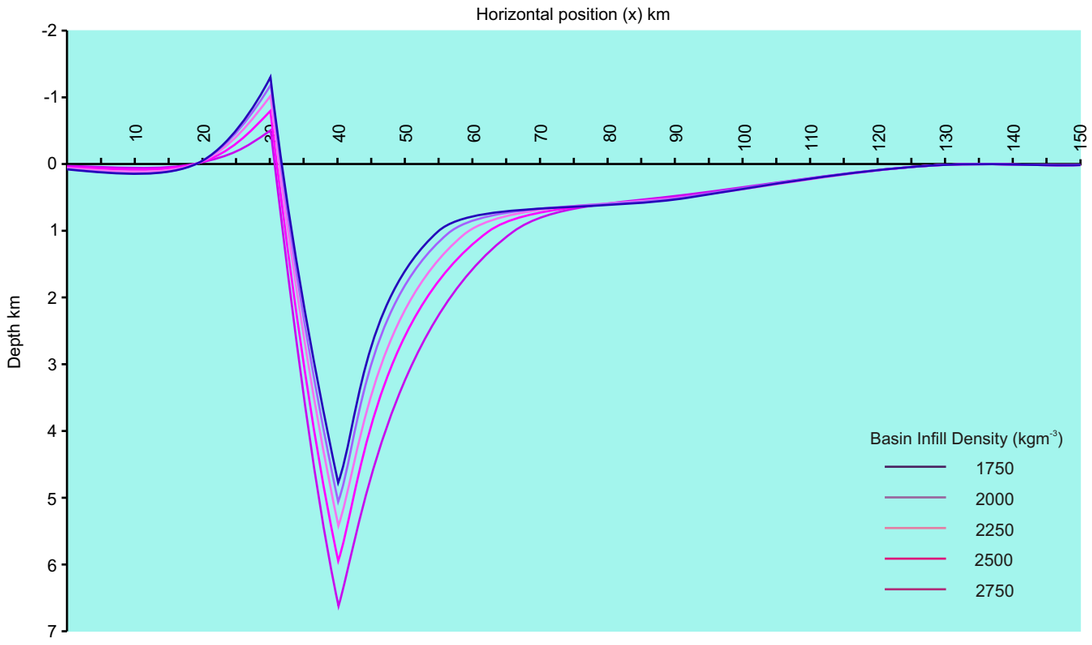


c)

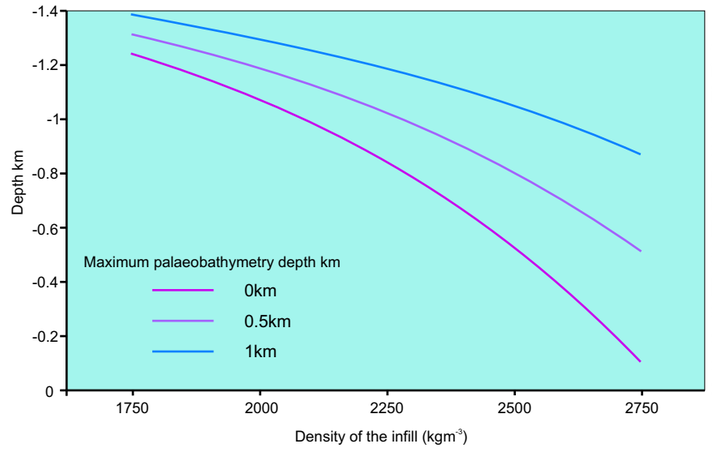


At x = 30 km, the maximum footwall uplift, decreases with increasing sediment density. The decrease in footwall uplift is smaller at greater palaeobathymetry depths. There is an average decrease of 0.00052 km for every 1kgm$^{-3}$ increase in sediment density when palaeobathymetry = 1km and an average decrease of 0.0014km for every 1kgm$^{-3}$ increase in sediment density when palaeobathymetry = 0km.

d)

At x = 40 km, the maximum basin depth increases with increasing sediment density. The decrease in basin depth is smaller at greater palaeobathymetry depths. There is an average increase of 0.0012km for every 1kgm$^{-3}$ increase in sediment density when palaeobathymetry = 1km and an average increase of 0.0026km for every 1kgm$^{-3}$ increase in sediment density when palaeobathymetry = 0km.

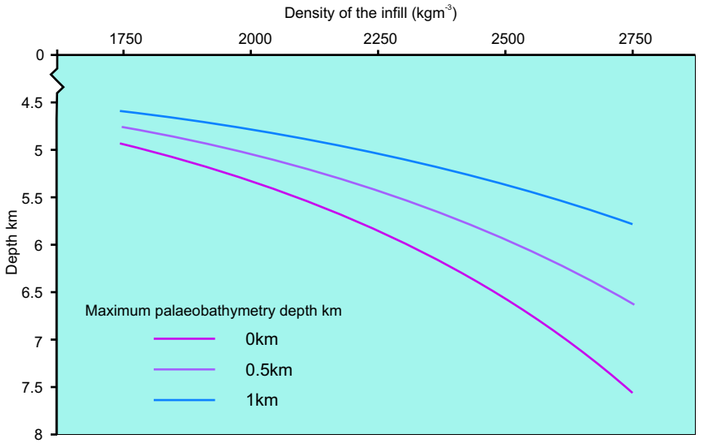


e)

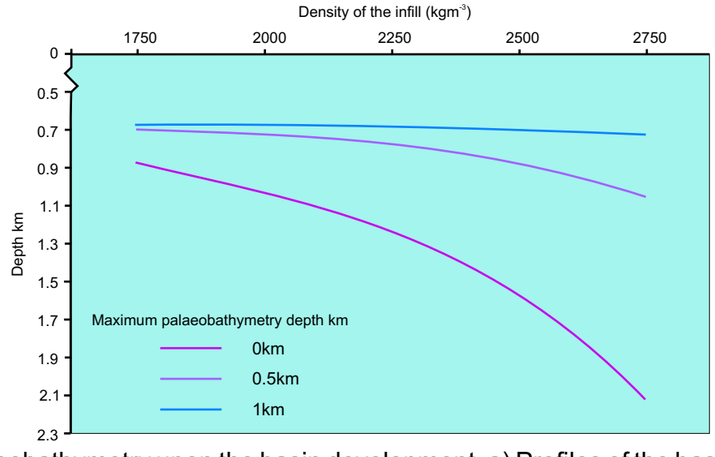


At a distal position in the basin, x=65km, increasing the palaeobathymetry decreases basin depth. The basin deepens with increasing sediment density. The increase in basin depth is smaller at greater palaeobathymetry depths.

Figure C5.56. The effect of increasing the density of the basin sediment, $p_s$, with varying maximum palaeobathymetry upon the basin development. a) Profiles of the basin at t = 0 Ma with a maximum palaeobathymetry of 500m. b) Profiles of the basin at t = 100 Ma, with a maximum palaeobathymetry of 500m. c) The footwall uplift with increasing sediment density, $p_s$, and varying palaeobathymetry depth, at time, t = 100 Ma, at horizontal position x = 30 km. d) The maximum basin depth, at x = 40 km, with increasing sediment density, $p_s$, and varying palaeobathymetry. e) The depth of the basin at x = 65 km at time, t = 100 Ma, with increasing sediment density, $p_s$, and varying palaeobathymetry.

a)

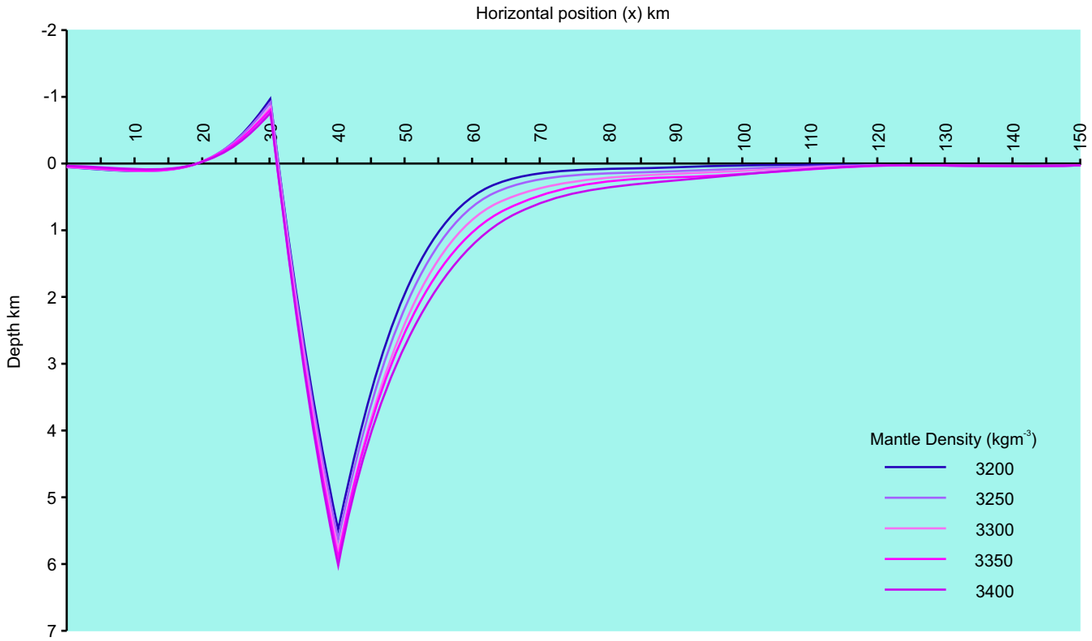


b)

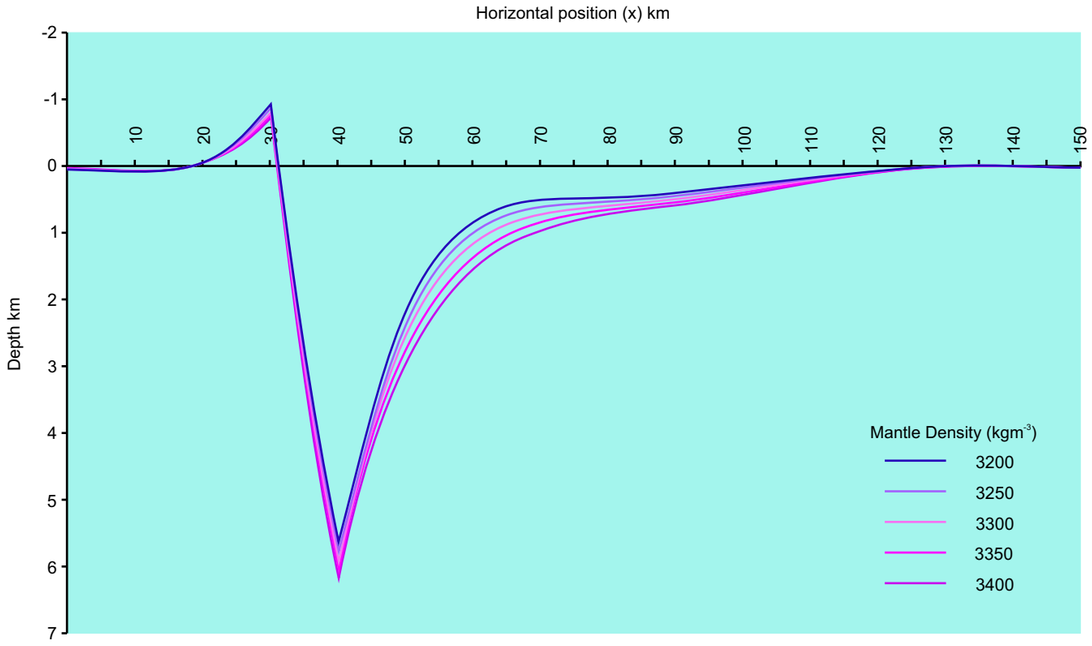


c)

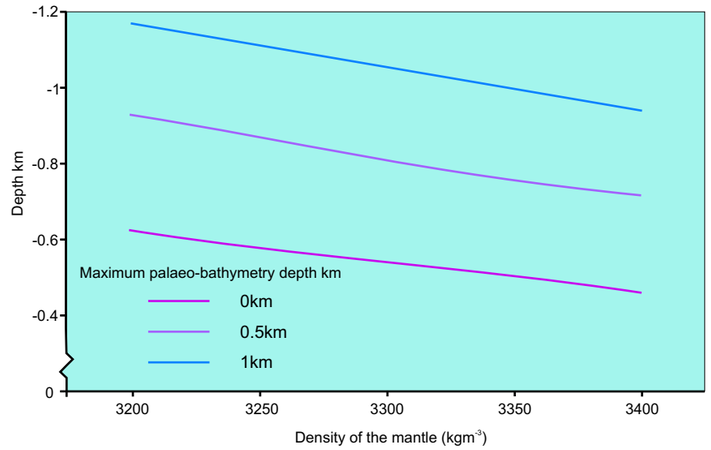


At x = 30 km, the maximum footwall uplift, decreases with increasing mantle density. The decrease in footwall uplift is larger at greater palaeo-bathymetry depths. There is an average decrease of 0.0011 km for every 1kgm$^{-3}$ increase in mantle density when palaeo-bathymetry = 1km and an average decrease of 0.0008km for every 1kgm$^{-3}$ increase in mantle density when palaeo-bathymetry = 0km.

d)

At x = 40 km, the maximum basin depth decreases with increasing mantle density. The decrease in basin depth is larger at greater palaeo-bathymetry depths. There is an average decrease of 0.0029 km for every 1kgm$^{-3}$ increase in mantle density when palaeo-bathymetry = 1km and an average decrease of 0.0024km for every 1kgm$^{-3}$ increase in mantle density when palaeo-bathymetry = 0km.

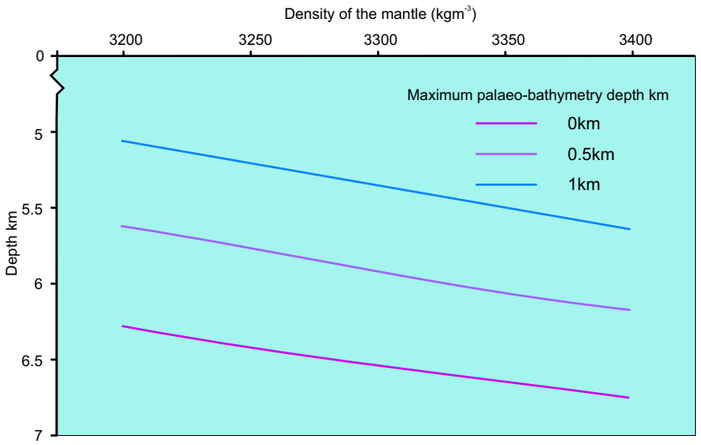


e)

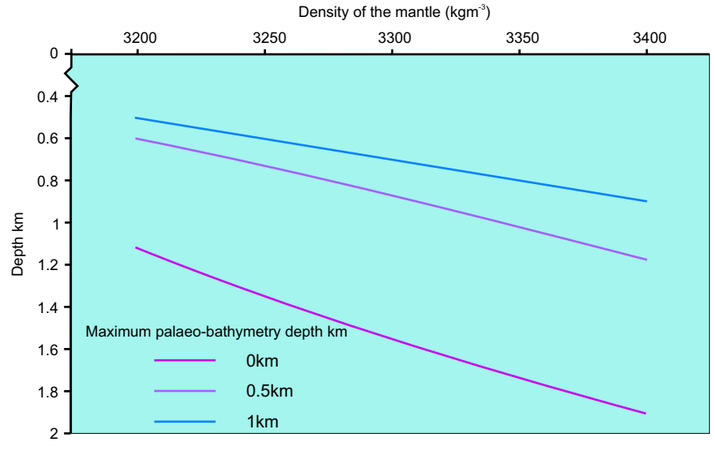


At a distal position in the basin, x=65km, increasing the palaeo-bathymetry decreases basin depth. The basin deepens with increasing mantle density. The increase in basin depth is smaller at greater palaeo-bathymetry depths. There is an average increase of 0.0010 km for every 1kgm$^{-3}$ increase in mantle density when palaeo-bathymetry = 1km and an average increase of 0.0025km for every 1kgm$^{-3}$ increase in mantle density when palaeo-bathymetry = 0km.

Figure C5.57. The effect of increasing the density of the mantle, $p_m$, with varying maximum palaeo-bathymetry depth upon the basin development. a) The profile of the basin at t = 0 Ma with a maximum palaeo-bathymetry depth of 500m. b) The profile of the basin at t = 100 Ma, with a maximum palaeo-bathymetry depth of 500m. c) The footwall uplift with increasing mantle density, $p_m$, and varying palaeo-bathymetry depth, at time, t = 100 Ma, at horizontal position x = 30 km. d) The maximum basin depth, at x = 40 km, with increasing mantle density, $p_m$, and varying palaeo-bathymetry. e) The depth of the basin at x = 90 km at time, t = 100 Ma, with increasing mantle density, $p_m$, and varying palaeo-bathymetry.

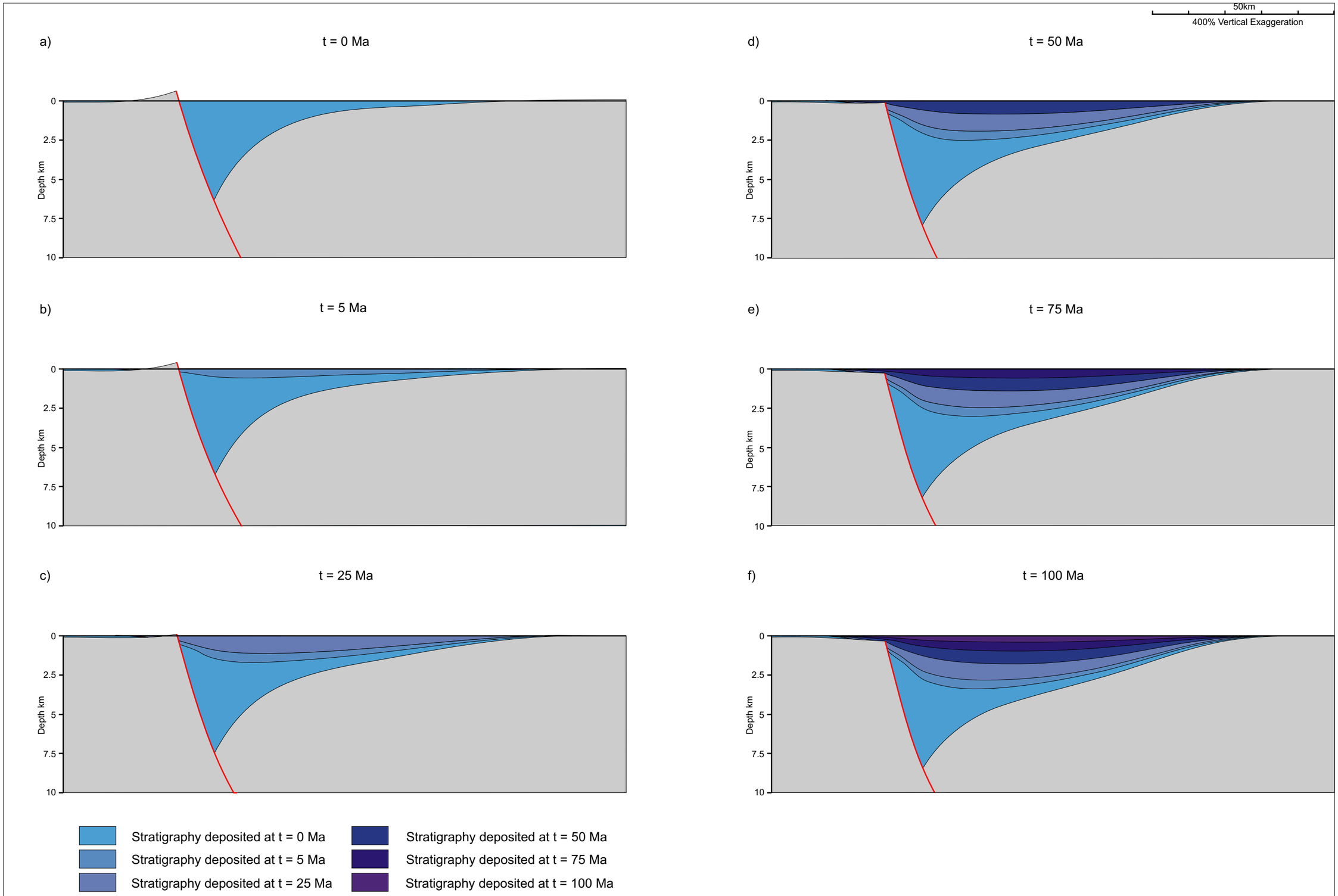


Figure C5.58. Development of basin stratigraphy over time including compaction. a) t = 0 Ma after rifting. b) t = 5 Ma after rifting. c) t = 25 Ma after rifting. d) t = 50 Ma after rifting. e) t = 75 Ma after rifting. f) t = 100 Ma after rifting. The basin is assumed to be filled to the sea level datum after each period of subsidence. The amount of subsidence produced decreases over time, as such the thickness of the units decreases over time.

a)

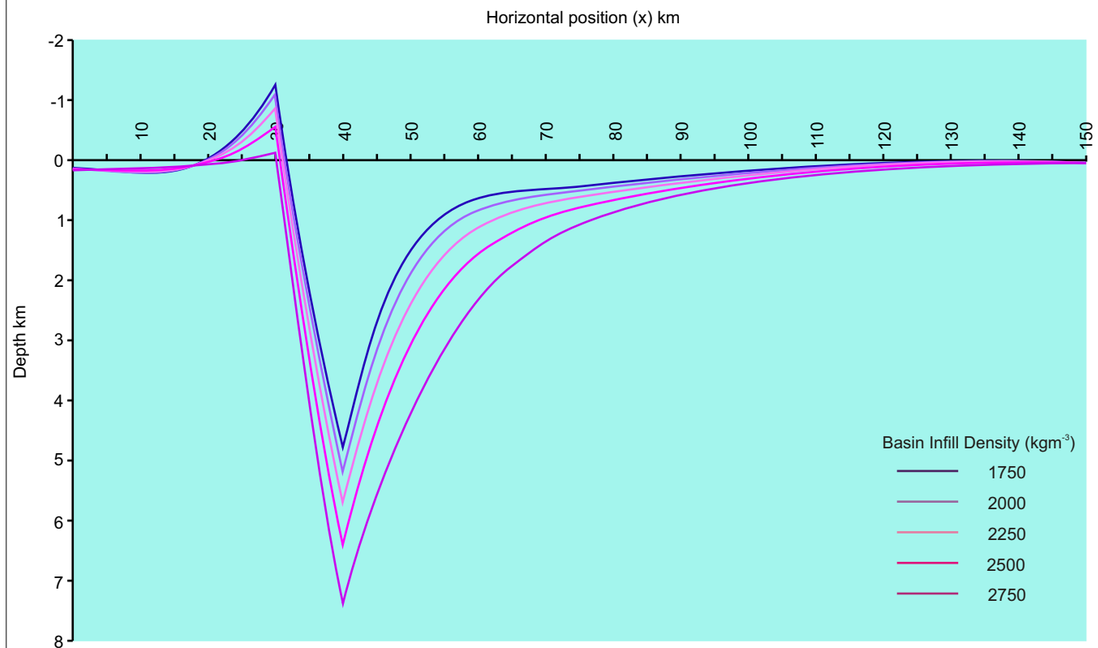


b)

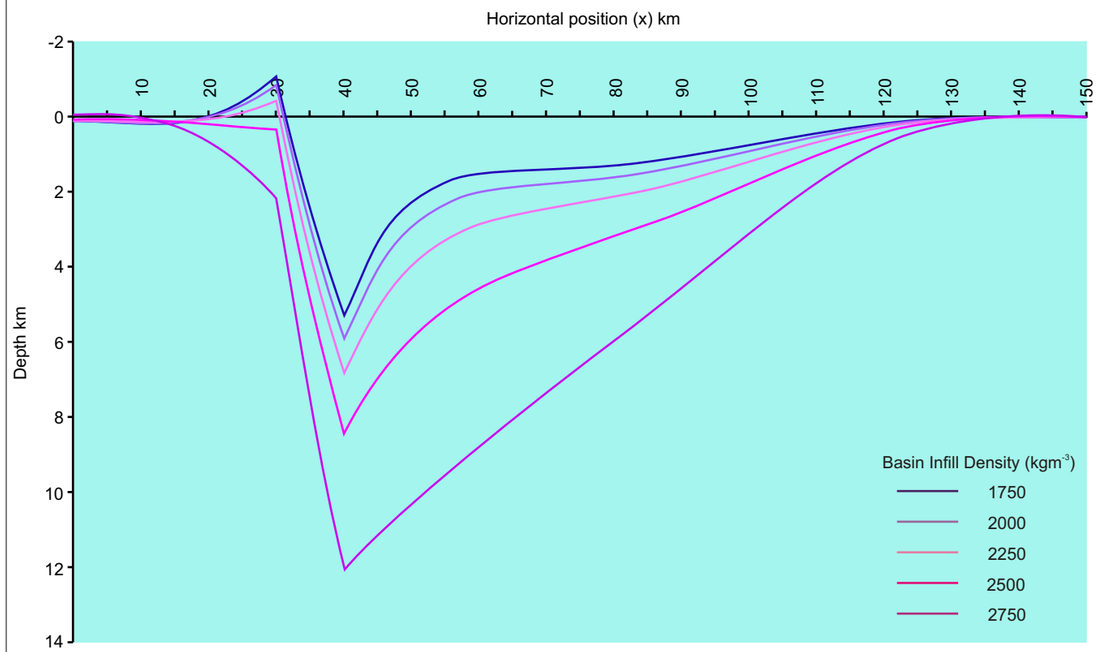


c)

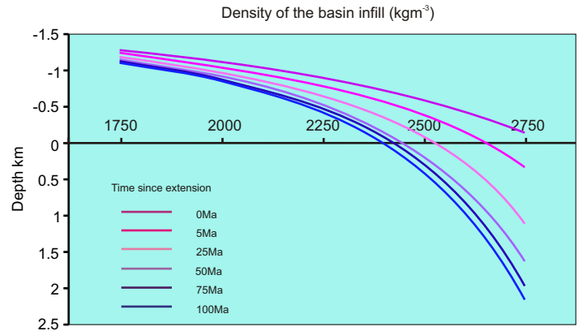


At x = 30 km, the footwall uplift generated at t = 0 Ma decreases with increasing sediment density. This affect is increased over time with compaction. the basement remains uplifted above the sea level datum at values of $\rho_s$ less than 2375 kgm$^{-3}$, after which the footwall subsides beneath the sea level datum to form part of the basin.

d)

At x = 40 km, the rate of increase in basin depth increases with increasing sediment density. At t = 100 Ma after rifting, the increase in basin depth with increasing $\rho_s$ has an average of 0.003km per 1kgm$^{-3}$ increase in $\rho_s$ when $\rho_s$ is between 1750kgm$^{-3}$ and 2250kgm$^{-3}$ and 0.01 km per 1kgm$^{-3}$ increase in $\rho_s$ between $\rho_s$ of 2250kgm$^{-3}$ and 2750kgm$^{-3}$.

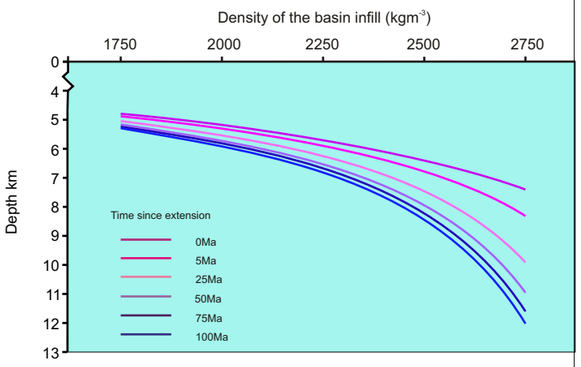


e)

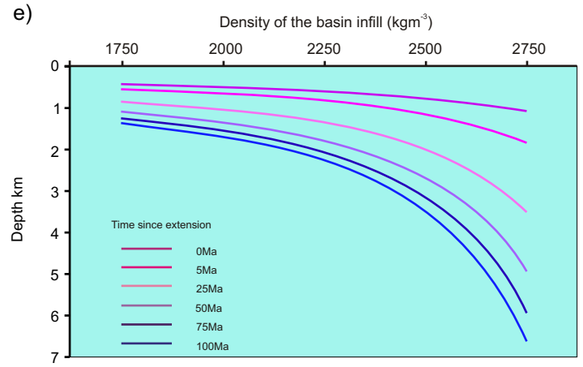


In a more distal position within the basin, x = 75 km, the effect of increasing the sediment density upon the increasing basin depth is greater than in the distal positions within the basin. At t = 100 Ma after rifting, there is an average increase in basin depth of 0.0018km per 1kgm$^{-3}$ increase in $\rho_s$ when $\rho_s$ is between 1750kgm$^{-3}$ and 2250kgm$^{-3}$ and 0.0087 km per 1kgm$^{-3}$ increase in $\rho_s$ between $\rho_s$ of 2250kgm$^{-3}$ and 2750kgm$^{-3}$.

f)

As time since extension increases, the thickness of the deposit decreases. The rate of decrease in thickness is greater with increasing sediment density. The thickness of sediment decreases at a greater rate when sediment density is higher because it is buried deeper and therefore compacted more.

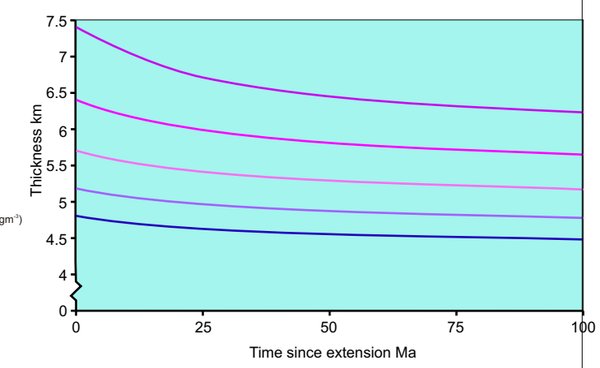


Figure C5.59. The effect of increasing the density of the sediment, $\rho_s$, upon the basin development with compaction. a) Profiles of the basin at t = 0 Ma. b) Profiles of the basin at t = 100 Ma. c) The footwall uplift generated adjacent to the fault at x = 30 km. d) The depth of the basin at x = 40 km over time with increasing sediment density, $\rho_s$. e) The depth of the basin over time at x = 75 km. f) The compaction of the first stratigraphic layer over time at x = 40 km.

a)

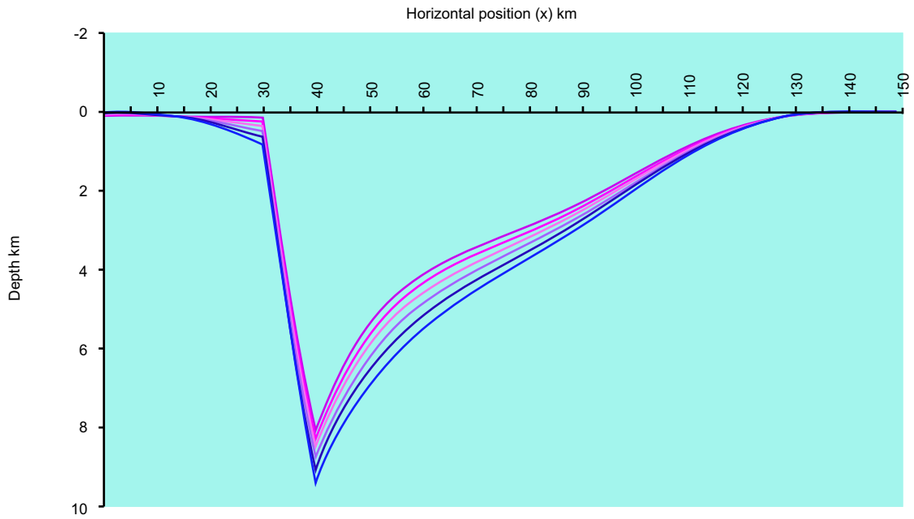


b)

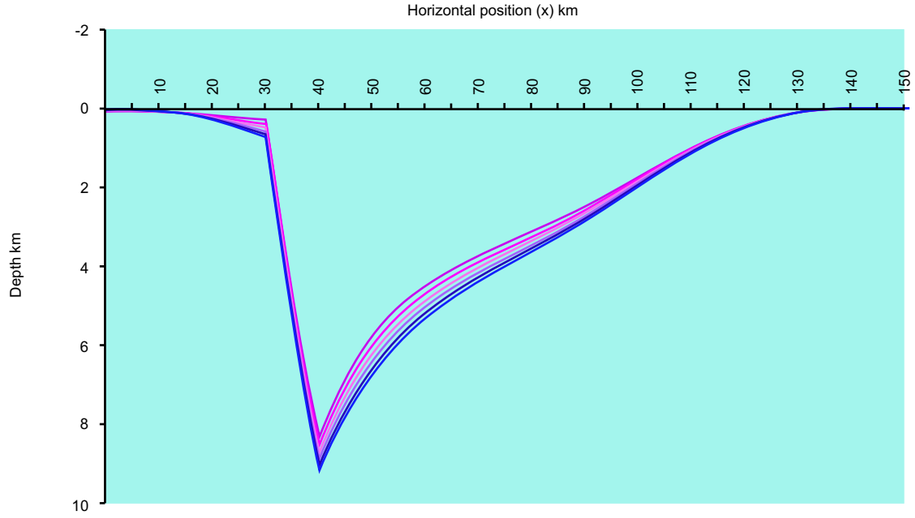


ai)

At x = 30 km, the increase in subsidence with increasing surface porosity gets greater as time since extension increases. At t = 100 Ma after extension, there is an increase in the depth of the footwall of 0.027 km per 1% increase in $\Phi_s$.

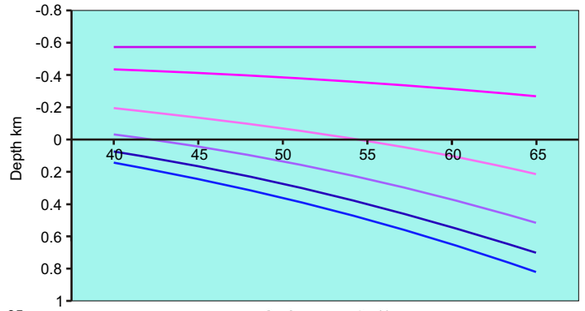


bi)

At x = 30 km over time, with increasing compaction co-efficient, as time since extension increases, the depth of the footwall increases. At t = 100 Ma after extension, there is an increase in the depth of the footwall of 0.018 km per 0.1 increase in c.

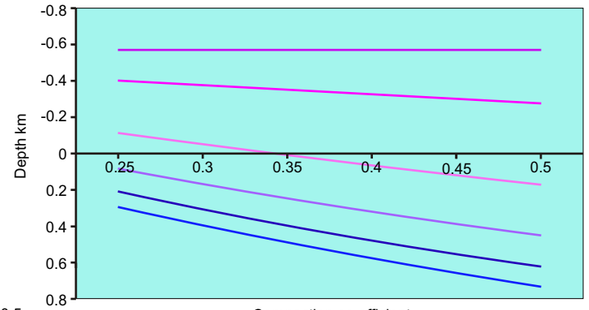


aii)

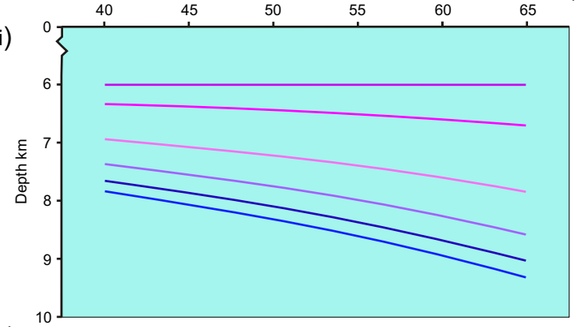


At x = 40 km, there is an increase in basin depth with increasing surface porosity. At t = 100 Ma after extension, there is an increase in basin depth of 0.054 km per 1% increase in $\Phi_s$.

bii)

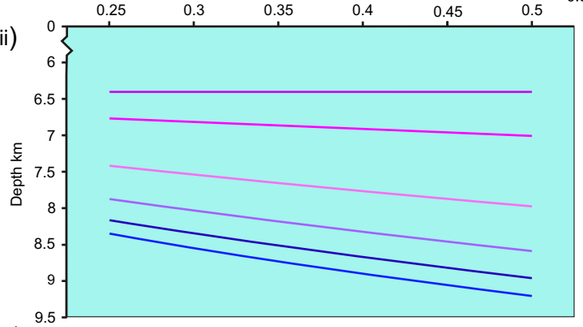


At x = 40 km, the maximum basin depth increases by 0.034 km per 0.1 increase in c at t = 100 Ma after extension.

aiii)

In a more distal position, x = 75 km, the increase in basin depth with increasing is reduced to 0.038 km per 1% increase in $\Phi_s$ at t = 100 Ma.

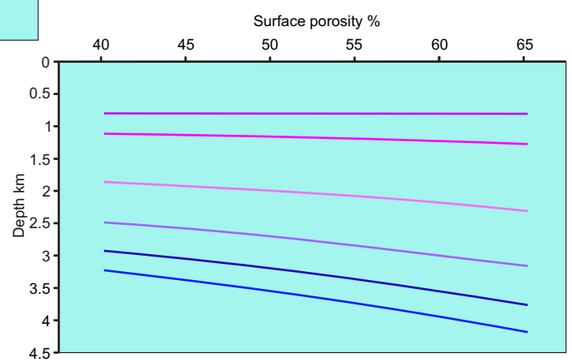


biii)

.At x = 75 km, in a more distal position within the basin, there is an increase in basin depth of 0.022 km per 0.1 increase in c at t = 100 Ma after extension.

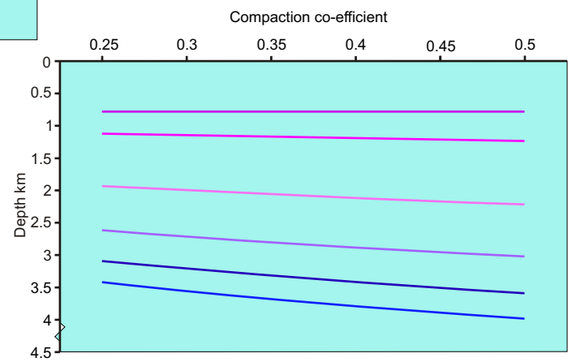


Figure C5.60. The effect of varying porosity with depth upon basin development with compaction. a) The effect of varying the surface porosity on basin development. Profiles of the basin at t = 100 Ma. ai) The basin at x = 30 km with varying surface porosity. aii) The basin at x = 40 km. aiii) The basin at x = 75 km. b) The effect of varying the compaction co-efficient, c, on basin development. Profiles of the basin at t = 100 Ma. bi) The basin at x = 30 km with varying compaction co-efficient. bii) The basin at x = 40 km. biii) The basin at x = 75 km.

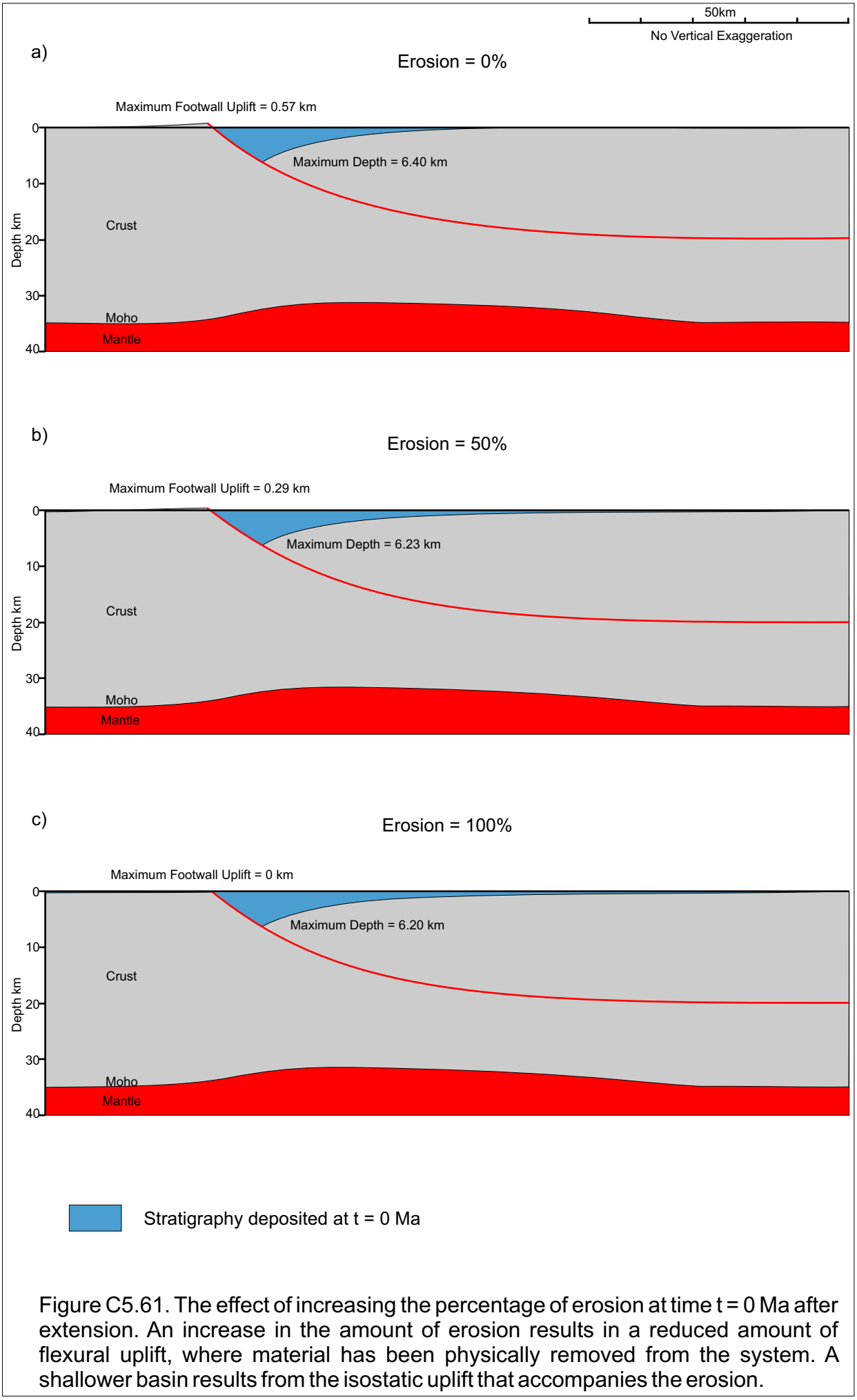


Figure C5.61. The effect of increasing the percentage of erosion at time t = 0 Ma after extension. An increase in the amount of erosion results in a reduced amount of flexural uplift, where material has been physically removed from the system. A shallower basin results from the isostatic uplift that accompanies the erosion.

a)

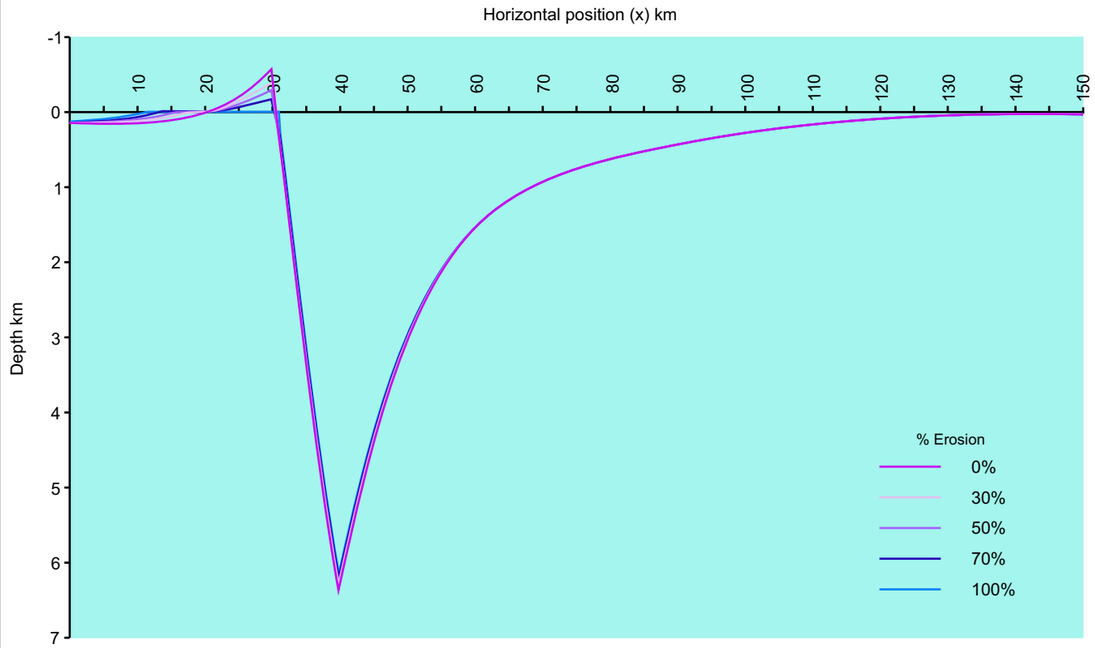


b)

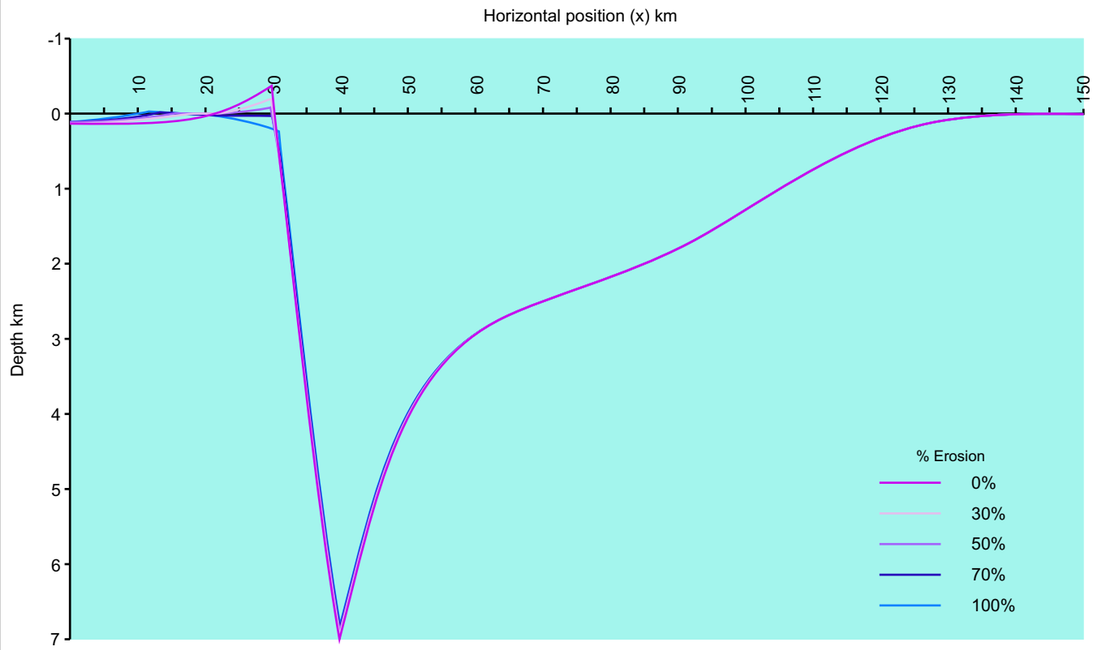


c)

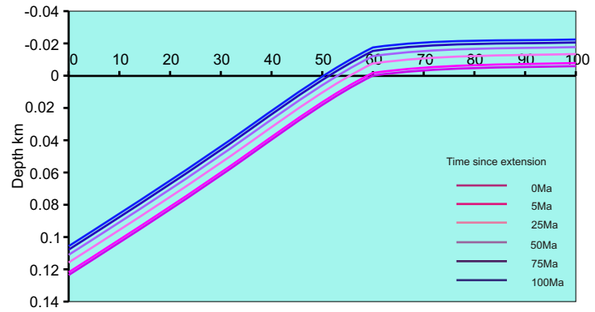


Subsidence in front of the fault, before the footwall uplift, decreases with increasing % erosion up to 60% erosion, with an decrease of 0.021km per 10% increase in erosion at x = 15 km. When the amount of erosion is greater than 60% the increase in footwall uplift decreases to 0.001km per 10% increase in erosion.

d)

The amount of footwall uplift generated decreases with increasing % erosion. At x=30km there is a decrease of 0.056 km for every 10% increase in erosion adjacent to the fault.

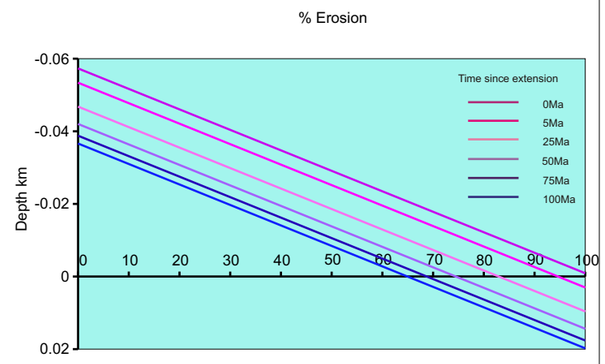


e)

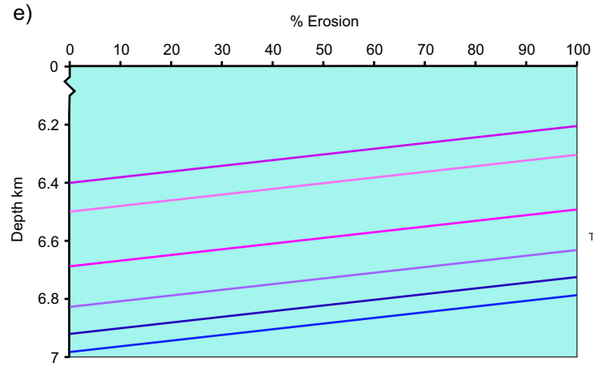


At x = 40 km, where the maximum basin depth is achieved, there is a decrease in basin depth of 0.02 km for every 10% increase in erosion.

f)

At a distal position in the basin, x=75km, the amount of erosion has little affect at this distal position within the basin due to its distance from the position of the eroded uplift.

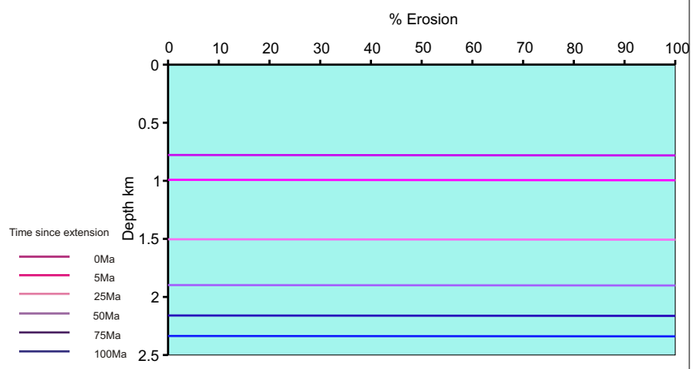


Figure C5.62. The effect of increasing the percentage of erosion upon the basin development. a) Profiles of the basin at t = 0 Ma. b) Profiles of the basin at t = 100 Ma. c) The depth to the basement with increasing % erosion over time at horizontal position x = 15 km. d) The footwall uplift generated adjacent to the fault at x = 30 km. e) The depth of the basin at x = 40 km over time with varying % erosion. f) The depth of the basin over time at x = 75 km.

a)

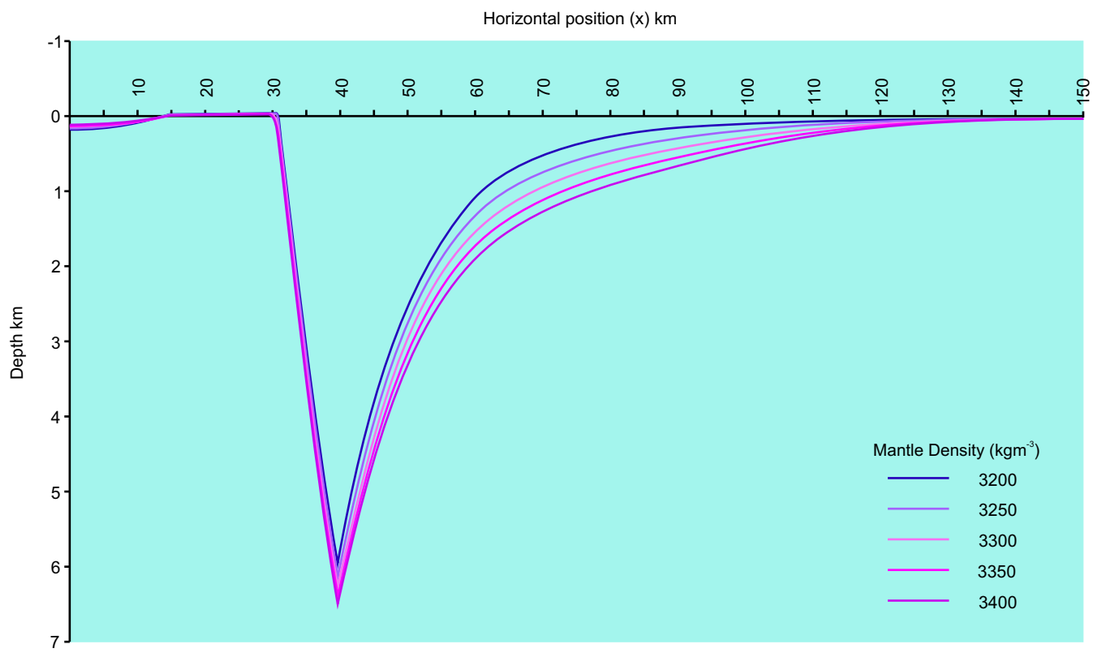


b)

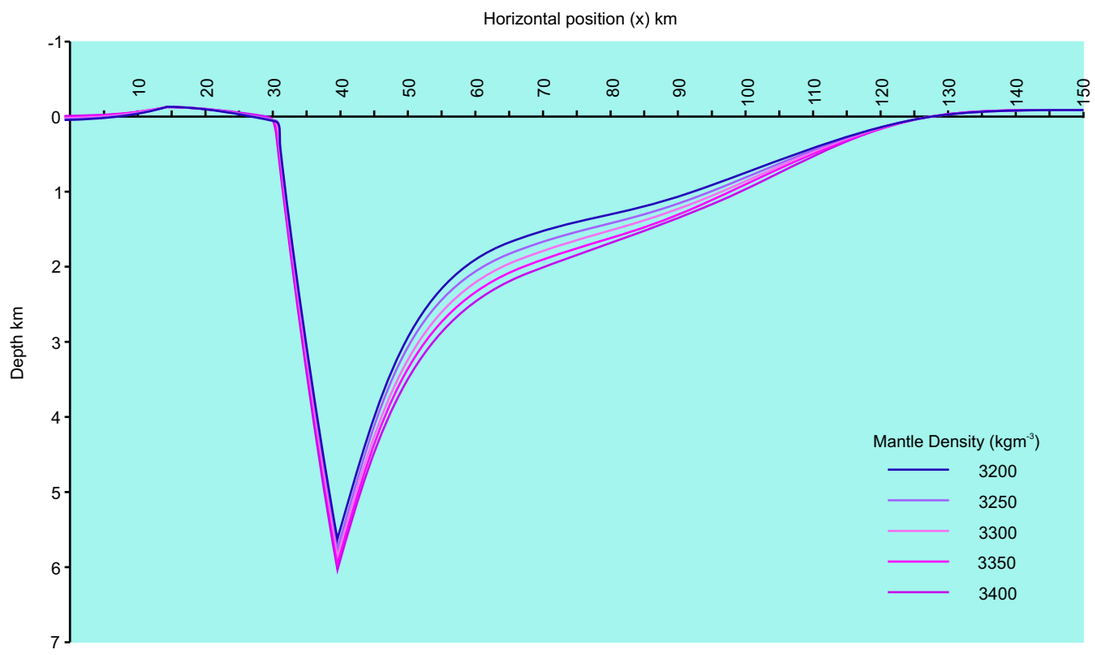


c)

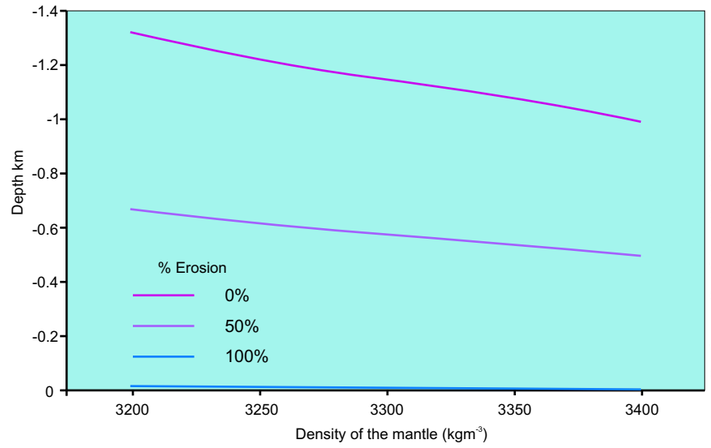


At x = 30 km, the maximum footwall uplift, decreases with increasing mantle density. With increasing % erosion, the amount by which footwall uplift is reduced with increasing mantle density decreased. There is an average decrease of 0.0008km for every 1kgm$^{-3}$ increase in mantle density when there is no erosion, this decreases to 0.0004km for every 1kgm$^{-3}$ increase in mantle density when erosion = 50% and 0.0003km when erosion = 100%.

d)

At x = 40 km, the maximum basin depth, increases with increasing mantle density. With increasing % erosion, the amount by which basin depth is increased with increasing mantle density isincreased. There is an average decrease of 0.0029km for every 1kgm$^{-3}$ increase in mantle density when there is 100% erosion, this decreases to 0.0026km for every 1kgm$^{-3}$ increase in mantle density when erosion = 50% and 0.0023km when there is no erosion.

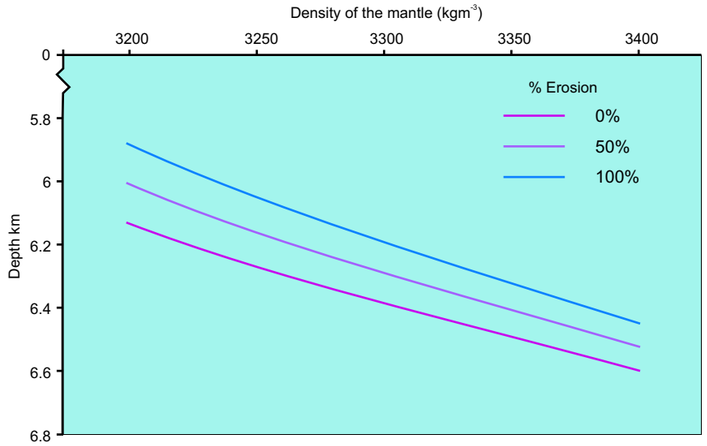


e)

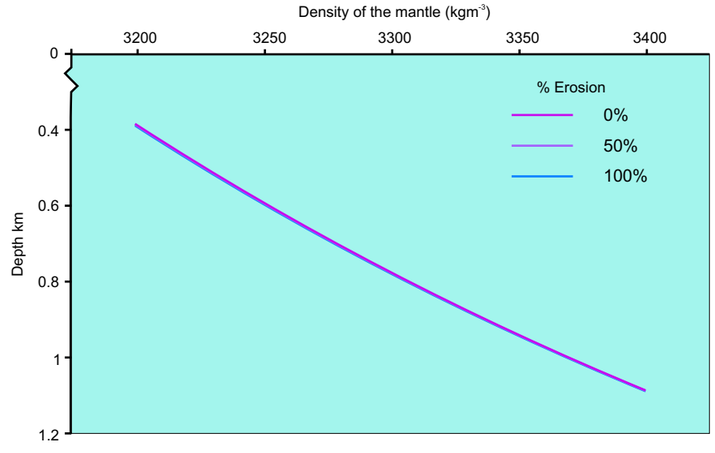


At a distal position in the basin, x=75km, increasing the basin deepens with increasing mantle density. The amount of erosion has little affect at this distal position within the basin due to its distance from the position of the eroded uplift.

Figure C5.63. The effect of increasing the density of the mantle, $\rho_m$, upon the flexural isostatic response to extension, including erosion and basin development. a) The profile of the basin at t = 0 Ma. b) The profile of the basin at t = 100 Ma. c) The footwall uplift with increasing mantle density and erosion at horizontal position x = 30 km and t = 0 Ma. d) The maximum basin depth generated adjacent to the fault at x = 40 km, with varying mantle density and erosion. e) The depth of the basin at x = 75 km with varying mantle density and erosion at t = 0 Ma.

a)

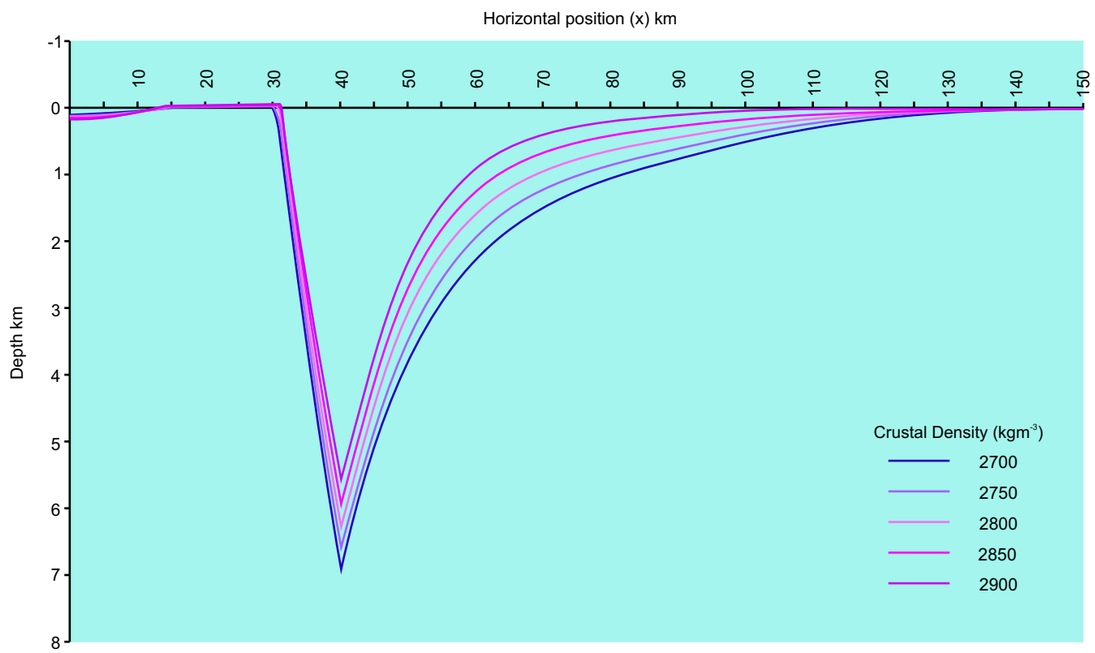


b)

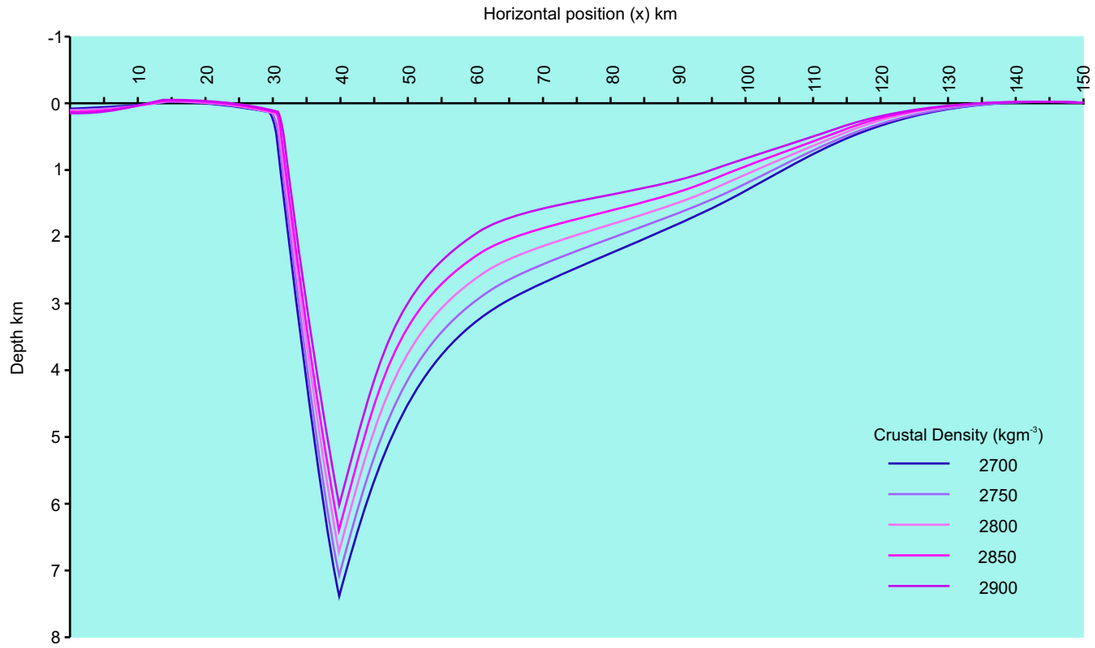


c)

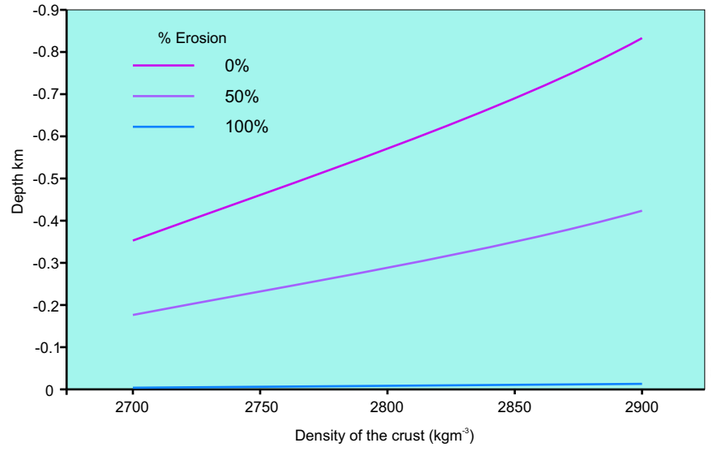


At x = 30 km, the maximum footwall uplift, increases with increasing crustal density. With increasing % erosion, the amount by which footwall uplift increases with increasing crustal density decreased. There is an average increase of 0.0024km for every 1kgm$^{-3}$ increase in crustal density when there is no erosion, this decreases to 0.0012km for every 1kgm$^{-3}$ increase in crustal density when erosion = 50% and 0.0005km when erosion = 100%.

d)

At x = 40 km, the maximum basin depth, increases with increasing crustal density. With increasing % erosion, the amount by which basin depth is increased with increasing crustal density is increased. There is an average decrease of 0.007km for every 1kgm$^{-3}$ increase in crustal density when there is 100% erosion, this decreases to 0.006km when there is no erosion.

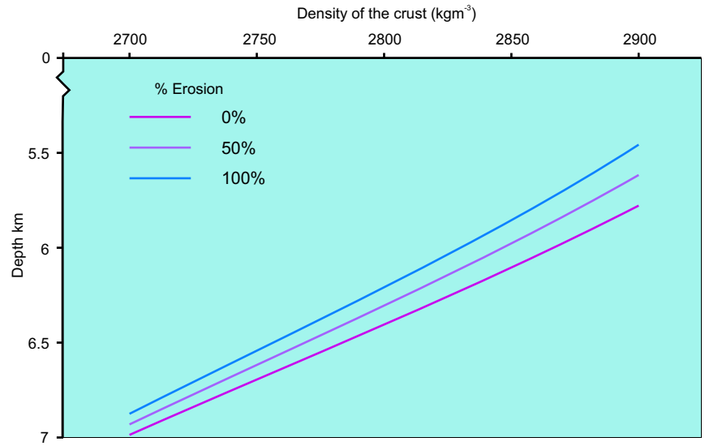


e)

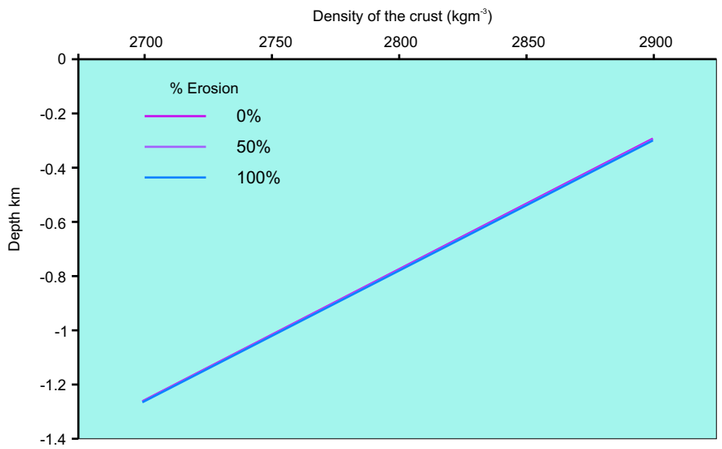


At a distal position in the basin, x=75km, increasing the basin depth is reduced with increasing crustal density. The amount of erosion has little affect at this distal position within the basin due to its distance from the position of the eroded uplift.

Figure C5.64. The effect of increasing the density of the crust, $\rho_c$, upon the flexural isostatic response to extension, including erosion and basin development. a) The profile of the basin at t = 0 Ma. b) The profile of the basin at t = 100 Ma. c) The footwall uplift with increasing crustal density and erosion at horizontal position x = 30 km and t = 0 Ma. d) The maximum basin depth generated adjacent to the fault at x = 40 km, with varying crustal density and erosion. e) The depth of the basin at x = 75 km with varying crustal density and erosion at t = 0 Ma.

a)

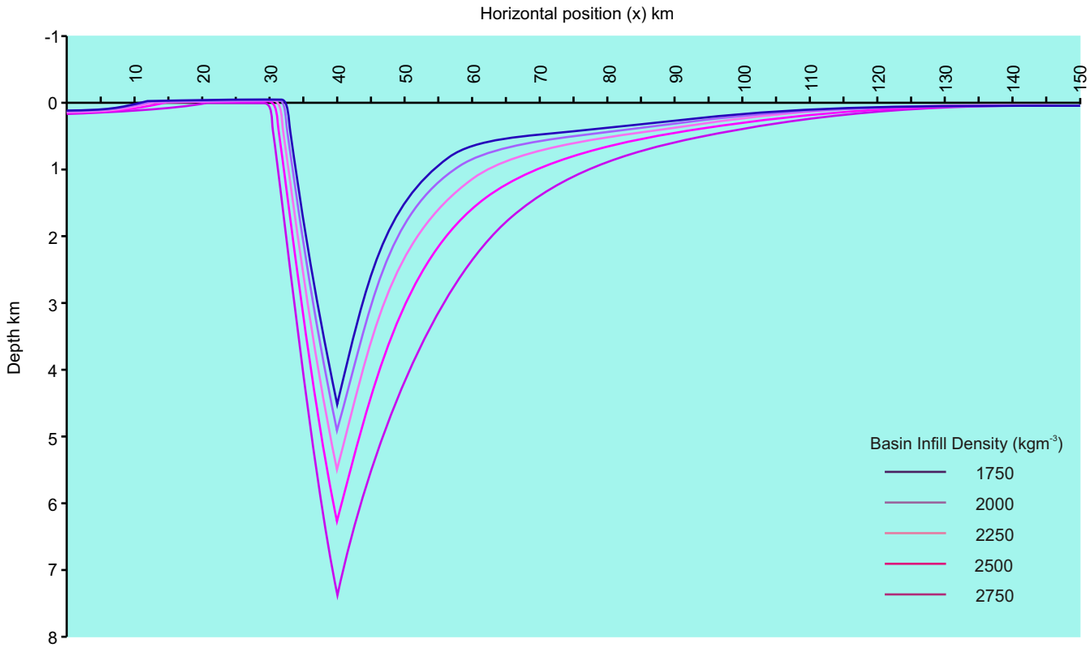


b)

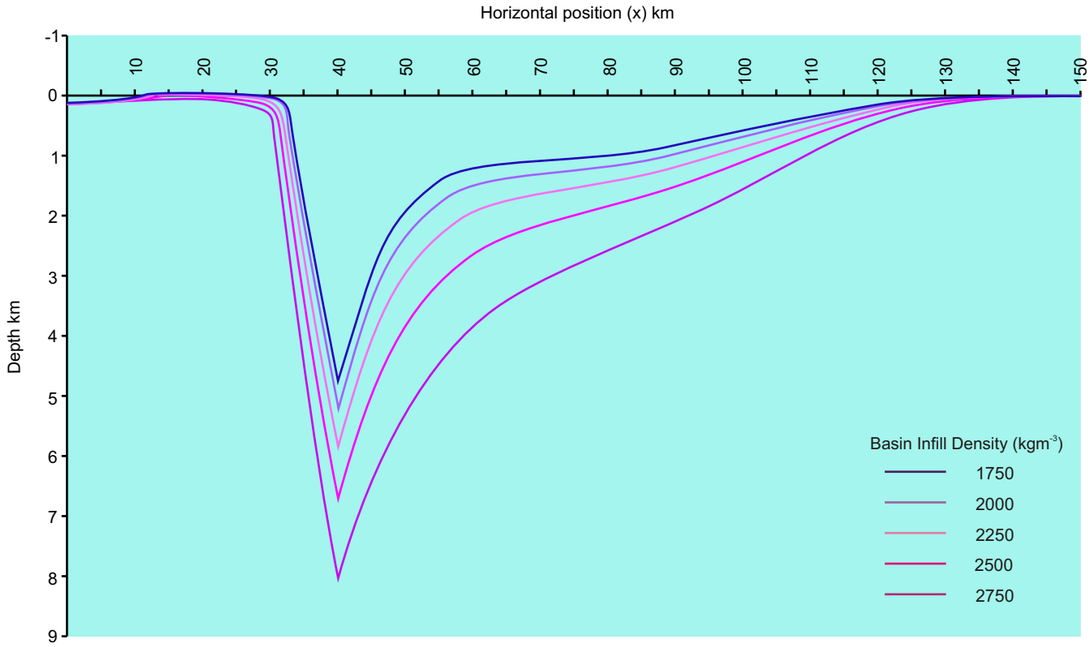


c)

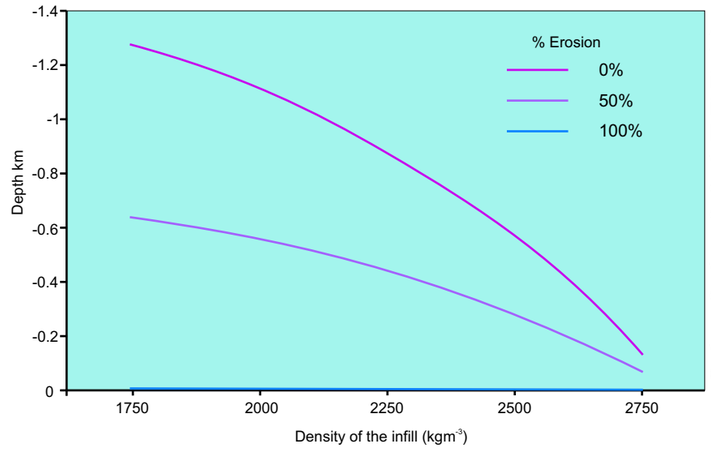


At x = 30 km, the maximum footwall uplift, decreases with increasing infill density. With increasing % erosion, the amount by which footwall uplift is reduced with increasing infill density decreased. There is an average decrease of 0.0011km for every 1kgm$^{-3}$ increase in infill density when there is no erosion, this decreases to 0.0006km for every 1kgm$^{-3}$ increase in infill density when erosion = 50% and 0.00001km when erosion = 100%.

d)

At x = 40 km, the maximum basin depth, increases with increasing mantle density. With increasing % erosion, the amount by which basin depth is increased with increasing infill density is increased. There is an average decrease of 0.0029km for every 1kgm$^{-3}$ increase in infill density when there is 100% erosion, this decreases to 0.00275km for every 1kgm$^{-3}$ increase in infill density when erosion = 50% and 0.0026km when there is no erosion.

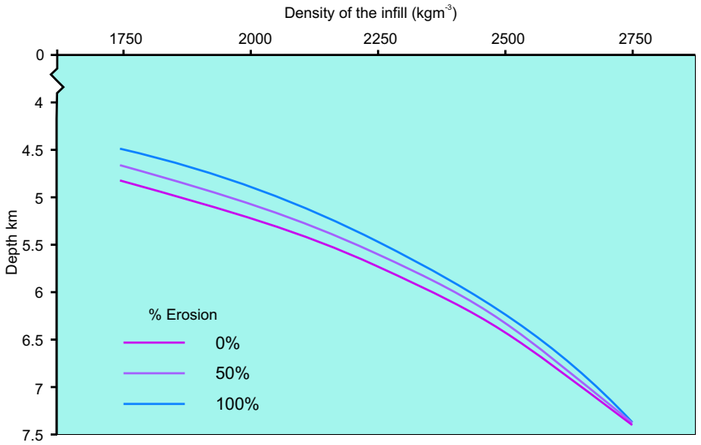


e)

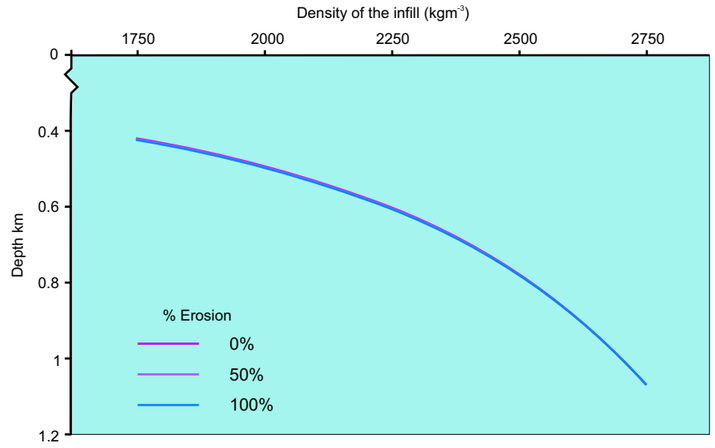


At a distal position in the basin, x=75km, increasing the basin deepens with increasing infill density. The amount of erosion has little affect at this distal position within the basin due to its distance from the position of the eroded uplift.

Figure C5.65. The effect of increasing the density of the basin infill, $\rho_i$, upon the flexural isostatic response to extension, including erosion and basin development. a) The profile of the basin at t = 0 Ma. b) The profile of the basin at t = 100 Ma.c) The footwall uplift with increasing infill density and erosion at horizontal position x = 30 km and t = 0 Ma. d) The maximum basin depth generated adjacent to the fault at x = 40 km, with varying infill density and erosion. e) The depth of the basin at x = 75 km with varying infill density and erosion at t = 0 Ma.

```
/*
 * LithosphereExtension.java
 *
 * Created on 14 December 2006, 18:24
 *
 */

package LithosphereExtension;

/**
 * @author Linda Austin
 */
public class LithosphereExtension {


    // Set up Variables

    /**
     * Thickness of Lithosphere
     * @see #ThermalUplift()
     * @see #FlexModelEt()
     * @see #ModelEt()
     * @see Parameters#Parameters()
     */
    static double A;

    /**
     * Original Thickness of Crust
     * @see #PSThinning()
     * @see #Beta()
     * @see Parameters#Parameters()
     */
    static double Co;

    /**
     * Thermal Expansion Co-eficient
     * @see #ThermalUplift()
     * @see #FlexModelEt()
     * @see #ModelEt()
     * @see Parameters#Parameters()
     */
    static double alpha;
```

```
/**
 * Temperature at the base of the Lithosphere
 * @see #ThermalUplift()
 * @see #FlexModelEt()
 * @see #ModelEt()
 * @see Parameters#Parameters()
 */
static double To;

/**
 * Density of the Mantle
 * @see #Granite()
 * @see #IsostaticRebound()
 * @see #Flex()
 * @see #ModelEt()
 * @see Parameters#Parameters()
 */
static double pm;

/**
 * Density of the Crust
 * @see #GranDensity()
 * @see #Granite()
 * @see #IsostaticRebound()
 * @see #Flex()
 * @see Parameters#Parameters()
 */
static double pc;

/**
 * Density of the Infill
 * @see #IsostaticRebound()
 * @see #Flex()
 * @see #ModelEt()
 * @see Parameters#Parameters()
 */
static double pi;

/**
 * a squared/ (pi squared * k)
 * @see #FlexModelEt()
 * @see #ModelEt()
 * @see Parameters#Parameters()
 */
static double tau;
```

```
/**
 * Used for carrying out a summation
 * @see #FlexModelEt()
 * @see #ModelEt()
 */
static double ModelSum;

/**
 * Used for carrying out a summation
 * @see #ThermalUplift()
 */
static double ModelSum1;

/**
 * Detachment Depth of Faults
 * @see #FaultProfile()
 * @see #PSThinning()
 * @see Parameters#Parameters()
 * @see FaultDialog#OKjButtonActionPerformed()
 * @see FaultDialog#CanceljButtonActionPerformed()
 * @see FaultDialog#ZdjTetFieldActionPerformed()
 */
static double Zd;

/**
 * The maximum value of Beta within the pure shear distribution
 * @see #PureShear()
 */
static double BetaMax;

/**
 * The value of extension by pure shear
 * @see #PureShear()
 */
static double TotalHeave =10;

/**
 * The width of the pure shear distribution
 * @see #PureShear()
 */
static double PS_Width;

/**
 * Used for intermediate calculations
 * @see #ThermalUplift()
 */
static double A1;
```

```
/**
 * Used for intermediate calculations
 * @see #ThermalUplift()
 */
static double A2;

/**
 * Distance between horizontal data points
 * @see #FaultProfile()
 * @see #InclinedShear()
 * @see #DefFaultProfileInclined()
 * @see #BasinInclined()
 * @see #PureShear()
 * @see #PSThinning()
 * @see #BaseGran()
 * @see #TopGran()
 * @see #GranDensity()
 * @see #Granite()
 * @see FaultDialog#HeavejTextFieldActionPerformed()
 * @see FaultDialog#SurfacePositionjTextFieldActionPerformed()
 * @see ModelDialog#CanceljButtonActionPerformed()
 * @see ModelDialog#djTextFieldActionPerformed()
 * @see ModelDialog#TotalXjTextFieldActionPerformed()
 */
static double d = 1;

/**
 * Value of x – distance between points x = i * d
 * @see #InclinedShear()
 * @see #DefFaultProfileInclined()
 */
static double x;

/**
 * Position of the start of the pure shear extension distribution
 * @see #PureShear()
 */
static double PS_Start;

/**
 * Position of the end of the pure shear extension distribution
 * @see #PureShear()
 */
static double PS_Finish;
```

```
    /**
     * Horizontal position of the start of the granite batholith in crust
     * @see #BaseGran()
     * @see #TopGran()
     * @see #GranDensity()
     * @see #Granite()
     */
    static double Granite_Start;

    /**
     * Horizontal position of the end of the granite batholith in crust
     * @see #BaseGran()
     * @see #TopGran()
     * @see #GranDensity()
     * @see #Granite()
     */
    static double Granite_Finish;

    /**
     * XNext a step in the calcultaion of e' during the inclined shear
     * calculation
     * @see #InclinedShear()
     * @see #DefFaultProfileInclined()
     */
    static double XNext;

    /**
     * Specific gravity of the Earth
     * @see #Flex()
     */
     final double g = 9.81;

    /**
     * Flexural Rigidity of the Lithosphere
     * @see #Flex()
     */
     static double D;

    /**
     * Response function applied to the data that has been through the
forward
     * transform process
     * @see #Flex()
     */
     static double resp1;
```

```
/**
 * Response function applied to the data that has been through the
 * forward transform process
 * @see #Flex()
 */
 static double resp2 = 0;

/**
 * Young's Modulus
 * @see #Flex()
 */
 static double E = 70*Math.pow(10, 9);

/**
 * Poisson's Ratio
 * @see #Flex()
 */
static double v = 0.25;

/**
 * Elastic thickness of the Lithosphere in m
 * @see #Flex()
 */
 static double te = 5000;

/**
 * Elastic thickness of the Lithosphere in m at time t=0
 * @see #Flex()
 */
 static double te0 = 5000;

/**
 * Elastic thickness of the Lithosphere in m
 * @see #Flex()
 */
 static double ElasticThickness;

/**
 * Surface position of the first forward facing fault
 * @see #BasinInclined()
 */
 static double Flt_Forwards_1;

/**
 * Surface position of the first backwards facing fault
 * @see #BasinInclined()
 */
 static double Flt_Backwards_1;
```

```
/**
 * IHW is the array position for the value of x-e'
 * @see #InclinedShear()
 */
static double IHW;

/**
 * Surface porosity of sediment
 * @see #Compaction()
 * @see #PorosityAtDepth()
 */
static double SPorosity;

/**
 * Compaction co-efficient
 * @see #Compaction()
 * @see #PorosityAtDepth()
 */
static double ck;

/**
 * Density of water
 * @see #Flex()
 */
static double pw = 1000;

/**
 * Density of sediment for flexural isostacy algorithm
 * @see #Flex()
 */
static double ps;

/**
 * Number of times to carry out summation and ModelSummation
 * @see #ThermalUplift()
 * @see #FlexModelEt()
 * @see #Compaction()
 * @see #ModelEt()
 * @see #IsostaticRebound()
 * @see #FlexStratigraphy()
 * @see Parameters#Parameters()
 */
static int m;
```

```
/**
 * Loop Variable, most often represents increments in the x value
 * @see #FaultProfile()
 * @see #InclinedShear()
 * @see #DefFaultProfileInclined()
 * @see #BasinInclined()
 * @see #PureShear()
 * @see #PSThinning()
 * @see #Moho()
 * @see #BaseGran()
 * @see #TopGran()
 * @see #GranDeansity()
 * @see #Granite()
 * @see #Beta()
 * @see #ThermalUplift()
 * @see #IsostaticRebound()
 * @see #FlexModelEt()
 * @see #FlexModelSt()
 * @see #Flex()
 * @see #Compaction()
 * @see #PorosityAtDepth()
 * @see #IsostaticBasin()
 * @see #IsostaticFault()
 * @see #IsostaticMoho()
 * @see #ModelEt()
 * @see #ModelSt()
 * @see #ThermalIsostaticBasin()
 * @see #ThermalIsostaticFaults()
 * @see #ThermalIsostaticMoho()
 * @see #ThermalBasin()
 * @see #ThermalFaults()
 * @see #ThermalMoho()
 * @see #FlexStratigraphy()
 */
static int i;
```

```
/**
 * Loop Variable, most often represents fault numbers
 * @see #FaultProfile()
 * @see #InclinedShear()
 * @see #DefFaultProfileInclined()
 * @see #BasinInclined()
 * @see #ThermalUplift()
 * @see #FlexModelEt()
 * @see #Flex()
 * @see #Erosion()
 * @see #IsostaticFault()
 * @see #ModelEt()
 * @see #ThermalIsostaticFaults()
 * @see #ThermalFaults()
 * @see #FlexStratigraphy()
 */
static int j;

/**
 * Loop Variable, most often represents increments in time stages
 * @see #InclinedShear()
 * @see #DefFaultProfileInclined()
 * @see #BasinInclined()
 * @see #IsostaticRebound()
 * @see #FlexModelEt()
 * @see #FlexModelSt()
 * @see #Flex()
 * @see #Erosion()
 * @see #Compaction()
 * @see #PorosityAtDepth()
 * @see #IsostaticBasin()
 * @see #IsostaticFault()
 * @see #IsostaticMoho()
 * @see #ModelEt()
 * @see #ModelSt()
 * @see #ThermalIsostaticBasin()
 * @see #ThermalIsostaticFaults()
 * @see #ThermalIsostaticMoho()
 * @see #ThermalBasin()
 * @see #ThermalFaults()
 * @see #ThermalMoho()
 */
static int k;
```

```
/**
 * Total Number of Faults
 * @see #FaultProfile()
 * @see #DefFaultProfileInclined()
 * @see #BasinInclined()
 * @see #Flex()
 * @see #Erosion()
 * @see #IsostaticFault()
 * @see #ThermalIsostaticFaults()
 * @see #ThermalFaults()
 * @see FaultDialog#OKjButtonActionPerformed()
 * @see FaultDialog#CanceljButtonActionPerformed()
 * @see FaultDialog#NFltjTextFieldActionPerformed()
 * @see FaultDialog#FaultNojComboBoxActionPerformed()
 */
static int NFlt;

/**
 * Number of horizontal data points
 * @see #FaultProfile()
 * @see #InclinedShear()
 * @see #DefFaultProfileInclined()
 * @see #BasinInclined()
 * @see #IsostaticRebound()
 * @see #Flex()
 * @see #IsostaticBasin()
 * @see #IsostaticFault()
 * @see #IsostaticMoho()
 * @see #ModelEt()
 * @see #ModelSt()
 * @see #ThermalIsostaticBasin()
 * @see #ThermalIsostaticFaults()
 * @see #ThermalIsostaticMoho()
 * @see #ThermalBasin()
 * @see #ThermalFaults()
 * @see #ThermalMoho()
 * @see #FlexStratigraphy()
 * @see FaultDialog#SurfacePositionjTextFieldActionPerformed()
 * @see ModelDialog#CanceljButtonActionPerformed()
 * @see ModelDialog#djTextFieldActionPerformed()
 * @see ModelDialog#TotalXjTextFieldActionPerformed()
 */
static int Xt = 150;
```

```
/**
 * maximum total no. horizontal data points - for use in arrays
 * @see #FaultProfile()
 * @see #PureShear()
 * @see #Moho()
 * @see #BaseGran()
 * @see #TopGran()
 * @see #GranDensity()
 * @see #Granite()
 * @see #FlexModelEt()
 * @see #FlexModelSt()
 * @see #Flex()
 * @see #fft()
 */
static int XtMax = 4096;

/**
 * total no. horizontal data points - for use in arrays
 */
static int XtMin = 2000;

/**
 * Number of Time divisions
 * @see #FlexModelEt()
 * @see #FlexModelSt()
 * @see #IsostaticRebound()
 * @see #Flex()
 * @see #Compaction()
 * @see #PorosityAtDepth()
 * @see #IsostaticBasin()
 * @see #IsostaticFault()
 * @see #IsostaticMoho()
 * @see #ModelEt()
 * @see #ModelSt()
 * @see #ThermalIsostaticBasin()
 * @see #ThermalIsostaticFauls()
 * @see #ThermalIsostaticMoho()
 * @see #ThermalBasin()
 * @see #ThermalFauls()
 * @see #ThermalMoho()
 * @see #FlexStratigraphy()
 */
static int Td = 5;

/**
 * Maximum number of Faults for use in array.
 */
static int FltMax = 26;
```

```
/**
 * Inc a step in the calcultaion of e' during the inclined shear calculation
 * @see #InclinedShear()
 * @see #DefFaultProfileInclined()
 */
static int Inc;

/**
 * Establishes which switch statement to carry out
 * @see #Flex()
 */
static int flexLoad;

/**
 * First case of switch statement
 * @see #Flex()
 */
static int flexStart;

/**
 * Last case of switch statement
 * @see #Flex()
 */
static int flexEnd;

/**
 * Calls forward or reverse FFT
 * 1 for forward transform, -1 for inverse transform
 * @see #Flex()
 * @see #fft()
 * @see #four1()
 */
static int Isign;

/**
 * the maximum number of values for the fft/2
 * @see #fft()
 * @see #four1()
 */
static int NN;

/**
 * e is the array position for the value of x-e
 * @see #InclinedShear()
 */
static int e;
```

```
/**
 * Boolean to determine if there is a granite batholith present to be
 * modelled
 * @see #runFaults()
 */
static boolean GranitePresent;

/**
 * Boolean that sets the infill state of the basin
 * @see #IsostaticRebound()
 * @see #Flex()
 * @see ModelDialog#CanceljButtonActionPerformed()
 * @see ModelDialog#NoInfilljRadioButtonActionPerformed()
 */
static boolean Infill =true;

/**
 * Boolean that sets the erosional state of the model
 * @see #Flex()
 */
static boolean Erode = false;

/**
 * Boolean that determines whether the amount of deformation by pure
 * shear equals the amount of deformation by faulting.
 * @see #PureShear()
 */
static boolean BalancedDeformation = true;

/**
 * Boolean that determines whether the amount first faults modelled
 * belong to the forwards fault system or the backwards fault system
 * @see #DefFaultProfileInclined()
 * @see #BasinInclined()
 */
static boolean System_Forwards;

/**
 * Boolean that determines whether the model is isostatically
 * compensated using the flexural isostasy or Airy isostasy method
 * @see #runFaults()
 */
static boolean FlexuralIsostasy =true;
```

```
/**
 * Boolean that determines whether compaction occurrs
 * @see #Flex()
 */
static boolean Compact = false;

/**
 * Boolean that determines method of calculating porosity at depth
 * @see #PorosityAtDepth()
 */
static boolean ChristieAndSchlater = true;

/**
 * Array containing the depth to the basement
 * @see #Flex()
 * @see #Erosion()
 */
static double [] Basement = new double[XtMax+1];

/**
 * Array containing the depth to the infilled basement
 * @see #Flex()
 * @see #Erosion()
 */
static double [] InfilledBasement = new double [XtMax+1];

/**
 * Array containing the amount of infill
 * @see #Flex()
 * @see #Erosion()
 * @see #Compaction()
 */
static double [] Infilled = new double[XtMax+1];

/**
 * Array containing the amount of sediment to be compacted
 * @see #Flex()
 * @see #Compaction()
 */
static double [] CompactData = new double[(XtMax*2)+2];

/**
 * Array containing the adjustment of the fault for any erosion of the
 * fault surface
 * @see #Flex()
 * @see #Erosion()
 */
static double [][] FaultAdj = new double [XtMax+1][FltMax];
```

```
/**
 * Array containing the amount of erosion where 0 = 0% and 1 = 100%
 * @see #Flex()
 * @see #Erosion()
 */
static double [] Erosion = new double [Td+1];


/**
 * Array containing the density data for the granite across the batholith
 * @see #GranDensity()
 * @see #Flex()
 */
static double [] pg = new double [XtMax+1];



/**
 * Array to carry out summation  to calculate Thermal Subsidence for
 * the Model
 * @see #FlexModelEt()
 * @see #ModelEt()
 */
static double [] ModelSummation;

/**
 * Array containing Fault Profile data
 * @see #FaultProfile()
 * @see #InclinedShear()
 * @see #DefFaultProfileInclined()
 * @see #BasinInclined()
 * @see #Flex()
 * @see #IsostaticFault()
 * @see #ThermalFaults()
 */
 static double [][]Flt = new double [XtMax+1][FltMax];

/**
 * Reverses the direction of the fault surface for backwards facing faults
 * @see #FaultProfile()
 * @see #InclinedShear()
 * @see #DefFaultProfileInclined()
 */
static double [][]FltA = new double [Xt+1][FltMax];
```

```
/**
 * Fault Surface Position Array
 * @see #FaultProfile()
 * @see #DefFaultProfileInclined()
 * @see FaultDialog#SurfacePositionjTextFieldActionPerformed()
 * @see FaultDialog#NFltjTextFieldActionPerformed()
 */
static double []Flt_pos = new double [FltMax];

/**
 * Extensional heave along faults
 * @see #InclinedShear()
 * @see #DefFaultProfileInclined()
 * @see FaultDialog#HeavejTextFieldActionPerformed()
 * @see FaultDialog#NFltjTextFieldActionPerformed()
 */
static double []Heave = new double [FltMax];

/**
 * Array containing the data for the depth to the basin
 * @see #BasinInclined()
 * @see #Flex()
 * @see #Compaction ()
 * @see #IsostaticBasin()
 * @see #ThermalBasin()
 */
static double []B = new double [XtMax+1];

/**
 * For Isostatic response to crustal thinning
 * @see #IsostaticRebound()
 * @see #Flex()
 * @see #Compaction()
 * @see #IsostaticBasin()
 * @see #IsostaticFault()
 * @see #IsostaticMoho()
 */
static double [][]Wx = new double [XtMax+1][Td+1];

/**
 * Isostatically compensated depth of basin
 * @see #IsostaticBasin()
 * @see #ThermalIsostaticBasin()
 * @see # FlexStratigraphy()
 */
static double [][]BWx = new double[XtMin+1][Td+1];
```

```
/**
 * Isostatically compensated fault profiles
 * @see #IsostaticFault()
 * @see #ThermalIsostaticFaults()
 */
static double [][][]FWx = new double [XtMin+1][FltMax][Td+1];

/**
 * Isostatically compensated Moho
 * @see #IsostaticMoho()
 * @see #ThermalIsostaticMoho()
 */
static double [][]MWx = new double [XtMin+1][Td+1];

/**
 * Depth to the Moho
 * @see #Moho()
 * @see #IsostaticMoho()
 * @see #ThermalMoho()
 */
static double [] Moho = new double [XtMax+1];

/**
 * Array containing Time stages for calculations
 * @see #FlexModelEt()
 * @see #Flex()
 * @see #ModelEt()
 */
static double []Time = new double [Td+1];

/**
 * Values for the basin for different stratigrapic horizons
 * @see #FlexStratigraphy()
 */
static double [][] TopStratigraphy = new double [XtMin+1][Td+1];

/**
 * Values for the thickness of each unit
 * @see #FlexStratigraphy()
 */
static double [][] UnitThickness = new double[XtMin+1][Td + 1];
```

```
/**
 * Values of beta calculated for the basin from pure shear
 * @see #PureShear()
 * @see #ThermalUplift()
 * @see #FlexModelEt()
 * @see #ModelEt()
 */
static double [] BetaP = new double [XtMax+1];

/**
 * Values of beta calculated for the basin from crustal thinning
 * @see #Beta()
 */
static double [] BetaT = new double [XtMax+1];

/**
 * Values of thermal subsidence at time T
 * @see #FlexModelEt()
 * @see #ModelEt()
 */
 static double [][]ModelThermalSubsidenceT = new double
      [XtMax+1][Td+1];

/**
 * Total thermal subsidence values
 * @see #FlexModelEt()
 * @see #Flex()
 * @see #ModelSt()
 * @see #ThermalIsostaticBasin()
 * @see #ThermalIsostaticFaults()
 * @see #ThermalIsostaticMoho()
 */
 static double [][]ModelThermalSubsidence = new double
      [XtMax+1][Td+1];

/**
 * Thermal Uplift at time t=0
 * @see #ThermalUplift()
 * @see #IsostaticRebound()
 * @see #FlexModelSt()
 * @see #Flex()
 */
 static double []ThermalUplift = new double [XtMax+1];
```

```
/**
 * Intermediate step in the Airy isostatic rebound calculation
 * @see #IsostaticRebound()
 */
 static double [] intermediateA = new double [Xt+1] ;

/**
 * Intermediate step in the Airy isostatic rebound calculation
 * @see #IsostaticRebound()
 */
 static double [] intermediateB = new double [Xt+1];

/**
 * Intermediate step in the Airy isostatic rebound calculation
 * @see #IsostaticRebound()
 */
 static double [] intermediateC = new double [Xt+1];

/**
 * Array containing basin profile for thermally subsided basin.
 * @see #ThermalBasin()
 */
static double [][]BTx = new double [XtMin+1][Td+1];

/**
 * Array containing basin profile for thermally subsided isostatically
 * compensated basin.
 * @see #ThermalIsostaticBasin()
 */
static double [][]BWTx = new double [XtMin+1][Td+1];

/**
 * Array containing fault profiles for thermally subsided basin
 * @see #ThermalFaults()
 */
static double [][][]FTx = new double[XtMin+1][FltMax][Td+1];

/**
 * Array containing fault profiles for thermally subsided isostatically
 * compensated basin.
 * @see #ThermalIsostaticFaults()
 */
static double [][][]FWTx = new double[XtMin+1][FltMax][Td+1];
```

```
/**
 * Array containing Moho profile for thermally subsided basin
 * @see #ThermalMoho()
 */
static double [][]MTx = new double [XtMin+1][Td+1];

/**
 * Array containing Moho profile for thermally subsided isostatically
 * compensated basin.
 * @see #ThermalIsostaticMoho()
 */
static double [][]MWTx = new double [XtMin+1][Td+1];

/**
 * Crustal thinning by pure shear
 * @see #PSThinning()
 * @see #Moho()
 * @see #Beta()
 * @see #IsostaticRebound()
 * @see #Flex()
 */
static double []CTPS = new double [XtMax+1];

/**
 * Crustal thinning by faulting
 * @see #BasinInclined()
 * @see #Beta()
 * @see #IsostaticRebound()
 * @see #Flex()
 */
 static double []CTF = new double [XtMax+1];

/**
 * Thickness of granite intrusion
 * @see #Granite()
 * @see #Flex()
 */
static double []Granite = new double [XtMax+1];

/**
 * Position of the top surface of the granite body
 * @see #Granite()
 * @see #BaseGran()
 * @see #TopGran()
 */
static double []TopGran = new double [XtMax+1];
```

```
/**
 * Position of the bottom surface of the granite body
 * @see #Granite()
 * @see #TopGran()
 */
static double []BaseGran = new double [XtMax +1];

/**
 * Airy isostatic effect of the granite body
 * @see #Granite()
 */
static double [] Granite_Effect = new double [XtMax+1];

/**
 * data to be carried through the fast forward transfer routine
 * @see #Flex()
 * @see #Compaction()
 * @see #fft()
 * @see #four1()
 */
static double []data = new double [(XtMax*2)+2];

/**
 * This array determines the direction of dip of each individual fault. If
   synthetic, the fault dips towards the right end of the model
 * @see #FaultProfile()
 * @see #InclinedShear()
 * @see #DefFaultProfileInclined()
 * @see #BasinInclined()
 */
static boolean [] Flt_Synthetic = new boolean [FltMax];

/**
 * This array determines the system which the fault is in
 * @see #DefFaultProfileInclined()
 * @see #BasinInclined()
 */
static boolean [] Flt_Forwards = new boolean[FltMax];

/**
 * Array containing the shear angle in degrees value for each fault
 * @see #InclinedShear()
 * @see #DefFaultProfileInclined()
 */
static double []ShearAngleDeg = new double [FltMax];
```

```
/**
 * Array containing the shear angle in radians value for each fault
 * @see #InclinedShear()
 * @see #DefFaultProfileInclined()
 */
static double []ShearAngleRad = new double [FltMax];

/**
 * Array containing x' values
 * @see #InclinedShear()
 * @see #DefFaultProfileInclined()
 */
static double [][] xInc = new double [XtMax][FltMax];

/**
 * Array containing Hanging wall x values
 * @see #InclinedShear()
 * @see #DefFaultProfileInclined()
 */
static double [][] HxInc = new double [XtMax][FltMax];

/**
 * Array containing y' values for the fault profile
 * @see #InclinedShear()
 * @see #DefFaultProfileInclined()
 */
static double [][]FltInc = new double [XtMax][FltMax];

/**
 * Array containing heave' values
 * @see #InclinedShear()
 * @see #DefFaultProfileInclined()
 */
static double []HeaveInc = new double[FltMax];

/**
 * Array containing the value of d, distance between values of x
 * @see #InclinedShear()
 * @see #DefFaultProfileInclined()
 */
static double [][]dNew = new double[XtMax][FltMax];

/**
 * Array containing incremental data for the inclined shear construction
 * @see #InclinedShear()
 * @see #DefFaultProfileInclined()
 */
static double [][]Next = new double[XtMax][FltMax];
```

```
/**
 * ZFW represents the first part of the deformed hanging wall, that is
 * the difference between the fault and the hanging wall at the current
 * location
 * @see #InclinedShear()
 * @see #DefFaultProfileInclined()
 */
static double [][]ZFW = new double[XtMax][FltMax];

/**
 * ZHW is the second part of the deformed hanging wall, the difference
 * between the fault and hangingwall at x-e'
 * @see #InclinedShear()
 * @see #DefFaultProfileInclined()
 */
static double [][]ZHW = new double[XtMax][FltMax];

/**
 * Deformed hanging wall thinning values HTInc = ZFW-ZHW
 * @see #InclinedShear()
 * @see #DefFaultProfileInclined()
 */
static double [][]HTInc = new double[XtMax][FltMax];

/**
 * Hx'
 *@see #InclinedShear()
 * @see #DefFaultProfileInclined()
 */
static double [][]OHWInc = new double[XtMax][FltMax];

/**
 * HWx' deformed hanging
 * @see #InclinedShear()
 * @see #DefFaultProfileInclined()
 */
static double [][]OHWInc2 = new double[XtMax][FltMax];

/**
 * Hx
 * @see #InclinedShear()
 * @see #DefFaultProfileInclined()
 */
static double [][]HWInc = new double[XtMax][FltMax];
```

```
/**
 * xH
 * @see #InclinedShear()
 * @see #DefFaultProfileInclined()
 */
static double [][]HX = new double [XtMax][FltMax];

/**
 * crustal thinning due to faulting, This is the position of the hanging
 * wall
 * @see #InclinedShear()
 * @see #DefFaultProfileInclined()
 * @see #BasinInclined()
 */
static double [][]CTFx = new double [XtMax][FltMax];

/**
 * determines the thickness of each unit prior to compaction at any point
 * in the compaction algorithm
 * @see #Compaction()
 */
static double [][] OriginalUnitThickness = new double
      [XtMax*2 +2][Td+1];

/**
 * determines the porosity of each unit at depth during compaction
 * @see #Compaction()
 * @see #PorosityAtDepth()
 */
static double [] PorosityAtDepth = new double [Td+1];

/**
 * determines the 'solid' thickness of the unit during compaction
 * @see #Compaction()
 */
static double [][] ThicknessSolid = new double [XtMax*2+2][Td+1];

/**
 * determines the cumulative amount decrease in thickness of deposits
 * due to compaction
 * @see #Compaction()
 */
static double [] CumulativeAmountOfCompaction= new
      double[XtMax*2+2] ;
```

```
/**
 * determines the ‘maximum’ palaeobathymetry
 * @see #Flex()
 * @see #IsostaticBasin()
 */
static double [] PB = new double [XtMax+1];

/**
 * determines the ‘actual’ palaeobathymetry
 * @see #Flex()
 * @see #IsostaticBasin()
 * @see #FlexStratigraphy()
 */
static double [][] PAb = new double [XtMax + 1][Td +1];

/**
 * determines the subsidence generated by infilling with water
 * @see #Flex()
 */
static double [] waterSub = new double [XtMax*2 +2];

/**
 * determines the basin depth during the flexural isostasy algorithm
 * @see #Flex()
 */
static double [] basinDepth = new double [XtMax+1];
```

```
    /** Creates a new instance of LithosphereExtension */
    public LithosphereExtension() {
    }

   /**
    * employs the methods associated with running the basin model
    * @see #FaultProfile()
    * @see #InclinedShear()
    * @see #DefFaultProfileInclined()
    * @see #BasinInclined()
    * @see #PureShear()
    * @see #PSThinning()
    * @see #Moho()
    * @see #BaseGran()
    * @see #TopGran()
    * @see #GranDensity()
    * @see #Granite()
    * @see #Beta()
    * @see #ThermalUplift()
    * @see #IsostaticRebound()
    * @see #FlexModelEt()
    * @see #FlexModelSt()
    * @see #Flex()
    * @see #Erosion()
    * @see #Compaction()
    * @see #PorosityAtDepth()
    * @see #IsostaticBasin()
    * @see #IsostaticFault()
    * @see #IsostaticMoho()
    * @see #ModelEt()
    * @see #ModelSt()
    * @see #ThermalIsostaticBasin()
    * @see #ThermalIsostaticFaults()
    * @see #ThermalIsostaticMoho()
    * @see #ThermalBasin()
    * @see #ThermalFaults()
    * @see #ThermalMoho()
    * @see #FlexStratigraphy()
    * @see #fft()
    * @see #four1()
    * @see LithosphereExtensionGUI#jButtonRunActionPerformed()
    * @see
LithosphereExtensionGUI#RunFaultsjMenuItemActionPerformed()
    */
    public void runFaults(){
    FaultProfile();
    InclinedShear();
    DefFaultProfileInclined();
```

```
BasinInclined();
Moho();
Beta();
ThermalUplift();
if (GranitePresent){
BaseGran();
TopGran();
GranDensity();
Granite();}
if (FlexuralIsostasy){
FlexModelEt();
FlexModelSt();
Flex();
fft();
four1();
}
else {
ModelEt();
ModelSt();
IsostaticRebound();
}
IsostaticBasin();
IsostaticFault();
IsostaticMoho();
FlexStratigraphy();
ThermalIsostaticBasin();
ThermalIsostaticFaults();
ThermalIsostaticMoho();
ThermalBasin();
ThermalFaults();
ThermalMoho();

}
```

```
    /**
     * This method calculates the fault profile
     */
    public void FaultProfile(){
    for (j=0; j<NFlt; j++){
        if (Flt_Synthetic[j]){ //if fault surface dips towards the right of the
model
    for (i=0; i<=XtMax; i++){
    if (i*d < Flt_pos[j]) //if x > xf
        Flt[i][j] = 0;
    else Flt[i][j] =
            -Zd*(1-Math.exp(-((i*d)-Flt_pos[j])/Zd));
    }}
        else{ // fault surface dips towards left of the model
            for (i=0; i<=XtMax; i++){
    if (i*d > Flt_pos[j]) //if x > xf
        Flt[i][j] = 0;
    else Flt[i][j] =
            -Zd*(1-Math.exp(-(Flt_pos[j]-(i*d))/Zd));
    }
          for (i=0; i<=Xt; i++){
           FltA[i][j] = Flt[(Xt-i)][j];
           //turns the fault in the right direction as fault calculated dipping to
the right
          }
        }
    }
    }
```

```
/**
 * Inclined Shear Construction
 */
  public void InclinedShear(){

      j =0;
      ShearAngleRad[j]=(ShearAngleDeg[j]/180 *Math.PI);
      // converts shear angle in degrees to shear angle in radians
      HeaveInc[j] = Heave[j] * Math.cos(ShearAngleRad[j]);

 if (Flt_Synthetic[j]){ //fault surface dipping right

      for (i=0; i<=Xt; i++){
      x=i*d;
      xInc[i][j] = (x * Math.cos(ShearAngleRad[j]))+ (Flt[i][j] *
Math.sin(ShearAngleRad[j])); //rotated x co-ordinate of fault
      FltInc[i][j] = (-x * Math.sin(ShearAngleRad[j]))+ (Flt[i][j] *
Math.cos(ShearAngleRad[j])); //rotated y co-ordinate of fault
      HxInc[i][j] = xInc[i][j]; //rotated x co-ordinate of hanging wall
      OHWInc[i][j] = -HxInc[i][j] * Math.tan(ShearAngleRad[j]);
      //rotated y co-ordinate of hanging wall
                              }
                        }

 else{ //fault surface dipping left

      for (i=0; i<=Xt; i++){
      x=i*d;
      xInc[i][j] = (x * Math.cos(ShearAngleRad[j]))+ ((FltA[i][j]) *
Math.sin(ShearAngleRad[j]));  //rotated x co-ordinate of fault
      FltInc[i][j] = (-x * Math.sin(ShearAngleRad[j]))+ ((FltA[i][j]) *
Math.cos(ShearAngleRad[j]));  //rotated y co-ordinate of fault
      HxInc[i][j] = xInc[i][j];  //rotated x co-ordinate of hanging wall
      OHWInc[i][j] = -xInc[i][j] * Math.tan(ShearAngleRad[j]);
      //rotated y co-ordinate of hanging wall
                              }
       }

for (i=0; i<Xt; i++){ //method for determining x-e'
         dNew[i][j] = xInc[(i+1)][j]-xInc[i][j];
       // distance between x co-ordinates
                        }
for (i=1; i<Xt; i++){
      XNext = 0;
      Inc = 0;

      for (k=(i-1); k>=1; k--){
            XNext = XNext + dNew[k][j];
```

```
                if (XNext < (HeaveInc[j]+0.001)) Inc = Inc+1;
                //increment increases by 1
                else break;
                                }
        Next[i][j] = Inc; //no of increments in dNew that represent e
                        }

        Next[Xt][j] = Next[(Xt-1)][j];

for (i=0; i<=Xt; i++){
        IHW = i - Next[i][j];
        e = (int)IHW; //array position xe
           if(e > Xt) e = Xt;
           if(e < 0) e = 0;

        ZFW[i][j] = FltInc[i][j] - OHWInc[i][j]; //Fx' – HWx'
        ZHW[i][j] = FltInc[e][j] - OHWInc[e][j]; //Fxe' – HWxe'
        if (i==e){
           HTInc[i][j] = ZFW[i][j];
        }
        else{
           HTInc[i][j] = ZFW[i][j]-ZHW[i][j]; //HTx'
        }
        OHWInc2[i][j]= OHWInc[i][j]+ HTInc[i][j];
        //HWx' deformed hanging wall

        HX[i][j] = (HxInc[i][j] * Math.cos(ShearAngleRad[j]))- (OHWInc2[i][j]
                  * Math.sin(ShearAngleRad[j]));
         //rotation of x co-ordinate HW
        HWInc[i][j] = (HxInc[i][j] * Math.sin(ShearAngleRad[j]))+
                        (OHWInc2[i][j] * Math.cos(ShearAngleRad[j]));
         //rotation of y co-ordinate HW

                }


for (i=0; i<=Xt; i++){
           if (Flt_Synthetic[j]){
              CTFx[i][j]  = HWInc[i][j];
                                }
           else{
             CTFx[i][j] = HWInc[(Xt-i)][j];
              }

                        }
}
```

```
/**
 * Deformed fault profile for multiple faults
 */

 public void DefFaultProfileInclined (){

for (j=1; j<NFlt; j++){

        ShearAngleRad[j]=(ShearAngleDeg[j]/180 *Math.PI);
         //convert shear angle from degrees to radians
         HeaveInc[j] = Heave[j] * Math.cos(ShearAngleRad[j]);


   if (Flt_Synthetic[j]){ //fault surface dipping to the right

        for (i=0; i<=Xt; i++){
        x=i*d;
        xInc[i][j] = (x * Math.cos(ShearAngleRad[j]))+ (Flt[i][j] *
                        Math.sin(ShearAngleRad[j]));
        FltInc[i][j] = (-x * Math.sin(ShearAngleRad[j]))+ (Flt[i][j] *
                         Math.cos(ShearAngleRad[j]));
        HxInc[i][j] = xInc[i][j];
        OHWInc[i][j] = -HxInc[i][j] * Math.tan(ShearAngleRad[j]);
                                }
                        }

   else{ //fault surface dipping left

        for (i=0; i<=Xt; i++){
        x=i*d;
        xInc[i][j] = (x * Math.cos(ShearAngleRad[j]))+ ((FltA[i][j]) *
                        Math.sin(ShearAngleRad[j]));
        FltInc[i][j] = (-x * Math.sin(ShearAngleRad[j]))+ ((FltA[i][j]) *
                        Math.cos(ShearAngleRad[j]));
        HxInc[i][j] = xInc[i][j];
        OHWInc[i][j] = -xInc[i][j] * Math.tan(ShearAngleRad[j]);
                                }
                }

for (i=0; i<Xt; i++){
         dNew[i][j] = xInc[(i+1)][j]-xInc[i][j];
                        }
for (i=1; i<Xt; i++){
        XNext = 0;
        Inc = 0;

        for (k=(i-1); k>=1; k--){
        XNext = XNext + dNew[k][j];
```

```
        if (XNext < (HeaveInc[j]+0.001)) Inc = Inc+1;
        else break;
                                }
        Next[i][j] = Inc;
                    }

         Next[Xt][j] = Next[(Xt-1)][j];


for (i=0; i<=Xt; i++){
        IHW = i - Next[i][j];
        e = (int)IHW;
           if(e > Xt) e = Xt;
           if(e < 0) e = 0;

        ZFW[i][j] = FltInc[i][j] - OHWInc[i][j];
        ZHW[i][j] = FltInc[e][j] - OHWInc[e][j];
        if (i==e){
        HTInc[i][j] = ZFW[i][j];
                  }
        else{
        HTInc[i][j] = ZFW[i][j]-ZHW[i][j];
             }
        OHWInc2[i][j]= OHWInc[i][j]+ HTInc[i][j];


        HX[i][j] = (HxInc[i][j] * Math.cos(ShearAngleRad[j]))- (OHWInc2[i][j]
*
                        Math.sin(ShearAngleRad[j]));
        HWInc[i][j] = (HxInc[i][j] * Math.sin(ShearAngleRad[j]))+
(OHWInc2[i][j] *
                        Math.cos(ShearAngleRad[j]));

                            }

for (i=0; i<=Xt; i++){
       if (Flt_Synthetic[j]){
         CTFx[i][j] = HWInc[i][j];
                                }
       else{
         CTFx[i][j] = HWInc[(Xt-i)][j];
            }
                        }


if(Flt_Forwards[j]){
// if fault being modelled is part of the forwards dipping system
        if (Flt_Synthetic[j]){
```

```
//if the fault being modelled dips towards the end of the section i.e. is synthetic to the main detachment fault
            for (i=0; i<Xt; i++){
            for (k=0; k<j; k++){
                Flt[i][j] = Flt[i][j] + CTFx[i][k];
                                }
            for (k=0; k<j; k++){
                if(System_Forwards){} // if system forwards first
                else{ // if system backwards first
                 if(Flt_Forwards[k]){
// if previous fault is part of the forwards system i.e. the same system as the fault being modelled
                        if (Flt_Synthetic[(k)]){}
// if previous fault dips towards the end of the section i.e. is synthetic to the main detachment fault and the fault being modelled
                        else{
// if previous fault dips towards the beginning of the section i.e. is antithetic to the main detachment fault and the fault being modelled
                            if (i<Flt_pos[j]){
                                Flt[i][j] = Flt[i][k];
                                                }
                            }
                                    }
                    else{
// if previous fault is part of the backwards system i.e. the other system from the fault being modelled
                        if (Flt_Synthetic[(k)]){
// if previous fault dips towards the end of the section i.e. is antithetic to the main detachment fault
                            if (i<Flt_pos[j]){
                                Flt[i][j] = Flt[i][k];
                                                }
                                                    }
                        else {
// if previous fault dips towards the beginning of the section i.e. is synthetic to the main detachment fault
                            if (i<Flt_pos[j]){
                                Flt[i][j] = Flt[i][k];
                                                }
                            }
                        }
                    }
                                }
                            }
        else{
//if the fault being modelled dips towards the beginning of the section i.e. is antithetic to the main detachment fault
```

```
            for (i=0; i<Xt; i++){
            for (k=0; k<j; k++){
                Flt[i][j] = Flt[i][j] + CTFx[i][k];
                                    }
            for (k=0; k<j; k++){
                if(Flt_Forwards[k]){
// if the previous faults are part of the forwards system
                    if (Flt_Synthetic[k]){
// if the previous fault dips towards the end of the section i.e. antithetic to
the fault being modelled
                        if (i>Flt_pos[j]){
                            Flt[i][j] = CTFx[i][k];
                                            }
                        else if (Flt[i][j]<Flt[i][(k)]){
                            Flt[i][j] = Flt[i][k];        }
                                            }
                    else{
// if the previous fault dips towards the beginning of the section i.e. is
synthetic to the fault being modelled
                        if (Flt[i][k]>0){
                            if (Flt[i][j]<Flt[i][k]){
                                Flt[i][j] = Flt[i][k];}
                                            }
                      }
                            }
                else{ //if the previous faults are part of the backwards system
                    if (Flt_Synthetic[(k)]){}
// if the previous faults dip towards the end of the section i.e. antithetic to
the main detachment fault in the system
                    else{
//if the previous faults dip towards the beginning of the section i.e.
synthetic to the main detachment fault
                        if(i<Flt_pos[k]){
                            Flt[i][j]=Flt[i][k];
                                            }
                      }
                    }

                            }
                             }
                      }
                      }


        else{ //if the fault being modelled is part of the backwards system
         if (Flt_Synthetic[j]){
// if the fault being modelled dips towards the end of the section i.e. is
antithetic to the main detachment fault
```

```
          for (i=0; i<Xt; i++){
          for (k=0; k<j; k++){
       Flt[i][j] = Flt[i][j] + CTFx[i][k];}
          for (k=0; k<j; k++){
             if(Flt_Forwards[k]){}
// if the previous faults are part of the forwards system
             else{// if the previous faults are part of the backwards system
       if (Flt_Synthetic[(k)]){}
// if the previos faults dip towards the end of the section i.e are antithetic
to the main detachment fault and synthetic to the fault being modelled
       else {
// if the previous faults dip towards the beginning gof the section i.e.
synthetic to the main detachment fault and antithetic to the fault being
modelled
          if (Flt_pos[j] <= Flt_pos[k]){
          if (Flt[i][j]<Flt[i][(k)]){
          Flt[i][j] = Flt[i][k];     }
                                        }
           }
               }
                                    }
                                    }
                        }
     else{
// if fault being modelled dips towards the beginning of the section i.e.
synthetic to the main detachment in this system

       for (i=0; i<Xt; i++){

          for (k=0; k<j; k++){
       Flt[i][j] = Flt[i][j] + CTFx[i][k];}
          for (k=0; k<j; k++){
             if(Flt_Forwards[k]){
// if previous faults are part of the forwards dipping system
             if (i>=Flt_pos[j]){
               Flt[i][j]=Flt[i][k];
             }
                                 }
             else{// if previous faults are part of the backwards dipping system
       if (Flt_Synthetic[(k)]){}
// if previous faults dip towards the end of the section i.e antithetic to the
main detachment and the fault being modelled
       else{
// if previous faults dip towards the beginning of the section i.e. synthetic
to the main detachment and the fault being modelled
          if(System_Forwards){//if forwards system is modelled first
          if(i>=Flt_pos[j] && i<Flt_pos[k]){
          Flt[i][j] = Flt[i][j] + CTFx[i][k];
```

```
            }
            }
        }
         }}
         }
    }
    }
          }
    }
```

```
    /**
     * Basin Profile
     * This method populates the shaoe of the basin by taking into account all of the
     * fault movement
     */
 public void BasinInclined(){
      for (i=0; i<=Xt; i++){ //increasing x position
      for (j=0; j<NFlt; j++){ //increasing fault no.
         B[i] = CTFx[i][j] +B[i] ;
         CTF[i] = -B[i];
                                }
       for (j=0; j<NFlt; j++){ //increasing fault no.
          if(System_Forwards){ // if the forwards facing system is applied first
                  if (Flt_Forwards[j]){ //if the fault being modelled is part of the forward system
                  if (Flt_Synthetic[j]){ //if fault being modelled dips towards the end of the section i.e synthetic to the main detachment and the fault being modelled
                  if(i>=Flt_pos[j]){ // if i is on or after the surface position of the fault
                  if (B[i] < Flt[i][j]){ // if the basin is shallower than the fault position
                              B[i] = Flt[i][j];
                                    }
                                 }
                                    }
                                     }


          else{ // if the fault being modeller is part of the backwards facing system
                              if (Flt_Synthetic[j]){ //if fault being modelled dips towards the end of the section i.e antithetic to the main detachment and the fault being modelled
                                                  }
```

```
                    else{ //if fault being modelled dips towards the end of
the section i.e synthetic to the main detachment and the fault being
modelled
                if(i>=Flt_pos[j]){ // if i is on or after the surface position of the
fault
                if (B[i] < Flt[i][j]){ // if the basin is shallower than the fault
position
                    B[i] = Flt[i][j];
                            }
                        }
                    }
                        }
                    }
        else{ //system backwards first
                if (Flt_Forwards[j]){ //if the fault being modelled is part of the
forward system
                if (Flt_Synthetic[j]){ //if fault being modelled dips towards the
end of the section i.e synthetic to the main detachment and the fault being
modelled
                                }
                else{ //if fault being modelled dips towards the end of the
section i.e antithetic to the main detachment and the fault being modelled
                if(i<=Flt_pos[j]){ // if i is on or after the surface position of the
fault
                if (B[i] < Flt[i][j]){ // if the basin is shallower than the fault
position
                    B[i] = Flt[i][j];
                            }
                        }
                    }
                            }
                 else{ //if the fault being modelled is part of the backwards
system
                    if (Flt_Synthetic[j]){ //if fault being modelled dips
towards the end of the section i.e antithetic to the main detachment and
the fault being modelled
                        }
                    else{ //if fault being modelled dips towards the end of
the section i.e synthetic to the main detachment and the fault being
modelled
                if(Flt[i][j]<0){ //if fault plane is above the ordinance datum
                if(i >=Flt_pos[j]){ // if i is on or after the surface position of the
fault
                if (B[i] < Flt[i][j]){ // if the basin is shallower than the fault
position
                    B[i] = Flt[i][j];
                            }
                                }
```

```
                    }
                }
                }
                }
                    }
    if((i*d)>(Flt_Backwards_1-1) && (i*d)<(Flt_Forwards_1+1)){ //the
position between the two fault systems
        B[i] = 0;
                                                                    }
                    }
                        }


 /**
  * calculates pure shear distribution
  */

  public void PureShear(){
        PS_Width = PS_Finish-PS_Start; // width of pure shear
                if (BalancedDeformation) {
                        BetaMax = (Math.PI/2)*(TotalHeave/(PS_Width-
TotalHeave));
                                                }
                else {
                        BetaMax = BetaMax - 1;
                    }
    for (i=0; i<=XtMax; i++){ //increments of x position
                if (i*d < PS_Start) {// if x < position of ps start
                                BetaP[i] = 1;
                                    }
                else if (i*d > PS_Finish) { // if x > position of ps finish
                                BetaP[i] = 1;
                                        }
                else { // if x pos within ps distribution band
                        BetaP[i] = (1 + BetaMax * Math.sin(Math.PI * ((i*d) -
                PS_Start)/(PS_Width)));
                    }
                                }
                            }

 /**
  * calculates amount of crustal thinning resulting from pure shear
  */
 public void PSThinning(){
        for (i=0; i<=XtMax; i++){
                CTPS[i] = 0;
```

```
        if (i*d >= PS_Start && i*d <= PS_Finish){ // if x pos within ps
distribution band
                CTPS[i] = (Co-Zd)*(1-(1/BetaP[i]));
                                                }
        else {
                CTPS[i] = 0;
            }
                                }
                        }

 /**
  * calculates the position of the Moho
  */
 public void Moho(){
        for (i=0; i<=XtMax; i++){
                Moho[i]= -Co + CTPS[i];
                                }
                    }


 /**
  * sets the position of the base of the granite
  */
 public void BaseGran(){
        for (i=0; i<=XtMax; i++){
                if (i*d < Granite_Start) { //before start position of the granite
                        BaseGran[i] = 0;
                                        }
                else if (i*d > Granite_Finish){ //after end position of the
granite
                        BaseGran[i] = 0;
                                                }
                else BaseGran[i] = -10;
                                }
                        }
```

```
 /**
  * sets the position of the top of the granite
  */
 public void TopGran(){
        for (i=0; i<=XtMax; i++){
                if (i*d < Granite_Start) {//before start position of the granite
                        TopGran[i] = BaseGran[i];
                                                }
                else if (i*d > Granite_Finish){ //after end position of the
granite
                        TopGran[i] = BaseGran[i];
                                                }
                                }
                           }

 /**
  * sets the density of the granite
  */
 public void GranDensity(){
        for (i=0; i<=XtMax; i++){
                if (i*d < Granite_Start){ //before start position of the granite
                        pg[i] = pc;
                                                }
                else if (i*d > Granite_Finish){ //after end position of the
granite
                        pg[i] = pc;
                                                }
                else{
                        pg[i] = 2630;
                    }
                                }
                           }

 /**
  * calculates the thickness and effect of the granite density
  */
 public void Granite(){
        for (i=0; i<=XtMax; i++){
                if (i*d >= Granite_Start && i*d <= Granite_Finish){//if x pos
within granite distribution
                        Granite[i] = -(BaseGran[i] - TopGran[i]);
                                                                }
                else{
                         Granite[i] = 0;
                    }
        Granite_Effect[i]= Granite[i]* ((pg[i]-pc)/pm);
                                }
                           }
```

```
/**
   * Beta value magintude of crustal thinning
   */
public void Beta() {
        for (i=0; i<=XtMax; i++){
                BetaT[i] = Co/ (Co - (CTF[i]+ CTPS[i]));
                                }
                }

/**
  * Calculates the amount of thermal uplift at Time, t =0Ma after
extension
  */
 public void ThermalUplift(){
    double [] ModelSummation1 = new double[m+1];
//array used for temporary storage of data for cumulative addition
    double [] A3 = new double [XtMax+1];
//array used for temporary storage of data
        for (i=0; i<=XtMax; i++){
                ModelSum1 = 0;
        for (j=0; j<=m; j++){
        A1 = 2*j+1;
        A2 = (1/Math.pow((A1),2.0));
        A3[i]  =
(BetaP[i]/((A1)*Math.PI))*(Math.sin(((A1)*Math.PI)/BetaP[i]));
        ModelSummation1[j] = A2*A3[i];
        ModelSum1 = ModelSum1 + ModelSummation1[j];
                        }
        ThermalUplift[i] = (A*alpha*To)*((4/Math.pow(Math.PI,
2.0))*ModelSum1);
                                }
                        }

 /**
  * Isostatic Rebound including thermal uplift using Airy Isostasy
  */
 public void IsostaticRebound(){
        for (i=0; i<=Xt; i++){// for increasing x position
        intermediateA[i] = CTF[i] * (pc/pm); // Crustal thinning by faulting
        intermediateB[i] = CTPS[i] * ((pm-pc)/pm); //Crustal thinning by
pure shear
        intermediateC[i] = -intermediateA[i] + intermediateB[i] -
ThermalUplift[i];
                if(Infill) {
                        Wx[i][0] =-intermediateC[i]-((CTF[i] +
intermediateC[i]) *
                        (pi/(pm-pi))) - Granite_Effect[i] ;
                         }
```

```
                else {
                        Wx[i][0] = -intermediateC[i] - Granite_Effect[i];
                    }
        for (k=1; k<=Td; k++){  //for increasing time increments
                Wx[i][k]=Wx[i][0];
                                }
                            }
                              }
/**
 * Thermal Subsidence at time =t
 */
public void FlexModelEt() {
      for (k=0; k<=Td; k++){ //for time incerements
      for (i=0; i<XtMax; i++){ //for increasing x position
         ModelSum = 0;
      for (j=0; j<=m; j++){
        ModelSummation = new double[m+1];
        ModelSummation[j] =
        (1/Math.pow((2*j+1),2.0))*((BetaP[i]/((2*j+1)*Math.PI))*(Math.sin(((
        2*j+1)*Math.PI)/BetaP[i]))*Math.exp(-
        (Math.pow((2*j+1),2.0))*(Time[k]/tau)));
        ModelSum = ModelSum + ModelSummation[j];
                          }
        ModelThermalSubsidenceT[i][k] =
        (A*alpha*To)*((4/Math.pow(Math.PI, 2.0))*ModelSum);
                              }
                            }
                           }


   /**
    * Cumulative model of thermal subsidence
    */
   public void FlexModelSt(){
        for (k=0; k<=Td; k++){
        for (i=0; i<=XtMax; i++){
         if (k==0){
                ModelThermalSubsidence[i][k]= ThermalUplift[i];
                  }
                else{
                ModelThermalSubsidence[i][k] = -
                ModelThermalSubsidenceT[i][k] +
                ModelThermalSubsidenceT[i][k-1];
                    }
                                  }
                                }
                                }
```

```
/**
*
*Flexural isostatic compensation routine to main loads
*/
  public void Flex() {
      ps = pi; //sediment density
      double [] Iso_adj = new double [XtMax+1]; //array for the temporary
storage if isostatic adjustment data
      double [] IsoBasin = new double [XtMax +1]; //array for the temporary
storage of isostatically compensated basin depth
      double [] Pab = new double [XtMax + 1]; //array for the temporary
storage of palaeobathymetry data
      int f;

 for (k=0; k<=Td; k++){

 if (Time[k] == 0){ //i.e. this is the first time step
            ElasticThickness = te0;
            flexStart = 1; //start at case 1
              if(Infill){ //if basin infilled end at case 28
            flexEnd = 28;
            }
            else
            flexEnd = 5;} // without infill end at case 5

else{ //for all subsequent time steps
            ElasticThickness = te;
            flexStart = 29; //start at case 29
            flexEnd =32; //end at case 32
     }

    D = (E* Math.pow(ElasticThickness,3))/(12*(1-Math.pow(v,2)));
//calculates flexural wavelength []


 for(flexLoad =flexStart; flexLoad <= flexEnd; flexLoad = flexLoad +1){
//Note working in metres

          j = 0; //resets j to 0 at the beginning of each step

       for(i = 1; i <= XtMax*2; i=i+1){ //loop of x positions

         switch (flexLoad) {
           case 1:   //Load 1 = crustal thinning/thickening due to faulting
                    data[i] = -(CTF[j]*1000)*pc*g;
                      //Note data array starts from element 1 not zero
                    break;
```

```
case  2:  //Load 2 = crustal thinning/thickening due to pure shear

        data[i] = (CTPS[j]*1000)*(pm-pc)*g;
        break;

case 3:  //Load 3 = thermal uplift/subsidence at time = 0
        data[i] = -(ThermalUplift[j]*1000)*pm*g;
        break;

 case 4: //Load 4 - granite intrusion
        data[i] = (Granite[j]*1000)* (pg[j]-pc)*g;
        break;

 case 5: // Load 5 Erosion if no basin infill
        if(Infill)
                data[i] = 0;
        else{ // no infill
                if (Erode){ // erode option selected
                        Basement[j] = B[j]+ Iso_adj[j];
                        for (f=0; f<NFlt; f++){
                                        FaultAdj[j][f] = Flt[j][f]+ Iso_adj[j];
                        //adjusts fault surfaces to consider the material
                removed
                                                }
                 if (Basement[j] > 0){ // above sea level
                        Erosion();
                        data[i] = -((B[j]+
Iso_adj[j])*Erosion[k]*1000)*pc*g;}
                else{ // below ordinance datum i.e sea level
                        data[i] = 0;}
                for (f=0; f<NFlt; f++){
                        Flt[j][f]= FaultAdj[j][f]-Iso_adj[j];
                                }
                        B[j] = Basement[j]- Iso_adj[j];
                          }
                }
                break;
case 6: //Load 6 = first infill load of sea water at time = 0
        basinDepth[j] = CTF[j]-Iso_adj[j];
        data[i] = (basinDepth[j]*1000)*pw*g;
        if(data[i] < 0)
                data[i] = 0;
        break;


case 7: //Load 7 = first infill load of sediment at time t=0
          waterSub[i] = data[i];
          data[i] = ((basinDepth[j]-PB[j])*1000)*(ps-pw)*g;
```

```
                // already loaded with sea water therefore additional density
is ps-pw
                        if ((basinDepth[j]-PB[j])<0){
                        Pab[j] = basinDepth[j];
                        data[i] = 0;
                                                }
                        else{
                        Pab[j]=PB[j];
                             }
                break;

        case 8:// Load 8 = infill of additional subsidence at t=0 below th
        palaeo-sea level infill of sed, above, infill of water
                 data[i] = data[i] + waterSub[i];
                        if ((CTF[j]-Iso_adj[j])<0){ //if above sea level
                        data[i] = 0;
                                                }
                        else if ((CTF[j]-Iso_adj[j])<PB[j]){ //if above
palaeo-sea level
                        Pab[j] = CTF[j]-Iso_adj[j];
                        data[i] = data[i]*pw*g;
                                                }
                        else if ((CTF[j]-Iso_adj[j])> PB[j] &&
basinDepth[j]<PB[j] ){
                        //sediment infill below palaeo-sea level, water above
                        data[i]= ((PB[j]-Pab[j])*pw*g) + (((data[i])-(PB[j]-
                        Pab[j]))*ps*g);
                        Pab[j]= PB[j];

           }
                        else {//below palaeo-sea level
                        data[i] = data[i]*ps*g;
                             }
                 break;

        case 9: //Load 9+ = infill load increments, below palaeo sea level
        infill sed, above water
         case 10:
         case 11:
         case 12:
         case 13:
         case 14:
         case 15:
         case 16:
         case 17:
                if ((CTF[j]-Iso_adj[j])<0){ //if above sea level
                  data[i] = 0;
                                        }
```

```
                else if ((CTF[j]-Iso_adj[j])<PB[j]){ //water infill above palaeo-
                sea level
                  Pab[j] = CTF[j]-Iso_adj[j];
                  data[i] = data[i]*pw*g;
                                                    }
                else if ((CTF[j]-Iso_adj[j])> PB[j] && basinDepth[j]<PB[j] ){
                //sediment infill below palaeo-sea level water above
                  data[i]= ((PB[j]-Pab[j])*pw*g) + ((data[i]-(PB[j]-
Pab[j]))*ps*g);
                  Pab[j]= PB[j];
                                                                                    }
                        else { //entirely below palaeo-sea level
                     data[i] = data[i]*ps*g;
                       }
                break;

        case 18://load 18 - erode if infill
                        if (Erode){
                        Basement[j] = B[j]+ Iso_adj[j];
                        if (Basement[j] < 0){ //below sea level
                        Infilled[j] = - Basement[j] - PB[j];
                                        }
                        else{ //basement above sea level
                                Infilled[j] = 0;
                             }
                        for (f=0; f<NFlt; f++){ //increasing fault no
                        FaultAdj[j][f] = Flt[j][f]+ Iso_adj[j];
                                        }
                        if (Basement[j] > 0){ // basement above sea level
                        Erosion();
                        data[i] = -((B[j]+ Iso_adj[j])*Erosion[k]*1000)*pc*g;
                                        }
                        else{
                        data[i] = 0;
                             }
                        for (f=0; f<NFlt; f++){ //increasing fault no
                        Flt[j][f]= FaultAdj[j][f]-Iso_adj[j];
                                        }
                        B[j] = Basement[j]- Iso_adj[j];
                          }
                        else{ //erode not selected
                data[i] = 0;
                                }
                break;

        case 19: //load19+ erode increments
        case 20:
        case 21:
```

```
        case 22:
        case 23:
        case 24:
        case 25:
        case 26:
        case 27:
        case 28:
              if (Erode){ //erode option selected
                Basement[j] = B[j]+ Iso_adj[j];
              //adjusting the basement for previous isostatic adjustments
                InfilledBasement[j]= Basement[j]+Infilled[j];
              //determining height of infilled basin with isostatic
adjustments
                for (f=0; f<NFlt; f++){ //increasing fault no
                FaultAdj[j][f] = Flt[j][f]+ Iso_adj[j];
              //fault surface with isostatic adjustments
                                    }
                    if (Basement[j] > 0){ //above sea level
                    Basement[j] = Basement[j] + (data[i]/1000);
                    FaultAdj[j][f] = FaultAdj[j][f] + (data[i]/1000);
                    data[i] = data[i]*pc*g;
                                          }
                    else if (InfilledBasement[j] > 0){ //above sea level
                    data[i] = data[i]*pi*g;
                                                }
                    else if (InfilledBasement[j] < 0 &&
                    (InfilledBasement[j]+PB[j])>0){
                    // water level pushed above sea level – water drains
                    away
                    data[i] = data[i]*pw*g;
                                                }
                    else{ //below sea level = no erosion
                    data[i] = 0;
                         }
                    for (f=0; f<NFlt; f++){ //increasing fault no
                Flt[j][f]= FaultAdj[j][f]-Iso_adj[j];
                                    }
                B[j] = Basement[j]- Iso_adj[j];
                                    }
              break;

        case 29: //Load 29 - thermal subsidence
              IsoBasin[j]= CTF[j]-Iso_adj[j];
              data[i] = (ModelThermalSubsidence[j][k]*1000)*pm*g;
              break;

        case 30:
```

```
        //Load 30 - Load due to sediment deposited in thermal subsidence
with water
                if (Infill){ //if the basin is infilled
                CompactData[i]=  data[i];
                //loads the compact data array with data for compacting the
        sediments
                data[i] = data[i]*pw*g;
                if(((-B[j])-Iso_adj[j]) < 0){ //above sea level
                  data[i] = 0;
                                        }
                        }
                else{ //below sea level
                  data[i] = 0;
                     }
                break;

         case 31:
        //Load 31 - infill of thermal subsidence with sediment below palaeo
sea level
                pi =ps;
                waterSub[i]=data[i];
                if ((IsoBasin[j]-(CompactData[i]+ waterSub[i]))> 0){
                //basin above ordinance datum
                  data[i] = 0;
                                                                }

                        else if ((IsoBasin[j]-(CompactData[i]+ waterSub[i]))> -
PB[j]){
                //basin above palaeo-sea level
                        data[i] = 0;
                                                                        }
                        else if ((IsoBasin[j]-(CompactData[i]+ waterSub[i]))
                < -PB[j] && IsoBasin[j]>-PB[j] ){
                //below palaeo-sea level after compaction and water induced
                subsidence
                  data[i]= (((CompactData[i]+ waterSub[i])-(PB[j]-
Pab[j]))*ps*g);
                   Pab[j]= PB[j];
                                                        }
                        else { //below palaeo-sea level
                    data[i] = data[i]*ps*g;
                        }
                break;

         case 32:
        // Compaction of sediments and infill of additional accommodation
space
                if (Infill){ //basin infill selected
```

```
        if (Compact){ //compaction selected
          CompactData[i] = CompactData[i]+ data[i]+ waterSub[i];
        Compaction(); //calls the Compaction method
        data[i]= data[i]*pi*g;
                    }
        else{ //no compaction
          data[i] = 0;
             }
                  }
        else{ //no infill
          data[i] = 0;
             }
        break;


                        }

if(i >=2048  && i < 6144 ){
j = j +1;
                                }
        }

          Isign = 1;                    // 1 for forward transform
          fft();                        // Call FFT method

int h = 0;
for( i=1; i <= XtMax*2; i=i+2){
resp1 = (float)Math.pow((2*Math.PI*h/(XtMax*2*1000f)),4);
if(flexLoad >= 30) {
resp2 = 1/(((pm-pi)*g)+(D*resp1));
                    }
else {
resp2 = 1/((pm*g)+(D*resp1));
      }
data[i] = data[i]*resp2;
data[i+1] = data[i+1]*resp2;
h = h + 1;
     }

        Isign = -1;                     // -1 for inverse transform
        fft();                          // Call FFT method

j = 0;
for( i = 1; i <= XtMax*2; i=i+1){
if(i >= 2048 && i <= 6144){
Iso_adj[j] = Iso_adj[j]-(data[i]/1000);
j=j+1;
                                }
```

```
                                        }
}
        for (j = 0; j<Xt; j++){
        Wx[j][k] =  Iso_adj[j];
                                        }
  }
}

/**
 * Calcultes the amount of erosion and the uplift generated by the erosion
 */
public void Erosion(){
    int f;
    if (Basement[j] > 0){ //if basin over ordinance datum
    Basement[j] = Basement[j]-(Basement[j]*Erosion[k]);
    for (f=0; f<NFlt; f++){
    FaultAdj[j][f] = FaultAdj[j][f]-(FaultAdj[j][f]*Erosion[k]);
        // adjusts the fault surface for erosion
                            }
                        }
   else{
   Infilled[j] = InfilledBasement[j]-(InfilledBasement[j]*Erosion[k])-
Basement[j];
        }
}
```

```
/**
 * Calculates the amount of compaction and the new accommodation space
generated by compaction
 */
  public void Compaction(){
      double [] CompactedUnitThickness = new double [Td+1];
      double [] AmountOfCompaction = new double [Td+1];
      double [][] ThicknessPore = new double [XtMax*2+2][Td+1];
      double addition;
      SPorosity = 0.49; //surface porosity
      if(k==1){
      //time step 1 therefore the first time the sediments are loaded by other
sediments
          Basement[j] = (B[j]+ Wx[j][0]);
          if(Basement[j]+Infilled[j] > 0){ //above ordinane datum
          OriginalUnitThickness[i][0] = Infilled[j];
          }
          else{
         OriginalUnitThickness[i][0] = -Basement[j];
          }
         if (OriginalUnitThickness[i][0]<0){
         OriginalUnitThickness[i][0] = 0;
                                          }

         OriginalUnitThickness[i][1] = CompactData[i]/1000;
         if (OriginalUnitThickness[i][1]<0) {
         OriginalUnitThickness[i][1] = 0;
                                          }
         ThicknessSolid[i][0]=OriginalUnitThickness[i][0]* (1-SPorosity) ;
         ThicknessSolid[i][1]=OriginalUnitThickness[i][1]* (1-SPorosity) ;
                  }

      else if (k>1){
          addition = 0;
          for (m=0; m < (k-1); m++){ //time increments
          addition = addition + OriginalUnitThickness[i][m];
           // cumulative thickness
                                       }
     OriginalUnitThickness[i][(k-1)] = -((B[j]+ Wx[j][(k-1)])+ addition);
     OriginalUnitThickness[i][k]= CompactData[i]/1000;

      if (OriginalUnitThickness[i][k]<0) {
        OriginalUnitThickness[i][k] = 0;
                                         }
     ThicknessSolid[i][(k-1)]=OriginalUnitThickness[i][(k-1)]* (1-SPorosity) ;
     ThicknessSolid[i][k]=OriginalUnitThickness[i][k]* (1-SPorosity) ;
                  }
```

```
        CumulativeAmountOfCompaction[i] = 0;
        for (m=k-1; m >= 0; m--){ //decreasing time increments
        PorosityAtDepth(); //calls the porosity at depth method
        ThicknessPore[i][m]= ThicknessSolid[i][m]/
          (1- PorosityAtDepth[m])*PorosityAtDepth[m];
        CompactedUnitThickness[m] =
ThicknessSolid[i][m]+ThicknessPore[i][m];
        AmountOfCompaction[m] = OriginalUnitThickness[i][m]-
          CompactedUnitThickness[m];
          //caulculates the amount this layer has been compacted at time m
        CumulativeAmountOfCompaction[i] =
CumulativeAmountOfCompaction[i] +
          AmountOfCompaction[m];
        OriginalUnitThickness[i][m] = CompactedUnitThickness[m];
                                    }

        data[i]= CumulativeAmountOfCompaction[i]*1000;
                                  }

/**
 * Calculates the porosity at depth by either the Sclater and Christie
(1980) or Falvey
 * & Middleton (1981) methods
 */
  public void PorosityAtDepth(){
     double BurialDepth;
     double CumulativeBurialDepth;
     double [] InversePorosityAtDepth = new double [Td+1];
     double Cy;
     ck = 0.27;

     for(m=0; m<k; m++){
                CumulativeBurialDepth = 0;
     for (int n=m+1; n<=k; n++){
                CumulativeBurialDepth = CumulativeBurialDepth +
                OriginalUnitThickness[i][n];
                //determines the depth of burial of the sediments
                                  }
                BurialDepth = CumulativeBurialDepth ;
                          }

     if (ChristieAndSchlater){
        // if Sclater and Christie (1980) method is used
          for(m=0; m<k; m++){
                Cy = ck *BurialDepth;
                PorosityAtDepth[m]= SPorosity* Math.exp(-Cy);
                                  }
                                 }
```

```
      else{
        // if Falvey and Middleton (1981) method is used
         for(m=0; m<k; m++){
                InversePorosityAtDepth[m]=1/SPorosity + ck *BurialDepth;
                PorosityAtDepth[m]= 1/InversePorosityAtDepth[m];
                                }
         }
                                    }
/**
 * Basin following isostatic and thermal uplift
 */
public void IsostaticBasin(){
    for (i=0; i<=Xt; i++){
       BWx[i][k] = B[i]  + Wx[i][k];
           if (BWx[i][k] > -PB[i] ){
                PAb[i][k] = -BWx[i][k];
                                    }
           if (BWx[i][k] > 0){
                PAb[i][k] = 0;
                                }
          else if (BWx[i][k] < -PB[i] ){
                PAb[i][k] = PB[i];
                                }
                            }
                                 }

/**
 * Fault Profiles following isostatic and thermal uplift
 */
public void IsostaticFault(){
   for (k=0; k<=Td; k++){
   for (j=0; j<NFlt; j++){
   for (i=0; i<Xt; i++){
        FWx[i][j][k] = Flt[i][j] + Wx[i][k] ;
                        }
                          }
                            }
                              }

/**
 * Moho Profile following isostatic and thermal uplift
 */
public void IsostaticMoho(){
   for (k=0; k<=Td; k++){
   for (i=0; i<=Xt; i++){
        MWx[i][k]= Moho[i] + Wx[i][k];
                          }
                            }
```

```
                    }

/**
 * Thermal Subsidence at time =t
 */
public void ModelEt() {
      for (k=0; k<=Td; k++){
      for (i=0; i<=Xt; i++){
        ModelSum = 0;
      for (j=0; j<=m; j++){
        ModelSummation = new double[m+1];
        ModelSummation[j] =
        (1/Math.pow((2*j+1),2.0))*((BetaP[i]/((2*j+1)*Math.PI))*
        (Math.sin(((2*j+1)*Math.PI)/BetaP[i]))*
        Math.exp(-(Math.pow((2*j+1),2.0))*(Time[k]/tau)));
        ModelSum = ModelSum + ModelSummation[j];
                    }
        ModelThermalSubsidenceT[i][k] = ((A*pm*alpha*To)/
        (pm-pi))*((4/Math.pow(Math.PI, 2.0))*ModelSum);
                  }
                    }
                }

   /**
    * Model thermal subsidence
    */
   public void ModelSt(){
      for (k=0; k<=Td; k++){
        if(k>0){
        for (i=0; i<=Xt; i++){
        ModelThermalSubsidence[i][k] = ModelThermalSubsidenceT[i][0] -
        ModelThermalSubsidenceT[i][k];
                    }
              }
                    }
                  }

   /**
    * Basin with Isostatic compensation and thermal subsidence
    */
   public void ThermalIsostaticBasin(){
      for (k=0; k<=Td; k++){
      for (i=0; i<Xt; i++){
        BWTx[i][k]= BWx[i][k]- ModelThermalSubsidence[i][k];
                  }
                    }
                        }
```

```
/**
 * Fault Profiles with Isostatic Compensation and Thermal Subsidence
 */
public void ThermalIsostaticFaults(){
   for (k=0; k<=Td; k++){
   for (j=0; j<NFlt; j++){
   for (i=0; i<=Xt; i++){
     FWTx[i][j][k]= FWx[i][j][k]-ModelThermalSubsidence[i][k];
                        }
                         }
                          }
                                  }
/**
 * Moho porfile for basin woth Isostatic Compensation and Thermal
Subsidence
 */
public void ThermalIsostaticMoho(){
    for (k=0; k<=Td; k++){
    for (i=0; i<Xt; i++){
      MWTx[i][k]= MWx[i][k]-ModelThermalSubsidence[i][k];
                       }
                          }
                                  }

/**
 * Basin with thermal subsidence
 */
public void ThermalBasin(){
   for (k=0; k<=Td; k++){
   for (i=0; i<=Xt; i++){
      BTx[i][k]= B[i]- ModelThermalSubsidence[i][k];
                       }
                         }
                           }

/**
 * Fault Profiles Thermal Subsidence
 */
public void ThermalFaults(){
   for (k=0; k<=Td; k++){
   for (j=0; j<NFlt; j++){
   for (i=0; i<Xt; i++){
   FTx[i][j][k]= Flt[i][j]-ModelThermalSubsidence[i][k];

                       }
                         }
                           }
                              }
```

```
    /**
     * Moho porfile for basin with Isostatic Compensation and Thermal
Subsidence
     */
    public void ThermalMoho(){
       for (k=0; k<=Td; k++){
       for (i=0; i<=Xt; i++){
          MTx[i][k]= Moho[i] - ModelThermalSubsidence[i][k];
                                }
                                  }
                                    }
```

```
/**
 * Stratigraphy – calculates the stratigraphy for display
 */
public void FlexStratigraphy(){
   double add;
   for (j=0; j<=Td; j++){   //increasing time increments
      for (i=0; i<=Xt; i++){ //increasing x
                  if(j ==0){ //timestep 1
            UnitThickness[i][j] = (-BWx[i][j]) - PAb[i][j];
            if (UnitThickness[i][j] < 0){
            UnitThickness[i][j] = 0;
                                    }
                  }
            else{
                  UnitThickness[i][j] = (-(BWx[i][j] - BWx[i][j-1])) –
                  (PAb[i][j]-PAb[i][j-1]);
            if (BWx[i][j-1]>0){
                  UnitThickness[i][j] = (-BWx[i][j]);
                              }
            if (UnitThickness[i][j] < 0){
                  UnitThickness[i][j] = 0;
                                    }
               }
    add = 0;
      for (m=0; m<=j; m++){
      add = add + UnitThickness[i][m];
                           }
      TopStratigraphy[i][j]= BWx[i][j] - add;
                        }
                     }
                           }

/**
 * FFT algorithm - includes fft() method and sub-method four1()
 * Based upon standard Cooley & Tukey (1965) methodology
 * This method mostly prepares data array for processing by four1()
method
 */
public void fft(){
int nm, k1j, k1i, k2j, k2i ;
double s, fn, wr, wi, ex, wwr, wwi, wrr, a1, a2, b1, b2;
    NN = (XtMax)/2;
     if(Isign == 1){
            data[XtMax +1] = 0;
            data[XtMax +2] = 0;
            four1();
     }
     s = data[1];
```

```
nm = NN/2;
fn = (float) XtMax ;
ex = (2*(float)Math.PI)/fn;
j = NN;
wr = 1;
wi = 0;
wwr = (float)Math.cos(ex);
wwi = (float)-Math.sin(ex);

if(Isign > 0){
        data[1] = data[1] + data[2];
        data[XtMax +1] = s-data[2];
        data[2] = 0;
        data[XtMax+2] = 0;
}else{
        data[1] = 0.5*(data[1]+data[XtMax +1]);
        data[2] = 0.5*(s-data[XtMax +1]);
        data[XtMax +1] = 0;
        data[XtMax +2] = 0;
}
data[NN+2] = -data[NN+2];

for(i = 2; i <= nm; i=i+1){
        wrr = wr*wwr-wi*wwi;
        wi = wr*wwi+wi*wwr;
        wr = wrr;
        k1j = 2*j-1;
        k1i = 2*i-1;
        k2j = 2*j;
        k2i = 2*i;
        a1 = 0.5*(data[k1i]+data[k1j]);
        a2 = 0.5*(data[k2i]-data[k2j]);
        b1 = 0.5*(-data[k1i]+data[k1j]);
        b2 = 0.5*(-data[k2i]-data[k2j]);
        s = b1;
        b1 = b1*wr+b2*wi;
        b2 = b2*wr-s*wi;
        data[k1i] = a1-b2;
        data[k2i] = -a2-b1;
        data[k1j]= a1+b2;
        data[k2j] = a2-b1;
        j = j-1;
}

if(Isign == -1){
        four1();
        for(i=1; i<= XtMax;i=i+1)
                data[i] =data[i]/NN;
```

```
                data[XtMax +1] = 0;
            data[XtMax +2] = 0;
        }
}


 /**
 * Sub-method to fft() - contains main FFT calculation
 */
 public void four1(){
int ipo, ip1, ip2, i2a, i2b, ip3, i3rev, i1, i3;
double tempr, tempi, theta, sinth, wstpr, wstpi, wr, wi;

      ipo = 2;
      ip3 = ipo * NN;
      i3rev = 1;
       for(i3 = 1; i3 <=ip3; i3=i3+ipo){
            if(i3 < i3rev){
                  tempr = data[i3];
                  tempi = data[i3+1];
                  data[i3] = data[i3rev];
                  data[i3+1] = data[i3rev+1];
                  data[i3rev] = tempr;
                  data[i3rev+1] = tempi;
            }
            ip1 = ip3/2;
                  while(i3rev > ip1){
                        i3rev = i3rev - ip1;
                        ip1 = ip1/2;
                        if(ip1 < ipo)
                              break;
                  }
         i3rev = i3rev+ip1;
       }

       ip1 = ipo;
       while(ip1 < ip3){
            ip2 = ip1*2;
            theta = (2 * (float)Math.PI)/((float)(Isign*ip2/ipo));
            sinth = (float)Math.sin(theta/2);
            wstpr = -2*sinth*sinth;
            wstpi = (float)Math.sin(theta);
            wr = 1;
            wi = 0;
            for(i1 = 1; i1 <=ip1; i1=i1+ipo){
                  for(i3 = i1; i3 <= ip3; i3=i3+ip2){
                        i2a = i3;
                        i2b = i2a +ip1;
```

```
                                tempr = wr*data[i2b]-wi*data[i2b+1];
                                tempi = wr*data[i2b+1]+wi*data[i2b];
                                data[i2b] = data[i2a]-tempr;
                                data[i2b+1] = data[i2a+1]-tempi;
                                data[i2a] = data[i2a]+tempr;
                                data[i2a+1] = data[i2a+1]+tempi;
                        }
                tempr = wr;
                wr = wr*wstpr-wi*wstpi+wr;
                wi = wi*wstpr+tempr*wstpi+wi;
                }
                ip1 = ip2;
        }

  }
}
```

# 6 Appendix D: Modelling of the subsidence history of the Northumberland Trough Region

## 6.1 Burial History Modelling

Burial history is a quantitative method for calculating the amount of tectonic subsidence generated from extension within a lithified column of strata (Bond and Kominz, 1984). In order to determine the amount of tectonic related subsidence, the strata must first be decompacted. Once the strata have been decompacted, the effect of isostasy, palaeobathymetry and palaeoeustacy can be corrected for to leave the tectonic subsidence (Allen and Allen, 1990).

### *6.1.1 Decompaction*

As demonstrated in section 5.4. compaction occurs as deposition of sediment increases the overburden stress, which results on a reduction in porosity (Lerche, 1990). In order to calculate tectonic subsidence, it is necessary to know the thickness of sediment deposited before it was compacted. This is achieved by stripping layers of sediment and decompacting the layers beneath them. As discussed in section 5.4.3.1, there is an empirical relationship between porosity and depth. This relationship was quantified by Sclater and Christie (1980) and Falvey and Middleton (1981) in equations [5.67] and [5.68] respectively. By removing the top layer of sediment, each underlying layer of sediment moves up their respective porosity-depth curve, increasing the thickness of the pore

space within the layer and thus causing them to decompact. The total thickness of sediment ($y_t$) between two vertical points, $y_1$ and $y_2$ is comprised of the thickness of pore space ($y_p$) and the thickness of sediment grains ($y_s$) such that:

$$y_t = y_s + y_p \qquad \text{[D6.1]}$$

The thickness of the sediment grains remains constant but the amount of pore space decreases as sediments are compacted, and increases as the sediments are decompacted. The thickness of the pore space between $y_1$ and $y_2$ is calculated by integrating the porosity over the depth interval (Allen and Allen, 1990).

$$y_p = \int_{y_1}^{y_2} \phi_o e^{-cy}\, dy \qquad \text{[D6.2]}$$

where: $\phi_o e^{-cy}$ is the porosity at depth y given by equation [5.68]

When integrated, this gives:

$$y_p = \frac{\phi_0}{c}\left(\exp^{(-cy_1)} - \exp^{(-cy_2)}\right) \qquad \text{[D6.3]}$$

On decompaction, the pore space ($y'_p$) is given by:

$$y'_p = \frac{\phi_0}{c}\left(\exp^{(-cy'_1)} - \exp^{(-cy'_2)}\right) \qquad \text{[D6.4]}$$

where: $y'_1$ and $y'_2$ are the new position of the top and bottom of the unit respectively

The decompacted thickness of sediment ($y'_t$) is given by:

$$y'_t = y_s - y'_p$$
$$y'_t = y_2 - y_1 - \frac{\phi_0}{c}\left(\exp^{(-cy_1)} - \exp^{(-cy_2)}\right) + \frac{\phi_0}{c}\left(\exp^{(-cy'_1)} - \exp^{(-cy'_2)}\right) \qquad \text{[D6.5]}$$

Figure D6.1 illustrates the method of sediment decompaction. A sediment layer at present depth $y_1$, $y_2$ is moved vertically to a shallower depth $y'_1$, $y'_2$. The volume of the pore space increases according to equation [D6.4] and the new decompacted thickness of sediment is calculated using equation [D6.5].

### 6.1.1.1 Interlayered Bedding

The method for modelling decompaction described above assumes a single lithology to determine the porosity of each unit. However, units within the lithified column of strata undergoing decompaction are often interbedded. Assuming a quasihomogeneous distribution of sublayers within the layer, with each lithology occurring in the same proportions, the average porosity ($\phi_{(z)}$) can be calculated (Ungerer *et al.*, 1990).

$$\frac{1}{\phi_{(y)}} = \sum_{m=1}^{n} \frac{c_m}{\phi_{(y)\,m}} \qquad [D6.6]$$

where: $c_m$ is the fully compacted proportion of the lithology m

n is the number of lithologies

each lithology, m, is characterised by a porosity depth relation $\phi = \phi_{(y)\,m}$

### 6.1.1.2 Erosion

Compaction is assumed to be an inelastic process that is largely irreversible. As such uplift and removal of material by erosion do not reverse porosity changes that resulted from deeper burial (Springer, 1993; Holliday, 1999). In this way the basic decompaction model described in section D6.1.1 needs to be adapted to consider the maximum burial depth

that the layer has experienced during its existence, not its present day burial depth. If the strata that have been eroded were originally on the top of the stratigraphy in the section being decompacted, it can simply be added as the first layer of stratigraphy to be removed, if the amount of erosion is known. If however, the strata within the sedimentary column have experienced erosion, the effect of the eroded material on compaction can be determined by calculating the maximum burial depth of each layer, which can be determined as follows:

- For layers of sediment above the erosional event this is the same as the present day burial depth.
- For layers of sediment beneath the erosional event, the maximum burial depth depends upon the amount of sediment removed by erosion and the amount of sediment subsequently deposited.
- If the amount of material subsequently deposited is greater than the amount of material eroded, the present day burial depth will be the maximum burial depth.
- If the amount of material deposited after the erosion event is less than the amount of material removed, the maximum burial depth will equal the present day burial depth plus the amount of material erode minus the amount of material deposited after the erosional event. The solid thickness of the layer ($y_s$) is calculated from the maximum burial depth. This

remains constant throughout the decompaction modelling. At the time stage where erosion occurs, no decompaction event accompanies the removal of material.

#### 6.1.1.3 Igneous Intrusions

The basic theory of decompaction described above does not take into account the effect that the imposition of an igneous intrusion has on sediment compaction. Within the Northumberland Trough Region, the Whin Sill swarm was intruded into the sediments of the Tyne Limestone Formation and the Alston Formation. The intrusion of a sill or dyke will bury the sediments beneath them deeper, causing further compaction. In addition, due to the crystalline nature of igneous rocks, the intrusive body will not be subject to physical compaction under the pressure of the overlying rocks or any additional sediment deposited. Figure D6.2 illustrates the decompaction model with an igneous intrusion. Igneous intrusions should be modelled as layers in the correct position within the strata. If they are within a formation or unit that forms a layer within the decompaction model, the formation should be split into two layers located either side of the intrusion, as only the strata beneath the intrusion are compacted by it. Due to their crystalline nature, the intrusions should be modelled with 100% thickness solid ($y_s$) and 0% thickness pore space ($y_p$). In this way the layer will not decompact when layers of sediment are removed, or compact when layers of sediment are added. The intrusions should be removed from the decompaction model at the correct chronological stage during which they were intruded, rather than in layer

order. This is necessary in order to decompact the sediments beneath them at the correct time.

### *6.1.2 Isostatic, palaeobathymetric and palaeoeustatic corrections*

The subsidence curve generated following decompaction is a record of the subsidence generated by tectonics and sediment loading. To calculate the tectonic subsidence it is necessary to first remove the subsidence that results from the isostatic response to loading of the lithosphere. The isostatic response to the sediment load can be calculated for Airy or flexural isostasy.

The loading effect of the sediment using an Airy isostatic approach is given by:

$$Y_b = S\left(\frac{\rho_m - \overline{\rho_s}}{\rho_m - \rho_w}\right) \qquad \text{[D6.7]}$$

where: $Y_b$ is the depth of the basement corrected for sediment loading

$S$ is the total thickness of the sedimentary column corrected for compaction

$\rho_m$ is the density of the mantle

$\overline{\rho_s}$ is the bulk sediment density of the entire column

$\rho_w$ is the density of water

The bulk sediment density of each layer ($\rho_s$) is related to its porosity and the density of the sediment grains ($\rho_{sg}$) such that the density of each sediment layer is given by:

$$\rho_s = \phi_y \rho_w + \left(1 - \phi_y\right)\rho_{sg} \qquad \text{[D6.8]}$$

The bulk sediment density of the entire sediment column is made up of the density of m layers of sediment such that:

$$\overline{\rho_s} = \sum_{m=1}^{n} \left( \frac{\phi_m \rho_w + (1 - \phi_m) \rho_{sg_m}}{S} \right) y_m \qquad [D6.9]$$

where: $\phi_m$ is the porosity of the $m^{th}$ layer

$\rho_{sg_m}$ is the sediment grain density of the $m^{th}$ layer

$y_m$ is the thickness of the $m^{th}$ layer

These calculations assume that subsidence was filled to sea level with sediment and that the palaeoeustatic sea level was the same as the present day eustatic sea level. In order to accurately calculate the subsidence associated with tectonic processes, the data must be corrected for palaeobathymetry and palaeoeustacy. The depth of the water at the time the sediment was deposited is an important consideration because the depth to the basement is equal to the thickness of the sediment plus the thickness of the water column. In addition, the isostatic effect of the eustatic sea level must be considered as an increase in the eustatic sea level results in subsidence as the excess weight of water is compensated for. Conversely, a decrease in eustatic sea level results in uplift as a result of the removal of the weight of the water from the lithosphere (Allen and Allen, 1990).

These corrections for sediment loading, palaeobathymetry and eustacy are incorporated into a calculation for tectonic subsidence (Steckler and Watts, 1978; Bond and Kominz, 1984):

$$Y_t = \Phi \left[ S \left( \frac{\rho_m - \overline{\rho_s}}{\rho_m - \rho_w} \right) - \Delta SL \left( \frac{\rho_w}{\rho_m - \rho_w} \right) \right] + \left[ w_d - \Delta SL \right] \qquad \text{[D6.10]}$$

where: $Y_t$ is the amount of tectonic subsidence

$\Phi$ is a basement response function relating sediment and water loads to tectonic subsidence equal to 1 for Airy isostasy

$\Delta SL$ is the difference between present day eustatic sea level and the palaeoeustatic sea level

This equation is applied to the data from the decompaction model in order to calculate the tectonic subsidence (including thermal post-rift subsidence) and the subsidence resulting from sedimentary loading using Airy isostatic compensation.

The flexural isostatic approach to burial history has to account for the strength of the lithosphere supporting loads by bending. Assuming the load upon the lithosphere to be periodic and sinusoidal, the load exerted on the lithosphere is given by (Allen and Allen, 1990):

$$L_{h(x)} = h_o \sin \left( \frac{2\pi x}{\lambda_f} \right) \rho_s g \qquad \text{[D6.11]}$$

where: $\lambda_f$ is the flexural wavelength given by equation [4.51]

$h_o$ is the maximum height of the load

$g$ is the specific gravity

The flexural response of the lithosphere to this load, $W_h$, is given by:

$$\frac{d^2}{dx^2} D \frac{d^2 W_h}{dx^2} + \left( \rho_m - \rho_s \right) g W_h = h_o \sin \left( \frac{2\pi x}{\lambda} \right) \rho_s g \qquad \text{[D6.12]}$$

Due to the assumed periodic and sinusoidal nature of the load, the flexural response of the lithosphere will also be periodic and sinusoidal. As such, if the flexural wavelength is short, the lithosphere behaves more rigidly and

the deflection caused by the load is small compared to the height. This is reflected in the degree of compensation of the load, $C_f$; the ratio of the flexural deflection compared to the maximum hydrostatic deflection resulting from the Airy isostatic hypothesis.

$$C_f = \frac{\left(\rho_m - \rho_s\right)}{\rho_m - \rho_s + \frac{D}{g}\left(\frac{2\pi}{\lambda}\right)^4} \qquad \text{[D6.13]}$$

where: $D$ is the flexural rigidity of the lithosphere, given by equation [4.50]

The tectonic subsidence can then be calculated:

$$Y_t = S\left[1 - C_f\left(1 - \frac{\rho_m - \overline{\rho_s}}{\rho_m - \rho_w}\right)\right] \qquad \text{[D6.14]}$$

This method does not compensate for palaeobathymetry and palaeoeustacy. The flexural rigidity and flexural wavelength used within this research to model the response of the lithosphere have been calculated using an estimated elastic thickness, *Te* (section 5..2 provides a more detailed explanation of *Te*).

Both the Airy and the flexural approach to isostatic compensation for sedimentary loading have been considered within this research.

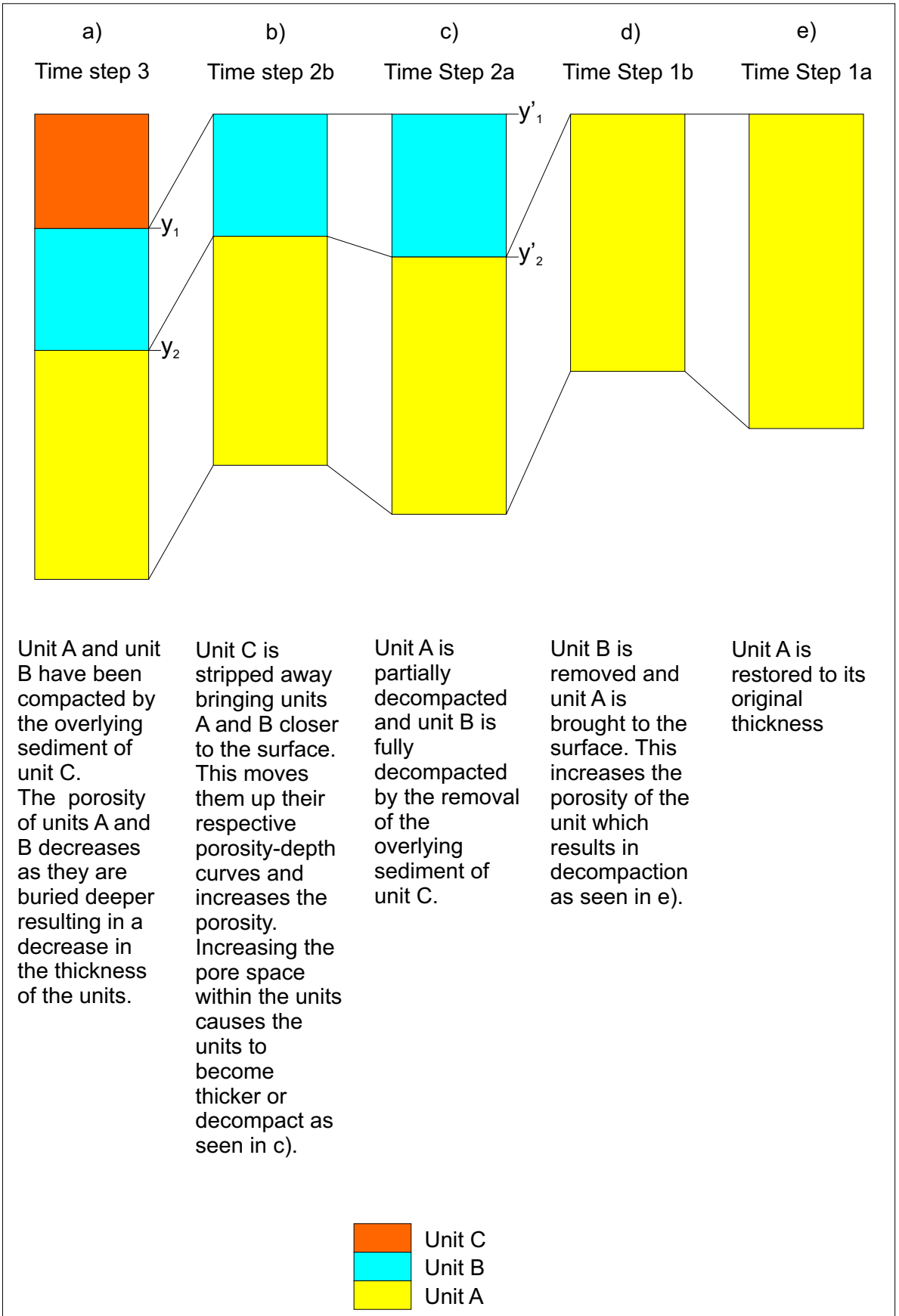


Figure D6.1. The stratigraphical effect of the decompaction algorithm. a) Time step 3, unit C has been deposited and has compacted units A and B. b) Time step 2, unit C has been removed and unit B is now at the surface. c) Time step 2b, unit B is fully decompacted and unit A is partially decompacted. d) Time step 1a, overlying sediment has been removed, the unit is now at the surface. e) Time step 1b, this is the first unit as it was before compaction.

Figure D6.2. The stratigraphical effect of the decompaction algorithm with an igneous intrusion. a) Time step 4, units A and B contain igneous intrusions. b) Time step 3b. The igneous intrusions have been removed moving units Bii and Ai and Aii closer to the surface. C) Time step 3a, units A and B have been partially decompacted. d) Time step 2, unit C has been removed and unit B is now at the surface. e) Time step 2b, unit B is fully decompacted and unit A is partially decompacted. f) Time step 1a, overlying sediment has been removed, the unit is now at the surface. g) Time step 1b, this is the first unit as it was before compaction.

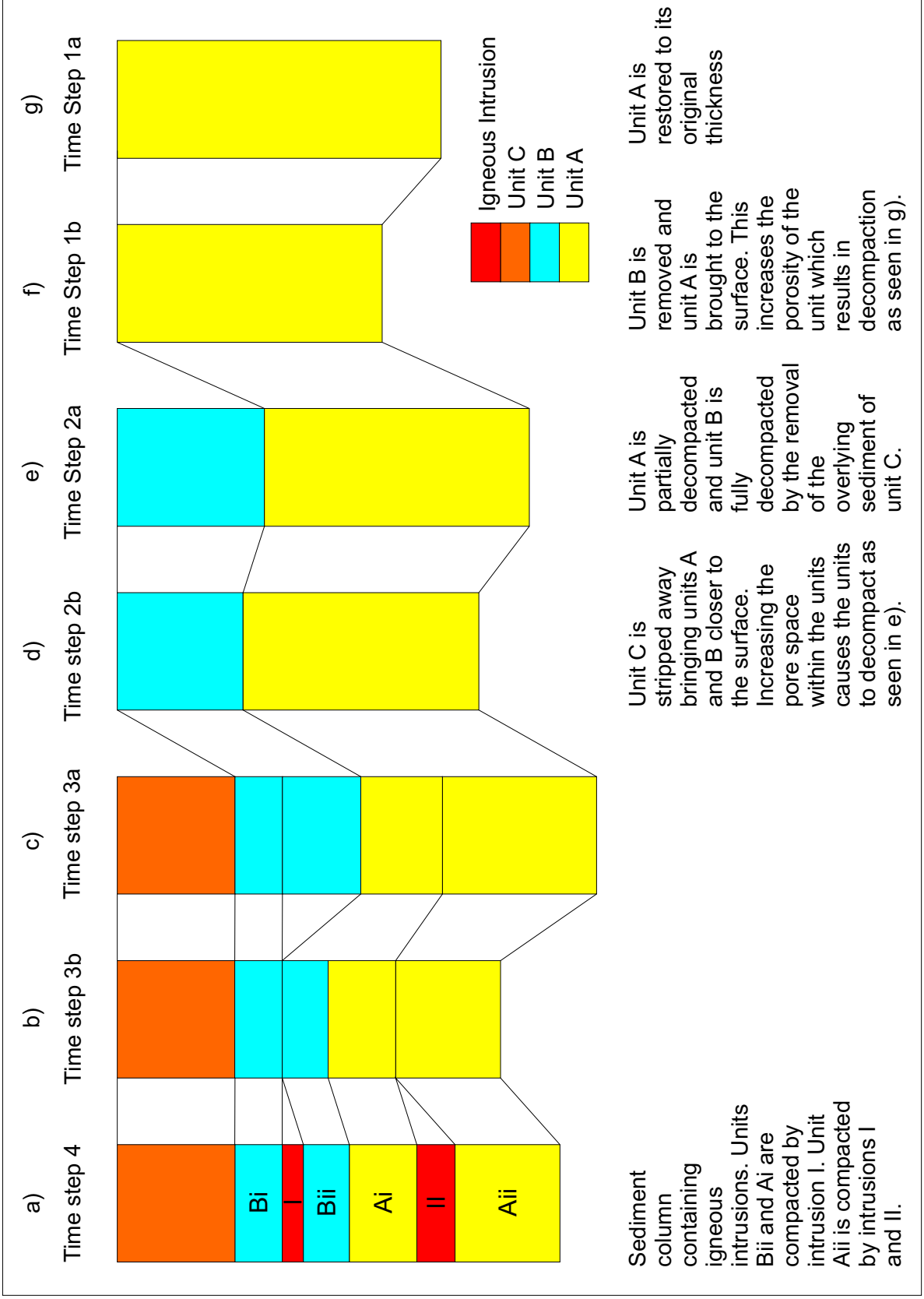

| | A | B | C | D | E | F | G | H |
|---|---|---|---|---|---|---|---|---|

**Time step Present**

| | Porosity | Solidity | Thickness Pore | Thickness Solid | Unit Thickness | Burial Depth |
|---|---|---|---|---|---|---|
| Erosion | 49 | 51 | 490 | 510 | 1000 | 0 |
| UCM | 37.40559522 | 62.59440478 | 28.42825237 | 47.57174763 | 76 | 1000 |
| MCM | 36.64585401 | 63.35414599 | 68.16128846 | 117.8387115 | 186 | 1076 |
| LCM | 34.85094657 | 65.14905343 | 64.47425116 | 120.5257488 | 185 | 1262 |
| Stainmore | 33.15290345 | 66.84709655 | 142.8890139 | 288.1109861 | 431 | 1447 |
| Alston | 29.51091805 | 70.48908195 | 151.0959004 | 360.9040996 | 512 | 1878 |
| Tyne | 25.70075318 | 74.29924682 | 104.3450579 | 301.6549421 | 406 | 2390 |
| Basement | | | | | | 2796 |

| | Depth | Porosity |
|---|---|---|
| Surface | 0 | 0.49 |
| UCM | 1 | 0.374056 |
| MCM | 1.076 | 0.366459 |
| LCM | 1.262 | 0.348509 |
| Stainmore | 1.447 | 0.331529 |
| Alston | 1.878 | 0.295109 |
| Tyne | 2.39 | 0.257008 |

**Time step 199Ma**

| | Porosity | Solidity | Thickness Pore | Thickness Solid | Unit Thickness | Burial Depth |
|---|---|---|---|---|---|---|
| Erosion | 49 | 51 | 490 | 510 | 1000 | 0 |
| UCM | 37.40559522 | 62.59440478 | 28.42825237 | 47.57174763 | 76 | 1000 |
| MCM | 36.64585401 | 63.35414599 | 68.16128846 | 117.8387115 | 186 | 1076 |
| LCM | 34.85094657 | 65.14905343 | 64.47425116 | 120.5257488 | 185 | 1262 |
| Stainmore | 33.15290345 | 66.84709655 | 142.8890139 | 288.1109861 | 431 | 1447 |
| Alston | 29.51091805 | 70.48908195 | 151.0959004 | 360.9040996 | 512 | 1878 |
| Tyne | 25.70075318 | 74.29924682 | 104.3450579 | 301.6549421 | 406 | 2390 |
| Basement | | | | | | 2796 |

| | | |
|---|---|---|
| Surface | 0 | 0.49 |
| UCM | 1 | 0.374056 |
| MCM | 1.076 | 0.366459 |
| LCM | 1.262 | 0.348509 |
| Stainmore | 1.447 | 0.331529 |
| Alston | 1.878 | 0.295109 |
| Tyne | 2.39 | 0.257008 |

**Time step 306Ma**

| | Porosity | Solidity | Thickness Pore | Thickness Solid | Unit Thickness | Burial Depth |
|---|---|---|---|---|---|---|
| UCM | 49 | 51 | 45.7061889 | 47.57174763 | 93.27793653 | 0 |
| MCM | 47.78134327 | 52.21865673 | 107.8252923 | 117.8387115 | 225.6640039 | 93.27793653 |
| LCM | 44.95697738 | 55.04302262 | 98.44069432 | 120.5257488 | 218.9664432 | 318.9419404 |
| Stainmore | 42.37612163 | 57.62387837 | 211.8744267 | 288.1109861 | 499.9854128 | 537.9083836 |
| Alston | 37.02483757 | 62.97516243 | 212.1854895 | 360.9040996 | 573.0895891 | 1037.893796 |
| Tyne | 31.71706246 | 68.28293754 | 140.1171213 | 301.6549421 | 441.7720634 | 1610.983385 |
| Basement | | | | | | 2052.755449 |

| | | |
|---|---|---|
| UCM | 0 | 0.49 |
| MCM | 0.093278 | 0.477813 |
| LCM | 0.318942 | 0.44957 |
| Stainmore | 0.537908 | 0.423761 |
| Alston | 1.037894 | 0.370248 |
| Tyne | 1.610983 | 0.317171 |

**Time step 311Ma**

| | Porosity | Solidity | Thickness Pore | Thickness Solid | Unit Thickness | Burial Depth |
|---|---|---|---|---|---|---|
| MCM | 49 | 51 | 113.2175856 | 117.8387115 | 231.0562971 | 0 |
| LCM | 46.03652476 | 53.96347524 | 102.8211507 | 120.5257488 | 223.3468996 | 231.0562971 |
| Stainmore | 43.34240279 | 56.65759721 | 220.4015529 | 288.1109861 | 508.512539 | 454.4031967 |
| Alston | 37.78200947 | 62.21799053 | 219.159796 | 360.9040996 | 580.0638956 | 962.9157357 |
| Tyne | 32.30479908 | 67.69520092 | 143.9526313 | 301.6549421 | 445.6075734 | 1542.979631 |
| Basement | | | | | | 1988.587205 |

| | | |
|---|---|---|
| MCM | 0 | 0.49 |
| LCM | 0.231056 | 0.460365 |
| Stainmore | 0.454403 | 0.433424 |
| Alston | 0.962916 | 0.37782 |
| Tyne | 1.54298 | 0.323048 |

**Time step 313Ma**

| | Porosity | Solidity | Thickness Pore | Thickness Solid | Unit Thickness | Burial Depth |
|---|---|---|---|---|---|---|
| LCM | 49 | 51 | 115.7992489 | 120.5257488 | 236.3249977 | 0 |
| Stainmore | 45.9710821 | 54.0289179 | 245.142311 | 288.1109861 | 533.2532971 | 236.3249977 |
| Alston | 39.80665696 | 60.19334304 | 238.6706729 | 360.9040996 | 599.5747725 | 769.5782948 |
| Tyne | 33.85710825 | 66.14289175 | 154.4106065 | 301.6549421 | 456.0655486 | 1369.153067 |
| Basement | | | | | | 1825.218616 |

| | | |
|---|---|---|
| LCM | 0 | 0.49 |
| Stainmore | 0.236325 | 0.459711 |
| Alston | 0.769578 | 0.398067 |
| Tyne | 1.369153 | 0.338571 |

**Time step 314Ma**

| | Porosity | Solidity | Thickness Pore | Thickness Solid | Unit Thickness | Burial Depth |
|---|---|---|---|---|---|---|
| Stainmore | 49 | 51 | 276.8125161 | 288.1109861 | 564.9235022 | 0 |
| Alston | 42.06815127 | 57.93184873 | 262.0763637 | 360.9040996 | 622.9804633 | 564.9235022 |
| Tyne | 35.55519321 | 64.44480679 | 166.427681 | 301.6549421 | 468.0826231 | 1187.903965 |
| Basement | | | | | | 1655.986589 |

| | | |
|---|---|---|
| Stainmore | 0 | 0.49 |
| Alston | 0.564924 | 0.420682 |
| Tyne | 1.187904 | 0.355552 |

**Time step 326Ma**

| | Porosity | Solidity | Thickness Pore | Thickness Solid | Unit Thickness | Burial Depth |
|---|---|---|---|---|---|---|
| Alston | 49 | 51 | 346.7509977 | 360.9040996 | 707.6550973 | 0 |
| Tyne | 40.47778973 | 59.52221027 | 205.1389768 | 301.6549421 | 506.7939189 | 707.6550973 |
| Basement | | | | | | 1214.449016 |

| | | |
|---|---|---|
| Alston | 0 | 0.49 |
| Tyne | 0.707655 | 0.404778 |

**Time step 333Ma**

| | Porosity | Solidity | Thickness Pore | Thickness Solid | Unit Thickness | Burial Depth |
|---|---|---|---|---|---|---|
| Tyne | 49 | 51 | 289.8253365 | 301.6549421 | 591.4802786 | 0 |
| Basement | | | | | | 591.4802786 |

| | | |
|---|---|---|
| Tyne | 0 | 0.49 |

A = G x 100

B = 100 - A

C = E x (A /100)

D = E (for present day taken from borehole) x (B /100) Thickness Solid does not change

E (other than present day) = C + D

Eqn. [D6.1]

F = (F-1 i.e. Cumulative thickness) + E

Porosity at depth $\Phi_y$ (H) is calculated from equation [4.53]

$\Phi_y = \Phi_s e^{-cy}$

Surface porosity $\Phi_s$ = 0.49

Compaction co-efficient c = 0.27

Burial depth y (G)

Figure D6.3. The calculations for the burial history modelling of the Harton borehole. The data for the present day thickness of the units is taken from the borehole data and used to calculate the thickness of the solid particles in each unit.

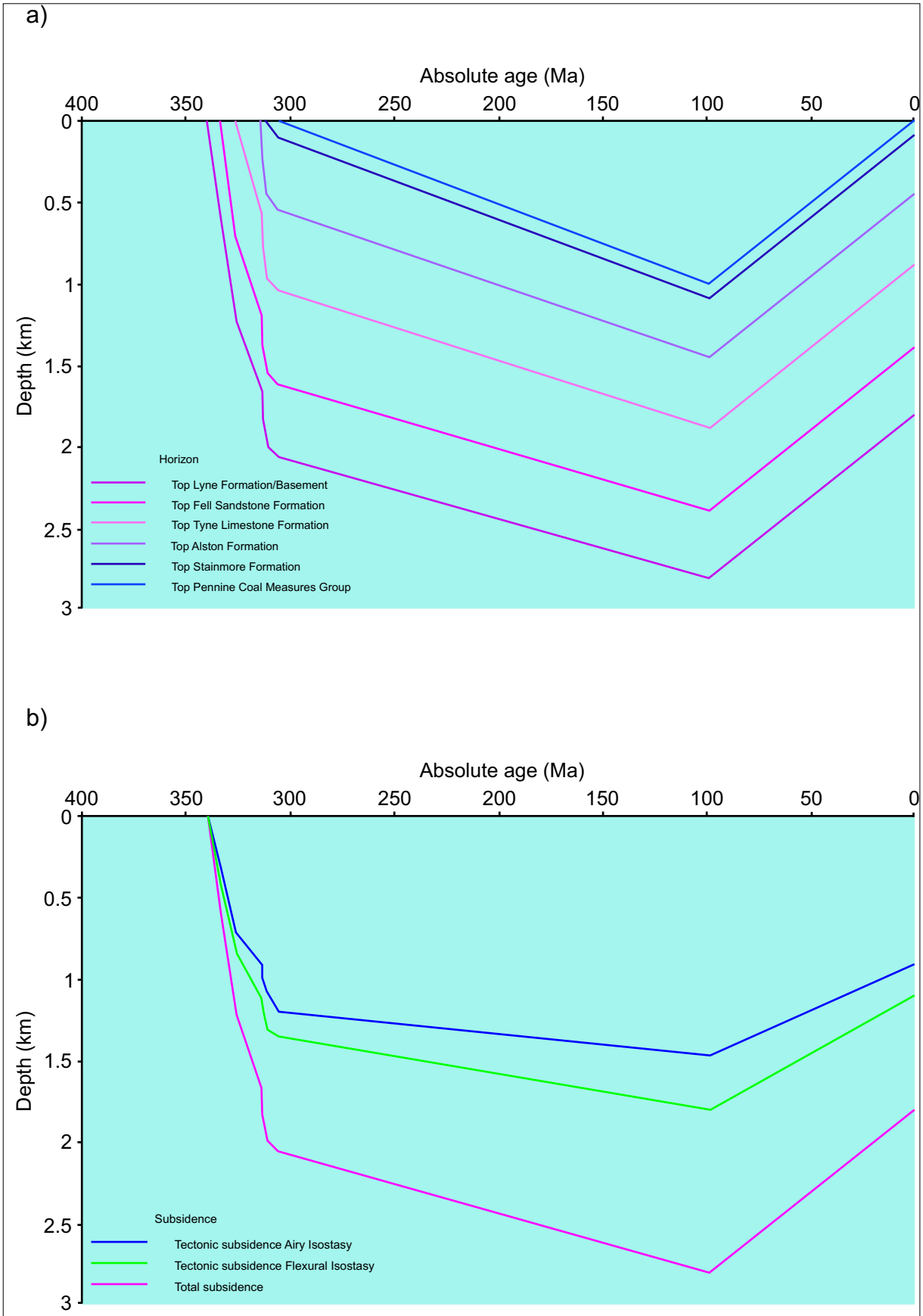


Figure D6.4. The burial history for the Harton borehole dataset with 1 km erosion. a) Decompacted subsidence history for each unit. b) Tectonic subsidence corrected for sediment loading, palaeobathymetry and palaeoeustacy and the total subsidence of the basement.

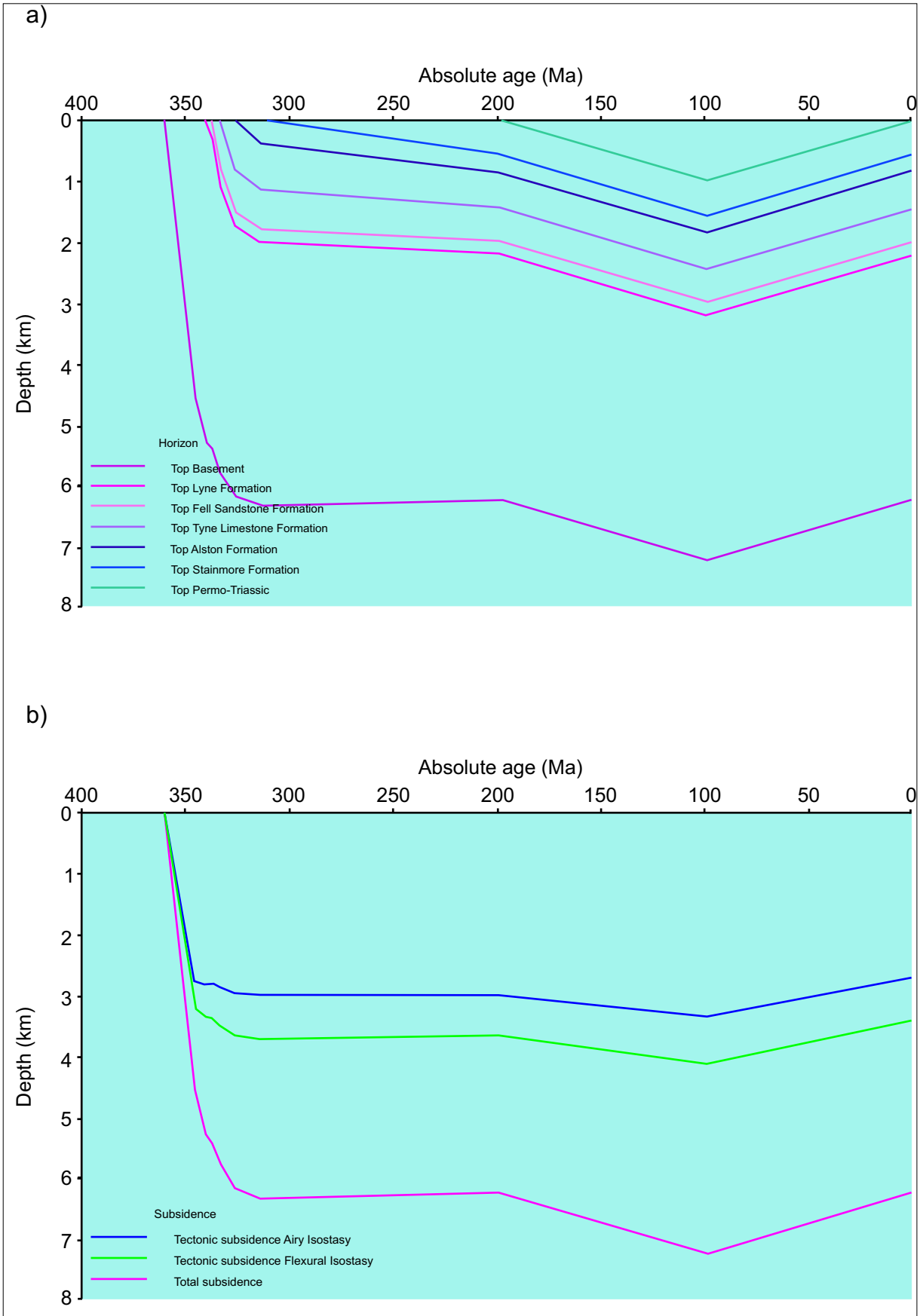


Figure D6.5. The burial history for cross-section B-B' at horizontal position x = 22 km with 1 km erosion. This burial history curve is located within the Solway Basin, in the hanging wall of the Maryport Fault. a) the decompacted subsidence history for each unit. b) the tectonic subsidence corrected for sediment loading using a flexural isostasy approach and an Airy isostasy approach also corrected for palaeobathymetry and palaeoeustacy.

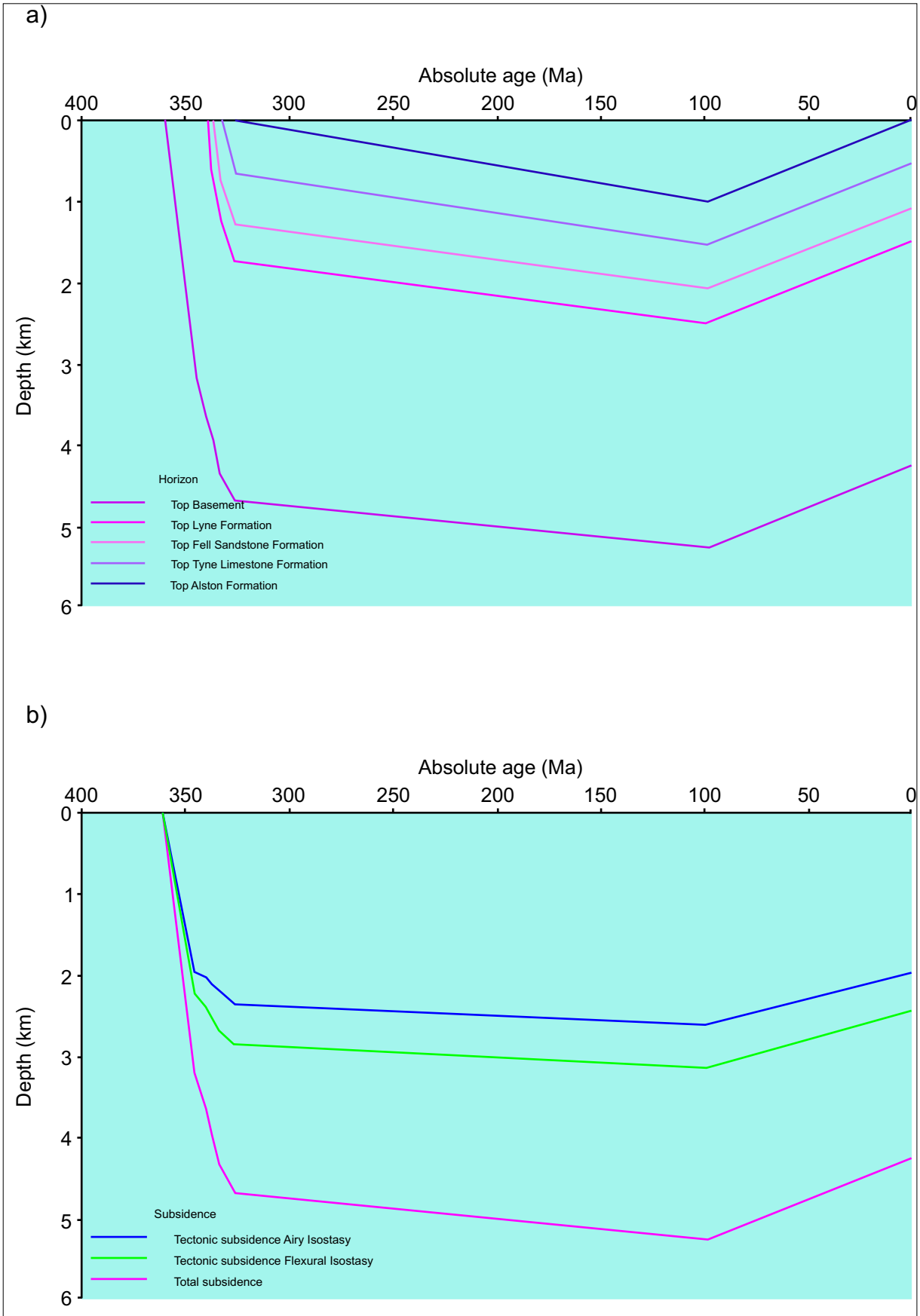


Figure D6.6. The burial history for cross-section G-G' at horizontal position x = 42 km with 1 km erosion. This burial history profile is located within the Northumberland Trough, in the hanging wall of the Stublick Fault. a) the decompacted subsidence history for each unit. b) the tectonic subsidence corrected for sediment loading using a flexural isostasy approach and an Airy isostasy approach also corrected for palaeobathymetry and palaeoeustacy.

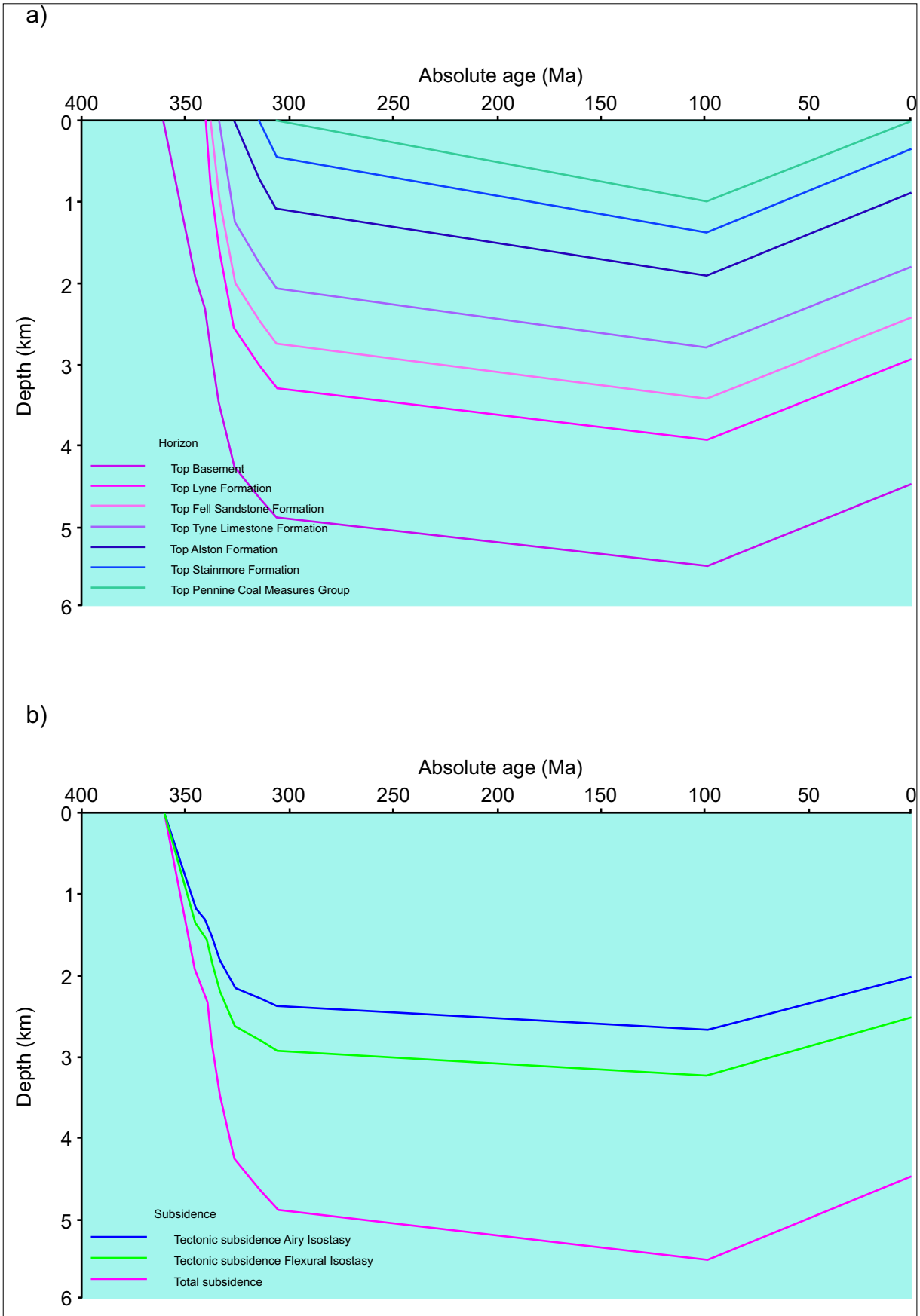


Figure D6.7. The burial history for cross-section I-I' at horizontal position x = 42 km with 1 km erosion. This burial history profile is located within the Northumberland Trough, in the hanging wall of the Ninety Fathom Fault. a) the decompacted subsidence history for each unit. b) the tectonic subsidence corrected for sediment loading using a flexural isostasy approach and an Airy isostasy approach also corrected for palaeobathymetry and palaeoeustacy.

Afonso, J.C. and Ranalli, G., 2004. Crustal and mantle strengths in continental lithosphere: is the jelly sandwich model obsolete? *Tectonophysics,* **394**, 3-4, 221-232.

Afonso, J.C., Ranalli, G. and Fernāndez, M., 2005. Thermal expansivity and elastic properties of the lithospheric mantle: results from mineral physics of composites. *Physics of the Earth and Planetary Interiors,* **149**, 3-4, 279-306.

Airy, G.B., 1855. On the computation of the effect of the attraction of mountain-masses, as disturbing the apparent astronomical latitude of stations in geodetic surveys. *Philosophical Transactions of the Royal Society of London,* **145** 101-104.

Allen, P.A. and Allen, J.R., 1990. Basin analysis principles and applications. Blackwell Scientific, Oxford.

Anderson, O.L., 1982. The Earth's core and the phase diagram of iron. *Philosophical Transactions of the Royal Society of London.Series A, Mathematical and Physical Sciences,* **306**, 1492, 21-35.

Artemjev, M.E. and Artyushkov, E.V., 1971. Structure and isostasy of the Baikal rift and the mechanism of rifting. *Journal of Geophysical Research,* **76**, 5, 1197-1211.

Artemjev, M.E., Kaban, M.K., Kucherinenko, V.A., Demyanov, G.V. and Taranov, V.A., 1994. Subcrustal density inhomogeneities of Northern Eurasia as derived from the gravity data and isostatic models of the lithosphere. *Tectonophysics,* **240**, 1-4, 249-280.

Bond, G.C. and Kominz, M.A., 1984. Construction of tectonic subsidence curves for the early Paleozoic miogeocline, southern Canadian Rocky Mountains: Implications for subsidence mechanisms, age of breakup, and crustal thinning. *Geological Society of America Bulletin,* **95**, 2, 155-173.

Bosworth, W., 1985. Discussion on the structural evolution of extensional basin margins. *Journal of the Geological Society,* **142**, 5, 939-942.

Bott, M.H.P., 1976. Formation of sedimentary basins of graben type by extension of the continental crust. *Tectonophysics,* **36**, 1-3, 77-86.

Bott, M.H.P., 1982. Interior of the earth: its structure, constitution and evolution. 2nd Edn. Edward Arnold, London

Braun, J. and Beaumont, C., 1989. A physical explanation of the relation between flank uplifts and the breakup unconformity at rifted continental margins. *Geology,* **17**, 8, 760-764.

Brewer, J.A. and Smythe, D.K., 1984. MOIST and the continuity of crustal reflector geometry along the Caledonian-Appalachian orogen. *Journal of Geological Society,* **141**, 1, 105-120.

Brown, J.M. and McQueen, R.G., 1986. Phase transitions, Grüneisen parameter, and elasticity for shocked iron between 77 GPa and 400 GPa. *Journal of Geophysical Research-Solid Earth,* **91**, 7, 7485-7494.

Brown, J.M. and Shankland, T.J., 1981. Thermodynamic parameters in the Earth as determined from seismic profiles. *Geophysical Journal of the Royal Astronomical Society,* **66**, 3, 579-596.

Busse, F.H., 1989. Fundamentals of thermal convection. In: W.R. Peltier (Ed) *Mantle convection: Plate tectonics and global dynamics.* Gordon and Breach, New York, 23-95.

Christensen, N.I. and Mooney, W.D., 1995. Seismic velocity structure and composition of the continental crust: A global view. *Journal of Geophysical Research-Solid Earth,* **100**, 6, 9761-9788.

Clarke, S.M., 2002. Faulting, fault zone processes and hydrocarbon flow through three-dimensional basin models. 2 vols. PhD Edn. Keele. University. Department of Earth Sciences and Geography.

da Silva, C.R.S., Wentzcovitch, R.M., Patel, A., Price, G.D. and Karato, S.I., 2000. The composition and geotherm of the lower mantle: constraints from the elasticity of silicate perovskite. *Physics of the Earth and Planetary Interiors,* **118**, 1-2, 103-109.

Dahlstrom, C.D.A., 1969. Balanced cross sections. *Canadian Journal of Earth Sciences,* **6**, 4, 743-757.

Darbyshire, F.A., White, R.S. and Priestley, K.F., 2000. Structure of the crust and uppermost mantle of Iceland from a combined seismic and gravity study. *Earth and Planetary Science Letters,* **181**, 3, 409-428.

Davies, G.F., 1999. Dynamic Earth: Plates, Plumes and Mantle Convection. Cambridge University Press, New York.

Doin, M.P. and Fleitout, L., 1996. Thermal evolution of the oceanic lithosphere: an alternative view. *Earth and Planetary Science Letters,* **142**, 1-2, 121-136.

Dula, W.F., 1991. Geometric models of listric normal faults and rollover folds. *Bulletin American Association of Petroleum Geologists,* **75**, 10, 1609-1625.

Egan, S.S., Kane, S., Buddin, T.S., Williams, G.D. and Hodgetts, D., 1999. Computer modelling and visualisation of the structural deformation caused by movement along geological faults. *Computers & Geosciences,* **25**, 3, 283-297.

Falvey, D.A. and Middleton, M.F., 1981. Passive continental margins: Evidence for a prebreakup deep crustal metamorphic subsidence mechanism. In: R. Blanchet and L. Montadert (Eds) *Proceedings of 26th International Geological Congress, Geology of Continental Margins Symposium, Paris, 7–17 July 1980.* Oceanologica Acta, 103-114.

Fjeldskaar, W., ter Voorde, M., Johansen, H., Christiansson, P., Faleide, J.I. and Cloetingh, S., 2004. Numerical simulation of rifting in the northern Viking Graben: the mutual effect of modelling parameters. *Tectonophysics,* **382**, 3-4, 189-212.

Fourier, J., 1878. The Analytical Theory of Heat. Cambridge University Press, London.

Geikie, A., 1882. Text-book of geology. Macmillan, London.

Gibbs, A.D., 1983. Balanced cross-section construction from seismic sections in areas of extensional tectonics. *Journal of Structural Geology,* **5**, 2, 153-160.

Gibbs, A.D., 1984. Structural evolution of extensional basin margins. *Journal of the Geological Society,* **141**, 4, 609-620.

Goguel, J., 1962. Tectonics. English translation of Traite de tectonique. Paris, 1952. Thalmann. H.E. Edn. W.H. Freeman, San Francisco.

Gueydan, F., Morency, C. and Brun, J.P., 2008. Continental rifting as a function of lithosphere mantle strength. *Tectonophysics,* **460**, 1-4, 83-93.

Heath, T.L., 1897. The works of Archimedes. Cambridge University Press, Cambridge.

Heiskanen, W., 1931. Isostatic tables for the reduction of gravimetric observations calculated on the basis of Airy's hypothesis. *Bulletin Géodésique,* **30**, 1, 110-153.

Holliday, D.W., 1999. Palaeotemperatures, thermal modelling and depth of burial studies in northern and eastern England. *Proceedings of the Yorkshire Geological Society,* **52**, 4, 337-352.

Jackson, J., 2002. Strength of the continental lithosphere: time to abandon the jelly sandwich? *GSA today,* **12**, 9, 4-9.

Kearey, P., Klepeis, K.A. and Vine, F., 2009. Global tectonics. Blackwell Pub.

Kern, H. and Schenk, V., 1988. A model of velocity structure beneath Calabria, southern Italy, based on laboratory data. *Earth and Planetary Science Letters,* **87**, 3, 325-337.

Kimbell, G.S., Carruthers, R.M., Walker, A.S.D. and Williamson, J.P., 2006. Regional geophysics of Southern Scotland and Northern England. British Geological Survey [Version 1.0 on CD-ROM], Keyworth, Nottingham.

Kohlstedt, D.L., Evans, B. and Mackwell, S.J., 1995. Strength of the lithosphere: Constraints imposed by laboratory experiments. *Journal of Geophysical Research-Solid Earth,* **100**, 9, 17587-17602.

Kooi, H. and Cloetingh, S., 1992. Lithospheric necking and regional isostasy at extensional basins 2. Stress-induced vertical motions and relative sea level changes. *Journal of Geophysical Research-Solid Earth,* **97**, 12, 17573-17591.

Kusznir, N.J., 1991. The distribution of stress with depth in the lithosphere: thermo-rheological and geodynamic constraints. *Royal Society of London Philosophical Transactions Series A,* **337** 95-107.

Kusznir, N.J. and Park, G., 1987. The extensional strength of the continental lithosphere: its dependence on geothermal gradient, crustal composition and thickness. In: M.P. Coward, J.F. Dewey and P.L. Hancock (Eds) *Continental Extensional Tectonics.* Geological Society of London Special Publication No.28, 35-52.

Kusznir, N.J. and Park, R.G., 1982. Intraplate lithosphere strength and heat flow. *Nature,* **299** 540-542.

Kusznir, N.J. and Park, R.G., 1984. Intraplate lithosphere deformation and the strength of the lithosphere. *Geophysical Journal of the Royal Astronomical Society,* **79**, 2, 513-538.

Kusznir, N.J. and Park, R.G., 1986. Continental lithosphere strength: the critical role of lower crustal deformation. In: J.B. Dawson, D.A. Carswell, J. Hall and K.H. Wedepohl (Eds) *The Nature of the Lower Continental Crust.* Geological Society of London Special Publication No. 24, London, 79-93.

Lee, M.K., 1989. *Upper crustal structure of the Lake District from modelling and image processing of potential field data.* Keyworth, Nottingham: British Geological Survey, Technical Report WK/89/1.

Lerche, I., 1990. Basin analysis: Quantitative Methods. Academic Press, San Diego.

Lowrie, W., 1997. Fundamentals of geophysics. Cambridge University Press, Cambridge.

Lyustkikh, E.N., 1960. Isostasy and isostatic hypotheses. English Translation. American Geophysical Union, New York.

Maggi, A., Jackson, J.A., McKenzie, D. and Priestley, K., 2000. Earthquake focal depths, effective elastic thickness, and the strength of the continental lithosphere. *Geology,* **28**, 6, 495-498.

McKenzie, D., 1978. Some remarks on the development of sedimentary basins. *Earth and Planetary Science Letters,* **40**, 1, 25-32.

McKenzie, D. and Jackson, J., 2002. Conditions for flow in the continental crust. *Tectonics,* **21**, 6, 1055-1062.

McKenzie, D., Jackson, J. and Priestley, K., 2005. Thermal structure of oceanic and continental lithosphere. *Earth and Planetary Science Letters,* **233**, 3-4, 337-349.

McLennan, S.M. and Taylor, S.R., 1996. Heat flow and the chemical composition of continental crust. *The Journal of geology,* **104**, 4, 369-377.

Menzies, M.A., 1990. Petrology and Geochemistry of the Continental Mantle: An historical Perspective. In: M.A. Menzies (Ed) *Continental Mantle.* 31-54.

Morgan, P., 1984. The thermal structure and thermal evolution of the continental lithosphere. *Physics and Chemistry of the Earth,* **15** 107-193.

Nyblade, A.A. and Pollack, H.N., 1993. A comparative study of parameterized and full thermal-convection models in the interpretation of heat flow from cratons and mobile belts. *Geophysical Journal International,* **113**, 3, 747-751.

Özişik, M.N., 1980. Heat conduction. Wiley, Chichester.

Parsons, B. and McKenzie, D., 1978. Mantle convection and the thermal structure of the plates. *Journal of Geophysical Research-Solid Earth,* **83**, 9, 4485-4496.

Parsons, B. and Sclater, J.G., 1977. An analysis of the variation of ocean floor bathymetry and heat flow with age. *Journal of Geophysical Research,* **82**, 5, 803-827.

Poirier, J.P., 1986. Dislocation-mediated melting of iron and the temperature of the Earth's core. *Geophysical Journal of the Royal Astronomical Society,* **85**, 2, 315-328.

Poirier, J.P., 1991. Introduction to the Physics of the Earth's Interior. 1st Edn. Cambridge University Press, New York.

Pollack, H.N. and Chapman, D.S., 1977. On the regional variation of heat flow, geotherms, and lithospheric thickness. *Tectonophysics,* **38**, 3-4, 279-296.

Poudjom Djomani, Y.H., O'Reilly, S.Y., Griffin, W.L. and Morgan, P., 2001. The density structure of subcontinental lithosphere through time. *Earth and Planetary Science Letters,* **184**, 3-4, 605-621.

Priestley, K. and McKenzie, D., 2006. The thermal structure of the lithosphere from shear wave velocities. *Earth and Planetary Science Letters,* **244**, 1-2, 285-301.

Rao, R.U.M. and Jessop, A.M., 1975. A comparison of the thermal characters of shields. *Canadian Journal of Earth Sciences,* **12**, 3, 347-360.

Richardson, S.W. and Oxburgh, E.R., 1978. Heat flow, radiogenic heat production and crustal temperatures in England and Wales. *Journal of Geological Society,* **135**, 3, 323-337.

Ringwood, A., 1975. Composition and petrology of the earth's upper mantle. McGraw-Hill, London.

Röhm, A.H.E., Snieder, R., Goes, S. and Trampert, J., 2000. Thermal structure of continental upper mantle inferred from S-wave velocity and surface heat flow. *Earth and Planetary Science Letters,* **181**, 3, 395-407.

Rudnick, R.L. and Fountain, D.M., 1995. Nature and composition of the continental crust: a lower crustal perspective. *Reviews of Geophysics,* **33**, 3, 267-309.

Rudnick, R.L., McDonough, W.F. and O'Connell, R.J., 1998. Thermal structure, thickness and composition of continental lithosphere. *Chemical Geology,* **145**, 3-4, 395-411.

Sass, J.H., Lachenbruch, A.H. and Munroe, R.J., 1971. Thermal conductivity of rocks from measurements on fragments and its application to heat-flow determinations. *Journal of geophysical research,* **76**, 14, 3391-3401.

Sclater, J.G. and Christie, P.A.F., 1980. Continental stretching: an explanation of the post-mid-Cretaceous subsidence of the central North Sea basin. *Journal of Geophysical Research-Solid Earth,* **85**, 7, 3711-3739.

Sclater, J.G., Jaupart, C. and Galson, D., 1980. The heat flow through oceanic and continental crust and the heat loss of the Earth. *Reviews of Geophysics and Space Physics,* **18**, 1, 269-311.

Shaw, D.M., Cramer, J.J., Higgins, M.D. and Truscott, M.G., 1986. Composition of the Canadian Precambrian shield and the continental crust of the earth. In: J.B. Dawson, D.A. Carswell, J. Hall and K.H. Wedepohl (Eds) *The Nature of the Lower Continental Crust.* Geological Society of London Special Publication No. 24, London, 275-282.

Shaw, D.M., Dostal, J. and Keays, R.R., 1976. Additional estimates of continental surface Precambrian shield composition in Canada. *Geochimica et Cosmochimica Acta,* 73-84.

Simon, N.S.C. and Podladchikov, Y.Y., 2008. The effect of mantle composition on density in the extending lithosphere. *Earth and Planetary Science Letters,* **272**, 1-2, 148-157.

Springer, J., 1993. Decompaction and backstripping with regard to erosion, salt movement, and interlayered bedding. *Computers & Geosciences,* **19**, 8, 1115-1125.

Stacey, F.D., 1992. Physics of the Earth. 3rd Edn. Brookfield, New York.

Stacey, F.D., 1995. Theory of thermal and elastic properties of the lower mantle and core. *Physics of the Earth and Planetary Interiors,* **89**, 3-4, 219-245.

Steckler, M.S. and Watts, A.B., 1978. Subsidence of the Atlantic-type continental margin off New York. *Earth and Planetary Science Letters,* **41**, 1, 1-13.

Taylor, S.R. and McLennan, S.M., 1985. The continental crust: its composition and evolution. Blackwell Scientific, Oxford.

Ter Voorde, M. and Cloetingh, S., 1996. Numerical modelling of extension in faulted crust: effects of localized and regional deformation on basin stratigraphy. In: P.G. Buchanan and D. Nieuwland (Eds) *Modern developments in structural interpretation, validation and modelling.* Geological Society of London Special Publication No. 99, 283-296.

Turcotte, D.L. and Schubert, G., 2002. Geodynamics. Cambridge Univ Pr.

Ungerer, P., Burrus, J., Doligez, B., Chenet, P.Y. and Bessis, F., 1990. Basin evaluation by integrated two-dimensional modeling of heat transfer, fluid flow, hydrocarbon generation, and migration. *AAPG Bulletin,* **74**, 3, 309-335.

Verrall, P., 1981. Structural interpretation with applications to North Sea problems. Joint Association for Petroleum Exploration Courses (UK).

Watts, A.B., 2001. Isostasy and Flexure of the Lithosphere. Cambridge University Press, Cambridge.

Watts, A.B. and Burov, E.B., 2003. Lithospheric strength and its relationship to the elastic and seismogenic layer thickness. *Earth and Planetary Science Letters,* **213**, 1-2, 113-131.

Wedepohl, H., 1995. The composition of the continental crust. *Geochimica et Cosmochimica Acta,* **59**, 7, 1217-1232.

Weissel, J.K. and Karner, G.D., 1989. Flexural uplift of rift flanks due to mechanical unloading of the lithosphere during extension. *Journal of Geophysical Research-Solid Earth,* **94**, 10, 13919-13950.

Wheeler, J., 1987. Variable-heave models of deformation above listric normal faults: the importance of area conservation. *Journal of Structural Geology,* **9**, 8, 1047-1049.

White, N.J., Jackson, J.A. and McKenzie, D.P., 1986. The relationship between the geometry of normal faults and that of the sedimentary layers in their hanging walls. *Journal of Structural Geology,* **8**, 8, 897-909.

White, S., 1976. The effects of strain on the microstructures, fabrics, and deformation mechanisms in quartzites. *Philosophical Transactions of the Royal Society of London.Series A, Mathematical and Physical Sciences,* **283** 69-86.

Williams, G.D. and Vann, I., 1987. The geometry of listric normal faults and deformation in their hangingwalls. *Journal of Structural Geology,* **9**, 7, 789-795.

Yegorova, T.P., Kozlenko, V.G., Pavlenkova, N.I. and Starostenko, V.I., 1995. 3-D density model for the lithosphere of Europe: construction method and preliminary results. *Geophysical journal international,* **121**, 3, 873-892.

Yegorova, T.P. and Starostenko, V.I., 2002. Lithosphere structure of European sedimentary basins from regional three-dimensional gravity modelling. *Tectonophysics,* **346**, 1-2, 5-21.

Yegorova, T.P., Starostenko, V.I., Kozlenko, V.G. and Pavlenkova, N.I., 1997. *Geophysical Journal International,* **129**, 2, 355-367.